Conjugated Macrocycles in Organic Electronics

Melissa L. Ball

Submitted in partial fulfillment of the
requirements for the degree of
Doctor of Philosophy
in the Graduate School of Arts and Sciences

COLUMBIA UNIVERSITY

2019

ABSTRACT

Conjugated Macrocycles in Organic Electronics

Melissa L. Ball

The discipline of organic electronics encompasses the design and synthesis of molecules for use in organic field effect transistors, organic photovoltaics, organic photodetectors, single molecule electronics, sensors, and many more. The rationale for studying organic electronic materials is compelling: organics have the potential to be low cost, processable, and flexible complements to silicon technologies to combat some of the most pressing environmental issues.

Organic molecules that transport carriers are used as the active layer in many device applications. Molecules that possess energy levels that allow for electron or hole transport are typically π-conjugated materials. There has been swift progress on the design and synthesis of π-conjugated materials that possess a large density of high energy electrons such as acenes. Yet there has been less growth on materials with low energy vacant orbitals to accept an electron. Fullerenes are the ubiquitous acceptor materials used in organic electronics. Over the past few years, there have been several groups, including our own, that have synthesized non-fullerene materials for use in organic field effect transistors and solar cells. In particular, the Nuckolls laboratory has pioneered the design and synthesis of a class of molecules called contorted aromatics and studied these molecules in range of organic electronic applications. Conjugated macrocycles are one sub-class of the contorted aromatic family.

This Thesis describes a body of research on the design, synthesis, and application of a new class of electronic materials made from conjugated macrocycles. Each of the macrocycles comprises perylenediimide cores wound together with various electronic linkers. The perylenediimide building block endows each macrocycle with the ability to transport electrons,

while the synthetic flexibility to install different linkers allows us to create macrocycles with different electronic and physical properties.

We use these materials in organic photovoltaics, field effect transistors, sensors, and photodetectors. The macrocycles possess vivid colors, absorb in the visible range of the solar spectrum, and are an exemplary class of materials to study how rigidity and strain affect device performance. We find that the strained and rigid macrocyclic framework affords each macrocycle with the ability to absorb lower energy visible light with respect to acyclic counterparts and the macrocycles outperform in photovoltaic applications. Rigidity was an important concept in our organic photodetector study: we found rigidity was one of the reasons our macrocycles outperformed both fullerenes and acyclic controls. The macrocycles all possess intramolecular cavities, and our recent studies focused on using this nanospace for sensing applications. Each of the studies described in this Thesis will demonstrate how macrocyclization is a design technique to enhance organic electronic performance.

Table of Contents

List of Tables and Figures

ACKNOWLEDGEMENTS

I am indebted to all mentors, mentees, teachers, friends, and family who have supported, encouraged and inspired me throughout my life. In particular, I am beholden to those who provided me courage to pursue a doctorate despite possessing a non-traditional background. I have always been motivated by those around me, and academia has provided endless reasons to be motivated over the past five years.

I remain in disbelief that my advisor Colin Nuckolls took me - a pre-medical, economics students – into his group five years ago. That one decision has steered my life into a different direction, and I am not sure how to convey in words what this has meant to me. His unconditional support of me as a scientist has made me who I am today; he was never too busy to discuss science and macrocycles together. I am proud of what we accomplished, and its fulfilling to see other students admitted from non-traditional backgrounds over the past five years. I had the unique experience of being an undergraduate in CHEM 3444 with Colin, and this is where my passion for organic chemistry was developed, in a large part thanks to him.

Mike Steigerwald served as a friend, colleague, and, especially, mentor over the past five years. I am appreciative for all the hours together discussing science; his office served as one of the best classrooms I have experienced. Yet I am most grateful for his support and friendship. He supported me through some difficult times in graduate school, not least, with the death of my father, and provided a space where I could just be.

I am indebted to my Committee members. I know I am a better scientist for their mentorship and encouragement. Tristan Lambert was one of the first people to give me courage to change my career and pursue a doctorate. I am indebted to him for his continued support. Tomislav Rovis is an academic mentor. I am grateful for all of our conversations, his support, and candor.

Both their examples excite me for a career in academia. I am thankful to Xavier Roy for his support and his guidance on my future over the past five years.

Latha Venkataraman has served as a role model throughout graduate school. I am grateful for our frank and open conversations; her encouragement helped me decide to pursue a post-doctoral position. Fay Ng was my first mentor in lab. She taught me how to be a rigorous scientist in the laboratory and shaped how I approach lab work. We started the conjugated macrocycles project, and I have her to thank for an amazing five years of learning. I am thankful to David Reichman and Laura Kaufman for their openness to listen to the students and their desire to improve our community as the Chair and Director of Graduate Studies. I am grateful to Ruben Gonzalez for his support of my candidacy as DGS. Willem Buiter was my first academic mentor at the London School of Economics. His support and friendship have taught me how special this mentor-mentee bond can be.

I am also indebted to David Reichman for his support of Women in Chemistry. Co-founding this group with Anastasia Voevodin is one of the things I am most proud of during my time at Columbia University. The Chemistry Department's support was invaluable. I am grateful to all the female students, post-docs, and professors who attended our events: this group would be nothing without each of you.

I have been fortunate to collaborate with wonderful scientist and friends. Brandon Fowler and Yu Zhong served as mentors and friends both in my early days and now. Boyuan Zhang has been my better half in lab for five years. I am fortunate to have been in the same year as her, as her support and friendship have been invaluable. Brandon, Yu, Boyuan and I were the first students and post-docs to develop and work on the macrocycle project. I am proud to be part of this team.

I am indebted to Cary Ritter, Ayden Schattman, and Pan Pan Li. Mentoring these three women was one of most joyful experiences of graduate school. I am thankful to all my students as a teaching assistant. I loved being in the classroom because of them.

Thank you to my graduating class and accepting me as one of you despite having pursued a different path to get here. In particular, I am thankful to Anastasia Voevodin and Evan Doud for their friendship. Some of my best memories in graduate school are with you both. I am thankful for both Makeda Tekle-Smith and Prakriti Joshi for their support and excitement for academia; they both are inspiring peers and I am proud to be their friend. I can't imagine graduate school without the friendship of Anouck Champsaur. Tim Su, Nate Schuster, Dan Paley, Raul Hernandez Sanchez, and Michael Inkpen served as mentors and friends; I am grateful for their support. I am thankful for Ilana Berenson Stone ("Mini"). She was another student that followed the path from post-bac to Ph.D. Watching her grow as a scientist has been fulfilling. Natalia Gadjieva has been by my side for five years. I am indebted to her for her friendship. I am thankful to all past and present lab members; it has been a wonderful environment to pursue science. I am thankful for Ryan Hastie's advice and friendship through the years, but mostly for all the laughs together. Thank you to all those that keep the department running, especially Alison Doyle for keeping me organized. I am thankful for the Guthikonda family for their financial support in my fifth year. Thank you to Brandon Fowler and Nate Schuster too for their helpful edits in Chapter 1.

I am thankful for all my friendships. My group of friends have been my biggest supporters. There are too many to name, but I could not have done this without their love. I am particularly thankful for the love and support over the past decade from both Paul and Jo Parsonson.

I owe everything to my mother and father, Alicia and Mitchell. Neither of them completed high school, yet instilled a work ethic and love of education into me and my twin sister. My mother

sacrificed her entire life so I would have one. When I was seven, she told me I could be whatever I put my mind to, and I believed her. My father was in disbelief when I told him I was pursuing a Ph.D. at Columbia University, and I am grateful I was able to share my experiences with him before he passed away in my third year. I know he is proud today. I am who I am today because of these two individuals. I am not sure either parent knew they would raise two doctors.

My twin sister Melinda is my best friend and biggest supporter. She has been my partner throughout my life. We have conquered many obstacles and accomplished many feats together, and without one another's support, I have no doubt our lives would be fundamentally different. Nothing in life seems too difficult when you have Melinda next to you.

Last, none of this would be possible without my loving husband Mark Parsonson. His unconditional love and support fuel me daily. This year we celebrated my ten year remission anniversary from cancer. Experiencing an illness at a young age impacted us; we wanted our lives to mean more. I will never forget where we were in Notting Hill when we decided to quit our finance jobs, and apply to Columbia University together. I am more fulfilled now than ever, and am indebted to him for pushing me forward, then and now, and picking me up when needed. Life is the best adventure with him. I love you.

For my mother and father:

Future generations and I are forever indebted to you.

Chapter 1: Introduction

Chapter 1 Section 1A. Contorted Aromatics as Electronic Materials

1A.1. Preface

Chapter 1A is inspired by conversations with both Prof. Colin Nuckolls and Dr. Michael L. Steigerwald and a recent published Accounts article titled "Conjugated Macrocycles in Organic Electronics" by Melissa L. Ball, Boyuan Zhang, Yu Zhong, Brandon Fowler, Shengxiong Xiao, Fay Ng, Michael L. Steigerwald, and Colin Nuckolls, published in the Accounts of Chemical Research (2019).[1]

1A.2. Introduction

The discipline of organic electronics encompasses the design and synthesis of molecules for use in organic field effect transistors (OFETs), organic photovoltaics (OPVs), organic photodetectors (OPDs), single molecule electronics (SME), sensors, and many more. The rationale for synthesizing organic electronic materials is compelling: organics have the potential to be low cost, processable, and flexible complements to silicon technologies to combat some of the most pressing environmental issues and be used in logic-based systems and memory storage. A bottom-up approach to synthesis is beneficial as it allows one to understand the electronic and physical structure of a molecule and provides a better chance of rationalizing device properties. One can also tune both the energetics and structural properties of the molecule and this can result in different physical properties. A bottom-up approach also provides an opportunity to study device physics on a fundamental level, as chemists can make nuanced changes to a molecular backbone and see how the device properties change.

This Thesis describes our efforts to design and study a new class of conjugated macrocycles materials that incorporate perylenediimide (PDI).[1–6] Our conjugated macrocycles are enveloped within a broader class of contorted aromatics that include discs and ribbons from the Nuckolls

labortory.[7,8] The macrocycles absorb low energy visible light, and function as electron-accepting materials for device applications. Before I provide a general overview of the conjugated macrocycles in Chapter 1B, I provide a brief background on OFETs and the importance of π-conjugated materials for electronic applications.

1A.3. Output and Transport Curves: What Do They Tell Us?

A necessary condition for a molecule to be considered for use in (opto)electronic applications is whether the molecule can carry current.[9–14] One device to test carrier mobility is an OFET. An idealized transistor can function as a binary logic gate, operating in either an "on" state, where there is current, or in an "off" state in the absence of current. Figure 1A.1 shows a schematic of a bottom-contact OFET. For the data presented in this Thesis, we used a three-probe setup to bias the device: a source electrode (V_s), a drain electrode (V_d), and a gate electrode (V_g). Current flows through a conduction channel comprised of the semiconducting material.

The semiconducting material in the channel ("Semiconducting layer" in Figure 1A.1) can be either a p-type molecule (a molecule that transports holes, or the absence of an electron) or n-type molecule (a molecule that transports electrons) or both (ambipolar). The semiconducting material lies within a channel between a source and drain electrode (gold in Figure 1A.1). In the case of electron transport, we empirically know that a positive electrical potential is applied to the gate electrode (silicon), and electrons, which are attracted to the positive gate bias, collect to form a conduction pathway between the source and drain electrodes to form a current. A negative gate potential is required to transport holes for p-type materials for the analogous electrostatic reasons.

Two types of curves are often presented for OFETs: the output curve and the transfer curve. Figure 1A.1 shows representative data for both an output and transfer curve. The output curve

shows the amount of current produced by sweeping the source-drain bias at a constant gate potential and is used to assess where the saturation point is in the device.

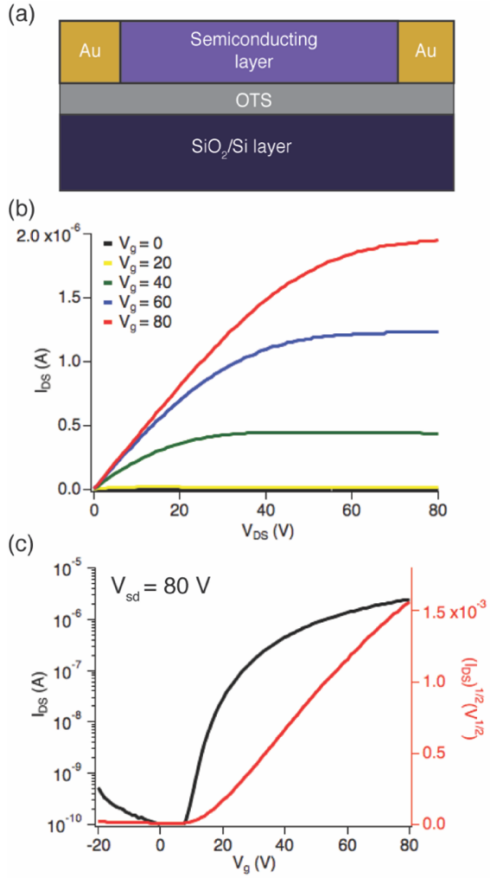

Figure 1A.1. (a) A schematic of an OFET device. The semiconducting layer comprises a conjugated molecule with p-type characteristics, n-type characteristics, or both; (b) a representative output curve showing the current between the source and drain electrodes as a function of a gate bias; we show the device is saturated at a gate bias of 80 V and transports electrons; and (c) a representative transfer curve that shows the current generated between the source and drain electrodes as a function of sweeping the gate.

In the example presented in Figure 1A.1b, a gate potential ranging from 0 V – 80 V is applied, and one can observe the device transports electrons and saturates (or plateaus) at 80 V. We use the saturation current to produce a transfer curve by sweeping the gate potential. Figure 1A.1c shows a device with a constant source-drain bias of 80 V. One sweeps the gate potential from -20 V – 80 V to produce transfer characteristics (black line in Figure 1A.1c). In order to calculate the mobility of the device, one takes the square root of the I_{DS} curve to produce the red

line (transfer curve) in Figure 1A.1c. The mobility is calculated from the transfer curve in the saturation regime using $I_{DS} = (W/2L)C_i\mu(V_G-V_T)^2$, where W and L are the width and length of the channel, C_i (11.5 nFcm^{-2}), μ, and V_T correspond to the capacitance per unit area of the gate insulator, the field effect mobility, and the threshold voltage, respectively.[11,15]

Each application discussed in this Thesis (OFETs, OPVs, OPDs, and sensors) requires the efficient transport of a carrier. Transport requires an otherwise localized carrier to be "freed" so it can move through a conduction channel and collected at an electrode, and this is where π-conjugation and energy levels matter. There are additional requirements (and often overlapping) for each application: the absorption of visible light, too, is important for OPVs (Chapter 3) and a rigid structure is important for OPDs (Chapter 5).

1A.4. A Chemist's Approach to Understanding Electronic Materials

Section 1A.3 defined n-type materials as electron-transporting and p-type materials as hole transporting. A molecule can be "electron transporting" if it possesses low energy unoccupied space to accept an electron that has been "freed" from its local environment; this energy level is often referred to as the lowest unoccupied molecular orbital (LUMO). Likewise, a molecule is "hole transporting" if it possesses a large density of high energy electrons or a high energy highest occupied molecular orbital (HOMO) that provides an electron (often after prompted by a stimulus e.g. light or a potential).

As the basic principles of molecular electronics require transport of a charge carrier, the first question then is what molecular design causes a molecule to possess a high energy HOMO and low energy LUMO? A second related question is why do these two energy levels matter for organic electronics? Pi-conjugated molecules remain the ubiquitous materials for organic electronics.[11,16–19] Pi-conjugation comprises alternating single and double bonds within the same

plane (or nearly so), which facilitates carrier transport through the molecular backbone. All else being equal, for a homologous series of conjugated molecules, a longer conjugation length gives a higher energy HOMO and a lower energy LUMO.[20]

A higher energy HOMO is advantageous in organic electronics as it suggests the molecule is easier to oxidize, and a lower energy LUMO suggests the molecule is easier to reduce (the HOMO and LUMO are often referred to as the frontier orbitals). Both properties are helpful if the goal is to create a conduction channel in an OFET as we need molecules that can rapidly accept and give up electrons (or holes). Thus, we have answered the first two questions: π-conjugated materials endow a molecule with hole or electron transport properties because conjugation can raise the energy of the HOMO and lower the energy of the LUMO, all else being equal.[19,21,22]

The third question to address is what molecular designs can be utilized to tune the frontier orbitals energy levels and decrease the HOMO/LUMO gap? Through the past several decades, a donor/acceptor strategy remains the primary method to tune the energy levels of molecules. I define donor as a molecule with a relatively high energy HOMO and an acceptor as a molecule (or part of a molecule) with a low energy LUMO. Given their large density of high energy electrons, donor molecules are often referred to as p-type materials. Analogously, acceptor molecules and n-type molecules are used interchangeably.[17] Arrow-pushing may help classify some molecules (or part of a molecule) as donors or acceptors (donor and acceptor classifications can be misleading as it often can depend on the state of reference e.g. ground or excited state). For example, a molecule with a lone pair could be a potent donor; such as a thiophene, as the lone pair can be pushed or "donated" into an acceptor. Molecules or a part of a molecule that can accept or "pull" electron density are often classified as acceptors; for example, atoms with high electron affinities like the oxygen of a carbonyl group. Often cyclic voltammetry (CV) is used to approximate HOMO

and LUMO levels of a molecule.[23] Thus, chemists design acceptor molecules because they can possess low energy LUMOs, which would make them potential candidates as n-type materials, and design donor molecules because they have high energy HOMOs to function as p-type materials in organic electronics.

1A.5. Evolution of Molecules for Organic Electronics

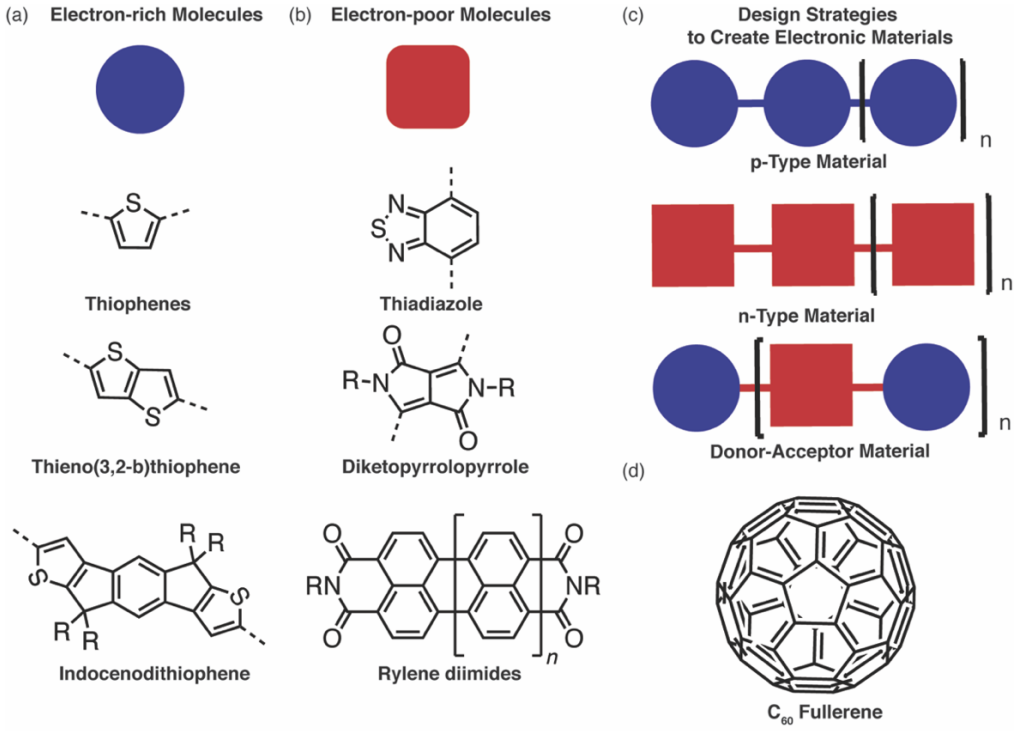

Figure 1A.2. (a) Common donor molecules and (b) common acceptor molecules used to construct small molecules and polymers for organic electronics; (c) design strategies to create electronic materials; and (d) C_{60}.

Typical donor molecules for small molecules and polymers include thiophenes, pentacene, indaceno-dithiophene (IDT), hexabenzocoronene, and thieno(3,2-b)thiophene (TT). Each of these molecules possess either a lone pair that can add electron density, or donate to an adjacent atom or molecule, or possess extended conjugation. [15,24,25]

N-type molecules are often composed of thiadiazole, diketopyrrolopyrrole, rylene diimides-based structures, and $C_{60}/_{70}$ and their derivatives.[26–31]Figure 1A.2 provides examples of common donor and acceptor molecules used to build small molecules and polymers used in

OFETs. This is by no means an exhaustive list, but illustrative of the types of molecules chemists consider in their design of materials. The evolution of bottom-up synthesis to synthesize materials that exhibit p-type characteristics has been rapid over the past few decades, with n-type materials recently garnering greater attention.

1A.6. Contorted Aromatics as Electronic Materials

Fullerene derivatives, such as [6,6]-phenyl-$C_{61}/_{71}$-butyric acid methyl ester ($PC_{61}BM$ and $PC_{71}BM$), have been used historically as the electron acceptor in bulk heterojunction due to efficient charge separation in fullerenes.[27,32–37] Fullerenes present four useful structural and electronic properties: (1) a three-dimensional shape with a π-surface that can participate in π-to-π interactions; (2) a conjugated and fully delocalized π-space; (3) the presence of an interior and exterior to the π-surface; and (4) a low-energy unoccupied molecular orbital(s) allowing them to accept electrons. These electronic and structural elements have inspired chemists to design non-fullerene molecules that exhibit "fullerene-like" properties.

Over the past few years, there have been several groups, including our own, that have synthesized non-fullerene materials for use in OFETs and OPVs.[8,8,28,30,31,38–50] In particular, the Nuckolls laboratory has pioneered the design and synthesis of new contorted aromatics for materials applications. We named these compounds 'contorted aromatics' because steric congestion in their periphery results in non-planar structures. We have synthesized both discs and ribbon versions of contorted aromatics (Figure 1A.3.).[8] These molecules have been an exciting complement to planar polyaromatic hydrocarbons. Contorted structures change both the physical and electronic structure of the molecules. This allows one to build different supramolecular assemblies with different binding motifs to probe on a fundamental level the relationship between structure and function in device applications.

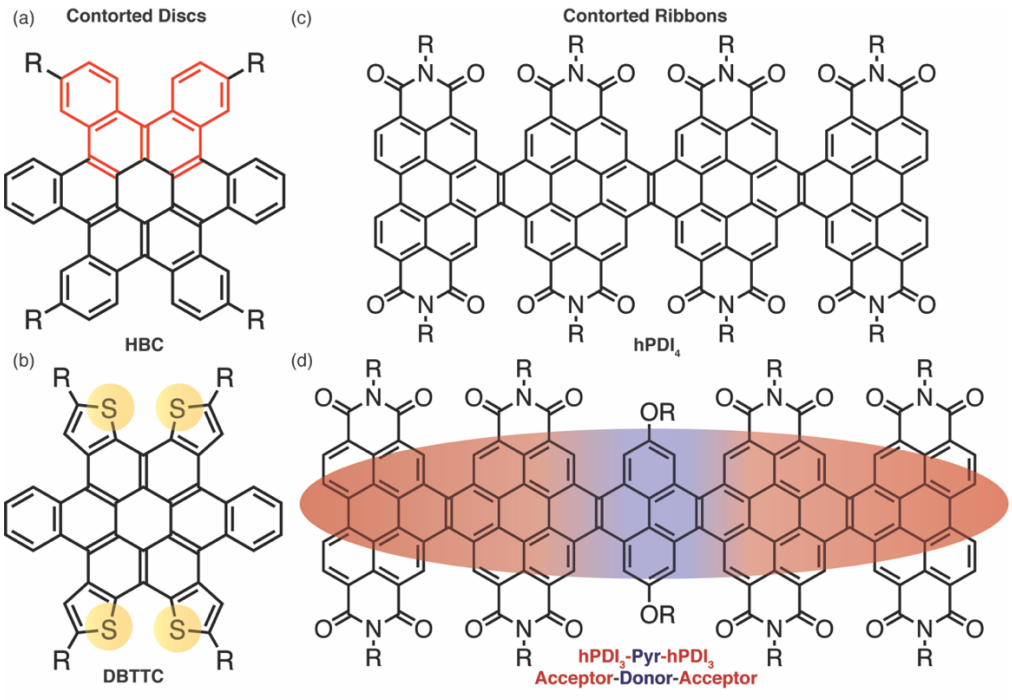

Figure 1A.3. Representative molecule of two contorted aromatics (a) **HBC** and (b) **DBTCC**. Both **HBC** and **DBTCC** are composed of [4]helicene structures outlined in red; (c) $hPDI_4$ tetramer. One of the helical PDI series that showed exceptional solar cell performance; and (d) a donor-acceptor $hPDI_3$-based ribbon, where the HOMO resides on a pyrene-centered orbital and the LUMO resides on a $hPDI_3$-centered orbital.

The disc-shaped contorted molecules have well-defined conformations that create concave π-surfaces. The molecular feature incorporated into the design of these contorted structures is benzophenanthrene, also known as [4]helicene, the smallest carbohelicene (indicated in red in Figure 1A.3a).[51] Steric congestion in the bay positions causes the molecule to bend out of planarity. Hexabenzocoronene (**HBC**) and dibenzotetrathienocoronene (**DBTTC**) are two examples of disc-shaped molecules in Figure 1A.3a,b.[7,52,53] The concave surfaces of these disc-shaped contorted molecules form ideal receptors for the molecular recognition and assembly with shape-matched molecules.[54]

The ribbon-shaped, contorted molecules can be conceptualized as ultra-narrow pieces of graphene.[55] PDI is the building block for the ribbons. PDI has many advantages: (1) it is an efficient material in n-type organic field effect transistors;[33,42,44,56,57] (2) it has high molar

absorptivities;[8,55,58] (3) it is an efficient electron acceptor in organic photovoltaics;[41,44] and (4) it is easily functionalized from inexpensive starting materials and photostable.[59–61] Upon substitution in the bay region of the molecule, PDI exists as two isomeric forms: *1,6* and *1,7*-substituted PDI that possess different electronic properties (Figure 1A.4).[62–65] *1,*6-PDI and *1,*7-PDI are also referred to as cis and trans-PDI, respectively. Chapter 4 and Chapter 8 both present interesting studies where we found substitution patterns impacted device performance.

The Nuckolls lab fuses PDI moieties to make atomically-defined graphene ribbons, the helical-PDI family ($hPDI_n$).[8,55] The bottom-up approach allows for exquisite structural control and versatility to synthesize oligomeric derivatives. Figure 1A.4 shows the three oligomers synthesized: the dimer ($hPDI_2$), trimer ($hPDI_3$), and tetramer ($hPDI_4$). The contortion in these ribbons causes them to wind into helical ribbons and exists in multiple conformations. Density Functional Theory (DFT) calculations performed by Dr. Nathanial Schuster in the Nuckolls laboratory suggest the barrier to inversion is approximately 11 kcal/mol between conformers. The PDI ribbons have been used in OFETs,[28] OPVs,[28,41,66] and OPDs[67,68].

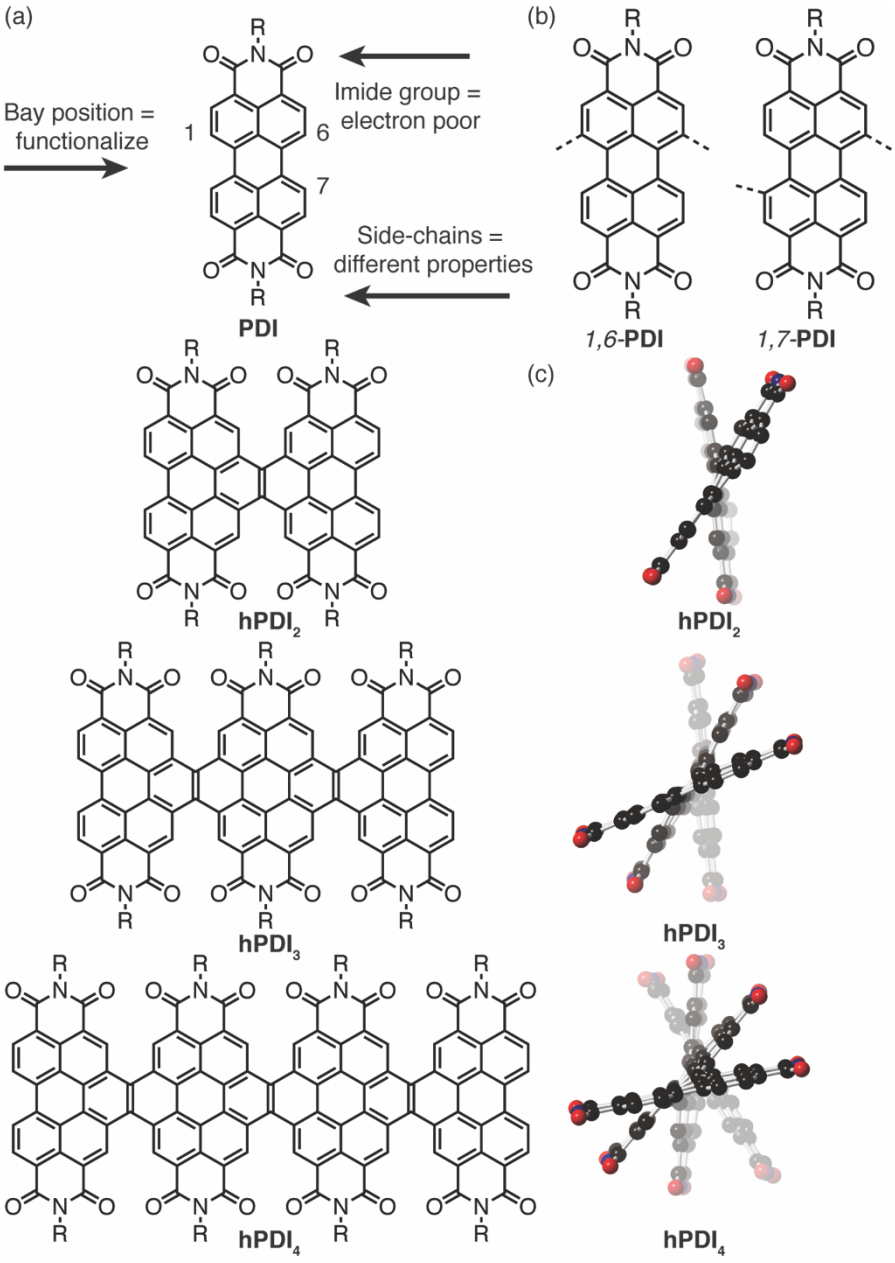

Figure 1A.4. (a) Helical PDI oligomer family. The imide position creates an area of low-energy unoccupied space on the molecule, the bay position can be readily substituted. (b) The most common substitution patterns are *1,7* and *1,6* which will be discussed in the following chapters. The R groups can be altered to affect processing of material and photophysical properties; (c) the helical conformation of the hPDI oligomers using DFT performed by Dr. Michael L. Steigerwald.

My research into the design and synthesis of the PDI-based conjugated macrocycles was inspired by much of the work produced in the Nuckolls laboratory over the past two decades. Ultimately, I was interested in how physical organic principles such as strain, rigidity, and chirality

impact materials applications in three-dimensional conjugated macrocycles. Conjugated macrocycles had not been used in (opto)electronic devices until our studies. Chapter 1B provides an overview of the conjugated macrocycles; including, the design and inspiration for the materials. I also provide an overview of key concepts that feature in this thesis such as strain and rigidity.

1A.7. References

1. Ball, M. *et al.* Conjugated Macrocycles in Organic Electronics. *Acc. Chem. Res.* (2019).

2. Ball, M. *et al.* Chiral Conjugated Corrals. *J. Am. Chem. Soc.* **137**, 9982–9987 (2015).

3. Ball, M. *et al.* Macrocyclization in the Design of Organic n-Type Electronic Materials. *J. Am. Chem. Soc.* **138**, 12861–12867 (2016).

4. Zhang, B. *et al.* Rigid, Conjugated Macrocycles for High Performance Organic Photodetectors. *J. Am. Chem. Soc.* **138**, 16426–16431 (2016).

5. Zhang, B. *et al.* Hollow organic capsules assemble into cellular semiconductors. *Nat. Commun.* **9**, 1957 (2018).

6. Ball, M. L. *et al.* Influence of Molecular Conformation on Electron Transport in Giant, Conjugated Macrocycles. *J. Am. Chem. Soc.* **140**, 10135–10139 (2018).

7. Kang, S. J. *et al.* A Supramolecular Complex in Small-Molecule Solar Cells based on Contorted Aromatic Molecules. *Angew. Chem. Int. Ed.* **51**, 8594–8597 (2012).

8. Ball, M. *et al.* Contorted Polycyclic Aromatics. *Acc. Chem. Res.* **48**, 267–276 (2015).

9. Brédas, J. L. *et al*. Organic semiconductors: A theoretical characterization of the basic parameters governing charge transport. *Proc. Natl. Acad. Sci.* **99**, 5804 LP – 5809 (2002).

10. Bendikov, M. *et al*. Tetrathiafulvalenes, Oligoacenenes, and Their Buckminsterfullerene Derivatives: The Brick and Mortar of Organic Electronics. *Chem. Rev.* **104**, 4891–4946 (2004).

11. Newman, C. R. *et al.* Introduction to Organic Thin Film Transistors and Design of n-Channel Organic Semiconductors. *Chem. Mater.* **16**, 4436–4451 (2004).

12. Anthony, J. E. Functionalized Acenes and Heteroacenes for Organic Electronics. *Chem. Rev.* **106**, 5028–5048 (2006).

13. Gundlach, D. J. *et al*. Thin-film transistors based on well-ordered thermally evaporated naphthacene films. *Appl. Phys. Lett.* **80**, 2925–2927 (2002).

14. Lin, Y. *et al*. Stacked pentacene layer organic thin-film transistors with improved characteristics. *IEEE Electron Device Lett.* **18**, 606–608 (1997).

15. Zaumseil, J. *et al*. Electron and Ambipolar Transport in Organic Field-Effect Transistors. *Chem. Rev.* **107**, 1296–1323 (2007).

16. Brédas, J.-L. *et al*. Charge-Transfer and Energy-Transfer Processes in π-Conjugated Oligomers and Polymers: A Molecular Picture. *Chem. Rev.* **104**, 4971–5004 (2004).

17. Coropceanu, V. *et al.* Charge Transport in Organic Semiconductors. *Chem. Rev.* **107**, 926–952 (2007).

18. Roncali, J. Molecular engineering of the band gap of pi-conjugated systems: Facing technological applications. *Macromol. Rapid Commun.* **28**, 1761–1775 (2007).

19. Havinga, E. E. *et al*. A new class of small band gap organic polymer conductors. *Polym. Bull.* **29**, 119–126 (1992).

20. Anslyn, E. V. *et al*. *Modern Physical Organic Chemistry*. (University Science Books, 2006).

21. Guo, X. *et al*. Designing π-conjugated polymers for organic electronics. *Prog. Polym. Sci.* **38**, 1832–1908 (2013).

22. Havinga, E. E. *et al*. Alternate donor-acceptor small-band-gap semiconducting polymers; Polysquaraines and polycroconaines. *Synth. Met.* **55**, 299–306 (1993).

23. You, J. B. *et al.* A polymer tandem solar cell with 10.6% power conversion efficiency. *Nat. Commun.* **4**, 10 (2013).

24. Facchetti, A. π-Conjugated Polymers for Organic Electronics and Photovoltaic Cell Applications. *Chem. Mater.* **23**, 733–758 (2011).

25. Dou, L. *et al.* 25th Anniversary Article: A Decade of Organic/Polymeric Photovoltaic Research. *Adv. Mater.* **25**, 6642–6671 (2013).

26. Kroto, H. W. *et al*. C60: Buckminsterfullerene. *Nature* **318**, 162–163 (1985).

27. Haddon, R. C. *et al.* C60 thin film transistors. *Appl. Phys. Lett.* **67**, 121–123 (1995).

28. Zhong, Y. *et al.* Molecular helices as electron acceptors in high-performance bulk heterojunction solar cells. *Nat Commun.* **6**, 8242 (2015).

29. Lin, Y. Z. *et al.* High-performance fullerene-free polymer solar cells with 6.31% efficiency. *Energy Environ. Sci.* **8**, 610–616 (2015).

30. Nielsen, C. B. *et al*. Non-Fullerene Electron Acceptors for Use in Organic Solar Cells. *Acc. Chem. Res.* **48**, 2803–2812 (2015).

31. Yan, C. *et al.* Non-fullerene acceptors for organic solar cells. *Nat. Rev. Mater.* **3**, 18003 (2018).

32. Savoie, B. M. *et al.* Unequal Partnership: Asymmetric Roles of Polymeric Donor and Fullerene Acceptor in Generating Free Charge. *J. Am. Chem. Soc.* **136**, 2876–2884 (2014).

33. Anthony, J. E. *et al*. n-Type Organic Semiconductors in Organic Electronics. *Adv. Mater.* **22**, 3876–3892 (2010).

34. Huang, Q. *et al.* Photoconductive Curved-Nanographene/Fullerene Supramolecular Heterojunctions. *Angew. Chem. Int. Ed.* **58**, 6244 (2019).

35. Li, H. *et al.* High-Mobility Field-Effect Transistors from Large-Area Solution-Grown Aligned C60 Single Crystals. *J. Am. Chem. Soc.* **134**, 2760–2765 (2012).

36. Zhang, Y. *et al*. Development of fullerenes and their derivatives as semiconductors in field-effect transistors: exploring the molecular design. *J. Mater. Chem. C* **6**, 3514–3537 (2018).

37. Zhao, Y. *et al*. 25th Anniversary Article: Recent Advances in n-Type and Ambipolar Organic Field-Effect Transistors. *Adv. Mater.* **25**, 5372–5391 (2013).

38. Hou, J. *et al*. Organic solar cells based on non-fullerene acceptors. *Nat. Mater.* **17**, 119 (2018).

39. Matsuno, T. *et al*. Self-Sorting of Two Hydrocarbon Receptors with One Carbonaceous Ligand. *Angew. Chem. Int. Ed.* **55**, 15339–15343 (2016).

40. Zhong, Y. *et al.* Efficient Organic Solar Cells with Helical Perylene Diimide Electron Acceptors. *J. Am. Chem. Soc.* **136**, 15215–15221 (2014).

41. Zhong, Y. *et al.* Efficient Organic Solar Cells with Helical Perylene Diimide Electron Acceptors. *J. Am. Chem. Soc.* **136**, 15215 (2014).

42. Sharenko, A. *et al.* A High-Performing Solution-Processed Small Molecule: Perylene Diimide Bulk Heterojunction Solar Cell. *Adv. Mater.* **25**, 4403–4406 (2013).

43. Lin, Y. *et al.* A Star-Shaped Perylene Diimide Electron Acceptor for High-Performance Organic Solar Cells. *Adv. Mater.* **26**, 5137–5142 (2014).

44. Cai, Y. *et al.* High Performance Organic Solar Cells Based on a Twisted Bay-Substituted Tetraphenyl Functionalized Perylenediimide Electron Acceptor. *Adv. Energy Mater.* **5**, 1500032 (2015).

45. Segawa, Y. *et al.* Efficient Organic Solar Cells with Helical Perylene Diimide Electron Acceptors. *J. Am. Chem. Soc.* **137**, 3122–3125 (2015).

46. Lin, H. *et al.* Reduced Intramolecular Twisting Improves the Performance of 3D Molecular Acceptors in Non-Fullerene Organic Solar Cells. *Adv. Mater.* **28**, 8546–8551 (2016).

47. Meng, D. *et al.* High-Performance Solution-Processed Non-Fullerene Organic Solar Cells Based on Selenophene-Containing Perylene Bisimide Acceptor. *J. Am. Chem. Soc.* **138**, 375–380 (2016).

48. Lin, Y. *et al*. Non-fullerene acceptors for organic photovoltaics: an emerging horizon. *Mater. Horizons* **1**, 470–488 (2014).

49. Chen, W. *et al.* A perylene diimide (PDI)-based small molecule with tetrahedral configuration as a non-fullerene acceptor for organic solar cells. *J. Mater. Chem. C* **3**, 4698–4705 (2015).

50. Zhang, J. *et al*. Material insights and challenges for non-fullerene organic solar cells based on small molecular acceptors. *Nat. Energy* **3**, 720–731 (2018).

51. Gingras, M. One hundred years of helicene chemistry. Part 1: non-stereoselective syntheses of carbohelicenes. *Chem. Soc. Rev.* **42**, 968–1006 (2013).

52. Chiu, C.-Y. *et al.* Shape-shifting in contorted dibenzotetrathienocoronenes. *Chem. Sci.* **2**, 1480–1486 (2011).

53. Roncali, J. Synthetic Principles for Bandgap Control in Linear π-Conjugated Systems. *Chem. Rev.* **97**, 173–206 (1997).

54. Tremblay, N. J. *et al.* Photovoltaic Universal Joints: Ball-and-Socket Interfaces in Molecular Photovoltaic Cells. *ChemPhysChem* **11**, 799–803 (2010).

55. Zhong, Y. *et al.* Helical Ribbons for Molecular Electronics. *J. Am. Chem. Soc.* **136**, 8122–8130 (2014).

56. Zhou, E. J. *et al.* All-Polymer Solar Cells from Perylene Diimide Based Copolymers: Material Design and Phase Separation Control. *Angew. Chem. Int. Ed.* **50**, 2799–2803 (2011).

57. Li, C. & Wonneberger, H. Perylene Imides for Organic Photovoltaics: Yesterday, Today, and Tomorrow. *Adv. Mater.* **24**, 613–636 (2012).

58. Nolde, F. *et al*. Synthesis and self-organization of core-extended perylene tetracarboxdiimides with branched alkyl substituents. *Chem. Mater.* **18**, 3715–3725 (2006).

59. Yan, Q. F. *et al*. Conjugated Dimeric and Trimeric Perylenediimide Oligomers. *Org. Lett.* **11**, 3426–3429 (2009).

60. Huo, L. J. *et al*. Synthesis and absorption spectra of n-type conjugated polymers based on perylene diimide. *Macromol. Rapid Commun.* **29**, 1444–1448 (2008).

61. Würthner, F. *et al.* Perylene Bisimide Dye Assemblies as Archetype Functional Supramolecular Materials. *Chem. Rev.* **116**, 962–1052 (2016).

62. Ahrens, M. J. *et al*. R. Bis(n-octylamino)perylene-3,4:9,10-bis(dicarboximide)s and Their Radical Cations: Synthesis, Electrochemistry, and ENDOR Spectroscopy. *J. Org. Chem.* **71**, 2107–2114 (2006).

63. Osswald, P. *et al*. Effects of Bay Substituents on the Racemization Barriers of Perylene Bisimides: Resolution of Atropo-Enantiomers. *J. Am. Chem. Soc.* **129**, 14319–14326 (2007).

64. Schmidt, R. *et al*. Synthetic Routes to Core-fluorinated Perylene Bisimide Dyes and their Properties. *Z. Naturforsch. B* **64**, 735–746 (2009).

65. Chen, Z. *et al*. Effect of Core Twisting on Self-Assembly and Optical Properties of Perylene Bisimide Dyes in Solution and Columnar Liquid Crystalline Phases. *Chem. – A Eur. J.* **13**, 450–465 (2007).

66. Edison, C. *et al.* Cove-Edge Nanoribbon Materials for Efficient Inverted Halide Perovskite Solar Cells. *Angew. Chem. Int. Ed.* **56**, 14648–14652 (2017).

67. Zhong, Y. *et al.* Helical Nanoribbons for Ultra-Narrowband Photodetectors. *J. Am. Chem. Soc.* **139**, 5644–5647 (2017).

Chapter 1 Section 1B. Conjugated Macrocycles in Organic Electronics

1B.1. Preface

Chapter 1B contains excerpts from a published accounts article entitled "Conjugated Macrocycles in Organic Electronics" by Melissa L. Ball, Boyuan Zhang, Yu Zhong, Brandon Fowler, Shengxiong Xiao, Fay Ng, Michael Steigerwald, and Colin Nuckolls, published in the Accounts of Chemical Research.[1] Copyright 2019 American Chemical Society.

1B.2. Introduction: Inspiration for Design

Here I describe our efforts to design and synthesize a new class of n-type materials: conjugated macrocycles. Conjugated macrocycles[2–28] have several potential advantages as organic electronic materials.[11,28–33] Our macrocyclic design takes into consideration the useful attributes of fullerenes and what properties make fullerenes efficient n-type materials. In order to create electronic materials that complement fullerenes, we asked ourselves what makes fullerenes effective as n-type materials, and then used the power of synthetic chemistry to try to install these features into new materials. Fullerenes present four useful structural and electronic properties: 1) a three-dimensional shape; 2) a conjugated and fully delocalized pi-space; 3) the presence of an interior and exterior to the pi-surface; and 4) a low-energy unoccupied molecular orbital(s) allowing them to accept electrons.[34,35]

While designing the macrocycles, we wondered how "fullerene-like" the macrocycles needed to be in order to remain "fullerene-like" electronic materials. We synthesized the macrocycles to mimic the three dimensional shape of fullerenes, yet our design offers several advantages: synthetic flexibility (allowing us to control the electronic properties of the macrocycles), extensive pi-conjugation, and intramolecular cavities that facilitate guest incorporation and sensing. My research goal was to design and synthesize three-dimensional

conjugated macrocycles that could absorb visible light and be used as the n-type material in electronic applications.

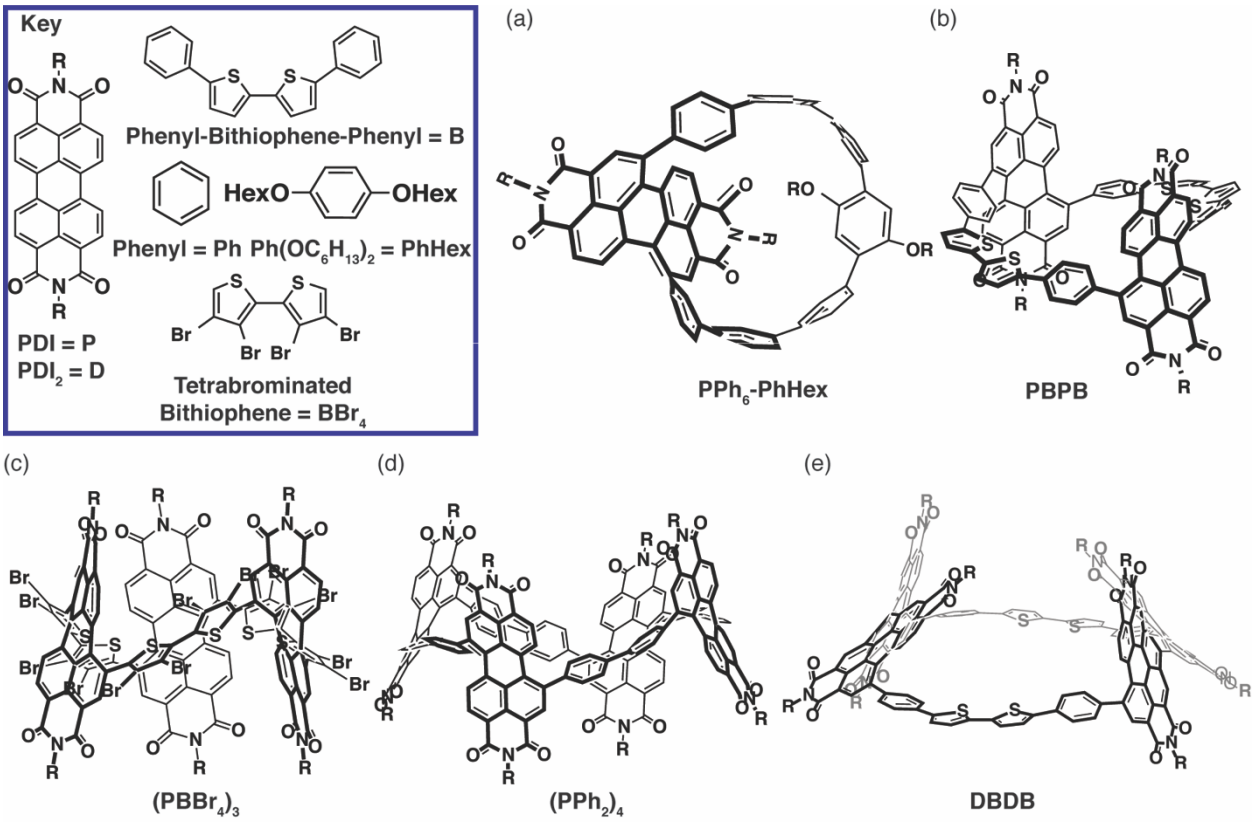

Figure 1B.1. The five conjugated macrocycles: (a) **PPh_6-PhHex**; (b) **PBPB**; (c) **$(PBBr_4)_3$**; (d) **$(PPh_2)_4$**; and (e) **DBDB**.

Figures 1B.1a-d show the four macrocycles studied that comprise monomeric PDI. The four molecules differ in the number of PDI (PDI = "**P**" in the names of each macrocycle) and linking groups that wind them into a macrocyclic structure. I studied three main linkers: a Phenyl-Bithiophene-Phenyl belt (**B**), a phenyl group (**Ph** and **PhHex**), and a tetrabrominated bithiophene (**BBr_4**) (Figure 1B.1a-d). We also synthesized and studied a $hPDI_2$-based ($hPDI_2$ = "**D**") macrocycle that exchanged monomeric PDI for **$hPDI_2$** (Figure 1A.4), and called this macrocycle **DBDB** (Figure 1B.1e).

There was both a structural and electronic consideration in the design of the conjugated macrocycles. First, the choice of subunits was paramount. We considered subunits that absorbed

visible light as this would allow provide utility in optoelectronic application. Each of the macrocycles contain at least one PDI (or **hPDI$_2$**) due to its many advantages: it is an efficient material in n-type organic field effect transistors;[36–40] (2) it has high molar absorptivities;[41–43] (3) it is an efficient electron acceptor in organic photovoltaics;[10,44] (4) it forms small band gap polymers with electron-donating moieties; and (5) it is easily functionalized from inexpensive starting materials and photostable.[42,45–47] The choice of linker between the PDI moieties was both a structural and electronic decision. The geometry of the linking group can facilitate macrocyclization by reducing strain. The linker groups, too, had a profound effect on the electronic structure of each macrocycle by modulating the HOMO-LUMO gap (Section 1B.7).

The macrocycles exist as chiral materials and exhibit size-dependent isomerization between stereoisomers (Section 1B.4.). Two of the monomer PDI macrocycles **PPh$_6$-PhHex** and **(PBBr$_4$)$_3$** are conformationally rigid, and unable to isomerize, while both **PBPB** and **(PPh$_2$)$_4$** show dynamic stereochemistry (Sections 1B.4 and 1B.5).

The conjugated macrocycles, too, are electronic and optoelectronic materials, and these "pseudo-fullerenes" are useful in an array of devices. This Thesis will describe how the macrocycles are effective n-type semiconductors in OFETs,[11,33,48] and can act as the electron-accepting materials in a bulk heterojunction.[11] Moreover, we find the internal cavities can be used as a locus of guest binding to create sensors and nanoscale reaction chambers (Chapter 6 and 9).[33]

1B.3. Synthetic Approaches to Build in Strain

We based our synthetic strategy on the pioneering studies by the Yamago[21,49] and the Jasti laboratories[50,51] in their syntheses of cycloparaphenylenes (CPPs). CPPs possess interesting topologies, but do not absorb in the visible portion of the solar spectrum and thus have not been explored in optoelectronic devices.

Figure 1B.2 shows two synthetic approaches to synthesize strained CPPs. The first approach builds in strain by performing the macrocyclization and reductive elimination steps before a final reductive aromatization to yield their desired product. One of the interesting design features is the two-fold addition of 4-bromo-4'-lithiobiphenyl to 1,4-benzoquinone: the two biphenyl appendages are on the same face of the aryl ring aiding the macrocyclization step. The hypothesis is that after the first addition, the oxygen anion is on one face of the aryl ring, and as the second mole of the lithio-biphenyl approaches, it preferentially attacks the carbonyl from the side anti to the oxygen anion as it is electronically favored due to Coulombic repulsion.

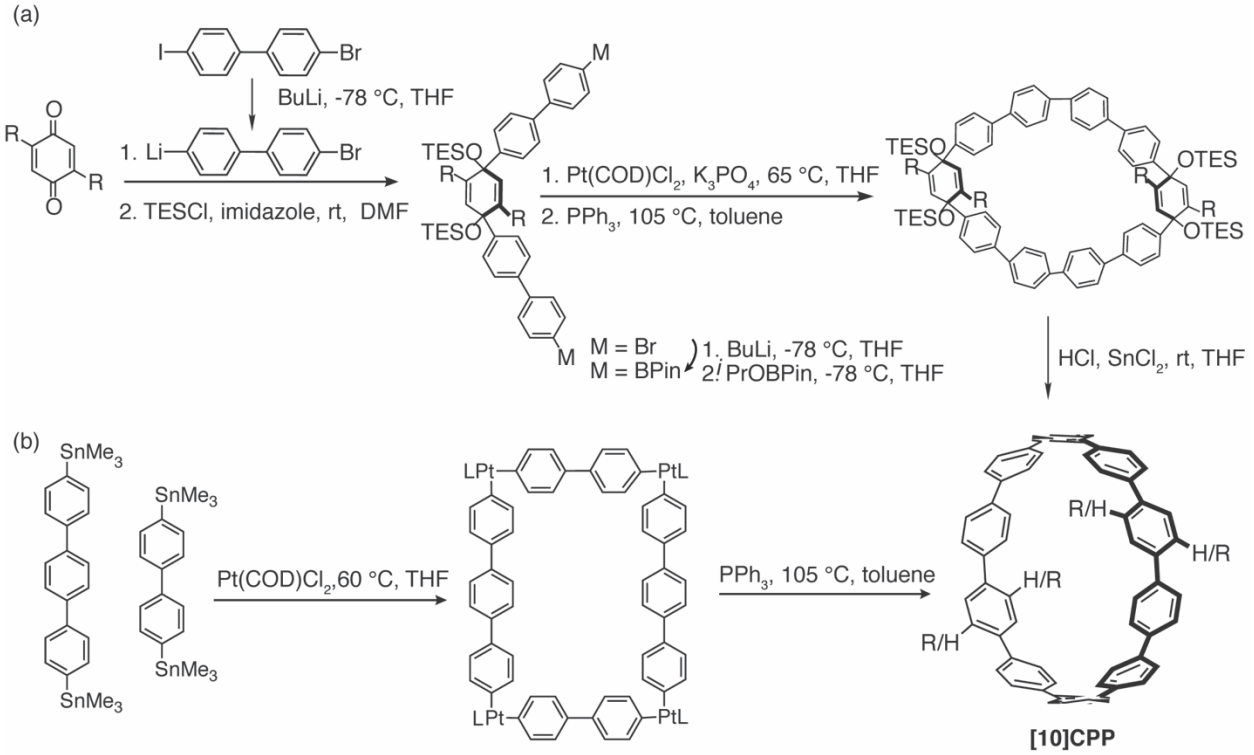

Figure 1B.2. (a) Synthetic approach utilizing an unstrained precursor to perform the macrocyclization before the final aromatization step; (b) a Pt-based strategy that relies on transmetalation from an aryl-tin bond to an aryl- Pt bond. R = alkyl, alkoxy groups.

The second strategy involves the transmetalation of a tin group onto a platinum (Pt). While both approaches take advantage of the square planar geometry of Pt in the macrocyclization step, the latter strategy does not possess a final reductive aromatization step. One of the theoretical

downsides to both strategies is the reversibility of the transmetalation step, which can lead to multiple unwanted byproducts, yet it only seemed to impact the latter approach.[21,52] We employed both approaches in the syntheses of the conjugated macrocycles, and the following chapters provide the details of each macrocycle's synthesis.

Several important physical organic concepts arise in each chapter of this Thesis including strain, rigidity, conjugation, and chirality, and each have interesting effects on the macrocycles structural and electronic properties. Thus, Sections 1B.4 - IB.7 provide a brief background on these topics insomuch as how they relate to the conjugated macrocycles. This knowledge will support and aid one's understanding of the remaining chapters.

1B.4. Bay Substitution of PDI Induces Chirality

The PDI macrocycles possess chiral axes about each PDI as described below. For macrocycles that are sufficiently rigid, these chiral axes are locked; however, for more flexible macrocycles, mechanisms exist for stereoisomerization of these chiral axes. The stereoisomers of macrocyclic PDIs arise from di-substitution of the PDI bay positions, which results in two observed isomeric forms, a *1,6*- and a *1,7*-substituted PDI or *cis*- and *trans*-substituted PDI (Figure 1A.4). The *1,7*-substitution exhibits axial chirality (or helicity), with a stereogenic axis down the long axis of the PDI moeity.[53–58] Axial chirality arises when a molecules possesses a stereogenic axis, rather than a stereogenic center, and the substituents about this axis are spatially arranged so they are not superimposable.[59] When *1,7*-substituted PDI (*1,7*-PDI, for short) possesses a bulky group in the bay position (phenyl groups in Figure 1B.3), the two naphthyl groups that comprise the perylene backbone twist out of planarity to avoid steric congestion between the substituent and the hydrogen in the adjacent bay position (top naphthyl is in a solid rectangle and the bottom naphthyl is indicated with a dashed rectangle in Figure 1B.3a,b). The twist angle is approximately

22° for a *1,7*-phenyl PDI (Compound **1.1**). The twisting of the naphthyl groups places the bay substituents on the same face of the PDI molecule. Figure 1B.3c and Figure 1B.3d provide a view of the stereogenic axis and a schematic detailing the designation of substituents. The top naphthyl contains the two "near" groups and the bottom naphthyl contains the two "far" groups.

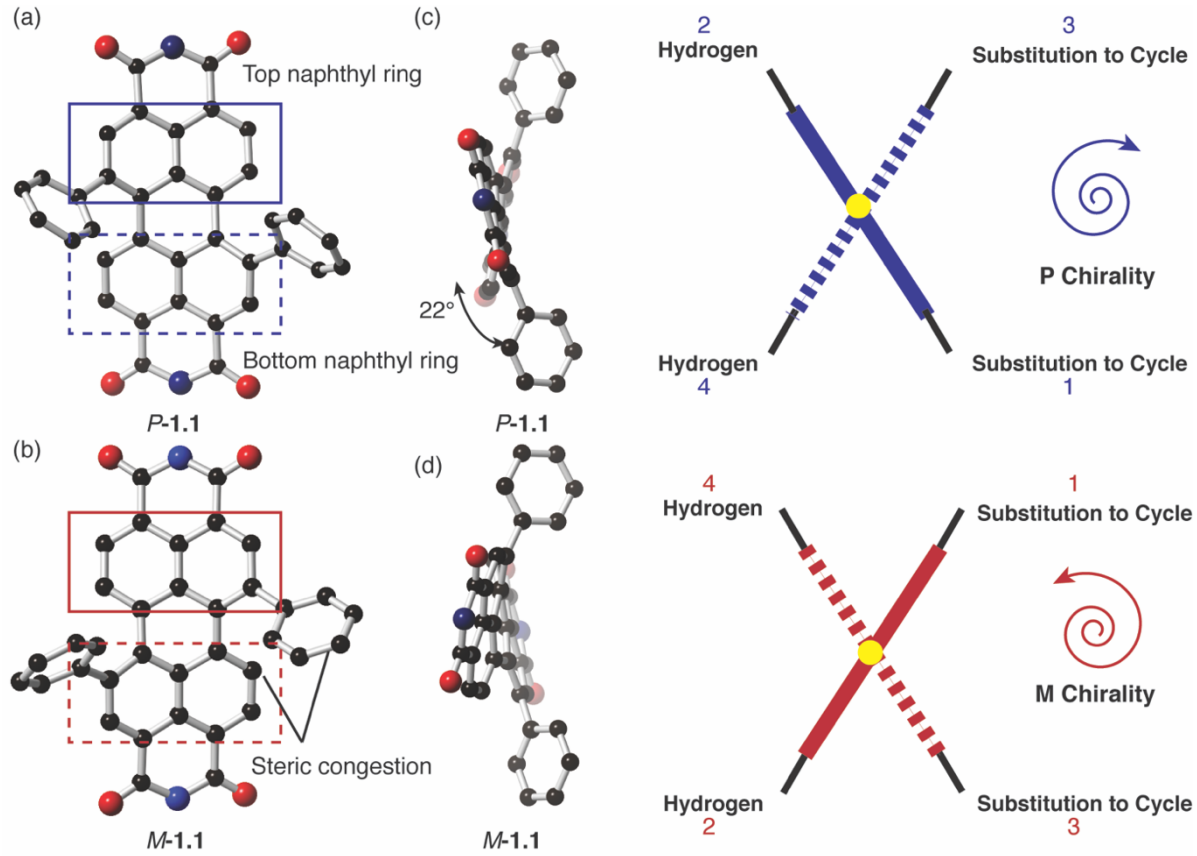

Figure 1B.3. (a) *P*-diphenyl PDI (*P*-**1.1**) and (b) *M*-diphenyl PDI (*M*-**1.1**) from DFT calculations carried out at 6-31G/B3LYP level of theory; (c) and (d) show how the *P* and *M* designations are assigned. One looks down the stereogenic axis (indicated with a yellow dot) and assigns the groups off the top naphthyl (solid line) a 1 or 2 priority before assigning 3 and 4 to the bottom naphthyl (dashed line) ring substituents.

One assigns the substituents from 1 - 4 with the near groups taking priority. If the assignment produces a clockwise rotation, this produces a right-handed, *P* (or Plus) helix, and a counterclockwise rotation yields a left-handed helix *M* (or Minus). An analogous procedure can be used to assign the helicity of **DBDB**. When conformationally restricted in a macrocycle,

isomerization between a *P* or *M* enantiomer depends on the size of the cavity. Section 1B.5 introduces how rigidity affects the ability to isomerize between stereoisomers.

1B.5. Rigidity in the Macrocycles and its Effects on Isomerization

The number of stereoisomers is directly related to the number of PDI subunits constrained within the cycle. For example, **PBPB** contains two PDI subunits and each can take a *P* or *M* designation. Thus, theoretically in solution, there are the enantio-pair (*P,P*)-, (*M,M*)-, and meso diastereomer (*P,M*). Likewise **(PPh$_2$)$_4$** possesses four *1,7*-PDI units, and exists as six stereoisomers in solution (two pairs of enantiomers*, P,P,P,P,*/*M,M,M,M* and *P,P,P,M*/*M,M,M,P* and two meso compounds, *P,M,P,M* and *P,P,M,M*).

One of the most obvious differences among the macrocycles is the size of their intramolecular cavities. According to structures determined DFT, the cavity is the smallest in **(PBBr$_4$)$_3$** (1.1 nm from PDI to thiophene), largest in **(PPh$_2$)$_4$** (2.0 nm across its transannular axis from PDI to PDI), and intermediate (1.6 nm) in **PBPB** and (1.3 nm) in **PPh$_6$-PhHex**. The size of the cavity directly affects the intramolecular fluctional behavior and the macrocycles ability to isomerize between stereoisomers.

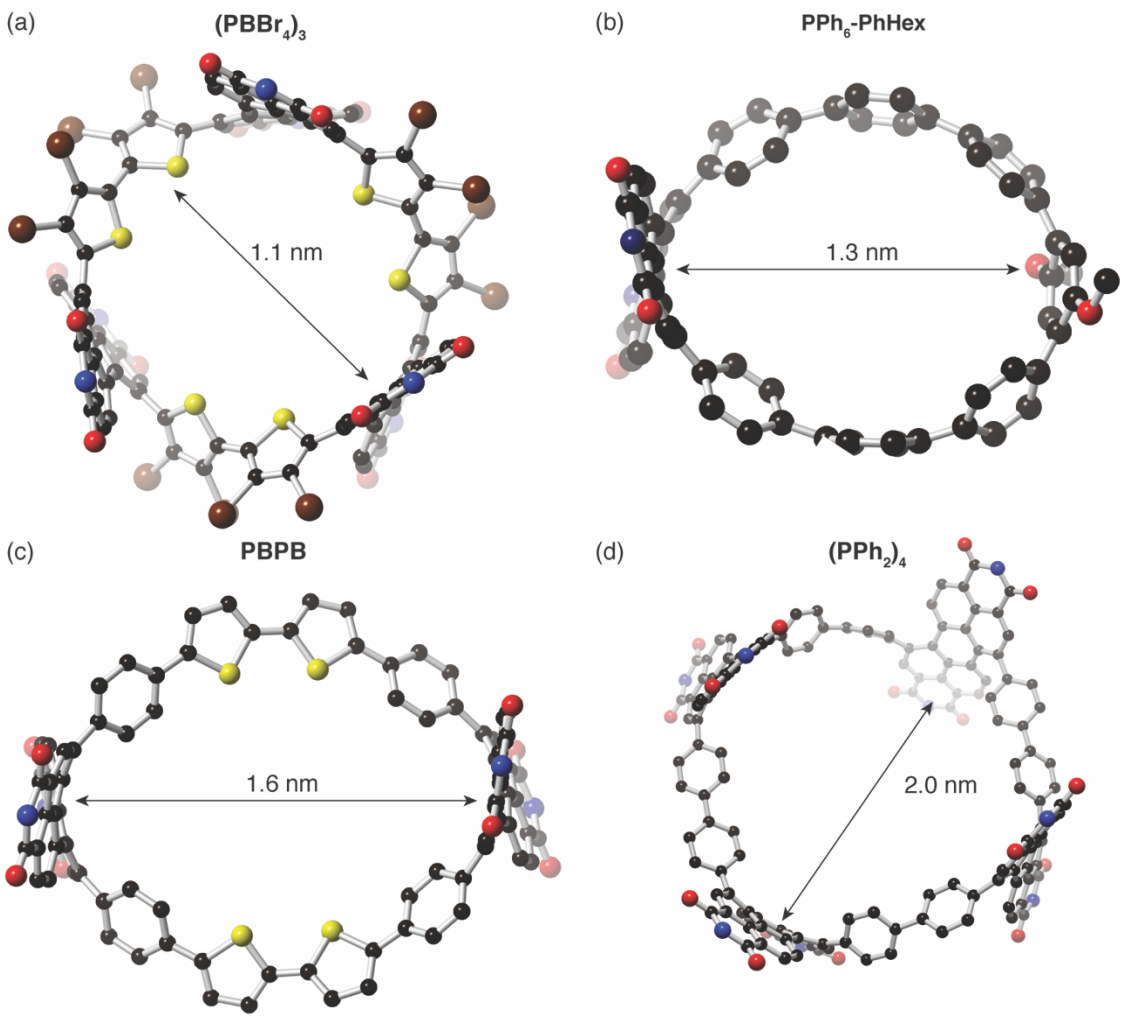

Figure 1B.4. Monomeric PDI-based macrocycles. The smallest macrocycles are (a) **$(PBBr_4)_3$** and (b) **PPh_6-PhHex**; (c) **PBPB**; and the largest cavity is for (d) **$(PPh_2)_4$**.

Both **$(PBBr_4)_3$** and **PPh_6-PhHex** possess fewer rotational degrees of freedom, resulting in conformationally locked macrocycles that are unable to isomerize between stereoisomers. We are able to isolate the two enantiomers of **PPh_6-PhHex** from chiral high performance liquid chromatography (HPLC), and find the two enantiomers do not interconvert at temperature up to 100 °C. We also are able to isolate one pair of the enantiomers for **$(PBBr_4)_3$**, and find no interconversion up to 160 °C. With larger cavities, **PBPB**, **$(PPh_2)_4$**, and **DBDB** exhibit dynamic stereo-isomerization. These macrocycles isomerize rapidly at room temperature, and are we are unable to isolate individual stereoisomers.

1B.6. Strain as a Function of Design

The macrocycles are an exemplary model system to test the interplay between rigidity and strain. As the macrocycles' topologies differ, so does the amount of strain within each system. We calculate the amount of strain within the macrocycles using a group equivalent homodesmotic calculation.[49,60–62] Before discussing the macrocycles, Figure 1B.5 shows an example of an homodesmotic calculations using a cyclobutane molecule.

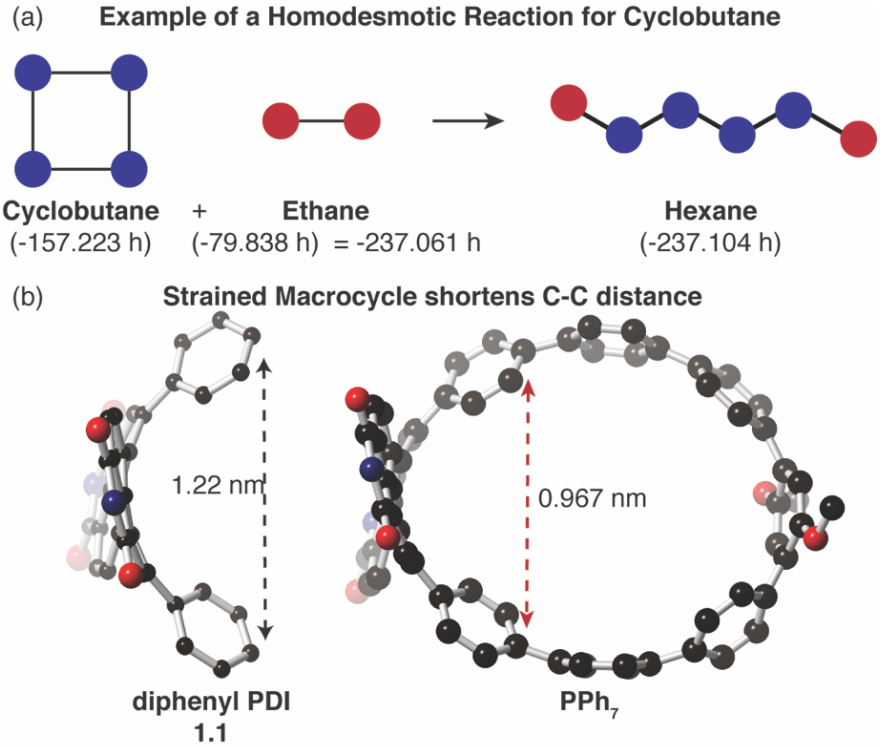

Figure 1B.5. (a) An example of an homodesmotic reaction to calculate the strain in cyclobutane. Two carbon-carbon bonds must break and then form in order to yield the hexane product. The two products possess a ΔH_f of -237.061 hartrees (1 hartree = 627.51 kcal/mol), and ΔH_f is -237.104 for hexane. The difference of 43 mH/ 27.2 kcal/mol is close to the experimentally determined value of 26.5 kcal/mol. (b) The aryl-aryl distance in an unsubstituted diphenyl PDI (Compound 1.1) and **PPh_6-PhHex**. Our findings suggest a negative correlation between aryl-aryl distance and strain: as this distance increases, the strain energy decreases.

Both the reactants and products contain six sp^3 → sp^3 with the same number of carbons and hydrogens. One can envision breaking and forming two C-C bonds on the reactants side to form hexane (Figure 1B.5). According to DFT, the difference in energy between an unstrained hexane

molecule and its group equivalent cyclobutane and ethane is 27.2 kcal/mol, consistent with -26.4 kcal/mol experimentally determined, and considered to be the amount of strain in the molecule. The strain energy encompasses deviations from ideal bond lengths and angles by restricting the four carbon atoms into a cyclic geometry.[59]

Both **$(PBBr_4)_3$** (2 kcal/mol) and **$(PPh_2)_4$** (~0 kcal/mol) possess a small amount of strain by DFT, while **PBPB** (21 kcal/mol) and **PPh_6-PhHex** (63 kcal/mol) contain a relatively significant amount of strain. It is interesting to note that although **$(PBBr_4)_3$** possesses the smallest cavity, the syn geometry of the three bithiophene subunits alleviates strain in the macrocycle as the syn geometry provides a natural curvature. The role of the bithiophene in macrocyclization is discussed in Chapter 2.

Table 1B.1. The transannular aryl-aryl distance from the phenyl rings adjacent to the PDI

	Aryl-Aryl Distances		Strain
	Distance (nm)	Deviation (nm)	Energy (kcal/mol)
1.1	1.22	-	-
PPh_6-PhHex	0.97	0.26	63
PBPB	0.99	0.24	23
$(PBBr_4)_3$	1.0	0.18	2
$(PPh_2)_4$	1.1	0.10	0

Table 1B.1. The transannular aryl-aryl distance from the phenyl rings adjacent to the PDI. There is a negative correlation with distance and strain: as the distance increases, the strain decreases in the conjugated macrocycles.

One possibility to assess strain visually in these systems is to consider the *para* carbon-carbon distance from the adjacent phenyl rings to the PDI. In an unsubstituted diphenyl PDI (**1.1**), this distance is approximately 1.22 nm (Figure 1B.5b); however, this distance changes when restricted into a macrocyclic framework: for the least strained macrocycles **$(PPh_2)_4$** and **$(PBBr_4)_3$**, the carbon-carbon distance is the least perturbed, and measures 1.13 and 1.05 nm, respectively.

There is a greater perturbation in **PPh$_6$-PhHex** (0.26 nm) followed by **PBPB** (0.24 nm), analogous to the same trend in strain energy.

1B.7. Macrocyclic Design Promotes Absorption of Visible Light

The first indication that the macrocycles could be efficient optoelectronic materials was their color. Figure 1B.6 shows the colors of the conjugated macrocycles: by visual inspection, **PBPB** is black, **PPh$_6$-PhHex** is teal, **(PPh$_2$)$_4$** and **DBDB** are purple, and **(PBBr$_4$)$_3$** is red. The UV-Visible spectra confirm light absorption across much of the visible range (Figure 1B.6b).

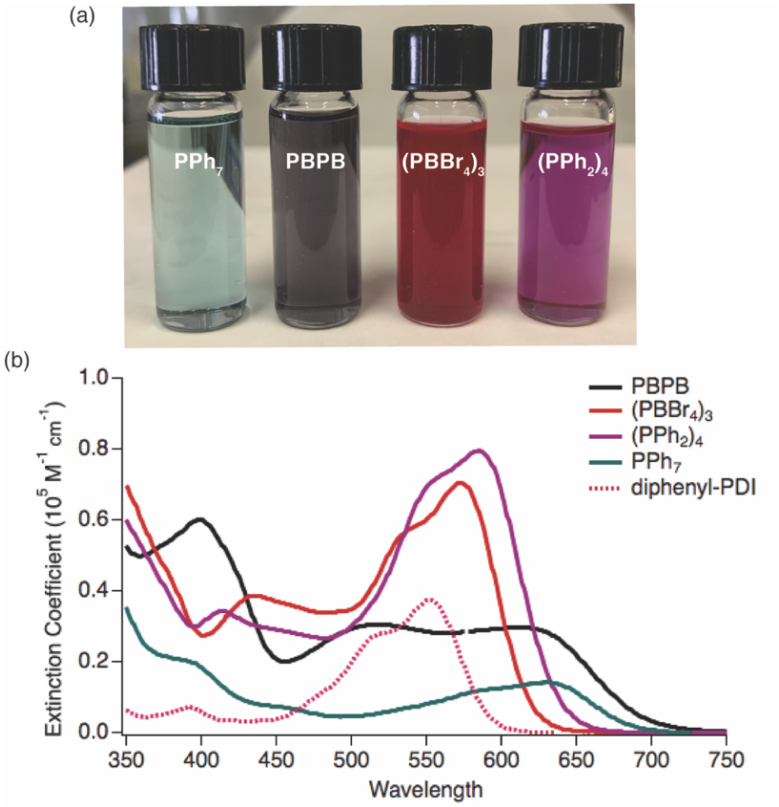

Figure 1B.6. (a) Vials containing the macrocycles in micromolar solutions. (b) The UV-Vis absorption spectrum of the four PDI-based macrocycles are at 10^{-5} M.

Each macrocycle functions as a n-type material in devices. DFT calculations and estimates from electrochemistry reveal that each molecule possesses a LUMO energy level that can accept at least two electrons per PDI (or four electrons for each hPDI$_2$ molecule) due to PDI's electron accepting ability (Table 1B.2). From the potential of the first reduction peak in the CV, we estimate

the LUMO energy levels to be approximately –3.9 eV for **PBPB**, **$(PPh_2)_4$**, and **$(PBBr_4)_3$**. For **DBDB**, the LUMO value is -3.90 eV. These values are similar to the common n-type semiconductors like [6,6]-phenyl C_{61}-butyric acid methyl ester (PCBM), whose LUMO is also –3.9 eV, and an unsubstituted PDI at -3.89.[63,64]

Table 1B.2: Electrochemistry, UV/vis and DFT Data for Conjugated Macrocycles

	Electrochemical[a]			DFT[b]			Optical[c]
	E_{LUMO}/eV	E_{HOMO}/eV	E_{gap}/eV	E_{LUMO}/eV	E_{HOMO}/eV	E_{gap}/eV	E_{gap}/eV
PBPB	–3.87	–5.39	1.52	-3.46	-5.31	1.85	1.79
PPh_6-PhHex	-	-	-	-3.46	-5.28	1.81	1.82
$(PPh_2)_4$	–3.90	–5.69	1.79	-3.54	-5.74	2.20	1.94
$(PBBr_4)_3$	–3.90	–6.06	2.16	-3.78	-6.12	2.34	2.00

Table 1B.2. [a]DFT calculations carried out at 6-31G/B3LYP level of theory. [b]HOMO and LUMO levels were estimated from onset of the first oxidation and reduction peaks and are relative to Fc/Fc+. [c]Optical band gaps were estimated from the onset of absorption.

We care about strain because strain affects the electronic structure and properties of the macrocycles. For example, we find the electronic structures of the macrocycles differ from their acyclic counterparts, with the macrocycles absorbing more visible light (Chapter 3). Chapter 1A discussed the effects of conjugation on the HOMO/LUMO levels and the importance of a narrow energy gap for electronics. These same principles apply to the conjugated macrocycles and are discussed throughout this Thesis. I spent five years trying to understand the overlap between strain, rigidity, and the effects of conjugation. These concepts matter because we observe an appreciable effect on device performance that we can attribute to these physical organic concepts. Yet I would

not say that these concepts alone are sufficient to design materials that perform well in devices: devices and how they work are complicated. But these molecules allowed us to probe on a fundamental level, from a physical organic chemistry point of view, what design features may be important for organic materials applications, and for this I am grateful.

Chapters 1A provided background on non-fullerene, contorted aromatics. It also described the role of conjugation and its effects on molecules. Chapter 1B describes an overview of the conjugated macrocycles. Here, I discussed the role of strain and rigidity on the macrocycles' electronic and physical structures. This background will be advantageous for Chapters 2-8, as I show how macrocyclization impacts device performance. The most interesting results described in this Thesis involve the interplay between strain and rigidity and device performance.

Chapters 2 and 3 focus on **PBPB** as an electronic material. Chapter 2 will describe the molecular structure of **PBPB**, and the exciting stereochemistry observed for this molecule. This Chapter will also show how the electronic structure of **PBPB** is not just a sum of the two linker components. Chapter 3 describes **PBPB** and **$(PPh_2)_4$** in both OFETs and OPVs. Here we study how the macrocyclic framework affects device performance by comparing **$(PPh_2)_4$** and **PBPB** to several acyclic control molecules. The macrocycles outperform the acyclic controls in each of the parameters tested.

The focus in Chapter 4 is how a *1,7* or *1,6* substitution affects OFET mobility. We design a cis analog to **PBPB**, and using a combination of single molecule junction conductance measurements of the components of the macrocycles, control experiments with acyclic counterparts to the macrocycles, and analyses of each of the materials using spectroscopy, electrochemistry, and DFT, we show the difference in electron mobility is due to a difference in intramolecular conductivity between the two isomers. The ability to synthesize and probe the

effects from nuanced differences in the macrocyclic framework is an advantage to this bottom-up approach.

Chapter 5 describes a direct relationship between structure and function for **$(PPh_2)_4$**. We compare the macrocycle relative to an acyclic control and show that the rigidity of the macrocycle aides its ability to function as a photodetector. This is a beautiful demonstration of structure and function. The macrocyclic structure minimizes the number of charged defects from deformed sp^2 bonds, resulting in a low dark current and a detectivity comparable to the best fullerene-based photodetectors.

Chapter 6 focuses on **$(PBBr_4)_3$** and its role as a sensor of small molecule guests. The macrocycle detects subtle differences in a series of alkanes (n-hexanes, 1-hexyne, and 3-hexyne), and is the first demonstration of the utility of designing a macrocycle with open pores. One of the key features of **$(PBBr_4)_3$** is that it is conformationally restricted, which could help aide its ability to function as a sensor. Chapter 7 describes the synthesis and characterization of the second conformationally locked macrocycle: **PPh_6-PhHex**. Intrigued by the possibility of creating enantio-pure sensors, we sought to make this synthetically-challenging macrocycle. The cavity of **PPh_6-PhHex** is larger than **$(PBBr_4)_3$**, and future work will include using **PPh_6-PhHex** in sensing applications with larger guests.

Chapter 8 includes our work on incorporating $hPDI_2$ within a macrocyclic framework. The motivation for this design was based off the success of the hPDI oligomers in electronic applications, as discussed in Chapter 1A. The final chapter (Chapter 9) discusses recent work using **PBPB** as a host system with fullerenes, and shows the utility of the conjugated macrocycles in sensing applications. Future work will explore how fullerene encapsulation affects electron mobility in OFET devices.

1B.8. Appendix

Diphenyl PDI – M enantiomer
***M*-1.1**

Heat of Formation = -1871.869720

H	2.421580	-5.686988	-0.551058
H	3.860773	-8.435283	-3.524222
H	6.186046	-7.757314	-3.025221
H	4.743387	-5.003344	-0.056350
H	-5.235350	-4.313873	-0.075358
H	-3.053109	-5.445250	0.183032
C	0.063429	-8.658829	2.182835
C	1.354330	-9.098917	2.557639
C	1.222168	-7.291460	-3.777648
C	3.245686	-6.147253	-1.086950
C	-2.431049	-7.903858	-3.776694
N	-1.689364	-7.474598	-6.078272
C	-2.757680	-7.780617	-5.217513
C	-0.357107	-7.310014	-5.680969
C	0.840232	-8.334762	-0.130028
C	-3.159428	-8.235104	-1.500815
C	2.087104	-8.822222	0.273119
C	-1.102189	-7.752569	-3.316804
C	-0.678482	-8.863838	4.580959
C	2.340622	-9.211722	1.592968
C	-3.438594	-8.185504	-2.870359
C	5.364271	-7.303038	-2.479653
C	-1.870104	-8.036055	-0.999218
C	1.568694	-7.466248	-2.420058
C	-0.065986	-7.469688	-4.235812
O	-3.894388	-7.930031	-5.645188
O	-1.522365	-8.761482	5.461979
C	-3.953270	-5.910130	0.573547
C	5.619295	-6.342311	-1.502386
C	1.659110	-9.458139	3.964323
C	-6.261116	-7.086369	1.600913
N	0.613495	-9.305846	4.890345
C	-5.028341	-7.721744	1.752521
O	0.504953	-7.045766	-6.509222
C	2.975958	-7.120537	-2.062834
C	-6.342068	-5.862174	0.938829
C	0.866299	-9.632578	6.297183
O	2.760010	-9.864893	4.311023
C	-3.859753	-7.148013	1.230666
C	-5.182302	-5.273796	0.429999
C	4.554260	-5.762086	-0.810244

C	4.052702	-7.684487	-2.762991
C	-0.228581	-8.336572	0.824523
C	-2.527987	-7.780686	1.454983
C	-1.572964	-8.020981	0.443818
C	-2.195747	-8.065949	2.797319
C	-0.792754	-7.885935	-1.931405
C	-0.951585	-8.538327	3.160011
C	0.573956	-7.865349	-1.500910
H	-2.930259	-7.902932	3.578354
H	2.889882	-8.897009	-0.446732
H	-4.446242	-8.338187	-3.240152
H	3.316019	-9.584932	1.884983
H	1.984016	-6.998213	-4.491384
H	-3.974710	-8.422972	-0.817385
H	-4.971899	-8.677025	2.266916
H	-7.157630	-7.549857	2.002095
C	-1.961508	-7.315325	-7.510367
H	-1.656182	-6.318177	-7.834399
H	1.904695	-9.942237	6.383852
H	0.670165	-8.757095	6.919588
H	0.198223	-10.435131	6.617291
H	-3.027841	-7.460423	-7.663121
H	-1.388093	-8.049013	-8.080981
H	-7.300991	-5.365623	0.824024
H	6.639889	-6.042220	-1.284028

Diphenyl PDI – P enantiomer

***P*-1.1**

Heat of Formation = -1871.869710

H	4.322695	-4.627155	-2.086531
H	6.480589	-5.862076	-2.055867
H	4.650901	-8.975413	0.274756
H	-4.891827	-4.606365	1.896083
H	-3.018507	-5.461131	0.529059
C	0.036188	-8.549338	2.206044
C	1.360381	-8.489346	2.697902
C	1.249969	-8.317575	-3.846104
C	3.350203	-7.345556	-0.272590
C	-2.353403	-7.449330	-3.769315
N	-1.621648	-7.593664	-6.106551
C	-2.674522	-7.340354	-5.214359
C	-0.311331	-7.924194	-5.733733
C	0.879325	-8.039485	-0.063985
C	-3.111843	-7.313839	-1.451999
C	2.171546	-7.866160	0.479106
C	-1.047709	-7.773041	-3.332459

C	-0.756740	-9.211659	4.501099
C	2.384079	-8.113769	1.852792
C	-3.337629	-7.184319	-2.839593
C	5.608811	-6.275320	-1.557396
C	-1.853697	-7.763373	-0.995845
C	1.544893	-8.339257	-2.478450
C	-0.024960	-8.001632	-4.281475
O	-3.793546	-7.047292	-5.614377
O	-1.637249	-9.539410	5.285896
C	-4.016481	-5.866593	0.393221
C	5.696657	-7.494934	-0.887807
C	1.663560	-8.773137	4.122977
C	-6.585148	-6.883830	0.027340
N	0.572123	-9.113920	4.936071
C	-5.528854	-7.361337	-0.749333
O	0.536459	-8.132376	-6.591711
C	3.276631	-6.113740	-0.942459
C	-6.360320	-5.896162	0.985156
C	0.815217	-9.409690	6.351669
O	2.799872	-8.713242	4.573569
C	-4.228087	-6.868107	-0.568471
C	-5.072527	-5.385789	1.161639
C	4.577663	-8.023362	-0.243505
C	4.395533	-5.584000	-1.577943
C	-0.217747	-8.261087	0.831885
C	-2.586272	-8.600041	1.263823
C	-1.576556	-8.199940	0.382779
C	-2.316233	-8.958394	2.588984
C	-0.776681	-7.869792	-1.935325
C	-1.022638	-8.897038	3.077478
C	0.575327	-8.073823	-1.506675
H	-3.113243	-9.264222	3.257586
H	-4.308019	-6.858907	-3.197689
H	3.377808	-7.998465	2.270927
H	2.016802	-8.525811	-4.583933
H	-5.709908	-8.132118	-1.493412
H	-7.583986	-7.284223	-0.119677
C	-1.884900	-7.512086	-7.546949
H	-1.268735	-6.728588	-7.994165
H	1.874965	-9.261487	6.543485
H	0.212902	-8.745703	6.974879
H	0.525989	-10.439737	6.571753
H	-2.940502	-7.287045	-7.677409
H	-1.628667	-8.460776	-8.022649
H	-7.183060	-5.521546	1.586846
H	6.636801	-8.038191	-0.864073

H	-3.610913	-8.631871	0.923819
H	2.556709	-8.565503	-2.176293
H	2.336950	-5.569898	-0.955767

Cyclobutane

Heat of Formation = -157.2230

C	-0.58524	0.51356	0.77860
C	-0.58085	0.51852	-0.77860
C	0.58085	-0.51852	-0.77860
C	0.58524	-0.51356	0.77860
H	-1.51202	0.14734	1.22988
H	-0.34799	1.47692	1.23946
H	-0.32995	1.48292	-1.22992
H	-1.50826	0.16598	-1.23943
H	1.50826	-0.16598	-1.23943
H	0.32995	-1.48292	-1.22992
H	1.51202	-0.14734	1.22988
H	0.34799	-1.47692	1.23946

Ethane

Heat of Formation = -79.83871

C	-0.14076	-0.65454	0.37030
C	0.14076	0.65454	-0.37030
H	0.20291	-1.52032	-0.20548
H	0.36684	-0.68106	1.34028
H	1.21215	0.78569	-0.55513
H	-0.36684	0.68106	-1.34028
H	-0.20291	1.52032	0.20548
H	-1.21215	-0.78569	0.55513

Hexanes

Heat of Formation = -237.10497

C	-0.76632	0.02456	0.00000
C	-1.33586	1.44885	0.00000
C	0.76632	-0.02456	0.00000
C	1.33586	-1.44885	0.00000
C	2.86683	-1.48805	0.00000
C	-2.86683	1.48805	0.00000
H	-1.14729	-0.51733	0.87764
H	-1.14729	-0.51733	-0.87764
H	-0.95626	1.99032	-0.87716
H	-0.95626	1.99032	0.87716
H	1.14729	0.51733	0.87764
H	1.14729	0.51733	-0.87764
H	0.95626	-1.99032	-0.87716
H	0.95626	-1.99032	0.87716

H	3.24204	-2.51681	0.00000
H	3.27553	-0.98490	-0.88375
H	3.27553	-0.98490	0.88375
H	-3.24204	2.51681	0.00000
H	-3.27553	0.98490	-0.88375
H	-3.27553	0.98490	0.88375

1B.9. References

1. Ball, M. *et al.* Conjugated Macrocycles in Organic Electronics. *Acc. Chem. Res.* (2019). doi:10.1021/acs.accounts.9b00017
2. Krömer, J. *et al.* Synthesis of the First Fully α-Conjugated Macrocyclic Oligothiophenes: Cyclo[n]thiophenes with Tunable Cavities in the Nanometer Regime. *Angew. Chem. Int. Ed.* **39**, 3481–3486 (2000).
3. Nakao, K. *et al.* Giant Macrocycles Composed of Thiophene, Acetylene, and Ethylene Building Blocks. *J. Am. Chem. Soc.* **128**, 16740–16747 (2006).
4. Darzi, E. R. *et al.* Synthesis, Properties, and Design Principles of Donor–Acceptor Nanohoops. *ACS Cent. Sci.* **1**, 335–342 (2015).
5. Ball, M. *et al.* Chiral Conjugated Corrals. *J. Am. Chem. Soc.* **137**, 9982–9987 (2015).
6. Ito, H. *et al*. Thiophene-Based, Radial pi-Conjugation: Synthesis, Structure, and Photophysical Properties of Cyclo-1,4-phenylene-2 ',5 '-thienylenes. *Angew. Chem. Int. Ed.* **54**, 159–163 (2015).
7. Xue, J. Y. *et al.* Aromatic hydrocarbon macrocycles for highly efficient organic light-emitting devices with single-layer architectures. *Chem. Sci.* **7**, 896–904 (2016).
8. Kayahara, E. *et al*. Synthesis and Characterization of {[}n]CPP (n=5, 6, 8, 10, and 12) Radical Cation and Dications: Size-Dependent Absorption, Spin, and Charge Delocalization. *J. Am. Chem. Soc.* **138**, 338–344 (2016).
9. Kayahara, E. *et al*. Size Dependence of {[}n]Cycloparaphenylenes (n=5-12) in Electrochemical Oxidation. *Chem. Asian J.* **11**, 1793–1797 (2016).
10. Zhang, B. *et al.* Rigid, Conjugated Macrocycles for High Performance Organic Photodetectors. *J. Am. Chem. Soc.* **138**, 16426–16431 (2016).
11. Ball, M. *et al.* Macrocyclization in the Design of Organic n-Type Electronic Materials. *J. Am. Chem. Soc.* **138**, 12861–12867 (2016).
12. Van Raden, J. *et al*. Synthesis and characterization of a highly strained donor-acceptor nanohoop. *Org. Biomol. Chem.* **14**, 5721 (2016).
13. Peeks, M. D. *et al*. Aromatic and antiaromatic ring currents in a molecular nanoring. *Nature* **541**, 200 (2017).
14. Zang, L. *et al*. One-Dimensional Self-Assembly of Planar π-Conjugated Molecules: Adaptable Building Blocks for Organic Nanodevices. *Acc. Chem. Res.* **41**, 1596–1608 (2008).
15. Izumi, T. *et al.* Efficient Blue Electroluminescence from a Single-layer Organic Device

Composed Solely of Hydrocarbons. *Chem. Asian J.* **12**, 730–733 (2017).

16. Nishigaki, S. *et al.* Synthesis, Structures, and Photophysical Properties of Alternating Donor–Acceptor Cycloparaphenylenes. *Chem. Eur. J.* **23**, 7227–7231 (2017).
17. Thakellapalli, H. *et al.* Synthesis and Properties of Conjugated Macrocycles Containing 2,7-Bis(2-thienyl)-9H-fluoren-9-one Units. *Org. Lett.* **19**, 2674–2677 (2017).
18. Li, T. *et al.* Synthesis, solvent-dependent emission and two- photon absorption of a triangular -{[}D-pi-A](3)- macrocycle. *Org. Chem. Front.* **4**, 737–742 (2017).
19. Hahn, S. *et al.* Synthesis and Characterization of Heterobenzenacyclooctaphanes Derived from Cyclotetrabenzoin. *Chem. Eur. J.* **23**, 10543–10550 (2017).
20. Van Raden, J. *et al*. 2,2′-Bipyridyl-Embedded Cycloparaphenylenes as a General Strategy To Investigate Nanohoop-Based Coordination Complexes. *J. Am. Chem. Soc.* **139**, 2936–2939 (2017).
21. Kayahara, E. *et al.* Gram-Scale Syntheses and Conductivities of [10]Cycloparaphenylene and Its Tetraalkoxy Derivatives. *J. Am. Chem. Soc.* **139**, 18480–18483 (2017).
22. Zhang, F. *et al*. Giant Cyclo n thiophenes with Extended pi Conjugation. *Angew. Chem. Int. Ed.* **48**, 6632–6635 (2009).
23. Fenwick, O. *et al.* Linear and Cyclic Porphyrin Hexamers as Near-Infrared Emitters in Organic Light-Emitting Diodes. *Nano Lett.* **11**, 2451–2456 (2011).
24. Zhang, F. *et al.* Molecular and electronic structure of cyclo[10]thiophene in various oxidation states: polaron pair vs. bipolaron. *Chem. Sci.* **2**, 781–784 (2011).
25. Iyoda, M. *et al*. Conjugated Macrocycles: Concepts and Applications. *Angew. Chem. Int. Ed.* **50**, 10522–10553 (2011).
26. Jiang, H.-W. *et al.* Cyclic 2,12-Porphyrinylene Nanorings as a Porphyrin Analogue of Cycloparaphenylenes. *J. Am. Chem. Soc.* **137**, 2219–2222 (2015).
27. Kuwabara, T. *et al*. Curved Oligophenylenes as Donors in Shape-Persistent Donor–Acceptor Macrocycles with Solvatofluorochromic Properties. *Angew. Chem. Int. Ed.* **54**, 9646–9649 (2015).
28. Chen, Q. *et al.* Strain-Induced Stereoselective Formation of Blue-Emitting Cyclostilbenes. *J. Am. Chem. Soc.* **137**, 12282–12288 (2015).
29. Iwamoto, T. *et al*. Size-Selective Encapsulation of C60 by [10]Cycloparaphenylene: Formation of the Shortest Fullerene-Peapod. *Angew. Chem. Int. Ed.* **50**, 8342–8344 (2011).
30. Kylberg, W. *et al.* Oligothiophene dendron-decorated squaraine dyes: Synthesis, thin film formation, and performance in organic solar cells. *Org. Electron.* **13**, 1204–1212 (2012).
31. Iwamoto, T. *et al.* Size- and Orientation-Selective Encapsulation of C70 by Cycloparaphenylenes. *Chem. Eur. J.* **19**, 14061–14068 (2013).
32. Nakanishi, Y. *et al.* Size-Selective Complexation and Extraction of Endohedral Metallofullerenes with Cycloparaphenylene. *Angew. Chem. Int. Ed.* **53**, 3102–3106 (2014).
33. Zhang, B. *et al.* Hollow organic capsules assemble into cellular semiconductors. *Nat. Commun.* **9**, 1957 (2018).

34. Dou, L. *et al.* 25th Anniversary Article: A Decade of Organic/Polymeric Photovoltaic Research. *Adv. Mater.* **25**, 6642–6671 (2013).

35. Savoie, B. M. *et al.* Unequal Partnership: Asymmetric Roles of Polymeric Donor and Fullerene Acceptor in Generating Free Charge. *J. Am. Chem. Soc.* **136**, 2876–2884 (2014).

36. Anthony, J. E. *et al*. n-Type Organic Semiconductors in Organic Electronics. *Adv. Mater.* **22**, 3876–3892 (2010).

37. Sharenko, A. *et al.* A High-Performing Solution-Processed Small Molecule: Perylene Diimide Bulk Heterojunction Solar Cell. *Adv. Mater.* **25**, 4403–4406 (2013).

38. Cai, Y. *et al.* High Performance Organic Solar Cells Based on a Twisted Bay-Substituted Tetraphenyl Functionalized Perylenediimide Electron Acceptor. *Adv. Energy Mater.* **5**, 1500032 (2015).

39. Zhou, E. J. *et al.* All-Polymer Solar Cells from Perylene Diimide Based Copolymers: Material Design and Phase Separation Control. *Angew. Chem. Int. Ed.* **50**, 2799–2803 (2011).

40. Li, C. *et al*. Perylene Imides for Organic Photovoltaics: Yesterday, Today, and Tomorrow. *Adv. Mater.* **24**, 613–636 (2012).

41. Ball, M. *et al.* Contorted Polycyclic Aromatics. *Acc. Chem. Res.* **48**, 267–276 (2015).

42. Zhong, Y. *et al.* Helical Ribbons for Molecular Electronics. *J. Am. Chem. Soc.* **136**, 8122–8130 (2014).

43. Nolde, F. *et al*. Synthesis and self-organization of core-extended perylene tetracarboxdiimides with branched alkyl substituents. *Chem. Mater.* **18**, 3715–3725 (2006).

44. Meng, D. *et al.* High-Performance Solution-Processed Non-Fullerene Organic Solar Cells Based on Selenophene-Containing Perylene Bisimide Acceptor. *J. Am. Chem. Soc.* **138**, 375–380 (2016).

45. Yan, Q. F. *et al*. Conjugated Dimeric and Trimeric Perylenediimide Oligomers. *Org. Lett.* **11**, 3426–3429 (2009).

46. Huo, L. J. *et al*. Synthesis and absorption spectra of n-type conjugated polymers based on perylene diimide. *Macromol. Rapid Commun.* **29**, 1444–1448 (2008).

47. Wuerthner, F. *et al.* Perylene Bisimide Dye Assemblies as Archetype Functional Supramolecular Materials. *Chem. Rev.* **116**, 962–1052 (2016).

48. Ball, M. L. *et al.* Influence of Molecular Conformation on Electron Transport in Giant, Conjugated Macrocycles. *J. Am. Chem. Soc.* **140**, 10135–10139 (2018).

49. Fujitsuka, M. *et al*. Size-dependent fluorescence properties of n cycloparaphenylenes (n=8-13), hoop-shaped pi-conjugated molecules. *Phys. Chem. Chem. Phys.* **14**, 14585–14588 (2012).

50. Darzi, E. R. *et al*. An Operationally Simple and Mild Oxidative Homocoupling of Aryl Boronic Esters To Access Conformationally Constrained Macrocycles. *J. Am. Chem. Soc.* **139**, 3106–3114 (2017).

51. Evans, P. J. *et al*. Efficient room-temperature synthesis of a highly strained carbon

nanohoop fragment of buckminsterfullerene. *Nat. Chem.* **6**, 404–408 (2014).

52. Iwamoto, T. *et al*. Selective and Random Syntheses of n Cycloparaphenylenes (n=8-13) and Size Dependence of Their Electronic Properties. *J. Am. Chem. Soc.* **133**, 8354–8361 (2011).

53. Ahrens, M. J. *et al*. Bis(n-octylamino)perylene-3,4:9,10-bis(dicarboximide)s and Their Radical Cations: Synthesis, Electrochemistry, and ENDOR Spectroscopy. *J. Org. Chem.* **71**, 2107–2114 (2006).

54. Osswald, P. *et al*. Effects of Bay Substituents on the Racemization Barriers of Perylene Bisimides: Resolution of Atropo-Enantiomers. *J. Am. Chem. Soc.* **129**, 14319–14326 (2007).

55. Chen, Z. *et al*. Effect of Core Twisting on Self-Assembly and Optical Properties of Perylene Bisimide Dyes in Solution and Columnar Liquid Crystalline Phases. *Chem. Eur. J.* **13**, 450–465 (2007).

56. Goretzki, G. *et al.* Bis-morpholine-Substituted Perylene Bisimides: Impact of Isomeric Arrangement on Electrochemical and Spectroelectrochemical Properties. *J. Org. Chem.* **73**, 8808–8814 (2008).

57. Dubey, R. K. *et al*. 1,7- And 1,6-Regioisomers of Diphenoxy and Dipyrrolidinyl Substituted Perylene Diimides: Synthesis, Separation, Characterization, and Comparison of Electrochemical and Optical Properties. *Chem. Mater.* **23**, 778–788 (2011).

58. Würthner, F. *et al.* Perylene Bisimide Dye Assemblies as Archetype Functional Supramolecular Materials. *Chem. Rev.* **116**, 962–1052 (2016).

59. Anslyn, E. V. & Dougherty, D. A. *Modern Physical Organic Chemistry*. (University Science Books, 2006).

60. George, P. *et al*. An alternative approach to the problem of assessing stabilization energies in cyclic conjugated hydrocarbons. *Theor. Chim. Acta* **38**, 121–129 (1975).

61. Bachrach, S. M. *et al*. DFT Study of Cycloparaphenylenes and Heteroatom-Substituted Nanohoops. *J. Org. Chem.* **75**, 6595–6604 (2010).

62. Segawa, Y. *et al*. Theoretical Studies on the Structures and Strain Energies of Cycloparaphenylenes. *Org. Lett.* **12**, 2262–2265 (2010).

63. Li, Y. *et al.* Synthesis and Properties of Ethylene-Annulated Di(perylene diimides). *Org. Lett.* **14**, 5278–5281 (2012).

64. White, B. M. *et al.* Expanding the Chemical Space of Biocompatible Fluorophores: Nanohoops in Cells. *ACS Cent. Sci.* **4**, 1173–1178 (2018).

Chapter 2. Chiral Conjugated Corrals

2.1. Preface

Chapter 2 is reproduced with permission from the authors: Melissa Ball, Brandon Fowler, Panpan Li, Leo A. Joyce, Fang Li, Taifeng Liu, Daniel W. Paley, Yu Zhong, Hexing Li, Shengxiong Xiao, Fay Ng, Michael L. Steigerwald, and Colin Nuckolls published in the *Journal of the American Chemical Society*.[1] Copyright 2015 American Chemical Society. I synthesized all compounds, with valuable input from Shengxiong Xiao and coworkers. I performed calculations with essential input from Michael L. Steigerwald. Brandon Fowler and I performed HPLC experiments**.** Daniel W. Paley performed XRD analysis. Leo A. Joyce performed circular dichroism experiments. Yu Zhong performed CV.

2.2. Introduction

This manuscript describes the design, synthesis and study of a new type of conjugated aromatic macrocycle formed from the linkage of donor and acceptor subunits into a strained cycle (Figure 2.1.). These macrocycles are members of an ever-growing class of cyclic, conjugated belts, such as, CPPs[2–24] and cycloporphyrins (CPs).[25–34] CPPs consist of para-connected phenylene rings and possess size-dependent optical and electronic properties.[21] However, CPPs do not absorb at a sufficiently broad part of the visible spectrum for them to be useful in optoelectronic devices. The optical gaps for CPs are smaller, but they have not been used in devices.[17] Alternation of electron donor and acceptor subunits is a proven strategy to engineer the energetics of linear, conjugated oligomers and polymers, but it has not been explored in the context of conjugated, cyclic oligomers.[35–37]

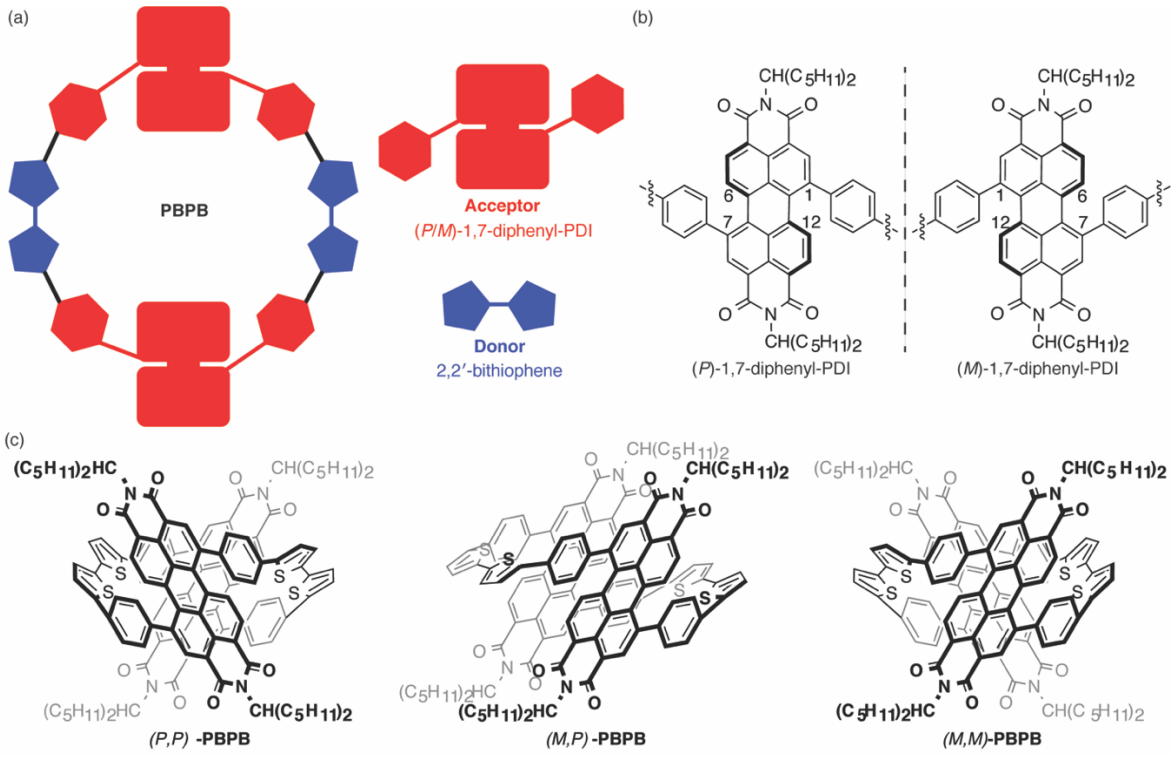

Figure 2.1. (a) Schematic structure of the -a-b-a-b pattern for **PBPB**. (b) The stereoisomerism of **PBPB** results from the chirality of the (*P*)- and (*M*)-*1,7*-diphenyl-PDI (1.1) subunits. (c) **PBPB** exists in chiral [(*P,P*)-**PBPB** and (*M,M*)-**PBPB**] and meso [(*M,P*)-**PBPB**] forms.

For this study, we designed and synthesized the molecules shown in Figure 2.1, comprising a PDI and a phenyl-bithiophene-phenyl linker. We incorporated PDI as the electron acceptor in **PBPB**'s design because PDI derivatives have shown a number of desirable behaviors for organic electronics, as discussed in Chapter 1. We employed oligothiophenes as the electron-rich counterpart because they are ubiquitous as electron-donor molecules in electronic materials. Each of these macrocycles has a persistent, elliptiform cavity that is lined with electron deficient π-faces of the PDI and the lone pairs of the sulfur atoms from the thiophene subunits. We named these molecules **PBPB** reflecting their ability to perform intramolecular charge transfer upon excitation. The macrocycle is black in color and has a broad absorption spectrum that spans the entire visible range. The onset of strong absorbance occurs at approximately 700 nm (HOMO-to-LUMO excitation at 1.8 eV), hinting at **PBPB**'s favorable prospects as optical materials (*vida infra*

Chapter 3). Furthermore, we find **PBPB** exists in a dynamical equilibrium between both chiral-[(*P*,*P*)-**PBPB** and (*M*,*M*)-**PBPB**] and meso-[(*M*,*P*)-**PBPB**] forms due to the handedness of the helical PDI subunits (Chapter 1B.4, Figure 2.1). The essential point of this study is that this new -a-b-a-b- motif for cyclic conjugated molecules (Figure 2.1a) provides interesting chiral information and an unusual electronic structure.

2.3. Synthesis of PBPB

Our synthesis is based on the strategies developed by Bäuerle[2,18] and Yamago[21] in the syntheses of conjugated macrocycles via square planar platinum intermediates. Figure 2.2 displays the synthesis of **PBPB**.

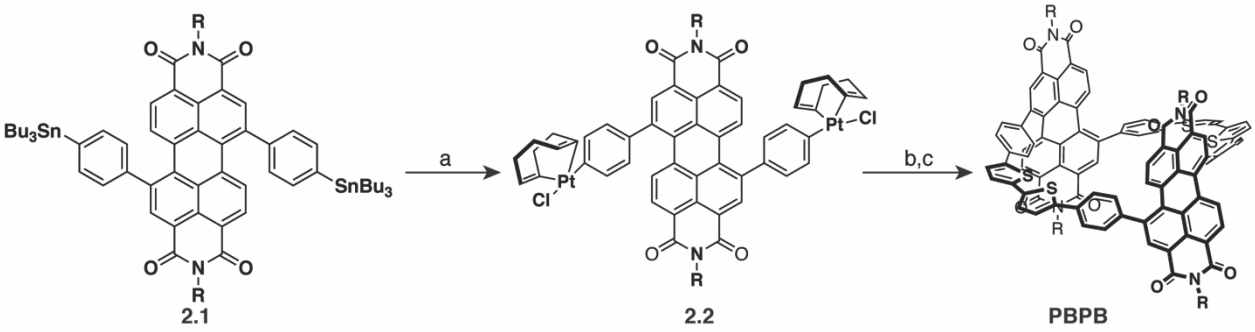

Figure 2.2. Scheme for synthesis of PBPB. (a) $Pt(COD)Cl_2$, toluene, 100 °C, 24.5 h 63% yield. (b) 5,5′ bis(trimethylstannyl)-2,2′-bithiophene, THF, 55 °C, 48 h. (c) PPh_3, toluene, 100 °C, 12 h, 49% yield (2 steps).

The key intermediate is the bis-platinated diphenyl-PDI, **2.2**. We synthesize this important building block by a double Stille coupling of 1,4-bis(tributylstannyl)benzene with the 1,7-dibromo-PDI to afford the bis-tributyltin substituted aromatic, **2.1**. Transmetalation of **2.1** with dichloro(1,5-cyclooctadiene)platinum(II) provides **2.2**. We heat equimolar amounts of **2.2** and 5,5′-bis(trimethylstannyl)-2,2′-bithiophene for 48 h to afford a tetra-platinum intermediate. This organometallic intermediate macrocycle proved difficult to isolate, so we carried the crude material on to the ultimate product by heating it with excess triphenylphosphine. This initiates the four-fold reductive elimination that forms **PBPB**. I found the yield was concentration dependent.

If we perform the macrocyclization step at 20 mili-molar (mM), then we isolate **PBPB** in a 16% yield over the two steps. Yet if we run the macrocyclization step at 3.0 mM, **PBPB** is isolated in a 49% yield (over the two steps), as lower concentrations promote macrocyclization. This yield is exceptional given that it incorporates two steps (macrocyclization and reductive elimination) without a template to yield a complex, strained macrocycle.

Scrambling of aryl-tin/aryl-platinum bonds has been observed in the formation of platinum macrocycles from unsubstituted aromatics;[21,24] such scrambling is suppressed here due to the electron deficiency of the PDI subunit. Others have found scrambling less pronounced when aryl groups possessed electron-withdrawing substituents.[38,39] We find no evidence of scrambling in the Pt–phenyl bond in **2.2** when heated to 50 °C with tributyltin chloride for 48 h. The lack of reversibility is a new design feature that allows the synthesis, for the first time, of conjugated macrocycles with an alternating -a-b-a-b- pattern.

2.4. Single Crystal Analysis of PBPB

The structure of **PBPB** was unambiguously confirmed via single crystal XRD (SCXRD). Figure 2.3 shows the relationship between two **PBPB** adjacent diphenyl subunits with their π faces orthogonal to the b axis, the direction of the π-stacked wires. **PBPB** can exist as one of three different stereoisomers (a *P*- or *M*-enantiomer and a meso form), but exists as the two enantiomers in the solid-state. Neighboring diphenyl PDIs have opposite handedness, such that, a *P* enantiomer (red molecule in Figure 2.3a) always packs with the *M* stereoisomer (blue molecule).[40] The interaction between adjacent PDIs in the stack can be thought of as a left hand clasping a right hand. This, in turn, maximizes the π-π interaction between adjacent molecules by positioning the π faces within ~3.7 Å of each other. Neighboring macrocycles are orthogonal and create a one-dimensional wires down the b axis. Section 2.12 contains crystallographic information.

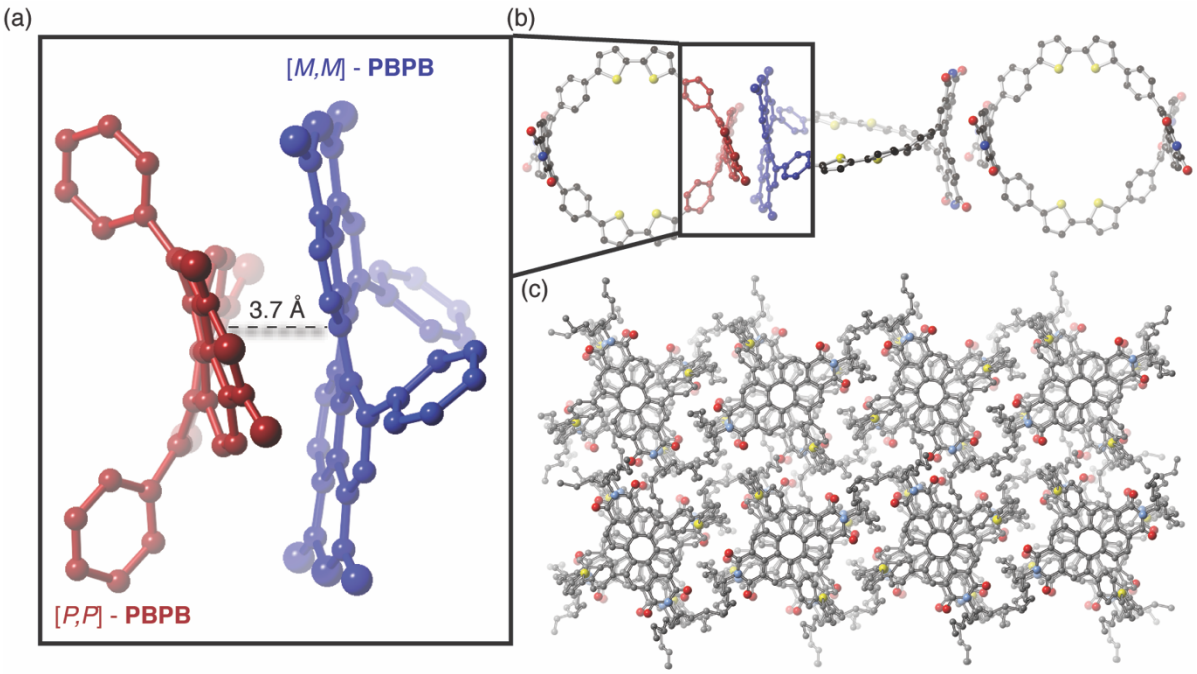

Figure 2.3. (a) Two adjacent diphenyl PDIs. The shortest PDI-PDI distance is ~3.7 Å. Only one PDI unit of (*P*,*P*)-**PBPB** (red) and (*M*,*M*)-**PBPB** (blue) is shown; (b) a one-dimensional molecular wire formed from π-π interactions between neighboring macrocycles viewed down the a axis. Side chains and hydrogen atoms have been removed for clarity; and (c) a view down the b axis showing adjacent PBPB wires. Carbon = gray, nitrogen = blue, oxygen = red, sulfur = yellow. Hydrogen atoms have been removed to clarify the view.

2.5. NMR Studies of PBPB

While the ^{1}H NMR spectrum of **PBPB** contains several broad peaks in the aromatic region at room temperature, suggesting that dynamical processes (rotation of the phenyl rings and the undecyl sidechains)[41] occur on the NMR timescale (Figure 2.9), acquiring the NMR data at 88 °C (in 1,1,2,2-tetrachloroethane-d_2), however, provides a well-resolved ^{1}H NMR spectrum (Figure 2.4a). In the downfield region of the spectrum (Figure 2.4a), we observe resonances consistent with the macrocycle alongside a smaller set of resonances that have analogous splitting and multiplicity. This pattern suggests that **PBPB** exists as two closely related isomers, and integration of the resonances reveals that the two isomers occur in a ratio of approximately 6:1 (at 87 °C). The gas phase calculations provide a ratio of 316:1 at 87 °C (Section 2.16). The effects of the medium,

solvation, dielectric constant, and guest inclusion must account for the difference between the calculated and the observed ratios. We attempted to find the coalescence point of the two isomers using variable temperature NMR, however, full coalescence was not observed even at temperatures of 147 °C.

The two sets of resonances we observe in the NMR in Figure 2.4a are a result of stereoisomerism. The diphenyl PDI moiety, when linked in the *1,7*-position and constrained in a macrocycle, introduces chirality (Chapter 1B, Figure 1B.3). With this information in hand, we used DFT to determine energy-optimized structures for the stereoisomers, and these are represented in Figures 2.4b and 2.4c. When linked together by a pair of bithiophenes, two diphenyl-PDI subunits possessing the same chirality produce a pair of enantiomers [(*P*,*P*)-**PBPB** and (*M*,*M*)-**PBPB**]. Alternatively, linking two PDI subunits with opposite chirality produces an achiral, meso form [(*P*,*M*)-**PBPB**, Figure 2.4c.]. The enantiomeric forms of **PBPB** have an effective C_2 axis with respect to two PDIs in the macrocycle. The achiral, meso isomer, contains a mirror plane between the two PDIs. Both the chiral and meso forms of **PBPB** have PDI core structures that resemble the diphenyl-PDI conformation. The twist of the PDI core in the meso isomer is the same as that of the diphenyl PDI derivative, 22° (Figure 1B.3 and Figure 2.7); whereas, the chiral isomer has a larger twist in its PDI subunit (25°, shown in Figure 2.4b). We believe this twist and orientation of the phenyls facilitates formation of **PBPB** by giving curvature to the otherwise planar PDI**.**

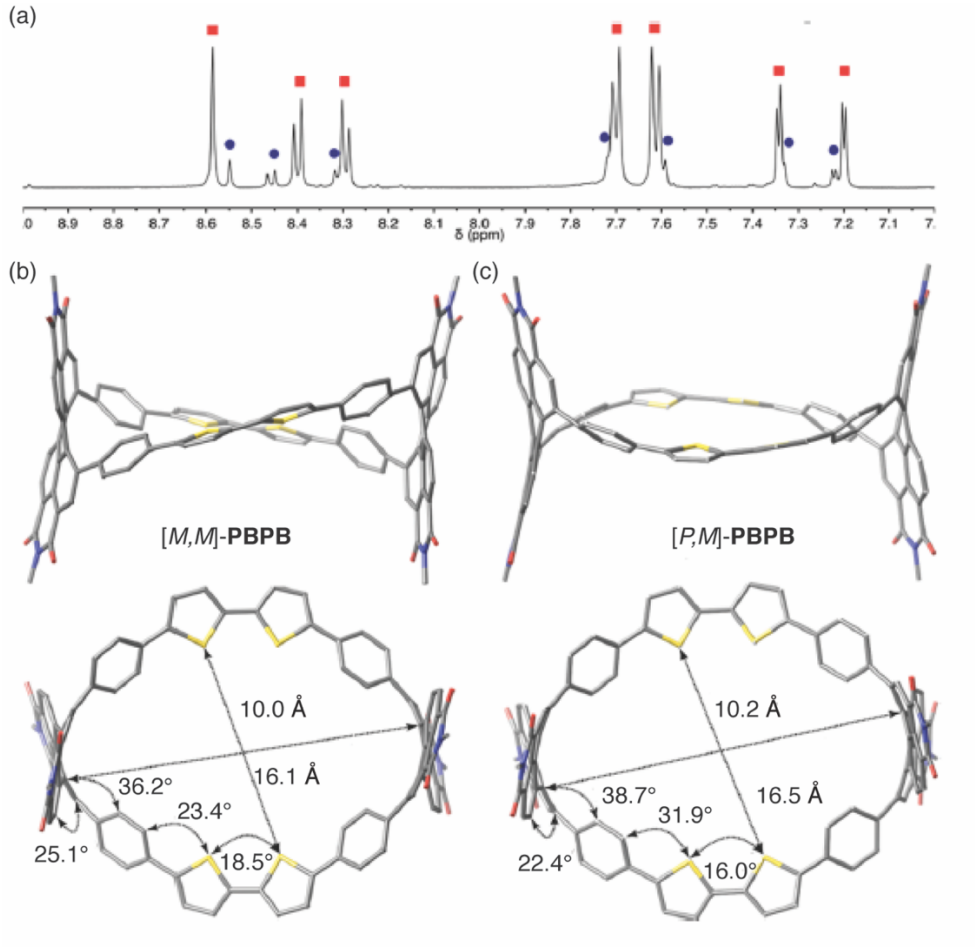

Figure 2.4. (a) Downfield region of the ^{1}HNMR spectrum of macrocycle **PBPB** recorded at 88 °C. The red squares (chiral) and blue circles (achiral) identify resonances from the two stereoisomers. (b) DFT minimized model (side-on and face-on views) of chiral stereoisomer (*M*,*M*)-**PBPB**. (c) DFT minimized model (side-on and face-on views) of meso stereoisomer (*P*,*M*)-**PBPB** (undecyl sidechains have been truncated to a methyl group to simplify the calculations). Carbon = grey, nitrogen = blue, oxygen = red, sulfur = yellow. Hydrogens have been removed to clarify the view.

2.6. Bithiophene Acts as Strain Reliever

In both stereoisomers of **PBPB**, the macrocycle has a persistent elliptiform cavity, measuring 1.6 nm from PDI to PDI and 1.2 nm from bithiophene to bithiophene. One striking difference between these two stereoisomers is the apparent strain in the tetracyclic linkers connecting the PDIs. The meso isomer forces the linkers to bow in order to accommodate the rigidity of the cycle (Figure 2.4c), while in the chiral isomer the tetracyclic linkers are essentially

flat (Figure 2.4b), which make the chiral isomer appear less strained. In both isomers, the sulfur atoms of the four thiophenes point into the cavity while the diphenyl PDIs cap the ends of the macrocycle. Oligothiophenes typically possess an anti-geometry of their sulfur atoms rather than syn orientation, reflecting decreased steric repulsion in the former.[42–44] However, this is not the case for **PBPB**. The bithiophene orientation plays a crucial role in the assembly of **PBPB** by relieving strain. In order to quantify this effect, we modeled the syn and anti conformers of simple bithiophene, $C_8H_6S_2$. The angle between the two terminal C-H bond vectors defines the curvature supported by the bithiophene. This angle is 117° in the syn geometry and 180° in the anti geometry. Thus, the syn orientation of the bithiophene promotes the formation and stabilization of **PBPB**. Conversely, the incorporation of the bithiophenes into **PBPB** promotes the otherwise unfavorable syn orientation in the bithiophenes. Reports from Bäuerle and Itami describe a similar conformation preference in macrocyclic, 2,5-linked oligothiophenes.[9,18]

2.7. HPLC Analysis of Stereoisomers

Chiral Higher Performance Liquid Chromatography (HPLC) allowed us to separate and characterize the stereoisomers of **PBPB**. The chromatogram of **PBPB** (Figure 2.5a) shows both the pair of enantiomers and the meso isomer. In the chromatogram, peaks **A** and **C** have equal integrated intensity and therefore represent the enantiomeric pair. A third peak, **B**, corresponds to the meso stereoisomer. Using HPLC with a circular dichroism (CD) detector, we were able to confirm this assignment (Figure 2.5b). The two peaks in the chromatogram assigned to the two enantiomers gave opposite CD signals (225–800 nm, Figures 2.5b & 2.5c). As anticipated, the peak assigned to the meso compound had no detectable CD signal.

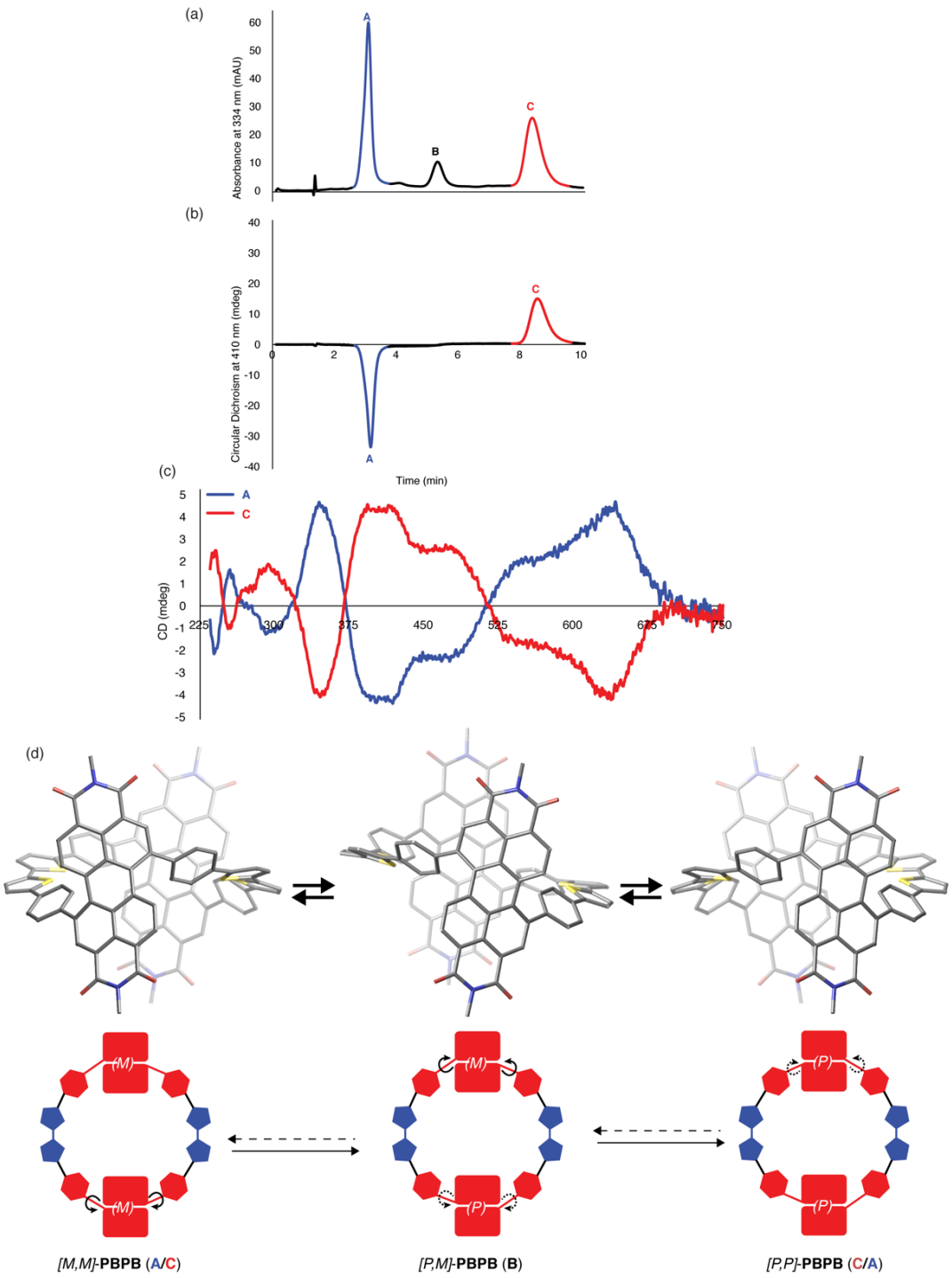

Figure 2.5. (a) HPLC chromatogram of **PBPB** using a CHIRALPAK® IA-3 column. (b) HPLC-CD chromatogram of **PBPB** showing peaks A and C exhibit opposite optical activity (270–410 nm). (c) CD spectra for both enantiomers of **PBPB**. (D) Interconversion of the stereoisomers of **PBPB** by sequential rotation of one PDI subunit through the macrocycle and then rotation of the other PDI to convert between enantiomers. The hydrocarbon sidechains have been replaced with a methyl group in the DFT structures. Carbon = grey, nitrogen = blue, oxygen = red, sulfur = yellow. Hydrogen atoms have been removed to clarify the view.

2.8. Intramolecular Somersault Mode of Isomerization

It is interesting that **A** and **C** interconvert at room temperature, albeit not directly; the interconversion requires the intermediacy of **B**, the meso compound. To confirm the intermediacy of **B**, we used preparative HPLC. We obtained a pure fraction of **C**, and immediately re-injected it into the HPLC and monitored for the appearance of the **A** and **B** stereoisomers (Figure 2.6). Within 20 min, the concentration of **B** had already reached 62% of its equilibrium value, yet that of **A** had reached only 8% of its equilibrium value. After 2 h at room temperature, all peaks had reached their equilibrium intensities (Figure 2.6b). This result is remarkable because it suggests the mode of isomerization is a PDI 'intramolecular somersault' in which one of the PDIs rotates around its transverse axis, thereby moving one of its diimide heads through the plane of the cavity. This somersault converts a chiral molecule into an achiral one and vice versa. Figure 2.5d shows a schematic of this conversion process between **A** and **B**.

We were also interested in the rate of interconversion, and we used variable temperature HPLC to study this process. Maintaining the temperature of both the HPLC column and the sample at 0 °C, we analyzed the freshly isolated *meso* isomer, **B**, monitoring its conversion to both of the enantiomers (**A**/**C**) over time. Figure 2.11 shows the natural log of the diastereomeric excess as a function of time. If we assume this process is a simple first-order reaction, the rate constant was $\sim 10^{-4}$ s^{-1} at 0 °C. It is difficult to relate this rate to other macrocycles, given there have been just a few kinetic studies concerning the racemization of conjugated belt-like compounds. Yet, we see experimentally that equilibrium is reached within two hours at room temperature as discussed above.

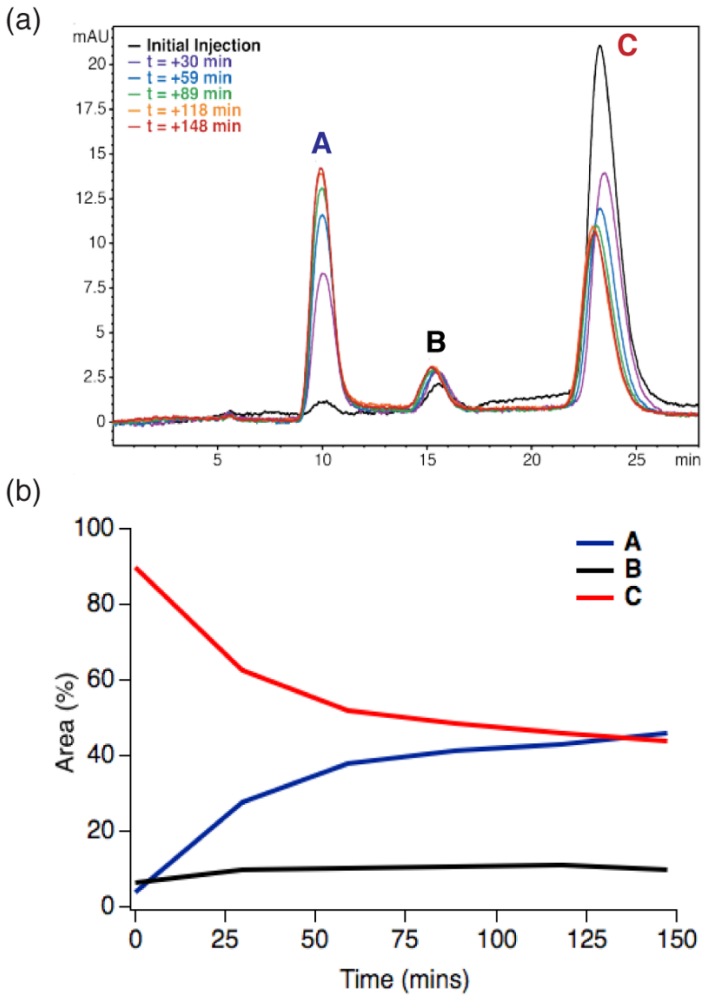

Figure 2.6. (a) The interconversion of **C** to **A** through the intermediacy of **B**. (b) Plot of relative intensities (via integration of the area under each peak) as a function of time.

2.9. Charge Transfer Characteristics in PBPB

The electronic properties of **PBPB** can be appreciated by consideration of its UV-Vis absorption spectrum (Figure 2.7), particularly when compared to the spectra of its constituent parts, *viz*., **1.1**, and a bithiophene derivative. **PBPB** retains the shorter-wavelength absorptions (~300–400 nm) characteristic of bithiophene and the intermediate-wavelength absorptions (~450–550 nm) characteristic of PDIs, but a new, strong absorption band appears at longer wavelength (~550–700 nm). The optical gap is estimated to be 1.8 eV from the absorption band edge. It is the addition of this latter band that completes the absorption of the visible and renders **PBPB** black.

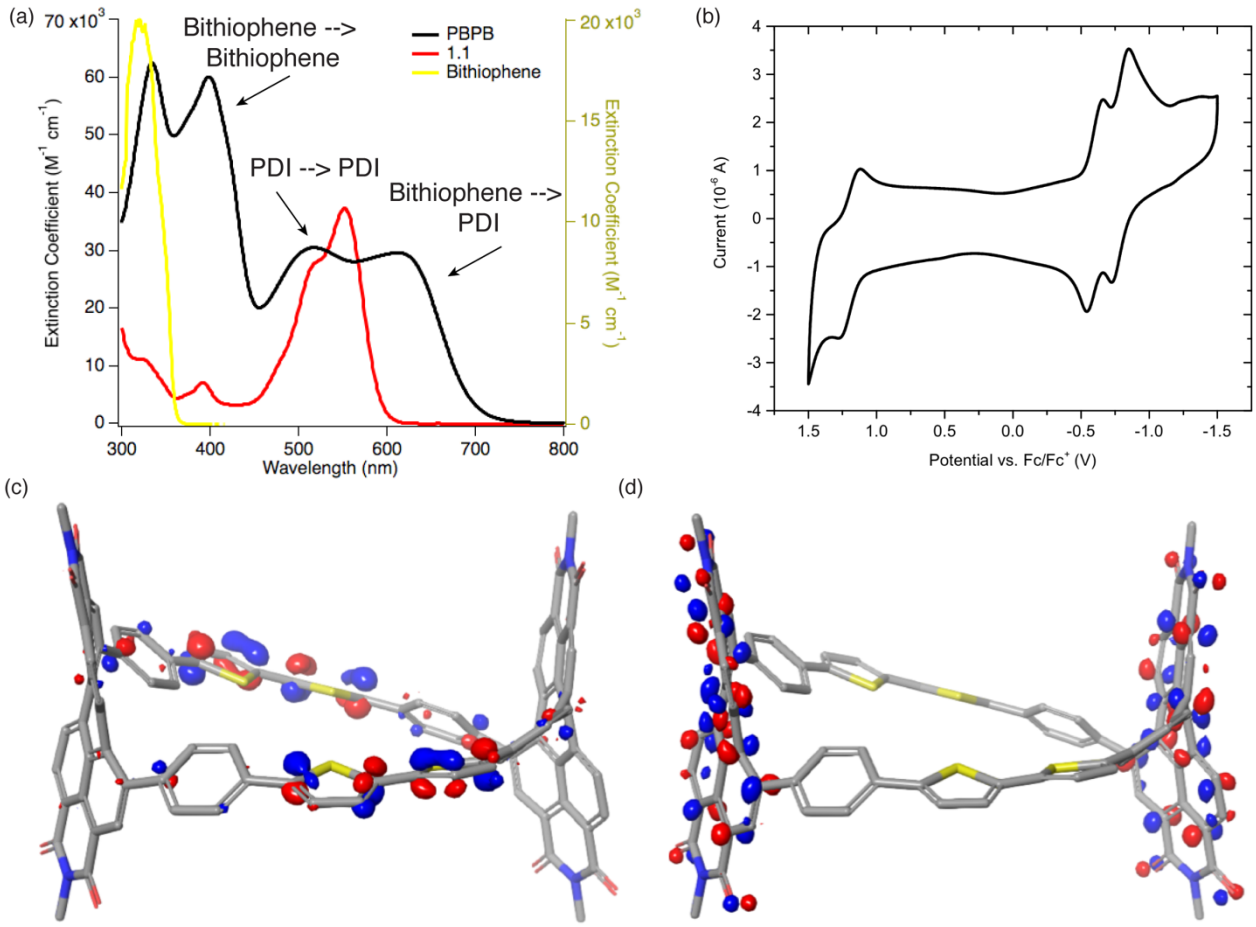

Figure 2.7. (a) UV-vis absorption spectrum of **PBPB** (black line), 5,5′-bis(tributylstannyl)-2,2′-bithiophene (yellow) and 1.1 (diphenyl PDI), red) in CH_2Cl_2 (concentration = 1.6×10^{-5} M, 1.3×10^{-4} and 1.5×10^{-5}, respectively, path length = 1.0 cm). The yellow trace is plotted with respect to the right ordinate, and the black and red traces are plotted with respect to the left ordinate; (b) CV of **PBPB** showing two reversible reduction and one reversible oxidation peak; (c) and (d) the HOMO and LUMO orbitals of **PBPB** from TDDFT, respectively.

The electronic properties of **PBPB** can be appreciated by consideration of its UV-vis absorption spectrum (Figure 2.7a), particularly when compared to the spectra of its constituent parts, *viz*., a helically-deformed PDI (**1.1**), and a bithiophene derivative. **PBPB** retains the shorter-wavelength absorptions (~300–400 nm) characteristic of bithiophene and the intermediate-wavelength absorptions (~450–550 nm) characteristic of PDIs, but a new, strong absorption band appears at longer wavelength (~550–700 nm). The optical gap is estimated to be 1.8 eV from the absorption band edge. It is the addition of this latter band that completes the absorption of the

visible and renders **PBPB** black.

We also studied the energetics of the frontier orbitals of **PBPB** using CV (Figure 2.7b). The onset of the first oxidation (0.58 V) and reduction (–1.07 V) peaks relative to Fc/Fc^+ provide an estimate of the HOMO-LUMO gap (1.6 eV). Similar to other aryl-substituted PDI compounds, **PBPB** has one oxidation and two one-electron reductions, revealing that the PDIs within **PBPB** retain their ability to accept two electrons.[45,46] We also used quantum chemical calculations (TDDFT) to characterize the low-lying excited states of **PBPB**, and found that while there is little charge-transfer from the electron-rich thiophenes to the electron-accepting PDIs in the ground state of the molecule, there is such charge-transfer in the lowest-energy excited states: the long-wavelength absorptions are best viewed as forming bithiophene-to-PDI charge-transfer states (Figure 2.7c-d).

2.10. Conclusion

This Chapter describes a new class of fully-conjugated macrocycles that incorporate donor and acceptors subunits to form a chiral conjugated corral. **PBPB** is the first example of a conjugated macrocycle with alternating aromatic subunits in an -a-b-a-b- pattern. These new macrocycles possess an interesting topology and useful electronic properties that is a result of the pattern written into the cycle. The macrocycle's unusual electronic structure provides a small HOMO/LUMO gap and broad absorbance across the entire visible light spectrum. Excited-state DFT calculations reveal intramolecular charge transfer in the frontier orbitals. Not only does **PBPB**'s conformational dynamics allow for the interconversion of this macrocycle between chiral and achiral forms, but this easy propensity for shape-shifting offers the appealing opportunity for sterically-forgiving host-guest chemistry (Chapter 9). This unusual set of properties makes the macrocycles exciting new candidates for use in energy applications such as in photovoltaics in the

following chapter.

2.11. Additional Thoughts and Observations

It is suggested that the reversibility of the transmetalation step is akin to electrophilic aromatic substitution.[38,39] In the reaction for **PBPB**, once the bithiophene has been transferred to the platinum center, the transmetalation process is reversible, yet he lack of scrambled products in suggest that the mechanism for the back reaction is selective. Figure 2.8 shows a proposed mechanism. In Figure 2.8a, R_1 and R_2 are different structures (e.g. a biphenyl and *p*-terphenyl) with similar electronics. The reversibility step can result in scrambled products.[21]

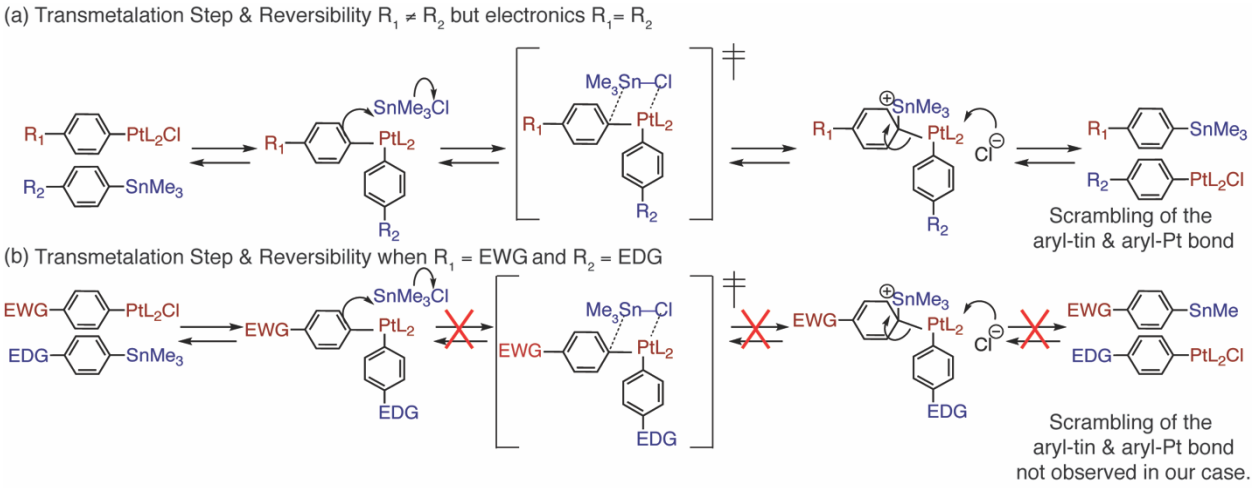

Figure 2.8. (a) A proposed mechanism for the reversibility of the transmetalation step when R_1 and R_2 are different substituents, but have similar electronics; and (b) reversibility is not observed in our system as there is a large difference in the aryl groups electronics e.g. one if electron rich and the other is electron deficient.

Figure 2.8b is an analogous situation to the synthesis of **PBPB**. If R_1 and R_2 possess different electronics e.g. one is electron rich and the other is electron poor, then the electrophilic addition will likely occur on the more electron rich ring (larger density of high energy electrons) theoretically and not from the electron deficient ring as shown in Figure 2.8b. This results in starting material and doesn't provide the opportunity to create scrambled products. This is one possible mechanism that explains the lack of reversibility in the synthesis of **PBPB**.

2.12. Appendix – Supplementary Figures

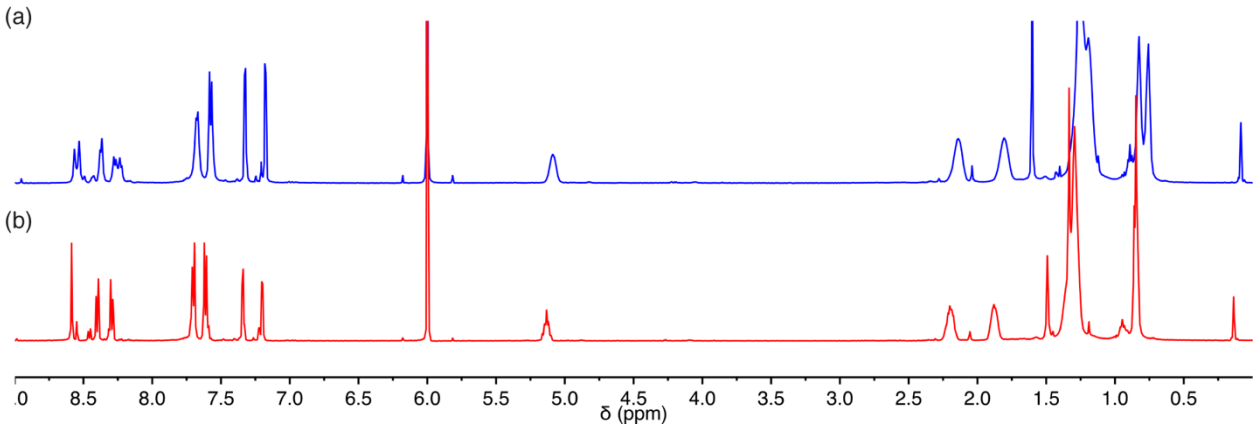

Figure 2.9. (a) ^{1}H NMR of **PBPB** at 300 K in $C_2D_2Cl_4$. (b) ^{1}HNMR of **PBPB** at 360 K in $C_2D_2Cl_4$.

Section 2.5 describes the twist angle of the PDI in **PBPB** relative to diphenyl PDI. Below is also the SCXRD structure of dibromo-diphenyl PDI that shows a 22° twist angle of the two naphthyl units. Two views of the single crystal structure of N,N′-di(6-undecyl)-1,7-di(4-bromophenyl)-perylene-3,4:9,10-tetracarboxylic diimide. Carbon = black, oxygen = red, nitrogen = blue, bromine = brown. Hydrogen atoms are omitted for clarity; in the side-on view the C_{11} chains are also omitted. The $C_{11}H_{23}$ chains were disordered over several positions. In addition, the crystal contained 25% of PDI(C_6H_4Br)(C_6H_5). The minor positions of these disordered atoms are omitted. Thermal ellipsoids are rendered at the 50% level.

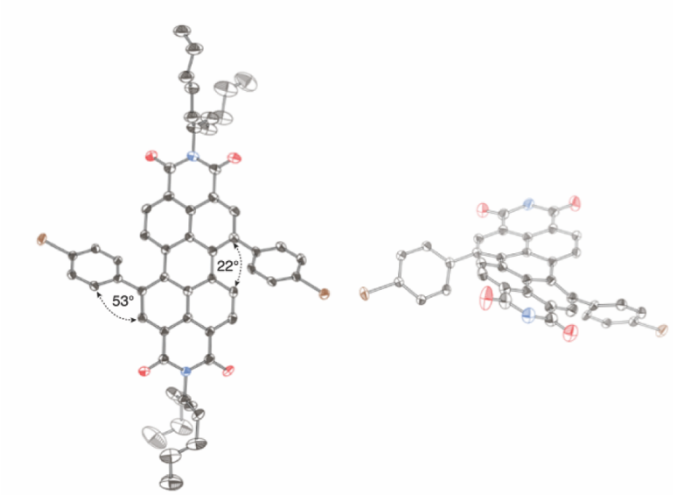

Figure 2.10. Single crystal X-ray structure of *N,N′*-di(6-undecyl)-1,7-di(4-bromophenyl)-perylene-3,4:9,10-tetracarboxylic diimide. (a) Face-on view. (b) Side-on view.

The rapid equilibration of *(P,M)*-**PBPB** into *(P,P)*-**PBPB** and *(M,M)*-**PBPB** was monitored by analytical HPLC using 30% CH_2Cl_2/hexanes at 0 ± 0.2 °C at 1.5 mL/min on a CHIRALPAK® IA-3 column (4.6 mm I.D. x 250 mm, 3 μm). The meso peak was isolated from a preparative HPLC column and injected onto the analytical HPLC within 1 minute before placing in an ice bath. The sample was kept in an ice bath for the first 185 minutes after the initial injection, then allowed to warm to room temperature (solid lines = sample kept at 0 °C; dashed lines = sample kept at 25 °C). Diastereomeric excess (de) was calculated for each HPLC injection and plotted as $\ln(de_0/de_t)$ vs. time, where de_0 is the d_e value for the initial injection and de_t is the d_e at a given time after the initial injection. The rate constant for conversion of the meso diastereomer to the chiral diastereomers is given by the slope.

Equation: $\ln(de_0/de_t) = 2kt$.

Slope = 4.0×10^{-4}; $R^2 = 0.9911$ $k = 1.7 \times 10^{-4}$ s^{-1}

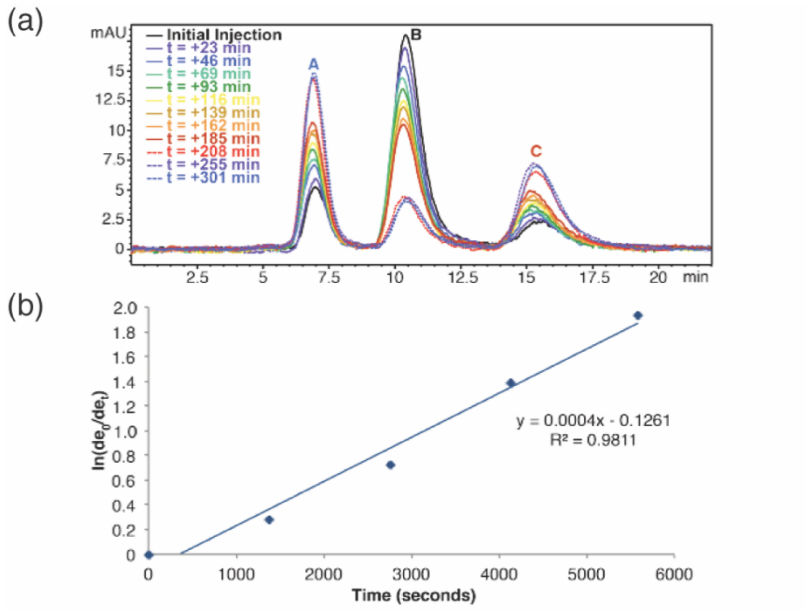

Figure 2.11. (a) Conversion of B into A and C. (b) Plot and linear fit of $\ln(de_0/de_t)$ vs. time.

2.13. General Experimental Information

Synthesis. All reactions were performed in oven-dried or flame-dried round bottom flasks, unless otherwise noted. The flasks were fitted with rubber septa and reactions were conducted under a positive pressure of nitrogen or argon, unless otherwise noted. Anhydrous and anaerobic solvents were obtained from a Glass Contour solvent system consisting of a Schlenk manifold with purification columns packed with activated alumina and supported copper catalyst. Reaction monitoring by thin layer chromatography (TLC) was performed on J.T. Baker Baker-flex Silica Gel IB2-F (25 mm x 75 mm) TLC plates. TLC visualization was accomplished by visible observation and irradiation with a UV lamp. Commercial reagents were used without further purification. $Pt(COD)Cl_2$ was purchased from Strem Chemicals, and all other reagents were purchased from Sigma-Aldrich

Purification. Automated flash chromatography was performed using a Teledyne Isco Combiflash Rf200 and Redisep Rf Silica columns. Preparative high performance liquid chromatography (HPLC) was performed on a Waters Prep150 instrument equipped with a UV-vis detector (335

nm), an automated fraction collector, and a Nacalai Tesque COSMOSIL Buckyprep column (20 mm I.D. x 250 mm, 5 μm).

Spectrometers. ^{1}H NMR spectra were recorded on a Bruker 400 or 500 MHz spectrometer. ^{13}C NMR spectra were recorded on a Bruker 125 or 100 MHz spectrometer with complete proton decoupling. NMR spectra were recorded at 300 K unless otherwise noted. Chemical shifts are reported in parts per million (ppm) Data are represented as follows: chemical shift, multiplicity (s = singlet, d = doublet, dd= doublet of doublets, t = triplet, m = multiplet), coupling constants in Hz, and integration. Broadening (br) of peaks in the 1H NMR spectrum is due to rotational isomers about the imide side chains. **Multiple peaks for the same carbon in the ^{13}C NMR spectrum (indicated by **) reflect rotational isomers about the imide side chains that have been seen previously.[41] This was further confirmed by the HSQC spectrum of Compound **2.2** (pages 64). High-resolution mass spectrometry (HRMS) was performed on a Waters XEVO G2XS instrument equipped with a UPC SFC inlet, electrospray (ESI) and atmospheric pressure chemical (APCI) ionization, and a QToF mass spectrometer. UV-Vis absorption spectra were recorded on a Shimadzu UV-1800 spectrophotometer. Infrared (IR) spectra were recorded on a Perkin Elmer Spectrum400 FTIR spectrometer using a PIKE ATR attachment.

Chirality Analyses. Analytical HPLC was performed on an Agilent 1200 Series instrument equipped with a diode array detector (300 nm to 900 nm) and a CHIRALPAK® IA-3 column (4.6 mm I.D. x 250 mm, 3 μm) from Chiral Technologies. Analytical HPLC-circular dichroism (HPLC-CD) was performed on an Agilent 1100 system comprised of a G1311A quaternary pump, G1367A WPALS auto sampler, G1315B diode array detector, a CD-1595 circular dichroism detector, and a CHIRALPAK® IA-3 column (4.6 mm I.D. x 150 mm, 3 μm) from Chiral Technologies. Full CD spectra (225 nm to 750 nm) were measured on a Jasco 810 CD spectropolarimeter, equipped

with a 0.1 cm microcell and a Julabo thermostat.

HPLC-CD Instrument Method and CD Spectra: **PBPB** Separation was achieved using 30% CH_2Cl_2/hexanes at 20 °C at 1.5 mL/min on a CHIRALPAK® IA-3 column (4.6 mm I.D. x 150 mm, 3 μm). Analytical experiments were performed by injecting 5 μL of a 0.5 mg/mL solution of the macrocycle in CH_2Cl_2. Using this same method of separation, 10 μL of the sample at 0.75 mg/mL were injected, and the corresponding peak fractions were collected manually. The solvent from each fraction (approximately 1-2 mL) was immediately removed, and the remaining compound dissolved in approximately 200 μL CH_2Cl_2. The CD spectrum at 25°C was taken as quickly as possible, and baseline corrected against the CH_2Cl_2 blank.

Cyclic Voltammetry. CVs were recorded on a CH166 electrochemical workstation using Ag/AgCl electrode as the reference electrode at room temperature. Experiments were performed in CH_2Cl_2 with NBu_4PF_6 as the supporting electrolyte at a scan rate of 0.1 V/s.[47]

Single crystal X-ray diffraction.

Diphenyl-dibromo PDI

Data for all compounds was collected on an Agilent SuperNova diffractometer using mirror-monochromated Cu Kα or Mo Kα radiation. Data collection, integration, scaling (ABSPACK) and absorption correction (face-indexed Gaussian integration[48] or numeric analytical methods[49]) were performed in CrysAlisPro.[50] Structure solution was performed using ShelXS,[51] ShelXT,[52] or SuperFlip.[53] Subsequent refinement was performed by full-matrix least-squares on F^2 in ShelXL. Olex2[54] was used for viewing and to prepare CIF files. PLATON[55] was used extensively for SQUEEZE,[56] ADDSYM and TwinRotMat. Many disordered solvent molecules were modeled as rigid fragments from the Idealized Molecular Geometry Library. ORTEP graphics were prepared in CrystalMaker.[57] Thermal ellipsoids are rendered at the 50% probability level. A toluene solution

of PDI($C_6H_4Br)_2$ was diluted with methanol by vapor diffusion to afford bright red prisms. Part of a crystal (0.06 x 0.04 x 0.02 mm) was separated carefully, mounted with STP oil treatment, and cooled to 100 K on the diffractometer. Complete data (99.7%) were collected to 0.815 Å. 37417 reflections were collected (9236 unique, 7420 observed) with R(int) 5.8% and R(sigma) 5.2% after analytical absorption correction (Tmax 0.968, Tmin 0.914). The space group was assigned as $P2_1/c$ based on the systematic absences. The PDI($Ar)_2$ core was located easily and the C_{11} chains were located in two disordered positions. The geometries of the disordered side chains were stabilized with DFIX restraints on 1,2 and 1,3 distances for the intermediate refinements, which were converted to SAME restraints in the final refinement. The last three atoms of one chain were disordered over 3 positions, which were modeled with the aid of SUMP to restrain their total occupancy. All ADPs in the disordered side chains were stabilized with RIGU and SIMU.

In addition, the bromine atoms in the C_6H_4Br groups had significant negative Fourier peaks. The model was revised by splitting the entire group into two positions and freely refining the occupancy of the Br atom in the minor position. This amounted to a three-part disorder with the ratios (major,C-Br):(minor,C-Br):(minor,C-H) 73:13:14 and 76:14:10 for the two independent C_6H_4Br groups. Therefore the crystal was a 76:24 mixture of 1,7-bis(bromophenyl)-PDI and 1-bromophenyl-7-phenyl-PDI. Hydrodehalogenation is a known side reaction in Suzuki couplings.[58] All C-H hydrogens were placed in calculated positions and refined with riding coordinates and isotropic ADPs. The final refinement (9236 data, 2058 restraints, 926 parameters) converged with R_1 ($F_o > 4\sigma(F_o)$) = 5.8%, wR_2 = 13.5%, S = 1.11. The largest Fourier features were 0.59 and -0.45 $e^- A^{-3}$.

PBPB

Data for *trans*-**PBPB** was collected on an Agilent SuperNova diffractometer using mirror-monochromated Cu Kα radiation. Data integration, scaling (ABSPACK) and absorption correction (face-indexed Gaussian integration[48] or numeric analytical methods[49]) were performed in CrysAlisPro.[50] Structure solution was performed using ShelXT.[51] Subsequent refinement was performed by full-matrix least-squares on F2 in ShelXL.[54] Olex2[54] was used for viewing and to prepare CIF files. PLATON[55] was used extensively for SQUEEZE.[56] ORTEP graphics were prepared in CrystalMaker.[57] Thermal ellipsoids are rendered at the 20% probability level.

We grew crystals of **PBPB** for crystallography from a solution of toluene vapor diffused with methanol. A natural crystal (0.10 x 0.07 x 0.05 mm) was mounted with STP oil treatment and cooled to 100 K on the diffractometer. The diffraction was extremely weak and extended to low resolution, with no detectable intensity beyond 1 Å resolution. Complete data (99.3%) were collected to 0.985 Å. 116722 reflections were collected (15869 unique, 8603 observed) with R(int) 10.0% and R(sigma) 6.3% after analytical absorption correction (Tmax .979, Tmin .965).

According to the systematic absences, the space group was Cc or C2/c. Using ShelXT, the structure was solved readily in C2/c with two half-molecules in the asymmetric unit. Each molecule lies on a twofold axis with the PDI fragments normal to the axis. (Most non-H atoms appeared in the initial solution, but all four independent C_{11} side chains were disordered over two or three positions. These disorders were modeled with the aid of absolute (DFIX) restraints on all 1,2 and 1,3 distances, SAME similarity restraints for the two (three) components of each disordered chain, and SIMU restraints on the ADPs of all disordered atoms. In view of the poor data-to-parameters ratio, a global RIGU restraint was applied. C-H hydrogens were placed in calculated positions and refined with riding coordinates and ADPs.

The structure contained large voids with no Fourier peak larger than 1.1 e- $Å^{-3}$. Since there were no recognizable solvent molecules in the Fourier maps, the voids were treated with PLATON SQUEEZE. The unit cell contains 8853 Å3 of solvent-accessible volume with 2555 e- (equivalent to 51 toluene molecules) in the void space, giving 1 toluene per 174 Å3 of void space. Since crystalline toluene packs with 1 molecule per 145 Å3, the results of the SQUEEZE analysis are reasonable. When the solvent in void space had been included as a diffuse contribution to the scattering, R1 improved from 15.0% to 9.6%. The final refinement (15869 data, 3138 restraints, 1789 parameters) converged with R1 (Fo > 4σ(Fo)) = 9.7%, wR2 = 33.4%, S = 1.08. The largest Fourier features were 0.54 and -0.31 e- A-3.

2.14. Synthetic Procedures and Characterization

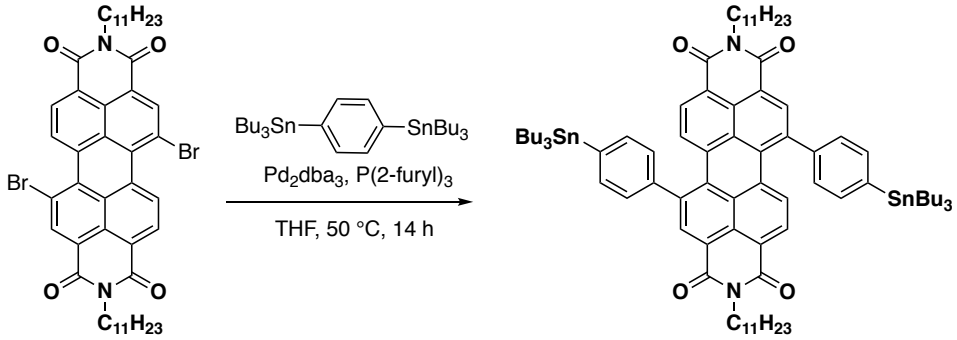

1,7-dibromo PDI **2.1**

Synthesis of 1,7-Bis[4-(tributylstannyl)-phenyl]-PDI **(2.1)**: Regio-pure 1,7-Bis[4-(tributylstannyl)-phenyl]-PDI was synthesized from regio-pure *N,N*-′di(6-undecyl)-1,7-dibromoperylene-3,4:9,10-tetracarboxylic diimide. The *1,6*- and *1,7*-regioisomers of *N,N*′-di(6-undecyl)-dibromoperylene-3,4:9,10-tetracarboxylic diimide were separated using prep HPLC on a COSMOSIL Buckyprep 20 x 250 mm, 18.9 mL/min and 12:88 CH_2Cl_2:hexanes prior to the Stille coupling. *1,7*-dibromo PDI (1.00 equiv, 0.350 mmol, 0.300 g), 1,4-bis(tributylstannyl)benzene (4.00 equiv, 1.40 mmol, 0.800 mL), tri(2-furyl)phosphine (0.400 equiv, 0.140 mmol, 0.0325 g), and THF (18.0 mL) were added to an oven-dried round bottom flask equipped with a stir bar. The

mixture was degassed for thirty minutes. While under N_2, tris(dibenzylideneacetone)dipalladium, Pd_2dba_3, (0.100 equiv, 0.0350 mmol, 0.0321 g) was added. The mixture was further degassed for ten minutes before being placed in a 55 °C oil bath and allowed to stir for 14 h. The crude mixture was concentrated and purified by column chromatography (Redisep Rf Silica) using a gradient from 0% to 60% CH_2Cl_2/hexanes to yield the Compound **2.1** as a magenta solid (0.276 g, 0.193 mmol, 55.1% yield). **^{1}H NMR** (500 MHz, $CDCl_3$) δ 8.64 (br, 2H), 8.12 (br, 2H), 7.91 (br s, 2H), 7.61* (d, J = 7.3 Hz, 4H), 7.54 (d, J = 7.4 Hz, 4H), 5.18 (br m, 2H), 2.25 (br m, 4H), 1.84 (br m, 4H), 1.64* (m, 12H), 1.42 (m, 12H), 1.29 (br m, 24H), 1.17* (m, 12H), 0.96 (m, 18H), 0.85 (br m, 12H). **^{13}C NMR** (125 MHz, $CDCl_3$) δ 164.76 (br), 163.67 (br), 143.09, 141.73, 141.25, 138.07*, 135.99**, 135.29**, 134.96, 132.46, 130.15, 129.86**, 129.28, 129.10**, 128.31*, 127.89, 122.80**, 122.49**, 122.08**, 121.73**, 54.60, 32.34, 31.78, 29.16*, 27.38*, 26.60, 22.57, 14.06, 13.75, 9.76*. **IR** (cm^{-1}) 2956, 2925, 2856, 1697, 1659, 1598, 1587, 1465, 1409, 1326, 1241, 1183, 1070, 863, 813. **HRMS** (APCI+) calculated m/z for $[C_{82}H_{114}N_2O_4Sn_2+Na]^+$ is 1453.6720, found 1453.6720. *Tin satellite peaks visible.

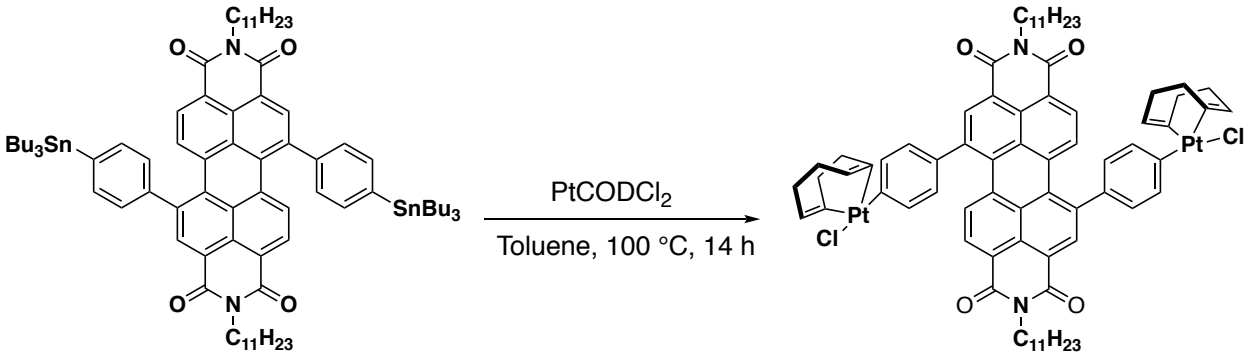

2.1 **2.2**

Synthesis of 1,7-Bis[4-(Pt(COD)Cl)-phenyl]-PDI (**2.2**). 1,7-Bis[4-(tributylstannyl)-phenyl]-PDI (**2.1**) (1.00 equiv, 0.193 mmol, 0.276 g) was added to an oven-dried round bottom flask equipped with a stir bar. Dichloro(1,5-cyclooctadiene)platinum(II) (2.20 equiv, 0.424 mmol, 0.158 g) was

added to the flask with anhydrous toluene (20 mL). The mixture was degassed for thirty minutes and then placed in a 100 °C oil bath and allowed to stir for overnight. The crude mixture was allowed to cool to room temperature and concentrated *in vacuo*. The crude product was purified by column chromatography using a gradient from 0% to 100% CH_2Cl_2/hexanes to elute the desired product. The product is re-precipitated from methanol three times to remove excess $PtCODCl_2$. The product is a purple solid (0.192 g, 0.121 mmol, 62.5% yield). **^{1}H NMR** (500 MHz, $CDCl_3$) δ 8.58 (br, 2H), 8.07 (br d, J = 8.2 Hz, 2H), 7.88 (br, 2H), 7.38 (d, J = 7.8 Hz, 4H), 7.29 (d, J = 7.7 Hz, 4H), 5.87 (s, 4H), 5.14 (br m, 2H), 4.72 (s, 4H), 2.75 (br m, 4H), 2.59 (br m, 4H), 2.45 (br m, 8H), 2.19 (br m, 4H), 1.80 (br m, 4H), 1.26 (br m, 24H), 0.82 (br m, 12H). **^{13}C NMR** (125 MHz, $CDCl_3$) δ 164.89**, 164.77**, 163.81**, 163.66**, 145.66, 141.21, 138.16, 136.15**, 135.64, 135.40**, 135.16, 132.39, 129.84, 129.70**, 129.34, 128.93**, 128.68, 127.76, 122.65**, 122.25**, 121.89**, 121.48**, 115.92, 87.94, 54.55**, 54.45**, 32.37, 32.30, 31.80, 28.04, 26.62, 22.60, 14.13. **IR** (cm^{-1}) 2953, 2924, 2854, 1694, 1652, 1598, 1584, 1408, 1323, 1236, 1181, 1015, 812. **HRMS** (ESI+) calculated m/z for $[C_{74}H_{84}Cl_2N_2O_4Pt_2+Na]^+$ is 1547.5001, found 1547.4994.

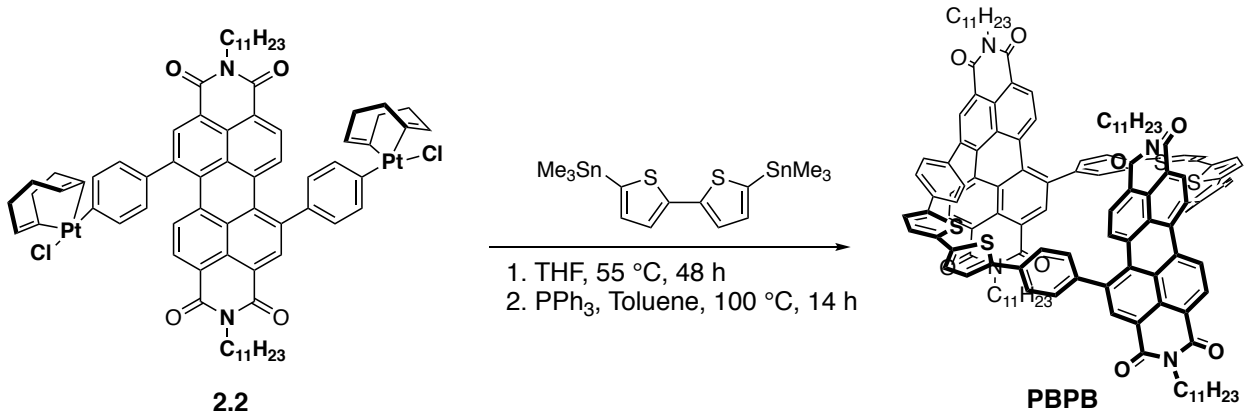

2.2 **PBPB**

Synthesis of **PBPB.** 1,7-Bis[4-(Pt(COD)Cl)-phenyl]-PDI (**2.2**) (1.00 equiv, 0.331 mmol, 0.505 g), commercially available 5,5′-bis(trimethylstannyl)-2,2′-bithiophene (1.00 equivalent, 0.331

mmol, 0.163 grams) and THF (110. mL) were added to a 250 ml two-neck round bottom flask. The mixture was degassed for thirty minutes and, then, stirred in a 55 °C oil bath for 48 h. The crude mixture was concentrated, and triphenylphosphine (20.0 equiv, 6.62 mmol, 1.93 g) and toluene (110. mL) were added. The mixture was degassed for fifteen minutes, then stirred for overnight in a 100 °C oil bath. The crude mixture was first purified by column chromatography using a gradient from 0% to 85% CH_2Cl_2/hexanes. Fractions that contained **PBPB** were collected and further purified on by preparative TLC using 70%:30% CH_2Cl_2/hexanes. The product is a black solid (0.163 g, 0.0805 mmol, 48.6% yield). **^{1}H NMR** (500 MHz, 370 K, $C_2D_2Cl_4$) δ [*major stereoisomer*] 8.59 (br s, 4H), 8.40 (br d, *J* = 7.9 Hz, 4H), 8.30 (br d, *J* = 7.9 Hz, 4H), 7.70 (d, *J* = 7.8 Hz, 8H), 7.62 (d, *J* = 8.0 Hz, 8H), 7.34 (d, *J* = 3.5 Hz, 4H), 7.22 (d, *J* = 3.7 Hz, 4H), 5.14 (br m, 4H), 2.19 (br m, 8H), 1.88 (br m, 8H), 1.30 (br m, 48H), 0.85 (br m, 24H); [*distinguishable minor stereoisomer peaks*] 8.55, 8.45 (br d), 7.54, 7.22 (d, *J* = 3.7 Hz). **^{13}C NMR** (125 MHz, 300 K, $C_2D_2Cl_4$) [*mixture of interconverting meso and racemic stereoisomers*] δ 164.22, 163.93, 163.10, 162.82, 141.89, 140.32, 140.05, 137.30, 134.92, 134.24, 134.14, 133.18, 132.15, 130.63, 129.78, 129.75, 129.30, 128.87, 128.45, 126.91, 126.84, 125.89, 123.26, 122.76, 122.25, 121.82, 121.49, 121.05, 119.77, 54.09, 33.68, 31.69, 31.40, 31.17, 29.60, 29.19, 29.15, 26.06, 22.21, 22.02, 20.41, 13.74, 13.61, 13.58. **IR** (cm^{-1}) 2952, 2924, 2855, 1695, 1657, 1583, 1456, 1405, 1323, 1239, 1181, 1126, 1094, 853, 836, 812, 794, 762. **HRMS** (ESI+) calculated m/z for $[C_{132}H_{128}N_4O_8S_4+Na]^+$ is 2047.8513, found 2047.8458. The list of ^{13}C NMR peaks above includes all distinguishable peaks for both diastereomers of **PBPB**.

2.15. NMR Spectra of Compounds

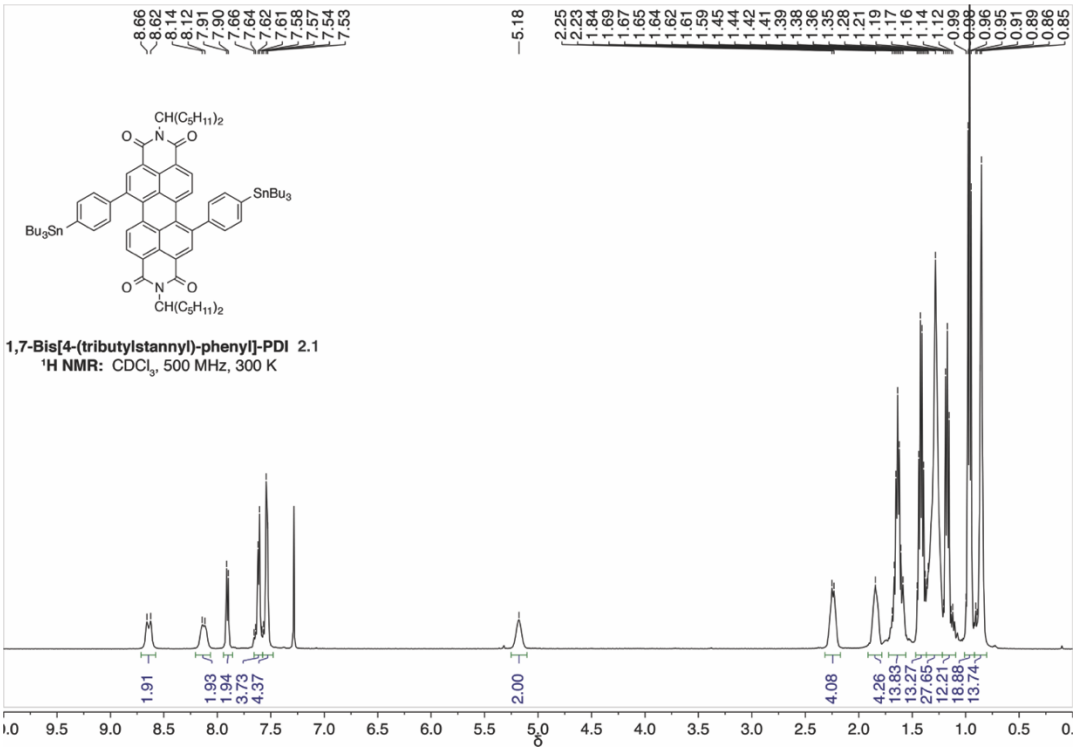

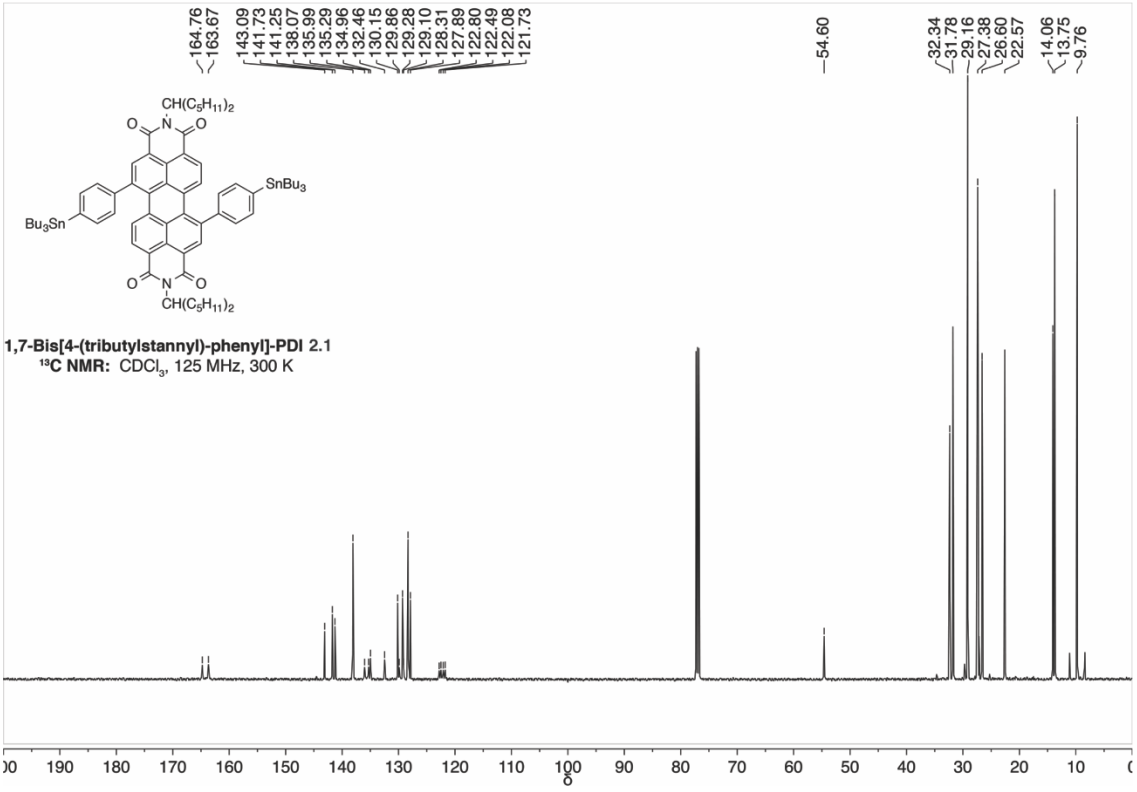

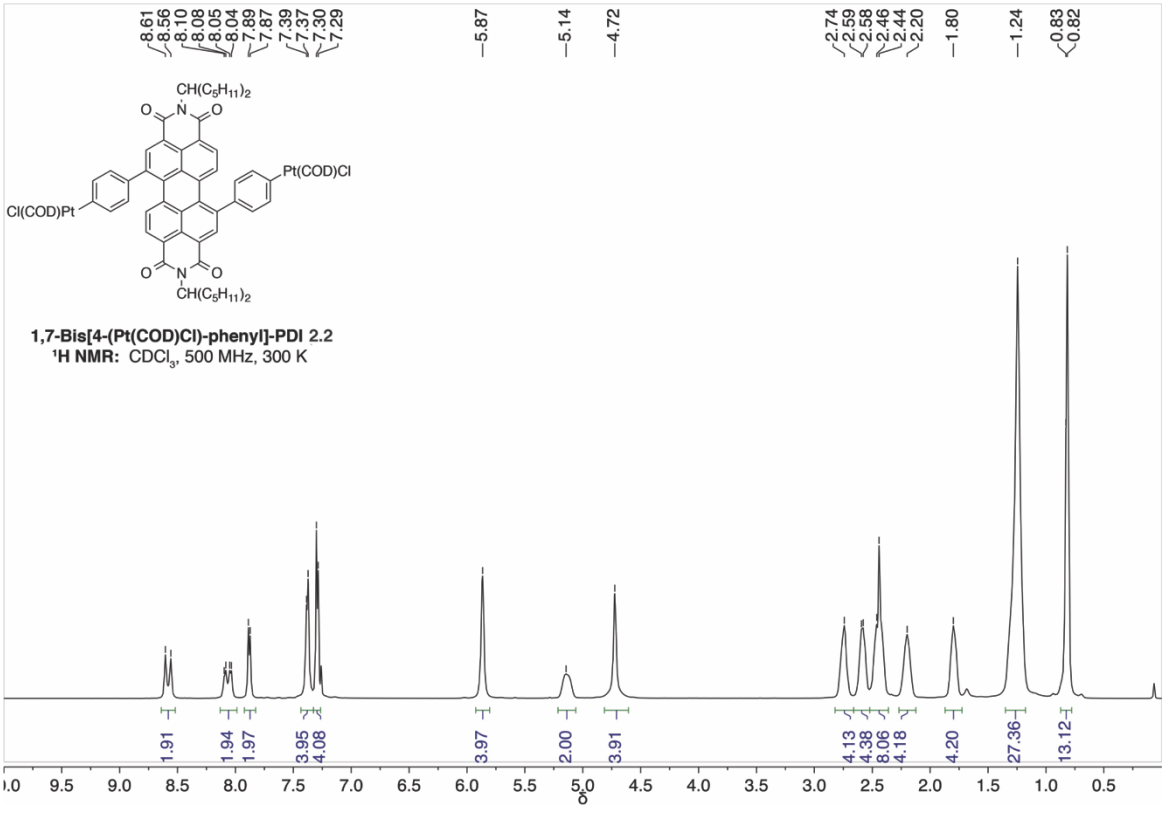
8.61
8.56
8.10
8.08
8.05
8.04
7.89
7.87
7.39
7.37
7.30
7.29
5.87
5.14
4.72
2.74
2.59
2.58
2.46
2.44
2.20
1.80
1.24
0.83
0.82
CH(C5H11)2
Pt(COD)Cl
Cl(COD)Pt
1,7-Bis[4-(Pt(COD)Cl)-phenyl]-PDI 2.2
1H NMR: CDCl3, 500 MHz, 300 K
1.91
1.94
1.97
3.95
4.08
3.97
2.00
3.91
4.13
4.38
8.06
4.18
4.20
27.36
13.12
δ

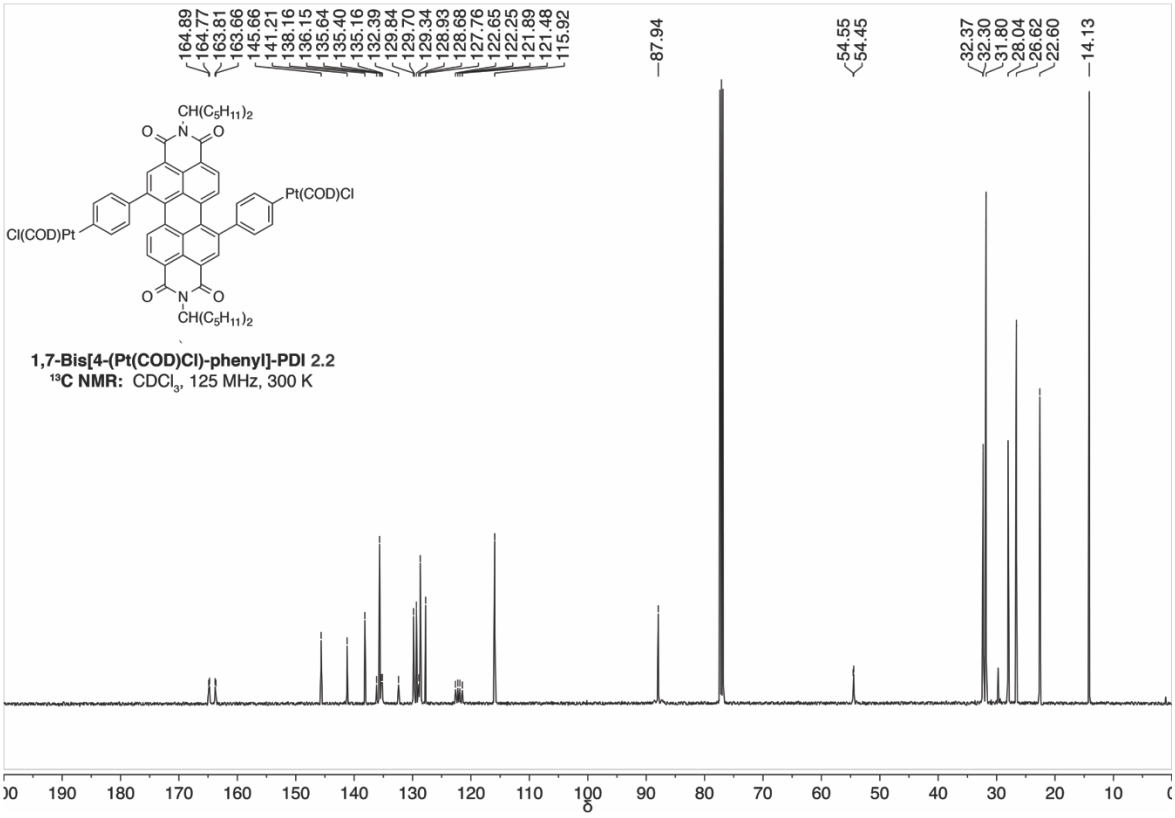
164.89
164.77
163.81
163.66
145.66
141.21
138.16
136.15
135.64
135.40
135.16
132.39
129.84
129.70
129.34
128.93
128.68
127.76
122.65
122.25
121.89
121.48
115.92
87.94
54.55
54.45
32.37
32.30
31.80
28.04
26.62
22.60
14.13
CH(C5H11)2
Pt(COD)Cl
Cl(COD)Pt
1,7-Bis[4-(Pt(COD)Cl)-phenyl]-PDI 2.2
13C NMR: CDCl3, 125 MHz, 300 K
δ

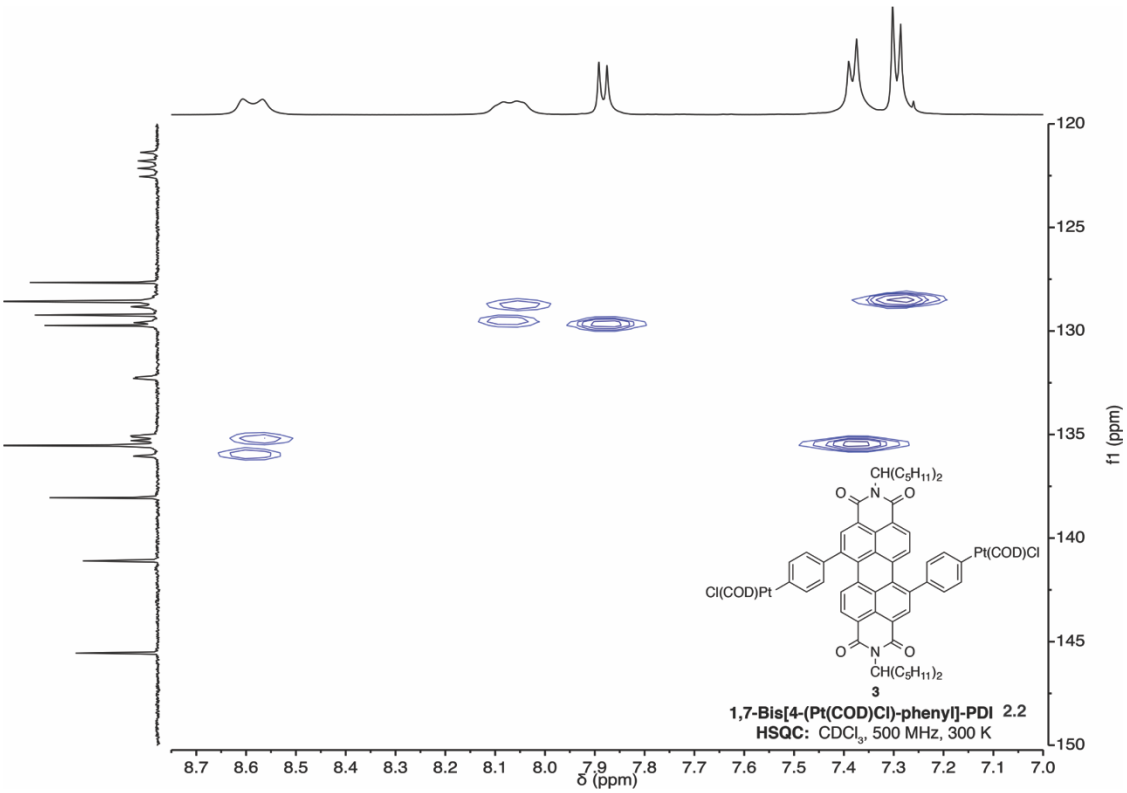
120
125
130
135
140
145
150
f1 (ppm)
8.7
8.6
8.5
8.4
8.3
8.2
8.1
8.0
7.9
7.8
7.7
7.6
7.5
7.4
7.3
7.2
7.1
7.0
δ (ppm)
CH(C5H11)2
O
N
O
Pt(COD)Cl
Cl(COD)Pt
O
N
O
CH(C5H11)2
3
1,7-Bis[4-(Pt(COD)Cl)-phenyl]-PDI 2.2
HSQC: CDCl3, 500 MHz, 300 K

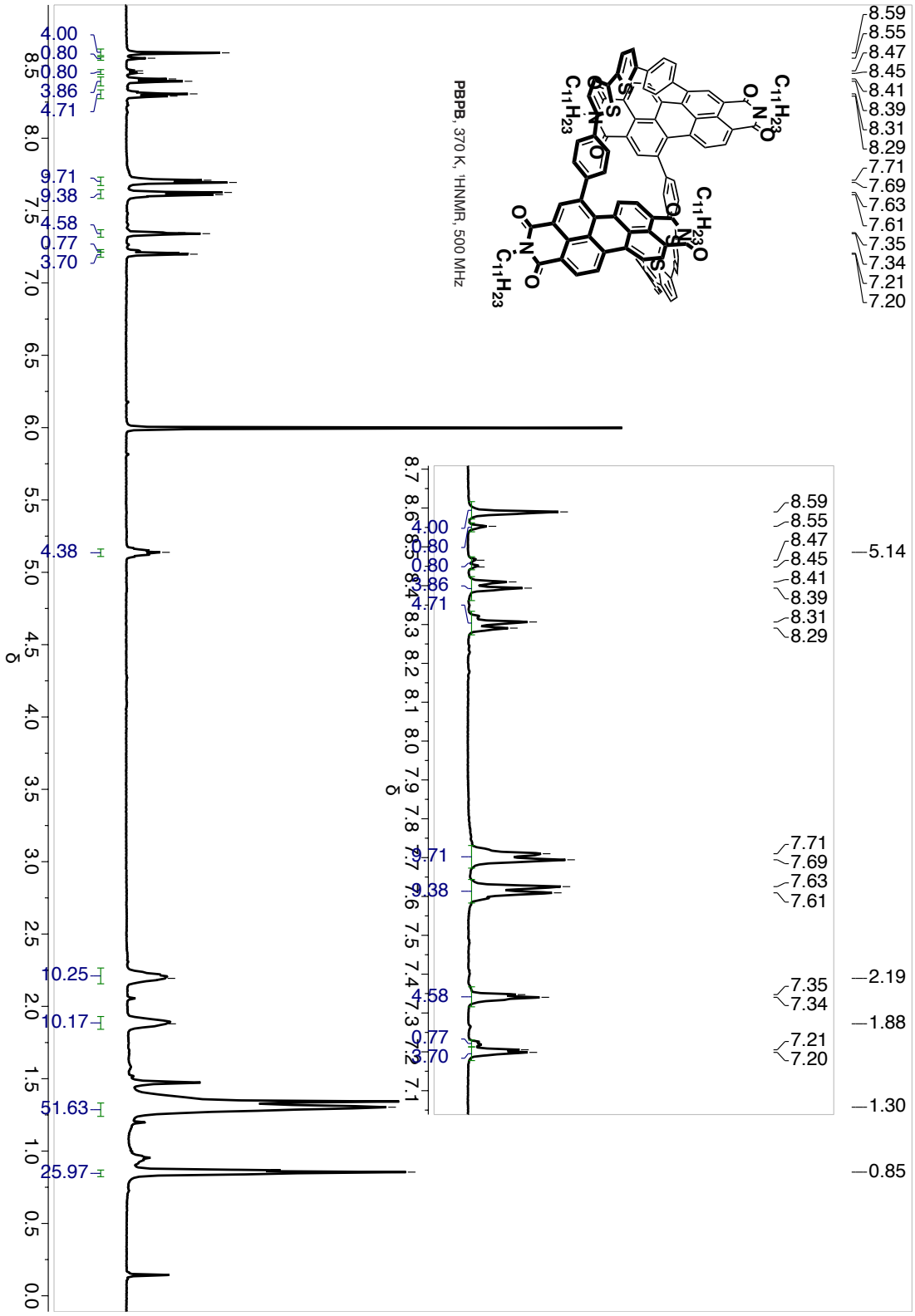
PBPB, 370 K, ¹HNMR, 500 MHz
δ
4.00
0.80
0.80
3.86
4.71
9.71
9.38
4.58
0.77
3.70
4.38
10.25
10.17
51.63
25.97
8.59
8.55
8.47
8.45
8.41
8.39
8.31
8.29
7.71
7.69
7.63
7.61
7.35
7.34
7.21
7.20
5.14
2.19
1.88
1.30
0.85

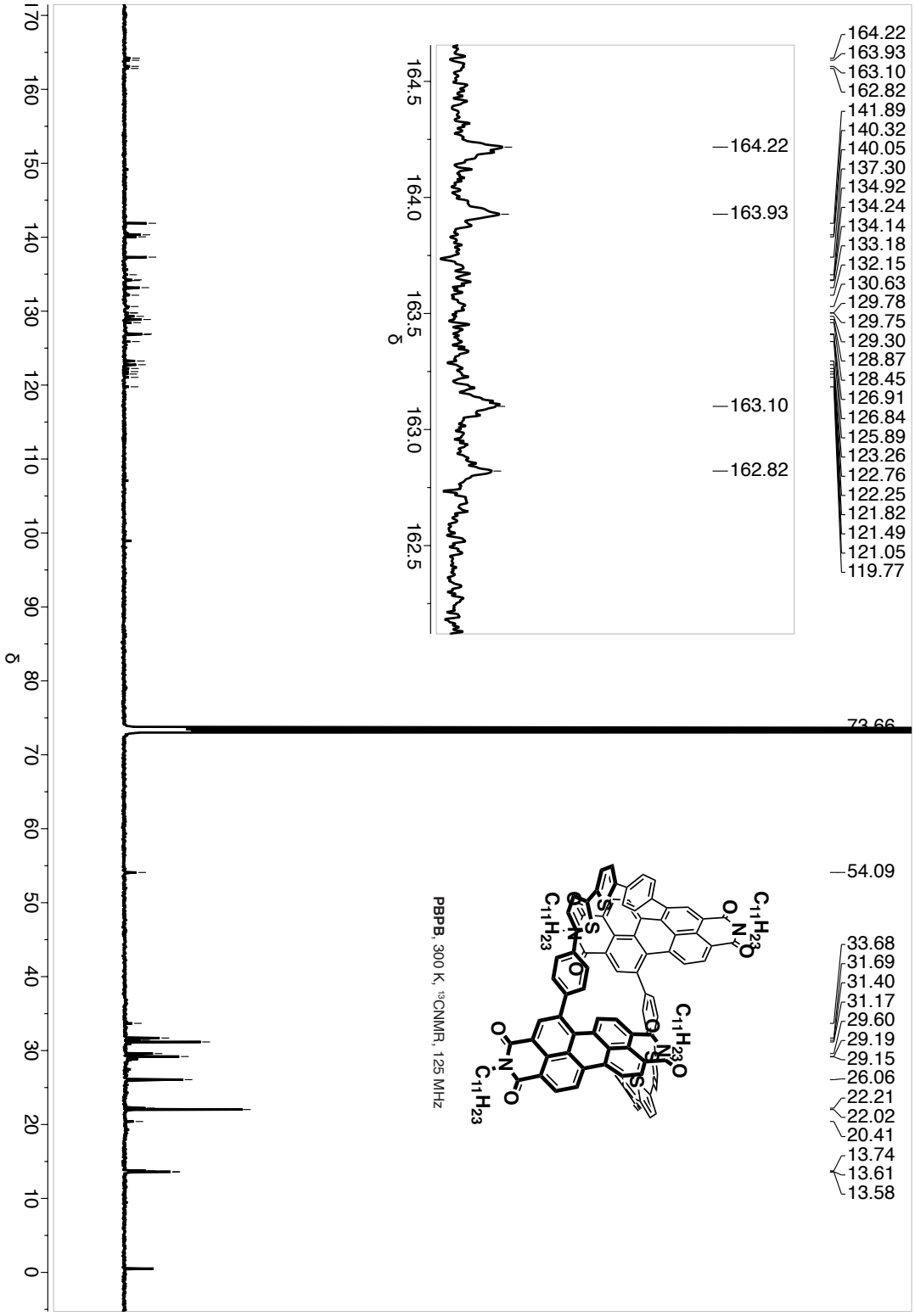
PBPB, 300 K, ^{13}CNMR, 125 MHz
δ
164.22
163.93
163.10
162.82
141.89
140.32
140.05
137.30
134.92
134.24
134.14
133.18
132.15
130.63
129.78
129.75
129.30
128.87
128.45
126.91
126.84
125.89
123.26
122.76
122.25
121.82
121.49
121.05
119.77
73.66
54.09
33.68
31.69
31.40
31.17
29.60
29.19
29.15
26.06
22.21
22.02
20.41
13.74
13.61
13.58

2.16. DFT Output

All quantum chemical calculations were performed using Jaguar, version 8.3, Schrodinger, Inc., New York, NY, 2013. (See A. D. Bochevarov, E. Harder, T. F. Hughes, J. R. Greenwood, D. A. Braden, D. M. Philipp, D. Rinaldo, M. D. Halls, J. Zhang, R. A. Friesner, "Jaguar: A High Performance Quantum Chemistry Software Program with Strengths in Life and Materials Sciences", Int. J. Quantum Chem., 2013, 113(18), 2110-2142). All geometries were optimized using the B3LYP functional and the 6-31G** basis set. Geometry optimization output information can be found in the online Supporting Information of Ref. 1.[1] For **PBPB**, we present the fifteen lowest energy roots determined by the TDDFT calculations. The HOMO is the doubly occupied orbital numbered 378.

TDDFT Output

Restricted Singlet Excited State 1: 1.5318 eV 809.41 nm

excitation	X coeff.
378 => 379	-0.98886

Transition dipole moment (debye):
X= -0.0890 Y= -0.0862 Z= -3.2537 Tot= 3.2560
Oscillator strength, f= 0.0616

Restricted Singlet Excited State 2: 1.6320 eV 759.68 nm

excitation	X coeff.
378 => 380	0.99758

Transition dipole moment (debye):
X= 4.2970 Y= -0.1207 Z= -0.1417 Tot= 4.3011
Oscillator strength, f= 0.1145

Restricted Singlet Excited State 3: 1.7453 eV 710.40 nm

excitation	X coeff.
377 => 379	0.99575

Transition dipole moment (debye):
X= 0.3000 Y= 6.6914 Z= 0.2086 Tot= 6.7013
Oscillator strength, f= 0.2972

```
 ---------------------------------------------------------------------------
 Restricted Singlet Excited State   4:     1.7937 eV       691.23 nm
  excitation     X coeff.
 ------------   ---------
  377 =>  380     0.99585
 Transition dipole moment (debye):
    X=    -0.2982     Y=     0.2533     Z=     0.1349  Tot=     0.4139
 Oscillator strength, f=     0.0012
 ---------------------------------------------------------------------------
 Restricted Singlet Excited State   5:     2.0218 eV       613.24 nm
  excitation     X coeff.
 ------------   ---------
  376 =>  379    -0.99748
 Transition dipole moment (debye):
    X=    -2.8177     Y=     0.2536     Z=     0.3220  Tot=     2.8474
 Oscillator strength, f=     0.0622
 ---------------------------------------------------------------------------
 Restricted Singlet Excited State   6:     2.0532 eV       603.87 nm
  excitation     X coeff.
 ------------   ---------
  376 =>  380    -0.98598
378 =>  379     0.10277
Transition dipole moment (debye):
 X=    -0.4137     Y=     0.8578     Z=    -5.4568  Tot=     5.5393
 Oscillator strength, f=     0.2389
 ---------------------------------------------------------------------------
 Restricted Singlet Excited State   7:     2.3079 eV       537.21 nm
  excitation     X coeff.
 ------------   ---------
  375 =>  379     0.99093
 Transition dipole moment (debye):
    X=     0.2428     Y=    -0.9048     Z=     6.0242  Tot=     6.0966
 Oscillator strength, f=     0.3253
 ---------------------------------------------------------------------------
 Restricted Singlet Excited State   8:     2.3427 eV       529.23 nm
  excitation     X coeff.
 ------------   ---------
  375 =>  380    -0.99473
 Transition dipole moment (debye):
    X=     0.4891     Y=     0.0763     Z=    -0.1334  Tot=     0.5127
 Oscillator strength, f=     0.0023
 ---------------------------------------------------------------------------
 Restricted Singlet Excited State   9:     2.6436 eV       469.00 nm

  excitation     X coeff.
 ------------   ---------
```

372 => 380 -0.18272
374 => 379 0.96735
Transition dipole moment (debye):
X= -0.2332 Y= -0.1825 Z= -0.0543 Tot= 0.3011
Oscillator strength, f= 0.0009

Restricted Singlet Excited State 10: 2.6744 eV 463.60 nm
excitation X coeff.
--- ---
372 => 379 0.19523
374 => 380 -0.96112
Transition dipole moment (debye):
X= -0.1319 Y= -3.5869 Z= -0.3162 Tot= 3.6032
Oscillator strength, f= 0.1317

Restricted Singlet Excited State 11: 2.7637 eV 448.62 nm
excitation X coeff.
--- ---
377 => 381 0.29688
378 => 381 0.79213
378 => 382 0.47433

Transition dipole moment (debye):
X= 0.0625 Y= 7.5012 Z= -3.1504 Tot= 8.1362
Oscillator strength, f= 0.6938

Restricted Singlet Excited State 12: 2.8174 eV 440.07 nm
excitation X coeff.
--- ---
377 => 381 -0.27881
377 => 382 0.15479
378 => 381 0.57112
378 => 382 -0.72298
Transition dipole moment (debye):
X= 0.4220 Y= 8.0581 Z= 2.7629 Tot= 8.5290
Oscillator strength, f= 0.7772

Restricted Singlet Excited State 13: 2.9360 eV 422.29 nm
excitation X coeff.
--- ---
369 => 380 0.14851
371 => 380 0.10405
373 => 379 0.93743
376 => 382 -0.15916
378 => 387 0.10576
Transition dipole moment (debye):

X= 2.3997 Y= 0.2431 Z= -0.3014 Tot= 2.4307
Oscillator strength, f= 0.0658

Restricted Singlet Excited State 14: 2.9377 eV 422.04 nm
excitation X coeff.
--- ---
369 => 379 -0.14275
371 => 379 -0.10186
373 => 379 0.12272
373 => 380 -0.66551
377 => 381 -0.56692
378 => 382 0.37436
Transition dipole moment (debye):
X= 0.3313 Y= -1.4637 Z= 2.2048 Tot= 2.6671
Oscillator strength, f= 0.0792

Restricted Singlet Excited State 15: 3.0155 eV 411.16 nm
excitation X coeff.
--- ---
373 => 380 0.11225
376 => 381 -0.15805
376 => 384 -0.23900
377 => 381 -0.11702
378 => 383 -0.90444
Transition dipole moment (debye):
X= -0.0650 Y= -0.1810 Z= -0.2065 Tot= 0.2821
Oscillator strength, f= 0.0009

The below provides the homodesmotic reaction employed in order to calculate strain within both the chiral and achiral isomers. Additionally, we include the Gibbs free energies and enthalpies of the enantiomers and the meso isomer used to calculate the theoretical equilibrium ratio. All thermochemical data employed single point calculations on the minimized geometries provided in the following pages.

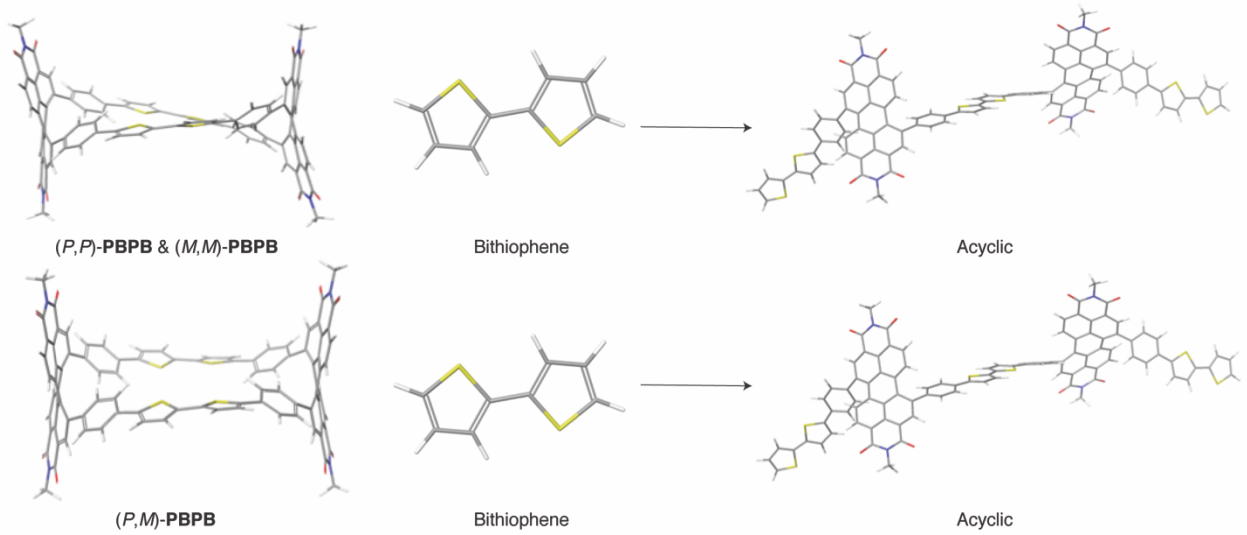

Table 2.1. Homodesmotic Calculations for Strain

Compound	Total energy (hartrees)	Strain energy (hartrees)	Strain energy (kcal/mol)
(*P*,*P*)-**PBPB**/(*M*,*M*)-**PBPB**	-5948.582452	0.032223	20
(*P*,*M*)-**PBPB**	-5948.579539	0.035138	22
Bithiophene	-1104.826802	-	-
Acyclic	-7053.441477	-	-

Table of energies for the Homodesmotic Reaction (enthalpy)

Table 2.2. Thermochemical Calculations for Strain

Compound	Gibbs free energy (hartrees)	Enthalpy (hartrees)
(*P*,*P*)-**PBPB**/(*M*,*M*)-**PBPB**	-5947.593171	-5947.309814
(*P*,*M*)-**PBPB**	-5947.587400	-5947.306842
Difference **(*M*,*M*)/(*P*,*P*)-(*M*,*P*)**	-0.005771	-0.002972
$K_{[P/M\ enantiomers]} = e^{-\Delta G/RT}$	158:1	14:1
(P+M):M	316:1	28:1

Temperature = 360 K, R = 8.3145 J mol^{-1} K^{-1}

2.17. References

1. Ball, M. *et al.* Chiral Conjugated Corrals. *J. Am. Chem. Soc.* **137**, 9982–9987 (2015).
2. Krömer, J. *et al.* Synthesis of the First Fully α-Conjugated Macrocyclic Oligothiophenes: Cyclo[n]thiophenes with Tunable Cavities in the Nanometer Regime. *Angew. Chem. Int. Ed.* **39**, 3481–3486 (2000).
3. Nakao, K. *et al.* Giant Macrocycles Composed of Thiophene, Acetylene, and Ethylene Building Blocks. *J. Am. Chem. Soc.* **128**, 16740–16747 (2006).
4. Hitosugi, S. *et al*. Bottom-up Synthesis and Thread-in-Bead Structures of Finite (n,0)-Zigzag Single-Wall Carbon Nanotubes. *J. Am. Chem. Soc.* **134**, 12442–12445 (2012).
5. Omachi, H. *et al*. Synthesis of Cycloparaphenylenes and Related Carbon Nanorings: A Step toward the Controlled Synthesis of Carbon Nanotubes. *Acc. Chem. Res.* **45**, 1378–1389 (2012).
6. Ishii, Y. *et al.* Size-selective synthesis of 9 - 11 and 13 cycloparaphenylenes. *Chem. Sci.* **3**, 2340–2345 (2012).
7. Evans, P. J. *et al*. Efficient room-temperature synthesis of a highly strained carbon nanohoop fragment of buckminsterfullerene. *Nat. Chem.* **6**, 404–408 (2014).
8. Kayahara, E. *et al*. Synthesis and Characterization of 5 Cycloparaphenylene. *J. Am. Chem. Soc.* **136**, 2284–2287 (2014).
9. Kuwabara, T. *et al*. Curved Oligophenylenes as Donors in Shape-Persistent Donor–Acceptor Macrocycles with Solvatofluorochromic Properties. *Angew. Chem. Int. Ed.* **54**, 9646–9649 (2015).
10. Ito, H. *et al*. Thiophene-Based, Radial pi-Conjugation: Synthesis, Structure, and Photophysical Properties of Cyclo-1,4-phenylene-2 ’,5 ’-thienylenes. *Angew. Chem. Int. Ed.* **54**, 159–163 (2015).
11. Darzi, E. R. *et al.* Synthesis, Properties, and Design Principles of Donor–Acceptor Nanohoops. *ACS Cent. Sci.* **1**, 335–342 (2015).
12. Chen, Q. *et al.* Strain-Induced Stereoselective Formation of Blue-Emitting Cyclostilbenes. *J. Am. Chem. Soc.* **137**, 12282–12288 (2015).
13. Chang, S.-W. *et al*. A Donor-Acceptor Conjugated Block Copolymer of Poly(arylenevinylene)s by Ring-opening Metathesis Polymerization. *Chem. Commun.* **51**, 9113–9116 (2015).
14. Jasti, R. *et al*. Synthesis, Characterization, and Theory of 9 -, 12 -, and 18 Cycloparaphenylene: Carbon Nanohoop Structures. *J. Am. Chem. Soc.* **130**, 17646-17647 (2008).
15. Asai, K. *et al*. A Cyclic Octithiophene Containing B,B'-linkages. *Chem. Commun.* **51**, 6096 (2015).
16. Nishigaki, S. *et al.* Synthesis, Structures, and Photophysical Properties of Alternating Donor–Acceptor Cycloparaphenylenes. *Chem. Eur. J.* **23**, 7227–7231 (2017).
17. Kayahara, E. *et al.* Gram-Scale Syntheses and Conductivities of [10]Cycloparaphenylene

and Its Tetraalkoxy Derivatives. *J. Am. Chem. Soc.* **139**, 18480–18483 (2017).

18. Zhang, F. *et al*. Giant Cyclo n thiophenes with Extended pi Conjugation. *Angew. Chem. Int. Ed.* **48**, 6632–6635 (2009).
19. Segawa, Y. *et al*. [9]Cycloparaphenylene: Nickel-mediated Synthesis and Crystal Structure. *Chem. Lett.* **40**, 423–425 (2011).
20. Iwamoto, T. *et al*. Size-Selective Encapsulation of C60 by [10]Cycloparaphenylene: Formation of the Shortest Fullerene-Peapod. *Angew. Chem. Int. Ed.* **50**, 8342–8344 (2011).
21. Iwamoto, T. *et al*. Selective and Random Syntheses of n Cycloparaphenylenes (n=8-13) and Size Dependence of Their Electronic Properties. *J. Am. Chem. Soc.* **133**, 8354–8361 (2011).
22. Segawa, Y. *et al.* Concise Synthesis and Crystal Structure of 12 Cycloparaphenylene. *Angew. Chem. Int. Ed.* **50**, 3244–3248 (2011).
23. Hitosugi, S. *et al* Atropisomerism in a Belt-Persistent Nanohoop Molecule: Rotational Restriction Forced by Macrocyclic Ring Strain. *Chem. Asian J.* **7**, 1550–1552 (2012).
24. Kayahara, E. *et al*. Selective Synthesis and Crystal Structure of [10]Cycloparaphenylene. *Org. Lett.* **14**, 3284–3287 (2012).
25. van der Boom, T. *et al.* Charge Transport in Photofunctional Nanoparticles Self-Assembled from Zinc 5,10,15,20-Tetrakis(perylenediimide)porphyrin Building Blocks. *J. Am. Chem. Soc.* **124**, 9582–9590 (2002).
26. Campbell, W. M. *et al.* Highly efficient porphyrin sensitizers for dye-sensitized solar cells. *J. Phys. Chem. C* **111**, 11760–11762 (2007).
27. Hoffmann, M. *et al*. Template-Directed Synthesis of a π-Conjugated Porphyrin Nanoring. *Angew. Chem. Int. Ed.* **46**, 3122–3125 (2007).
28. Bessho, T. *et al*. Highly Efficient Mesoscopic Dye-Sensitized Solar Cells Based on Donor-Acceptor-Substituted Porphyrins. *Angew. Chem. Int. Ed.* **49**, 6646–6649 (2010).
29. Song, J. *et al*. A Porphyrin Nanobarrel That Encapsulates C60. *J. Am. Chem. Soc.* **132**, 16356–16357 (2010).
30. Yella, A. *et al.* Porphyrin-Sensitized Solar Cells with Cobalt (II/III)-Based Redox Electrolyte Exceed 12 Percent Efficiency. *Science* **334**, 629–634 (2011).
31. Saito, S. *et al*. Expanded Porphyrins: Intriguing Structures, Electronic Properties, and Reactivities. *Angew. Chem. Int. Ed.* **50**, 4342–4373 (2011).
32. Fenwick, O. *et al.* Linear and Cyclic Porphyrin Hexamers as Near-Infrared Emitters in Organic Light-Emitting Diodes. *Nano Lett.* **11**, 2451–2456 (2011).
33. Sprafke, J. K. *et al.* Belt-Shaped π-Systems: Relating Geometry to Electronic Structure in a Six-Porphyrin Nanoring. *J. Am. Chem. Soc.* **133**, 17262–17273 (2011).
34. Jiang, H.-W. *et al.* Cyclic 2,12-Porphyrinylene Nanorings as a Porphyrin Analogue of Cycloparaphenylenes. *J. Am. Chem. Soc.* **137**, 2219–2222 (2015).
35. Havinga, E. E. *et al*. A New Class of Small Band Gap Organic Polymer Conductors. *Polym. Bull.* **29**, 119–126 (1992).

36. Havinga, E. E. *et al*. Alternate Donor-Acceptor Small Band-gap Semiconducting Polymers; Polysquaraines and Polycroconaines. *Synth. Met.* **55**, 299–306 (1993).

37. Roncali, J. Synthetic Principles for Bandgap Control in Linear π-Conjugated Systems. *Chem. Rev.* **97**, 173–206 (1997).

38. Eaborn, C. *et al*. Preparation of Aryl-Platinum(II) Complexes - Iinteraction of dichloro-(eta-cyclco-octa-1,5-diene)platinum(II) and Aryltrimethylstannanes. *J. Chem. Soc. Trans.* 357–368 (1978).

39. Shekhar, S. *et al*. Distinct electronic effects on reductive eliminations of symmetrical and unsymmetrical bis-aryl platinum complexes. *J. Am. Chem. Soc.* **126**, 13016–13027 (2004).

40. Würthner, F. *et al.* Perylene Bisimide Dye Assemblies as Archetype Functional Supramolecular Materials. *Chem. Rev.* **116**, 962–1052 (2016).

41. Rajasingh, P. *et al*. Selective Bromination of Perylene Diimides under Mild Conditions. *J. Org. Chem.* **72**, 5973–5979 (2007).

42. Samdal, S. *et al*. Molecular Conformation of 2,2'-Bithiophene Determined by by Gas-Phase Electron Diffraction and ab-initio calculations. *Synth. Met.* **59**, 259–265 (1993).

43. Quattrocchi, C. *et al*. Theoretical Investigation of the Conformaitonal Behavior of 2,2'-Bithiophene. *Chem. Phys. Lett.* **208**, 120–124 (1993).

44. Capozzi, B. *et al.* Length-Dependent Conductance of Oligothiophenes. *J. Am. Chem. Soc.* **136**, 10486–10492 (2014).

45. Chao, C. C. *et al.* Photophysical and electrochemical properties of 1,7-diaryl-substituted perylene diimides. *J. Org. Chem.* **70**, 4323–4331 (2005).

46. Goretzki, G. *et al.* Bis-morpholine-Substituted Perylene Bisimides: Impact of Isomeric Arrangement on Electrochemical and Spectroelectrochemical Properties. *J. Org. Chem.* **73**, 8808–8814 (2008).

47. You, J. B. *et al.* A polymer tandem solar cell with 10.6% power conversion efficiency. *Nat. Commun.* **4**, 10 (2013).

48. Blanc, E. *et al*. The evaluation of transmission factors and their first derivatives with respect to crystal shape parameters. *J. Appl. Crystallogr.* **24**, 1035–1041 (1991).

49. Clark, R. C. *et al*. The analytical calculation of absorption in multifaceted crystals. *Acta Crystallogr. Sect. A* **51**, 887–897 (1995).

50. Oxford Diffraction/Agilent Technologies UK Ltd. Version 1.171.37.35. (2014).

51. Sheldrick, G. M. Crystal structure refinement with {\it SHELXL}. *Acta Crystallogr. Sect. C* **71**, 3–8 (2015).

52. Sheldrick, G. M. {\it SHELXT} {--} Integrated space-group and crystal-structure determination. *Acta Crystallogr. Sect. A* **71**, 3–8 (2015).

53. Palatinus, L. *et al*. {\it SUPERFLIP} {--} a computer program for the solution of crystal structures by charge flipping in arbitrary dimensions. *J. Appl. Crystallogr.* **40**, 786–790 (2007).

54. Dolomanov, O. V. *et al.* {\it OLEX2}: A complete structure solution, refinement and

analysis program. *J. Appl. Crystallogr.* **42**, 339–341 (2009).

55. Spek, A. L. Structure validation in chemical crystallography. *Acta Crystallogr. Sect. D* **65**, 148–155 (2009).

56. van der Sluis, P. *et al*. BYPASS: an effective method for the refinement of crystal structures containing disordered solvent regions. *Acta Crystallogr. Sect. A* **46**, 194–201 (1990).

57. Crystalmaker Software Ltd.

58. Ahmadi, Z. *et al*. A mechanistic investigation of hydrodehalogenation using ESI-MS. *Chem. Commun.* **49**, 11488–11490 (2013).

Chapter 3. Macrocyclization in the Design of Organic n-Type Electronic Materials

3.1. Preface

Chapter 3 is reproduced with permission from the authors: Melissa Ball, Yu Zhong, Brandon Fowler, Boyuan Zhang, Panpan Li, Grisha Etkin, Daniel W. Paley, John Decatur, Ankur K. Dalsania, Hexing Li, Shengxiong Xiao, Fay Ng, Michael L. Steigerwald and Colin Nuckolls published in the *Journal of the American Chemical Society*.[1] Copyright 2016 American Chemical Society. Brandon Fowler and I carried out the synthesis and characterization of all compounds. Yu Zhong, Boyuan Zhang and Ankur K. Dalsania performed all device fabrication and characterization. Grisha Etkin performed GPC on polymer materials.

3.2. Introduction

We compare cyclic and acyclic π-conjugated molecules as n-type electronic materials and find that the cyclic molecules have numerous benefits in OPVS. Conjugated macrocycles[2–28] have several potential advantages as organic electronic materials: (1) their contorted structure[29] should facilitate intermolecular contacts and charge transport; (2) they lack endgroups that are known to create defects in linear polymers and act as trap-sites for charges as they move through materials;[30–34] (3) often they have an altered electronic structure;[2,25] and (4) they have a defined cavity that can be a host for electronically useful guest molecules.[16,24,35–37] Figure 3.1 and 3.2 display the cyclic and acyclic molecules designed and synthesized for this study. The two conjugated cycles here are **$(PPh_2)_4$** and **PBPB**. Section 3.12 contains the synthetic details for all compounds.

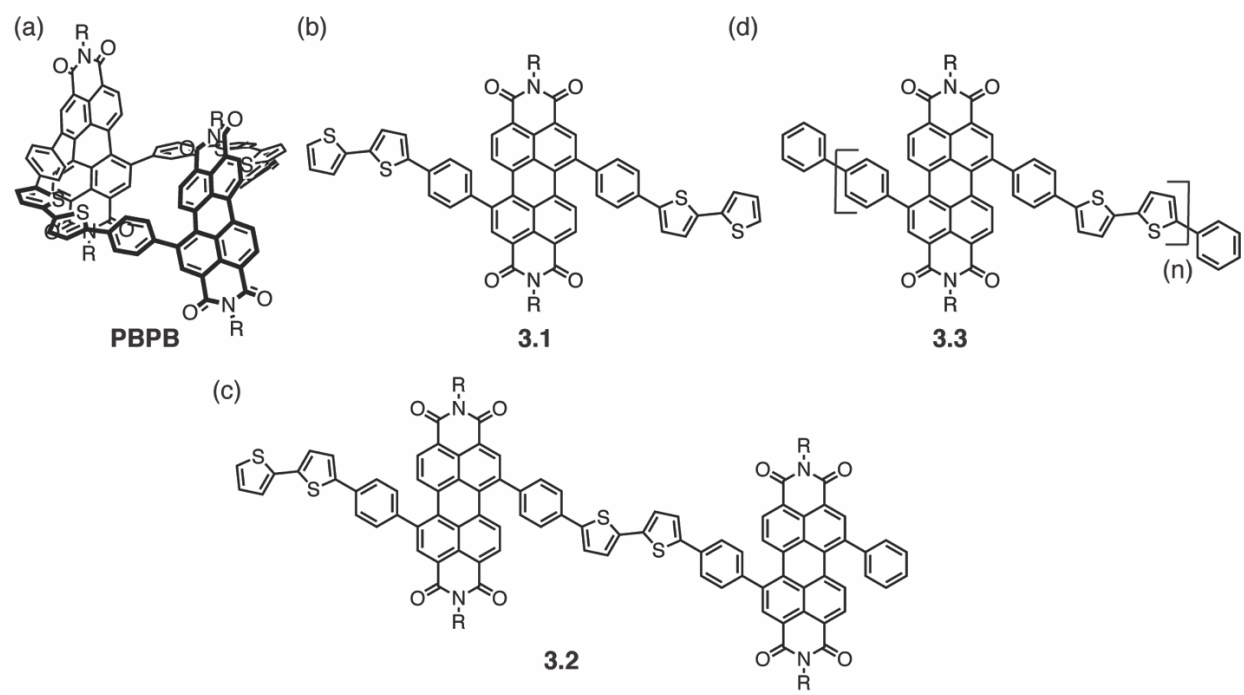

Figure 3.1. Structures of compounds designed and synthesized to compare acyclic and cyclic, π-conjugated molecules for n-type electronic materials. (a) **PBPB**; (b) a monomer version (**3.1**) of the macrocycle; (c) acyclic **PBPB** where the bond between one phenyl and a bithiophene is cut (**3.2**); and (d) a polymeric version (**3.3**). R = $C_{11}H_{23}$ side chains.

We compare these macrocycles to a series of acyclic molecules that link varying numbers of **P** subunits and find that the conjugated cycles have bathochromically shifted UV-vis absorbances, are more easily reduced, have higher electron mobility and have better morphology in blended films. All of these factors contribute to the more than doubling of the power conversion efficiency observed in solar cells using these macrocycles as n-type, electron-transporting material. This is first report directly comparing analogous cyclic and acyclic π-conjugated molecules as n-type materials in OPVs.

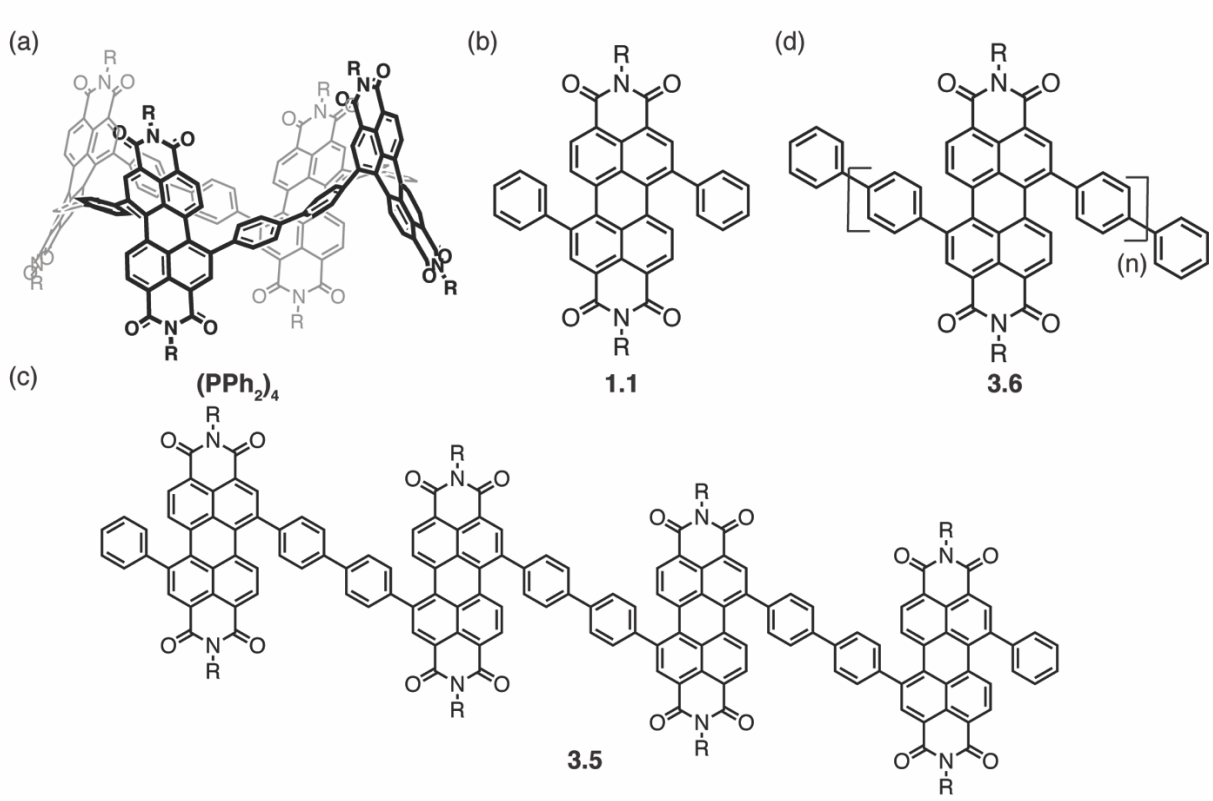

Figure 3.2. Structures of compounds designed and synthesized to compare acyclic and cyclic, π-conjugated molecules for n-type electronic materials. (a) **$(PPh_2)_4$**; (b) a monomer version (**1.1**) of the macrocycle introduced in Chapter 1B; (c) acyclic **$(PPh_2)_4$** where the bond between two phenyl groups is cut (**3.5**); and (d) a polymeric version (**3.6**).

3.3. Design of N-type Semiconductors

We designed a series of cyclic and acyclic π-conjugated molecules (Figures 3.1 and 3.2) that contain the redox active PDI subunit. PDIs possess many desirable properties such as efficient electron transport,[38–42] high molar absorptivities,[29,43,44] and ease of functionalization.[45–47] Derivatives of PDI are efficacious in solar cells when combined with electron rich conjugated polymers.[44,48–50] From these diaryl substituted PDI subunits, we build the two macrocycles, **PBPB** and **$(PPh_2)_4$**, using a tetranucleur platinum macrocyclization followed by reductive eliminations, analogous to the synthetic approach described in Chapter 1B and Chapter 2.[7,22,25] The DFT minimized structures for **PBPB**[20] and **$(PPh_2)_4$** are shown in Figure 3.3.

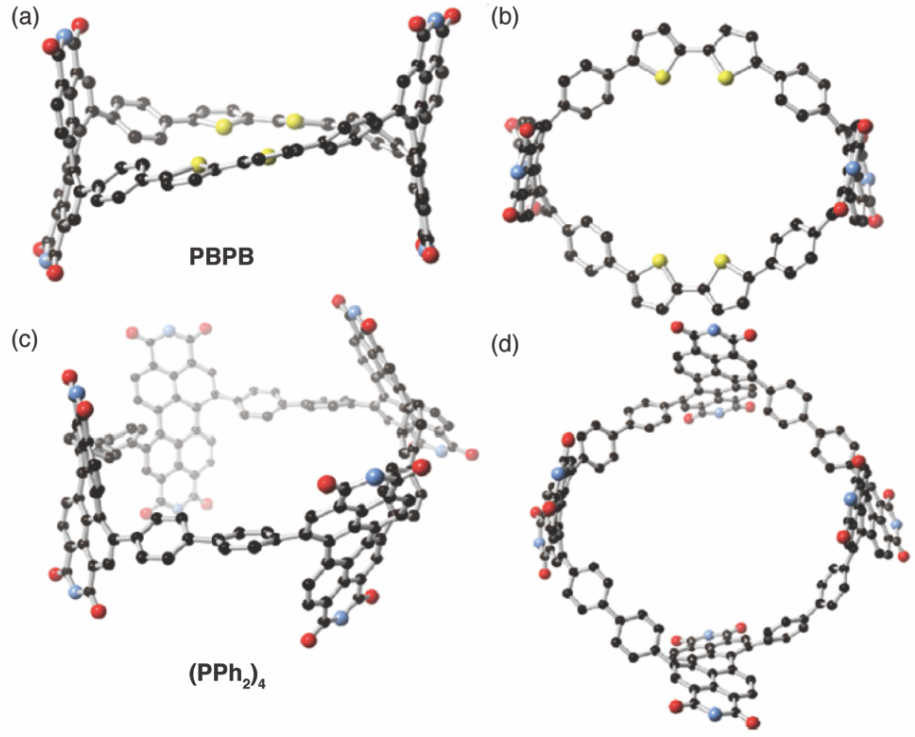

Figure 3.3. (a) Energy minimized structures from DFT for **PBPB**. The (*M,M*)-stereoisomer is shown.[20] (b) Cavity view of **PBPB**. (c) Energy minimized structures from DFT for **$(PPh_2)_4$**. The (*M,M,M,M*)-stereoisomer is shown. (d) Cavity view for **$(PPh_2)_4$**. Carbon = gray, nitrogen = blue, oxygen = red, sulfur = yellow. Hydrogen atoms have been removed to clarify the view. A methyl group substitutes the sidechains in the calculations. The methyl group, too, has been removed to clarify the view in the structures presented here.

For comparison to **PBPB** and **$(PPh_2)_4$**, we synthesized a series of acyclic molecules. The simplest structures are Compounds **3.1** and **1.1**; each possessing one PDI subunit (**1.1** was introduced in Chapter 1B). We created the polymeric version of the macrocycles [**3.3** and **3.6**] too, as these molecules would theoretically possess "infinite conjugation". As a final point of comparison, we also synthesized the precise analogs, "unfolded" macrocycles, that have one of their bonds cleaved and terminated with hydrogen atoms (**3.2** and **3.5**).

3.4. Conjugated Macrocycles in OPVs

We fabricated devices from each of these macrocyclic and acyclic molecules. We chose the low-bandgap semiconducting polymer poly[4,8-bis(5-(2-ethylhexyl)thiophen-2-yl)benzo[1,2-b;4,5-b′]dithiophene-2,6-diyl-alt-(4-(2-ethylhexyl)-3-fluorothieno[3,4-b]thiophene)-2-

carboxylate-2,6-diyl] (PTB7-Th)[51,52] as the electron donating component in our devices. PTB7-Th is widely used as a high-performance donor material in both fullerene and non-fullerene based solar cells.[53,54] PTB7-Th is complementary to all molecules synthesized, as it absorbs more low energy light (~550 nm to 800 nm). Figure 3.8 (in the Appendix) contains the film absorption spectra for all the compounds. We spin cast the mixture of PTB7-Th and the cyclic or acyclic molecules to form a bulk heterojunction (BHJ) solar cell.[55] We used an inverted configuration of ITO/ZnO(20 nm)/PTB7-Th:acceptor/MoO_3(7 nm)/Ag(100 nm) for all of our solar cell devices.[56] A schematic of the device is shown in Figure 3.4a.

Figure 3.4b-e displays the OPV properties and the EQE measurements for each of the cyclic and acyclic molecules. Details for the optimization including varying the ratio of donor and acceptor, the additives for annealing and the film thickness are included in the Supporting Information. The optimal active layers were ~100 nm in thickness. For the cyclic molecules, the optimal mass ratio was 1:2 for donor:acceptor. Furthermore, we optimized the films by using 1-chloronaphthalene (CN) as a solvent additive to control film morphology (Figure 3.11 in the Appendix).[42] **PBPB**'s PCE increases to 3.3% on average with a maximal value of 3.5%. Using an analogous procedure, we were able to achieve a PCE of 3.6% for **$(PPh_2)_4$** (see Figure 3.9, Figure 3.10, Table 3.3, and Table 3.4). This is the first example of a macrocycle being used as the electron acceptor in an OPV.

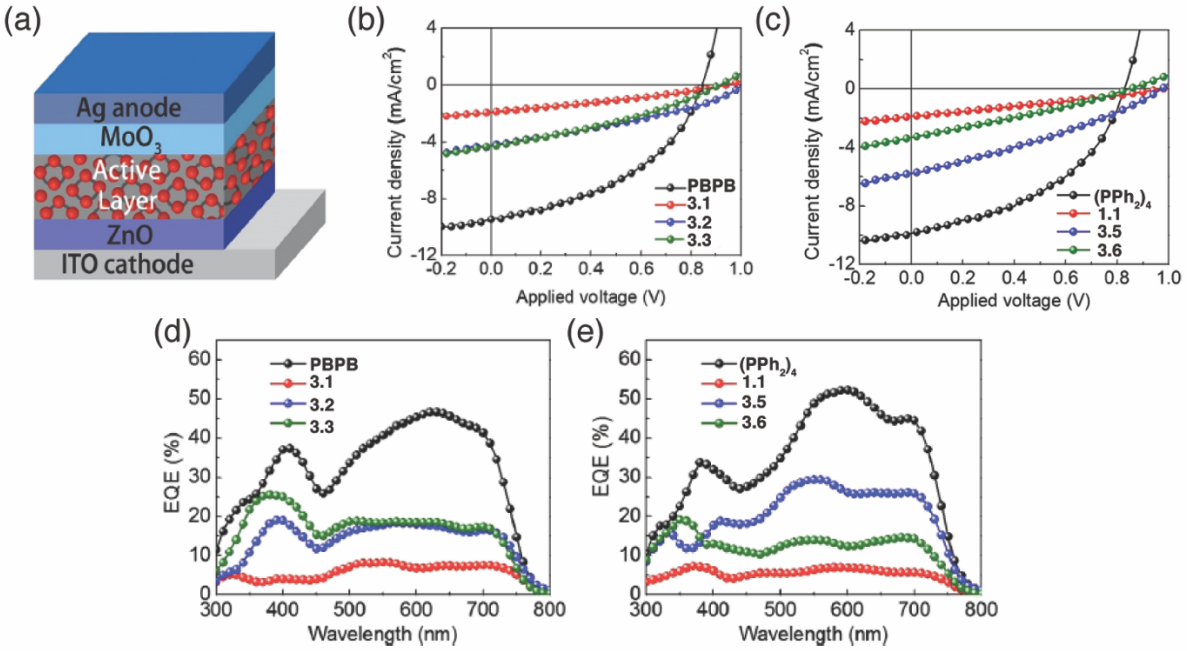

Figure 3.4. (a) Schematic of the solar cell device fabricated in this study. (b-e) J-V curves for (b) **PBPB**-series and (c) **$(PPh_2)_4$**-series solar cells under simulated AM 1.5G irradiation (100 $mWcm^{-2}$). EQE spectra for (d) **PBPB** -series and (e) **$(PPh_2)_4$**-series solar cells

Figure 3.4d and Figure 3.4e show the external quantum efficiency (EQE) curves for PTB7-Th:**PBPB** and the PTB7-Th:**$(PPh_2)_4$** solar cells. All the devices show broad photo-response from 350 nm to 800 nm, consistent with the absorption spectra (Figure 3.8). Each EQE spectrum shows two transitions; a narrow band centered at ~400 nm and a broad band centered at 620 nm for **PBPB** and at 600 nm for **$(PPh_2)_4$**. The EQE spectrum for **$(PPh_2)_4$** shows an increase relative to **PBPB** at ~700 nm. We note that both macrocycles show strong absorption from 400 nm to 650 nm (see Figure 3.5), indicating that photoexcitation in acceptor domains contributes to photocurrent in this type of solar cell. The integrated J_{sc} values are 9.2 and 9.8 $mAcm^{-2}$ for PTB7-Th:**PBPB** and the PTB7-Th:**$(PPh_2)_4$** solar cells , respectively. These values agree well with the measured J_{sc}, with mismatch < 3%. Upon addition of the CN additive, the EQE enhances over a broad range of wavelengths, particularly from 550 nm to 750 nm (Figure 3.9 and Figure 3.10). Atomic force microscopy (AFM) of the films confirms that CN changes the film morphology, resulting in more efficient charge dissociation and transport (Figure 3.11). Like $PC_{71}BM$ and some non-fullerene

acceptors,[48,53] complementary absorption between the macrocycles and the donor material is beneficial for harvesting light in the visible light region to maximize photocurrent.

Table 3.1. Summary of Device Parameters

	J_{sc} (mA cm^{-2})	V_{oc} (V)	FF	PCE (%)
PBPB	9.2 ± 0.3	0.84 ± 0.01	0.44 ± 0.01	3.3 ± 0.2 (3.5)
3.1	1.6 ± 0.2	0.94 ± 0.01	0.30± 0.01	0.46 ± 0.04 (0.53)
3.2	4.2 ± 0.1	1.00 ± 0.01	0.33 ± 0.01	1.3 ± 0.1 (1.4)
3.3	4.2 ± 0.2	0.90 ± 0.01	0.33 ± 0.01	1.1 ± 0.2 (1.3)
$(PPh_2)_4$	9.7 ± 0.2	0.83 ± 0.01	0.44 ± 0.01	3.5 ± 0.1 (3.6)
1.1	1.7 ± 0.1	0.97 ± 0.02	0.28 ± 0.01	0.46 ± 0.03 (0.51)
3.5	5.8 ± 0.1	0.97 ± 0.01	0.32 ± 0.01	1.6 ± 0.2 (1.8)
3.6	3.2 ± 0.1	0.85 ± 0.01	0.28 ± 0.01	0.73 ± 0.04 (0.78)

Table 3.1: Summary of device parameters of the solar cells based on the cycles and acyclic molecules. Highest PCE values are shown in parentheses.

We next compare the OPV results from the cyclic molecules to the acyclic molecules. Table 3.1 summarizes the device data. The key finding is that all of the acyclic molecules showed poor device performance on both an absolute and relative basis. Figure 3.4b and 3.4c display the *J-V* curves for all the devices. We observe a couple of trends from this study: (1) smaller oligomer acyclic molecules (**3.1**, **3.2**, **1.1**, and **3.5**) and the polymers (**3.3** and **3.6)** show decreased J_{sc} relative to the cyclic compounds; (2) the acyclic molecules also show higher V_{oc} values as compared to the cyclic acceptors; and (3) the poor PCEs in the devices from acyclic molecules are mainly attributed to the reduced J_{sc} and FFs relative to the cyclic ones. Figure 3.3d and 3.3e display comparison of external quantum spectra of the cyclics versus the acyclics. Overall, the photocurrent generation

in cyclic-based devices is much larger than the acyclic-based devices. These results indicate that the cyclic acceptors have enhanced photocarrier generation and better charge transport.

To better understand the performance difference between the cyclic and acyclic molecules, we examined the electrochemistry, UV-vis absorption, electron mobility and morphology of the films. These studies are described below.

3.5. Electrochemistry of N-type Semiconductors

We probe the variations in the frontier orbital energies for the macrocycles and their acyclic analogues using CV (see Figure 3.12 in the Appendix). The onset of the first oxidation and reduction peaks provide an estimate of the HOMO and LUMO levels, respectively.[57] We find the acyclic molecules possess a more negative first reduction potential than the cyclic molecules. As a result, we observe higher energies for the LUMO for each of the acyclic molecules. The electrochemical data are summarized in Table 3.2.

The energy offset between the donor's HOMO and acceptor's LUMO is one of the factors that determines the V_{oc}s in BHJ solar cells.[58] The values obtained from CV results are in good agreement with the V_{oc} trend from the devices. Previous studies show a direct correlation between relatively large V_{oc} values coupled with low J_{sc} when the band offset does not provide sufficient driving force for exciton dissociation at the donor/acceptor interfaces.[59,60] Here, the trend observed suggests that the high LUMO levels, particularly in the short acyclic compounds, result in a higher occurrence of recombination and lower $J_{sc.}$[60,61]

Table 3.2. Comparison of Electronic Data

	Electrochemical[a]			Optical[b]	FET
	E_{LUMO}/eV	E_{HOMO}/eV	E_{gap} /eV	E_{gap} /eV	μ /$cm^2V^{-1}s^{-1}$
PBPB	-3.87	-5.39	1.52	2.02	$(1.5 \pm 0.2)\times10^{-3}$
3.1	-3.80	-5.42	1.62	2.18	$(4.3 \pm 0.2)\times10^{-4}$
3.2	-3.80	-5.40	1.60	1.79	-
3.3	-3.86	-5.45	1.59	2.21	$(2.3 \pm 0.3)\times10^{-4}$
$(PPh_2)_4$	-3.90	-5.69	1.79	2.12	$(1.5 \pm 0.2)\times10^{-3}$
1.1	-3.75	-	-	2.25	$(2.0 \pm 0.3)\times10^{-5}$
3.5	-3.82	-5.77	1.95	2.23	-
3.6	-3.86	-5.75	1.89	2.21	$(1.9 \pm 0.3)\times10^{-5}$

Table 3.2: Comparison of the band-gaps estimated from CV and UV-vis absorption spectroscopy, and OFET performance. *a*HOMO and LUMO levels were estimated from onset of the first oxidation and reduction peaks. *c*Optical band gaps were estimated from the wavelength at the absorption maximum.

3.6. Absorption Spectroscopy

Figure 3.5 compares the UV-vis absorption spectra of **PBPB** and **$(PPh_2)_4$** to their acyclic counterparts. It is well documented that contorting linear molecules into cyclic structures significantly alters the electronic properties.[2,25] Absorptions in the cyclic compounds are shifted to lower energy relative to the linear, unstrained acyclic molecules. The CV data is also consistent with the UV-vis data. **PBPB** and **$(PPh_2)_4$** have smaller HOMO-LUMO gaps relative to each of the corresponding acyclic molecules studied (Figure 3.12). Greater visible light absorption contributes to the more efficient solar cells for the cyclic molecules, providing the higher J_{sc} parameter for the cyclic molecules relative to the acyclic molecules.

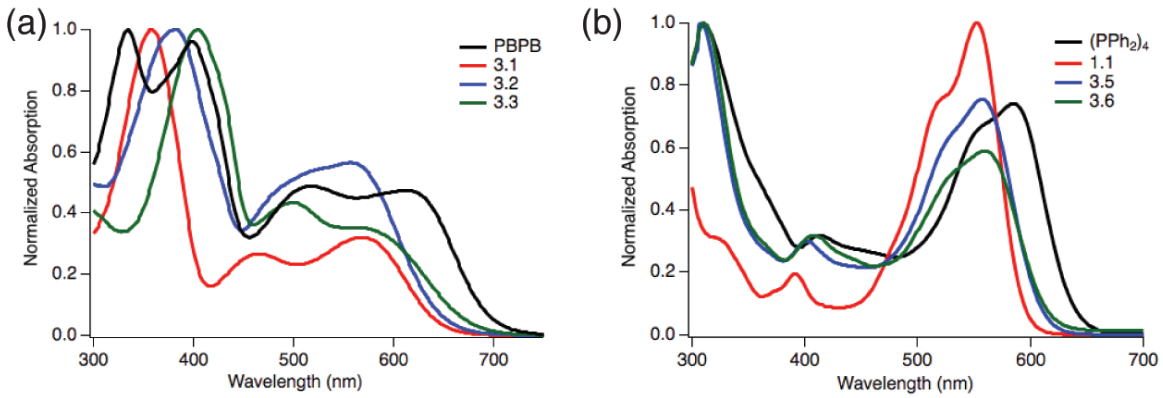

Figure 3.5. UV-vis absorption spectra measured in solution: (a) for **PBPB**, **3.1**, **3.2**, and **3.3**; (b) for **$(PPh_2)_4$**, **1.1**, **3.5**, and **3.6** normalized to each absorption maxima, where absorption max = 1.

3.7. OFET Characteristics

Another factor that is critical for OPV device performance is electron transport through the acceptor phase. Poor carrier mobility impedes the carrier extraction and results in increased carrier recombination inside OPV devices. This negatively impacts the J_{sc}, FF and overall solar cell performance. To investigate the electron mobility of these compounds, we fabricated OFETs. The Supporting Information describes the preparation of the devices and the methodology used to extract the OFET characteristics. All molecules measured form n-type, electron-transporting thin-film semiconductors.[38,62] Figure 3.6 displays typical transfer curves in the saturation regime. The mobility was calculated in the saturation regime using $I_{DS} = (W/2L)C_i\mu(V_G - V_T)^2$, where W and L are the width and length of the channel, C_i (11.5 nFcm^{-2}), μ, and V_T correspond to the capacitance per unit area of the gate insulator, the field effect mobility, and the threshold voltage, respectively.[63] Both **PBPB** and **$(PPh_2)_4$** show electron mobility of $(1.5 \pm 0.2) \times 10^{-3}$ cm^{2}V^{-1}s^{-1}. One of the key findings is the cyclic molecules have a far greater ability to transport electrons in thin-film devices relative to the acyclic molecules. Table 3.2 shows electron mobility for six of the compounds studied. **PBPB**'s average mobility is five-fold higher than its acyclic counterparts; **$(PPh_2)_4$**'s mobility is nearly two orders of magnitude higher than its counterparts. The cyclic

structures far greater ability to transport electrons contributes to the overall better solar cell performance.

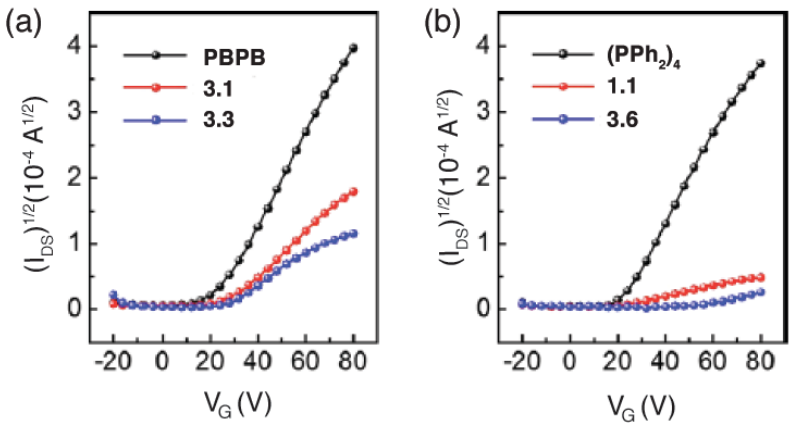

Figure 3.6. OFET transfer characteristics plotted in $(I_{DS})^{1/2}$-V_G axes for (a) **PBPB**, **3.1** and **3.3** and (b) for **$(PPh_2)_4$**, **1.1**, and **3.6**. The V_{DS} is 80 V.

3.8. Film Morphology

At the nanoscale level, phase separation between the donor and the acceptor plays an important role in providing an efficient donor/acceptor interface and a continuous pathway for carrier transport. Appropriate aggregation and phase separation is critical to device performance of BHJs in terms of charge dissociation and carrier transport. We performed AFM to study the surface morphology of the active layers. Figure 3.7 displays phase images of the six active layers studied. The corresponding height images are displayed in Figure 3.13. For both **PBPB** and **$(PPh_2)_4$**, the active layers possess clear phase separation as shown in Figure 3.7a and 3.7d. The average domain size is estimated to be 20-40 nm. For the polymeric **3.3** and **3.6**, the domain sizes are relatively small (10-30 nm) (Figure 3.7c,f). It is difficult to detect efficient phase segregation in these films. The active layers containing **3.1** and **1.1** have large domain sizes; they are in the range of 50-70 nm, as shown in Figure 3.7b and 3.7e. These features exceed twice the typical exciton diffusion length (ca. 10-20 nm) in organic semiconductors. Thus, photogenerated excitons within the domain recombine before they reach the donor/acceptor interface.[55,64] The over-

aggregation in the **3.1** and **1.1** solar cells likely results in carrier recombination and poor device performance. In the **PBPB**- and **$(PPh_2)_4$**-based BHJ systems, phase aggregation is essential to the device performance as it enables an efficient donor/acceptor interface and a three dimensional continuous pathway for efficient carrier transport.

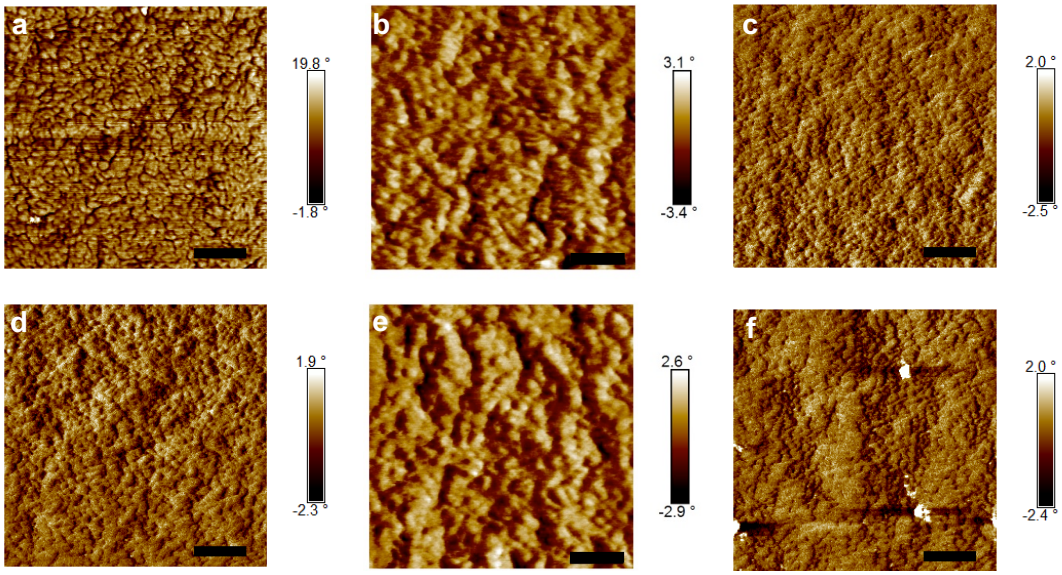

Figure 3.7. AFM phase images of bulkjunction films for (a) **PBPB**, (b) **3.1**, (c) **3.3**, (d) **$(PPh_2)_4$**, (e) **1.1**, and (f) **3.6**. The mass ratio of donor-to-acceptor is fixed at 1:2. 1 % CN additive was used. The scale bar is 200 nm.

3.9. Conclusion

This is the first study comparing cyclic structures to their acyclic counterparts in OPVs. We found that the cyclic structures far outperform the acyclic controls in organic photovoltaics. We find it interesting that **PBPB** and **$(PPh_2)_4$** perform similarly as the electron transporting material in OPVs even though **PBPB**'s UV-vis is shifted to lower energy compared to that of **$(PPh_2)_4$**. The origin of the increase in the efficiency of the devices when cyclic molecules are used in place of acyclic ones is multifaceted. When compared to the acyclic molecules, the macrocycles: (1) have better energy alignment with the donor material; (2) absorb more visible light; (3) are more efficient at transporting electrons; and (4) shows optimal phase separation for BHJ solar cells. The ease with which we can tune the energetics and therefore the properties of these

macrocycles – through a different linker subunit or incorporating oligomeric PDI subunits – will magnify these initial findings.[54] This study also offers the intriguing possibility of tuning the geometry of the donor so that it is shape matched to these cyclic electron accepting structures as a means to creating highly efficient devices.

3.10. Appendix – Supplementary Figures

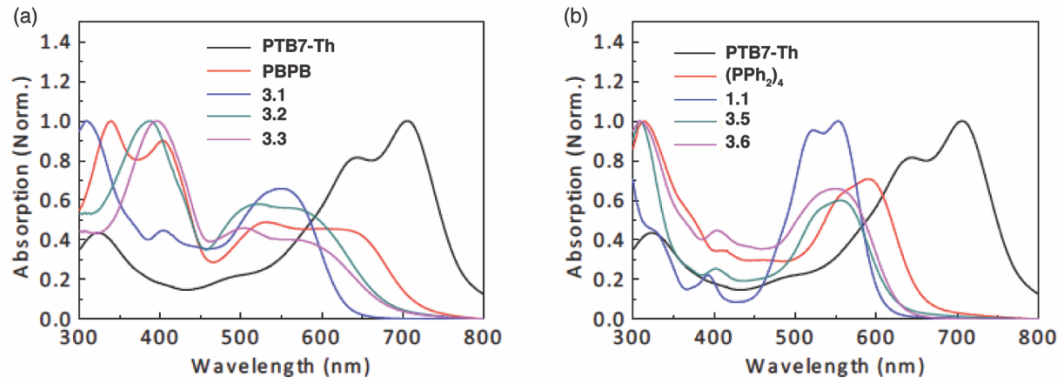

Figure 3.8. UV-vis absorption spectra measured in films: for (a) **PBPB**, **3.1**, **3.2**, and **3.3**; and (b) **$(PPh_2)_4$**, **1.1**, **3.5**, and **3.6** normalized to each absorption maxima, where absorption max = 1.

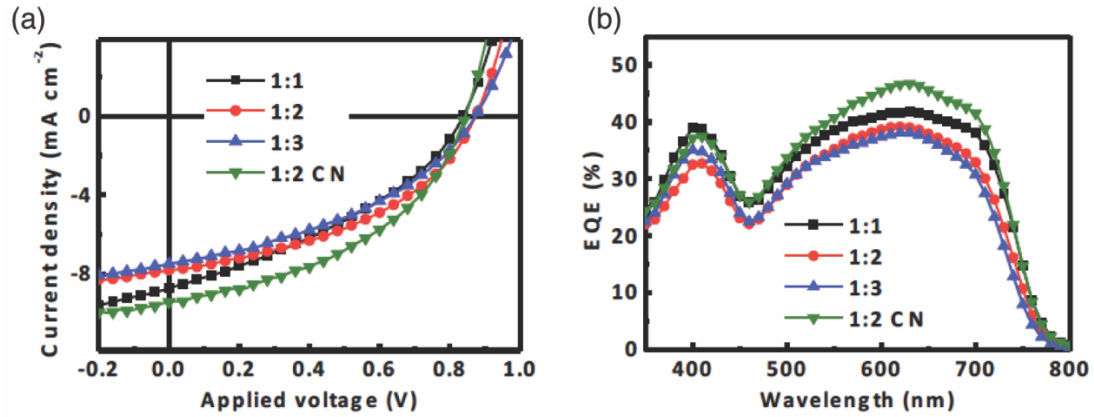

Figure 3.9. Device performance of PTB7-Th:**PBPB** solar cells. (a) Current density versus voltage (*J*–*V*) characteristics of PTB7-Th:**PBPB** solar cells with different blend ratios (PTB7-Th to **PBPB**) and 1% v/v CN. (b) EQE spectra of corresponding PTB7-Th:**PBPB** solar cells.

Table 3.3. Summary of Device Parameters for PTB7-Th:**PBPB** solar cell.

Mass ratio	J_{sc} (mAcm^{-2})	V_{oc} (V)	FF	PCE (%)
1:1	8.5 ± 0.3	0.83 ± 0.01	0.36 ± 0.01	2.5 ± 0.1 (2.6)
1:2	7.6 ± 0.2	0.87 ± 0.01	0.43 ± 0.01	2.8 ± 0.1 (2.9)
1:3	7.4 ± 0.1	0.87 ± 0.01	0.40 ± 0.01	2.5 ± 0.1 (2.6)
1:2 with CN	9.2 ± 0.3	0.84 ± 0.01	0.44 ± 0.01	3.3 ± 0.2 (3.5)

Table 3.3: Summary of device parameters of best PTB7-Th:**PBPB** solar cells with different conditions. Average PCE values were calculated from six devices for each condition; the highest PCE values are shown in parentheses.

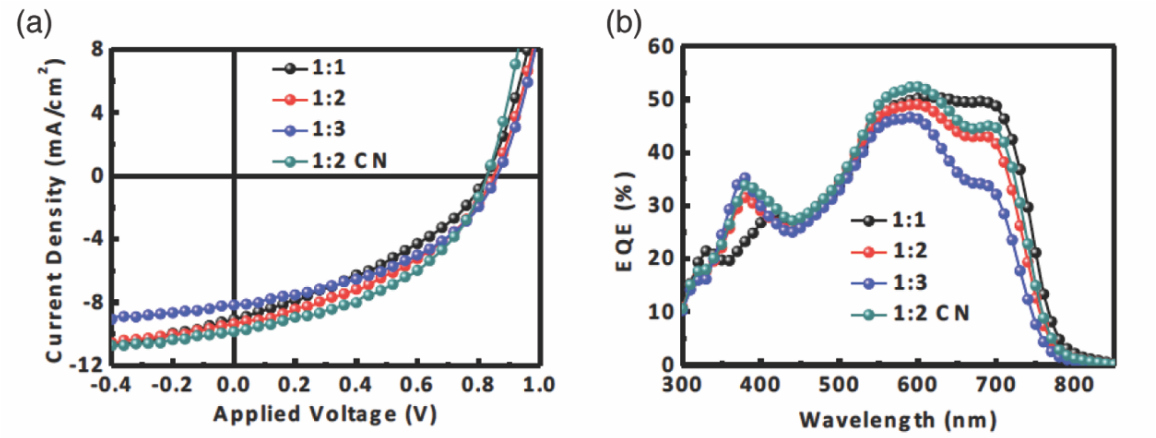

Figure 3.10. Device performance of PTB7-Th**:(PPh$_2$)$_4$** solar cells. (a) Current density versus voltage (*J–V*) characteristics of PTB7-Th:**(PPh$_2$)$_4$** solar cells with different blend ratios (PTB7-Th to **(PPh$_2$)$_4$)** and 1% v/v CN. (b) EQE spectra of corresponding PTB7-Th:**(PPh$_2$)$_4$** solar cells.

Table 3.4. Summary of Device Parameters for PTB7-Th:**(PPh$_2$)$_4$** solar cell.

Mass ratio	J_{sc} (mAcm^{-2})	V_{oc} (V)	FF	PCE (%)
1:1	8.6 ± 0.3	0.82 ± 0.01	0.37 ± 0.01	2.6 ± 0.2 (2.8)
1:2	8.8 ± 0.2	0.85 ± 0.01	0.41 ± 0.01	3.0 ± 0.1 (3.2)
1:3	7.6 ± 0.2	0.86 ± 0.01	0.43 ± 0.01	2.8 ± 0.2 (3.0)
1:2 with CN	9.7 ± 0.2	0.83 ± 0.01	0.44 ± 0.01	3.5 ± 0.1 (3.6)

Table 3.4: Summary of device parameters of best PTB7-Th:**(PPh$_2$)$_4$** solar cells with different conditions. Average PCE values were calculated from six devices for each condition; the highest PCE values are shown in parentheses.

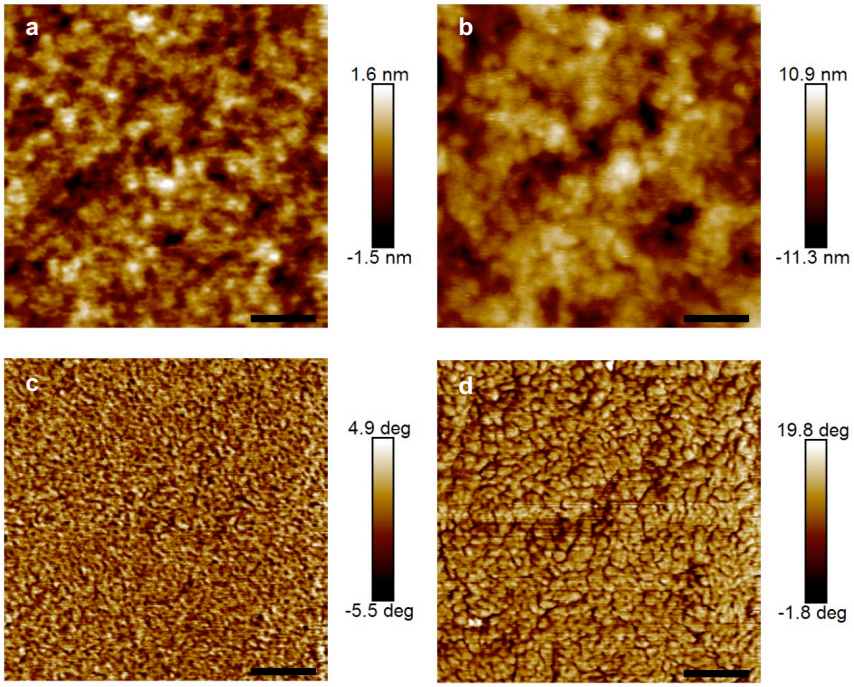

Figure 3.11. AFM height images of PTB7-Th:**PBPB** films at a donor:acceptor ratio of 1:2 (a) without CN and (C) with 1 % CN. AFM phase images of PTB7-Th:**PBPB** films at a donor:acceptor ratio of 1:2 (B) without CN and (d) with 1 % CN. The scale bar is 200 nm. Both of the active layers have very smooth surface, with root-mean-square roughness (RMS) of 0.5 nm and 2.6 nm for films both with/without 1% CN, respectively. When turning to the phase images, we observed fibrous domains in the active layer without CN. However, this feature is too fine to be quantified under the instrument limit (~8 nm). In contrast, the active layer with the 1% CN additive possesses clear phase separation as shown in d. The average domain size is estimated to be 20-40 nm. Here CN plays a critical role in phase aggregation, which is essential to the device performance.

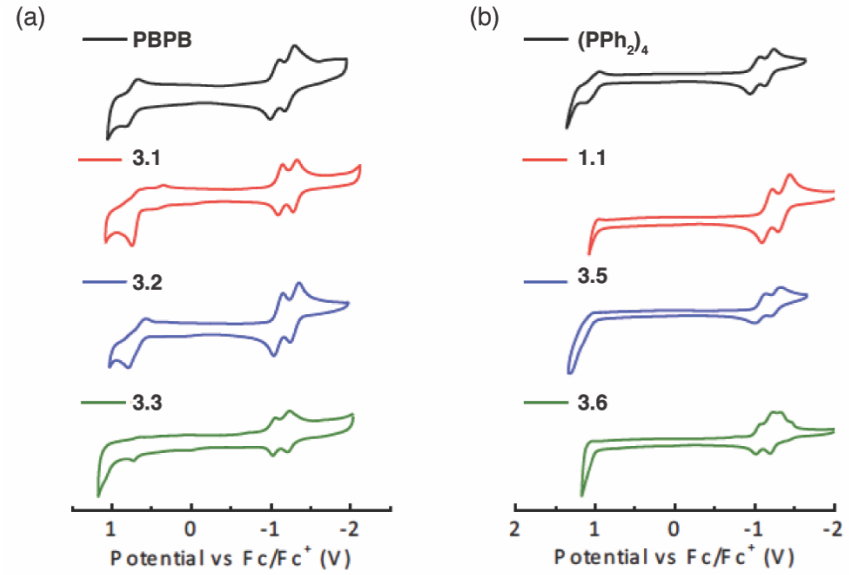

Figure 3.12. CV (a) for **PBPB**, **3.1**, **3.2**, and **3.3**; (b) for **$(PPh_2)_4$**, **1.1**, **3.5**, and **3.6**.

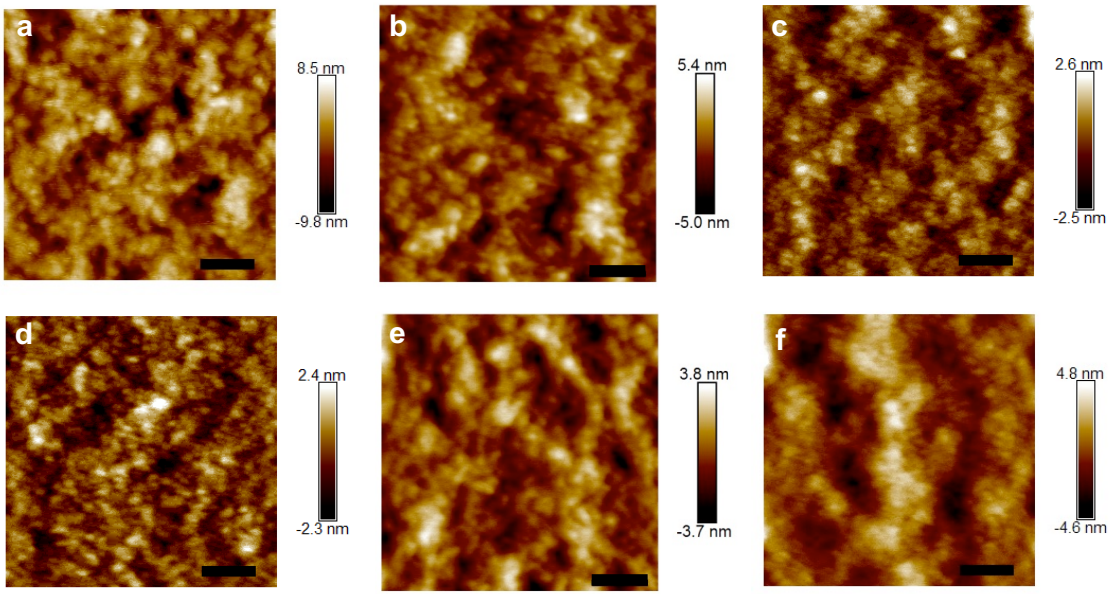

Figure 3.13. AFM height images of bulkjunction films for (a) **PBPB**, (b) **3.1**, (c) **3.3**, (d) **$(PPh_2)_4$**, (e) **1.1**, and (f) **3.6**. The mass ratio of donor-to-acceptor is fixed at 1:2. 1 % CN additive was used. The scale bar is 200 nm.

3.11. General Experimental Information

Synthesis. All reactions were performed in oven-dried or flame-dried round bottom flasks, unless otherwise noted. The flasks were fitted with rubber septa and reactions were conducted under a positive pressure of nitrogen or argon, unless otherwise noted. Anhydrous and anaerobic solvents were obtained from a Glass Contour solvent system consisting of a Schlenk manifold with purification columns packed with activated alumina and supported copper catalyst. Reaction monitoring by TLC was performed on J.T. Baker Baker-flex Silica Gel IB2-F (25 mm x 75 mm) TLC plates. TLC visualization was accomplished by visible observation and irradiation with a UV lamp. Commercial reagents were used without further purification. $Pt(COD)Cl_2$ was purchased from Strem Chemicals, and all other reagents were purchased from Sigma-Aldrich.

Purification. Automated flash chromatography was performed using a Teledyne Isco Combiflash Rf200 and Redisep Rf Silica columns. Preparative high performance liquid chromatography (HPLC) was performed on a Waters Prep150 instrument equipped with a UV-vis

detector, an automated fraction collector, and a Nacalai Tesque COSMOSIL Buckyprep column (20 mm I.D. x 250 mm, 5 μm).

Spectrometers. ^{1}H NMR spectra were recorded on a Bruker 400 or 500 MHz spectrometer. ^{13}C NMR spectra were recorded on a Bruker 125 or 100 MHz spectrometer with complete proton decoupling. NMR spectra were recorded at 300 K unless otherwise noted. Chemical shifts are reported in parts per million (ppm) Data are represented as follows: chemical shift, multiplicity (s = singlet, d = doublet, dd= doublet of doublets, t = triplet, m = multiplet), coupling constants in Hz, and integration. Broadening (br) of peaks in the ^{1}HNMR spectrum is due to rotational isomers about the imide side chains. Multiple peaks for the same carbon in the ^{13}C NMR spectrum arise due to rotational isomers about the imide side chains that have been seen previously.[13,65] HRMS was performed on a (1) Waters XEVO G2-XS QTOF instrument equipped with a UPC SFC inlet, and ESI and APCI ionization sources; or (2) a Bruker UltrafleXtreme MALDI TOF/TOF instrument using a dithranol matrix. UV-vis absorption spectra were recorded on a Shimadzu UV-1800 spectrophotometer using a 1.0 cm quartz cell. IR spectra were recorded on a Perkin Elmer Spectrum400 FTIR spectrometer using a PIKE ATR attachment. GPC analysis was done on an Agilent Technologies 1200 Infinity Series GPC fitted with a refractive index detector and a UV-visible detector. All samples were eluted at 1.0 mL/min through two Agilent Technologies PLgel 5 μm MIXED-D 300x7.5mm columns and monitored by their UV-vis signal. M_n and M_w were assigned based off of polystyrene standards.

Atomic force microscopy. AFM measurements were carried out in tapping mode on a Bruker Multi-Mode AFM at ambient conditions. A commercial silicon cantilever (RTESPA, MPP-11120-10, Bruker) was used in this study with a typical radius of curvature of ~8nm and a nominal spring constant of ~40 Nm^{-1}.

Cyclic Voltammetry. CVs were recorded on a CH166 electrochemical workstation using an Ag/AgCl electrode as the reference electrode at room temperature. Experiments were performed in CH_2Cl_2 with NBu_4PF_6 as the supporting electrolyte at a scan rate of 0.1 V/s.[57]

Thin film transistors. To create the devices, we first silanize the substrate (300 nm of SiO_2 on a Si wafer) with octadecyltrichlorosilane (OTS). Au is deposited onto the substrate as bottom-contact source and drain electrodes (40 nm) with a width of 105 μm and length of 20 μm. Next, we spin-cast organic films onto the surface at 1,000 r.p.m. for 1 min, to form transistors using the silicon wafer as the global back gate for the device. Finally, the samples were annealed under inert atmosphere at 160°C for 10 minutes to optimize device performance except that the **3.5** film was annealed at 120°C. The thin film transistors were tested on the Agilent 4155C semiconductor parameter analyzer.

Solar cell fabrication. PTB7-Th was purchased from 1-Material Inc. Synthesis of ZnO sol-gel precursor was described elsewhere.[56] Zinc acetate dihydrate, ethanolamine, 2-methoxyethanol, DIO and all of the solvents were purchased from Sigma Aldrich. Pre-patterned ITO-coated glass with a sheet resistance of ~15 Ωsq^{-1} was cleaned with detergent and ultrasonicated in deionized water, acetone and isopropanol for 30 min, respectively. Subsequently, we treated the substrates by ultraviolet-ozone for 10min. The prepared ZnO precursor was spin-cast onto the ITO substrate at 3,000 r.p.m. for 1 min, followed by annealing at 200 ^oC for 1h in air, to form a thin film with approximate thickness of 20 nm. Active layers were prepared by spin-coating a mixed solution containing polymer and acceptor in chlorobenzene at a total concentration of 25 $mgml^{-1}$. The thickness of the prepared active layers is about 100 nm. Finally, a 7 nm MoO_3 layer was deposited first and then a 100-nm Ag electrode was subsequently deposited through a shadow mask by thermal evaporation under a vacuum about 1×10^{-6} torr. The current density–

voltage (*J–V*) curves were measured by a Keithley 2635A source measure unit. The photocurrent was measured under AM 1.5G illumination at 100 $mWcm^{-2}$ under a Newport solar Simulator. A KG5-Si reference cell traceable to Newport was used to calibrate light intensity. The effective device area was defined as 6.25 mm^2 by an aperture mask. EQE measurements were performed using a QEXL system from PV Measurements Inc.

3.12. Synthetic Procedures and Characterization

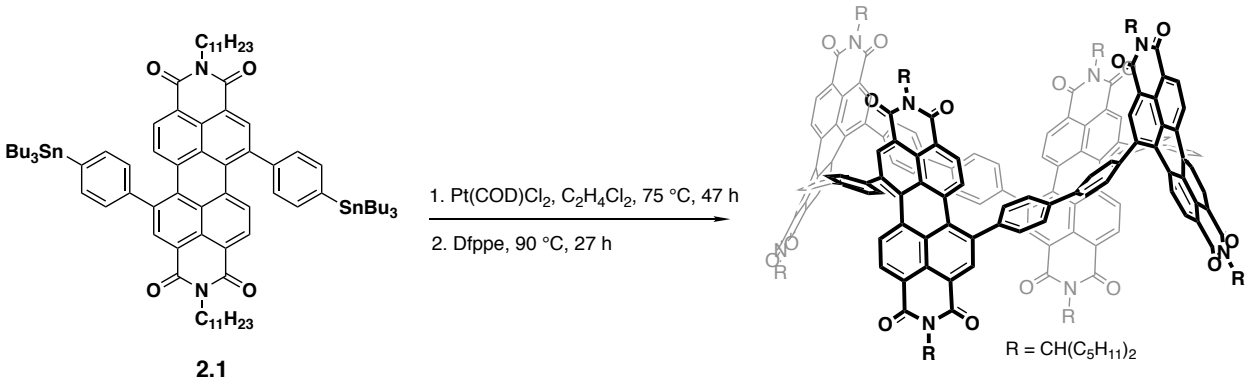

2.1

Synthesis of **$(PPh_2)_4$**: Compound **2.1** (1.04 g, 0.727 mmol, 1.00 equiv) and $Pt(COD)Cl_2$ (0.272 g, 0.727 mmol, 1.00 equiv) were added to an oven-dried, 2-neck, 500-mL round bottom flask with a stir bar. 1,2-Dichloroethane (300 mL) was added, and the mixture was sparged with N_2 for 30 min at ambient temperature. Under positive pressure of N_2, the flask was placed in an oil bath at 75 °C with stirring for 47 h. The mixture was allowed to cool to ambient temperature before adding 1,2-bis[bis(pentafluorophenyl)phosphino]ethane (2.76 g, 3.63 mmol, 5.00 equiv). The mixture was stirred at room temperature for 30 min, fitted with a reflux condenser, and placed in an oil bath at 90 °C for 27 h. The mixture was allowed to cool to room temperature then concentrated under reduced pressure. The crude mixture was loaded onto a silica column (120 g Redisep Rf Silica) and purified with a gradient from 9:1 CH_2Cl_2/hexanes to CH_2Cl_2 to 9:1 CH_2Cl_2/MeOH at 85 mL/min. Fractions containing **$(PPh_2)_4$** were identified by MALDI-TOF MS and were collected and concentrated. These fractions were further purified by preparative HPLC on a COSMOSIL

Buckyprep column (20 x 250 mm) with an eluent of 12% CH_2Cl_2/hexanes (v/v) at a flow rate of 18.9 mL/min. The pure fractions were concentrated to give **$(PPh_2)_4$** as a dark purple solid (0.0530 g, 0.0150 mmol, 8% yield). ^{1}H NMR (500 MHz, $C_2D_2Cl_4$, 413 K) δ 8.62 (s, 8H), 8.39 (d, J = 8.0 Hz, 8H), 8.32 (d, J = 8.0 Hz, 8H), 7.75 (d, J = 8.4 Hz, 16H), 7.64 (br d, J = 7.7 Hz, 16H), 5.21 – 5.13 (m, 8H), 2.30 – 2.18 (m, 16H), 2.00 – 1.89 (m, 16H), 1.44 – 1.29 (m, 96H), 0.89 (t, J = 7.0 Hz, 48H). ^{13}C NMR (125 MHz, C2D2Cl4, 383 K) δ 163.82, 163.57, 141.33, 140.40, 134.93, 134.52, 132.57, 130.13, 129.89, 129.52, 129.35, 128.46 (br), 127.45, 122.64, 122.30, 54.74, 32.34, 31.44, 26.38, 22.13, 13.53. IR (cm–1) 2955, 2927, 2860, 1695, 1657, 1595, 1585, 1456, 1407, 1324, 1238, 1180, 1127, 1096, 1003, 812. HRMS (MALDI–) calculated *m/z* for $[C_{232}H_{240}N_8O_{16}]^-$ 3393.821, found 3393.715.

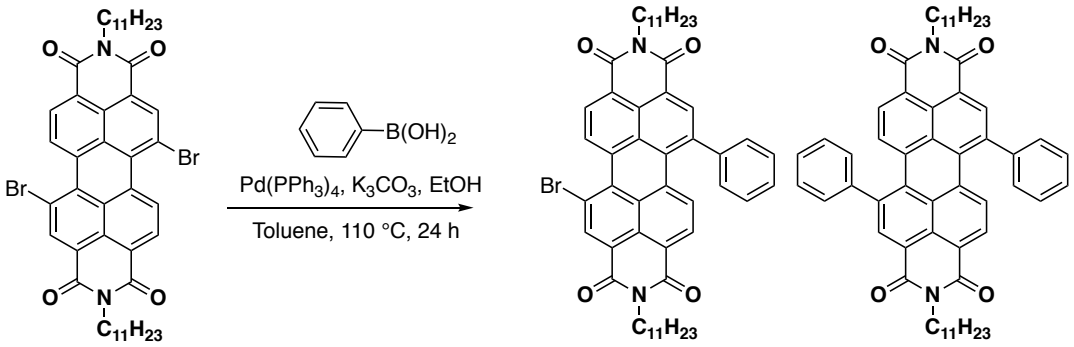

***1,7*-dibromo PDI** **SI-3.1** **1.1**

Synthesis of **SI-3.1** and **1.1**: *N,N′*-Di(6-undecyl)-1,7-dibromoperylene-3,4:9,10-tetracarboxylic diimide (0.600 g, 0.703 mmol, 1.00 equiv), phenyl boronic acid (0.0430 g, 0.352 mmol, 0.500 equiv), aqueous K_2CO_3 (2 M, 6.00 mL), EtOH (1.20 mL) and toluene (18.0 mL) were added to a two-neck 100-mL round bottom flask equipped with a stir bar. The mixture was sparged with N_2 for thirty minutes. While under N_2, tetrakis(triphenylphosphine)palladium(0) (0.0810 g, 0.0703 mmol, 0.100 equiv) was added. The mixture was further sparged for ten minutes before being fitted with a condenser and placed in a 100 °C oil bath under N_2, stirring for twenty-four hours. The

crude mixture was extracted with ethyl acetate and brine, concentrated and purified by column chromatography (40 g Redisep Rf Silica) using a gradient from 0% to 100% CH_2Cl_2/hexanes at 40 mL/min. Further purification by prep HPLC (COSMOSIL Buckyprep 20 x 250 mm, 18.9 mL/min and 3:93 CH_2Cl_2:hexanes) yielded **SI-3.1** (0.0930 g, 0.109 mmol, 16%) and **1.1** (0.0290 g, 0.0341, 5.0%) **SI-3.1**: **^{1}H NMR** (400 MHz, $CDCl_3$) δ 9.54 (d, J = 8.2 Hz, 1H), 8.90 (br, 1H), 8.66 (br, 2H), 8.11 (br, 1H), 7.80 (d, J = 8.2 Hz, 1H), 7.49 (br, 5H), 5.24 – 5.16 (m, 1H), 5.12 (br, 1H), 2.30 – 2.17 (m, 4H), 1.88 – 1.79 (m, 4H), 1.26 (br, 24H), 0.85 (br, 12H). **^{13}C NMR** (100 MHz, $CDCl_3$) δ 164.61, 164.26, 163.53, 162.54, 141.96, 141.43, 138.48, 137.83, 135.74, 135.07, 133.91, 133.70, 133.63, 131.62, 130.37, 130.30, 130.18, 129.99, 129.77, 129.58, 129.28, 128.99, 128.80, 128.67, 128.24, 127.70, 127.41, 123.87, 123.16, 122.45, 121.76, 120.29, 54.87, 54.76, 32.34, 32.26, 31.75, 31.72, 26.58, 22.57, 22.54, 14.04. **IR** (cm^{-1}) 2955, 2925, 2857, 1698, 1657, 1596, 1587, 1456, 1447, 1403, 1326, 1239, 1184, 914, 812, 734. **HRMS** (APCI+) calculated *m/z* for $[C_{52}H_{57}N_2O_4Br+H]^+$ 853.3580, found 853.3572. **3.1**: **^{1}H NMR** (400 MHz, $CDCl_3$) δ 8.62 (br, 2H), 8.12 (br, 2H), 7.82 (d, J = 8.2 Hz, 2H), 7.59 – 7.55 (m, 4H), 7.54 – 7.45 (m, 6H), 5.15 (br, 2H), 2.29 – 2.16 (m, 4H), 1.88 – 1.76 (m, 4H), 1.37 – 1.18 (m, 24H), 0.83 (t, J = 6.6 Hz, 12H). **^{13}C NMR** (100 MHz, $CDCl_3$) δ 164.70, 163.63, 142.23, 141.08, 135.78, 135.10, 134.81, 132.49, 130.22, 130.16, 129.91, 129.23, 129.17, 129.03, 128.59, 127.90, 122.87, 122.53, 122.13, 121.77, 54.65, 32.32, 31.75, 26.59, 22.55, 14.04. **IR** (cm^{-1}) 2956, 2925, 2860, 1695, 1657, 1598, 1585, 1409, 1325, 1242, 910, 814. **HRMS** (APCI-) calculated *m/z* for $[C_{58}H_{62}N_2O_4]^-$ 850.4710, found 850.4704. **1.1** was synthesized in Chapter 4 in a 97% yield using different conditions.

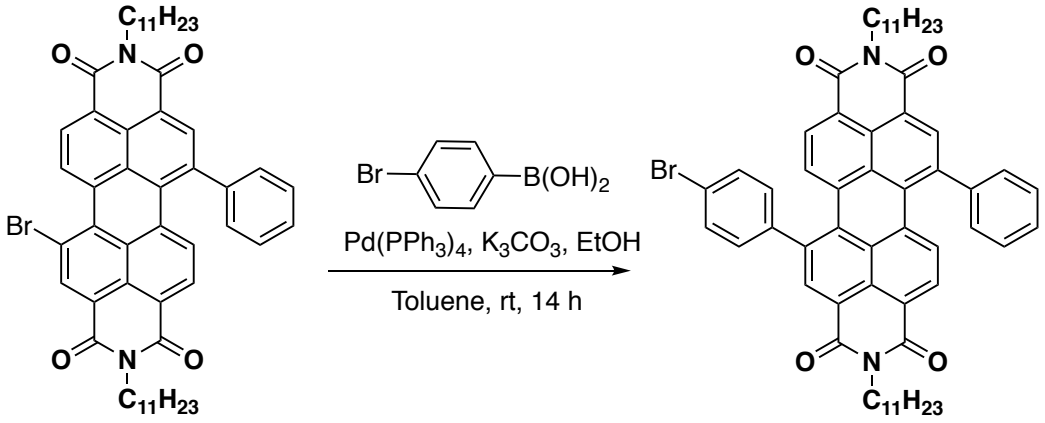

SI-3.1 **SI-3.2**

Synthesis of **SI-3.2**: **SI-3.1** (0.120 g, 0.141 mmol, 1.00 equiv), 4-bromophenylboronic acid (0.0850 g, 0.422 mmol, 3.00 equiv), aqueous K_2CO_3 (2 M, 1.20 mL), EtOH (0.240 mL) and toluene (3.60 mL) were added to 20 mL scintillation vial equipped with a stir bar. The mixture was sparged with N_2 for thirty minutes. While under N_2, tetrakis(triphenylphosphine)palladium(0) (0.0160 g, 0.0104 mmol, 0.100 equiv) was added. The mixture was further sparged for ten minutes and stirred overnight at room temperature. The crude mixture was extracted with ethyl acetate and brine, concentrated and purified by column chromatography (40 g Redisep Rf Silica) using a gradient from 0% to 100% CH_2Cl_2/hexanes at 40 mL/min. Impure fractions were further purified by prep HPLC (COSMOSIL Buckyprep 20 x 250 mm, 18.9 mL/min and 7:93 CH_2Cl_2:hexanes) to yield a total 0.0700 g (0.0750 mmol, 54%) of **SI-3.2**. **^{1}H NMR** (400 MHz, $C_2D_2Cl_4$, 390K) δ 8.65 (s, 1H), 8.60 (s, 1H), 8.24 (d, J = 8.2 Hz, 1H), 8.18 (d, J = 8.2 Hz, 1H), 7.92 (d, J = 8.1 Hz, 2H), 7.74 (d, J = 8.4 Hz, 2H), 7.65 – 7.51 (m, 7H), 5.23 – 5.14 (m, 2H), 2.32 – 2.24 (m, 4H), 1.98 – 1.93 (m, 4H), 1.38 (br, 24H), 0.93 (br, 12H). **^{13}C NMR** (100 MHz, $C_2D_2Cl_4$, 390K) δ 163.98, 163.92, 163.88, 142.54, 141.56, 141.36, 139.62, 135.32, 134.90, 134.83, 134.54, 133.46, 132.51, 132.34, 130.79, 130.22, 130.19, 130.10, 129.63, 129.44, 129.34, 129.04, 128.70, 128.19, 128.15, 123.17, 123.14, 123.08, 123.01, 122.75, 55.43, 32.67, 31.74, 26.68, 22.42, 13.80. **IR** (cm^{-1}) 2955, 2926, 2860,

1697, 1658, 1597, 1587, 1459, 1408, 1325, 1241, 1185, 813. **HRMS** (APCI+) calculated *m/z* for $[C_{58}H_{61}N_2O_4Br+H]^+$ 929.3893, found 929.3885.

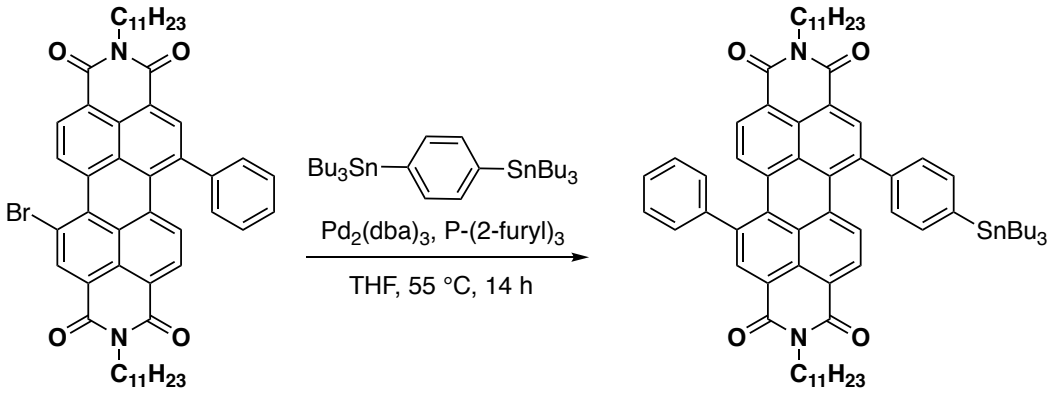

SI-3.1 **SI-3.3**

Synthesis of **SI-3.3**: **SI-3.1** (0.0930 g, 0.109 mmol, 1.00 equiv), 1,4-bis(tributylstannyl)benzene (0.0600 mL, 0.0720 mmol, 2.50 equiv) and THF (90.0 mL) were added to a 20 mL scintillation vial equipped with a stir bar. The mixture was sparged with N_2 for thirty minutes. While under N_2, tris(dibenzylideneacetone)dipalladium (0.0100 g, 0.0109 mmol, 0.100 equiv) and tri(2-furyl)phosphine (0.0110 g, 0.0436 mmol, 0.400 equiv) were added. The mixture was further sparged for ten minutes before being placed in a 55 °C oil bath and stirred overnight. The crude mixture was condensed and purified by column chromatography (40 g Redisep Rf Silica) using a gradient from 0% to 100% CH_2Cl_2/hexanes at 40 mL/min to yield **SI-3.3** (0.0770 g, 0.0680 mmol, 62% yield). **^{1}H NMR** (500 MHz, $CDCl_3$) δ 8.62 (br, 2H), 8.11 (br, 2H), 7.88 (d, J = 8.5 Hz, 1H), 7.81 (d, J = 6.3 Hz, 1H), 7.63 – 7.54* (m, J = 7.1 Hz, 4H), 7.52 – 7.48 (m, 5H), 5.15 (br, 2H), 2.25 – 2.21 (m, 4H), 1.82 (br, 4H), 1.66 – 1.54* (m, 6H), 1.43 – 1.35 (m, 6H), 1.26 (br, 24H), 1.18 – 1.09* (m, 6H), 0.94 (t, J = 7.3 Hz, 9H), 0.83 (br t, J = 6.6 Hz, 12H). **^{13}C NMR** (125 MHz, $CDCl_3$) δ 164.77, 163.66, 143.14, 142.28, 141.68, 141.33, 141.00, 138.19, 138.08, 135.87, 135.41, 135.16, 134.91, 134.76, 132.57, 132.40, 130.20, 130.17, 130.15, 129.97, 129.84, 129.26, 129.06, 128.58, 128.28, 127.92, 127.87, 122.83, 122.50, 122.14, 121.77, 54.63, 32.34, 31.77, 29.14*, 27.37*,

26.60, 26.59, 22.56, 14.05, 13.73, 9.75*. **IR** (cm^{-1}) 2956, 2925, 2855, 1697, 1657, 1598, 1586, 1459, 1447, 1408, 1325, 1264, 1239, 863, 814, 739. **HRMS** (APCI+) calculated *m/z* for $[C_{70}H_{88}N_2O_4Sn+H]^+$ 1141.5844, found 1141.5859. *Tin satellite peaks visible.

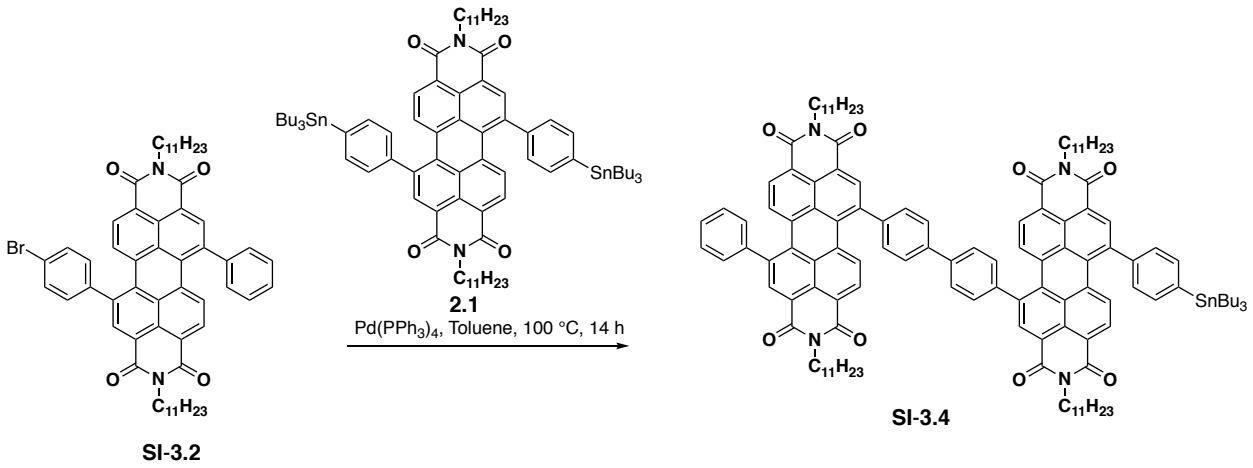

Synthesis of **SI-3.4**: **SI-3.2** (0.0750 g, 0.0810 mmol, 1.00 equiv) and **2.1** (0.463 g, 0.324 mmol, 4.00 equiv) were dissolved in toluene (8.00 mL) in a 20 mL scintillation vial equipped with a stir bar. The mixture was sparged with N_2 for thirty minutes. While under N_2, tetrakis(triphenylphosphine)palladium(0) (0.00900 g, 0.00810 mmol, 0.100 equiv) was added. The mixture was further sparged for ten minutes before being placed in a 110 °C oil bath and stirred overnight. The crude mixture was condensed and purified by column chromatography (40 g Redisep Rf Silica) using a gradient from 0% to 100% CH_2Cl_2/hexanes at 40 mL/min. Further purification by preparative HPLC (COSMOSIL Buckyprep 20 x 250 mm, 18.9 mL/min, 7:93 CH_2Cl_2:hexanes) yielded **SI-3.4** (0.0270 g, 0.0140 mmol, 17% yield). **^{1}H NMR** (500 MHz, $CDCl_3$) δ 8.67 (br, 4H), 8.17 (br, 4H), 8.03 (d, *J* = 3.2 Hz, 1H), 8.01 (d, *J* = 3.2 Hz, 1H), 7.91 (d, J = 8.5 Hz, 1H), 7.87 (d, J = 7.6, 4H), 7.85 (d, J = 9.1 Hz, 1H), 7.74 (d, J = 2.0 Hz, 2H), 7.73 (d, J = 2.3 Hz, 2H), 7.61 – 7.59* (m, 4H), 7.54 – 7.50* (m, 5H), 5.17 (br, 4H), 2.27 – 2.19 (br m, 8H), 1.83 (br, 8H), 1.67 – 1.60* (m, 6H), 1.44 – 1.35 (m, 6H), 1.35 – 1.21 (br m, 48H), 1.19 – 1.11* (m, 6H), 0.95 (t, J = 7.3 Hz, 9H), 0.86 – 0.81 (m, 24H). **^{13}C NMR** (100 MHz, $CDCl_3$) δ 164.70, 163.64,

143.19, 142.22, 141.78, 141.72, 141.66, 141.40, 141.15, 140.48, 140.39, 140.20, 140.15, 138.10, 135.82, 135.01, 134.82, 132.57, 130.28, 130.21, 130.03, 129.79, 129.35, 129.34, 129.28, 129.16, 129.07, 128.75, 128.64, 128.30, 127.97, 127.93, 122.90, 122.62, 122.21, 121.90, 54.68, 32.34, 31.78, 29.15*, 27.38*, 26.61, 22.58, 14.07, 13.75, 9.76*. **IR** (cm^{-1}) 2955, 2927, 2859, 1698, 1659, 1599, 1587, 1457, 1409, 1326, 1240, 1183, 814. **HRMS** (APCI+) calculated *m/z* for $[C_{128}H_{148}N_4O_8Sn+Na]^+$ 2012.0217, found 2012.0212. *Tin satellite peaks visible. that have been seen previously.

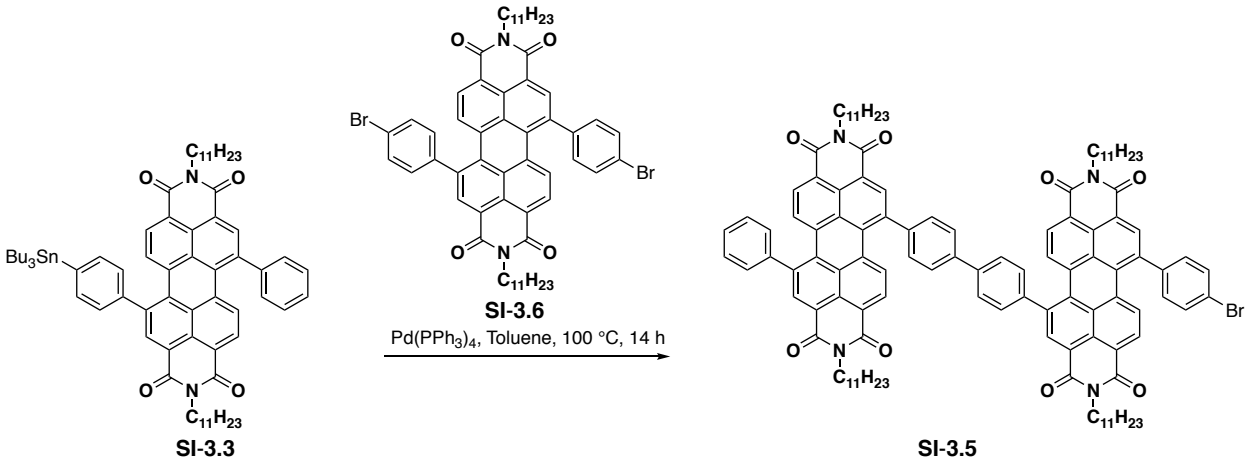

Synthesis of **SI-3.5**. **SI-3.3** (0.0550 g, 0.0480 mmol, 1.00 equiv) and *N,N′*-di(6-undecyl)-1,7-di(4-bromophenyl)- perylene-3,4:9,10-tetracarboxylic diimide (**SI-3.6**) (0.194 g, 0.193 mmol, 4.00 equiv) were dissolved in toluene (6 mL) in a 20 mL scintillation vial equipped with a stir bar. The mixture was sparged with N_2 for thirty minutes. While under N_2, tetrakis(triphenylphosphine)palladium(0) (0.00600 g, 0.00480 mmol, 0.100 equiv) was added. The mixture was further sparged for ten minutes before being placed in a 110 °C oil bath and stirred overnight. The crude mixture was condensed and purified by column chromatography (24 g Redisep Rf Silica) using a gradient from 0% to 100% CH_2Cl_2/hexanes at 40 mL/min. Further purification using preparative HPLC (Buckyprep, isocratic 15:85 CH_2Cl_2:hexane) yielded **SI-3.5** (0.0150 g, 0.00800 mmol, 18% yield). **^{1}H NMR** (500 MHz, $CDCl_3$) δ 8.71 – 8.58 (br m, 4H), 8.24

– 8.12 (br m, 4H), 8.02 (d, *J* = 8.4 Hz, 2H), 7.87 (d, *J* = 7.9 Hz, 4H), 7.85 (d, *J* = 8.2 Hz, 2H), 7.74 – 7.72 (m, 4H), 7.67 (d, *J* = 8.0 Hz, 2H), 7.60 (d, *J* = 7.1 Hz, 2H), 7.54 – 7.48 (m, 5H), 5.17 (br, 4H), 2.23 (br, 8H), 1.83 (br, 8H), 1.26 (br, 48H), 0.86 – 0.81 (br m, 24H). **^{13}C NMR** (100 MHz, $CDCl_3$) δ 164.70, 163.59, 142.20, 141.75, 141.60, 141.16, 141.07, 140.65, 140.45, 140.24, 140.12, 139.64, 135.89, 135.47, 135.17, 134.81, 134.49, 133.43, 132.53, 130.81, 130.36, 130.29, 130.20, 130.06, 130.01, 129.80, 129.76, 129.50, 129.33, 129.30, 129.26, 129.07, 128.79, 128.75, 128.65, 128.04, 127.99, 127.97, 123.08, 122.99, 122.65, 122.32, 121.88, 54.70, 32.33, 31.78, 26.62, 22.59, 14.09. **IR** (cm^{-1}) 2954, 2924, 2858, 1697, 1657, 1598, 1587, 1457, 1408, 1324, 1239, 1183, 814. **HRMS** (APCI+) calculated *m/z* for $[C_{116}H_{121}N_4O_8Br+Na]^+$ 1799.8265, found 1799.8259. Broadening (br) of peaks in the ^{1}H NMR spectrum is due to rotational isomers about the imide side chains.

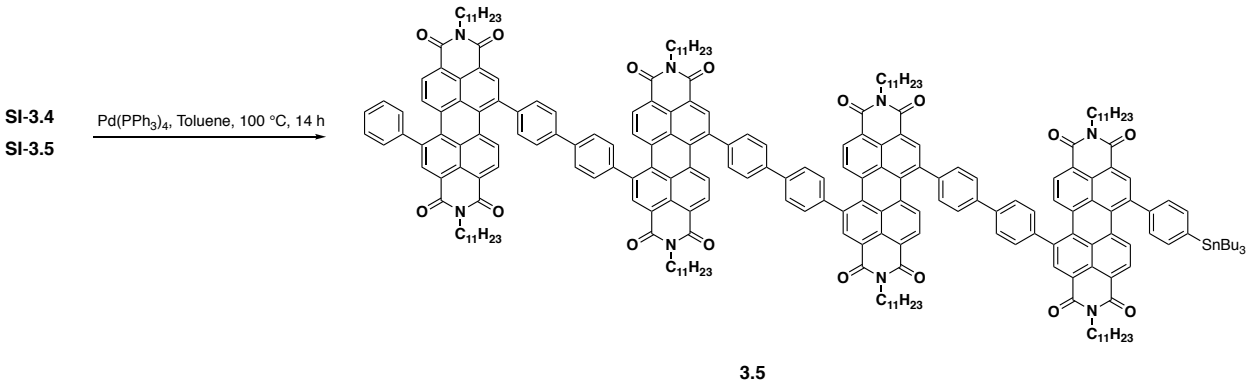

3.5

Synthesis of **3.5**: **SI-3.4** (0.0170 g, 0.00800 mmol, 1.00 equiv) and **SI-3.5** (0.0150 g, 0.00800 mmol, 1.00 equiv) were dissolved in toluene (2.0 mL) in a 20 mL scintillation vial equipped with a stir bar. The mixture was sparged with N_2 for thirty minutes. While under N_2, tetrakis(triphenylphosphine)palladium(0) (0.00600 g, 0.00480 mmol, 0.100 equiv) was added. The mixture was further sparged for ten minutes before being placed in a 110 °C oil bath and stirred for eight hours. The crude mixture was filtered through Celite, concentrated and purified by preparative TLC using a mobile phase of 70:30 CH_2Cl_2:hexanes. The product was washed with

hexanes and precipitated from methanol to yield **3.5** (0.00900 g, 0.00300 mmol, 62% yield). **^{1}H NMR** (500 MHz, $C_2D_2Cl_4$, 370 K) δ 8.75 (s, 4H), 8.72 (s, 2H), 8.67 (s, 2H), 8.32 – 8.26 (m, 6H), 8.19 (d, *J* = 8.2 Hz, 2H), 8.14 (d, J = 8.0 Hz, 2H), 8.14 (d, J = 8.2 Hz, 2H), 8.12 (d, *J* = 8.3 Hz, 2H), 7.99 – 7.91 (m, 14H), 7.84 – 7.78 (m, 12H), 7.66 (d, *J* = 7.0 Hz, 4H), 7.62 – 7.56 (m, 6H), 5.25 – 5.15 (br m, 8H), 2.33 – 2.21 (br m, 16H), 2.00 – 1.90 (br m, 16H), 1.45 – 1.27 (br m, 96H), 0.98 – 0.88 (br m, 48H). **^{13}C NMR** (125 MHz, $C_2D_2Cl_4$, 370 K) δ 163.81, 142.26, 141.79, 140.98, 140.40, 140.30, 140.27, 135.11, 134.68, 134.64, 132.34, 132.31, 132.26, 130.04, 129.97, 129.52, 129.23, 129.13, 128.83, 128.63, 128.46, 127.96, 127.88, 122.77, 122.50, 54.70, 32.36, 31.53, 26.47, 26.45, 22.24, 22.23, 13.69. **IR** (cm^{-1}) 2956, 2924, 2856, 1696, 1657, 1598, 1587, 1457, 1408, 1324, 1262, 1239, 1182, 1097, 1029, 861, 813, 740. **HRMS** (MALDI–) calculated *m/z* for $[C_{232}H_{242}N_8O_{16}]^-$ 3395.8369, found 3395.8363.

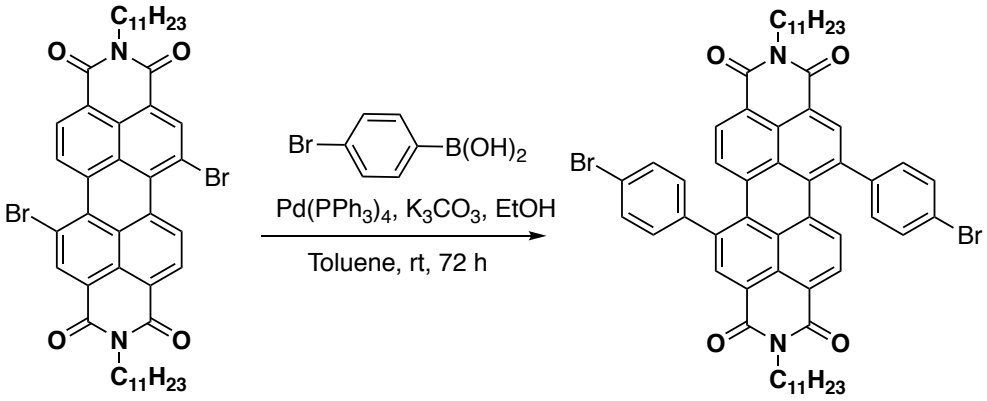

***1,7*-dibromo PDI** **SI-3.6**

Synthesis of 1,7-N,N′-di(6-undecyl)-1,7-di(4-bromophenyl)- perylene-3,4:9,10-tetracarboxylic diimide (**SI-3.6**): *N,N′*-Di(6-undecyl)-1,7-dibromoperylene-3,4:9,10-tetracarboxylic diimide (0.200 g, 0.234 mmol, 1.00 equiv), 4-bromophenylboronic acid (0.141 g, 7.01 mmol, 3.00 equiv), aqueous K_2CO_3 (2 M, 2.00 mL), EtOH (0.400 mL) and toluene (6.00 mL) were added to 20 mL scintillation vial equipped with a stir bar. The mixture was sparged with N_2 for thirty minutes. While under N_2, tetrakis(triphenylphosphine)palladium(0) (0.0270 g, 0.0234 mmol, 0.100 equiv)

was added. The mixture was further sparged for ten minutes and stirred overnight at room temperature. A small aliquot was taken 24 hours later and showed ~10% conversion to product by ^{1}H NMR. Additional tetrakis(triphenylphosphine)palladium(0) (0.108 g, 0.0936 mmol, 0.400 equiv) was added. The reaction was monitored for forty-eight hours and another 0.400 equiv of catalyst was added. In total, the reaction completed in 72 hours. The crude mixture was extracted with ethyl acetate and brine, concentrated and purified by column chromatography (40 g Redisep Rf Silica) using a gradient from 0% to 100% CH_2Cl_2/hexanes at 40 mL/min. Impure fractions were further purified by preparative TLC to yield a total 0.091 g (0.0905 mmol, 39%) of **SI-3.6**. **^{1}H NMR** (500 MHz, $CDCl_3$) δ 8.58 (br, 2H), 8.18 (br, 2H), 7.82 (d, J = 8.1 Hz, 2H), 7.65 (d, J = 8.3 Hz, 4H), 7.45 (d, J = 8.4 Hz, 4H). 5.16 (br, 2H), 2.28 – 2.16 (m, 4H), 1.88 – 1.77 (m, 4H), 1.38 – 1.18 (br m, 24H) 0.81 (br t, J = 6.9 Hz, 12H). **^{13}C NMR** (125 MHz, $CDCl_3$) δ 164.52, 163.43, 140.98, 139.73, 135.45, 134.73, 134.42, 133.43, 132.36, 130.74, 130.28, 130.10, 129.34, 129.20, 128.00, 123.11, 122.76, 122.38, 122.01, 54.76, 32.30, 31.74, 26.58, 22.56, 14.04. **IR** (cm^{-1}) 2955, 2928, 2858, 1697, 1657, 1598, 1587, 1487, 1456, 1409, 1324, 1239, 1183, 1072, 1012, 814. **HRMS** (APCI+) calculated *m/z* for $[C_{58}H_{60}N_2O_4Br_2+H]^+$ 1007.2998, found 1007.2994.

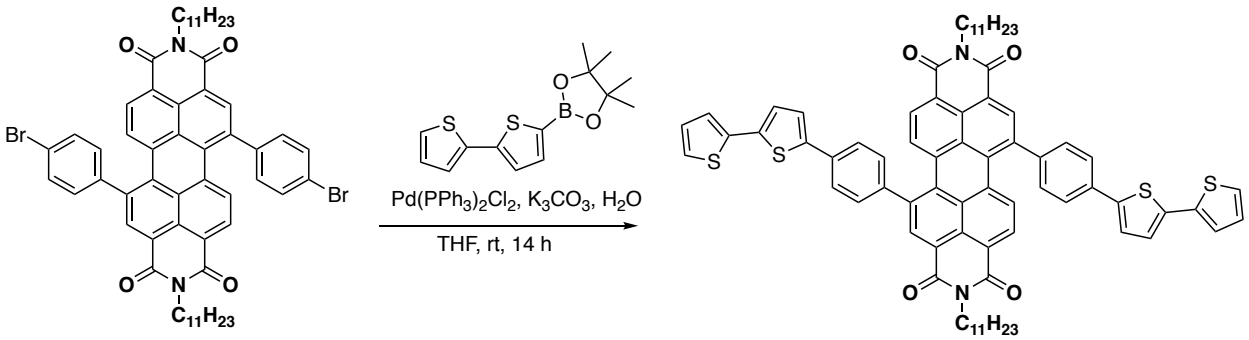

SI-3.6 **3.1**

Synthesis of **3.1**: **SI-3.6** (0.100 g, 0.0990 mmol, 1.00 equiv), 2,2′-bithiophene-5-boronic acid pinacol ester (1.74 g, 0.596 mmol, 6.00 equiv), K_2CO_3 (0.218 g, 1.58 mmol, 16.0 equiv), H_2O (1.00 mL) and THF (3.00 mL) were added to 20 mL scintillation vial equipped with a stir bar. The

mixture was sparged with N_2 for thirty minutes. While under N_2, bis(triphenylphosphine)palladium chloride (0.0110 g, 0.0150 mmol, 0.150 equiv) was added. The mixture was further sparged for ten minutes and stirred overnight at room temperature. The crude mixture was extracted with ethyl acetate and brine, concentrated and purified by column chromatography using a gradient from 0% to 100% CH_2Cl_2/hexanes to yield **3.1** (0.112 g, 0.0950 mmol, 94%). **^{1}H NMR** (500 MHz, $C_2D_2Cl_4$) δ 8.64 (br, 2H), 8.17 (br, 2H), 7.99 (br, 2H), 7.76 (d, J = 7.9 Hz, 4H), 7.65 (d, J = 8.3 Hz, 4H), 7.40 (d, J = 3.8 Hz, 2H), 7.30 (dd, J = 5.1, 1.1 Hz, 2H), 7.28 (dd, J = 3.6, 1.1 Hz, 2H), 7.24 (d, J = 3.7 Hz, 2H), 7.09 (dd, J = 5.1, 3.6 Hz, 2H), 5.12 (br, 2H), 2.26 – 2.11 (br m, 4H), 1.86 (br, 4H), 1.37 – 1.22 (br m, 24H), 0.88 – 0.82 (br m, 12H). **^{13}C NMR** (125 MHz, $C_2D_2Cl_4$) δ 164.47, 164.37, 163.41, 163.30, 141.70, 140.97, 140.11, 137.25, 136.99, 135.48, 134.77, 134.55, 134.08, 132.26, 130.00, 129.67, 129.24, 129.09, 128.00, 127.78, 126.91, 124.80, 124.77, 124.63, 123.91, 122.83, 122.42, 122.10, 121.74, 54.52, 32.16, 31.66, 26.53, 22.49, 14.09. **IR** (cm^{-1}) 2927, 2857, 1694, 1654, 1586, 1497, 1409, 1326, 1240, 1006, 950, 887, 838. **HRMS** (APCI+) calculated *m/z* for $[C_{74}H_{70}N_2O_4S_4+H]^+$ 1179.4297, found 1179.4301.

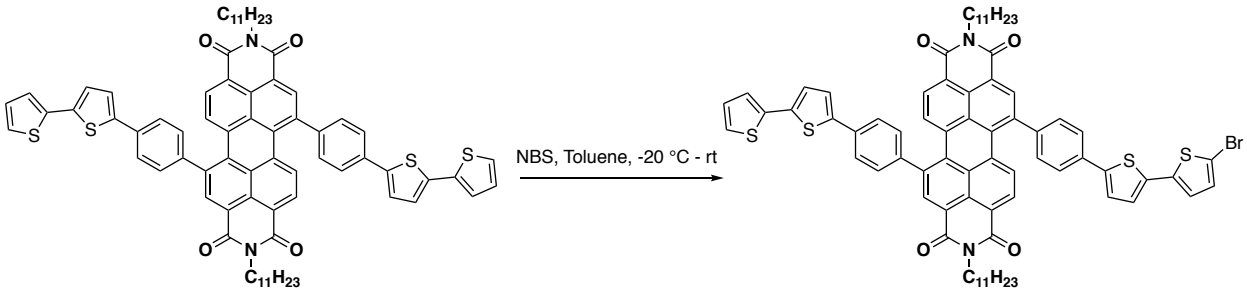

3.1 **SI-3.7**

Synthesis of **SI-3.7**: **3.1** (0.0740 g, 0.0640 mmol, 1.00 equiv) was dissolved in toluene (6.00 mL) and sparged with N_2 for fifteen minutes while at -20 ºC. *N*-Bromosuccinimide (0.0110 g, 0.0640 mmol, 1.00 equiv) was added and aluminum was placed over the reaction flask to protect from light. The reaction was stirred for twenty-four hours and allowed to warm to room temperature. The reaction mixture was concentrated and purified by column chromatography using a gradient

from 0% to 100% CH_2Cl_2/hexanes to yield **SI-3.7** (0.00800 g, 0.00600 mmol, 10%). **^{1}H NMR** (500 MHz, CD_2Cl_2) δ 8.62 (br, 2H), 8.15 (br, 2H), 8.00 (d, J = 6.9 Hz, 1H), 7.98 (d, J = 6.9 Hz, 1H), 7.80 – 7.77 (m, 4H), 7.65 (d, J = 8.1 Hz, 4H), 7.41 (d, J = 3.8 Hz, 1H), 7.39 (d, J = 3.8 Hz, 1H), 7.31 (d, J = 4.7 Hz, 1H), 7.29 (d, J = 3.5 Hz, 1H), 7.25 (d, J = 3.7 Hz, 1H), 7.19 (d, J = 3.8 Hz, 1H), 7.09 (dd, J = 5.1, 3.6 Hz, 1H), 7.06 (d, J = 3.8 Hz, 1H), 7.03 (d, J = 3.8 Hz, 1H), 5.12 (br, 2H), 2.24 – 2.12 (br m, 4H), 1.86 (br, 4H), 1.33 – 1.24 (br m, 24H), 0.89 – 0.83 (br m, 12H). **^{13}C NMR*** (100 MHz, $C_2D_2Cl_4$) δ 142.25, 141.70, 141.17, 140.13, 138.53, 137.27, 136.99, 136.10, 134.92, 134.58, 134.10, 133.88, 132.30, 130.84, 130.02, 129.69, 129.09, 128.00, 127.79, 126.96, 125.05, 124.79, 124.66, 123.96, 123.91, 111.12, 54.55, 32.16, 31.65, 26.53, 22.48, 14.08. **IR** (cm^{-1}) 2954, 2926, 2857, 1697, 1656, 1597, 1586, 1457, 1409, 1326, 1241, 1185, 838, 813, 796. **HRMS** (ESI+) calculated *m/z* for $[C_{74}H_{69}N_2O_4S_4Br+H]^+$ 1257.3402, found 1257.3392. *Partial spectrum reported due to limited solubility.

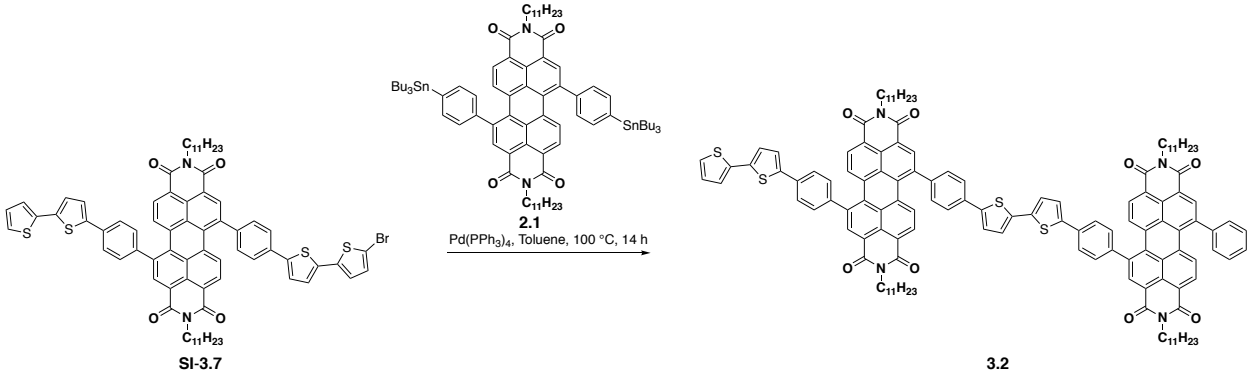

Synthesis of **3.2**: **SI-3.7** (0.0230 g, 0.0180 mmol, 1.00 equiv) and **2.1** (0.105 g, 0.0780 mmol, 4.00 equiv) were dissolved in toluene (6.00 mL) in a 20 mL scintillation vial equipped with a stir bar. The mixture was sparged with N_2 for thirty minutes. While under N_2, tetrakis(triphenylphosphine)palladium(0) (0.00200 g, 0.00200 mmol, 0.100 equiv) was added. The mixture was further sparged for ten minutes before being placed in a 107 °C oil bath and stirred overnight. The crude mixture was concentrated and purified by preparative TLC using a mobile

phase of 50:50 CH_2Cl_2:hexanes. The product was passed through a small silica plug to remove residual impurities. The product was then dissolved in CH_2Cl_2 (2.0 mL) and HCl (2.0 mL) and stirred at room temperature for two days. The crude mixture was extracted with water and CH_2Cl_2, concentrated and purified by column chromatography (4 g Redisep Rf Silica) using a gradient from 0% to 100% CH_2Cl_2/hexanes. The product was precipitated from CH_2Cl_2 and methanol to yield **3.2** as a purple solid (0.0050 g, 0.0020 mmol, 14%). **^{1}H NMR** (400 MHz, $C_2D_2Cl_4$) δ 8.62 (br, 4H), 8.17 (br, 4H), 8.03 – 7.98 (m, 3H), 7.84 (d, J = 8.4 Hz, 1H), 7.83 – 7.77 (m, 6H), 7.70 – 7.63 (m, 6H), 7.61 (br d, J = 6.3 Hz, 2H), 7.58 – 7.51 (m, 3H), 7.45 (br d, J = 3.1 Hz, 2H), 7.41 (d, J = 3.8 Hz, 1H), 7.32 (d, J = 3.9 Hz, 2H), 7.30 – 7.27 (m, 2H), 7.25 (d, J = 3.7 Hz, 1H), 7.11 – 7.06 (m, 1H), 5.16 (br, 4H), 2.31 – 2.13 (br m, 8H), 1.89 – 1.76 (br m, 8H) , 1.27 (br, 48H), 0.84 (br t, J = 6.6 Hz, 24H). **^{13}C NMR** (100 MHz, $C_2D_2Cl_4$) δ 165.13, 164.00, 142.97, 142.87, 142.53, 142.18, 142.14, 142.03, 141.56, 140.82, 140.79, 140.76, 137.89, 137.71, 137.67, 137.66, 135.90, 135.31, 134.72, 134.65, 134.62, 133.09, 130.79, 130.63, 130.47, 130.43, 129.89, 129.81, 129.66, 129.07, 128.56, 128.53, 128.49, 127.51, 127.47, 125.52, 125.34, 125.30, 125.23, 125.08, 124.45, 123.60, 123.26, 122.88, 122.52, 54.99, 54.48, 54.40, 32.84, 32.34, 27.14, 23.16, 14.38. **IR** (cm^{-1}) 2954, 2925, 2854, 1697, 1659, 1597, 1587, 1459, 1409, 1326, 1265, 1248, 1240, 814, 740. **HRMS** (ESI+) calculated *m/z* for $[C_{132}H_{130}N_4O_8S_4+H]^+$ 2027.8850, found 2027.8820.

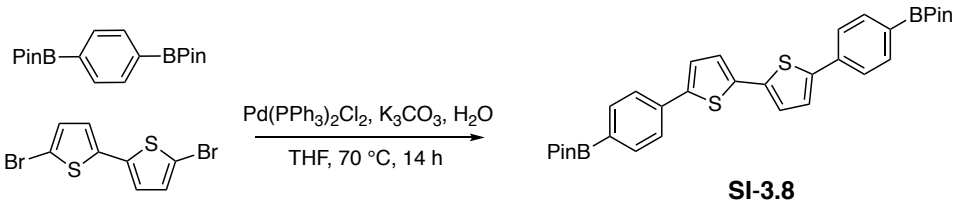

SI-3.8

Synthesis of **SI-3.8**: 1,4-Benzenediboronic acid bis(pinacol) ester (0.815 g, 2.47 mmol, 4.00 equiv), 5,5′-dibromo-2,2′-bithiophene (0.200 g, 0.617 mmol, 1.00 equiv) and K_2CO_3 (2.12 g, 15.0 mmol, 25.00 equiv) were dissolved in THF (21.0 mL) and H_2O (6.00 ml) in a 100 mL round bottom

flask equipped with a stir bar. The mixture was sparged with N_2 for thirty minutes. While under N_2, bis(triphenylphosphine)palladium chloride (0.0430 g, 0.0620 mmol, 0.100 equiv) was added. The mixture was further sparged for thirty minutes before being placed in a 70 °C oil bath and stirred overnight. The crude mixture was extracted with brine and ethyl acetate. The organic layer was collected, concentrated and purified by column chromatography using a gradient of 0 - 100% of hexanes/DCM. The final product was a pale yellow solid (0.030 g, 0.0526, 9%). **^{1}H NMR** (400 MHz, CD_2Cl_2) δ 7.80 (d, J = 8.2 Hz, 2H), 7.64 (d, J = 8.2 Hz, 2H), 7.36 (d, J = 3.8 Hz, 1H), 7.24 (d, J = 3.8 Hz, 1H), 1.36 (s, 24H). **IR** (cm^{-1}) 2973, 2934, 2857, 1605, 1399, 1362, 1145, 1093, 963, 859, 806. **HRMS** (ESI+) calculated *m/z* for $[C_{32}H_{36}B_2O_4S_2]^+$ 570.2241, found 570.2252.

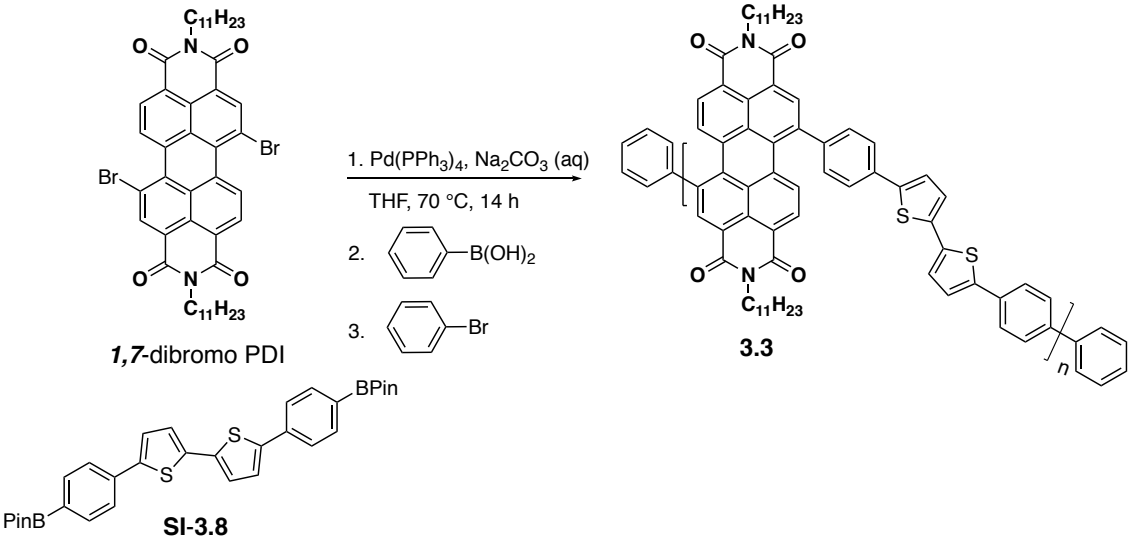

Synthesis of **3.3**: *N,N′*-Di(6-undecyl)-1,7-dibromoperylene-3,4:9,10-tetracarboxylic diimide (0.0420 g, 0.0490 mmol, 1.03 equiv), **SI-3.8** (0.027 g, 0.0474 mmol, 1.00 equiv), aqueous Na_2CO_3 (2 M, 2.20 mL) and THF (4.00 mL) were added to a 20 mL scintillation vial equipped with a stir bar. The mixture was sparged with N_2 for thirty minutes. While under N_2, tetrakis(triphenylphosphine)palladium(0) (0.002 g, 0.002 mmol, 0.0400 equiv) was added. The mixture was further sparged for ten minutes and stirred for 48 hours at 82 °C. Then phenylboronic acid (0.0170 g, 0.142 mmol, 3.30 equiv) was added to the reaction and allowed to stir for three

hours at 82 °C, followed by bromobenzene (0.200 mL, 1.90 mmol, 40 equiv). The reaction was left stirring overnight. The crude mixture was extracted with ethyl acetate and brine and concentrated. Solids were crashed out with methanol and further purified using soxhlet extraction using methanol, followed by hexanes. The final product was recovered using chloroform. The reaction yielded 0.040 g, 82% yield*. **^{1}H NMR*** (500 MHz, $C_2D_2Cl_4$) δ 8.71 (s, 2H), 8.27 (d, J = 8.0 Hz, 2H), 8.10 (d, J = 8.0 Hz, 2H), 7.86 (d, J = 7.5 Hz, 4H), 7.71 (d, J = 8.0 Hz, 4H), 7.47 (d, J = 3.0 Hz, 2H), 7.37 (d, J = 3.4 Hz, 2H), 5.26 – 5.16 (m, 2H), 2.28 (br, 4H), 1.99 (br, 4H), 1.43 (br, 24H)**, 0.95 (br, 12H). **GPC**: Mn = 6,388; Mw = 30,238 and PDI = 4.73; solvent = chloroform; λ = 440 nm. **HRMS** (MALDI) shows oligomers with repeating units of 1012 m/z up to the eight-mer. * Polymer yields do not incorporate phenyl caps.

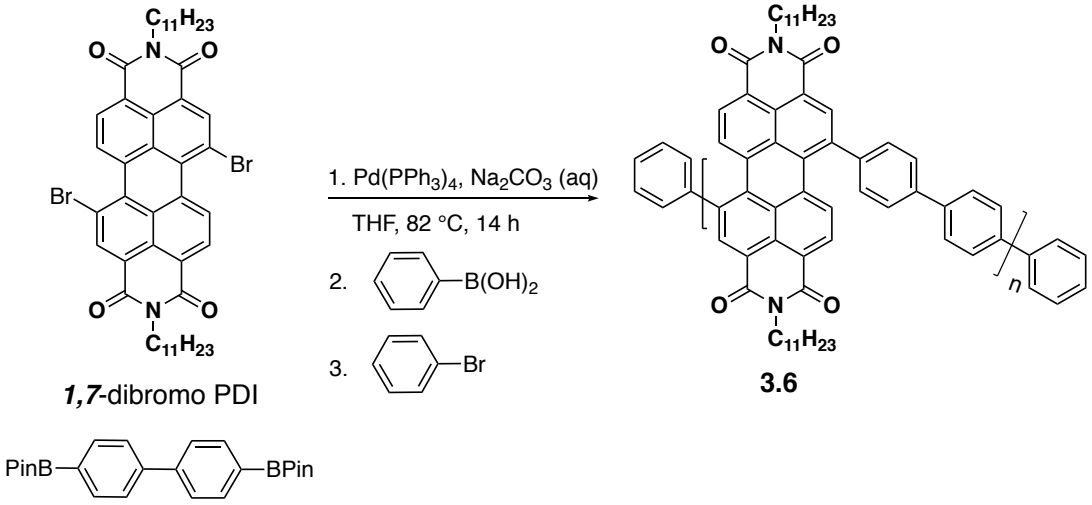

Synthesis of **3.6**: *N,N′*-Di(6-undecyl)-1,7-dibromoperylene-3,4:9,10-tetracarboxylic diimide (0.200 g, 0.234 mmol, 1.00 equiv), 4,4′-biphenyldiboronic acid bis(pinacol) ester (0.0950 g, 0.234 mmol, 1.00 equiv), aqueous Na_2CO_3 (2 M, 11.0 mL) and THF (19.0 mL) were added to 100 mL two-neck, round bottom flask equipped with a stir bar. The mixture was sparged with N_2 for thirty minutes. While under N_2, tetrakis(triphenylphosphine)palladium(0) (0.0110 g, 0.009 mmol, 0.0400 equiv) was added. The mixture was further sparged for ten minutes and stirred for 48 hours

at 78 °C. Then, commercially available phenylboronic acid (0.0940 g, 0.767 mmol, 3.30 equiv) was added to the reaction and allowed to stir for two hours at 78 °C, followed by bromobenzene (1.0 ml, 9.55 mmol, 41.0 equiv). The reaction was left stirring overnight. The crude mixture was extracted with ethyl acetate and brine and concentrated. Solids were crashed out with methanol and further purified using soxhlet extraction using methanol, followed by hexanes. The final product was recovered using chloroform. The reaction yielded 0.181 g for a 91% yield*. **^{1}H NMR*** (500 MHz, $C_2D_2Cl_4$) δ 8.77 (s, 2H), 8.33 (d, J = 8.5 Hz, 2H), 8.18 (d, J = 8.3 Hz, 2H), 7.99 (d, J = 8.1 Hz, 4H), 7.84 (d, J = 7.8 Hz, 4H), 5.27 – 5.20 (m, 2H), 2.31 (br, 4H), 1.99 (br, 4H), 1.42 (br, 24H)**, 0.95 (br, 12H). **GPC:** M_n = 16,950; M_w = 61,169 and PDI = 3.61; solvent = THF; λ = 500 nm. **HRMS** (MALDI) shows oligomers with repeating units of 849 m/z up to the nine-mer. *Polymer yields do not incorporate phenyl caps. **The broad peak at 1.43 ppm indicates water in the sample and prevents integration of the overlapping alkyl protons.

3.13. NMR Spectra of Compounds

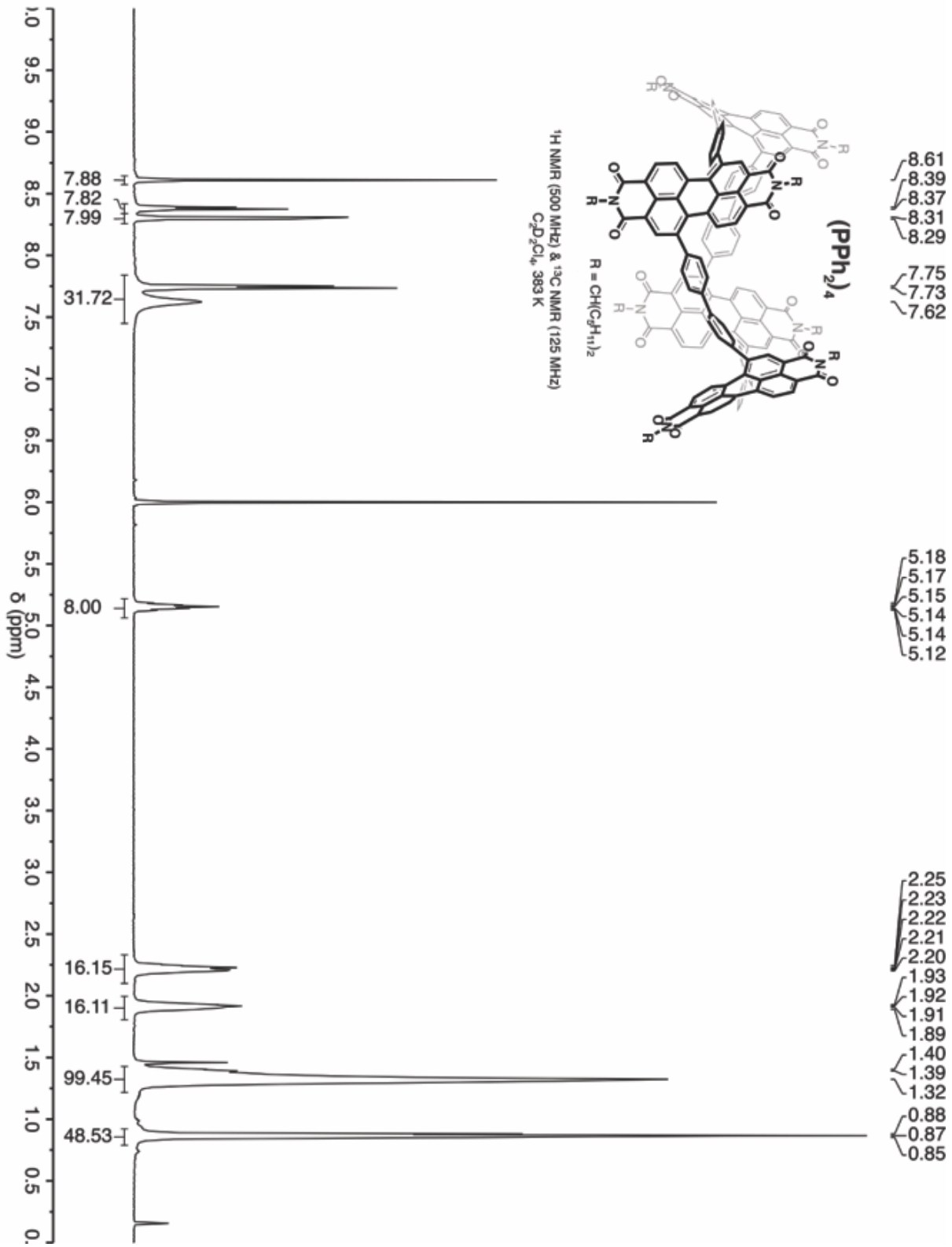

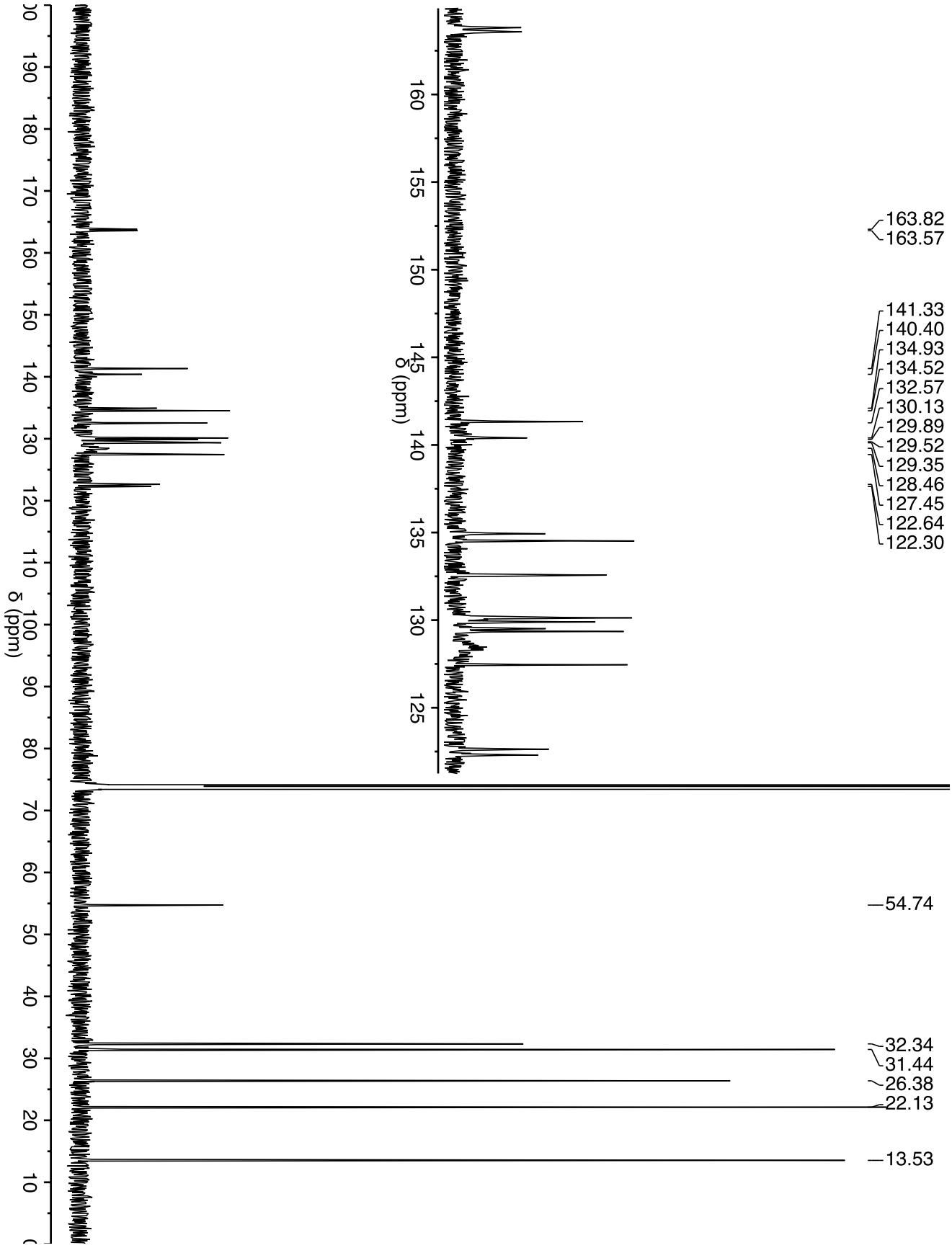
163.82
163.57
141.33
140.40
134.93
134.52
132.57
130.13
129.89
129.52
129.35
128.46
127.45
122.64
122.30
54.74
32.34
31.44
26.38
22.13
13.53
δ (ppm)

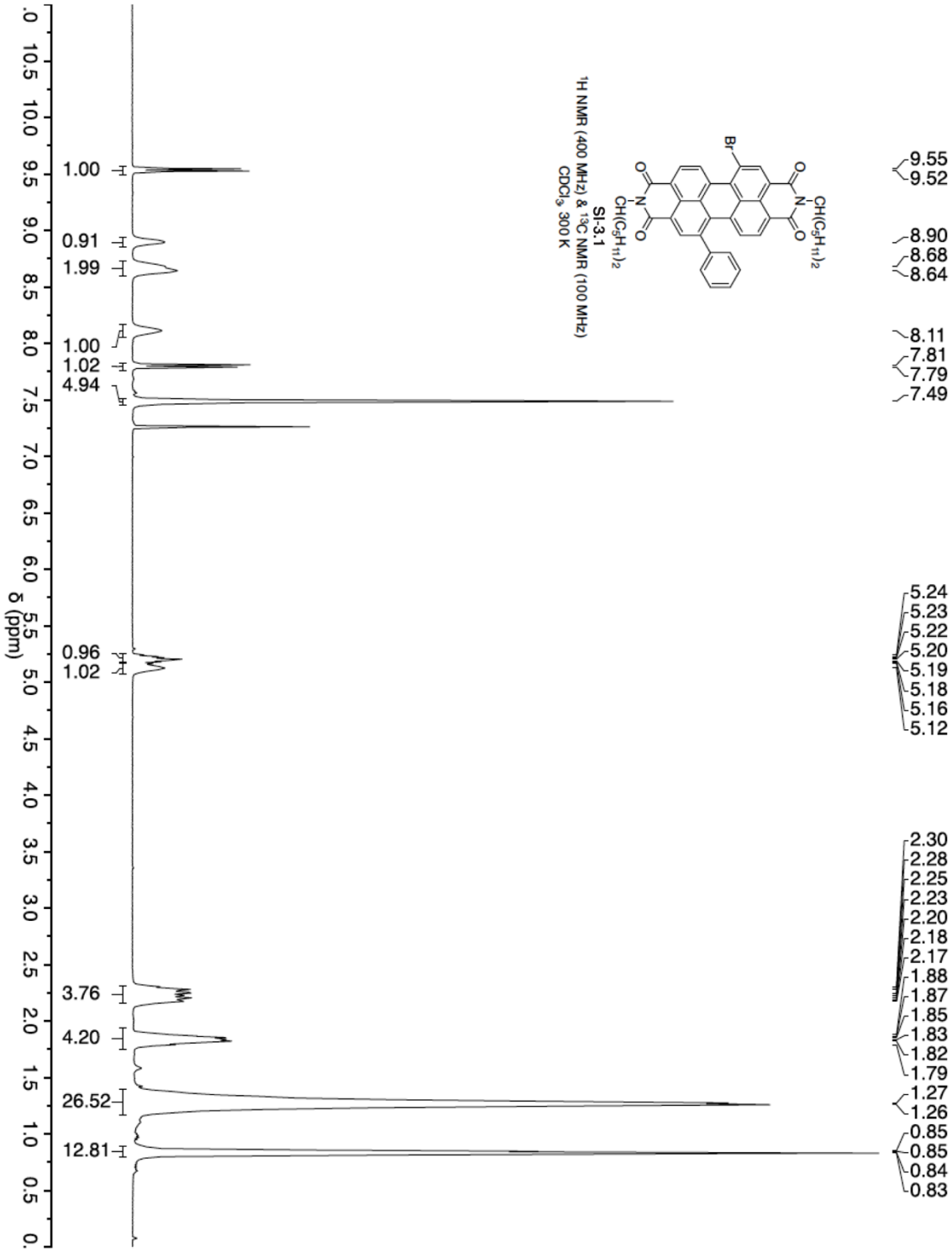
1H NMR (400 MHz) & 13C NMR (100 MHz)
CDCl3 300 K
SI-3.1
Br
CH(C5H11)2
CH(C5H11)2
δ (ppm)
1.00
0.91
1.99
1.00
1.02
4.94
0.96
1.02
3.76
4.20
26.52
12.81
9.55
9.52
8.90
8.68
8.64
8.11
7.81
7.79
7.49
5.24
5.23
5.22
5.20
5.19
5.18
5.16
5.12
2.30
2.28
2.25
2.23
2.20
2.18
2.17
1.88
1.87
1.85
1.83
1.82
1.79
1.27
1.26
0.85
0.85
0.84
0.83

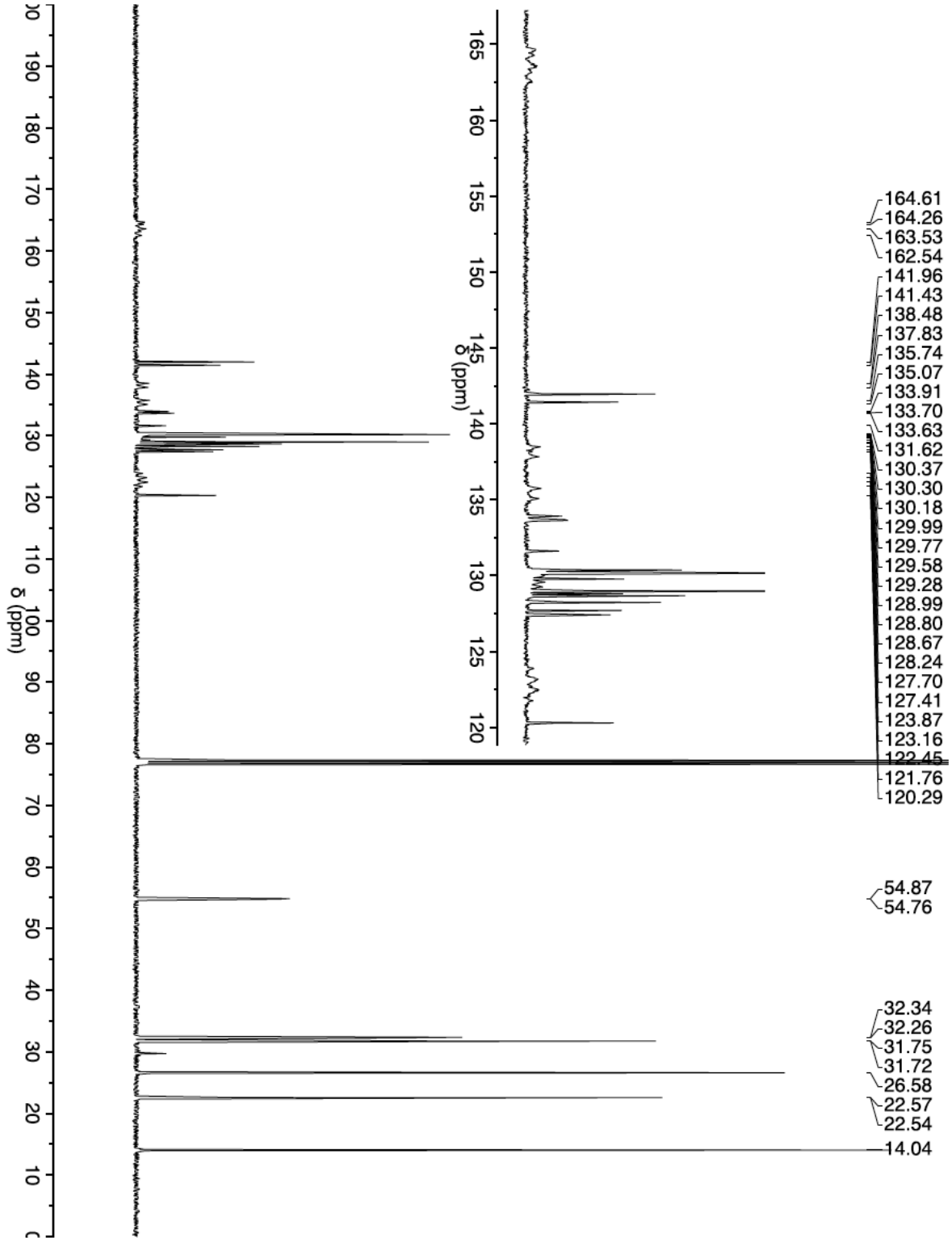
δ (ppm)
δ (ppm)
164.61
164.26
163.53
162.54
141.96
141.43
138.48
137.83
135.74
135.07
133.91
133.70
133.63
131.62
130.37
130.30
130.18
129.99
129.77
129.58
129.28
128.99
128.80
128.67
128.24
127.70
127.41
123.87
123.16
122.45
121.76
120.29
54.87
54.76
32.34
32.26
31.75
31.72
26.58
22.57
22.54
14.04

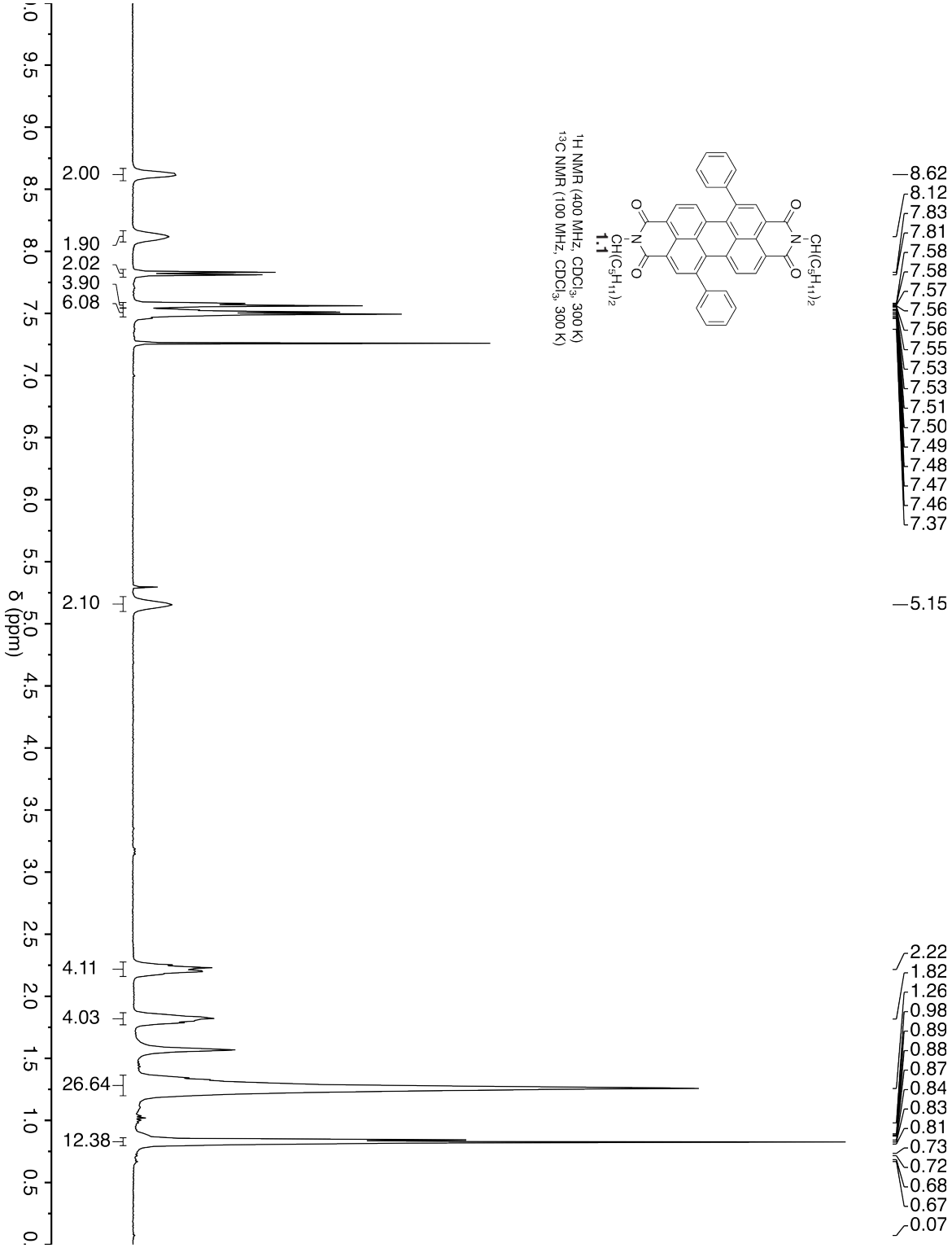
1H NMR (400 MHz, CDCl3, 300 K)
13C NMR (100 MHz, CDCl3, 300 K)
1.1
CH(C5H11)2
CH(C5H11)2
δ (ppm)
2.00
1.90
2.02
3.90
6.08
2.10
4.11
4.03
26.64
12.38
8.62
8.12
7.83
7.81
7.58
7.58
7.57
7.56
7.56
7.55
7.53
7.53
7.51
7.50
7.49
7.48
7.47
7.46
7.37
5.15
2.22
1.82
1.26
0.98
0.89
0.88
0.87
0.84
0.83
0.81
0.73
0.72
0.68
0.67
0.07

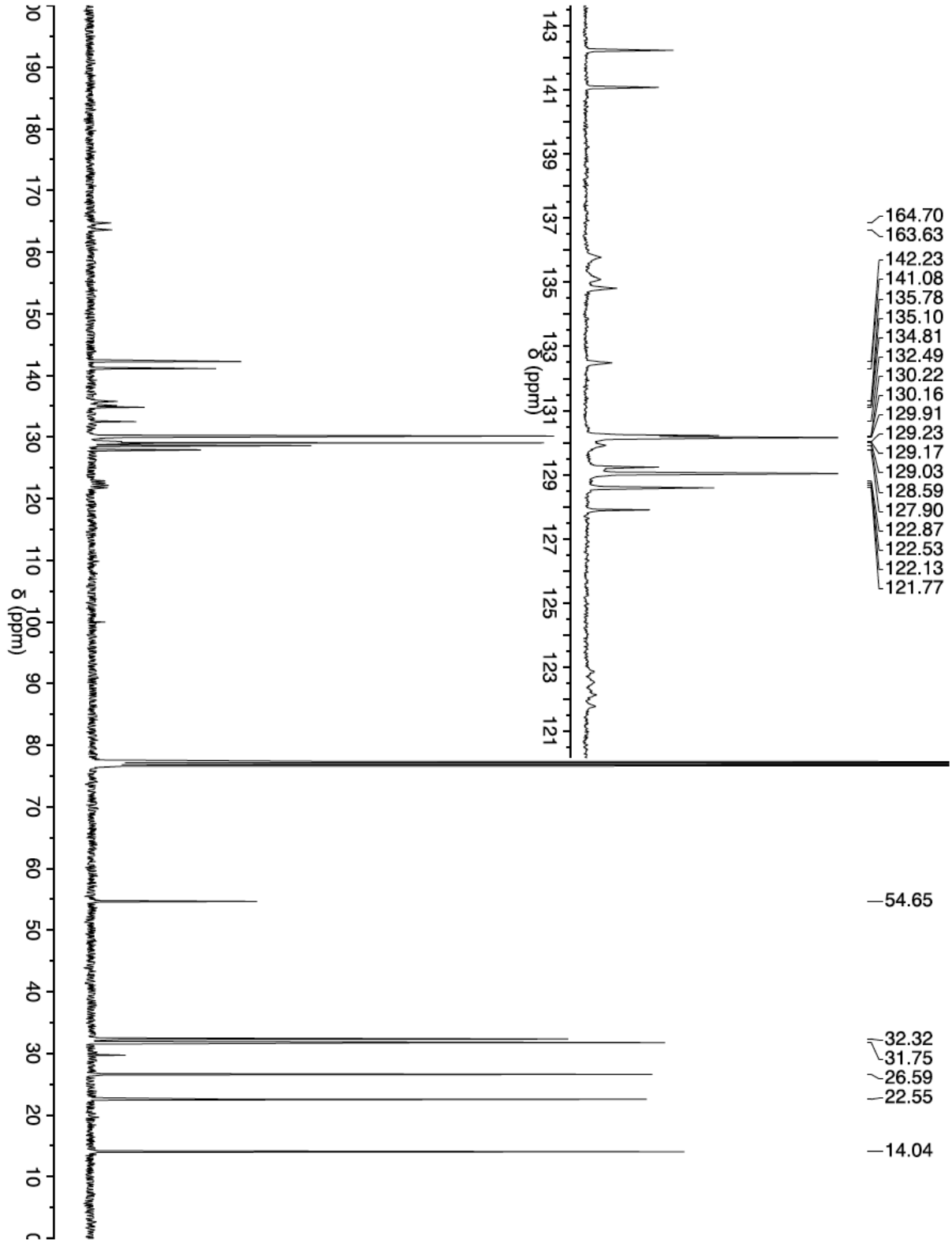
164.70
163.63
142.23
141.08
135.78
135.10
134.81
132.49
130.22
130.16
129.91
129.23
129.17
129.03
128.59
127.90
122.87
122.53
122.13
121.77
54.65
32.32
31.75
26.59
22.55
14.04
δ (ppm)

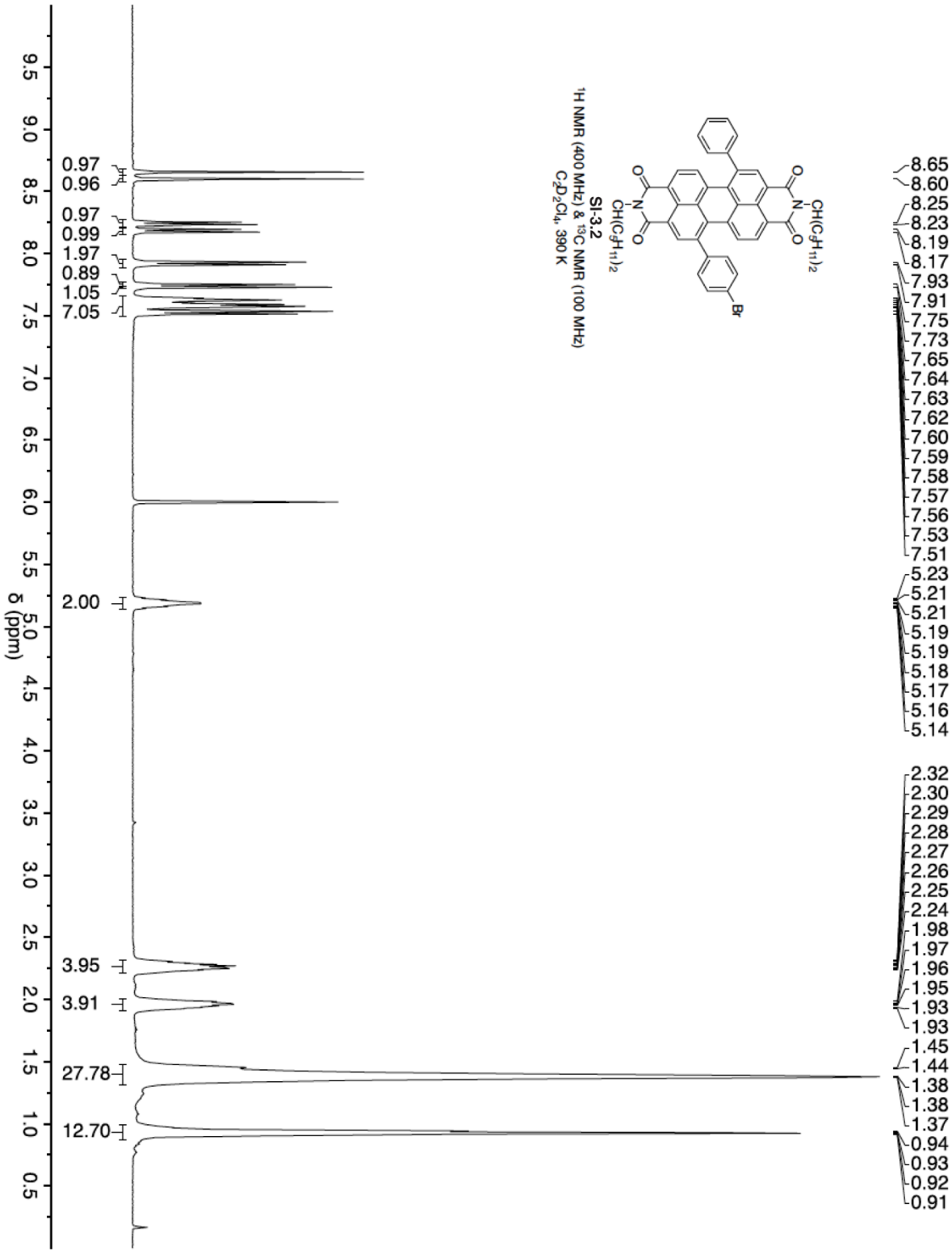
SI-3.2
^{1}H NMR (400 MHz) & ^{13}C NMR (100 MHz)
$C_2D_2Cl_4$, 390 K
δ (ppm)
0.97
0.96
0.97
0.99
1.97
0.89
1.05
7.05
2.00
3.95
3.91
27.78
12.70
8.65
8.60
8.25
8.23
8.19
8.17
7.93
7.91
7.75
7.73
7.65
7.64
7.63
7.62
7.60
7.59
7.58
7.57
7.56
7.53
7.51
5.23
5.21
5.21
5.19
5.19
5.18
5.17
5.16
5.14
2.32
2.30
2.29
2.28
2.27
2.26
2.25
2.24
1.98
1.97
1.96
1.95
1.93
1.93
1.45
1.44
1.38
1.38
1.37
0.94
0.93
0.92
0.91
Br

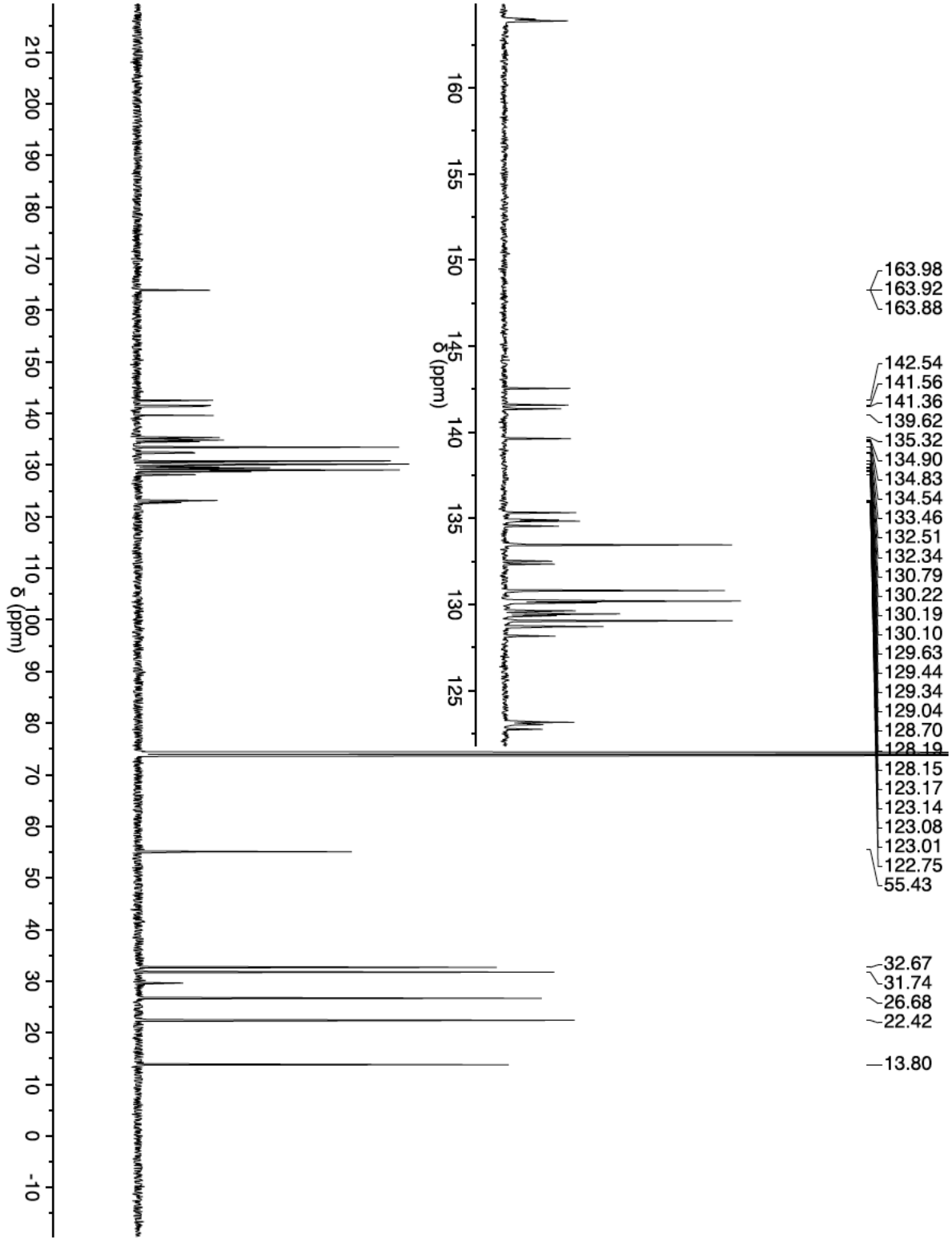
163.98
163.92
163.88
142.54
141.56
141.36
139.62
135.32
134.90
134.83
134.54
133.46
132.51
132.34
130.79
130.22
130.19
130.10
129.63
129.44
129.34
129.04
128.70
128.19
128.15
123.17
123.14
123.08
123.01
122.75
55.43
32.67
31.74
26.68
22.42
13.80
δ (ppm)
δ (ppm)

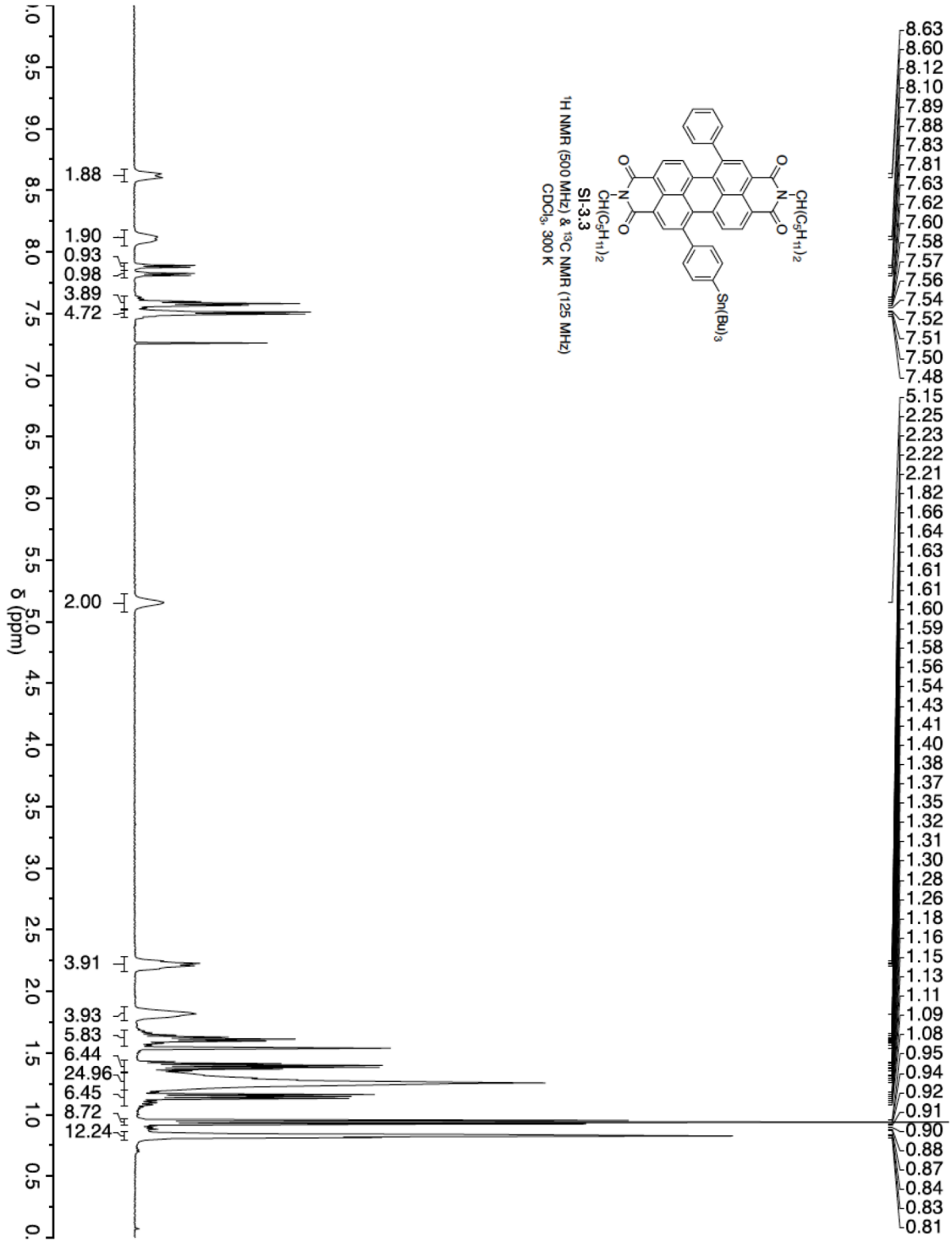
SI-3.3
^{1}H NMR (500 MHz) & ^{13}C NMR (125 MHz)
$CDCl_3$, 300 K
$CH(C_5H_{11})_2$
$CH(C_5H_{11})_2$
$Sn(Bu)_3$
δ (ppm)
1.88
1.90
0.93
0.98
3.89
4.72
2.00
3.91
3.93
5.83
6.44
24.96
6.45
8.72
12.24
8.63
8.60
8.12
8.10
7.89
7.88
7.83
7.81
7.63
7.62
7.60
7.58
7.57
7.56
7.54
7.52
7.51
7.50
7.48
5.15
2.25
2.23
2.22
2.21
1.82
1.66
1.64
1.63
1.61
1.61
1.60
1.59
1.58
1.56
1.54
1.43
1.41
1.40
1.38
1.37
1.35
1.32
1.31
1.30
1.28
1.26
1.18
1.16
1.15
1.13
1.11
1.09
1.08
0.95
0.94
0.92
0.91
0.90
0.88
0.87
0.84
0.83
0.81

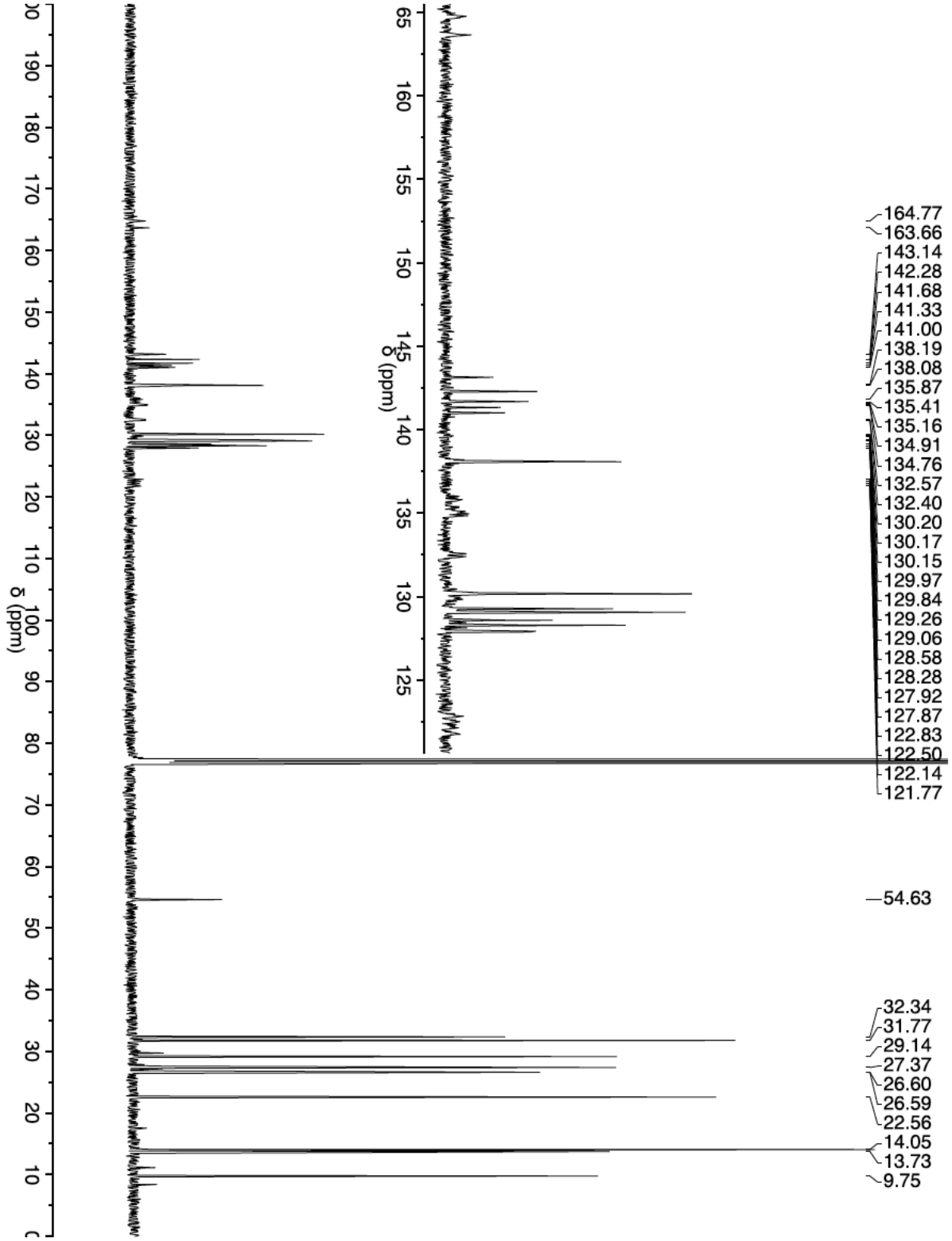
δ (ppm)
δ (ppm)
164.77
163.66
143.14
142.28
141.68
141.33
141.00
138.19
138.08
135.87
135.41
135.16
134.91
134.76
132.57
132.40
130.20
130.17
130.15
129.97
129.84
129.26
129.06
128.58
128.28
127.92
127.87
122.83
122.50
122.14
121.77
54.63
32.34
31.77
29.14
27.37
26.60
26.59
22.56
14.05
13.73
9.75

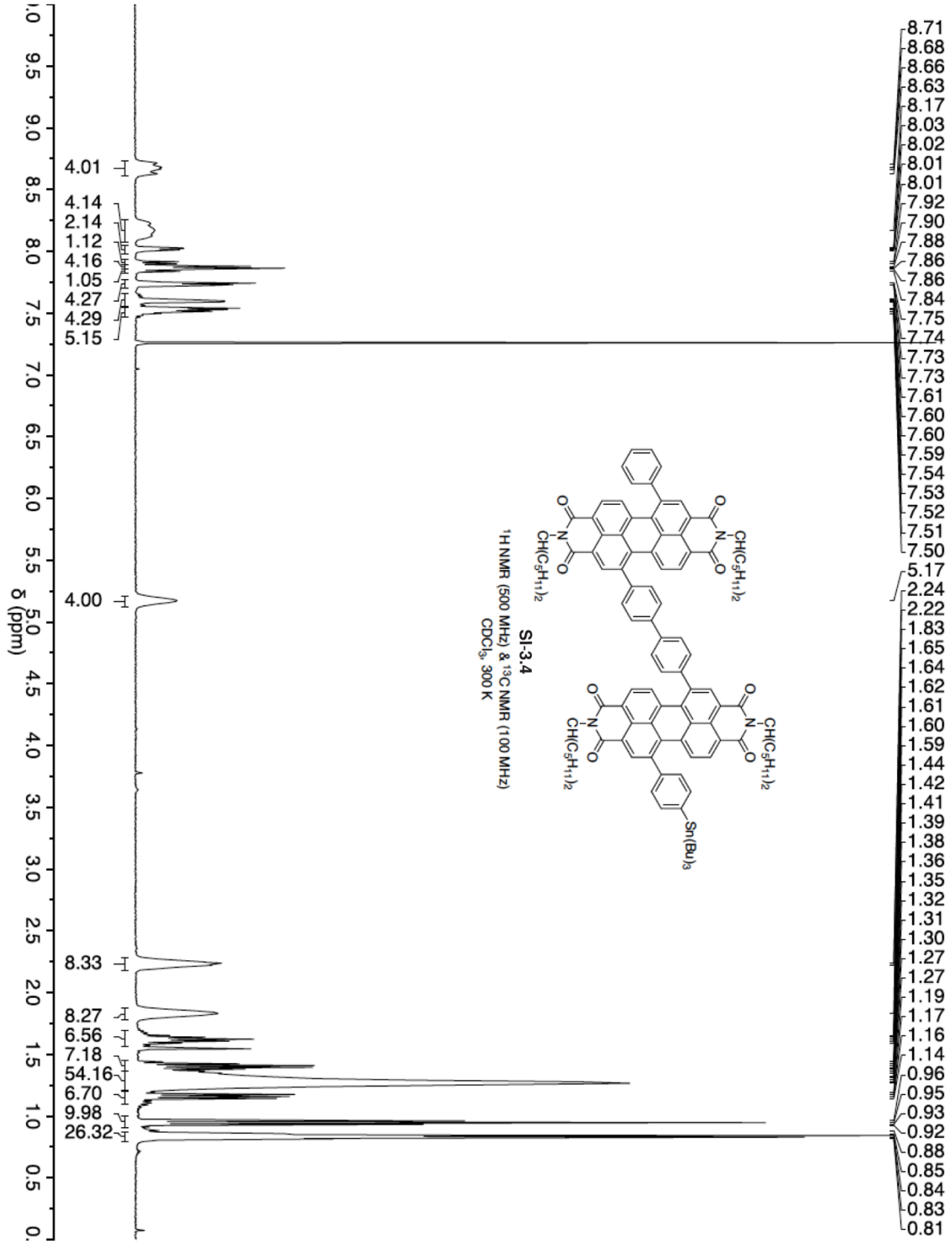
SI-3.4
^{1}H NMR (500 MHz) & ^{13}C NMR (100 MHz)
$CDCl_3$, 300 K
δ (ppm)
4.01
4.14
2.14
1.12
4.16
1.05
4.27
4.29
5.15
4.00
8.33
8.27
6.56
7.18
54.16
6.70
9.98
26.32
8.71
8.68
8.66
8.63
8.17
8.03
8.02
8.01
8.01
7.92
7.90
7.88
7.86
7.86
7.84
7.75
7.74
7.73
7.73
7.61
7.60
7.60
7.59
7.54
7.53
7.52
7.51
7.50
5.17
2.24
2.22
1.83
1.65
1.64
1.62
1.61
1.60
1.59
1.44
1.42
1.41
1.39
1.38
1.36
1.35
1.32
1.31
1.30
1.27
1.27
1.19
1.17
1.16
1.14
0.96
0.95
0.93
0.92
0.88
0.85
0.84
0.83
0.81

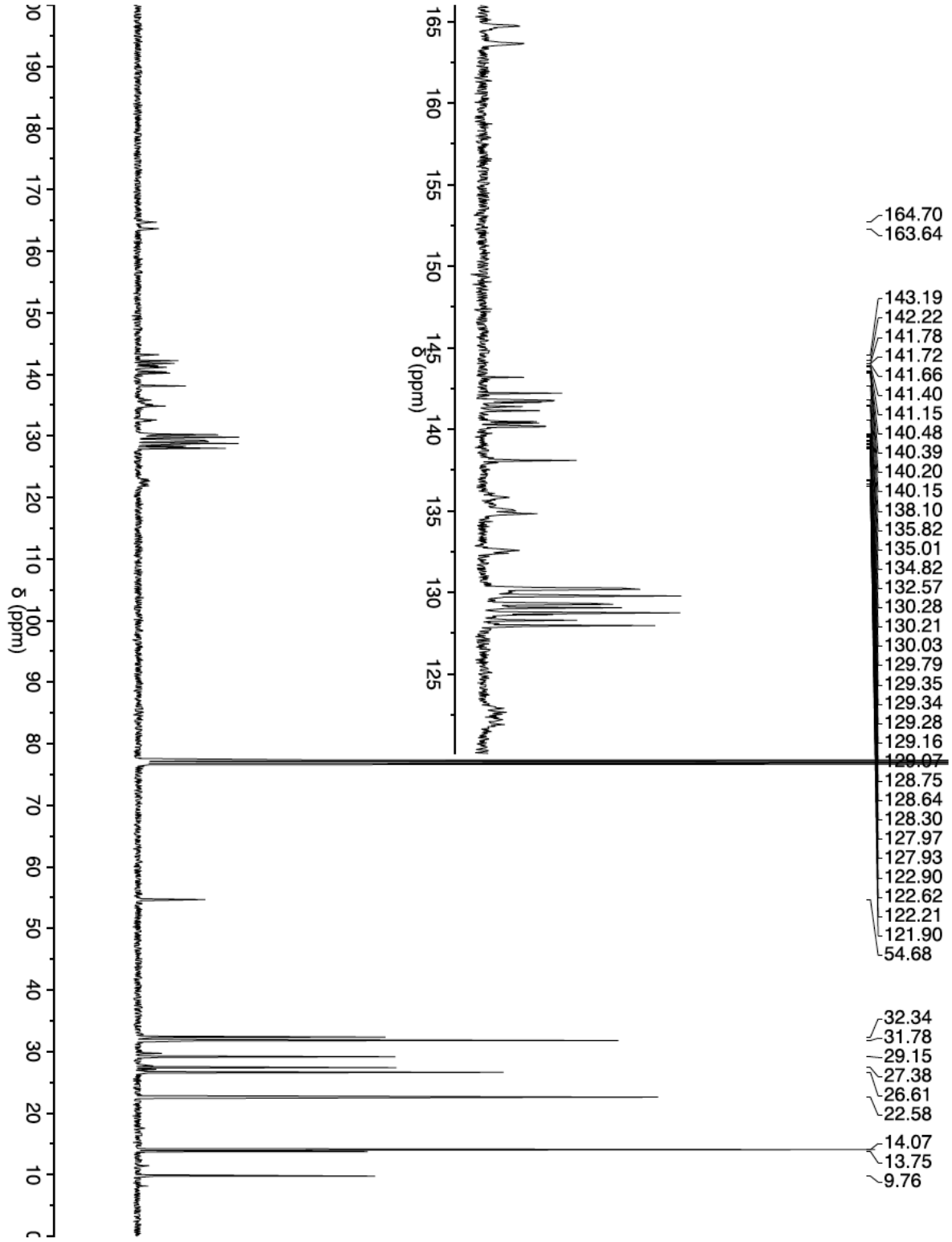
δ (ppm)
δ (ppm)
164.70
163.64
143.19
142.22
141.78
141.72
141.66
141.40
141.15
140.48
140.39
140.20
140.15
138.10
135.82
135.01
134.82
132.57
130.28
130.21
130.03
129.79
129.35
129.34
129.28
129.16
129.07
128.75
128.64
128.30
127.97
127.93
122.90
122.62
122.21
121.90
54.68
32.34
31.78
29.15
27.38
26.61
22.58
14.07
13.75
9.76

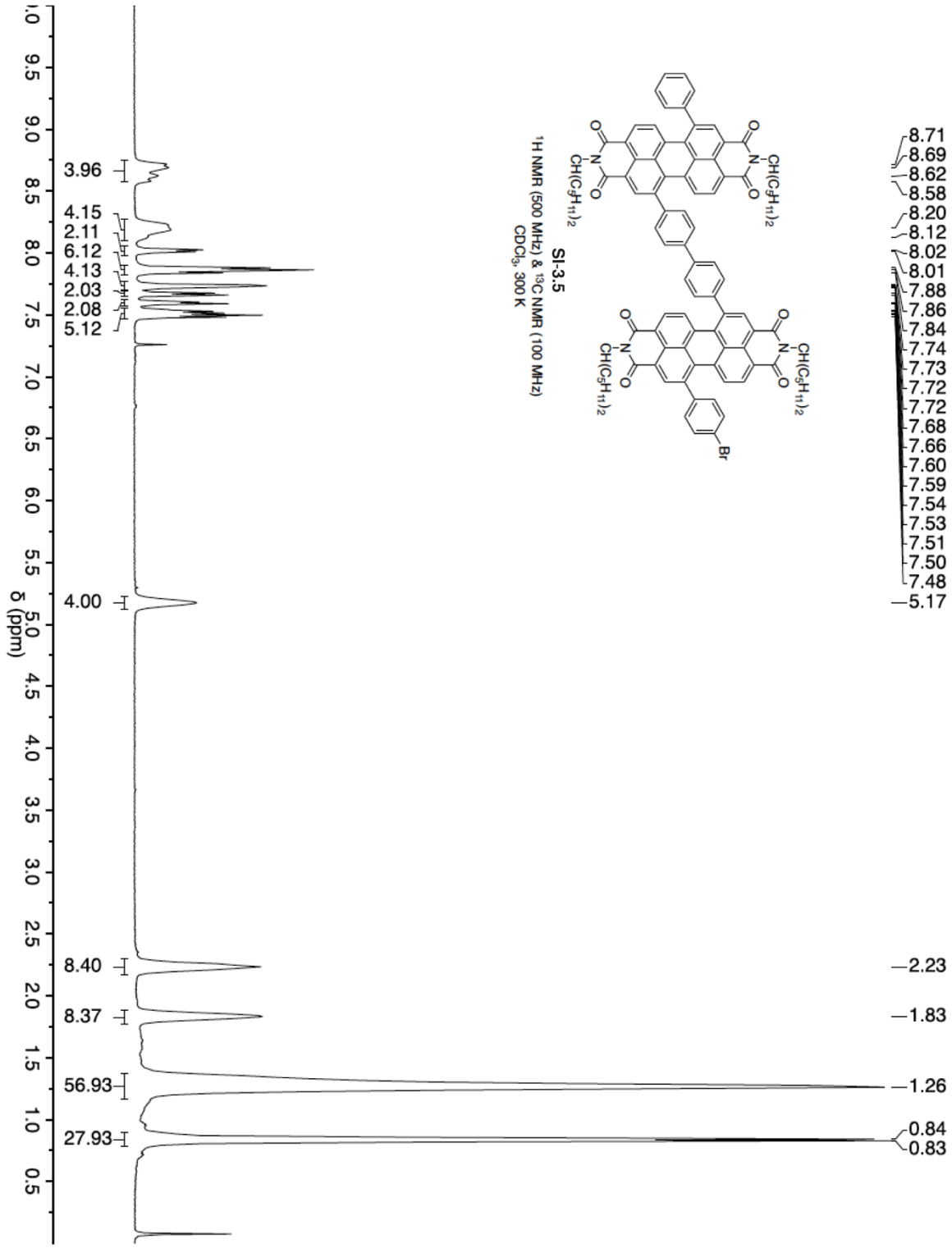
SI-3.5
^{1}H NMR (500 MHz) & ^{13}C NMR (100 MHz)
$CDCl_3$, 300 K
δ (ppm)
3.96
4.15
2.11
6.12
4.13
2.03
2.08
5.12
4.00
8.40
8.37
56.93
27.93
8.71
8.69
8.62
8.58
8.20
8.12
8.02
8.01
7.88
7.86
7.84
7.74
7.73
7.72
7.72
7.68
7.66
7.60
7.59
7.54
7.53
7.51
7.50
7.48
5.17
2.23
1.83
1.26
0.84
0.83

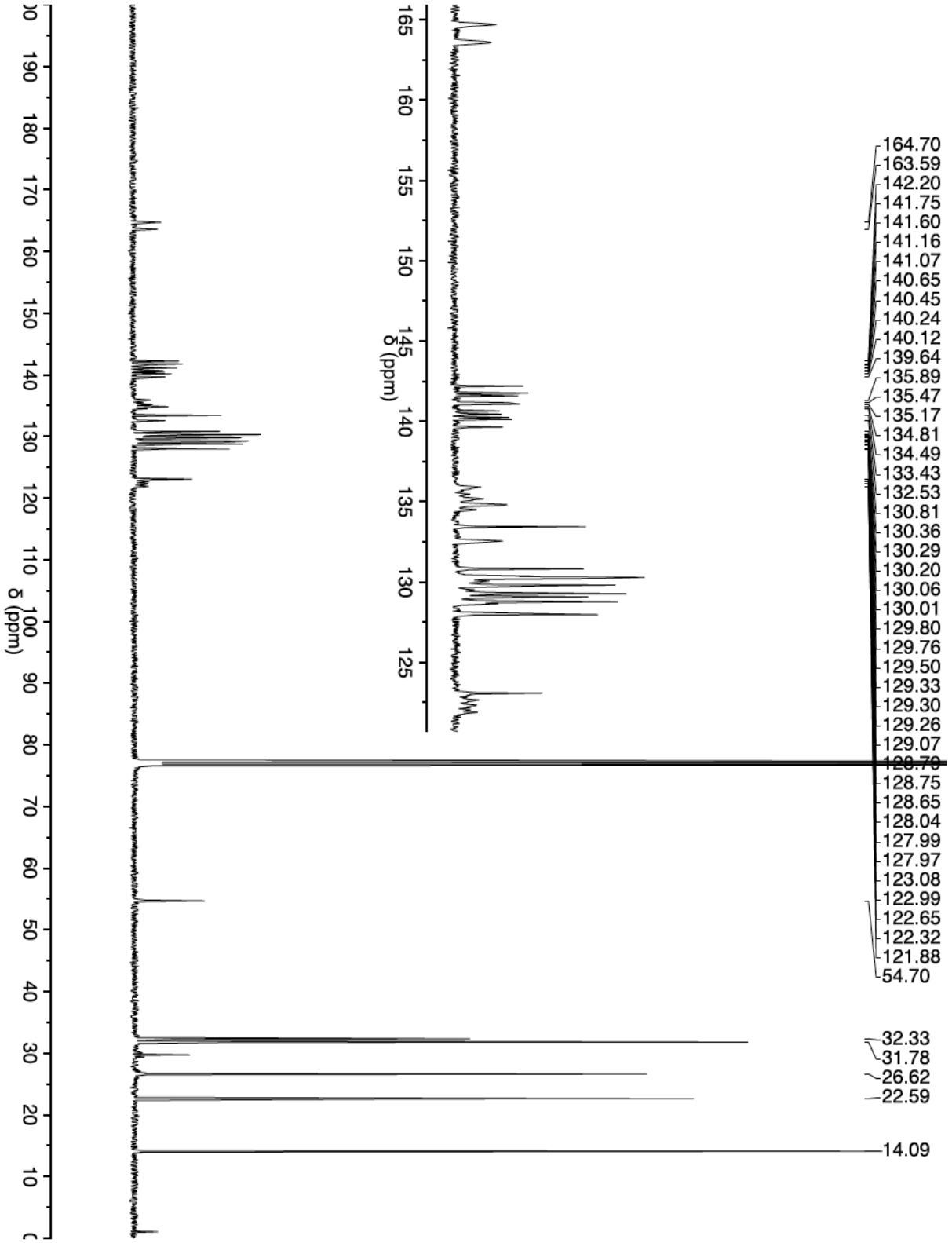
δ (ppm)
δ (ppm)
164.70
163.59
142.20
141.75
141.60
141.16
141.07
140.65
140.45
140.24
140.12
139.64
135.89
135.47
135.17
134.81
134.49
133.43
132.53
130.81
130.36
130.29
130.20
130.06
130.01
129.80
129.76
129.50
129.33
129.30
129.26
129.07
128.70
128.75
128.65
128.04
127.99
127.97
123.08
122.99
122.65
122.32
121.88
54.70
32.33
31.78
26.62
22.59
14.09

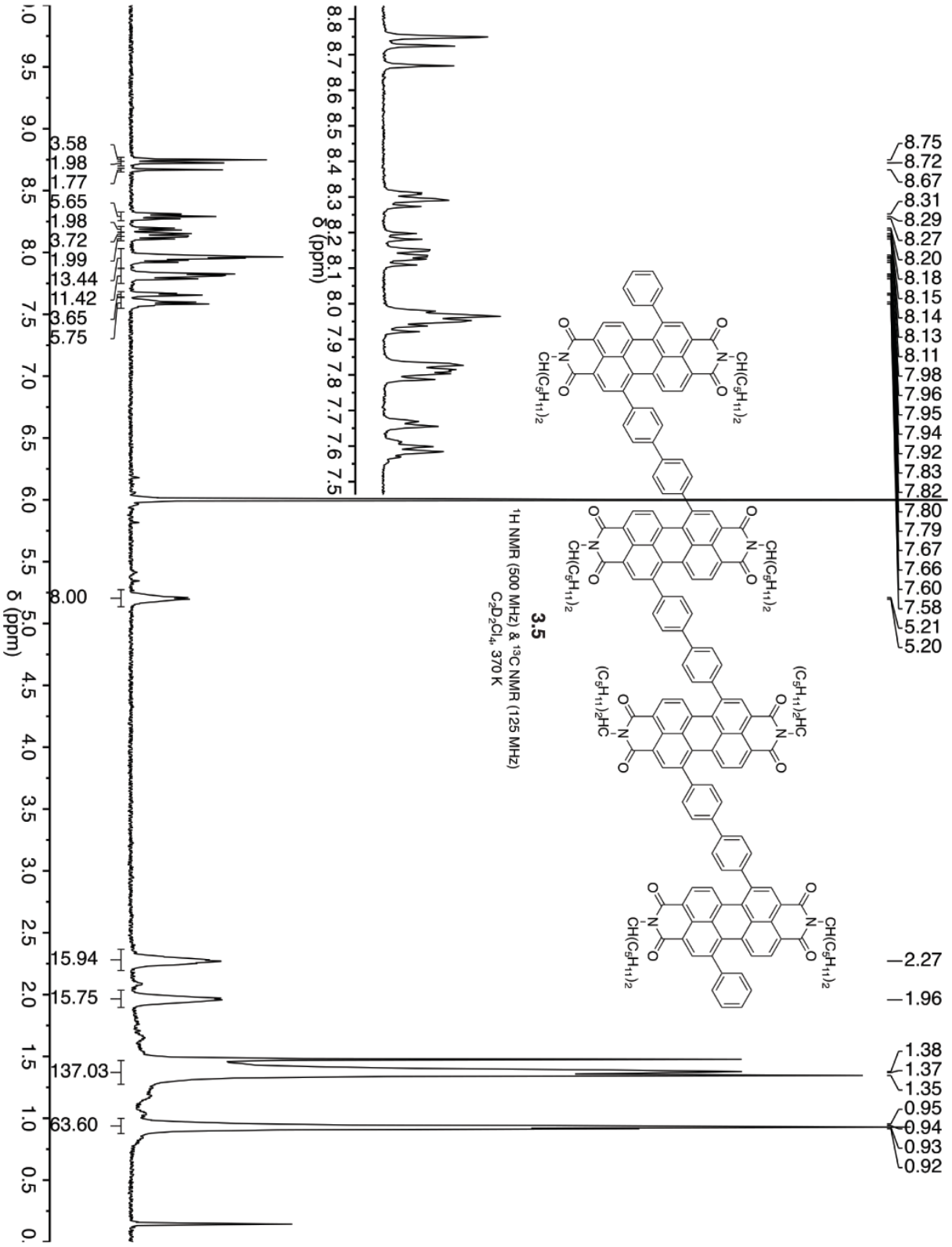
3.5
^{1}H NMR (500 MHz) & ^{13}C NMR (125 MHz)
$C_2D_2Cl_4$, 370 K
δ (ppm)
8.75
8.72
8.67
8.31
8.29
8.27
8.20
8.18
8.15
8.14
8.13
8.11
7.98
7.96
7.95
7.94
7.92
7.83
7.82
7.80
7.79
7.67
7.66
7.60
7.58
5.21
5.20
2.27
1.96
1.38
1.37
1.35
0.95
0.94
0.93
0.92
3.58
1.98
1.77
5.65
1.98
3.72
1.99
13.44
11.42
3.65
5.75
8.00
15.94
15.75
137.03
63.60

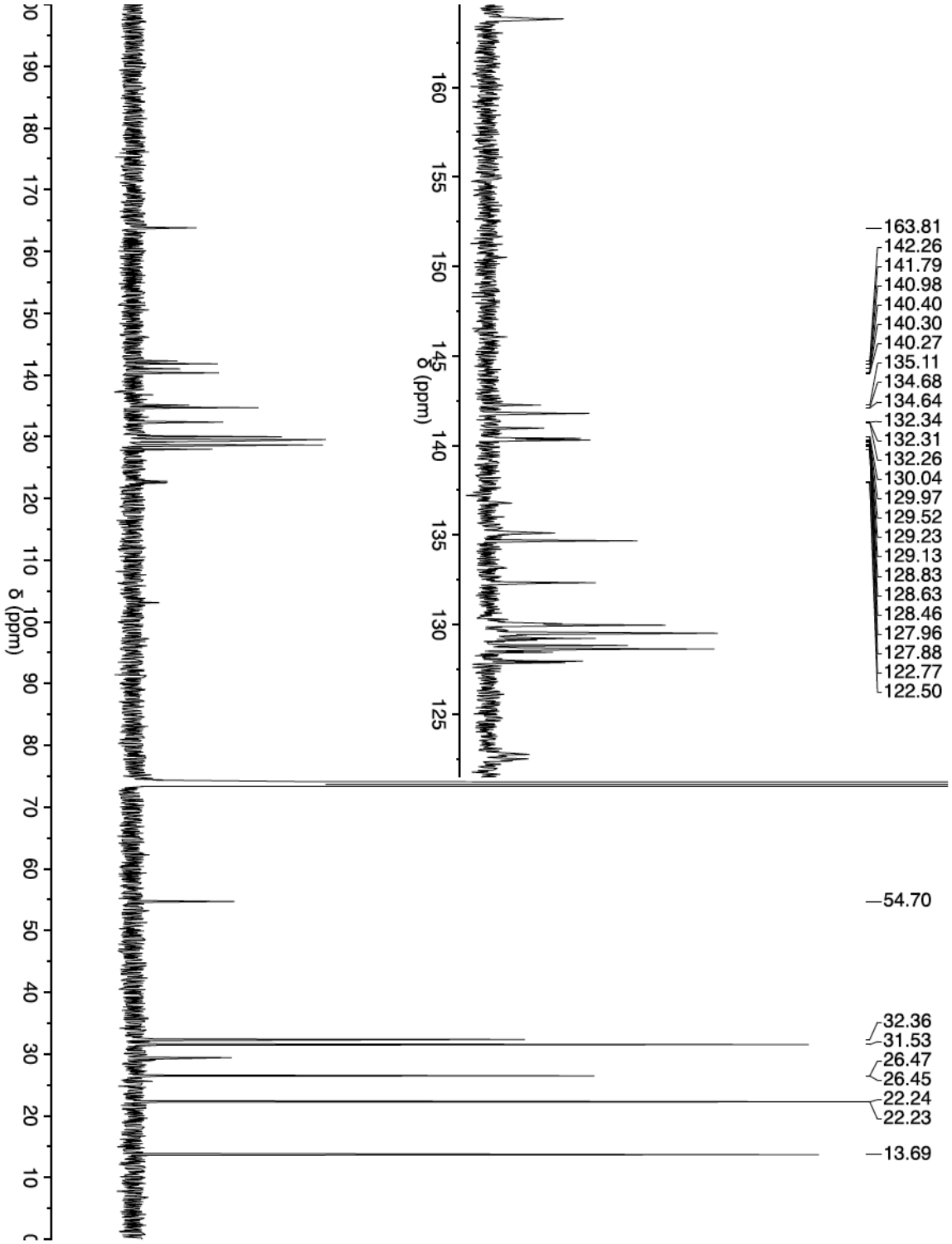
δ (ppm)
δ (ppm)
163.81
142.26
141.79
140.98
140.40
140.30
140.27
135.11
134.68
134.64
132.34
132.31
132.26
130.04
129.97
129.52
129.23
129.13
128.83
128.63
128.46
127.96
127.88
122.77
122.50
54.70
32.36
31.53
26.47
26.45
22.24
22.23
13.69

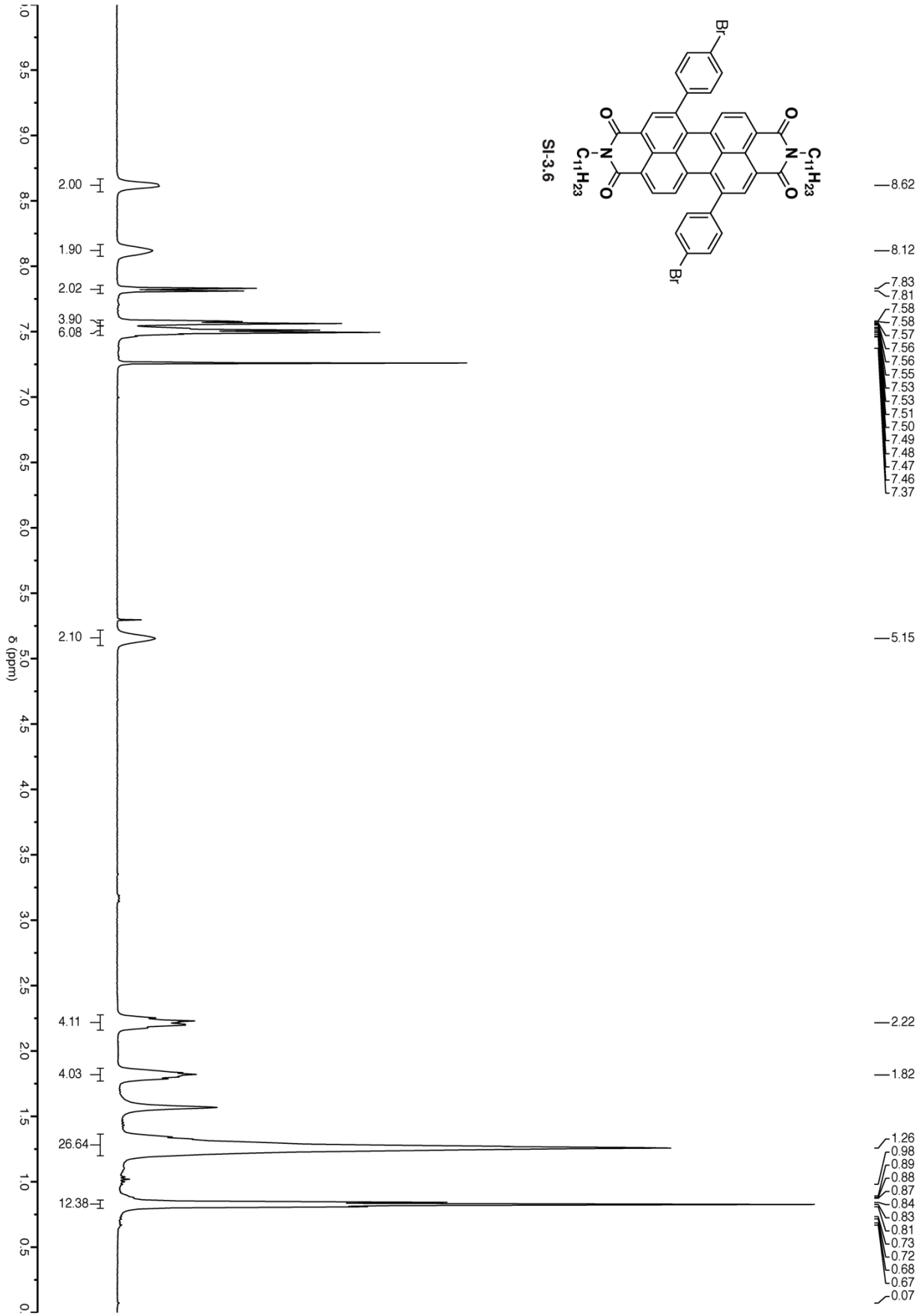
SI-3.6
Br
Br
O
O
N
C11H23
C11H23
δ (ppm)
2.00
1.90
2.02
3.90
6.08
2.10
4.11
4.03
26.64
12.38
8.62
8.12
7.83
7.81
7.58
7.58
7.57
7.56
7.56
7.55
7.53
7.53
7.51
7.50
7.49
7.48
7.47
7.46
7.37
5.15
2.22
1.82
1.26
0.98
0.89
0.88
0.87
0.84
0.83
0.81
0.73
0.72
0.68
0.67
0.07

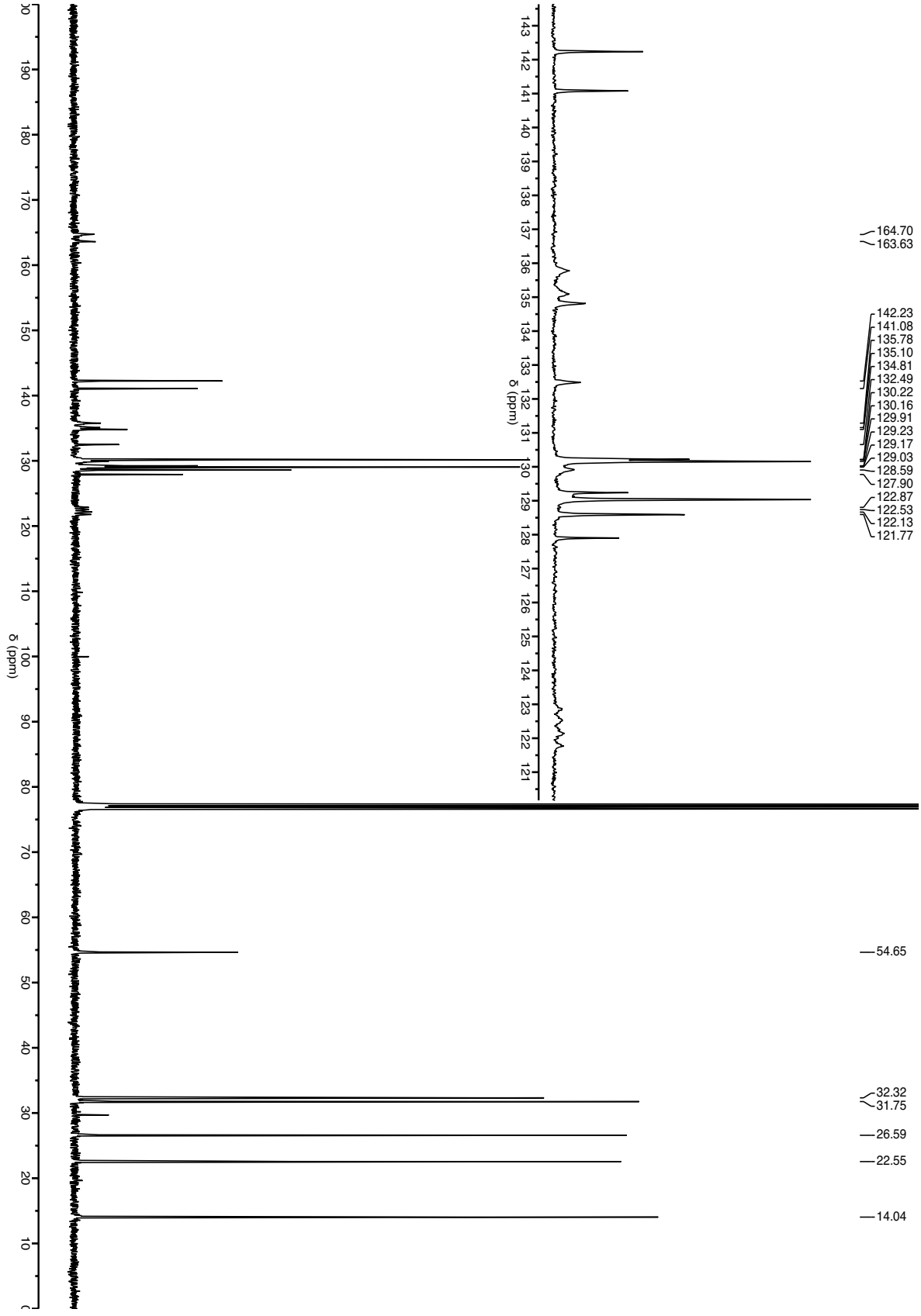
δ (ppm)
δ (ppm)
164.70
163.63
142.23
141.08
135.78
135.10
134.81
132.49
130.22
130.16
129.91
129.23
129.17
129.03
128.59
127.90
122.87
122.53
122.13
121.77
54.65
32.32
31.75
26.59
22.55
14.04

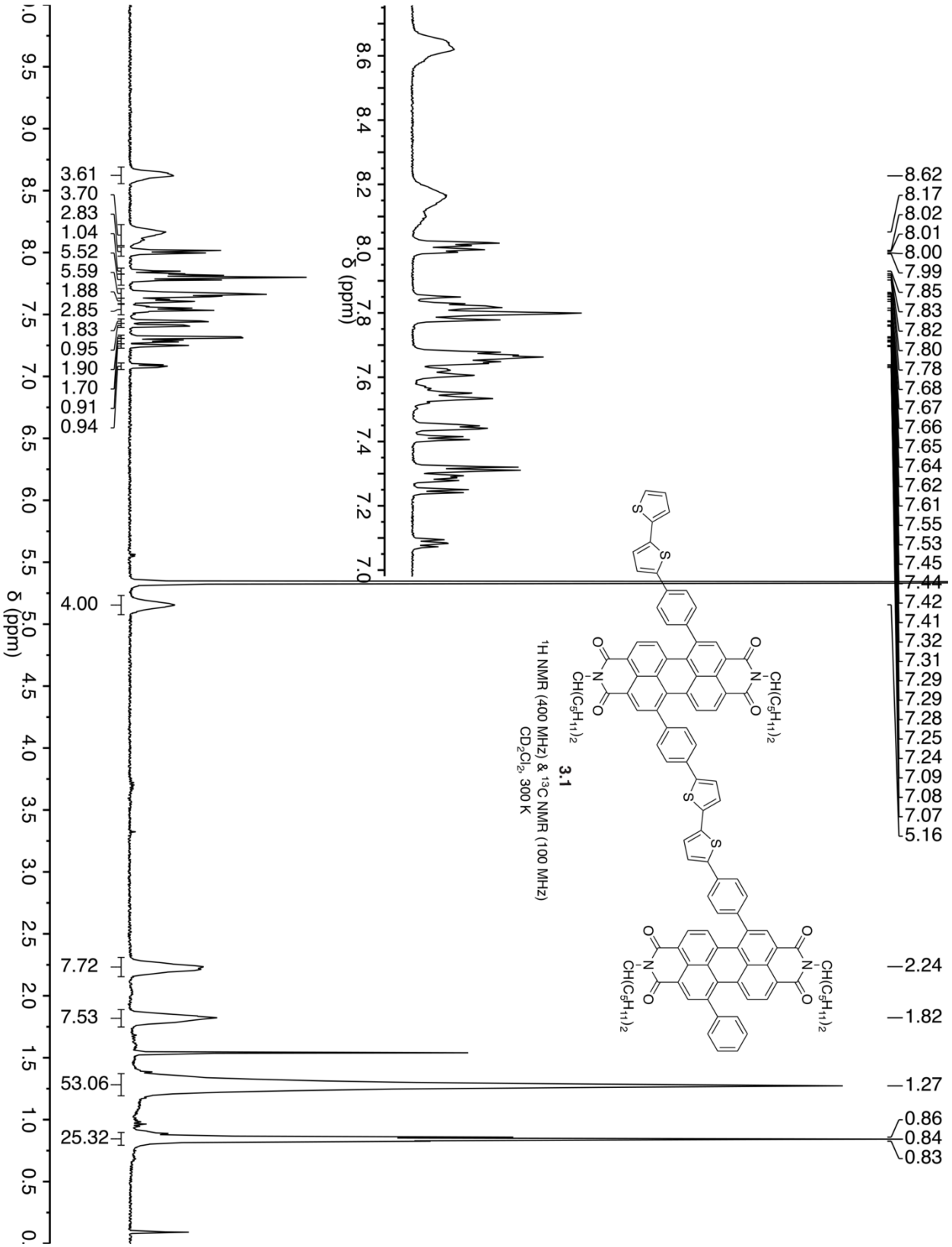
3.61
3.70
2.83
1.04
5.52
5.59
1.88
2.85
1.83
0.95
1.90
1.70
0.91
0.94
4.00
7.72
7.53
53.06
25.32
δ (ppm)
8.62
8.17
8.02
8.01
8.00
7.99
7.85
7.83
7.82
7.80
7.78
7.68
7.67
7.66
7.65
7.64
7.62
7.61
7.55
7.53
7.45
7.44
7.42
7.41
7.32
7.31
7.29
7.29
7.28
7.25
7.24
7.09
7.08
7.07
5.16
2.24
1.82
1.27
0.86
0.84
0.83
3.1
1H NMR (400 MHz) & 13C NMR (100 MHz)
CD2Cl2, 300 K

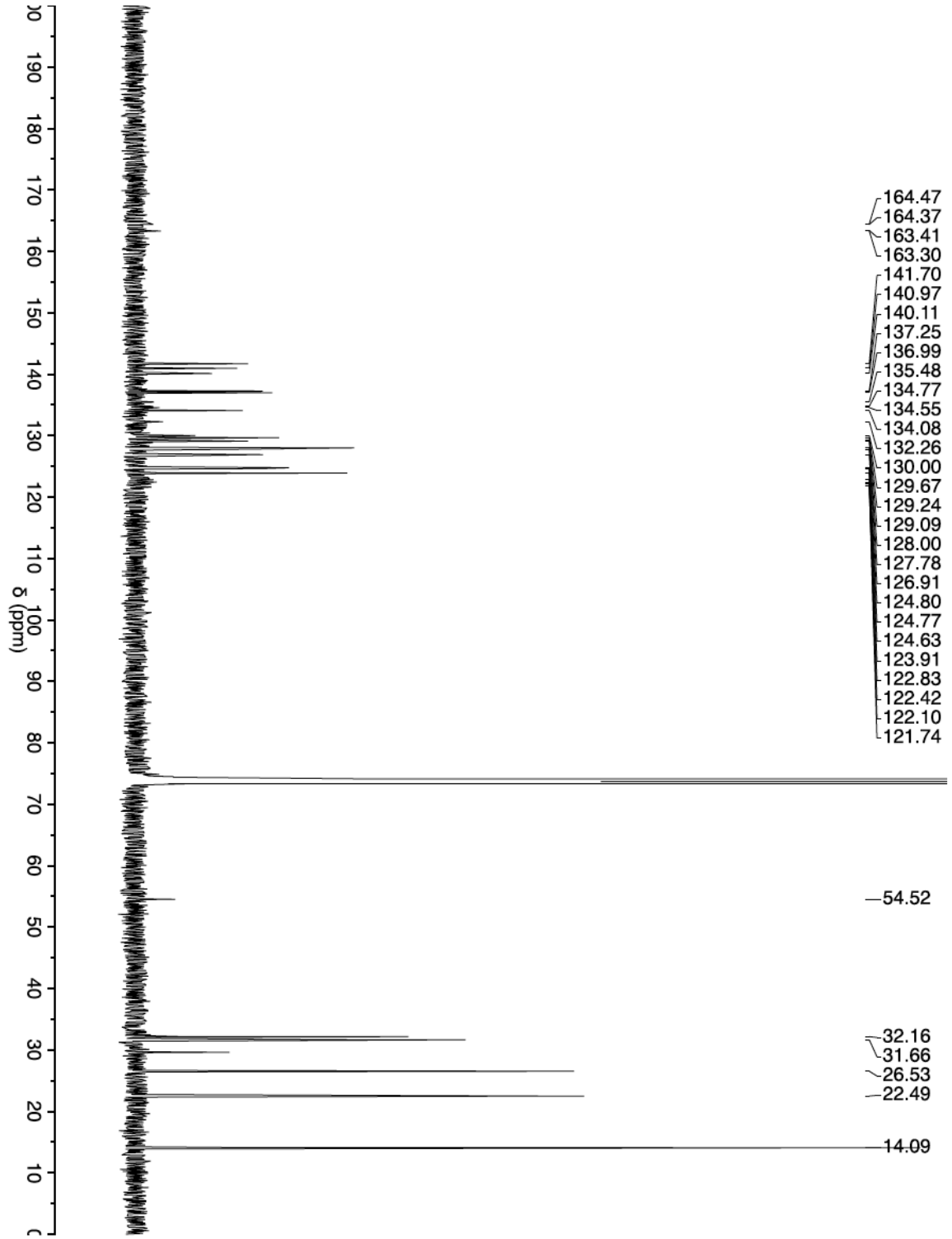
δ (ppm)
164.47
164.37
163.41
163.30
141.70
140.97
140.11
137.25
136.99
135.48
134.77
134.55
134.08
132.26
130.00
129.67
129.24
129.09
128.00
127.78
126.91
124.80
124.77
124.63
123.91
122.83
122.42
122.10
121.74
54.52
32.16
31.66
26.53
22.49
14.09

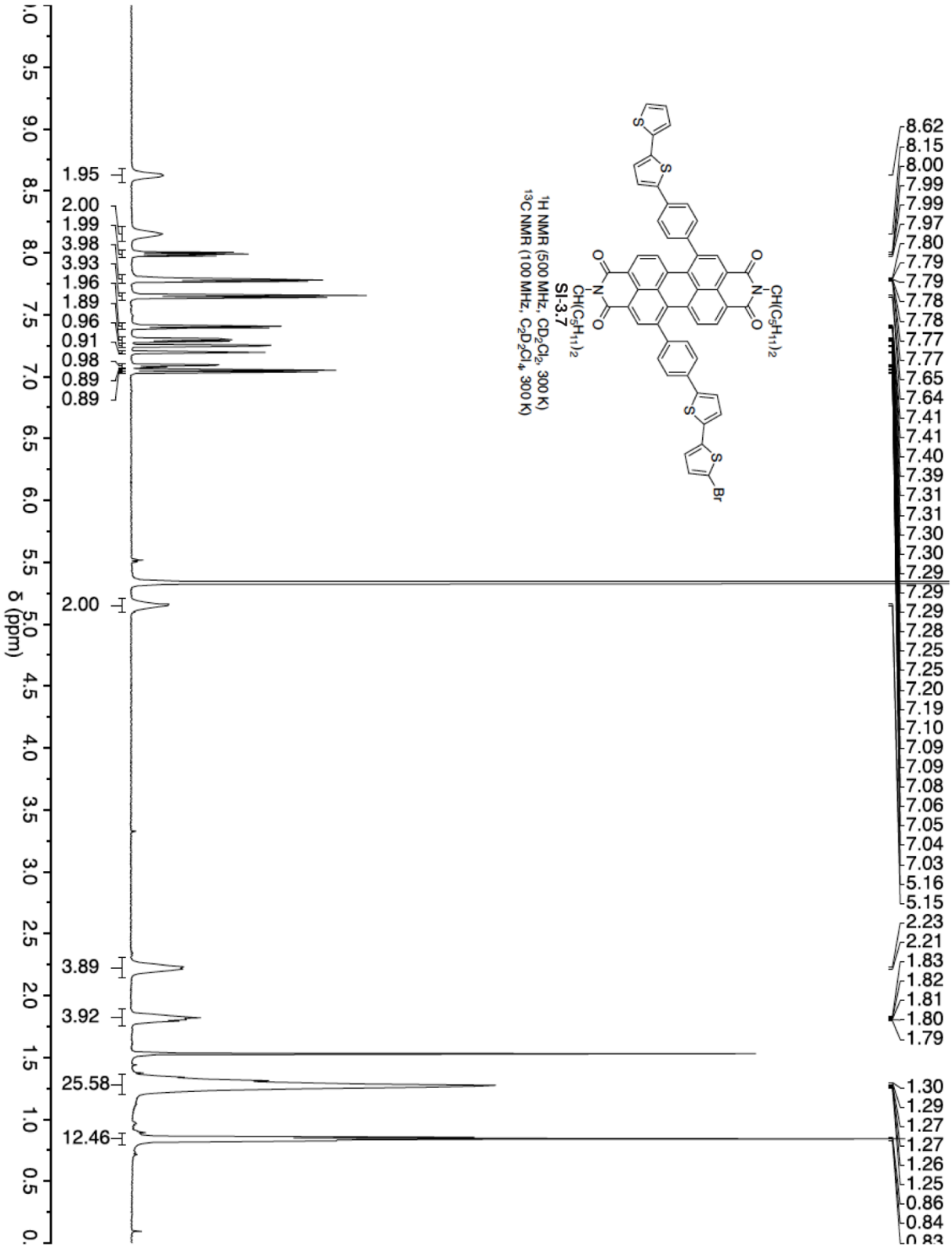
SI-3.7
1H NMR (500 MHz, CD2Cl2, 300 K)
13C NMR (100 MHz, C2D2Cl4, 300 K)
δ (ppm)
1.95
2.00
1.99
3.98
3.93
1.96
1.89
0.96
0.91
0.98
0.89
0.89
2.00
3.89
3.92
25.58
12.46
8.62
8.15
8.00
7.99
7.99
7.97
7.80
7.79
7.79
7.78
7.78
7.77
7.77
7.65
7.64
7.41
7.41
7.40
7.39
7.31
7.31
7.30
7.30
7.29
7.29
7.29
7.28
7.25
7.25
7.20
7.19
7.10
7.09
7.09
7.08
7.06
7.05
7.04
7.03
5.16
5.15
2.23
2.21
1.83
1.82
1.81
1.80
1.79
1.30
1.29
1.27
1.27
1.26
1.25
0.86
0.84

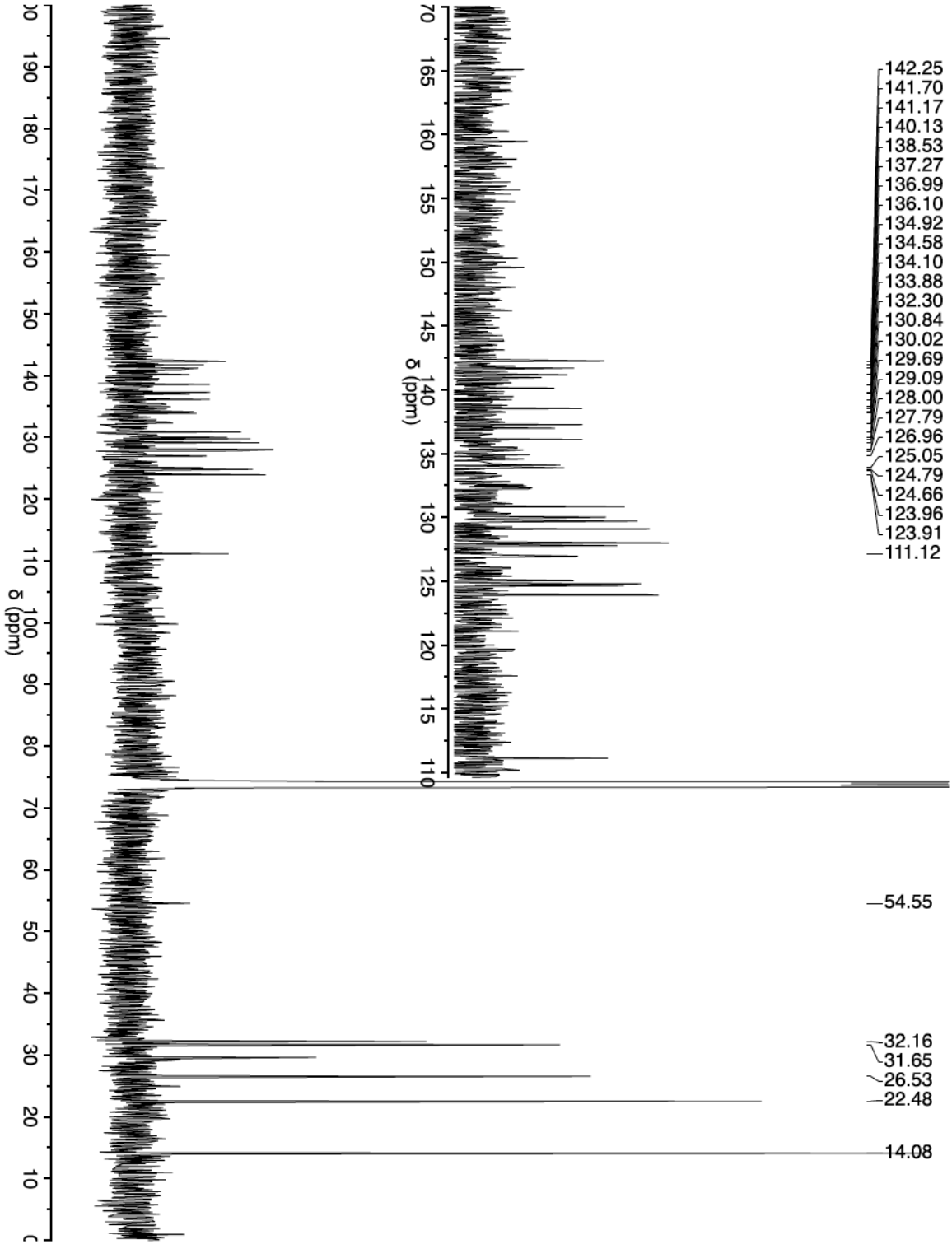
142.25
141.70
141.17
140.13
138.53
137.27
136.99
136.10
134.92
134.58
134.10
133.88
132.30
130.84
130.02
129.69
129.09
128.00
127.79
126.96
125.05
124.79
124.66
123.96
123.91
111.12
54.55
32.16
31.65
26.53
22.48
14.08
δ (ppm)

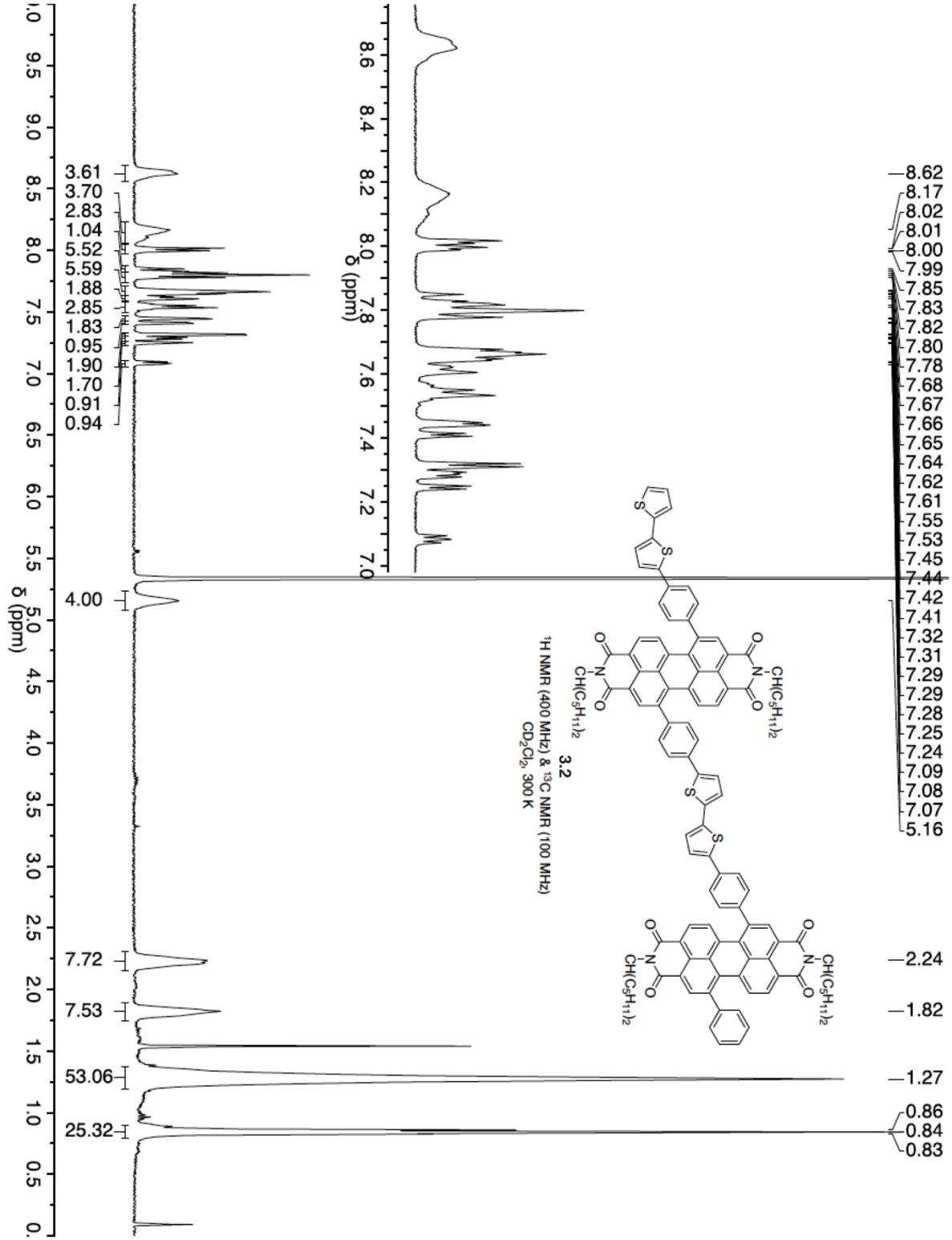
3.61
3.70
2.83
1.04
5.52
5.59
1.88
2.85
1.83
0.95
1.90
1.70
0.91
0.94
4.00
7.72
7.53
53.06
25.32
δ (ppm)
8.62
8.17
8.02
8.01
8.00
7.99
7.85
7.83
7.82
7.80
7.78
7.68
7.67
7.66
7.65
7.64
7.62
7.61
7.55
7.53
7.45
7.44
7.42
7.41
7.32
7.31
7.29
7.29
7.28
7.25
7.24
7.09
7.08
7.07
5.16
2.24
1.82
1.27
0.86
0.84
0.83
CH(C5H11)2
3.2
1H NMR (400 MHz) & 13C NMR (100 MHz)
CD2Cl2, 300 K

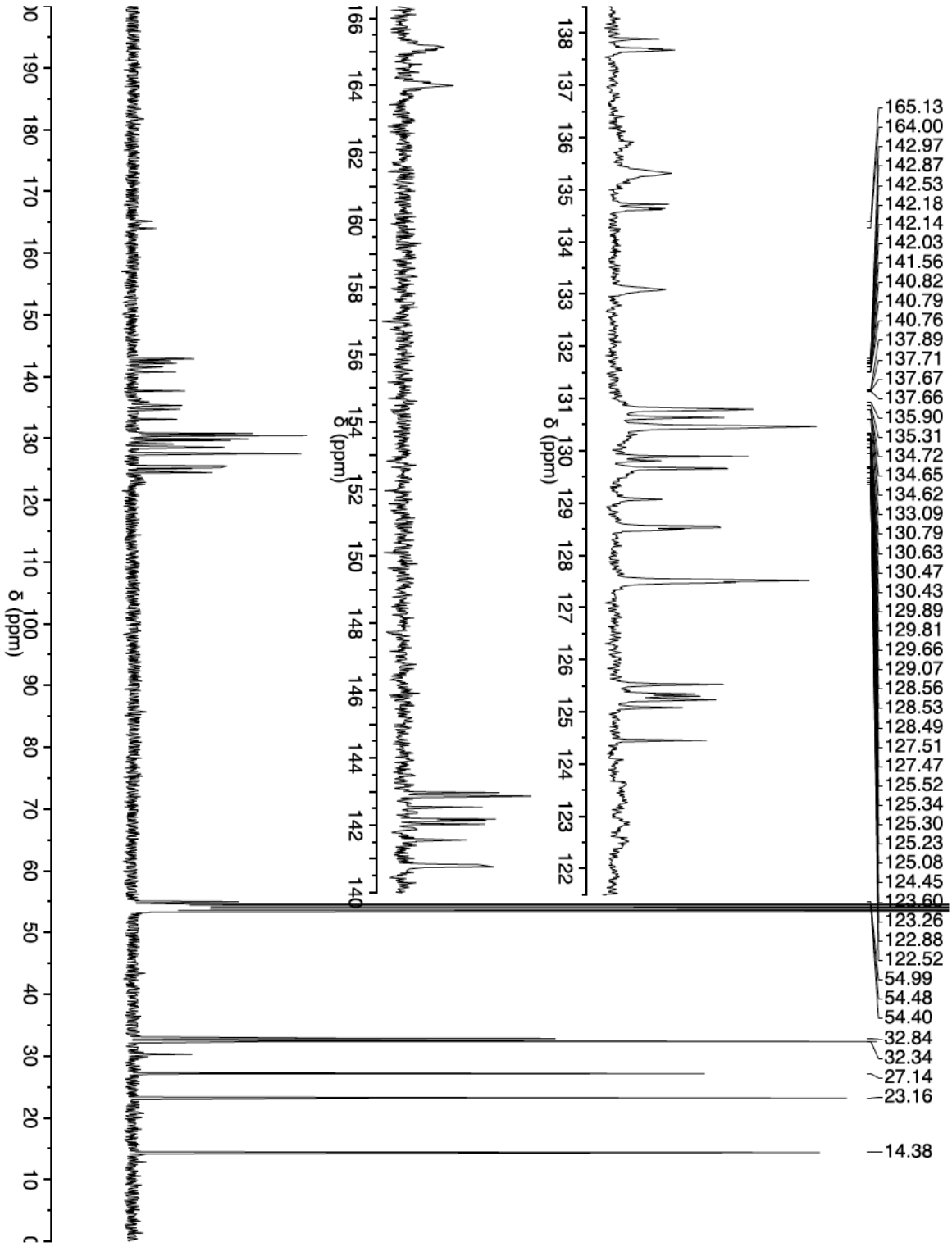
165.13
164.00
142.97
142.87
142.53
142.18
142.14
142.03
141.56
140.82
140.79
140.76
137.89
137.71
137.67
137.66
135.90
135.31
134.72
134.65
134.62
133.09
130.79
130.63
130.47
130.43
129.89
129.81
129.66
129.07
128.56
128.53
128.49
127.51
127.47
125.52
125.34
125.30
125.23
125.08
124.45
123.60
123.26
122.88
122.52
54.99
54.48
54.40
32.84
32.34
27.14
23.16
14.38
δ (ppm)

7.81
7.79
7.65
7.63
7.37
7.36
7.24
7.23
4.00
3.87
1.98
2.00
24.50
1.36
Me
Me
Me
Me
O
B
S
S
Me
Me
Me
Me
SI-3.8
^{1}H NMR (400 MHz, CD_2Cl_2, 300 K)
δ (ppm)

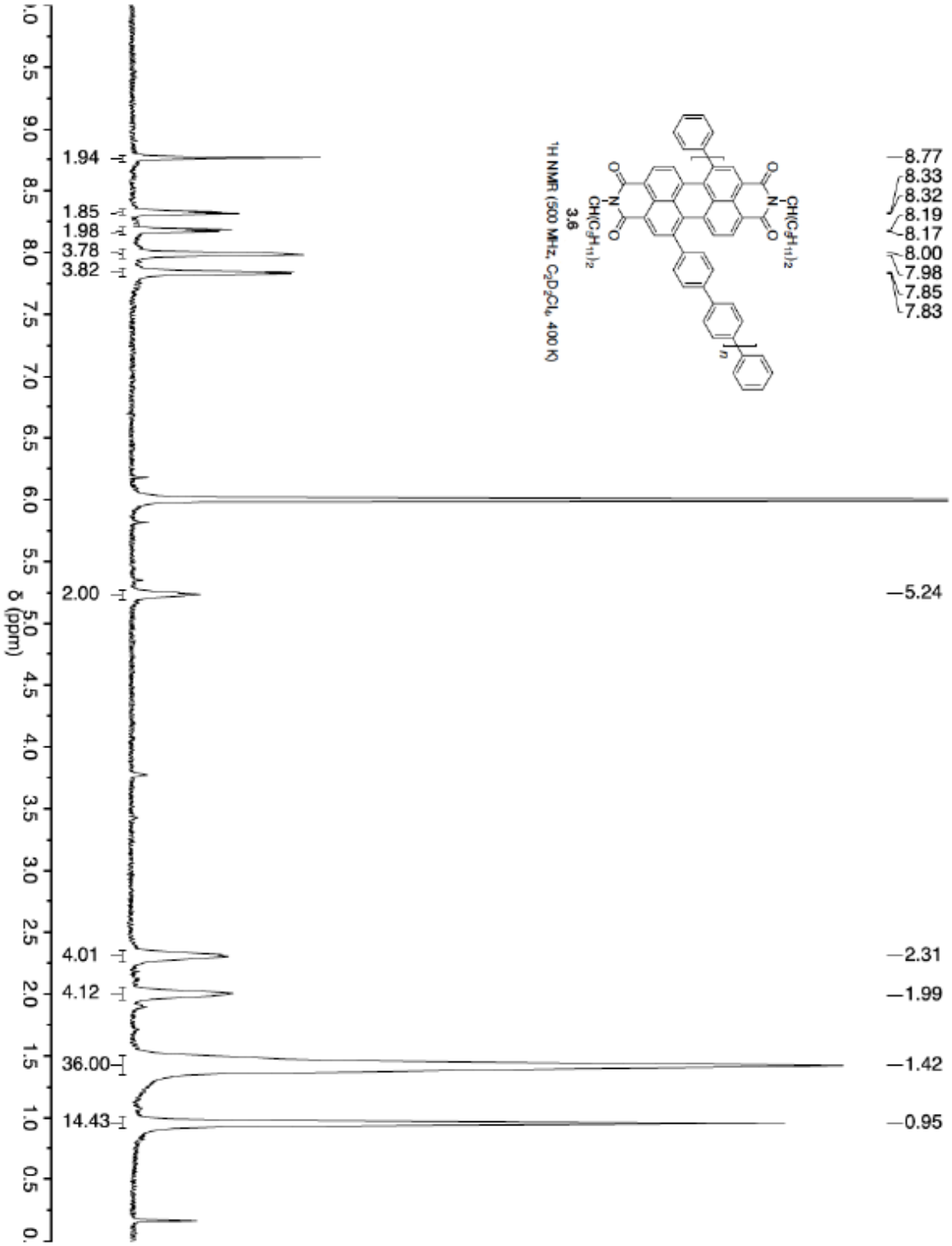
1.94
1.85
1.98
3.78
3.82
2.00
4.01
4.12
36.00
14.43
δ (ppm)
8.77
8.33
8.32
8.19
8.17
8.00
7.98
7.85
7.83
5.24
2.31
1.99
1.42
0.95
3.6
¹H NMR (500 MHz, C2D2Cl4, 400 K)

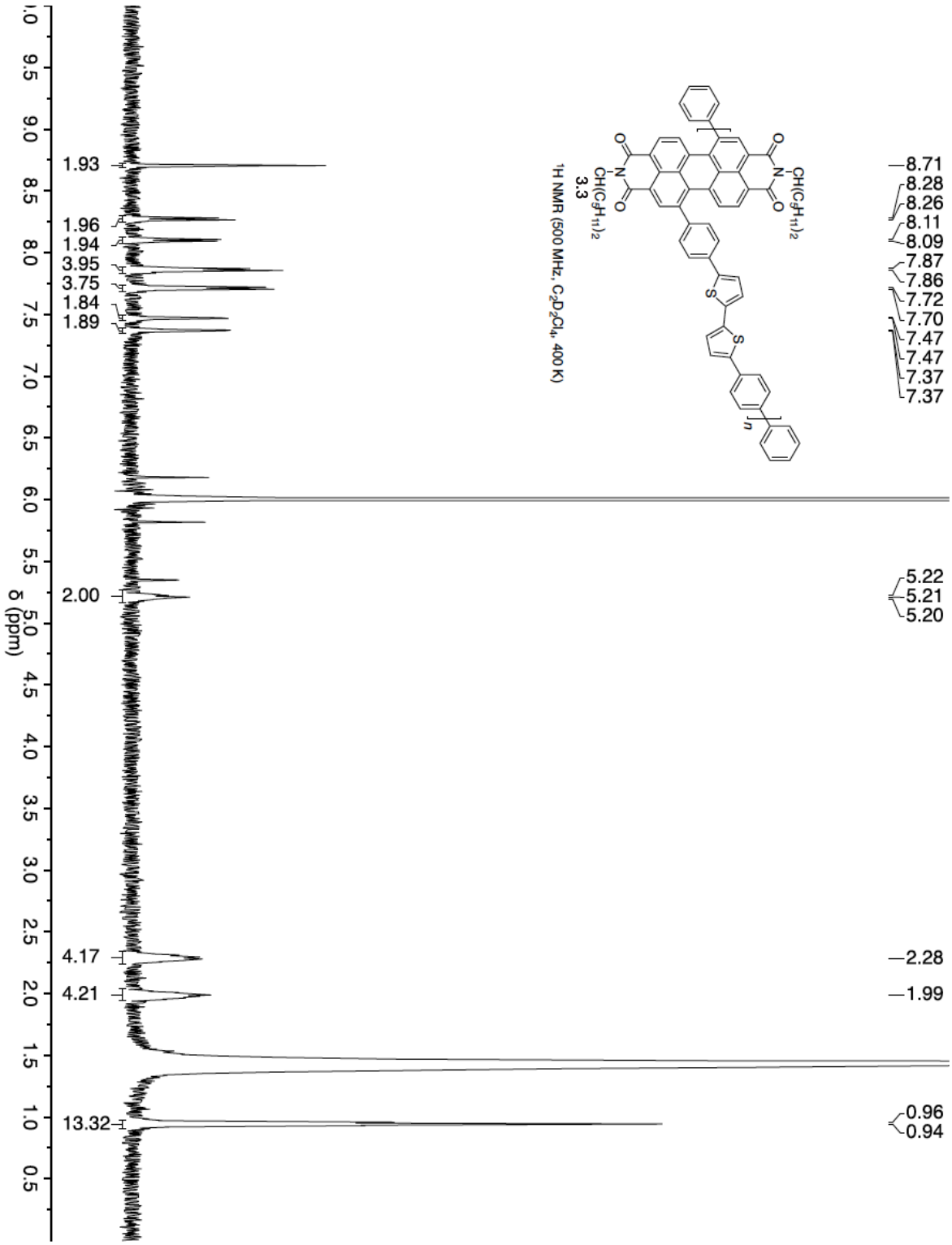
3.3
^{1}H NMR (500 MHz, $C_2D_2Cl_4$, 400 K)
δ (ppm)
1.93
1.96
1.94
3.95
3.75
1.84
1.89
2.00
4.17
4.21
13.32
8.71
8.28
8.26
8.11
8.09
7.87
7.86
7.72
7.70
7.47
7.47
7.37
7.37
5.22
5.21
5.20
2.28
1.99
0.96
0.94

3.14. DFT Output

All quantum chemical calculations were performed using Jaguar, version 8.3, Schrodinger, Inc., New York, NY,2013. (See A. D. Bochevarov, E. Harder, T. F. Hughes, J. R. Greenwood, D. A. Braden, D. M. Philipp, D. Rinaldo, M. D. Halls, J. Zhang, R. A. Friesner, "Jaguar: A High Performance Quantum Chemistry Software Program with Strengths in Life and Materials Sciences", Int. J. Quantum Chem., 2013, 113(18), 2110-2142). All geometries were optimized using the B3LYP functional and the 6-31G basis set. The optimized geometry for **$(PPh_2)_4$**'s can be found online at Reference 1 and **PBPB** can be found at Reference 13.[13]

3.15. References

1. Ball, M. *et al.* Macrocyclization in the Design of Organic n-Type Electronic Materials. *J. Am. Chem. Soc.* **138**, 12861–12867 (2016).
2. Krömer, J. *et al.* Synthesis of the First Fully α-Conjugated Macrocyclic Oligothiophenes: Cyclo[n]thiophenes with Tunable Cavities in the Nanometer Regime. *Angew. Chem. Int. Ed.* **39**, 3481–3486 (2000).
3. Nakao, K. *et al.* Giant Macrocycles Composed of Thiophene, Acetylene, and Ethylene Building Blocks. *J. Am. Chem. Soc.* **128**, 16740–16747 (2006).
4. Hitosugi, S. *et al*. Atropisomerism in a Belt-Persistent Nanohoop Molecule: Rotational Restriction Forced by Macrocyclic Ring Strain. *Chem. Asian J.* **7**, 1550–1552 (2012).
5. Hitosugi, S. *et al*. Bottom-up Synthesis and Thread-in-Bead Structures of Finite (n,0)-Zigzag Single-Wall Carbon Nanotubes. *J. Am. Chem. Soc.* **134**, 12442–12445 (2012).
6. Ishii, Y. *et al.* Size-selective synthesis of 9 - 11 and 13 cycloparaphenylenes. *Chem. Sci.* **3**, 2340–2345 (2012).
7. Kayahara, E. *et al*. Selective Synthesis and Crystal Structure of 10 Cycloparaphenylene. *Org. Lett.* **14**, 3284–3287 (2012).
8. Omachi, H. *et al*. Synthesis of Cycloparaphenylenes and Related Carbon Nanorings: A Step toward the Controlled Synthesis of Carbon Nanotubes. *Acc. Chem. Res.* **45**, 1378–1389 (2012).
9. Evans, P. J. *et al*. Efficient room-temperature synthesis of a highly strained carbon nanohoop fragment of buckminsterfullerene. *Nat. Chem.* **6**, 404–408 (2014).
10. Kayahara, E. *et al*. Synthesis and Characterization of 5 Cycloparaphenylene. *J. Am. Chem. Soc.* **136**, 2284–2287 (2014).
11. Yamago, S. *et al*. Organoplatinum-Mediated Synthesis of Cyclic pi-Conjugated Molecules: Towards a New Era of Three-Dimensional Aromatic Compounds. *Chem. Rec.* **14**, 84–100

(2014).

12. Asai, K. *et al*. A Cyclic Octithiophene Containing B,B'-linkages *Chem. Commun.* **51**, 6096 (2015).
13. Ball, M. *et al.* Chiral Conjugated Corrals. *J. Am. Chem. Soc.* **137**, 9982–9987 (2015).
14. Jasti, R. *et al*. Synthesis, Characterization, and Theory of 9 -, 12 -, and 18 Cycloparaphenylene: Carbon Nanohoop Structures. *J. Am. Chem. Soc.* **130**, 17646-17647 (2008).
15. Chang, S.-W. *et al*. A Donor-Acceptor Conjugated Block Copolymer of Poly(arylenevinylene)s by Ring-opening Metathesis Polymerization. *Chem. Commun.* **51**, 9113–9116 (2015).
16. Chen, Q. *et al.* Strain-Induced Stereoselective Formation of Blue-Emitting Cyclostilbenes. *J. Am. Chem. Soc.* **137**, 12282–12288 (2015).
17. Darzi, E. R. *et al.* Synthesis, Properties, and Design Principles of Donor–Acceptor Nanohoops. *ACS Cent. Sci.* **1**, 335–342 (2015).
18. Ito, H. *et al*. Thiophene-Based, Radial pi-Conjugation: Synthesis, Structure, and Photophysical Properties of Cyclo-1,4-phenylene-2 ',5 '-thienylenes. *Angew. Chem. Int. Ed.* **54**, 159–163 (2015).
19. Jiang, H.-W. *et al.* Cyclic 2,12-Porphyrinylene Nanorings as a Porphyrin Analogue of Cycloparaphenylenes. *J. Am. Chem. Soc.* **137**, 2219–2222 (2015).
20. Kuwabara, T. *et al*. Curved Oligophenylenes as Donors in Shape-Persistent Donor–Acceptor Macrocycles with Solvatofluorochromic Properties. *Angew. Chem. Int. Ed.* **54**, 9646–9649 (2015).
21. Van Raden, J. M. *et al*. Synthesis and characterization of a highly strained donor-acceptor nanohoop. *Org. Biomol. Chem.* **14**, 5721 (2016).
22. Zhang, F. *et al*. Giant Cyclo n thiophenes with Extended pi Conjugation. *Angew. Chem. Int. Ed.* **48**, 6632–6635 (2009).
23. Omachi, H. *et al*. A Modular and Size-Selective Synthesis of [n]Cycloparaphenylenes: A Step toward the Selective Synthesis of n, n Single-Walled Carbon Nanotubes. *Angew. Chem. Int. Ed.* **49**, 10202–10205 (2010).
24. Iwamoto, T. *et al*. Size-Selective Encapsulation of C60 by [10]Cycloparaphenylene: Formation of the Shortest Fullerene-Peapod. *Angew. Chem. Int. Ed.* **50**, 8342–8344 (2011).
25. Iwamoto, T. *et al*. Selective and Random Syntheses of n Cycloparaphenylenes (n=8-13) and Size Dependence of Their Electronic Properties. *J. Am. Chem. Soc.* **133**, 8354–8361 (2011).
26. Segawa, Y. *et al.* Concise Synthesis and Crystal Structure of [12]Cycloparaphenylene. *Angew. Chem. Int. Ed.* **50**, 3244–3248 (2011).
27. Segawa, Y. *et al*. [9]Cycloparaphenylene: Nickel-mediated Synthesis and Crystal Structure. *Chem. Lett.* **40**, 423–425 (2011).
28. Sprafke, J. K. *et al.* Belt-Shaped π-Systems: Relating Geometry to Electronic Structure in a Six-Porphyrin Nanoring. *J. Am. Chem. Soc.* **133**, 17262–17273 (2011).

29. Ball, M. *et al.* Contorted Polycyclic Aromatics. *Acc. Chem. Res.* **48**, 267–276 (2015).

30. Nicolai, H. T. *et al.* Unification of trap-limited electron transport in semiconducting polymers. *Nat. Mater* **11**, 882–887 (2012).

31. Mandoc, M. M. *et al*. Trap-limited electron transport in disordered semiconducting polymers. *Phys. Rev. B* **75**, 193202 (2007).

32. Arias, A. C. *et al*. Materials and Applications for Large Area Electronics: Solution-Based Approaches. *Chem. Rev.* **110**, 3–24 (2010).

33. Kaake, L. G. *et al*. Intrinsic Charge Trapping in Organic and Polymeric Semiconductors: A Physical Chemistry Perspective. *J. Phys. Chem. Lett.* **1**, 628–635 (2010).

34. Sirringhaus, H. *et al*. Device Physics of Solution-Processed Organic Field-Effect Transistors. *Adv. Mater.* **17**, 2411–2425 (2005).

35. Iyoda, M. *et al*. Conjugated Macrocycles: Concepts and Applications. *Angew. Chem. Int. Ed.* **50**, 10522–10553 (2011).

36. Iwamoto, T. *et al.* Size- and Orientation-Selective Encapsulation of C70 by Cycloparaphenylenes. *Chem. Eur. J.* **19**, 14061–14068 (2013).

37. Nakanishi, Y. *et al.* Size-Selective Complexation and Extraction of Endohedral Metallofullerenes with Cycloparaphenylene. *Angew. Chem. Int. Ed.* **53**, 3102–3106 (2014).

38. Anthony, J. E. *et al*. n-Type Organic Semiconductors in Organic Electronics. *Adv. Mater.* **22**, 3876–3892 (2010).

39. Zhou, E. J. *et al.* All-Polymer Solar Cells from Perylene Diimide Based Copolymers: Material Design and Phase Separation Control. *Angew. Chem. Int. Ed.* **50**, 2799–2803 (2011).

40. Li, C. & Wonneberger, H. Perylene Imides for Organic Photovoltaics: Yesterday, Today, and Tomorrow. *Adv. Mater.* **24**, 613–636 (2012).

41. Sharenko, A. *et al.* A High-Performing Solution-Processed Small Molecule: Perylene Diimide Bulk Heterojunction Solar Cell. *Adv. Mater.* **25**, 4403–4406 (2013).

42. Cai, Y. *et al.* High Performance Organic Solar Cells Based on a Twisted Bay-Substituted Tetraphenyl Functionalized Perylenediimide Electron Acceptor. *Adv. Energy Mater.* **5**, 1500032 (2015).

43. Nolde, F. *et al*. Synthesis and self-organization of core-extended perylene tetracarboxdiimides with branched alkyl substituents. *Chem. Mater.* **18**, 3715–3725 (2006).

44. Zhong, Y. *et al.* Helical Ribbons for Molecular Electronics. *J. Am. Chem. Soc.* **136**, 8122–8130 (2014).

45. Yan, Q. F. *et al*. Conjugated Dimeric and Trimeric Perylenediimide Oligomers. *Org. Lett.* **11**, 3426–3429 (2009).

46. Huo, L. J. *et al*. Synthesis and absorption spectra of n-type conjugated polymers based on perylene diimide. *Macromol. Rapid Commun.* **29**, 1444–1448 (2008).

47. Würthner, F. *et al.* Perylene Bisimide Dye Assemblies as Archetype Functional Supramolecular Materials. *Chem. Rev.* **116**, 962–1052 (2016).

48. Zhong, Y. *et al.* Efficient Organic Solar Cells with Helical Perylene Diimide Electron Acceptors. *J. Am. Chem. Soc.* **136**, 15215 (2014).

49. Meng, D. *et al.* High-Performance Solution-Processed Non-Fullerene Organic Solar Cells Based on Selenophene-Containing Perylene Bisimide Acceptor. *J. Am. Chem. Soc.* **138**, 375–380 (2016).

50. Wu, Q. *et al*. Covalently Bound Clusters of Alpha-Substituted PDI—Rival Electron Acceptors to Fullerene for Organic Solar Cells. *J. Am. Chem. Soc.* **138**, 7248–7251 (2016).

51. Liang, Y. *et al.* For the Bright Future—Bulk Heterojunction Polymer Solar Cells with Power Conversion Efficiency of 7.4%. *Adv. Mater.* **22**, E135--E138 (2010).

52. Liao, S.-H. *et al*. Fullerene Derivative-Doped Zinc Oxide Nanofilm as the Cathode of Inverted Polymer Solar Cells with Low-Bandgap Polymer (PTB7-Th) for High Performance. *Adv. Mater.* **25**, 4766–4771 (2013).

53. He, Z. *et al.* Single-junction polymer solar cells with high efficiency and photovoltage. *Nat Phot.* **9**, 174–179 (2015).

54. Zhong, Y. *et al.* Molecular helices as electron acceptors in high-performance bulk heterojunction solar cells. *Nat Commun.* **6**, 8242 (2015).

55. Heeger, A. J. 25th Anniversary Article: Bulk Heterojunction Solar Cells: Understanding the Mechanism of Operation. *Adv. Mater.* **26**, 10–28 (2014).

56. Sun, Y. *et al*. Inverted Polymer Solar Cells Integrated with a Low-Temperature-Annealed Sol-Gel-Derived ZnO Film as an Electron Transport Layer. *Adv. Mater.* **23**, 1679–1683 (2011).

57. You, J. B. *et al.* A polymer tandem solar cell with 10.6% power conversion efficiency. *Nat. Commun.* **4**, 10 (2013).

58. Elumalai, N. K. *et al*. Open circuit voltage of organic solar cells: An in-depth review. *Energy Environ. Sci.* **9**, 291 (2015).

59. Wang, M. *et al.* High Open Circuit Voltage in Regioregular Narrow Band Gap Polymer Solar Cells. *J. Am. Chem. Soc.* **136**, 12576–12579 (2014).

60. Li, W. *et al*. High Quantum Efficiencies in Polymer Solar Cells at Energy Losses below 0.6 eV. *J. Am. Chem. Soc.* **137**, 2231 (2015).

61. Hendriks, K. H. *et al*. Dichotomous Role of Exciting the Donor or the Acceptor on Charge Generation in Organic Solar Cells. *J. Am. Chem. Soc.* **138**, 10026-10031 (2016).

62. Zhao, Y. *et al*. 25th Anniversary Article: Recent Advances in n-Type and Ambipolar Organic Field-Effect Transistors. *Adv. Mater.* **25**, 5372–5391 (2013).

63. Newman, C. R. *et al.* Introduction to Organic Thin Film Transistors and Design of n-Channel Organic Semiconductors. *Chem. Mater.* **16**, 4436–4451 (2004).

64. Dou, L. *et al.* 25th Anniversary Article: A Decade of Organic/Polymeric Photovoltaic Research. *Adv. Mater.* **25**, 6642–6671 (2013).

65. Rajasingh, P. *et al*. Selective Bromination of Perylene Diimides under Mild Conditions. *J. Org. Chem.* **72**, 5973–5979 (2007).

Chapter 4. The Importance of Intramolecular Conductivity in Three Dimensional Molecular Solids

4.1. Preface

Chapter 4 is under review at *Chemical Science*. The manuscript was prepared by Melissa L. Ball, Boyuan Zhang, Tianren Fu, Ayden M. Schattman, Daniel W. Paley, Fay Ng, Latha Venkataraman, Colin Nuckolls, Michael L. Steigerwald. I synthesized *cis*-**PBPB** and its intermediates, with help from Ayden M. Schattman. Fay Ng synthesized the two single molecule control compounds. Boyuan Zhang fabricated the OFETs, and Tianren Fu performed the single molecule conductance measurements. Daniel W. Paley solved the crystal structure for **PBPB**.

4.2. Introduction

Understanding how molecular structure impacts mobility in OFETs has garnered much attention in recent years.[1–6] Small, flat aromatic molecules, such as linear acenes, have been widely used as the active layer in organic semiconductors due to their relatively high carrier mobilities in both films and single crystal devices. The high carrier mobilities are attributed to strong intermolecular interaction amongst adjacent molecules and low intramolecular reorganization energy.[7–9] While these two requirements govern charge transport for small, flat aromatic molecules, they are insufficient for complex, three dimensional molecules. In the latter, carriers can become localized, impeding transport. Examples of three dimensional molecular prototype are fullerene and its derivatives,[10] which are n-type materials used in OFETs,[11–13] OPVs,[14–16] and OPDs.[16,17] However, fullerenes are difficult to synthesize and functionalize, and their optical properties cannot be easily tuned. This prompts the search for alternatives that both absorb visible light and retain structural features, such as a three-dimensional shape.[18–22]

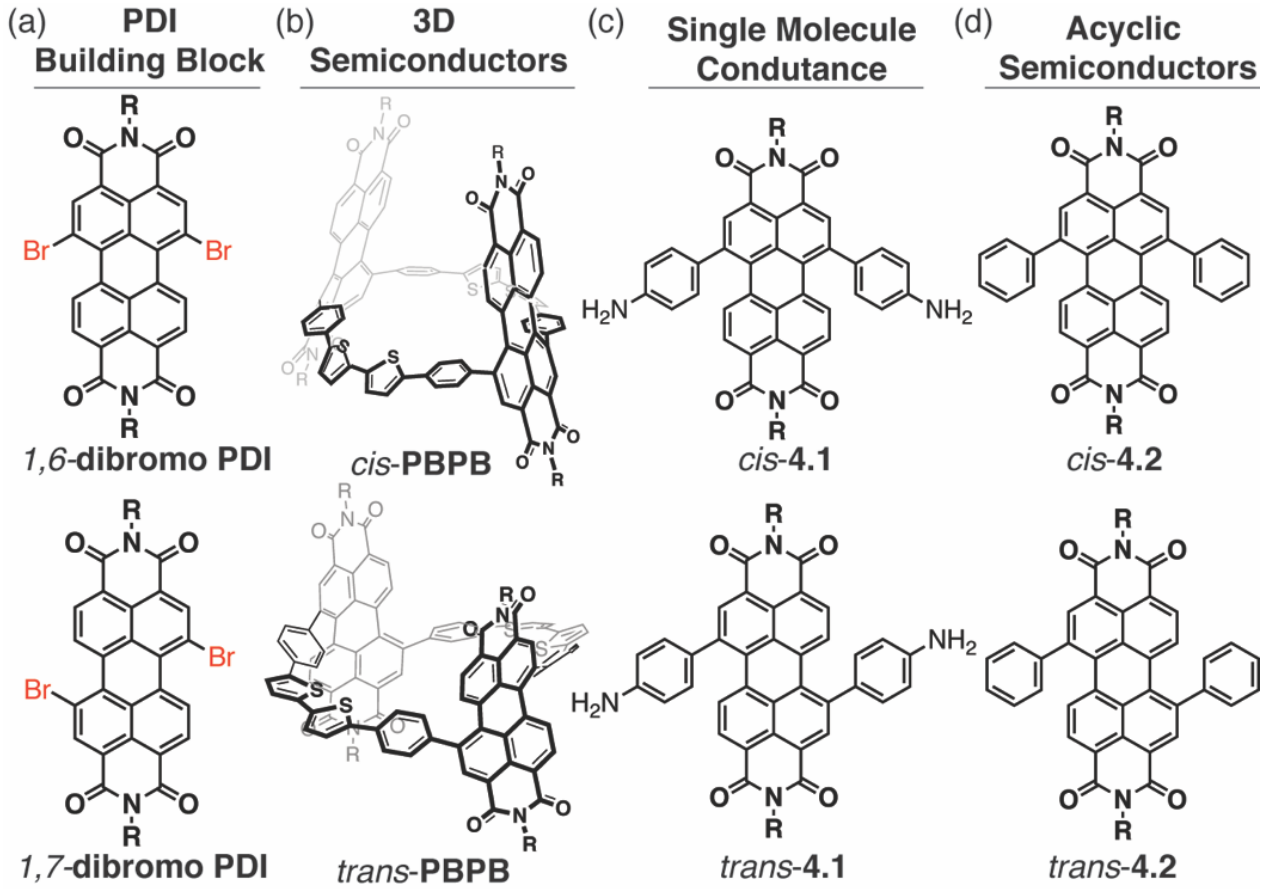

Figure 4.1. Structures of (a) *1,6* and *1,7*-dibromo PDI, with the cis/trans orientation indicated in red; (b) *cis*-**PBPB** and *trans*-**PBPB**; (c) molecules used for single molecule conductance measurements *cis*-**4.1** and *trans*-**4.1**; and (d) structures of acyclic PDI semiconductors *cis*-**4.2** and *trans*-**4.2**. *Cis*- and *trans*-based molecules are derived from *1,6*-dibromo PDI and *1,7*-dibromo PDI, respectively. R = branched $C_{11}H_{23}$ side chains.

Here, we study a sub-class of three dimensional, organic materials called conjugated macrocycles. Conjugated macrocycles possess several structural and electronic advantages over acyclic molecules: 1) their contorted structure can facilitate intermolecular contact and charge transport;[19,23] 2) they contain no end groups that can act as trap sites in linear molecules;[24–27] 3) they often absorb more visible light than linear molecules;[28,29] and 4) their intramolecular cavities can act as a host for electronic guests.[30–35] We create OFETs with three dimensional molecular solids made from macrocyclic organic semiconductors illustrated in Figure 4.1, and describe the role of intramolecular conductivity on their performance. While electronically active macrocycles

have been used in organic devices such as transistors, photovoltaics and detectors in recent years,[23,29,33,36–41] the impact of molecular structure on device performance is an ongoing field of research.[41] Our macrocycles were designed to enhance intermolecular interactions through π-π coupling while allowing for synthetic flexibility to control their electronic properties.

We utilize two types of PDI macrocycles that differ in their connectivity to the phenyl-bithiophene-phenyl linker: the PDI and linker are in a trans orientation for *trans*-**PBPB** and cis orientation for *cis*-**PBPB** (Figure 4.1b). *Trans*-**PBPB** incorporates a *1,7*-substituted PDI isomer into the synthesis while *cis*-**PBPB** comprises a *1,6*-substituted PDI isomer (Figure 4.1a). We call these macrocycles **PBPB**, where, **P** is PDI, and **B** is phenyl-bithiophene-phenyl belt. We previously reported the synthesis of *trans*-**PBPB** (Chapter 2).[42]. We measure the device performance in OFETs, and show that electrical mobilities are three times higher in the *trans*-based devices than in the *cis*-based devices. We study the materials on a single molecule level with macrocyclic components, use control experiments, computations, and spectroscopy to determine that the difference in electron mobility in OFETs made with the two macrocyclic isomers is due to the difference in intramolecular conductivity. This study demonstrates that intramolecular carrier pathways affect electron transport in three-dimensional molecular solids.

4.3. OFETs – Trans Linkage Produces Higher Current

We first investigate the impact from the *cis*- or *trans*-linkage on the electrical properties of OFETs made using *trans*- and *cis*-**PBPB** (Figure 4.2). Both *trans*-**PBPB** and *cis*-**PBPB** exhibit n-type characteristics and not p-type characteristics. To validate if the materials show any p-type characteristics, we set the source voltage at -80 V and swept the gate voltage to -80 V. From this measurement, we didn't observe any current in the negative gate region, which confirms the material doesn't show p-type characteristics. The devices show some leakage current due to the

large difference between the gate voltage when we sweep from 80 V to -20 V and the source-drain current (80 V). Figure 4.2 shows the output curves for both macrocycles, and shows both devices saturate at a source/drain voltage of 80 V.

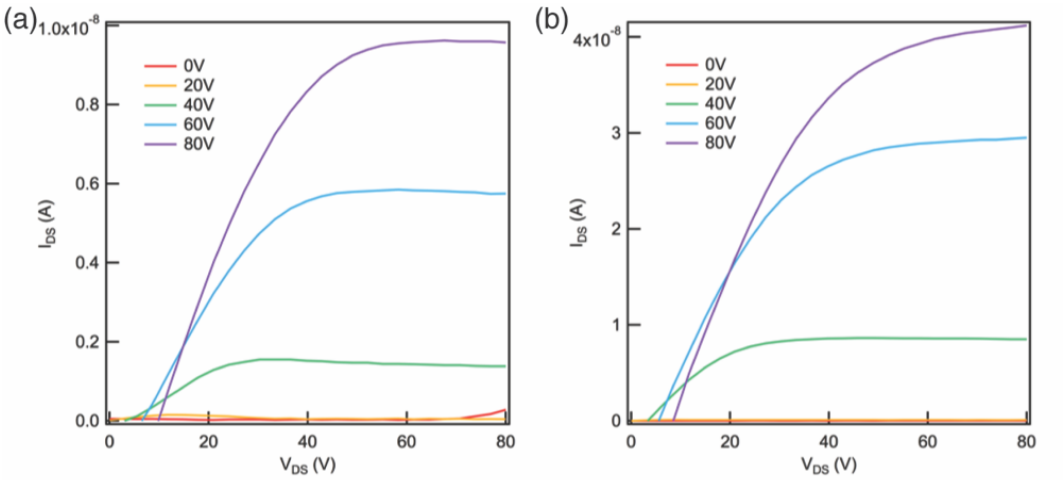

Figure 4.2. Output curves for (a) *cis*-**PBPB** and (b) *trans*-**PBPB** films from OFETs. In both devices, the source-drain voltage saturates at 80 V.

Figures 4.3a,b display the current versus applied gate voltages (transfer curves) for a trans and cis device. We collected the data for these transfer curves using a source-drain voltage of 80 V while sweeping the gate voltage from -20 V to 80 V. The mobility was calculated in the saturation regime[3,43] using $I_{DS} = (W/2L)C_i\mu(V_G-V_T)^2$, where W and L are the width and length of the channel, C_i (11.5 nFcm^{-2}), μ, V_G, and V_T correspond to the capacitance per unit area of the gate insulator, the field effect mobility, the gate voltage, and the threshold voltage, respectively. We find the mobility in *trans*-**PBPB** is three times that in *cis*-**PBPB** (1.3×10^{-3} cm^2/V•s versus 0.4×10^{-3} cm^2/V•s). We reproduce these mobility measurements across many samples. For example, we made ten devices with each isomer and found that the same values for the mobilities. Table 4.1 provides the averaged data for each macrocycle and Table 4.2 provides the OFET characteristics of both devices.

4.4. Film Morphology

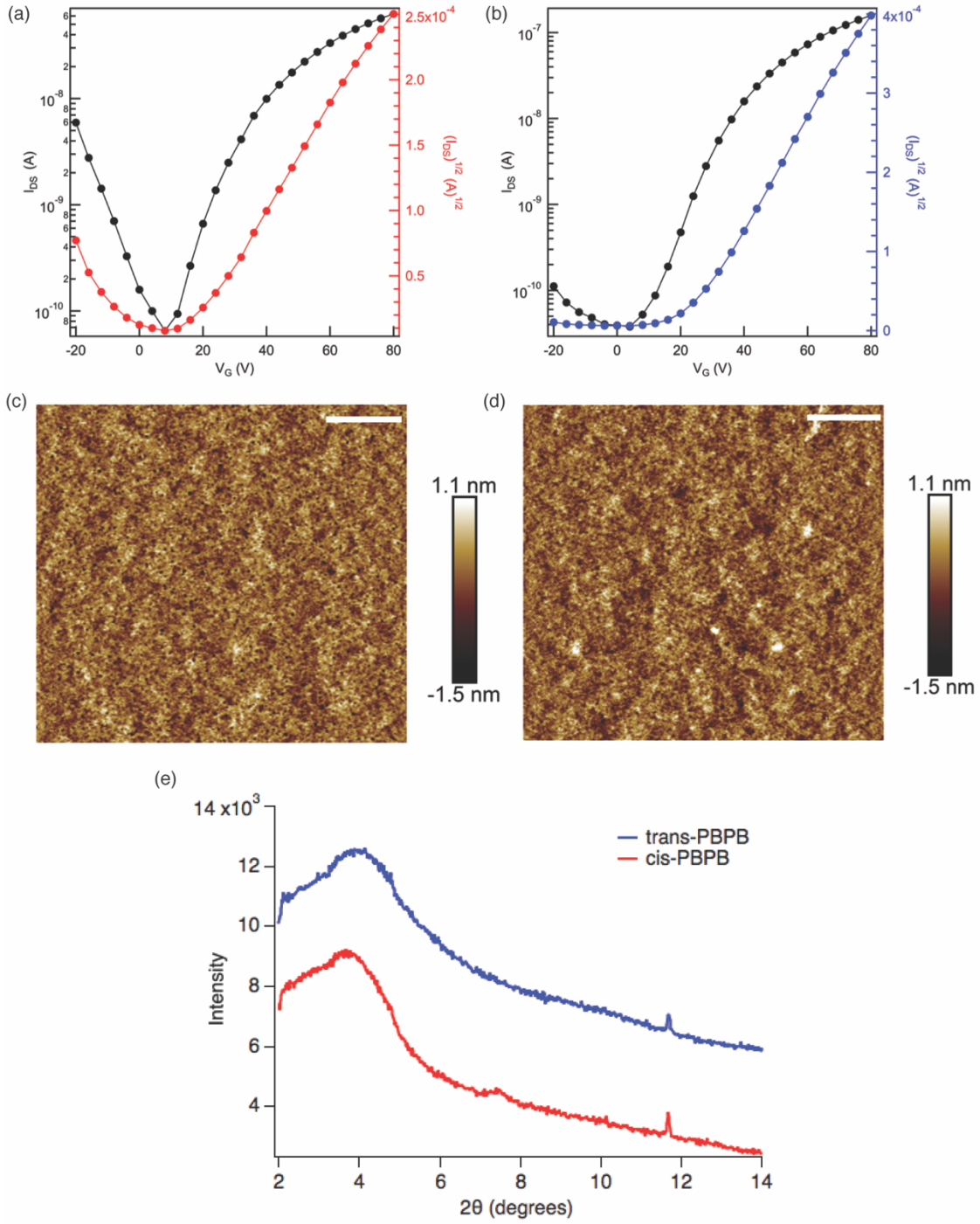

Figure 4.3. (a) Transfer curve for *cis*-**PBPB**; (b) transfer curve for *trans*-**PBPB**. Device current (left axis, black) and square root of current (right axis, red or blue) measured as a function of gate voltage at a constant source-drain voltage of 80 V. (c) Height image for *cis*-**PBPB** and (d) *trans*-**PBPB**. Both films are continuous and smooth and have a root mean square roughness of 0.35 and 0.37 nm for the *cis* and *trans*-based devices, respectively. The scale bar is 1.0 μm. (e) PXRD of both films showing no obvious signs of crystallinity. Films drop-cast from $CDCl_3$.

As morphology is known to have a profound effect on mobility, we first examined the film morphology using AFM to see if morphological differences could explain the difference in mobility.[2,5,44,45] Both films were continuous and smooth, and had a root mean square roughness of 0.35 nm and 0.37 nm for *cis*-**PBPB** and *trans*-**PBPB**, respectively (Figures 4.3c,d). The Powder/thin-film X-ray Diffraction (PXRD) of both films too show no obvious signs of crystallinity (Figure 4.3e). This suggests that morphology does not explain the different transport characteristics for the three-dimensional semiconductors.

4.5. Molecular Structures of Isomeric Macrocycles

The synthesis for *cis*-**PBPB** is based off our earlier synthesis of *trans*-**PBPB**.[42] We next considered the molecular structures of *trans*-**PBPB** and *cis*-**PBPB** using DFT calculations. Figure 4.4 contains the lowest energy structures for *cis*-**PBPB** and *trans*-**PBPB** determined from DFT using 6-31G/B3LYP level of computation. We see that the PDI units remain upright in *trans*-**PBPB** while they bow inward toward the cavity in *cis*-**PBPB**. The PDI-linker connection differs between the two isomers. The torsional angle is greater in the cis molecule relative to *trans*-**PBPB**. This causes the PDI and linker to possess a relatively more orthogonal relationship, and decreases the electronic coupling in *cis*-**PBPB** (Figures 4.4a,b). The colors of the macrocycles support *trans*-**PBPB** is more conjugated: *cis*-**PBPB** is purple by visual inspection, and *trans*-**PBPB** is black.

We next consider the packing of these macrocycles with the crystal structure of *trans*-**PBPB** (shown in Figure 4.4c and Figure 4.8 in the Appendix). We see that the macrocycles pack with the PDI face of one adjacent to that of another, though with opposite chirality.[46–48] We were unable to obtain crystal structures of *cis*-**PBPB** but anticipate a similar face-to-face packing, given the DFT-based structure presented here.

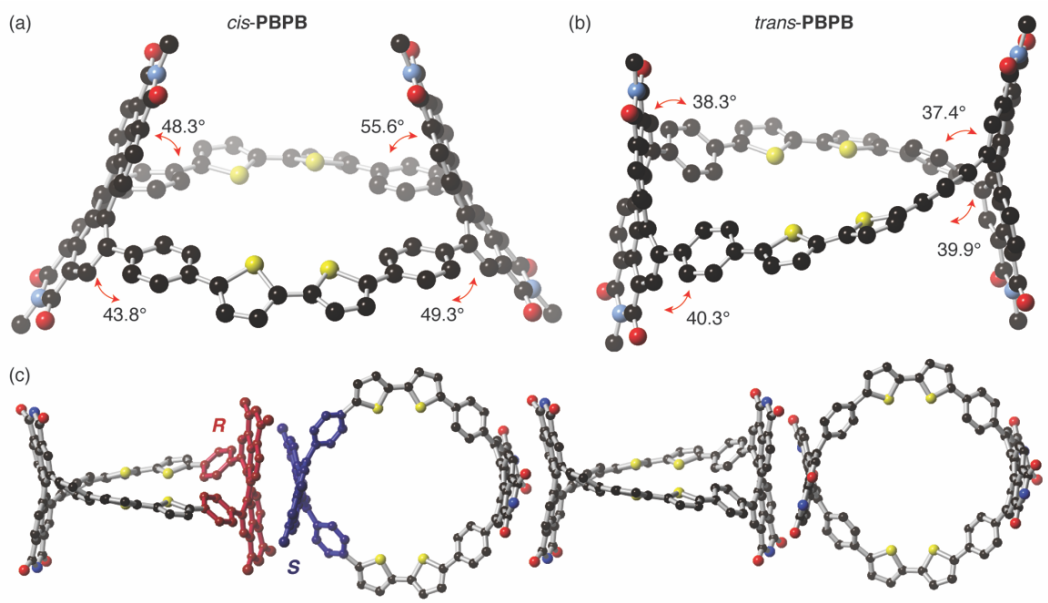

Figure 4.4. Molecular structures obtained with DFT using 6-31G/B3LYP basis set. (a) *cis*-**PBPB** and (b) *trans*-**PBPB**. (c) SCXRD solid-state packing of *trans*-**PBPB** as viewed down the *a* axis. Blue and red are the two enantiomers of the diphenyl PDI packing down the axis. Red = oxygen, blue = nitrogen, black = carbon, and yellow = sulfur. Hydrogens and side chains have been removed for clarity.

In addition, its known that molecular strain and rigidity can influence charge transport in macrocyclic semiconductor with the more strained systems having lower intermolecular coupling and hence lower intermolecular coupling and lower mobility.[41] We calculate the enthalpy difference between the macrocycle and an acyclic analog (i.e., a homodesmotic calculation[28,49–51]) to assess the strain energy in *trans*-**PBPB** and *cis*-**PBPB**. We found only a small (2 kcal/mol) difference in strain energy and therefore conclude that this does not explain the difference in mobility. Section 4.13 contains the details of the calculations used to assess the strain energy.

4.6. Cyclic Voltammetry Shows Similar Reduction Potentials

As these macrocyclic materials are n-type semiconductors, we wondered if a difference in reduction potentials would explain the difference in mobility. We used CV to estimate the LUMO energies for both *trans*- and *cis*-**PBPB** (Table 4.1, Figure 4.5). *Trans*-**PBPB** and *cis*-**PBPB** have similar reduction potentials, as estimated from the onset of the first reduction peak.[52] We also

studied the electronic structure using UV-Vis. The UV-vis spectrum suggests *trans*-**PBPB** is more conjugated: the lowest energy transition is at lower energy in *trans*-**PBPB** than in *cis*-**PBPB**. Moreover, *trans*-**PBPB** has a smaller optical gap than the *cis*-**PBPB** macrocycle (Table 4.1, Figure 4.6). This likely reflects greater orbital overlap between the linker and PDI, given the smaller torsional angle between the linker and the PDI (Figures 4.4a,b).

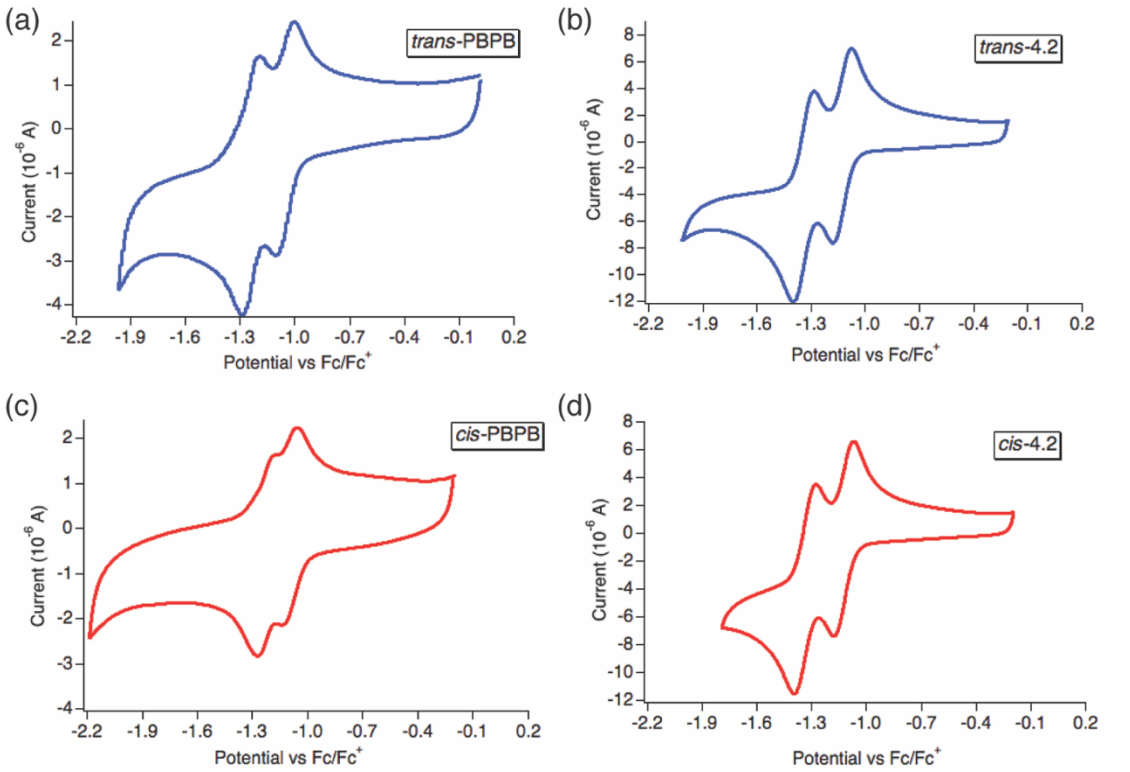

Figure 4.5. CV of (a) *trans*-**PBPB**; (b) *trans*-**4.2**; (c) *cis*-**PBPB**; and (d) *cis*-**4.2**. CVs taken in CH_2Cl_2 containing 0.1 M NBu_4PF_6 as the electrolyte.

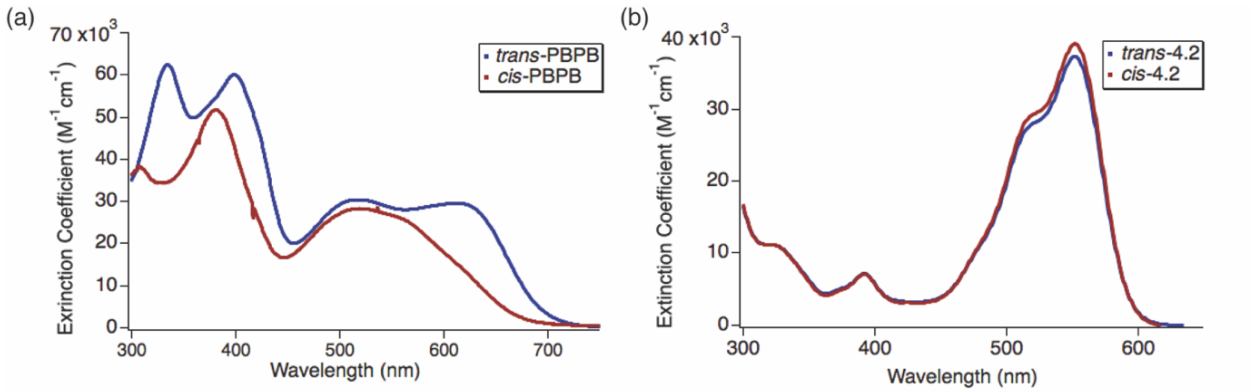

Figure 4.6. UV of (a) *trans*-**PBPB** and *cis*-**PBPB**; (b) *trans*-**4.2** and *cis*-**4.2**.

4.7. STM-BJ Studies Show Trans Conducts Better Than Cis Isomer

We next evaluate the intramolecular conductivity by deconstructing the macrocycles into *1,6*- and *1,7*-diphenyl PDI monomers that possess two aurophilic amino groups on the aryl rings. We refer to these molecules as *trans*-**4.1** and *cis*-**4.1** (Figure 4.7a). While the cis and trans PDI isomers are well known,[53–56] the difference in intramolecular conduction between the *cis* and *trans* isomers has not been reported until now. The two aurophilic amino groups on the aryl rings bind the Au electrodes in the STM-BJ setup[57–60] to form Au-**4.1**-Au- junctions (Fig. 4.7a). We found that *trans*-**4.1** has a conductance nearly one order of magnitude higher than *cis*-**4.1** at ~8.6×10^{-5} G_0 compared with ~1.0×10^{-5} G_0 (Fig. 4.7b), where $G_0 = e^2/h$ is the conductance quantum. Figure 4.8 contains the two-dimensional histograms for *cis*- and *trans*-**4.1**.

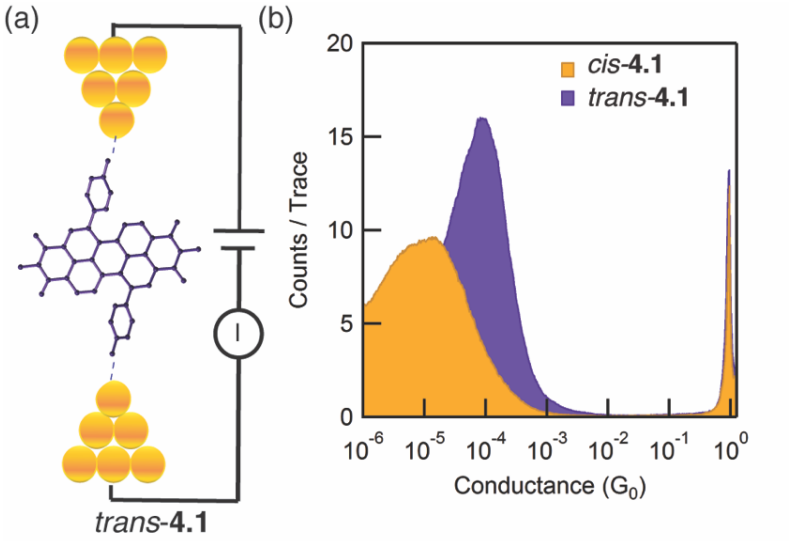

Figure 4.7. (a) Schematic of a single-molecule junction showing *trans*-**4.1** in the break junction. The diphenyl PDI contains two aurophilic amino groups on the aryl rings to bind the gold electrodes in the junction; (b) Logarithm conductance histograms for *cis*-**4.1** (yellow) and *trans*-**4.1** (purple) measured with an applied bias of 450 mV in a 1,2,4-trichlorobenzene solution.

Because the STM-BJ studies determined that *trans*-substituted PDI molecular junctions are better conductors than *cis*-substituted PDI junctions, we hypothesized that the difference in the mobilities seen for *trans*- and *cis*-**PBPB** based OFETs is due to the trans/cis substitution patterns. The experiments described next find that the substitution patterns in the acyclic subunits do not

explain the differences in mobility between the two three dimensional macrocyclic semiconductors.

4.8. Acyclic Controls Possess Analogous Electron Mobility in OFETs

We synthesized the acyclic relatives of *trans*- and *cis*-**PBPB**, *cis*- and *trans*-**4.2**, which comprise a diphenyl PDI substituted in a cis and trans orientation (Figure 4.1d). *Trans*-**4.2** was called **1.1** in the preceding chapters, but renamed here for ease of comparison to the cis-version. We made OFETs using *cis*- and *trans*-**4.2**, and find that the two have similar averaged electron mobilities: 1.9×10^{-4} $cm^2/V•s$ and 1.5×10^{-4} $cm^2/V•s$ for *cis*-**4.2** and *trans*-**4.2**, respectively (see Table 4.1, Table 4.1 and Figure 4.9 for details). We also studied the film morphology using AFM, and both films were smooth, with a root mean square roughness of 0.43 and 0.45 nm for *cis*- and *trans*-**4.2**, respectively (Figure 4.9). Since *cis*-**4.2** and *trans*-**4.2** show similar mobilities in OFETs, the cis and trans substitution pattern alone is not the reason for the difference in the performance found in the macrocyclic systems.

Table 4.1. Comparison of *trans*-**PBPB** and *cis*-**PBPB** Electronic Data

	Mobility μ ($cm^2V^{-1}s^{-1}$)	LUMO level[a] (eV)	Optical gap[b] (eV)
trans-**PBPB**	$(1.2 \pm 0.1) \times 10^{-3}$	-3.82	1.78
cis-**PBPB**	$(0.4 \pm 0.1) \times 10^{-3}$	-3.79	1.85
trans-**4.2**	$(1.5 \pm 0.3) \times 10^{-4}$	-3.74	2.10
cis-**4.2**	$(1.9 \pm 0.3) \times 10^{-4}$	-3.74	2.10

Table 4.1: CV, optical gap and FET performance for the two macrocycles and acyclic controls. [a]LUMO levels were estimated from onset of the first reduction peaks. [b]Optical band gaps were estimated from the onset of absorption.

Both *trans*-**PBPB** and *trans*-**4.2** possess a trans linkage, suggesting higher intramolecular conductivity than the cis analogues from the STM-BJ measurements. Yet OFET devices from

either *trans*- or *cis*-**4.2** show similar electron mobilities, while electron mobilities from *trans*-**PBPB** or *cis*-**PBPB** macrocycles show marked differences in their mobilities.

From this data, we conclude that the substitution pattern in the subunits is not responsible for the difference in charge transport in the acyclic controls, but influences charge transport for the relatively complex three dimensional semiconducting macrocycles. *Trans*-**PBPB** is more conjugated than *cis*-**PBPB**, as reflected in the UV-vis and electrochemistry data, suggesting that the intramolecular conductivity is higher in the *trans*-based macrocycle. Together, the acyclic control data, STM-BJ measurements, and spectroscopy support that intramolecular carrier pathways govern charge transport as the complexity of the molecule increases in molecular solids. We also found that film morphology and molecular strain are not the source of the difference in mobility for the macrocycles. This study reveals the importance of not just intermolecular interactions and reorganization energy as conditions for electrical conduction in OFETs but also shows the importance of intramolecular conduction.

4.9. Appendix – Supplementary Figures

Table 4.2. OFET Characteristics for Semiconductors

	cis-**PBPB**	*trans*-**PBPB**	*cis*-**4.2**	*trans*-**4.2**
Mobility	0.4×10^{-3} ($0.4 \pm 0.1 \times 10^{-3}$)	1.3×10^{-3} ($1.2 \pm 0.1 \times 10^{-3}$)	2.1×10^{-4} ($1.9 \pm 0.3 \times 10^{-4}$)	1.8×10^{-4} ($1.5 \pm 0.3 \times 10^{-4}$)

Table 4.2: Parentheses indicates average mobility and error. Mobility is in units of $cm^2V^{-1}s^{-1}$.

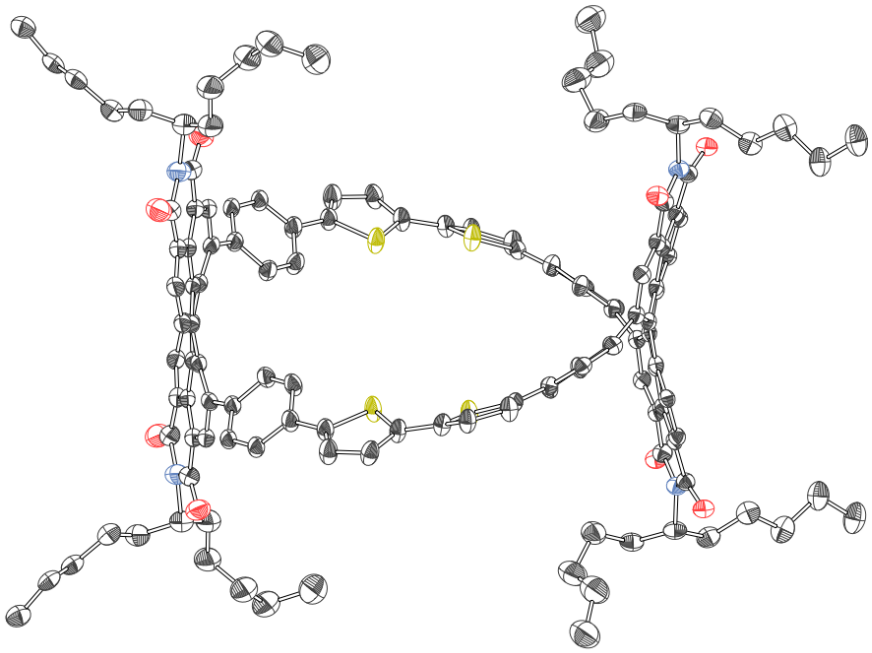

Figure 4.8. Molecular structure of *trans*-**PBPB**. One of the two independent molecules is shown. Thermal ellipsoids are rendered at the 20% probability level. Black, carbon; red, oxygen; blue, nitrogen; yellow, sulfur. Hydrogen atoms and the minor positions of disordered atoms are omitted. Crystallographic data is provided in Chapter 2.

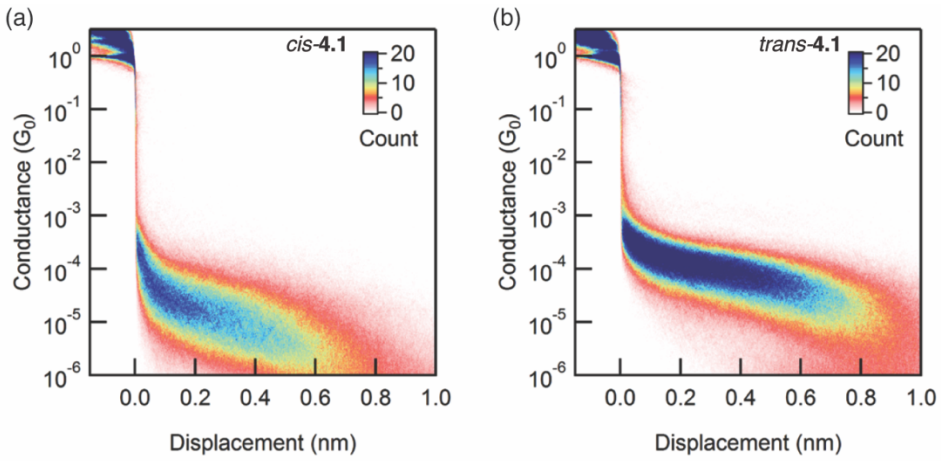

Figure 4.9. The two-dimensional conductance-displacement histograms of (a) *cis*-**4.1** and (b) *trans*-**4.1**.

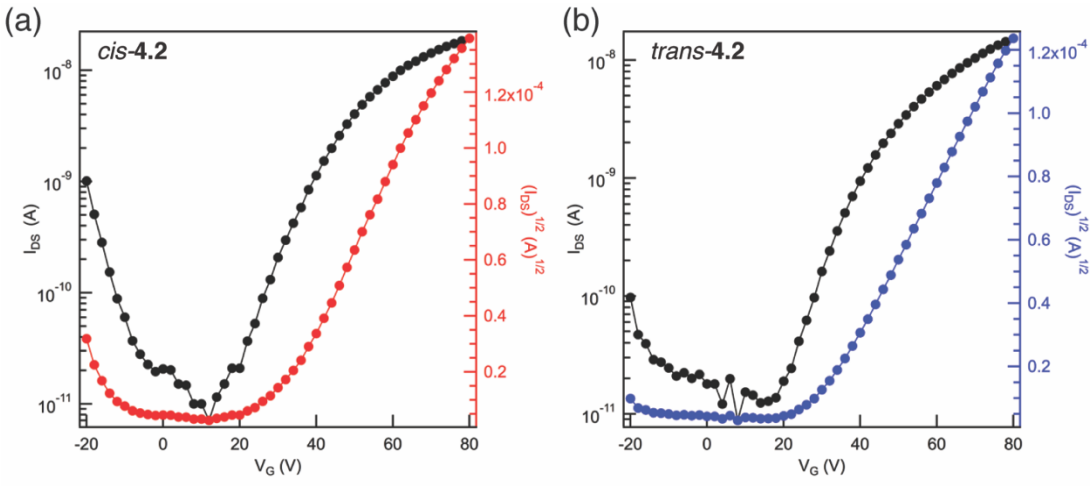

Figure 4.10. Transfer characteristics for (a) *cis*-**4.2** and (b) *trans*-**4.2**. The mobilities are similar: 2.1×10^{-4} $cm^2V^{-1}s^{-1}$ and 1.8×10^{-4} $cm^2V^{-1}s^{-1}$ for *cis*-**4.2** and *trans*-**4.2**, respectively.

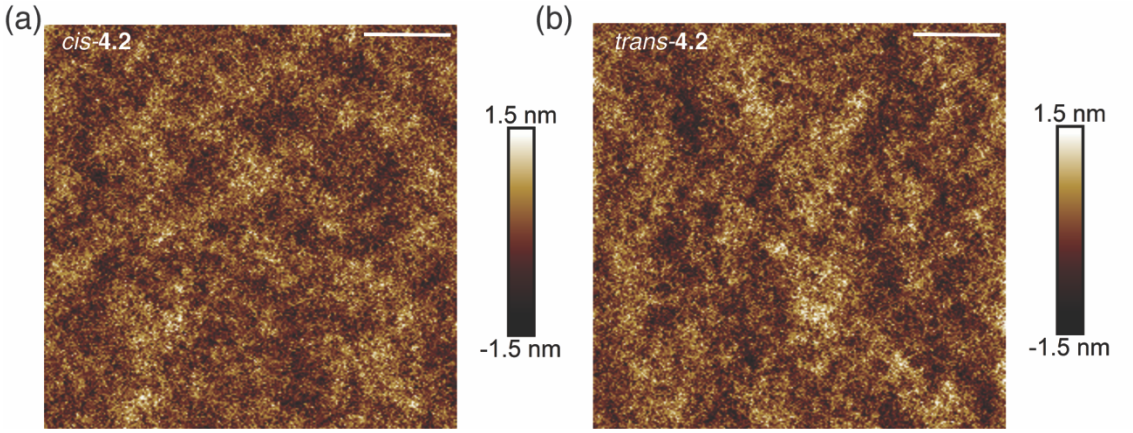

Figure 4.11. AFM micrograph height image for *cis*-**4.2** and (b) *trans*-**4.2**. Both films are continuous and smooth and have a root mean square roughness of 0.43 and 0.45 nm for the *cis* and *trans*-based films, respectively. The scale bar is 1.0 μm.

4.10. General Experimental Information

Synthesis. All reactions were performed in oven-dried or flame-dried round bottom flasks, unless otherwise noted. The flasks were fitted with rubber septa and reactions were conducted under a positive pressure of nitrogen or argon, unless otherwise noted. Anhydrous and anaerobic solvents were obtained from a Glass Contour solvent system consisting of a Schlenk manifold with purification columns packed with activated alumina and supported copper catalyst. Reaction monitoring by TLC was performed on J.T. Baker Baker-flex Silica Gel IB2-F (25 mm x 75 mm)

TLC plates. TLC visualization was accomplished by visible observation and irradiation with a UV lamp. Commercial reagents were used without further purification. $Pt(COD)Cl_2$ was purchased from Strem Chemicals, and all other reagents were purchased from Sigma-Aldrich.

Purification. Automated flash chromatography was performed using a Teledyne Isco Combiflash Rf200 and Redisep Rf Silica columns. Preparative HPLC was performed on a Waters Prep150 instrument equipped with a UV-vis detector, an automated fraction collector, and a Nacalai Tesque COSMOSIL Buckyprep column (20 mm I.D. x 250 mm, 5 μm).

Spectrometers. ^{1}H NMR spectra were recorded on a Bruker 400 or 500 MHz spectrometer. ^{13}C NMR spectra were recorded on a Bruker 125 or 100 MHz spectrometer with complete proton decoupling. NMR spectra were recorded at 300 K unless otherwise noted. Chemical shifts are reported in parts per million (ppm) Data are represented as follows: chemical shift, multiplicity (s = singlet, d = doublet, dd= doublet of doublets, t = triplet, m = multiplet), coupling constants in Hz, and integration. Broadening (br) of peaks in the 1H NMR spectrum is due to rotational isomers about the imide side chains. Multiple peaks for the same carbon in the ^{13}C NMR spectrum arise due to rotational isomers about the imide side chains that have been seen previously.[42,61] *Trans*-**4.2** was previously published and it represented as compound **1.1** in Chapters 1 and 3.[29] HRMS was performed on a (1) Waters XEVO G2-XS QTOF instrument equipped with a UPC SFC inlet, and ESI and APCI ionization sources; or (2) a Bruker UltrafleXtreme MALDI TOF/TOF instrument using a dithranol matrix. UV-vis absorption spectra were recorded on a Shimadzu UV-1800 spectrophotometer using a 1.0 cm quartz cell. IR spectra were recorded on a Perkin Elmer Spectrum400 FTIR spectrometer using a PIKE ATR attachment.

Atomic force microscopy. AFM measurements were carried out in tapping mode on a Bruker Multi-Mode AFM at ambient conditions. A commercial silicon cantilever (RTESPA, MPP-

11120-10, Bruker) was used in this study with a typical radius of curvature of ~8nm and a nominal spring constant of ~40 Nm^{-1}.

Cyclic Voltammetry. CVs were recorded on a CH166 electrochemical workstation using an Ag/AgCl electrode as the reference electrode at room temperature. Experiments were performed in CH_2Cl_2 with NBu_4PF_6 as the supporting electrolyte at a scan rate of 0.1 V/s.[52]

Thin film transistors. To create the devices, we first silanize the substrate (300 nm of SiO_2 on a Si wafer) with OTS. Au is deposited onto the substrate as bottom-contact source and drain electrodes (40 nm) with a width of 105 μm and length of 20 μm. Next, we spin-cast organic films onto the surface at 1,000 r.p.m. for 1 min, to form transistors using the silicon wafer as the global back gate for the device. Finally, the samples were annealed under inert atmosphere at 160℃ for 10 minutes to optimize device. The thin film transistors were tested on the Agilent 4155C semiconductor parameter analyzer.

STM-Break Junction Measurements. We measure the single-molecule conductance using the STM-BJ technique with a custom-built setup described previously.[58] Briefly, we drive a Au tip in and out of contact with an Au-on-mica substrate and record the conductance (current/voltage) of the junction as the tip is withdrawn. Upon rupture of the Au contact, a molecule may bridge the gap as evidenced by an additional plateau in the conductance versus displacement trace. We collect 10,000 such traces, which contain 2000 data points per nanometer of extension (40 kHz sampling rate) and construct the 1D and 2D conductance histograms without data selection from these data. The conductance histogram is binned logarithmically, with 100 bins per decade along the conductance axis. For two-dimensional histograms, traces are aligned along the displacement axis at the point when the conductance crosses 0.5 G_0 and then overlaid in 2D (see Figure 4.9). The histograms are normalized by the number of traces used to construct them. The

PDIs studied here were introduced into the setup in a 1,2,4-trichlorobenzene solution with 0.1~1 mM concentration.

4.11. Synthetic Procedures & Characterization

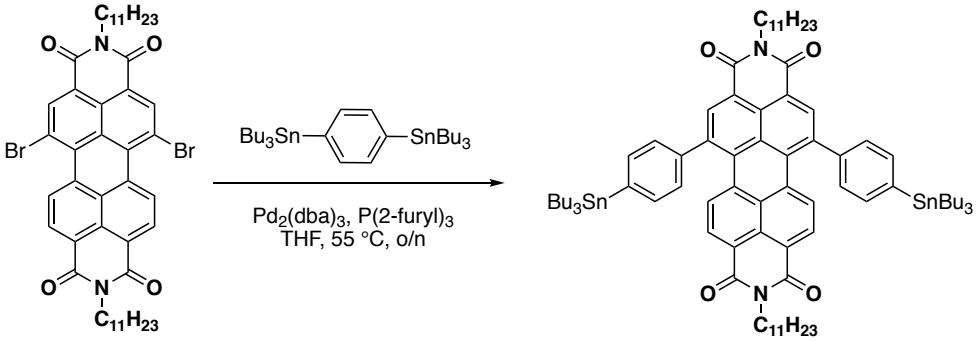

1,6-**PDI**
cis-**PDI**

SI-4.1

Synthesis of 1,6-Bis[4-(tributylstannyl)-phenyl]-PDI (**SI-4.1**). Pure 1,6-dibromo PDI (1.00 equiv, 0.199 mMol, 0.171 g), 1,4-bis(tributylstannyl)benzene (4.00 equiv, 0.799 mMol, 0.524 g), THF (9.95 mL), and tri(2-furyl)phosphine (0.400 equiv, 0.0796 mMol, 0.0180 g) were added to an oven-dried 25.0 mL round bottom flask under nitrogen and equipped with a stir bar. Solution was sparged with N_2 for 30 minutes. Tris(dibenzylidenacetone)dipalladium (0.100 equiv, 0.018 mMol, 0.0199 g) was added to the solution which was then degassed for an additional 30 minutes. Mixture was then placed in a 55ºC oil bath overnight. The crude mixture was concentrated and purified by column chromatography (40 g Redisep Rf Silica) with a gradient of 0% to 80% CH_2Cl_2/Hexanes flow to yield the 1,6-isomer as a magenta pink solid (0.083 mMol, 0.071 g). By-products were resubmitted to the same conditions described above to yield 0.119 g for a combined total yield of 42%. **^{1}H NMR** (400 MHz, 300K, $CDCl_3$) δ 8.59 (br s, 2H), 8.09 (br d, 2H), 7.84 (d, J = 8.1 Hz, 2H), 7.57* (d, J = 7.7 Hz, 4H), 7.39 (d, J = 7.9 Hz, 4H), 5.20 (br m, 1H), 5.11 (br m, 1H), 2.25 (br m, 2H), 2.16 (br m, 2H), 1.82 (br m, 4H), 1.61* (m, 12H), 1.40 (m, 12H), 1.26 (br m, 24H), 1.14* (m, 12H), 0.94 (t, 18H), 0.83 (br t, 12H). **^{13}C NMR** (100 MHz, 300K, $CDCl_3$) δ 164.78 (br), 163.73

(br), 142.83, 142.22, 142.18, 142.13, 138.05*, 135.97, 135.32, 134.34, 132.70, 130.00, 129.70, 129.50, 129.25, 128.70, 128.47, 128.06*, 127.25, 122.87, 122.03, 121.84, 54.68, 54.55, 32.34, 31.78, 31.76, 31.59, 29.13*, 27.35*, 26.65, 26.56, 22.65, 22.57, 22.54, 14.11, 14.04, 13.72, 13.75, 9.74*. **IR** (cm^{-1}) 2954, 2928, 2870, 2856, 1697, 1658, 1589, 1587, 1465, 1459, 1421, 1414, 1344, 1325, 1262, 1250, 813. **HRMS** (APCI+) calculated m/z for $[C_{82}H_{114}N_2O_4Sn_2+H]^+$ is 1431.6924, found 1431.6901. * Tin satellite peaks.

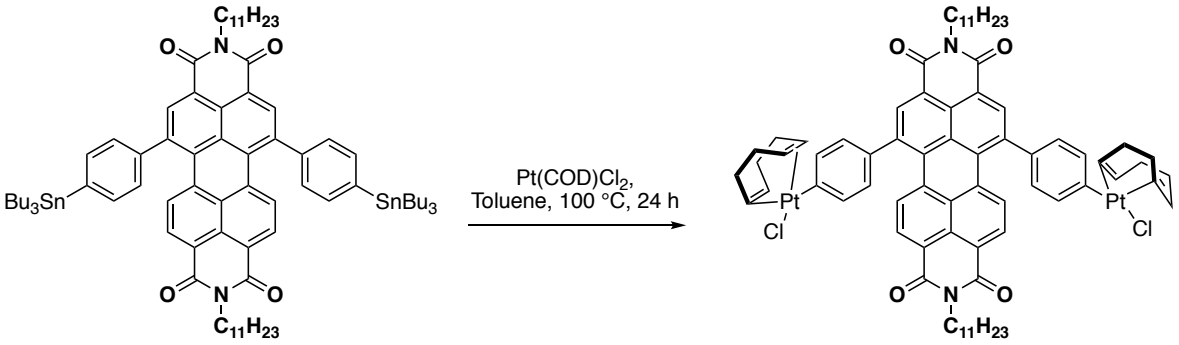

SI-4.1 **SI-4.2**

Synthesis of 1,6-Bis[4-(Pt(COD)Cl)-phenyl]-PDI (**SI-4.2**): 1,6-Bis[4-(tributylstannyl)-phenyl]-PDI (**SI-4.1**) (0.206 mMol, 0.295 g, 1 eq), Dichloro(1,5-cyclooctadiene)platinum(II) (0.433 mmol, 0.162 g, 2.1 eq) and toluene (21 mL) were added to an oven-dried two-neck, 50-mL round bottom flask equipped with a stir bar. The mixture was degassed for 30 minutes then placed in a 100 ºC oil bath and allowed to stir for 24 hours. The crude mixture was then concentrated and purified by column chromatography (24 g Redisep RF Silica) using a gradient from 0% to 80% CH_2Cl_2/hexanes at 60 mL/min. Product was collected and concentrated as a purple solid (0.123 g, 0.0771 mMol, 38% yield). **^{1}H NMR** (500 MHz, 300K, $CDCl_3$) δ 8.56 (br s, 1H), 8.54 (br s,1H), 8.09 (br d, 1H), 8.06 (br d, 1H), 7.85 (d, J = 8.2 Hz, 2H), 7.36 (d, J = 7.8 Hz, 4H), 7.16 (d, J = 8.2 Hz, 4H), 5.88 (s, 4H), 5.17 (br m, 1H), 5.11 (br m, 1H), 4.71 (s, 4H), 2.74 (br m, 4H), 2.60 (br m, 4H), 2.44 (br m, 8H), 2.24 (br m, 2H), 2.15 (br m, 2H), 1.82 (br m, 4H), 1.25 (br m, 24H), 0.85 (br t, 12H). **^{13}C NMR** (100 MHz, 300K, $CDCl_3$) δ 164.80, 163.84, 145.29, 142.26, 138.67, 135.92**,

135.58, 135.21**, 134.65, 129.99**, 129.51, 129.45, 129.25**, 128.75, 128.50, 128.39, 126.98, 122.80**, 122.29**, 121.94**, 121.43**, 115.91, 87.78, 54.58, 54.48, 32.41, 32.32, 32.28, 31.81, 31.76, 28.01, 26.68, 26.55, 22.57, 14.09, 14.05. **IR** (cm^{-1}) 2958, 2925, 2857, 1695, 1656, 1583, 1410, 1325, 1275, 1262, 763, 749. **HRMS** (ESI+) calculated m/z for $[C_{74}H_{84}Cl_2N_2O_4Pt_2+Na]^+$ is 1546.4923, found 1546.4922.

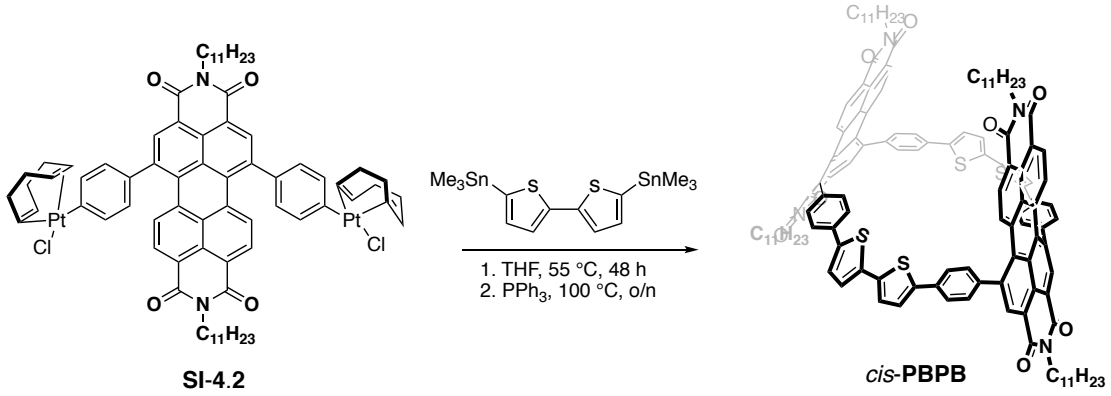

SI-4.2 *cis*-**PBPB**

Synthesis of cis-**PBPB**: Compound **SI-4.2** (0.105 mMol, 0.160 g), commercially available 5,5'-(bistrimethylstannyl)-2,2'-bithiophene (0.105 mMol, 0.0516 g), and THF were added to a 250 mL oven dried round bottom flask equipped with a stir bar. The mixture was sparged with nitrogen for 30 min then added to an oil bath at 55 ºC and allowed to stir for 48 h. Crude mixture was then removed from oil bath and concentrated. Triphenylphosphine (2.10 mMol, 0.613 g) and toluene (40.0 mL) were added to the flask. Mixture was sparged with nitrogen for 15 min then placed in a 100 ºC oil bath and allowed to stir overnight. The crude mixture was first washed with hexanes, followed by methanol and then purified by column chromatography (24 g Redisep Rf Silica) using a gradient from 0% to 85% CH_2Cl_2/hexanes at 35 mL/min. The polar fractions were further purified with prepatory TLC. Product was a dark purple solid (0.009 g, 8.5%). **^{1}H NMR** (400 MHz, 360 K, $C_2D_2Cl_4$) δ 8.75 (s, 4H), 8.18 (d, J = 8.3 Hz, 4H), 7.81 (d, J = 8.2 Hz, 8H), 7.57 (d, J = 8.2 Hz, 8H), 7.47 (d, J = 8.2 Hz, 4H), 7.41 (d, J = 3.7 Hz, 4H), 7.28 (d, J = 3.7 Hz, 4H), 5.23 (br m, 2H), 5.05 (br m, 2H), 2.30 (br m, 4H), 2.09 (br m, 4H), 1.95 (br m, 4H), 1.36 (br m, 28H)*,

1.05 (br m, 8H), 0.90 (br m, 28H), 0.58 (br m, 12H). **^{13}C NMR** (100 MHz, 328 K, $CDCl_3$) δ 166.17, 165.49, 165.07, 164.43, 144.44, 142.15, 141.98, 140.08, 136.12, 134.71, 134.16, 132.63, 131.73, 131.44, 130.73, 130.03, 129.62, 129.45, 128.57, 124.85, 124.44, 124.21, 123.96, 123.27, 56.23, 55.16, 33.74, 33.56, 33.10, 32.56, 31.05, 27.97, 27.58, 23.90, 23.49, 15.46, 15.15. **IR** (cm^{-1}) 2972, 2954, 2926, 2855, 1695, 1655, 1586, 1426, 1405, 1322, 1260, 1250, 1103, 1126, 811, 794, 751. **HRMS** (ESI+) calculated m/z for $[C_{132}H_{128}N_4O_8S_4+H]^+$ is 2025.8693, found 2025.8676. *There is a peak underneath that corresponds to four protons that are one of the methylenes of the side chains.

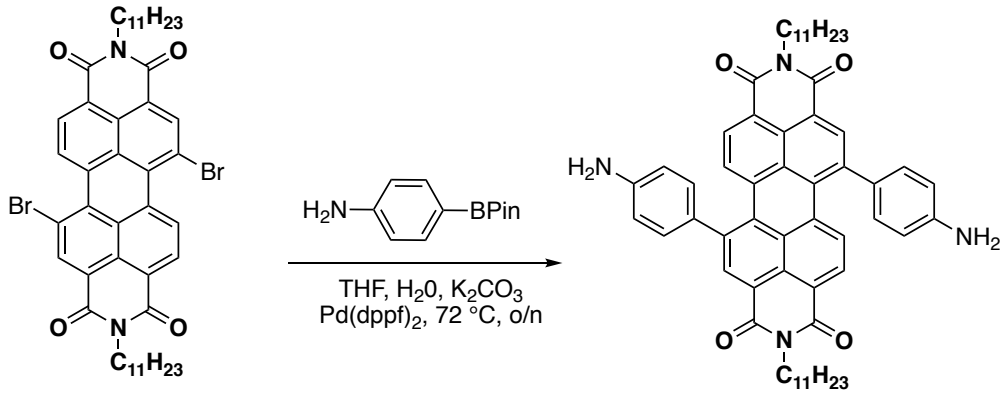

1,7-**PDI**
trans-**PDI**

trans-**4.1**

A solution of 1,7-dibromo PDI (100 mg, 0.117 mmol, 1.00 equiv) and 4-aminophenylboronic acid pinacol ester (150 mg, 0.685 mmol, 5.85 equiv) in THF (6 mL) was degassed under nitrogen for 30 mins. In a separate reaction vial, an aqueous solution of potassium phosphate (500 mg, 2.355 mmol, 20.13 equiv) in 2 mL water was degassed under nitrogen for 30 mins, and syringed into the degassing orange THF solution. The resultant reaction mixture was degassed for another 15 mins followed by addition of solid [1,1'-bis(diphenylphosphino)ferrocene]dichloropalladium (II) (10 mg, 0.012 mmol, 10 mol%). The orange solution was degassed for an additional 15 mins. It was placed in oil bath set at 72 °C under refluxing conditions for overnight. The blue solution was concentrated under reduced pressure to remove THF. The blue solution was diluted with brine (30

mL) and extracted with CH_2Cl_2 (50 mL) twice. The combined organic layer was dried ($MgSO_4$), filtered and concentrated under reduced pressure to a blue powdery residue. The solid was washed with methanol, and the residual solid was purified by silica gel chromatography (24 g Redisep Rf Silica) using a gradient from 100% CH_2Cl_2 to 5% ethyl acetate/CH_2Cl_2 to yield *trans*-**4.1** as dark blue solid (92 mg, 0.104 mmol, 89% yield). **^{1}H NMR** (500 MHz, $C_2D_2Cl_4$, 350K): δ 8.61 (s, 2H), 8.16 (d, J=8.2 Hz, 2H), 8.04 (d, J=8.2 Hz, 2H), 7.40 (d, J=8.5 Hz, 4H), 6.82 (d, J=8.5 Hz, 4H), 5.19-5.13 (m, 2H), 3.92 (br s, 4H), 2.27-2.20 (m, 4H), 1.94-1.88 (m, 4H), 1.40-1.31 (m, 24H), 0.90 (t, J=6.8 Hz, 12H). **^{13}C NMR** (100 MHz, $CDCl_3$, 323K): δ 163.92, 147.03, 141.21, 135.44, 132.29, 132.16, 130.33, 129.60, 129.42, 127.74, 122.34, 116.42, 54.59, 32.43, 31.75, 26.60, 22.50, 13.94. **IR** (ATR-ZnSe) [cm $^{-1}$] 3371, 2925, 2857, 1688, 1648, 1622, 1607, 1582, 1519, 1406, 1324, 1265, 1240, 1180. **HRMS** (ESI+) calculated m/z for $[C_{58}H_{64}N_4O_4+H]^+$ 881.5006; found 881.5009.

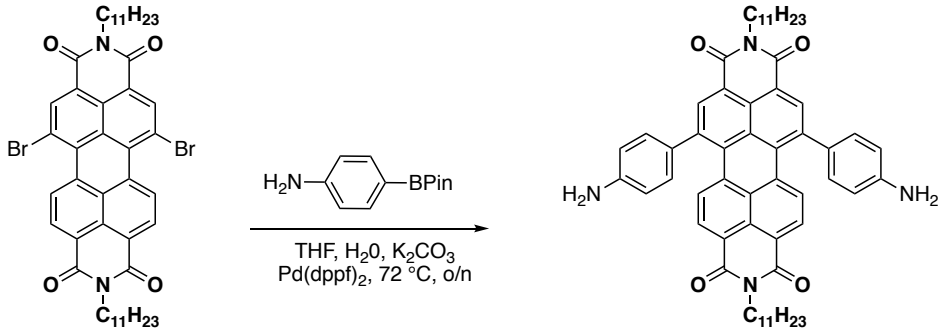

1,6-**PDI**
cis-**PDI**

cis-**4.1**

A solution of 1,6-dibromoPDI (90 mg, 0.105 mmol, 1.00 equiv) and 4-aminophenylboronic acid pinacol ester (90 mg, 0.411 mmol, 3.91 equiv) in THF (8 mL) was degassed under nitrogen for 30 mins. In a separate reaction vial, an aqueous solution of potassium phosphate (250 mg, 1.178 mmol, 11.22 equiv) in 2 mL water was degassed under nitrogen for 30 mins, and syringed into the orange THF solution. The resultant reaction mixture was degassed for another 15 mins followed by addition of solid [1,1'-bis(diphenylphosphino)ferrocene]dichloropalladium (II) (10 mg, 0.012

mmol, 11 mol%). The orange solution was degassed for another 15 mins. It was placed in oil bath set at 72 °C under refluxing conditions for overnight. The blue solution was concentrated under reduced pressure to remove THF. The blue solution was diluted with brine (30 mL) and extracted with CH_2Cl_2 (50 mL) twice. The combined organic layer was dried ($MgSO_4$), filtered and concentrated under reduced pressure to a blue powdery residue. The solid was washed with methanol, and the residual solid was purified by silica gel chromatography (24 g Redisep Rf Silica) using a gradient from 100% CH_2Cl_2 to 5% ethyl acetate/CH_2Cl_2 to yield *cis*-**4.1** as dark blue solid (77 mg, 0.087 mmol, 83% yield). **^{1}H NMR** (500 MHz, $C_2D_2Cl_4$, 350K): δ 8.56 (s, 2H), 8.17 (d, J=8.2 Hz, 2H), 8.00 (d, J=8.2 Hz, 2H), 7.26 (d, J=8.4 Hz, 4H), 6.80 (d, J=8.4 Hz, 4H), 5.20-5.11 (m, 2H), 3.90 (br s, 4H), 2.28-2.16 (m, 4H), 1.93-1.89 (m, 4H), 1.36-1.32 (m, 24H), 0.91-0.88 (m, 12H). **^{13}C NMR** (100 MHz, $CDCl_3$, 323K): δ 164.90, 164.80, 163.75, 146.79, 142.35, 135.59, 134.85, 132.27, 129.97, 129.57, 128.96, 128.85, 128.42, 126.66, 122.63, 121.97, 121.20, 116.29, 54.53, 54.42, 32.29, 31.73, 31.69, 26.58, 26.50, 22.51, 22.49, 14.01, 13.99. **IR** (ATR-ZnSe) [cm $^{-1}$] 3360, 2953, 2924, 2856, 1691, 1642, 1604, 1583, 1504, 1436, 1325, 1247, 1181. **HRMS** (ESI+) calculated m/z for $[C_{58}H_{64}N_4O_4+H]^+$ 881.5006; found 881.4988.

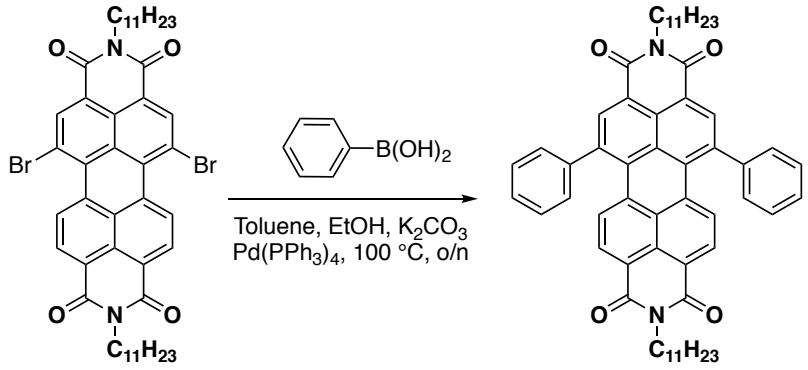

1,6-**PDI**
cis-**PDI**

cis-**4.2**

Synthesis of *cis*-**4.2**: *N,N'*-Di(6-undecyl)-1,6-dibromoperylene-3,4:9,10-tetracarboxylic diimide (0.0500 g, 0.0584 mmol, 1.00 equiv), phenyl boronic acid (0.0290 g, 0.234 mmol, 4.00 equiv),

aqueous K_2CO_3 (2 M, 1.00 mL), EtOH (0.200 mL) and toluene (3.00 mL) were added to a 20 ml scintillation vial equipped with a stir bar. The mixture was sparged with N_2 for thirty minutes. While under N_2, a spatula tip of tetrakis(triphenylphosphine)palladium(0) was added. The mixture was further sparged for ten minutes before placed in a 100 °C oil bath under N_2 for overnight. The crude mixture was extracted with ethyl acetate and brine, concentrated, and purified by column chromatography (24 g Redisep Rf Silica) using a gradient from 0% to 100% CH_2Cl_2/hexanes to yield *cis*-**4.2** (0.0480 g, 0.0565 mmol, 97%). **^{1}H NMR** (400 MHz, CDCl3, 300K): δ 8.61 (br s, 2H), 8.12 (br s, 2H), 7.83 (d, 2H), 7.59 – 7.55 (m, 4H), 7.54 – 7.47 (br d, 6H), 5.15 (br, 2H), 2.20 (m, 4H), 1.83 (m, 4H), 1.34 (m, 24H), 0.81 (t, 12H). **^{13}C NMR** (100 MHz,$CDCl_3$) δ 164.70, 163.60, 142.26, 141.10, 135.82, 135.19, 134.84, 132.50, 130.24, 130.17, 129.92, 129.25, 129.05, 128.61, 127.92, 122.86, 122.52, 122.16, 122.81, 54.65, 32.33, 31.76, 26.59, 22.56, 14.04. **IR** (cm^{-1}) 2953, 2928, 2868, 2861, 2856, 1697, 1659, 1598, 1589, 1408, 1326, 1240, 814. **HRMS** (ESI+) calculated m/z for $[C_{58}H_{62}N_2O_4+H]^+$ 851.4788, found 851.4780.

4.12. NMR Spectra of Compounds

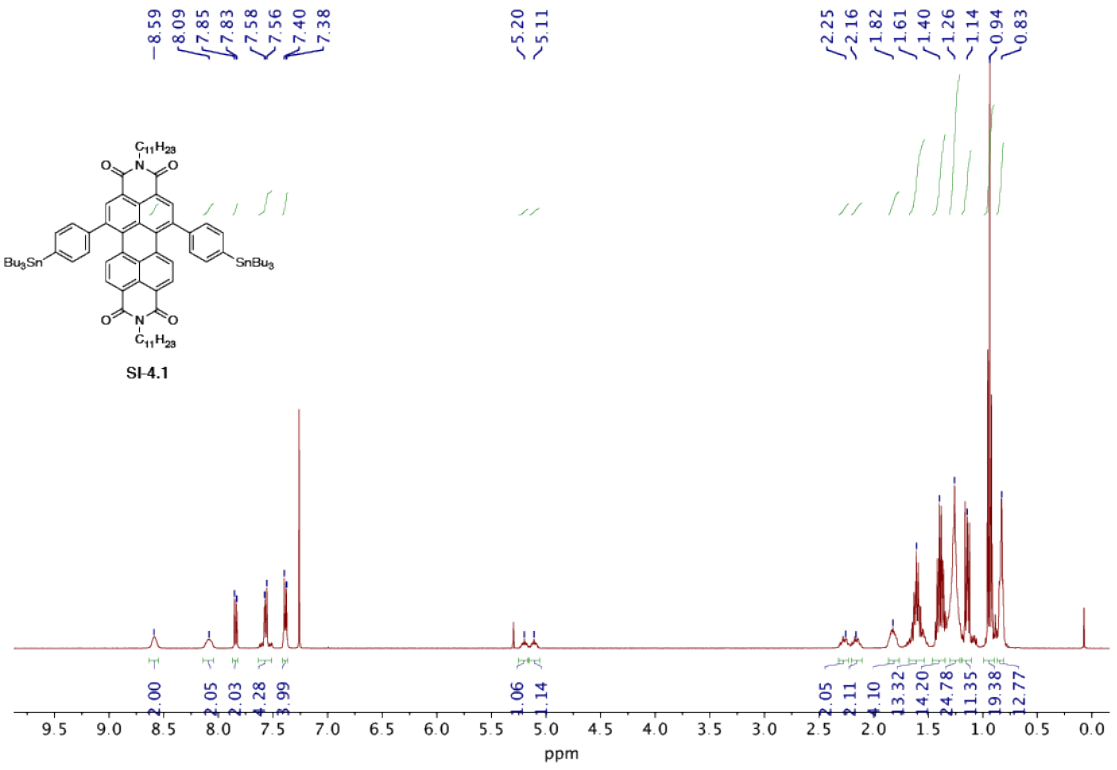

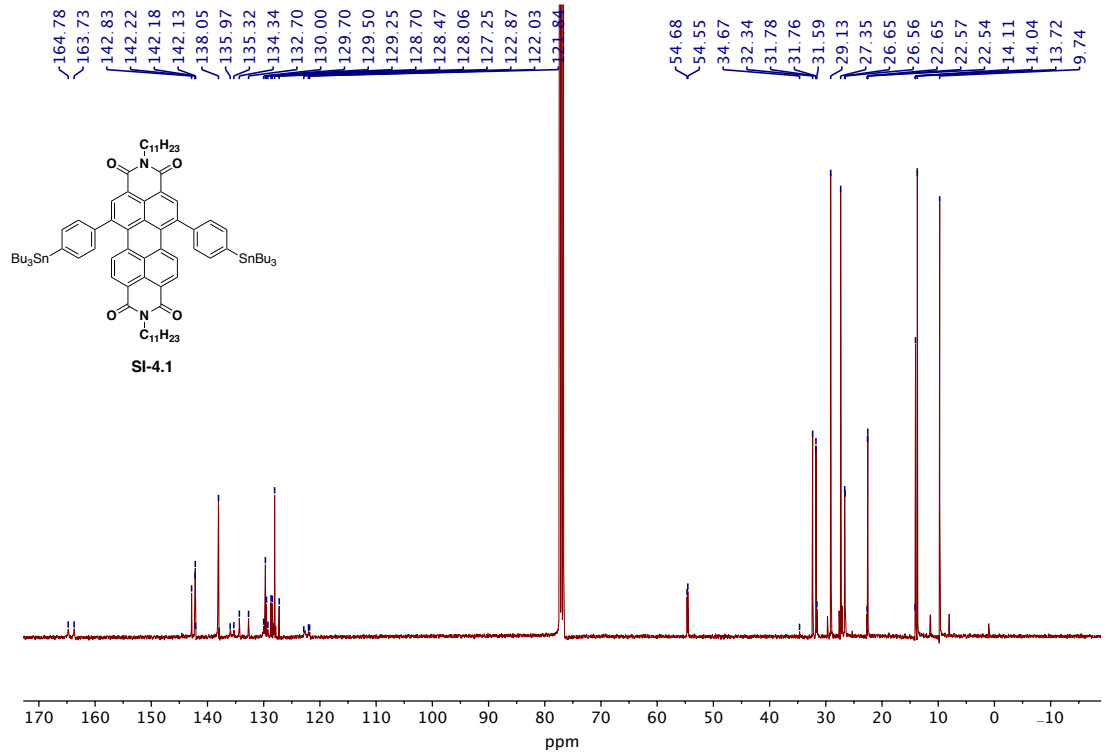

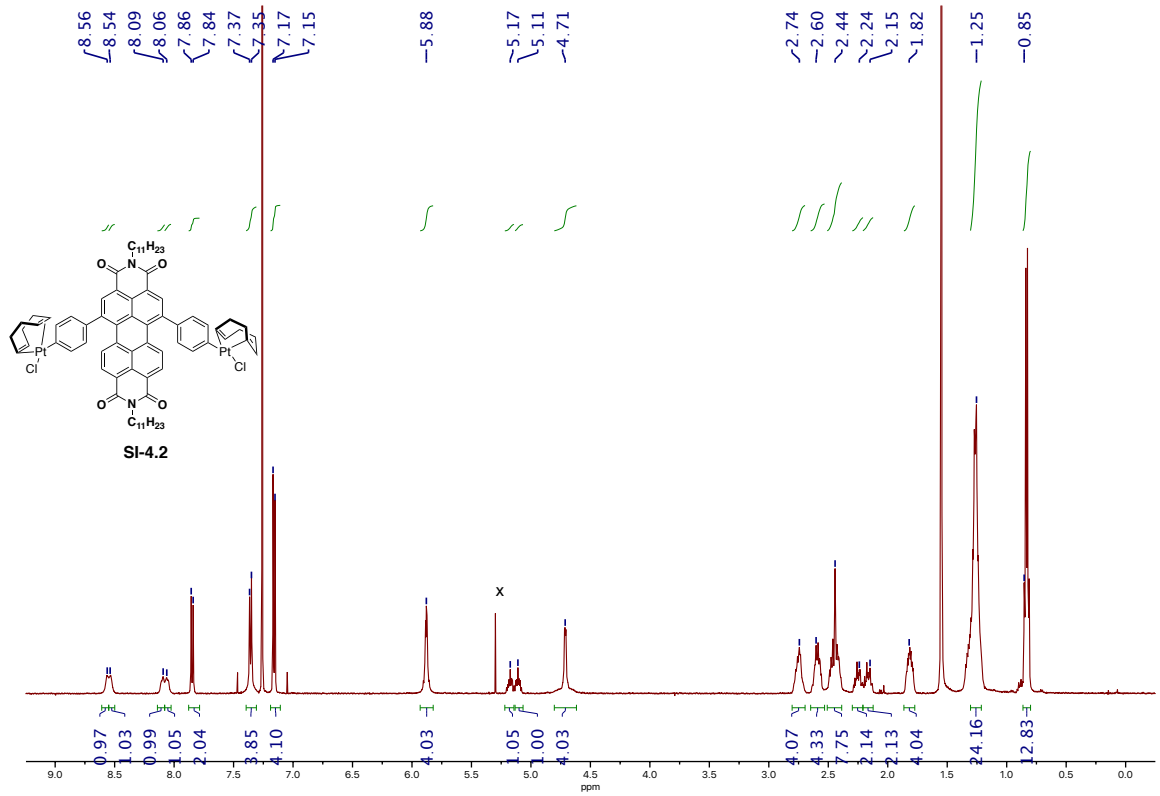
8.56
8.54
8.09
8.06
7.86
7.84
7.37
7.35
7.17
7.15
5.88
5.17
5.11
4.71
2.74
2.60
2.44
2.24
2.15
1.82
1.25
0.85
0.97
1.03
0.99
1.05
2.04
3.85
4.10
4.03
1.05
1.00
4.03
4.07
4.33
7.75
2.14
2.13
4.04
24.16
12.83
X
ppm

SI-4.2

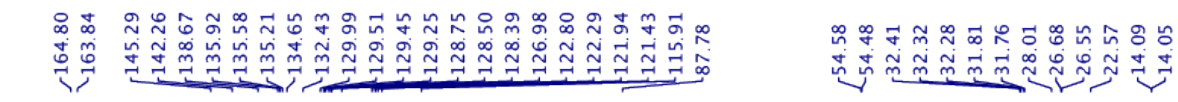
164.80
163.84
145.29
142.26
138.67
135.92
135.58
135.21
134.65
132.43
129.99
129.51
129.45
129.25
128.75
128.50
128.39
126.98
122.80
122.29
121.94
121.43
115.91
87.78
54.58
54.48
32.41
32.32
32.28
31.81
31.76
28.01
26.68
26.55
22.57
14.09
14.05

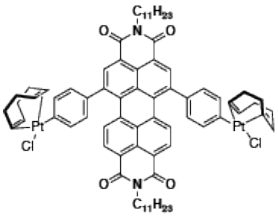

SI-4.2

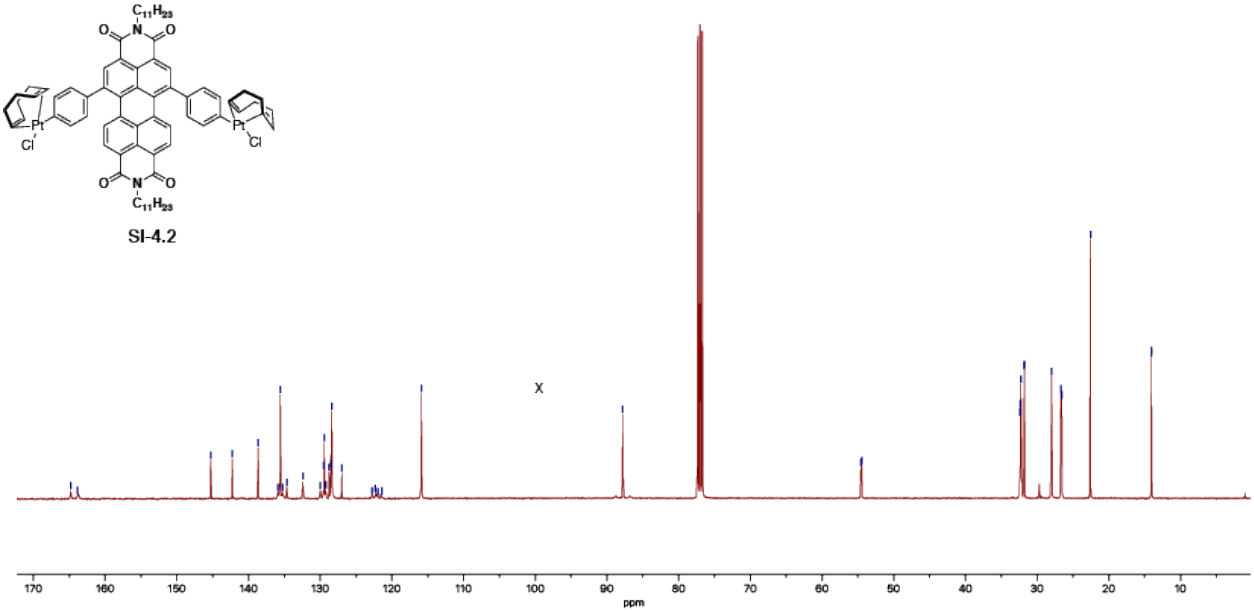
X
ppm

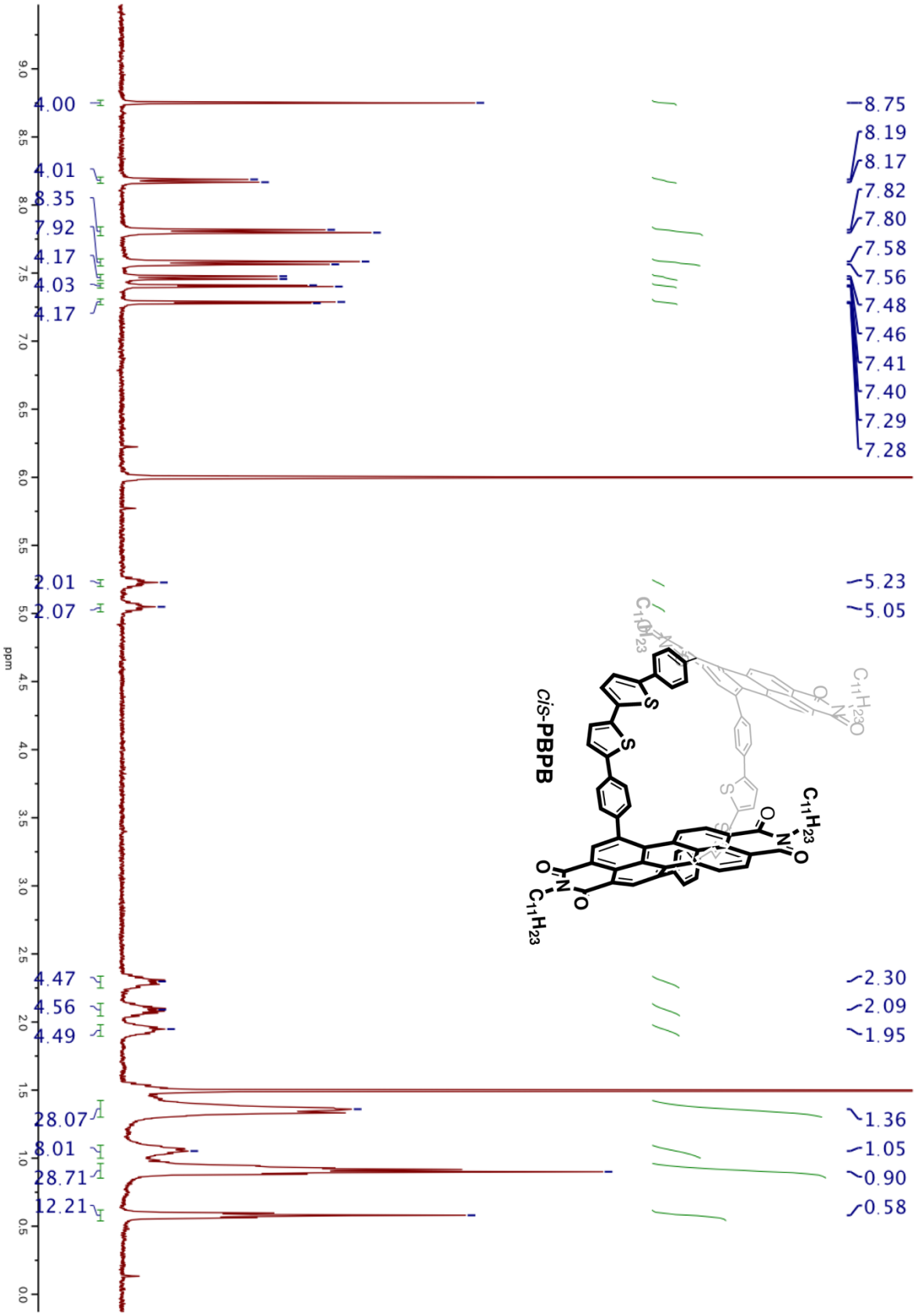
4.00
4.01
8.35
7.92
4.17
4.03
4.17
2.01
2.07
4.47
4.56
4.49
28.07
8.01
28.71
12.21
8.75
8.19
8.17
7.82
7.80
7.58
7.56
7.48
7.46
7.41
7.40
7.29
7.28
5.23
5.05
2.30
2.09
1.95
1.36
1.05
0.90
0.58
ppm
cis-PBPB

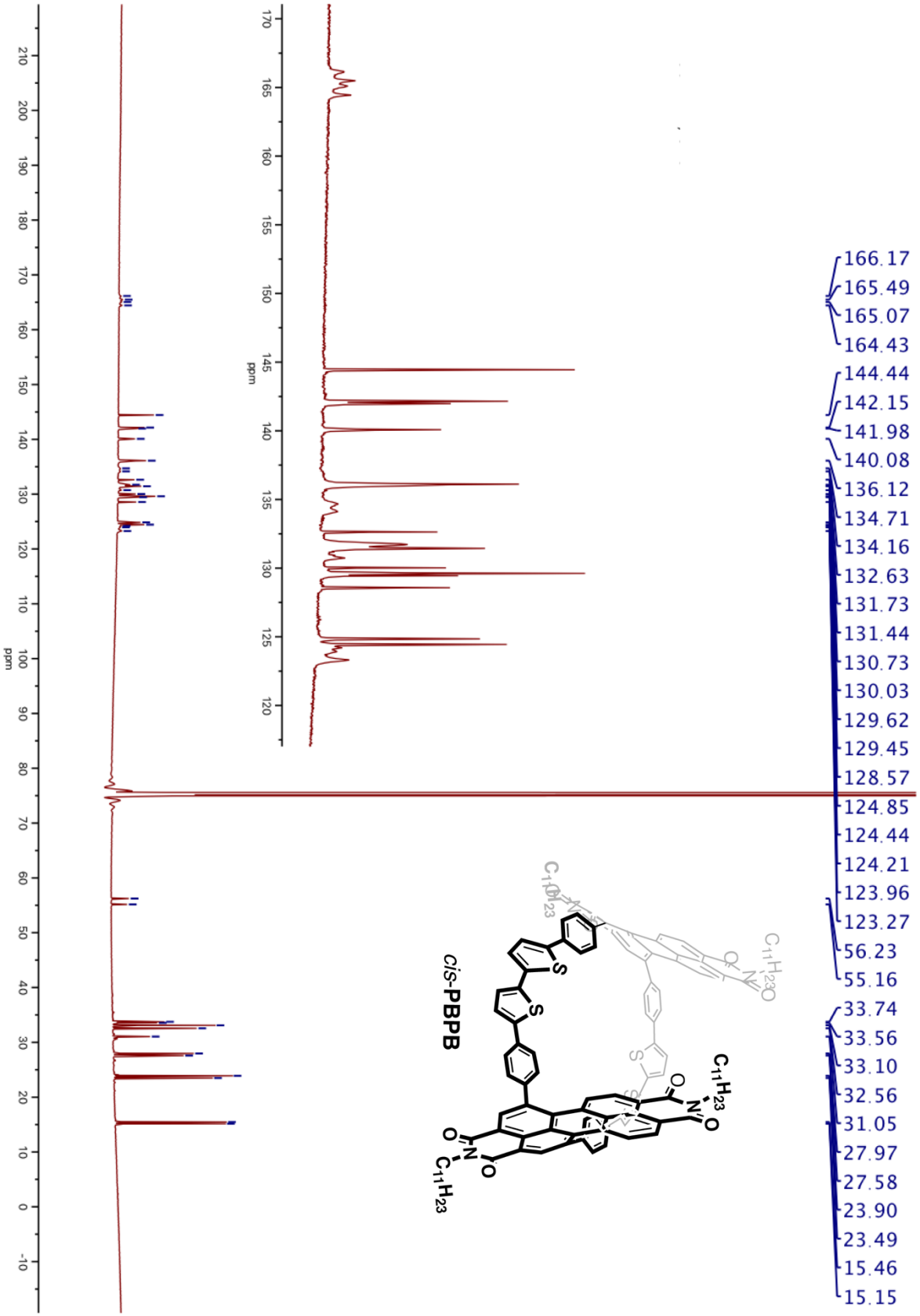
166.17
165.49
165.07
164.43
144.44
142.15
141.98
140.08
136.12
134.71
134.16
132.63
131.73
131.44
130.73
130.03
129.62
129.45
128.57
124.85
124.44
124.21
123.96
123.27
56.23
55.16
33.74
33.56
33.10
32.56
31.05
27.97
27.58
23.90
23.49
15.46
15.15
ppm
cis-PBPB
C11H23
C11H23O
O
N
S

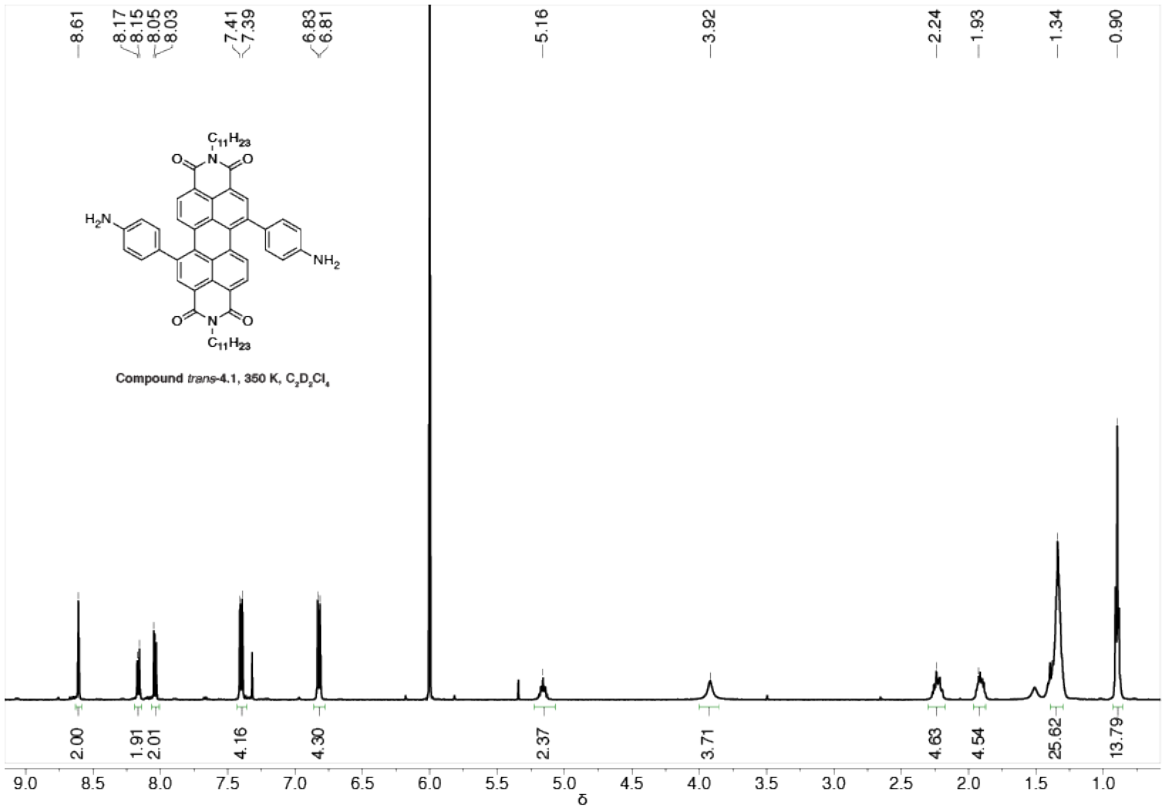
8.61
8.17
8.15
8.05
8.03
7.41
7.39
6.83
6.81
5.16
3.92
2.24
1.93
1.34
0.90
Compound trans-4.1, 350 K, C2D2Cl4
2.00
1.91
2.01
4.16
4.30
2.37
3.71
4.63
4.54
25.62
13.79
δ

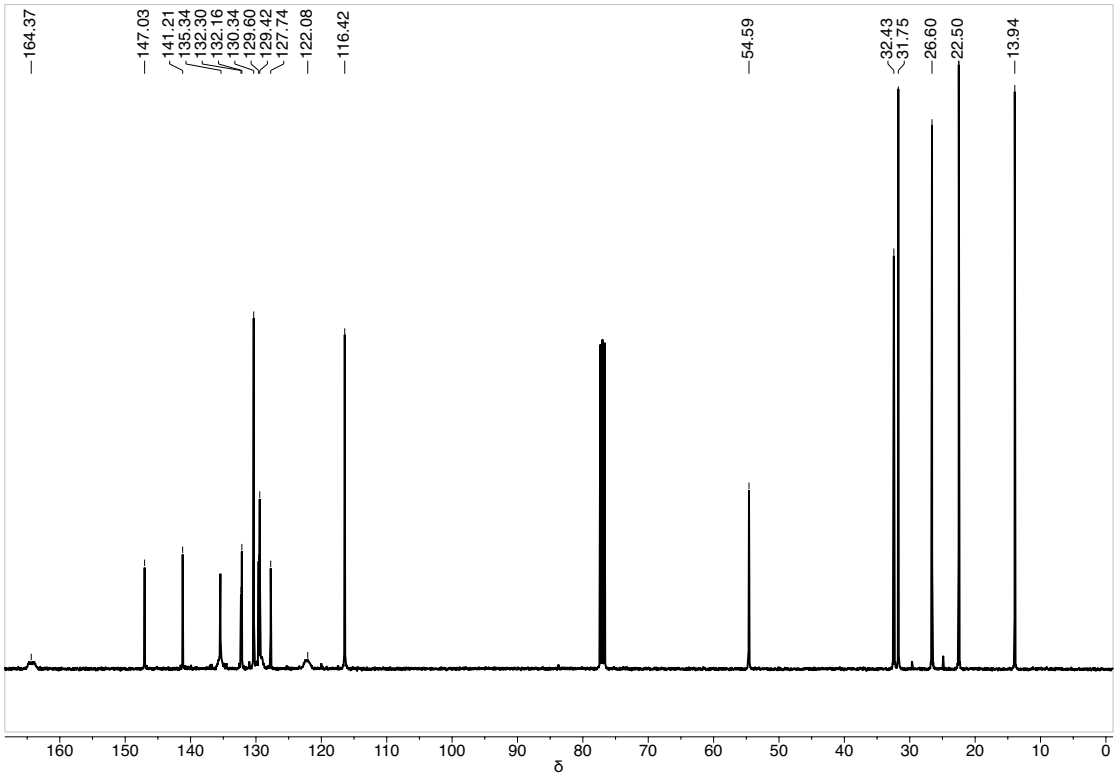
164.37
147.03
141.21
135.34
132.30
132.16
130.34
129.60
129.42
127.74
122.08
116.42
54.59
32.43
31.75
26.60
22.50
13.94
δ

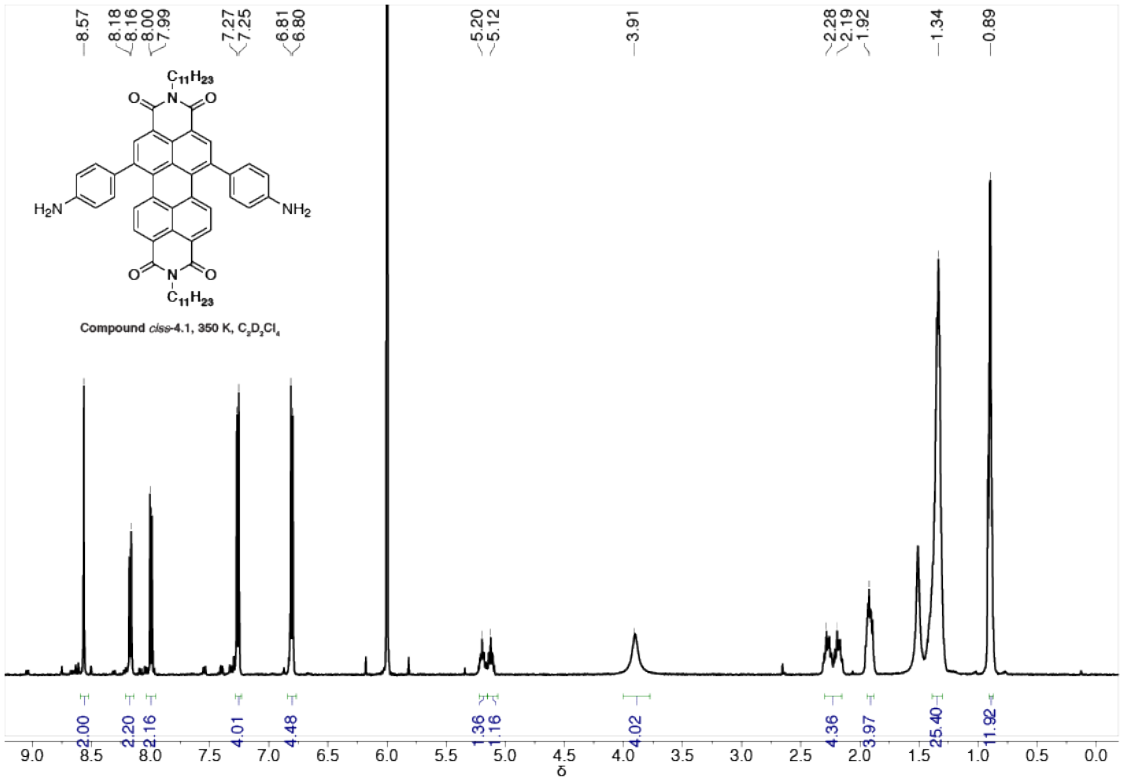
8.57
8.18
8.16
8.00
7.99
7.27
7.25
6.81
6.80
5.20
5.12
3.91
2.28
2.19
1.92
1.34
0.89
$C_{11}H_{23}$
H_2N
NH_2
Compound cis-4.1, 350 K, $C_2D_2Cl_4$
2.00
2.20
2.16
4.01
4.48
1.36
1.16
4.02
4.36
3.97
25.40
11.92
δ

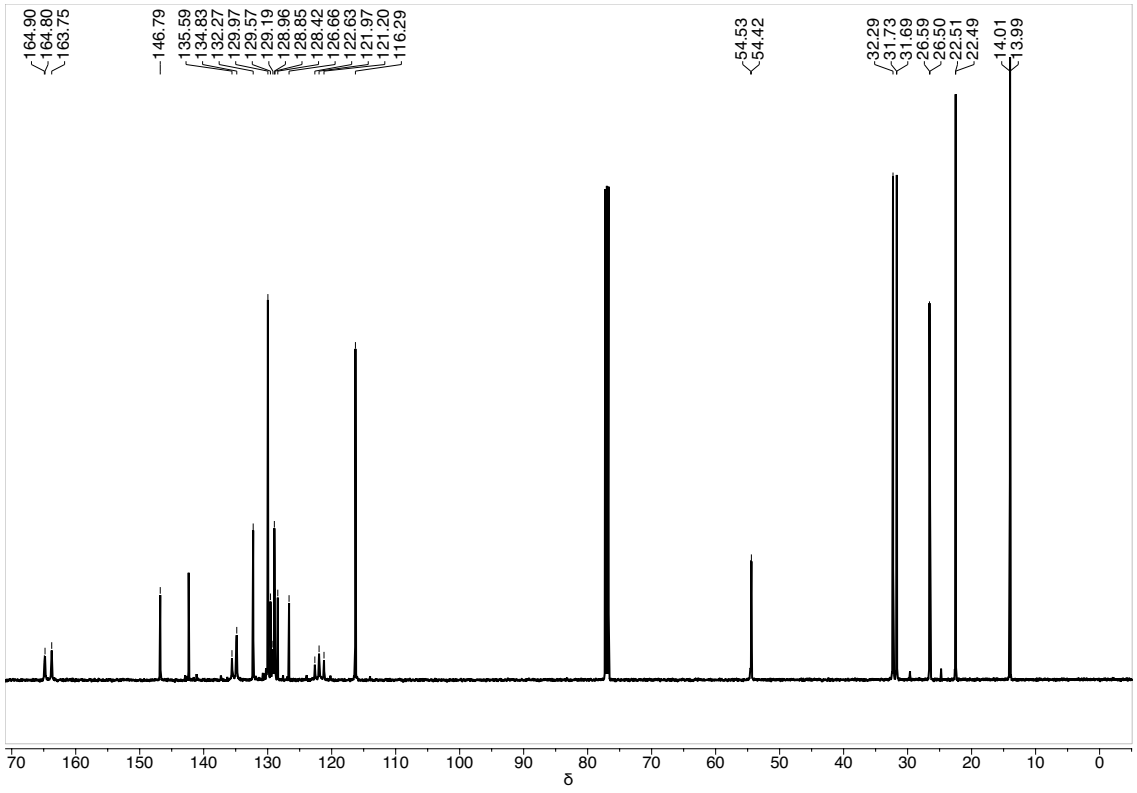
164.90
164.80
163.75
146.79
135.59
134.83
132.27
129.97
129.57
129.19
128.96
128.85
128.42
126.66
122.63
121.97
121.20
116.29
54.53
54.42
32.29
31.73
31.69
26.59
26.50
22.51
22.49
14.01
13.99
δ

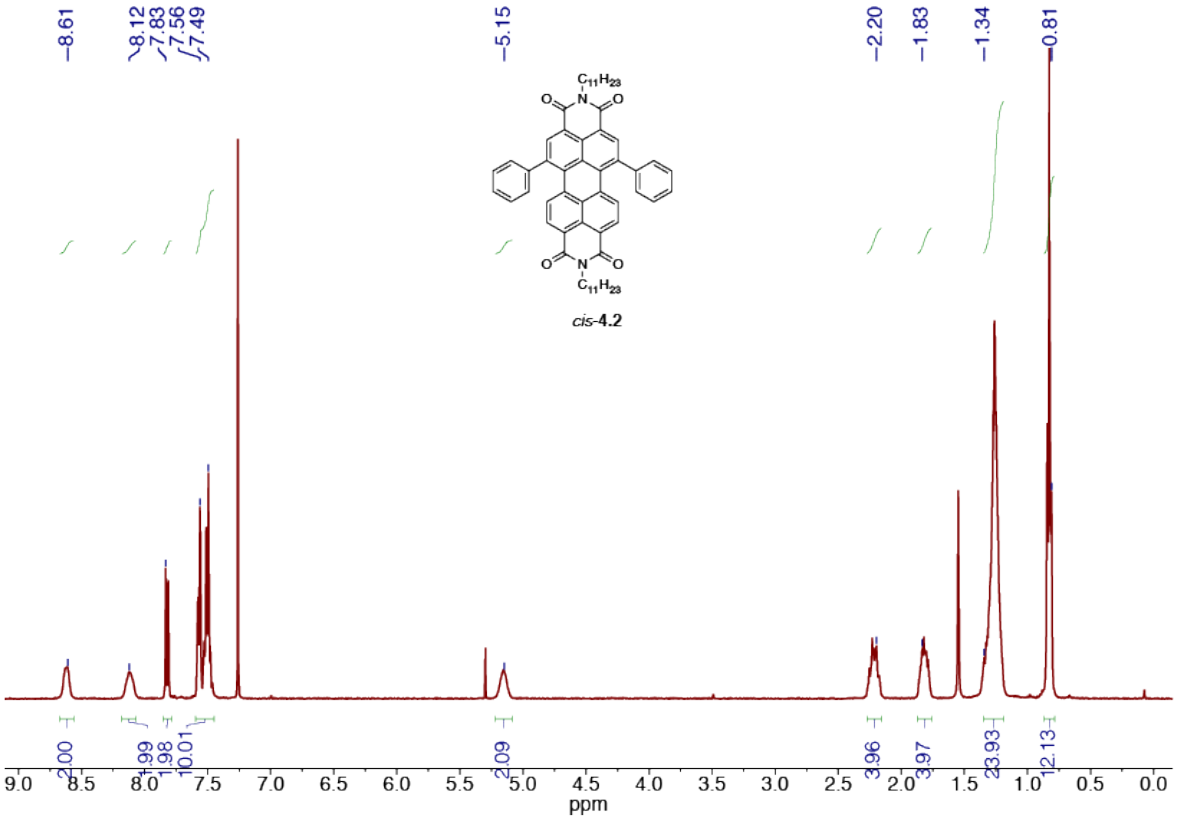
8.61
8.12
7.83
7.56
7.49
5.15
2.20
1.83
1.34
0.81
2.00
1.99
1.98
10.01
2.09
3.96
3.97
23.93
12.13
ppm
cis-4.2

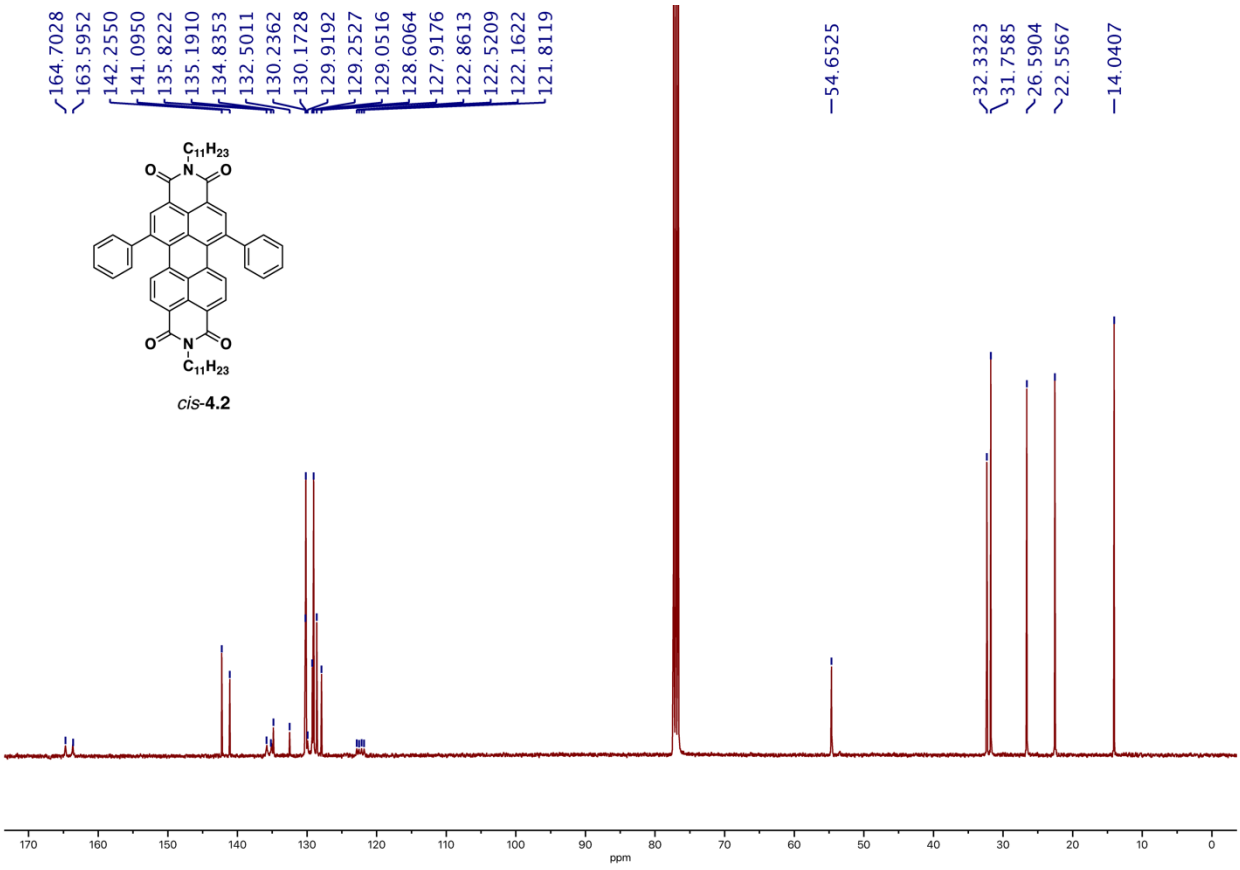
164.7028
163.5952
142.2550
141.0950
135.8222
135.1910
134.8353
132.5011
130.2362
130.1728
129.9192
129.2527
129.0516
128.6064
127.9176
122.8613
122.5209
122.1622
121.8119
54.6525
32.3323
31.7585
26.5904
22.5567
14.0407
ppm
cis-4.2

4.13. DFT Output

All quantum chemical calculations were performed using Jaguar, version 8.3, Schrodinger, Inc., New York, NY, 2013. (See A. D. Bochevarov, E. Harder, T. F. Hughes, J. R. Greenwood, D. A. Braden, D. M. Philipp, D. Rinaldo, M. D. Halls, J. Zhang, R. A. Friesner, "Jaguar: A High Performance Quantum Chemistry Software Program with Strengths in Life and Materials Sciences", Int. J. Quantum Chem., 2013, 113(18), 2110-2142). All geometries were optimized using the B3LYP functional and the 6-31G basis set. In the following pages, we include for each molecule its optimized geometry and total energy. The TD-DFT excited state calculations for *cis*-**PBPB** present the fifteen lowest energy roots. We also provide the results of the homodesmotic reaction employed in order to calculate strain within the two macrocycles. Computations for *trans*-**PBPB** were previously published.[42]

Minimized Geometries for Compounds

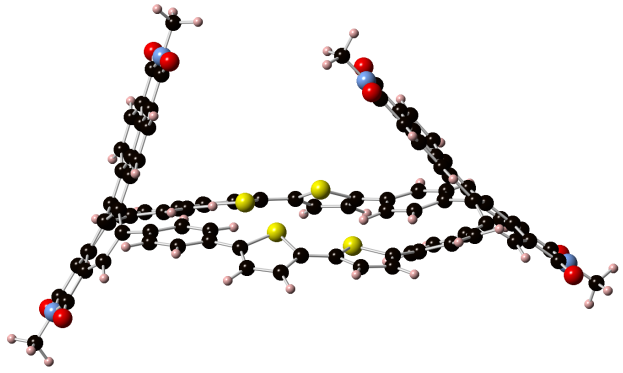

Cis-**PBPB**

Final Heat of Formation = -5948.571806

H	7.658252	-4.281555	1.179927
H	-8.874982	-1.420517	2.190158
H	-8.107008	3.709119	1.433691
H	7.719802	3.217096	2.202196
H	8.368280	0.696616	2.148717
H	8.550660	-1.838906	1.345177
H	1.503125	-5.313964	0.283514
H	4.795645	-8.075281	0.283243

H	6.359200	-6.194807	0.420670
H	3.043003	-3.451240	0.470003
H	-3.638890	-3.432346	0.980818
H	-8.959234	1.245785	1.345451
H	-8.210788	-3.931177	1.961736
H	-2.218948	-5.371265	0.671971
C	-1.305559	7.002332	-0.723196
C	-1.205260	7.406919	0.685651
C	0.079868	7.800864	1.186450
C	1.182332	7.012197	-0.898534
C	-2.289907	7.361151	1.600278
C	-0.999494	8.658602	3.215250
C	1.279853	7.405193	0.510582
C	-2.531978	6.907945	-1.389466
C	1.448254	8.655972	3.033108
C	-0.107704	6.816847	-1.481284
C	2.568696	8.077202	2.462638
C	0.893525	5.945135	-5.072414
C	-2.193082	8.087792	2.807701
C	2.482293	7.339931	1.262452
N	-0.386656	5.746760	-5.604420
C	2.208748	6.585116	-3.074341
C	2.306426	6.938609	-1.726755
C	0.973025	6.331054	-3.644307
C	-1.589110	5.923408	-4.901802
C	0.174657	8.407934	2.468801
C	-0.918883	9.373541	4.511688
C	-0.375440	-9.154493	1.211280
C	0.883319	-9.536258	1.732544
C	1.768974	-6.300892	-3.830104
C	5.218650	4.000800	0.897116
C	3.502771	6.283649	1.007915
C	3.833214	3.893761	0.668207
C	5.727861	-3.501620	0.570742
C	2.568147	-5.514289	0.287450
C	-0.201388	6.474688	-2.866895
C	-1.469358	6.309079	-3.474389
C	-1.902303	-5.934256	-4.229267
C	0.427694	10.440903	6.235532
O	2.653543	9.631303	4.831849
C	-2.617401	6.547637	-2.736937
N	-0.781901	-5.029181	-6.218563
C	-1.995878	-5.318033	-5.576284
C	6.654462	0.320731	0.873814
S	5.076212	-1.890935	0.324010
H	3.093576	6.510555	-3.696890

C	1.570393	9.365553	4.328839
O	-2.674023	5.760384	-5.444848
C	-3.370846	6.340768	1.474631
H	-1.906334	4.848630	0.948443
O	1.883810	5.794630	-5.776665
C	0.488318	-5.340402	-5.716353
C	0.776400	-7.781146	-0.480687
C	-0.446169	5.344275	-7.012413
C	-5.194214	4.143599	1.468332
C	-3.000729	-6.857083	-2.285204
C	-5.622602	5.447946	1.784473
C	1.964397	-7.900069	0.283013
C	-0.644559	-6.216849	-3.643449
C	-1.521941	-10.508172	2.984176
C	-2.951353	5.033259	1.166563
C	2.020994	-8.869701	1.308037
C	-3.063835	-6.268119	-3.551605
C	5.726553	5.287163	1.162811
C	5.294199	-5.989962	0.393320
C	-4.728630	6.523938	1.789638
C	4.886199	6.402668	1.226586
C	-1.782790	-7.101317	-1.641316
C	-3.832805	3.973275	1.151774
C	1.845697	-6.883040	-2.562814
C	0.542114	-5.952118	-4.368276
C	7.051956	-3.413092	0.948177
O	-3.068592	-5.065339	-6.109513
O	-1.903758	9.660457	5.179128
N	0.364420	9.721998	4.958961
O	-2.523601	-10.913284	3.558502
C	-3.292524	-5.511009	0.712508
C	4.838798	-4.658568	0.437958
C	0.971127	-10.510281	2.846555
C	-6.035450	-5.834770	0.911591
N	-0.252371	-10.968387	3.367876
C	-5.211306	-6.954784	0.760532
O	1.492168	-5.105095	-6.376516
C	3.017999	-6.847427	0.237567
C	6.588276	-1.122499	0.759394
C	-5.501135	-4.532660	0.968587
C	-0.224226	-11.948354	4.458249
S	5.406629	1.322323	0.162377
C	3.006959	4.995797	0.725719
C	7.178730	2.480114	1.620838
O	2.040622	-10.901788	3.293723
C	-7.443537	2.851734	1.452753

C	-3.820520	-6.813260	0.629770
C	-4.102038	-4.408236	0.881662
C	-7.910592	1.511426	1.404891
C	-6.899136	0.572415	1.390859
C	3.446615	-4.455191	0.388945
C	4.403172	-7.062239	0.308503
C	-6.951369	-0.875926	1.350626
C	-0.437671	-8.294152	0.081154
C	-6.069899	2.968447	1.473906
C	-7.571590	-3.118190	1.637747
C	7.537005	-2.083391	1.050288
C	-6.301822	-3.317076	1.139052
S	-5.343627	1.370223	1.483095
C	-7.937156	-1.751425	1.760341
S	-5.570612	-1.769266	0.752528
C	6.022098	2.776321	0.931282
C	7.532878	1.106599	1.593919
C	-2.801981	-7.900316	0.550778
H	-3.039400	8.131272	3.484953
H	-3.579244	6.458282	-3.229476
H	3.500220	8.112865	3.017692
H	5.317294	7.374627	1.450509
C	-1.706184	-7.782101	-0.341750
C	-2.744277	-8.863372	1.579379
C	-0.572765	-6.799340	-2.339454
H	-3.456721	2.989719	0.889833
C	-1.567441	-9.533439	1.870359
H	3.387626	2.918008	0.507693
C	0.707076	-7.108457	-1.782836
H	1.940693	4.852003	0.603421
H	-3.603515	-9.028916	2.221487
H	-6.659573	5.624485	2.050845
H	-4.017604	-6.076529	-4.030443
H	-5.096504	7.514470	2.043058
H	6.791817	5.420894	1.326745
H	2.947168	-9.038798	1.847549
H	2.663372	-6.124508	-4.417474
H	-5.661690	-7.942575	0.715813
H	-7.110383	-5.978125	0.970364
C	-0.830307	-4.412392	-7.547028
H	-1.492304	5.205793	-7.273610
H	0.007225	6.115406	-7.639107
H	0.114290	4.417737	-7.153124
H	1.465188	10.711586	6.414402
H	-0.204846	11.328638	6.184236
H	0.058753	9.805052	7.044161

H	-0.035905	-3.670462	-7.619416
H	0.809094	-12.252754	4.604714
H	-0.621028	-11.503225	5.373909
H	-0.849022	-12.804142	4.196444
H	-1.810680	-3.959678	-7.672299
H	3.283413	7.158074	-1.318685
H	-0.672982	-5.165758	-8.324581
H	-3.447393	7.118635	-0.854660
H	-3.925618	-7.137801	-1.799848
H	2.816461	-7.173473	-2.18655

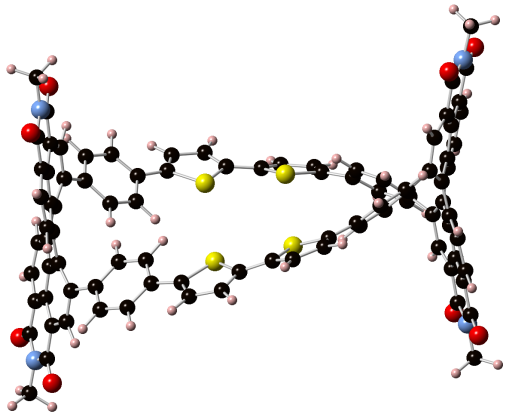

Trans-**PBPB**

Final Heat of Formation = -5948.582452

H	7.378979	-4.061255	-1.403716
H	-8.552342	-1.130130	0.960989
H	-7.808430	3.698092	-0.499800
H	7.723016	3.176686	0.618561
H	8.257131	0.651206	0.244544
H	8.121079	-1.589498	-1.014161
H	1.549809	-5.996235	-0.110919
H	4.264289	-7.363391	-3.155524
H	5.796426	-5.538855	-2.596380
H	3.101928	-4.215162	0.485313
H	-3.557266	-3.764780	-0.518083
H	-8.545919	1.229471	-0.107770
H	-7.951011	-3.655420	1.212110
H	-2.189449	-5.752749	-0.237154
C	-1.156063	7.863026	-0.595819
C	-1.240975	7.962287	0.863294
C	-0.035351	7.873851	1.625341
C	1.311428	8.099306	-0.421930
C	-2.443363	8.199950	1.535777
C	-1.345102	8.135796	3.686849
C	1.225487	7.683485	0.981719
C	-2.221768	7.496082	-1.450187

C	1.053574	7.613966	3.800389
C	0.101314	8.198406	-1.178366
C	2.197979	7.189738	3.152480
C	1.421477	9.480075	-4.509042
C	-2.493746	8.310023	2.929405
C	2.290310	7.148587	1.741085
N	0.210341	9.461060	-5.219887
C	2.545462	8.936712	-2.355348
C	2.513136	8.466821	-1.036156
C	1.384550	8.981980	-3.115281
C	-1.007695	8.944574	-4.744943
C	-0.111891	7.887293	3.044701
C	-1.415547	8.196847	5.163853
C	-0.165691	-9.052789	2.175949
C	1.089090	-9.526138	2.621649
C	1.414272	-7.558929	-3.635819
C	4.929477	4.016460	0.462769
C	3.335836	6.268971	1.153821
C	3.696590	4.257347	-0.169802
C	5.367256	-3.506402	-0.824260
C	2.495495	-5.927797	-0.636083
C	0.158635	8.565944	-2.548963
C	-1.017600	8.486300	-3.334723
C	-2.208465	-8.299149	-3.901923
C	-0.307612	8.029891	7.327945
O	2.001625	7.410603	5.969473
C	-2.149391	7.888691	-2.807137
N	-1.278891	-8.012767	-6.158693
C	-2.413230	-8.274304	-5.369769
C	6.150159	0.300998	-0.126483
S	4.597653	-2.021262	-0.293849
H	3.474185	9.266054	-2.808193
C	1.016225	7.647524	5.283179
O	-2.001069	8.896858	-5.458539
C	-3.247528	6.511953	-1.020909
H	-1.782595	5.406030	0.114289
O	2.437735	9.910639	-5.037677
C	0.023518	-7.821747	-5.672234
C	0.793222	-8.624118	-0.049522
C	0.257672	9.990555	-6.586232
C	-4.942190	4.288860	-0.461791
C	-3.115921	-8.425502	-1.663325
C	-5.403865	5.390176	-1.208318
C	2.022814	-9.080113	0.434201
C	-0.912883	-8.147992	-3.360556
C	-1.103828	-9.344304	4.486025

C	-2.805736	5.424842	-0.242497
C	2.164114	-9.551533	1.744678
C	-3.292850	-8.460161	-3.051526
C	5.396772	4.987581	1.368983
C	4.883721	-5.655206	-2.021698
C	-4.573671	6.475576	-1.484108
C	4.615365	6.089893	1.707630
C	-1.847975	-8.290602	-1.089375
C	-3.627804	4.351201	0.036349
C	1.631272	-7.607001	-2.237784
C	0.196457	-7.885452	-4.200579
C	6.703100	-3.280454	-1.073855
O	-3.505799	-8.463497	-5.887416
O	-2.450340	8.433582	5.772644
N	-0.220570	7.969656	5.865575
O	-2.006866	-9.257013	5.307671
C	-3.164273	-5.716718	0.235768
C	4.558964	-4.708104	-1.032247
C	1.264616	-9.984786	4.020392
C	-5.626425	-5.551667	1.497230
N	0.138628	-9.879192	4.856682
C	-4.852566	-6.703664	1.632534
O	0.954344	-7.610082	-6.438267
C	2.767541	-6.816409	-1.694561
C	6.088271	-1.113025	-0.432636
C	-5.173608	-4.449899	0.745960
C	0.256890	-10.330985	6.246681
S	4.715326	1.304978	-0.143918
C	2.920369	5.350298	0.170896
C	6.966703	2.436251	0.384513
O	2.323786	-10.437650	4.433455
C	-7.109242	2.893145	-0.305326
C	-3.591687	-6.804242	1.021345
C	-3.934139	-4.579377	0.092850
C	-7.512859	1.553862	-0.078528
C	-6.462093	0.688919	0.154610
C	3.366802	-4.902632	-0.312663
C	4.005942	-6.685420	-2.346945
C	-6.492063	-0.735925	0.410182
C	-0.342396	-8.673790	0.818154
C	-5.745970	3.085545	-0.245398
C	-7.228508	-2.897764	0.932056
C	7.110144	-1.942289	-0.850733
C	-5.905096	-3.184982	0.675235
S	-4.946352	1.563098	0.108522
C	-7.560627	-1.528190	0.781948

S	-5.050567	-1.713822	0.243775
C	5.632654	2.750703	0.250552
C	7.259848	1.067242	0.170126
C	-2.586073	-7.857098	1.320055
H	-3.428076	8.509312	3.442435
H	-2.980052	7.690456	-3.476168
H	3.022092	6.830193	3.758593
H	4.983361	6.788306	2.453730
C	-1.628147	-8.258887	0.360921
C	-2.398289	-8.259977	2.663276
C	-0.711874	-8.224294	-1.954879
H	-3.237357	3.534143	0.635062
C	-1.249508	-8.911113	3.076065
H	3.323487	3.552430	-0.906718
C	0.608421	-8.137935	-1.419943
H	1.940504	5.460379	-0.280465
H	-3.143673	-8.015725	3.412958
H	2.887520	-9.068311	-0.218566
H	-6.410104	5.379493	-1.615123
H	-4.278303	-8.585496	-3.486358
H	-4.960551	7.296303	-2.081765
H	6.348009	4.840491	1.870574
H	3.117400	-9.922927	2.103997
H	2.198226	-7.200088	-4.293774
H	-3.983376	-8.501508	-1.020115
H	-5.224000	-7.521995	2.243050
H	-6.575282	-5.491669	2.020933
C	-1.465338	-7.952602	-7.612388
H	-0.757612	9.998668	-6.974604
H	0.678198	10.997504	-6.569986
H	0.896112	9.363261	-7.212833
H	0.702342	7.963657	7.724491
H	-0.785249	8.964626	7.624361
H	-0.913098	7.201230	7.704026
H	-0.751046	-7.241437	-8.023064
H	1.251676	-10.750354	6.374781
H	0.106132	-9.489760	6.926877
H	-0.509098	-11.080434	6.455336
H	-2.490520	-7.648993	-7.813184
H	-3.358636	8.297589	0.965425
H	3.436168	8.414110	-0.471374
H	-1.288423	-8.933121	-8.065543

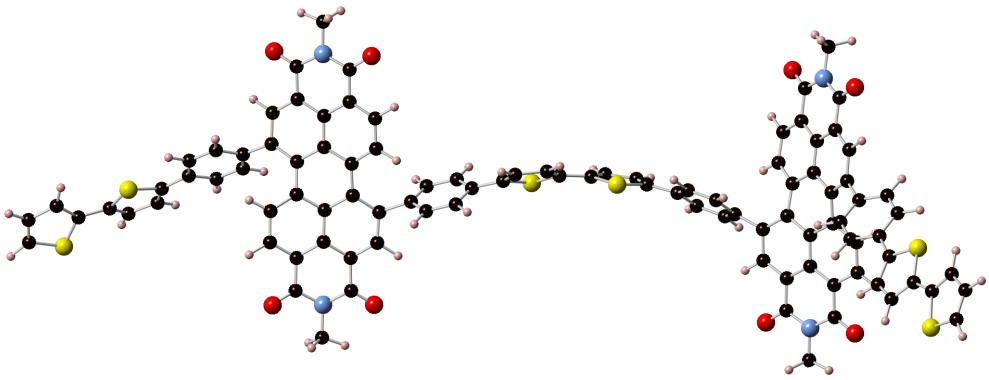

Trans-**PBPB-Acyclic for Homodesmotic Calculations**

Final Heat of Formation = -7053.442019

H	-3.233960	-6.432410	-14.857947
H	-2.058853	0.684038	-18.424512
H	-3.776636	-1.236636	-17.972620
H	-1.775695	-4.273604	-14.788876
H	-8.024836	-7.371139	-18.749207
H	-5.305647	-10.121626	-16.880256
H	-3.946001	-8.246249	-16.082889
H	-6.668862	-5.489172	-17.956364
H	-13.087586	-10.481150	-23.675002
H	-12.127208	-9.956352	-21.492947
C	5.143194	6.940450	-17.056760
C	5.884552	6.228233	-18.113325
C	5.492925	4.894972	-18.464409
C	3.349923	5.188678	-17.229018
C	6.929674	6.821555	-18.827061
C	7.429917	4.785823	-20.005890
C	4.275089	4.303227	-17.970355
C	5.620588	8.096059	-16.392319
C	6.031192	2.819424	-19.665553
C	3.832739	6.450572	-16.733042
C	4.921123	2.232647	-19.105361
C	0.732859	7.667324	-14.827264
C	7.690846	6.119120	-19.764944
C	4.021882	2.946163	-18.288108
N	1.272043	8.836722	-14.276367
C	1.160672	5.677884	-16.237118
C	2.009082	4.864450	-16.994992
C	1.635865	6.841485	-15.664527
C	2.588477	9.282185	-14.465736
C	6.326323	4.167719	-19.372049
C	8.282043	4.033311	-20.957340
C	-12.074580	-9.280565	-16.711511
C	-11.577682	-8.637659	-15.554208

C	-6.640533	-10.832438	-19.354676
C	0.594746	0.432678	-17.449397
C	2.818440	2.127554	-17.925458
C	1.541474	0.683750	-16.441317
C	-4.301763	-5.620524	-16.558499
C	-7.138023	-7.568038	-18.154061
C	2.971242	7.239758	-15.906411
C	3.451731	8.436162	-15.329428
C	-9.018513	-13.212032	-20.898969
C	8.819443	1.954878	-22.106506
O	6.652153	0.837853	-20.818110
C	4.754887	8.820633	-15.551556
N	-6.750433	-13.713256	-21.696851
C	-8.114489	-14.048233	-21.726660
C	-2.254004	-2.263606	-16.825720
S	-4.204908	-4.129654	-17.480170
H	0.125489	5.399831	-16.072229
C	6.878069	2.017080	-20.580885
O	2.992506	10.313757	-13.945710
C	7.012504	8.624026	-16.468127
H	6.430207	10.565371	-17.197500
O	-0.434022	7.366677	-14.609444
C	-6.193213	-12.677340	-20.938007
C	-9.770436	-9.791292	-17.423250
C	0.370007	9.635942	-13.441799
C	9.664700	9.623582	-16.639091
C	-11.248054	-12.666747	-20.161310
C	9.402377	8.330954	-16.137468
C	-9.328077	-9.170576	-16.250845
C	-8.515176	-12.148845	-20.112826
C	-14.416568	-8.651215	-16.026969
C	7.261696	9.933408	-16.898667
C	-10.213673	-8.614179	-15.321823
C	-10.374508	-13.485888	-20.881304
C	0.800240	1.023728	-18.708554
C	-4.852033	-8.041706	-16.644185
C	8.106101	7.844366	-16.056998
C	1.890535	1.848328	-18.940403
C	-10.801094	-11.563044	-19.428367
C	8.561541	10.419918	-16.992783
C	-7.468744	-10.047963	-18.522078
C	-7.128616	-11.877891	-20.107733
C	-3.355320	-5.612965	-15.556905
O	-8.524707	-14.980112	-22.406298
O	9.232857	4.537687	-21.540542
N	7.958248	2.687707	-21.173552

O	-15.626919	-8.633649	-16.210995
C	-13.049704	-10.526006	-21.544543
C	-5.195437	-6.712889	-16.953446
C	-12.497823	-8.000937	-14.579116
C	-15.446708	-11.926922	-21.709548
N	-13.867466	-8.048558	-14.888736
C	-14.911334	-11.598454	-20.464091
O	-4.988410	-12.462879	-20.979185
C	-6.774221	-8.895046	-17.872623
C	-2.889284	-3.518990	-16.486858
C	-14.789265	-11.565744	-22.897308
C	-14.819465	-7.425670	-13.964311
S	-0.586799	-1.921334	-16.385091
C	2.636147	1.519266	-16.676236
C	-1.825681	-0.207032	-17.853206
O	-12.095833	-7.461282	-13.556754
C	-13.689460	-10.917339	-20.354153
C	-13.589692	-10.831630	-22.781083
C	-6.365956	-6.502038	-17.705945
C	-5.619681	-9.105446	-17.101649
C	-11.186290	-9.917448	-17.627051
C	-2.563809	-4.439620	-15.514879
C	-0.593469	-0.410086	-17.274378
C	-2.759601	-1.239152	-17.597431
C	-13.097361	-10.519150	-19.046735
H	8.501506	6.602018	-20.299187
H	5.116606	9.714331	-15.054369
H	4.719112	1.192776	-19.336400
H	2.031556	2.286950	-19.924127
C	-11.725150	-10.655689	-18.729726
C	-13.946428	-9.860130	-18.131282
C	-9.389290	-11.346354	-19.317099
H	8.715936	11.430415	-17.359321
C	-13.467143	-9.295062	-16.967251
H	1.410826	0.238987	-15.458636
C	-8.847174	-10.354992	-18.429175
H	3.349067	1.706438	-15.878350
H	-15.005371	-9.769872	-18.346998
H	-8.271392	-9.112091	-16.043419
H	10.220599	7.693628	-15.825425
H	-10.745515	-14.329644	-21.452266
H	7.936256	6.837203	-15.687988
H	0.110797	0.804154	-19.517140
H	-9.846430	-8.142161	-14.417545
H	-5.582111	-10.606240	-19.419771
H	-12.305081	-12.893407	-20.188982

H	-15.435347	-11.908580	-19.564404
H	-16.372090	-12.493649	-21.754443
C	-5.816329	-14.491842	-22.516572
H	0.925256	10.501424	-13.089299
H	-0.497763	9.946419	-14.027586
H	0.016630	9.036247	-12.600264
H	8.449619	0.934420	-22.167438
H	8.793066	2.433237	-23.087939
H	9.850643	1.970492	-21.747498
H	-5.312220	-13.834470	-23.228329
H	-14.250864	-6.995900	-13.143554
H	-15.388833	-6.653726	-14.486091
H	-15.521410	-8.175998	-13.594369
H	-6.389517	-15.253876	-23.038713
H	7.170860	7.858140	-18.662184
H	1.594026	3.961550	-17.407899
H	-5.057059	-14.950241	-21.879594
C	-15.265772	-11.931290	-24.234574
C	-14.501453	-12.038111	-25.376890
C	-15.229742	-12.405567	-26.529472
C	-16.574803	-12.595063	-26.300577
S	-16.943360	-12.310567	-24.604618
H	-13.429975	-11.879955	-25.383939
H	-14.778035	-12.528283	-27.507372
C	-17.590847	-12.973175	-27.260133
C	-18.961639	-13.010824	-27.127594
C	-19.636894	-13.425681	-28.310068
C	-18.782956	-13.704403	-29.338830
S	-17.126249	-13.476729	-28.880570
H	-19.471608	-12.734404	-26.211814
H	-20.714586	-13.507354	-28.390304
C	11.043176	10.088055	-16.806316
C	12.213975	9.454434	-16.449800
C	13.386538	10.158255	-16.805777
C	13.139325	11.348257	-17.451992
S	11.412620	11.598582	-17.622670
H	12.239505	8.501847	-15.938141
H	14.387755	9.808455	-16.582166
C	14.095592	12.299548	-17.972307
C	13.929660	13.634723	-18.262454
C	15.109959	14.258654	-18.749761
C	16.170845	13.399446	-18.833180
S	15.742411	11.797992	-18.325320
H	12.991952	14.155616	-18.104750
H	15.168047	15.306800	-19.017837
H	17.179502	13.606874	-19.161314

H	-19.022186	-14.029030	-30.341418

Cis-PBPB-Acyclic for Homodesmotic Calculations

Final Heat of Formation = -7053.435400

H	-1.834122	-7.849178	-15.386708
H	0.585078	-2.296806	-20.657102
H	-1.203638	-4.109005	-20.081153
H	0.032051	-6.075792	-15.801352
H	-6.716251	-8.403724	-19.252300
H	-5.384920	-10.947647	-16.057199
H	-3.303308	-9.656397	-15.896592
H	-4.649469	-7.115692	-19.100859
H	-13.650605	-8.662737	-23.571423
H	-11.832841	-9.157944	-21.991861
C	5.184765	5.150000	-17.279303
C	6.384775	4.873091	-18.091168
C	6.476311	3.581346	-18.723017
C	4.054602	3.169999	-18.298256
C	7.450856	5.783429	-18.257328
C	8.761521	4.118088	-19.470327
C	5.368750	2.662793	-18.733857
C	5.121259	6.163265	-16.319804
C	7.852765	1.900306	-19.891748
C	4.017512	4.350963	-17.494047
C	6.825900	0.992858	-19.766042
C	0.295540	4.469725	-16.608928
C	8.612994	5.384702	-18.954948
C	5.591631	1.341826	-19.181767
N	0.331967	5.533863	-15.698172
C	1.621575	3.008471	-18.110790
C	2.840697	2.562884	-18.635836
C	1.587250	4.055848	-17.207503
C	1.487878	6.236659	-15.320929
C	7.696681	3.199154	-19.359493
C	10.022948	3.754300	-20.163558
C	-10.567710	-6.646406	-17.405416
C	-9.689138	-6.001871	-16.499859
C	-7.332012	-11.930861	-18.015977

C	2.785555	-1.927669	-18.933712
C	4.622606	0.215598	-19.075930
C	3.280766	-1.325949	-17.763988
C	-2.603969	-7.453500	-17.372487
C	-5.969983	-8.682193	-18.516351
C	2.783230	4.740896	-16.887640
C	2.755707	5.819241	-15.971028
C	-10.633270	-12.872562	-19.369603
C	11.372758	2.096795	-21.331978
O	9.262822	0.352228	-21.014658
C	3.928096	6.484370	-15.662178
N	-9.282591	-14.900990	-19.103070
C	-10.503840	-14.344090	-19.509726
C	-0.017443	-4.664935	-18.354864
S	-2.127713	-6.403790	-18.693989
H	0.690218	2.522599	-18.380282
C	9.108570	1.480081	-20.564831
O	1.440999	7.146828	-14.503609
C	7.523600	7.203878	-17.794913
H	5.966205	7.995279	-19.059764
O	-0.767899	3.925813	-16.878061
C	-8.202585	-14.173278	-18.588426
C	-9.068398	-8.598456	-17.465697
C	-0.951677	5.923567	-15.107074
C	8.007721	9.914547	-17.105107
C	-11.920401	-10.845043	-19.819211
C	8.761562	8.872812	-16.534668
C	-8.274651	-7.953230	-16.509242
C	-9.611009	-12.093513	-18.788301
C	-12.049287	-4.602380	-17.349511
C	6.739220	8.233262	-18.334905
C	-8.572387	-6.674105	-16.035693
C	-11.746339	-12.244643	-19.880366
C	3.288590	-1.489007	-20.170759
C	-4.046741	-9.372808	-16.634185
C	8.531747	7.550321	-16.882241
C	4.194679	-0.439992	-20.239009
C	-11.008126	-10.057842	-19.074383
C	6.976653	9.564103	-17.995954
C	-7.473431	-10.542383	-17.832568
C	-8.392041	-12.711034	-18.427853
C	-1.728623	-7.306896	-16.318620
O	-11.405422	-15.039530	-19.957630
O	10.954524	4.535657	-20.303349
N	10.117490	2.449379	-20.661465
O	-13.046343	-3.985674	-17.703726

C	-12.824336	-9.562094	-21.809557
C	-3.810105	-8.272501	-17.476310
C	-9.964756	-4.632120	-15.997589
C	-15.361243	-10.612856	-21.377020
N	-11.129475	-4.012055	-16.475513
C	-14.335680	-10.881397	-20.481239
O	-7.163046	-14.744683	-18.287365
C	-6.223901	-9.757770	-17.649450
C	-0.799487	-5.729253	-17.773487
C	-15.143549	-9.811957	-22.511698
C	-11.438057	-2.650100	-16.030048
S	1.499789	-4.118595	-17.660966
C	4.179241	-0.267258	-17.836145
C	0.675937	-2.986114	-19.826260
O	-9.219679	-4.063956	-15.209302
C	-13.045084	-10.368942	-20.681240
C	-13.852298	-9.288104	-22.706283
C	-4.796956	-7.956171	-18.430224
C	-5.228502	-10.104522	-16.724324
C	-10.284419	-7.970390	-17.877298
C	-0.716467	-6.339646	-16.540022
C	1.709898	-2.919059	-18.920169
C	-0.301489	-3.951870	-19.501480
C	-12.417696	-7.954398	-19.028991
H	9.422303	6.092848	-19.091020
H	3.897468	7.280609	-14.926725
H	6.981896	-0.017260	-20.127645
H	4.565218	-0.110829	-21.205599
C	-11.241930	-8.643778	-18.707927
C	-12.661574	-6.643716	-18.607065
C	-9.805434	-10.692836	-18.587957
H	6.389333	10.345057	-18.470712
C	-11.752213	-5.981919	-17.805423
H	2.920705	-1.658817	-16.794874
C	-8.752331	-9.944143	-17.965046
H	4.529997	0.203550	-16.922665
H	-13.578489	-6.135680	-18.885592
H	-7.404395	-8.451619	-16.111450
H	9.536804	9.107323	-15.813081
H	-12.480295	-12.850065	-20.399710
H	9.153122	6.768846	-16.454363
H	2.964323	-1.980020	-21.081912
H	-7.936979	-6.187466	-15.304328
H	-6.366963	-12.403796	-17.870589
H	-14.529558	-11.518529	-19.623235
H	-16.337064	-11.060093	-21.218628

C	-9.089729	-16.348093	-19.235164
H	-0.765619	6.752007	-14.428143
H	-1.646841	6.219527	-15.895619
H	-1.385030	5.076604	-14.570894
H	11.296563	1.060949	-21.653227
H	11.532335	2.754916	-22.188746
H	12.209300	2.225239	-20.641995
H	-8.244844	-16.549913	-19.896938
H	-10.633168	-2.325210	-15.375494
H	-11.523095	-1.989809	-16.895629
H	-12.392353	-2.640254	-15.498787
H	-10.005731	-16.767521	-19.643907
H	2.827812	1.722332	-19.312284
H	-8.869843	-16.782619	-18.257759
C	-16.237349	-9.626155	-23.470185
C	-17.592301	-9.650874	-23.220557
C	-18.391200	-9.538525	-24.386580
C	-17.659044	-9.412686	-25.544526
S	-15.942209	-9.442812	-25.187318
H	-18.002136	-9.733576	-22.220623
H	-19.475189	-9.532744	-24.381177
C	-18.134743	-9.352472	-26.917683
C	-17.747531	-8.521885	-27.942625
C	-18.428127	-8.779503	-29.166907
C	-19.312763	-9.818528	-29.076828
S	-19.356947	-10.482731	-27.476143
H	-17.004663	-7.743168	-27.812392
H	-18.258937	-8.219726	-30.079514
C	8.375129	11.296850	-16.790046
C	9.629450	11.746143	-16.441798
C	9.692895	13.134325	-16.184319
C	8.486360	13.781805	-16.334189
S	7.238944	12.634305	-16.802332
H	10.495107	11.095526	-16.407888
H	10.605623	13.649539	-15.908999
C	8.194712	15.180950	-16.108235
C	7.046902	15.892950	-16.376437
C	7.106161	17.250093	-15.952368
C	8.291357	17.569772	-15.351598
S	9.373735	16.214711	-15.308595
H	6.186834	15.455380	-16.871055
H	6.294520	17.956560	-16.081422
H	8.611831	18.523589	-14.957023
H	-13.185418	-8.437356	-19.608203
H	6.005956	6.732670	-16.079736
H	-19.962993	-10.213751	-29.844783

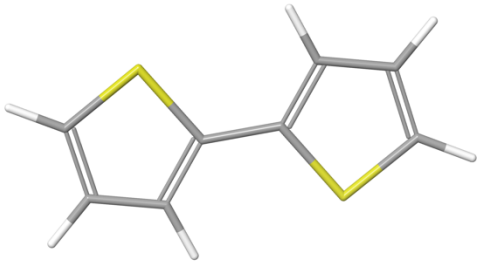

Bithiophene

Total Energy: -1104.826802 hartrees

S1	-0.5229025548	2.1569531073	0.0161859979
C2	0.3530028893	0.6332102763	0.0062644825
C3	1.7098905419	0.8694103010	0.0122565205
C4	2.0501584230	2.2514544128	0.0246320264
C5	0.9547258678	3.0684516605	0.0281022419
C6	-0.3530028893	-0.6332102763	-0.0062644825
S7	0.5229025548	-2.1569531073	-0.0161859979
C8	-0.9547258678	-3.0684516605	-0.0281022419
C9	-2.0501584230	-2.2514544128	-0.0246320264
C10	-1.7098905419	-0.8694103010	-0.0122565205
H11	2.4448343075	0.0724557652	0.0078978216
H12	3.0698389079	2.6188720882	0.0306528745
H13	0.9193525791	4.1486289730	0.0368265795
H14	-0.9193525791	-4.1486289730	-0.0368265795
H15	-3.0698389079	-2.6188720882	-0.0306528745
H16	-2.4448343075	-0.0724557652	-0.0078978216

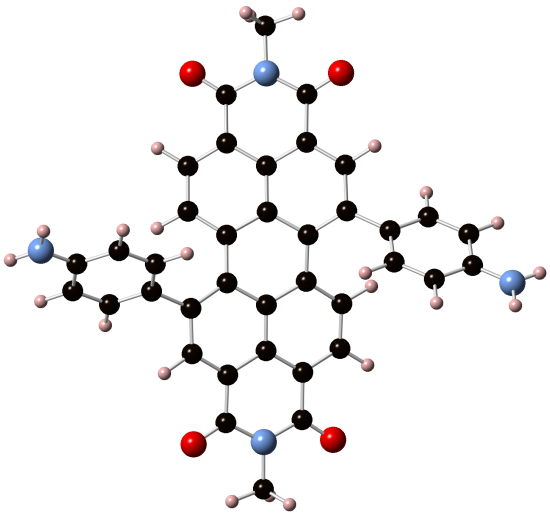

Trans-**4.1**

Final Heat of Formation = -1982.587675

C	5.032948	6.225155	-17.363312

C	5.682306	5.606906	-18.530798
C	5.252986	4.309444	-18.962953
C	3.237958	4.492861	-17.547763
C	6.663181	6.267517	-19.280581
C	6.976855	4.363053	-20.729424
C	4.132175	3.648390	-18.358431
C	5.571421	7.303917	-16.622909
C	5.629027	2.346437	-20.386541
C	3.729112	5.735657	-17.027782
C	4.663695	1.669432	-19.672272
C	0.672628	6.915148	-15.054415
C	7.291259	5.665129	-20.374295
C	3.911139	2.279609	-18.642108
N	1.234109	8.060289	-14.471619
C	1.062691	4.960849	-16.529560
C	1.898623	4.162757	-17.314924
C	1.554128	6.105671	-15.924910
C	2.557698	8.493394	-14.651381
C	5.960359	3.675106	-20.027806
C	7.690130	3.711318	-21.851673
C	1.366067	-0.479560	-16.480631
C	2.990730	1.381389	-17.894329
C	2.235855	0.393218	-15.796298
C	2.890370	6.500394	-16.163671
C	3.403477	7.668334	-15.549180
C	8.053023	1.756796	-23.259937
O	6.086214	0.494932	-21.806638
C	4.723826	8.017535	-15.744976
H	0.026088	4.687647	-16.365759
C	6.339673	1.649939	-21.487226
O	2.977790	9.500133	-14.094419
C	7.002732	7.702084	-16.635959
H	6.634024	9.814248	-16.871875
O	-0.497265	6.626347	-14.833968
C	0.347569	8.846857	-13.609350
C	9.740709	8.464511	-16.518030
C	9.357070	7.113290	-16.395816
C	7.391572	9.047747	-16.733486
C	1.329505	-0.407171	-17.885380
C	8.021488	6.748987	-16.455799
C	2.131755	0.497683	-18.569045
C	8.727586	9.426406	-16.686255
O	8.562403	4.271347	-22.504581
N	7.327963	2.390379	-22.154667
C	3.023314	1.298025	-16.491150
H	8.045957	6.194203	-20.945541

H	5.116518	8.863013	-15.191477
H	4.491123	0.626203	-19.912058
H	2.076760	0.529741	-19.653740
H	8.995080	10.475625	-16.780836
H	2.296104	0.346795	-14.711873
H	3.690640	1.948406	-15.934685
H	10.118396	6.351931	-16.245429
H	7.756851	5.701079	-16.352040
H	0.668303	-1.068415	-18.439677
H	0.914920	9.696799	-13.238721
H	-0.521409	9.181358	-14.180010
H	-0.006954	8.229938	-12.780725
H	7.670499	0.745039	-23.369271
H	7.901176	2.327457	-24.178676
H	9.122932	1.742354	-23.041207
H	6.952601	7.272600	-19.007703
H	1.491733	3.260078	-17.747457
N	11.063884	8.828903	-16.469162
N	0.581945	-1.376527	-15.797400
H	11.786475	8.140303	-16.353334
H	11.339296	9.792017	-16.548012
H	0.607789	-1.430199	-14.794383
H	-0.028594	-2.007096	-16.286587

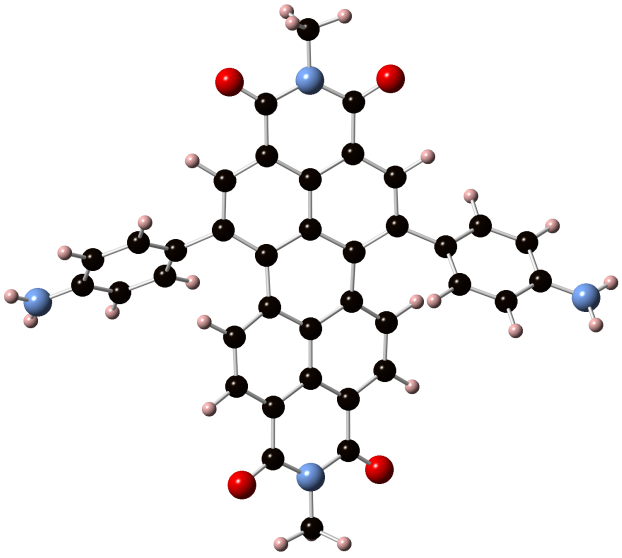

Cis-**4.1**

Final Heat of Formation = -1982.586248

C	4.546200	3.491118	-17.334244
C	5.817619	3.993776	-17.881884
C	6.692704	3.034674	-18.502647
C	4.815958	1.416413	-18.691877

C	6.220906	5.349039	-17.803832
C	8.448688	4.755158	-18.605100
C	6.257258	1.699163	-18.817767
C	3.820463	4.145600	-16.332963
C	8.929450	2.483281	-19.367294
C	4.030549	2.262541	-17.848753
C	8.526233	1.177541	-19.545626
C	0.714066	0.367041	-17.853819
C	7.549205	5.690880	-18.140277
C	7.210895	0.749749	-19.258845
N	0.047617	1.111575	-16.870666
C	2.827138	0.061271	-19.114296
C	4.169615	0.370365	-19.357602
C	2.103520	0.765493	-18.166551
C	0.589991	2.206815	-16.176132
C	8.026356	3.424542	-18.823728
C	9.832934	5.174420	-18.931893
C	6.722522	-3.543002	-19.572266
C	6.979402	-0.716402	-19.384030
C	6.367418	-2.857321	-18.392854
C	2.696063	1.875632	-17.518909
C	1.968168	2.603885	-16.547355
C	12.051007	4.625089	-19.774654
O	11.125652	2.063811	-20.175190
C	2.559531	3.694225	-15.927631
H	2.343021	-0.757282	-19.635663
C	10.324175	2.862066	-19.706697
O	-0.055435	2.794716	-15.316460
C	5.316661	6.488383	-17.486500
H	3.814363	5.944319	-18.934826
O	0.145416	-0.566280	-18.407528
C	-1.322268	0.692115	-16.562162
C	3.656394	8.750961	-17.012666
C	4.865699	8.579426	-16.313439
C	4.113053	6.674192	-18.189095
C	7.218463	-2.788145	-20.651002
C	5.676627	7.476758	-16.557043
C	7.350225	-1.408638	-20.547990
C	3.300586	7.774379	-17.965134
O	10.241330	6.315817	-18.761356
N	10.685308	4.195672	-19.459297
C	6.493411	-1.479066	-18.308162
H	7.874276	6.722250	-18.063120
H	2.006498	4.213772	-15.153062
H	9.257248	0.458554	-19.897223
H	7.736418	-0.853774	-21.398740

H	2.382092	7.891319	-18.534840
H	5.998260	-3.419006	-17.538482
H	6.218103	-0.981002	-17.383350
H	5.167731	9.318406	-15.575729
H	6.602664	7.372679	-15.998010
H	7.502928	-3.290673	-21.572020
H	-1.705737	1.355121	-15.790766
H	-1.938251	0.749297	-17.462267
H	-1.323958	-0.343571	-16.215285
H	12.589086	3.761450	-20.157304
H	12.026637	5.423638	-20.519409
H	12.533321	5.012851	-18.874991
H	4.719046	-0.235670	-20.063061
H	4.226303	5.034943	-15.871474
N	6.592868	-4.907601	-19.663347
N	2.849441	9.837752	-16.780963
H	6.855294	-5.397410	-20.500525
H	6.239814	-5.447817	-18.893298
H	3.105590	10.539386	-16.108998
H	1.984343	9.955241	-17.278311

Fifteen Lowest Roots for *cis*-PBPB

Restricted Singlet Excited State 1:

Excitation energy = 0.0610906005 hartrees 1.66235982 eV 745.83 nm

excitation	X coeff.
377 => 379	0.33699
378 => 379	-0.92552
378 => 380	-0.11201

Transition dipole moment (debye):
X= -0.7055 Y= 3.6338 Z= -1.2782 Tot= 3.9161

Oscillator strength, f= 0.0967

Restricted Singlet Excited State 2:

Excitation energy = 0.0625676576 hartrees 1.70255259 eV 728.23 nm

excitation	X coeff.

```
 ------------   ---------
 377 =>  379    -0.90608
 377 =>  380    -0.17843
 378 =>  379    -0.35791

 Transition dipole moment (debye):
   X=     1.0060     Y=     1.8391     Z=    -1.2889  Tot=     2.4608

 Oscillator strength, f=     0.0391

--------------------------------------------------------------------------------
 Restricted Singlet Excited State   3:
---------------------------------------

 Excitation energy =  0.0638476678 hartrees      1.73738344 eV      713.63 nm

  excitation     X coeff.
 ------------   ---------
 377 =>  379     0.11622
 378 =>  380     0.98095

 Transition dipole moment (debye):
   X=    -1.6218     Y=    -1.3297     Z=    -3.3019  Tot=     3.9116

 Oscillator strength, f=     0.1008

--------------------------------------------------------------------------------
 Restricted Singlet Excited State   4:
---------------------------------------

 Excitation energy =  0.0659836862 hartrees      1.79550746 eV      690.52 nm

  excitation     X coeff.
 ------------   ---------
 377 =>  379     0.18899
 377 =>  380    -0.97047
 378 =>  380    -0.11217

 Transition dipole moment (debye):
   X=    -3.5429     Y=     0.4476     Z=     1.2379  Tot=     3.7795

 Oscillator strength, f=     0.0973

--------------------------------------------------------------------------------
 Restricted Singlet Excited State   5:
---------------------------------------
```

Excitation energy = 0.0759310259 hartrees 2.06618834 eV 600.06 nm

excitation	X coeff.
376 => 379	-0.99402

Transition dipole moment (debye):
X= -0.5525 Y= -0.2414 Z= -5.4369 Tot= 5.4702

Oscillator strength, f= 0.2345

Restricted Singlet Excited State 6:

Excitation energy = 0.0777532387 hartrees 2.11577327 eV 586.00 nm

excitation	X coeff.
376 => 380	-0.98776

Transition dipole moment (debye):
X= -0.2331 Y= 0.6236 Z= -3.2380 Tot= 3.3057

Oscillator strength, f= 0.0877

Restricted Singlet Excited State 7:

Excitation energy = 0.0839091082 hartrees 2.28328301 eV 543.01 nm

excitation	X coeff.
375 => 379	-0.99157

Transition dipole moment (debye):
X= -0.2253 Y= -2.1072 Z= -2.3713 Tot= 3.1803

Oscillator strength, f= 0.0876

Restricted Singlet Excited State 8:

Excitation energy = 0.0864608397 hartrees 2.35271915 eV 526.98 nm

excitation	X coeff.
375 => 380	0.98990

Transition dipole moment (debye):
X= -0.3522 Y= 1.7551 Z= -5.4193 Tot= 5.7073

Oscillator strength, f= 0.2906

Restricted Singlet Excited State 9:

Excitation energy = 0.0948538603 hartrees 2.58110486 eV 480.35 nm

excitation	X coeff.
372 => 379	0.16804
374 => 379	-0.85580
374 => 380	0.25715
377 => 379	0.11098
377 => 382	0.15426
378 => 381	-0.33998

Transition dipole moment (debye):
X= 2.2358 Y= -0.6118 Z= -0.2839 Tot= 2.3353

Oscillator strength, f= 0.0534

Restricted Singlet Excited State 10:

Excitation energy = 0.0963328717 hartrees 2.62135081 eV 472.98 nm

excitation	X coeff.
372 => 380	-0.14821
374 => 379	-0.44565
374 => 380	-0.58636
377 => 382	-0.18366
378 => 381	0.60161

Transition dipole moment (debye):

X= 1.8757 Y= 0.9499 Z= -0.1500 Tot= 2.1079

Oscillator strength, f= 0.0442

Restricted Singlet Excited State 11:

Excitation energy = 0.0988396557 hartrees 2.68956388 eV 460.98 nm

excitation	X coeff.
374 => 380	0.71487
375 => 381	0.10446
376 => 383	-0.15476
378 => 381	0.63986

Transition dipole moment (debye):
X= -1.4208 Y= 1.2562 Z= 0.2145 Tot= 1.9086

Oscillator strength, f= 0.0372

Restricted Singlet Excited State 12:

Excitation energy = 0.1056867332 hartrees 2.87588233 eV 431.12 nm

excitation	X coeff.
377 => 381	0.97270

Transition dipole moment (debye):
X= -0.7305 Y= -10.9434 Z= -0.5560 Tot= 10.9818

Oscillator strength, f= 1.3153

Restricted Singlet Excited State 13:

Excitation energy = 0.1097775026 hartrees 2.98719783 eV 415.05 nm

excitation	X coeff.
373 => 379	-0.11909

```
 378 =>  382    -0.97130

 Transition dipole moment (debye):
   X=     0.0965     Y=    -7.8524     Z=    -0.3643  Tot=     7.8615

 Oscillator strength, f=     0.7001

--------------------------------------------------------------------------------
 Restricted Singlet Excited State  14:
---------------------------------------

 Excitation energy =  0.1099973014 hartrees      2.99317886 eV      414.22 nm

  excitation     X coeff.
 ------------   ---------
 372 =>  379     0.11890
 374 =>  379     0.13804
 375 =>  383    -0.17290
 376 =>  381     0.73838
 376 =>  386     0.15620
 377 =>  382     0.12515
 378 =>  383    -0.54733

 Transition dipole moment (debye):
   X=    -4.6623     Y=    -0.0028     Z=     0.0219  Tot=     4.6624

 Oscillator strength, f=     0.2467

--------------------------------------------------------------------------------
 Restricted Singlet Excited State  15:
---------------------------------------

 Excitation energy =  0.1117001572 hartrees      3.03951593 eV      407.91 nm

  excitation     X coeff.
 ------------   ---------
 368 =>  379     0.11729
 373 =>  379     0.94633
 376 =>  382     0.12027
 378 =>  382    -0.11004

 Transition dipole moment (debye):
   X=     0.4579     Y=    -1.1293     Z=    -1.7251  Tot=     2.1121

 Oscillator strength, f=     0.0514
--------------------------------------------------------------------------------
```

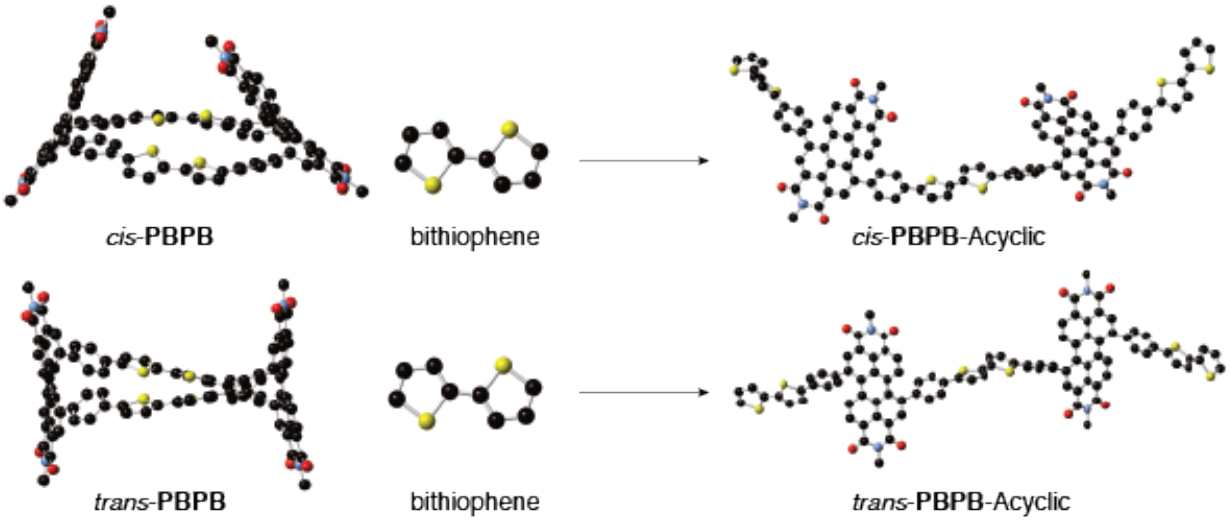

Table 4.3. Homodesmotic Calculations for Strain

Compound	Total energy (hartree)	Strain energy (hartree)	Strain energy (kcal/mol)
trans-**PBPB**	-5948.58245	0.033	21
cis-**PBPB**	-5948.57180	0.037	23
Bithiophene	-1104.82680	-	-
Trans-**PBPB-**Acyclic	-7053.44201	-	-
Cis-**PBPB-**Acyclic	-7053.43540		

Table 4.3: Table of energies for the Homodesmotic Reaction (enthalpy)

4.14. References

1. Brédas, J. L. *et al*. Organic semiconductors: A theoretical characterization of the basic parameters governing charge transport. *Proc. Natl. Acad. Sci.* **99**, 5804 LP – 5809 (2002).
2. Bendikov, M. *et al*. Tetrathiafulvalenes, Oligoacenenes, and Their Buckminsterfullerene Derivatives: The Brick and Mortar of Organic Electronics. *Chem. Rev.* **104**, 4891–4946 (2004).
3. Newman, C. R. *et al*. Introduction to Organic Thin Film Transistors and Design of n-Channel Organic Semiconductors. *Chem. Mater.* **16**, 4436–4451 (2004).
4. Anthony, J. E. Functionalized Acenes and Heteroacenes for Organic Electronics. *Chem. Rev.* **106**, 5028–5048 (2006).
5. Murphy, A. R. *et al*. Organic Semiconducting Oligomers for Use in Thin Film Transistors. *Chem. Rev.* **107**, 1066–1096 (2007).
6. Onwubiko, A. *et al*. Fused electron deficient semiconducting polymers for air stable electron transport. *Nat. Commun.* **9**, 416 (2018).
7. Lin, Y. *et al*. Stacked pentacene layer organic thin-film transistors with improved characteristics. *IEEE Electron Device Lett.* **18**, 606–608 (1997).

8. Gundlach, D. J. *et al*. Thin-film transistors based on well-ordered thermally evaporated naphthacene films. *Appl. Phys. Lett.* **80**, 2925–2927 (2002).

9. Coropceanu, V. *et al.* Charge Transport in Organic Semiconductors. *Chem. Rev.* **107**, 926–952 (2007).

10. Kroto, H. W. *et al*. C60: Buckminsterfullerene. *Nature* **318**, 162–163 (1985).

11. Haddon, R. C. *et al.* C60 thin film transistors. *Appl. Phys. Lett.* **67**, 121–123 (1995).

12. Li, H. *et al.* High-Mobility Field-Effect Transistors from Large-Area Solution-Grown Aligned C60 Single Crystals. *J. Am. Chem. Soc.* **134**, 2760–2765 (2012).

13. Zhang, Y. *et al*. Development of fullerenes and their derivatives as semiconductors in field-effect transistors: exploring the molecular design. *J. Mater. Chem. C* **6**, 3514–3537 (2018).

14. Dou, L. *et al.* 25th Anniversary Article: A Decade of Organic/Polymeric Photovoltaic Research. *Adv. Mater.* **25**, 6642–6671 (2013).

15. Savoie, B. M. *et al*. Mesoscopic Features of Charge Generation in Organic Semiconductors. *Acc. Chem. Res.* **47**, 3385–3394 (2014).

16. Savoie, B. M. *et al.* Unequal Partnership: Asymmetric Roles of Polymeric Donor and Fullerene Acceptor in Generating Free Charge. *J. Am. Chem. Soc.* **136**, 2876–2884 (2014).

17. Gong, X. *et al.* High-Detectivity Polymer Photodetectors with Spectral Response from 300 nm to 1450 nm. *Science.* **325**, 1665–1667 (2009).

18. Nielsen, C. B. *et al*. Non-Fullerene Electron Acceptors for Use in Organic Solar Cells. *Acc. Chem. Res.* **48**, 2803–2812 (2015).

19. Ball, M. *et al.* Contorted Polycyclic Aromatics. *Acc. Chem. Res.* **48**, 267–276 (2015).

20. Yan, C. *et al.* Non-fullerene acceptors for organic solar cells. *Nat. Rev. Mater.* **3**, 18003 (2018).

21. Zhang, J. *et al*. Material insights and challenges for non-fullerene organic solar cells based on small molecular acceptors. *Nat. Energy* **3**, 720–731 (2018).

22. Hou, J. *et al*. Organic solar cells based on non-fullerene acceptors. *Nat. Mater.* **17**, 119 (2018).

23. Ball, M. *et al.* Conjugated Macrocycles in Organic Electronics. *Acc. Chem. Res.* (2019). doi:10.1021/acs.accounts.9b00017

24. Mandoc, M. M. *et al*. Trap-limited electron transport in disordered semiconducting polymers. *Phys. Rev. B* **75**, 193202 (2007).

25. Kaake, L. G. *et al*. Intrinsic Charge Trapping in Organic and Polymeric Semiconductors: A Physical Chemistry Perspective. *J. Phys. Chem. Lett.* **1**, 628–635 (2010).

26. Arias, A. C. *et al*. Materials and Applications for Large Area Electronics: Solution-Based Approaches. *Chem. Rev.* **110**, 3–24 (2010).

27. Nicolai, H. T. *et al.* Unification of trap-limited electron transport in semiconducting polymers. *Nat. Mater.* **11**, 882–887 (2012).

28. Iwamoto, T. *et al*. Selective and Random Syntheses of n Cycloparaphenylenes (n=8-13) and

Size Dependence of Their Electronic Properties. *J. Am. Chem. Soc.* **133**, 8354–8361 (2011).

29. Ball, M. *et al.* Macrocyclization in the Design of Organic n-Type Electronic Materials. *J. Am. Chem. Soc.* **138**, 12861–12867 (2016).

30. Iyoda, M. *et al*. Conjugated Macrocycles: Concepts and Applications. *Angew. Chem. Int. Ed.* **50**, 10522–10553 (2011).

31. Iwamoto, T. *et al.* Size- and Orientation-Selective Encapsulation of C70 by Cycloparaphenylenes. *Chem. Eur. J.* **19**, 14061–14068 (2013).

32. Nakanishi, Y. *et al.* Size-Selective Complexation and Extraction of Endohedral Metallofullerenes with Cycloparaphenylene. *Angew. Chem. Int. Ed.* **53**, 3102–3106 (2014).

33. Zhang, B. *et al.* Hollow organic capsules assemble into cellular semiconductors. *Nat. Commun.* **9**, 1957 (2018).

34. Huang, Q. *et al.* Photoconductive Curved-Nanographene/Fullerene Supramolecular Heterojunctions. *Angew. Chem. Int. Ed.* **58**, 6244 (2019).

35. Nakamura, T. *et al*. Double-Circularly Connected Saloph-Belt Macrocycles Generated from a Bis-Armed Bifunctional Monomer. *J. Am. Chem. Soc.* **141**, 6462-6467 (2019).

36. Darzi, E. R. *et al.* Synthesis, Properties, and Design Principles of Donor–Acceptor Nanohoops. *ACS Cent. Sci.* **1**, 335–342 (2015).

37. Zhang, B. *et al.* Rigid, Conjugated Macrocycles for High Performance Organic Photodetectors. *J. Am. Chem. Soc.* **138**, 16426–16431 (2016).

38. Van Raden, J. M. *et al*. Synthesis and characterization of a highly strained donor-acceptor nanohoop. *Org. Biomol. Chem.* **14**, 5721 (2016).

39. Kayahara, E. *et al.* Gram-Scale Syntheses and Conductivities of {[}10]Cycloparaphenylene and Its Tetraalkoxy Derivatives. *J. Am. Chem. Soc.* **139**, 18480–18483 (2017).

40. Nishigaki, S. *et al.* Synthesis, Structures, and Photophysical Properties of Alternating Donor–Acceptor Cycloparaphenylenes. *Chem. Eur. J.* **23**, 7227–7231 (2017).

41. Ball, M. L. *et al.* Influence of Molecular Conformation on Electron Transport in Giant, Conjugated Macrocycles. *J. Am. Chem. Soc.* **140**, 10135–10139 (2018).

42. Ball, M. *et al.* Chiral Conjugated Corrals. *J. Am. Chem. Soc.* **137**, 9982–9987 (2015).

43. Zaumseil, J. *et al*. Electron and Ambipolar Transport in Organic Field-Effect Transistors. *Chem. Rev.* **107**, 1296–1323 (2007).

44. Dimitrakopolous, C.D. *et al*. Organic Thin Film Transistors for Large Area Electronics. *Adv. Mater.* **14**, 99–117 (2002).

45. Anthony, J. E. *et al*. n-Type Organic Semiconductors in Organic Electronics. *Adv. Mater.* **22**, 3876–3892 (2010).

46. Chen, Z. *et al*. Effect of Core Twisting on Self-Assembly and Optical Properties of Perylene Bisimide Dyes in Solution and Columnar Liquid Crystalline Phases. *Chem. Eur. J.* **13**, 450–465 (2007).

47. Kaiser, T. E. *et al*. Fluorescent J-Aggregates of Core-Substituted Perylene Bisimides:

Studies on Structure−Property Relationship, Nucleation−Elongation Mechanism, and Sergeants-and-Soldiers Principle. *J. Am. Chem. Soc.* **131**, 6719–6732 (2009).

48. Würthner, F. *et al.* Perylene Bisimide Dye Assemblies as Archetype Functional Supramolecular Materials. *Chem. Rev.* **116**, 962–1052 (2016).
49. George, P. *et al*. An alternative approach to the problem of assessing stabilization energies in cyclic conjugated hydrocarbons. *Theor. Chim. Acta* **38**, 121–129 (1975).
50. Bachrach, S. M. *et al*. DFT Study of Cycloparaphenylenes and Heteroatom-Substituted Nanohoops. *J. Org. Chem.* **75**, 6595–6604 (2010).
51. Segawa, Y. *et al*. Theoretical Studies on the Structures and Strain Energies of Cycloparaphenylenes. *Org. Lett.* **12**, 2262–2265 (2010).
52. You, J. B. *et al.* A polymer tandem solar cell with 10.6% power conversion efficiency. *Nat. Commun.* **4**, 10 (2013).
53. Ahrens, M. J. *et al*. Bis(n-octylamino)perylene-3,4:9,10-bis(dicarboximide)s and Their Radical Cations: Synthesis, Electrochemistry, and ENDOR Spectroscopy. *J. Org. Chem.* **71**, 2107–2114 (2006).
54. Goretzki, G. *et al.* Building Multistate Redox-Active Architectures Using Metal-Complex Functionalized Perylene Bis-imides. *Inorg. Chem.* **48**, 10264–10274 (2009).
55. Dubey, R. K. *et al*. 1,7- And 1,6-Regioisomers of Diphenoxy and Dipyrrolidinyl Substituted Perylene Diimides: Synthesis, Separation, Characterization, and Comparison of Electrochemical and Optical Properties. *Chem. Mater.* **23**, 778–788 (2011).
56. Dubey, R. K. *et al.* Direct Evidence of Significantly Different Chemical Behavior and Excited-State Dynamics of 1,7- and 1,6-Regioisomers of Pyrrolidinyl-Substituted Perylene Diimide. *Chem. Eur. J.* **19**, 6791–6806 (2013).
57. Xu, B. *et al*. Measurement of Single-Molecule Resistance by Repeated Formation of Molecular Junctions. *Science.* **301**, 1221–1223 (2003).
58. Venkataraman, L. *et al*. Dependence of single-molecule junction conductance on molecular conformation. *Nature* **442**, 904 (2006).
59. Hybertsen, M. S. *et al.* Amine-linked single-molecule circuits: systematic trends across molecular families. *J. Phys. Condens. Matter* **20**, 374115 (2008).
60. Su, T. A. *et al*. Chemical principles of single-molecule electronics. *Nat. Rev. Mater.* **1**, 16002 (2016).
61. Rajasingh, P. *et al*. Selective Bromination of Perylene Diimides under Mild Conditions. *J. Org. Chem.* **72**, 5973–5979 (2007).
62. Blanc, E. *et al*. The evaluation of transmission factors and their first derivatives with respect to crystal shape parameters. *J. Appl. Crystallogr.* **24**, 1035–1041 (1991).
63. Clark, R. C. *et al*. The analytical calculation of absorption in multifaceted crystals. *Acta Crystallogr. Sect. A* **51**, 887–897 (1995).
64. Oxford Diffraction/Agilent Technologies UK Ltd. Version 1.171.37.35. (2014).
65. Sheldrick, G. M. Crystal structure refinement with {\it SHELXL}. *Acta Crystallogr. Sect.*

C **71**, 3–8 (2015).

66. Dolomanov, O. V *et al*. {\it OLEX2}: A complete structure solution, refinement and analysis program. *J. Appl. Crystallogr.* **42**, 339–341 (2009).

67. Spek, A. L. Structure validation in chemical crystallography. *Acta Crystallogr. Sect. D* **65**, 148–155 (2009).

68. van der Sluis, P *et al*. BYPASS: an effective method for the refinement of crystal structures containing disordered solvent regions. *Acta Crystallogr. Sect. A* **46**, 194–201 (1990).

69. Crystalmaker Software Ltd.

Chapter 5. Rigid, Conjugated Macrocycles for High Performance Organic Photodetectors

5.1. Preface

Chapter 5 is reproduced with permission from the authors: Boyuan Zhang, M. Tuan Trinh, Brandon Fowler, Melissa Ball, Qizhi Xu, Fay Ng, Michael L. Steigerwald, X.-Y. Zhu, Colin Nuckolls, and Yu Zhong published in the *Journal of the American Chemical Society*.[1] Copyright 2016 American Chemical Society. Brandon Fowler and I synthesized all the compounds. I performed DFT calculations, with essential input from Michael L. Steigerwald. Boyuan Zhang and Yu Zhong fabricated and characterized all the devices with assistance from Qizhi Xu. M. Tuan Trinh conducted TA measurements and data analysis.

5.2. Introduction

Chapter 5 describes a new molecular design for creating OPDs with unparalleled ability to detect photons. The use of organic materials as the active component in photodetectors is attractive because of the potential ease of their fabrication as light-weight and mechanically flexible devices.[2–5] One critical parameter that limits OPDs performance is high dark current, because it determines the noise current level and sensitivity of an OPD. The current state-of-the-art for OPDs employs a number of modifications such as, carrier blocking layers,[6] vertical phase separation[7] and thick active layers,[8] to lower the dark current. An alternative approach is to use reaction chemistry to build the desired properties into the structure of the active molecule to minimize the charge carriers in the active layers.

The dark current in organic, electronic materials is multi-faceted, and its origins are not completely understood. Covalent defects formed upon photo/thermo-activation[9–11] and mechanically deformed sp^2 carbon-carbon bonds in π-conjugated molecules are known to produce charged defects that introduce carriers.[12–14] Fullerenes, which are one of the most ubiquitous organic electronic materials, undergo a facile dimerization when irradiated.[9,10] This also

contributes to the dark current.[12] To address these issues, we designed a macrocycle that consists of PDI and biphenyl moieties wrapped into a tetrameric structure and call this **$(PPh_2)_4$** (Figure 1B.1 and 5.1).[15]

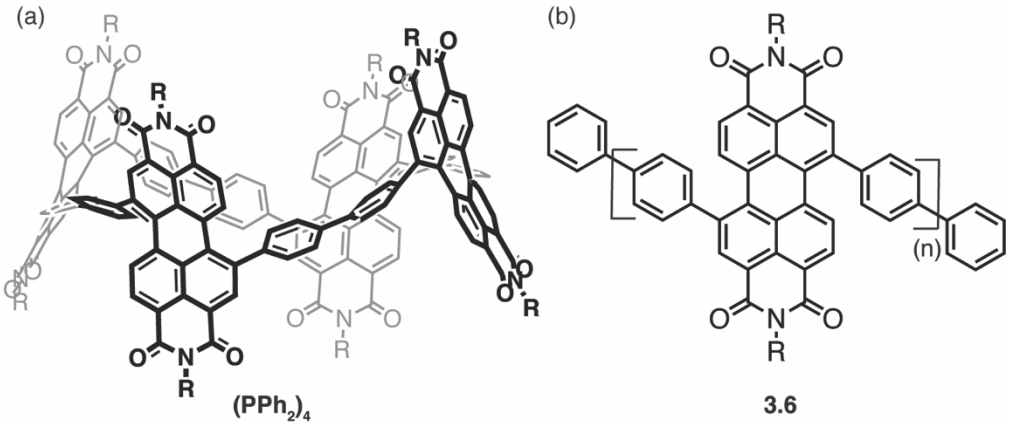

Figure 5.1. (a) Molecular structure of **$(PPh_2)_4$**. (b) Energy minimized structures from DFT for **$(PPh_2)_4$**. Carbon = gray, nitrogen = blue, oxygen = red. Hydrogen atoms have been removed to clarify the view. A methyl group substitutes the sidechains in the calculations. The methyl group, too, has been removed to clarify the view in the structures presented here.

We find **$(PPh_2)_4$**-based OPDs have high sensitivity for visible light detection in a simple device structure. The macrocycle contains several key design elements to yield the highly sensitive OPD result: (1) the rigid structure, constrained in a ring, minimizes the number of charged defects originating from deformed sp^2 carbons; (2) no covalent defects are formed upon photo/thermo-activation; (3) it is efficacious at transporting electrons; (4) and it has high visible light absorption that yields significant photocurrent in a bulk heterojunction photodiode.[15] Using this design we are able to suppress the dark current density while retaining high responsivity in an ultra-sensitive non-fullerene OPD. Without the need for extra carrier blocking layers, the highest detectivity in our device approaches 10^{14} Jones at near zero bias voltage. This detectivity is comparable to the best fullerene-based photodetectors, and the sensitivity at low working voltages (< 0.1 V) is a record for non-fullerene OPDs. A direct comparison between **$(PPh_2)_4$** and an acyclic, polymeric

control molecule (Compound **3.6**) reveals that **$(PPh_2)_4$**'s superior performance originates from its rigid, conjugated, and macrocyclic structure (Figure 5.1).

5.3. OPD Results for $(PPh_2)_4$

Chapter 3 described **$(PPh_2)_4$** as an n-type semiconductor that transports electrons in both field effect transistors and solar cells. **$(PPh_2)_4$**'s ~ 2 nm diameter interior cavity is large enough to thread donor polymers (Figure 1B.4); its branched sidechains impart high solubility in common organic solvents. In solution, the lowest-energy absorption peak at 585 nm has an extinction coefficient of 7.9×10^4 $M^{-1}cm^{-1}$ (Figure 1B.6). The active layer of the photodetector is a blended film of **$(PPh_2)_4$** and the commercially available polymer donor PTB7-Th.[16,17] The absorption of PTB7-Th is shifted to lower energy relative to **$(PPh_2)_4$** (Figure 5.2a). Figure 5.2b shows a model of a simple device structure that was used in this study. Figure 5.2c contains the energy diagram of the materials used in this device. We note the energy offset between the donor's LUMO and the acceptor's LUMO is well-matched (Figure 5.2c); energy levels were estimated from CV.[15,16] The thickness of the active film is ~150 nm.

Figure 5.2d displays the current-voltage curves for a typical OPD under dark conditions and simulated AM 1.5G irradiation (100 $mWcm^{-2}$). One of the exciting findings is that the OPD

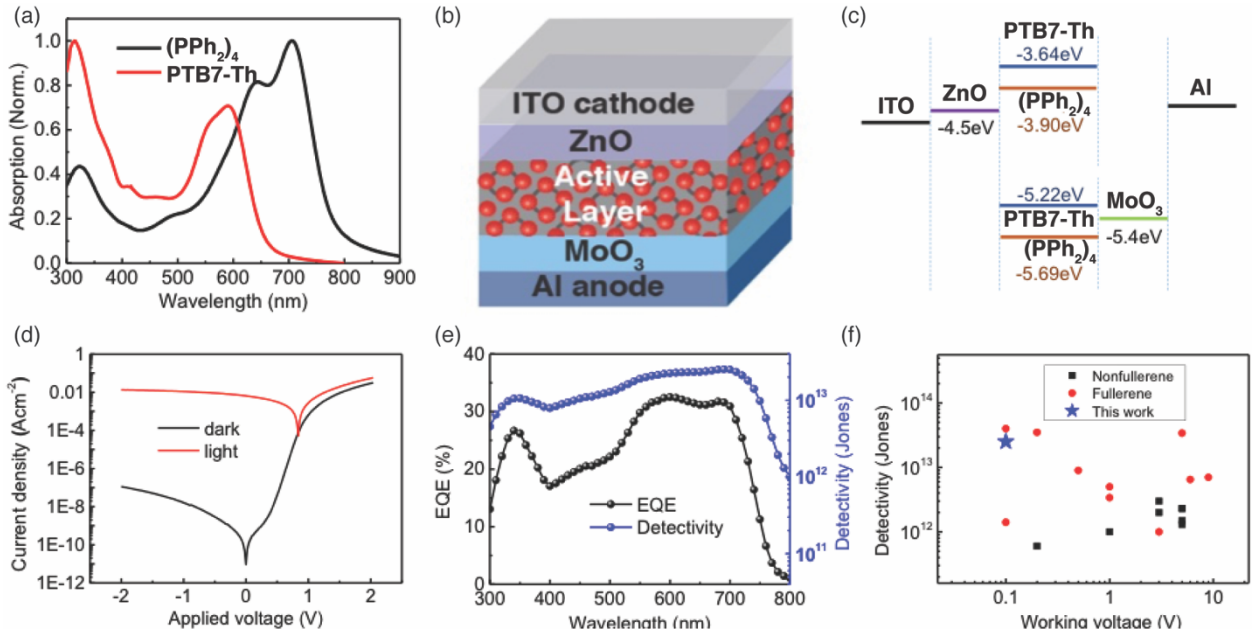

Figure 5.2. (a) Normalized film absorption spectra of PTB7-Th and **$(PPh_2)_4$**. (b) Device structure for the inverted organic photodetector. (c) Schematic of the energy levels of ITO, ZnO, PTB7-Th, **$(PPh_2)_4$**, MoO_3 and Al. Energy levels of PTB7-Th and **$(PPh_2)_4$** were estimated from cyclic voltammetry measurements in solution and adopted from ref. 16 and ref. 15, respectively. (d) Current density-voltage curves under dark condition and simulated AM 1.5 G irradiation (100mWcm^{-2}). (e) External quantum efficiency and specific detectivity spectra calculated at -0.1 V bias voltage. (f) Comparison of detectivity and working voltage in reported organic photodetectors and this work.

possesses extremely small dark current at reverse bias voltage. The dark *J-V* curve shows a high rectification ratio of >10^5 at ±2 V and a dark current density as small as 1.4×10^{-10} Acm^{-2} at -0.1 V. This dark current density is one order of magnitude lower than the best fullerene-free OPDs[8] and comparable with fullerene-based OPDs and perovskite photodetectors.[5,6] Notably, both fullerene-based OPDs and perovskite photodetectors need extra electron or hole blocking layers in order to achieve a low level of the dark current.[6,17] Equally important is the large photocurrent that is generated upon photoexcitation at small reverse bias voltages. The on/off ratio is >10^7 calculated at -0.1 V under simulated AM 1.5G irradiation (100 mWcm^{-2}). The OPD device described here can operate at small bias voltages and even at zero bias. This compares favorably with previously reported non-fullerene OPDs; they require much larger reverse bias voltages (typically -1V ~ -3 V) to operate due to the poor carrier extraction.[18–20]

Ultralow dark current could result from poor carrier transport ability. This is not the case for **$(PPh_2)_4$**. As discussed above, **$(PPh_2)_4$** effectively transports electrons generated upon photoexcitation. This allows the OPD to operate at a small bias voltage. We inherently achieve high photocurrent and low dark current simultaneously in the **$(PPh_2)_4$** OPD with a thin active layer and a simple device structure. **$(PPh_2)_4$** is an ideal design for an electron acceptor to create a highly sensitive non-fullerene OPD.

Table 5.1. A Summary of Responsivity, Detectivity, and EQE.

	J_d (Acm^{-2})	EQE (%)	R (AW^{-1})	D* (Jones)
$(PPh_2)_4$	1.5×10-10	33, 600nm	0.18, 690nm	2.5×10^{13}, 690nm
$PC_{71}BM$	5.6×10-7	70, 640nm	0.39, 710nm	9.2×10^{11}, 710nm
3.6	1.0×10-9	22, 350nm	0.09, 680nm	4.8×10^{12}, 680nm

Table 5.1: A summary of responsivity, detectivity, and EQE.

Table 5.1 summarizes the responsivity (R), specific detectivity (D^*), EQE and dark current (J_d) for the OPD device data for the PTB7-Th: **$(PPh_2)_4$** blended films. The devices have a linear dynamic range (LDR) > 140 dB (Figure 5.5) and cutoff frequency of 467 kHz (Figure 5.6). Overall the device characteristics are excellent. We find that the specific detectivity is more than 10^{13} Jones over the whole visible light region at -0.1V. The highest D^* was calculated to be 2.5×10^{13} Jones at 700nm (Figure 5.2e). At zero bias, the calculated specific detectivity is as high as 1×10^{14} Jones. These values are among the highest detectivities for the state-of-the-art fullerene photodetector[2,6,7,18,21–25] and much higher than the best non-fullerene OPDs[7,23-25,30,31,34] (Figure 5.2f). Moreover, the **$(PPh_2)_4$**-based OPD requires much smaller working voltage compared with other non-fullerene OPDs[2,6–8,20–22,25,26] because of their relatively high responsivity (R) near zero bias voltage (Figure 5.2f).

5.4. Transient Absorption Shows Fast Charge Separation

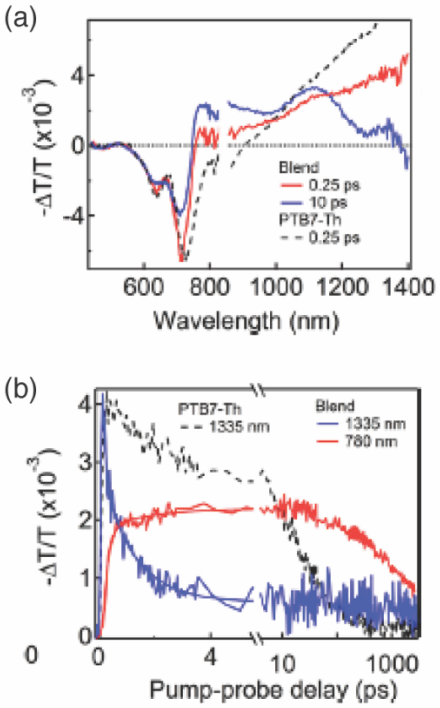

Figure 5.3. Transient absorption spectra (b) and dynamics (b) for the neat film of PTB7-Th and blended film of **$(PPh_2)_4$** and PTB7-Th pumped at 710 nm. The dashed-black curves are from PTB7-Th which were scaled for comparison.

One of the two key parameters responsible for high responsivity (*R*) is efficient charge generation from photo-excitation in the active layer. Extensive research on molecular donor/acceptor interfaces has pointed to the critical role of electronic delocalization in facilitating efficient charge separation at the donor/acceptor interfaces.[27,28] In particular, the spherical fullerene based electron acceptors are believed to transport charge efficiently due to their three dimensional connectivity in ensuring electronic delocalization on the acceptor side.[29,30] Can **$(PPh_2)_4$** provide similar connectivity and electronic delocalization that is necessary for charge separation? While the high responsivity near zero bias suggests the answer above is affirmative, we further support this by studying the efficient charge separation at the PTB7-Th/**$(PPh_2)_4$** interface using transient absorption (TA) spectroscopy (Figure 5.3).

The linear absorption spectra in Figure 5.2a show that the donor material, PTB7-Th can be selectively excited at 710 nm in the blended film; subsequently, we can monitor electron transfer from PTB7-Th to **$(PPh_2)_4$**. At a short pump-probe delay (0.25 ps), we observe features arising from PTB7-Th (red curve in Figure 5.3a) with the bleaching at 630 and 715 nm and excited state absorption (ESA) in the near IR range. This is similar to the TA spectrum from the neat PTB7-Th film (black dashed curve in Figure 5.3a). The bleaching in PTB7-Th is reduced and new ESA transitions from 770 to 1300 nm evolve as the delay time increases. These new ESA features centered at 840 and 1120 nm are attributed to the charge (polaron) absorptions in the PDI and PTB7-Th moieties, respectively.[13,31,32] While the ESA of the PTB7-Th singlet dominates in the long probe wavelength range (> 1300 nm), the ESA of charges in either donor or acceptor materials is negligible. Thus, dynamics at 1335 nm are a good measure of exciton dissociation at the donor/acceptor interface. Figure 5.3b shows that the biexponential fit (blue curve) to the dynamics at 1335 nm (blue dots) yields time constants of 0.11 ± 0.04 ps (42% weight) and 1.2 ± 0.1 ps (58% weight). The charge buildup monitored by polaron ESA at 780 nm (red dots) gives nearly identical time constants (red curve). These time constants indicate ultrafast electron transfer from PTB7-Th to **$(PPh_2)_4$**. The short time constant can be attributed to the instantaneous charge transfer near the interface upon photoexcitation, while the longer time constant is attributed to exciton diffusion in PTB7-Th prior to the dissociation event.[13,32] For comparison, the singlet exciton lifetime in neat PTB7-Th is of the order of nanoseconds (black dashed curve in Figure 5.3b). This is much longer than that in the blend. We also observe similarly ultrafast hole transfer from **$(PPh_2)_4$** to PTB7-Th when both donor and acceptor are excited at 560 nm. These measurements confirm that **$(PPh_2)_4$** photodetector performance is comparable, if not better than that of a fullerene, for exciton dissociation in blend films.[33–35]

The second important parameter that determines the high detectivity in these devices is the dark current density. To gain insight into the origin of the device characteristics, we analyze the *J-V* curve under dark conditions to calculate the reverse saturation dark current J_0. The fitting method is detailed in the Appendix. The saturation dark current density is as low as 7.7×10^{-13} Acm^{-2} (Figure 5.8). The intrinsic conductivity is determined by the intrinsic free carrier density and the mobility. Photocurrent and thin film field effect transistor measurements reveal efficacious electron transporting ability.[36] Therefore, such a low level of J_0 indicates a small amount of intrinsic free carrier density. To verify that the intrinsic conductivity of the thin films is dominated by the charged defects, we measured the dependence of the dark current density on temperature. The activation energies are calculated to be (0.15 ± 0.01) eV and (0.20 ± 0.01) eV at -2 V and -0.5 V, respectively (Figure 5.9). These values are much smaller than the band gaps of the active organic components (Figure 5.2c) and are consistent with thermal activation energy of locally bound charged defects.[12,37]

5.5 $PC_{71}BM$ Shows High Dark Current Density

To better understand the origin of the low density of charged defects in **$(PPh_2)_4$**, we made a direct comparison between a $PC_{71}BM$ and **$(PPh_2)_4$**-based OPD with the same device structure as shown in Figure 5.2b. Although the responsivity (*R*) of the $PC_{71}BM$-based OPD is approximately two fold higher than that of the **$(PPh_2)_4$**-based device (Table 5.1 and Figure 5.11), the dark current of the $PC_{71}BM$-based device is 2-3 orders of magnitude higher than that of the **$(PPh_2)_4$**-based one (Figure 5.4a). It is obvious that the dark current level dominates the detectivity in this type of OPD. Thus, the detectivity of the **$(PPh_2)_4$**-based OPD is more than one order of magnitude higher than that of the $PC_{71}BM$-based one (Figure 5.4b). One of the origins of the high dark current is from the chemistry of fullerenes. $PC_{71}BM$ is known to undergo dimerization that is initiated by electron

donors, metals, and photons.[9–11,38,39] In each of these cases, in a solid state film, the partners need to be unencumbered and in the correct orientation for the reaction to occur. In the absence of these conditions, the films will contain carriers that contribute to the relatively high dark current.[9–11] Fullerene-based OPDs made with fullerenes require extra blocking layers to minimize this relatively high dark current. Compared with fullerenes, PDIs are known to exhibit exceptional chemical, thermal and photochemical stability.[40–43] They have also been widely used as building blocks to construct macrocycles.[44–53] The PDI units in **$(PPh_2)_4$** have no readily accessible pathway to introduce these same type of covalent defects. This accounts for the low intrinsic conductivity in **$(PPh_2)_4$** OPDs.[12]

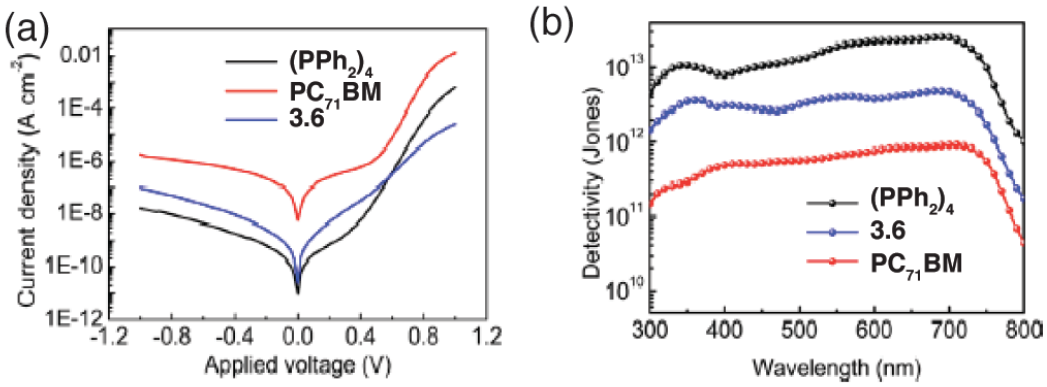

Figure 5.4. (a) Dark current density-voltage curves for $PC_{71}BM$, **3.6**, and **$(PPh_2)_4$** based photodetectors with the same device structure as shown in Figure 5.2b. (b) Specific detectivity spectra for **$(PPh_2)_4$**, **3.6** and $PC_{71}BM$ based OPDs calculated at -0.1V bias voltage.

5.6. Rigid Macrocyclic Design Impedes Charge Defects

In order to assess the importance of the cyclic, rigid structure of **$(PPh_2)_4$**, we fabricated a **3.6**-based OPD (Figure 5.1b). Overall, the **3.6** photodetector performs very well and shows high sensitivity. Although the responsivity of the **3.6** OPD is about one fourth of that in the $PC_{71}BM$ OPD, the dark current density in the **3.6** OPD is one order of magnitude lower than that in the $PC_{71}BM$ OPD (Figure 5.4a). As a result, the **3.6** OPD shows a doubling of the detectivity compared to the $PC_{71}BM$ OPD (Figure 5.4b). These results, once again, suggest that dark current dominates

the sensitivity and confirm the importance of incorporating chemically stable PDIs into electron acceptors in OPDs. Even so, the **3.6** OPD is still not as effective as the **$(PPh_2)_4$** OPD in terms of detectivity. As a comparison, the **3.6**-based OPD has a dark current 1.0×10^{-9} Acm^{-2} at -0.1 V, which is about ten-fold higher than that of the **$(PPh_2)_4$**-based device (see Table 5.1 and Figure 5.4a). In addition, the **3.6**-based OPD also shows lower responsivity compared to **$(PPh_2)_4$** devices (Table 5.1 and Figure 5.11). The resulting peak D^* for the **3.6**-based OPD is 4.8×10^{12} Jones at 680 nm, only about one third of the peak value in the **$(PPh_2)_4$**-based OPD. This is because intrinsic, charged defects in linear polymer semiconductors originate from endgroups[13,54,55] and deformed sp^2 carbons near the rotatable C-C single bonds.[12–14,56] The torsional effect is inevitable in linear molecules with flexible backbones. These problems are reduced by winding linear molecules into rigid, conjugated macrocycles with no endgroups.[15,36,57] The macrocyclic **$(PPh_2)_4$** possesses a locked conformation with higher rigidity (Figure 5.1a) and is expected to create fewer locally charged defects relative to the linear polymeric counterpart.

5.7. Conclusion

The results described above show that the rigid, cyclic molecular structure is an important design criterion to achieve ultralow intrinsic conductivity in OPDs. We found that the rigid, conjugated macrocycle is able to act as the electron acceptor in high performance OPDs. Using this molecular design, we suppress dark current density while retaining high responsivity in an ultra-sensitive non-fullerene OPD. Without the need for extra carrier blocking layers, this detectivity is comparable to the best fullerene-based photodetectors, and the sensitivity at low working voltages is a record for non-fullerene OPDs. It is clear from this study that the devices can be further improved by designing the electron donating material to form a shape and electronic match for these macrocyclic electron acceptors.

5.8. Appendix – Supplementary Figures

The linear dynamic range (LDR) is expressed as LDR=20log(J_{high}/J_d), where J_{high} is the highest measurable current density in the linear response range and J_d is the dark current density.

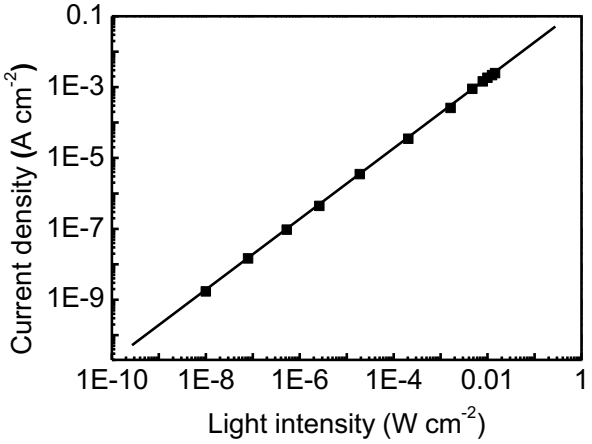

Figure 5.5. Linear dynamic range of the **$(PPh_2)_4$**-based OPD. A red light emitting diode (λ=625nm) was used as the light source.

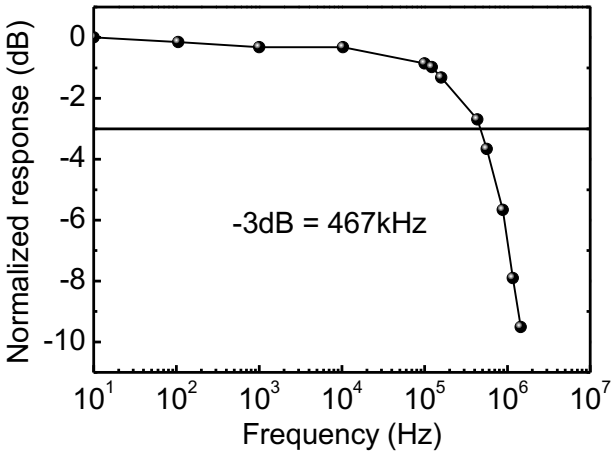

Figure 5.6. Frequency response of the **$(PPh_2)_4$**-based OPD. The device area is 0.09 cm^2.

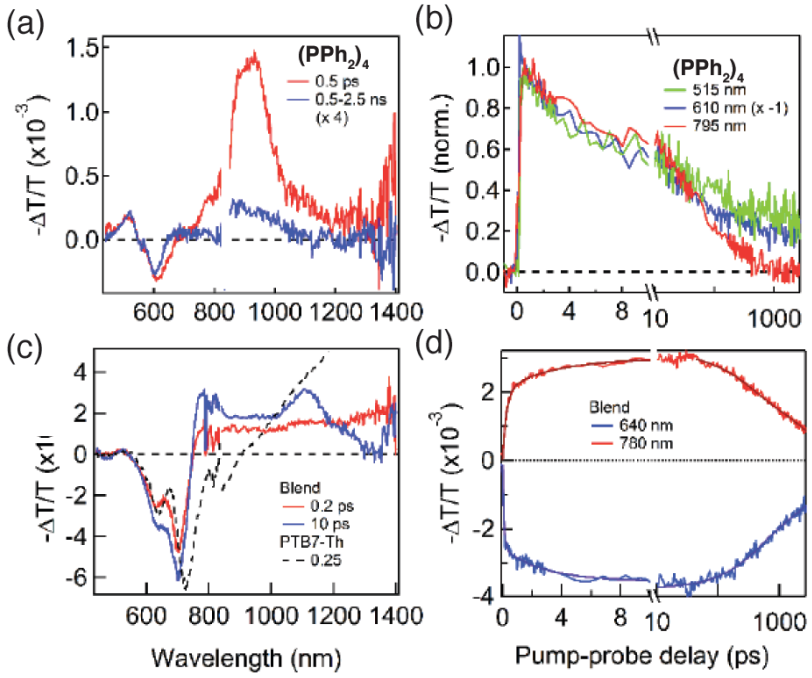

Figure 5.7. Transient absorption spectra and dynamics for the neat **$(PPh_2)_4$** (a, b) and the blended film of **$(PPh_2)_4$** and PTB7-Th (c,d) upon 560 nm excitation. The dashed-black curve in (c) is the spectrum from PTB7-Th upon the excitation of 710 nm. The signal from PTB7-th was scaled for comparison.

Figure 5.7a,b show the differential transmission spectra and dynamics for the neat film **$(PPh_2)_4$** upon 560 nm excitation. The negative feature centered at 600 nm is attributed to a bleaching of the ground state absorption under the presence of photo-excited excitons/charges. The positive features centered at 500 nm and from 700 nm to near IR are the excited state absorption (ESA) of the photo-excited excitons or charges. The ESA feature at 785 nm decays biexponentially with the time constants of 8 ± 0.7 ps (52%) and 122 ± 8 ps (48%) (red curve, Figure 5.7b). This feature is assigned to the singlet ESA, $S_1 \rightarrow S_N$ transition, similar to that of other PDI derivative compounds.

The ESA dynamics at 500 nm and ground state bleaching, however, behave differently. More than 50 % of the ESA signal at 500 nm decays with a time constant that is similarly to the dynamics at 785 nm. The remaining signal (20%) lasts for a long time, ns time scale (green and

blue curves). The long living signal can either come from photo-excited charges or from triplet excitons.

At the same excitation wavelength, 560 nm, for the blend of **$(PPh_2)_4$** and PTB7-Th, we observed the dominance of ground state bleaching from PTB7-Th at the range of 575-750 nm (Figure 5.7c, the dashed-black curve is from the neat PTB7-Th pumping at 710 nm). Note that at this excitation wavelength, we excite both donor and acceptor materials. The ESA cross section and the ground state bleaching from the polymer are much stronger than that of **$(PPh_2)_4$** resulting in a dominant feature from the polymer even when we excited both materials at 560 nm. At the longer time (10 ps, Figure S4 C), the bleaching from PTB7-Th increases and the hole ESA feature in PTB7-Th at 1100 nm appears. The increase of bleaching feature from PTB7-Th indicates the hole transfers from **$(PPh_2)_4$** to PTB7-Th. Since the ESA cross session at 780 nm for singlet in **$(PPh_2)_4$** is very small compared to that of charge ESA (compare Figure 5.7a,c), the ESA signal at this wavelength reflects the dynamics of charge generation from exciton dissociation. The fit to the dynamics at 780 nm gives two time constants, 0.2 ± 0.02 ps and 3.3 ± 0.4 ps (Figure 5.7d). These time constants reflect the electron and hole transfer upon 560 nm excitation. In addition, we observed a much longer charge lifetime in the blends (on the nanosecond time scale) when compared to that of the exciton dynamics in the neat films (Figure 5.7b,d). The longer charge lifetime is due to exciton dissociated into separating charges rather than charge transfer excitons.

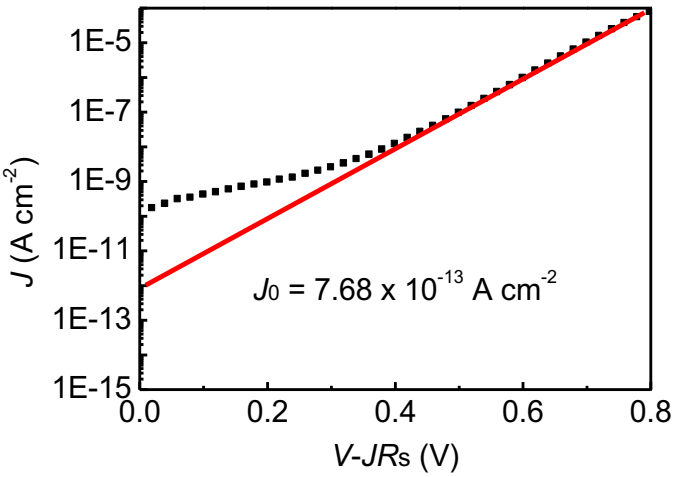

Figure 5.8. The device structure is ITO/ZnO/PBDTT-TT:**(PPh$_2$)$_4$** /MoO_3/Al. The original *J-V* curve is shown in Figure 5.2c Plot of d*V*/d*J* vs J^{-1} and linear fitting. (b) ln(*J*) vs (*V*-*JR*$_s$) and linear fitting. The J_0 is calculated to be 7.68×10^{-13} Acm^{-2}.

The dark current-voltage characteristics are described by $J_d=J_0\{\exp[e(V-JR_s)/nk_BT]-1\}$, where J_d is the dark current density, J_0 is the dark saturate current density, *V* is the applied voltage, n is the ideality factor, k_B is the Boltzmann constant, T is the temperature and e is the electron charge. The fitting method is described in ref. 17.[17]

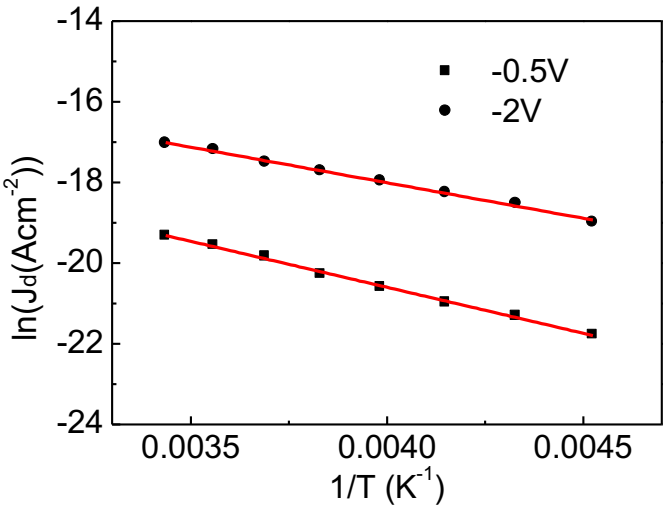

Figure 5.9. The dependence of the dark current density of the **(PPh$_2$)$_4$**-based OPD on temperature measured at −0.5 V and −2.0 V.

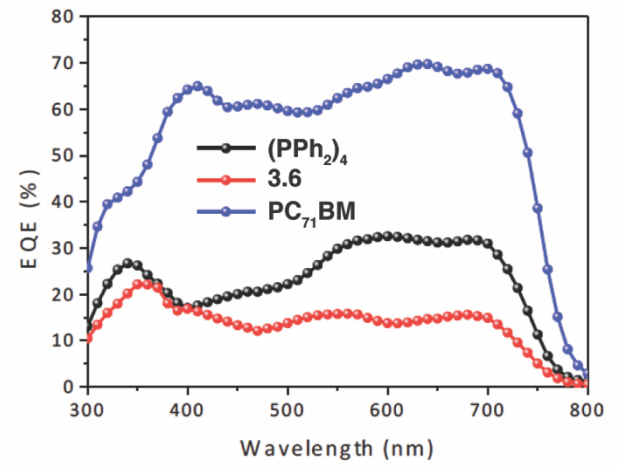

Figure 5.10. External quantum efficiency at different wavelength with inverted OPD structure at −0.1V.

The responsivity R was calculated from the following equation: $R=\lambda q/hc \times EQE$, where EQE is external quantum efficiency, λ the wavelength, q the electron charge, h the Planck constant, c the speed of light. When the noise current is dominated by the shot noise from the dark current, the specific detectivity (D^*) is given by $D^*=R/(2qJ_d)^{1/2}$, where R is the responsivity, q the electron charge and J_d the dark current density.

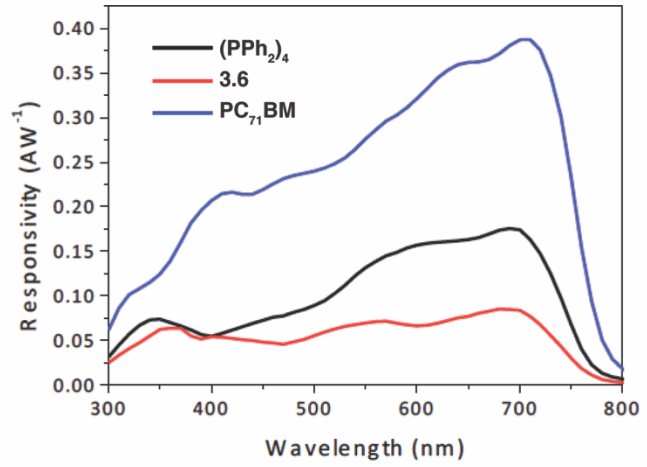

Figure 5.11. Calculated responsivity (R in AW^{-1}) spectra for different OPDs.

5.9. General Experimental Information

Device Fabrication. The synthesis of ZnO precursor was described elsewhere.[58] Prepatterned ITO-coated glass with a sheet resistance of ~15Ω/sq was cleaned with detergent, ultrasonicated in

DI water, acetone and isopropanol for 30 min, respectively. Subsequently, we treated the substrates by UV-Ozone for 10 min. The prepared ZnO precursor was spin-cast onto the ITO substrate at 3000 rpm for 1 min, followed by annealing at 200 ^{o}C for 1 h in air, to form a thin film with approximate thickness of 20 nm. The BHJ active layer was prepared by spin-coating a mixed solution containing polymer and acceptor in chlorobenzene. The thickness of the prepared active layers is about 150 nm. Finally, a 10 nm MoO_3 layer was deposited first and then a 100 nm Al electrode were subsequently deposited through a shadow mask by thermal evaporation under a vacuum about 1×10^{-6} torr. The active area of the device was 9 mm^2.

Characterization. The synthesis for **$(PPh_2)_4$** and **3.6** is provided in Chapter 3. Absorption spectra were obtained on Shimadzu UV 1800 UV-Vis. The current-density–voltage (J–V) curves were measured by a Keithley 2635A source measure unit. EQE measurements were performed using a QEXL system from PV Measurements Inc. For linear dynamic range measurement, a light-emitting diode (625 nm) was used as light source. For cutoff frequency measurement, the LED was modulated by a function generator (Tektronix CFG253). The photodetectors were connected to an oscilloscope (Tektronix TDS 224) with an input impedance of 50 Ω.

Temperature-dependent current-voltage measurements were realized in a vacuum cryogenic probe station (Lakeshore TTP4). Computer-controlled source units were used to apply DC potentials (Yokogawa 7651). Current measurements were obtained using a current preamplifier (Stanford Research System SR570) and a digital multimeter (Keysight 34401A). All device measurements were performed in vacuum ($P < 1\times10^{-4}$ Torr) at different temperatures.

In the transient absorption experiments, the pump pulse comes from an optical parametric amplifier (tunable from UV to the near IR, 100 fs pulse width, 1 KHz rep-rate). The probe pulse is a white-light supercontinuum (from 450 to 900 nm and from 850 to 1600 nm for the visible and

near IR range, respectively). The detection consists of a pair of high resolution multichannel detector arrays coupled to a high-speed data acquisition system (HELIOS, Ultrafast System Inc.). In order to avoid photo degradation, we kept samples in the inert gas both in storing and during measurements.

5.10. DFT Output

All quantum chemical calculations were performed using Jaguar, version 8.3, Schrodinger, Inc., New York, NY, 2013. (See A. D. Bochevarov, E. Harder, T. F. Hughes, J. R. Greenwood, D. A. Braden, D. M. Philipp, D. Rinaldo, M. D. Halls, J. Zhang, R. A. Friesner, "Jaguar: A High Performance Quantum Chemistry Software Program with Strengths in Life and Materials Sciences", Int. J. Quantum Chem., 2013, 113(18), 2110-2142). All geometries were optimized using the B3LYP functional and the 6-31G basis set. The geometry optimizations can be found in reference 1.[59]

5.11. References

1. Zhang, B. *et al.* Rigid, Conjugated Macrocycles for High Performance Organic Photodetectors. *J. Am. Chem. Soc.* **138**, 16426–16431 (2016).
2. Baeg, K.-J. *et al*. Organic Light Detectors: Photodiodes and Phototransistors. *Adv. Mater.* **25**, 4267–4295 (2013).
3. Sekitani, T. *et al.* A Rubberlike Stretchable Active Matrix Using Elastic Conductors. *Science.* **321**, 1468–1472 (2008).
4. Rogers, J. A. *et al*. Materials and Mechanics for Stretchable Electronics. *Science.* **327**, 1603–1607 (2010).
5. Ball, M. *et al.* Contorted Polycyclic Aromatics. *Acc. Chem. Res.* **48**, 267–276 (2015).
6. Gong, X. *et al.* High-Detectivity Polymer Photodetectors with Spectral Response from 300 nm to 1450 nm. *Science.* **325**, 1665–1667 (2009).
7. Zhang, L. *et al.* Toward Highly Sensitive Polymer Photodetectors by Molecular Engineering. *Adv. Mater.* **27**, 6496–6503 (2015).
8. Kim, I. K. *et al.* High-Performance, Fullerene-Free Organic Photodiodes Based on a Solution-Processable Indigo. *Adv. Mater.* **27**, 6390–6395 (2015).
9. Segura, J. L. *et al*. [60]fullerene dimers. *Chem. Soc. Rev.* **29**, 13–25 (2000).
10. Tsetseris, L. *et al*. Intermolecular bridges and carrier traps in defective C60 crystals. *Phys.*

Rev. B **84**, (2011).

11. Sheka, E. F. Donor-acceptor interaction and fullerene C-60 dimerization. *Chem. Phys. Lett.* **438**, 119–126 (2007).
12. Gregg, B. A. Charged defects in soft semiconductors and their influence on organic photovoltaics. *Soft Matter* **5**, 2985–2989 (2009).
13. Kaake, L. G. *et al*. Intrinsic Charge Trapping in Organic and Polymeric Semiconductors: A Physical Chemistry Perspective. *J. Phys. Chem. Lett.* **1**, 628–635 (2010).
14. Darling, S. B. Isolating the Effect of Torsional Defects on Mobility and Band Gap in Conjugated Polymers. *J. Phys. Chem. B* **112**, 8891–8895 (2008).
15. Ball, M. *et al.* Macrocyclization in the Design of Organic n-Type Electronic Materials. *J. Am. Chem. Soc.* **138**, 12861–12867 (2016).
16. Liao, S.-H. *et al*. Fullerene Derivative-Doped Zinc Oxide Nanofilm as the Cathode of Inverted Polymer Solar Cells with Low-Bandgap Polymer (PTB7-Th) for High Performance. *Adv. Mater.* **25**, 4766–4771 (2013).
17. Dou, L. *et al.* Solution-processed hybrid perovskite photodetectors with high detectivity. *Nat. Commun.* **5**, 5404 (2014).
18. Kim, I. K. *et al.* High-Performance, Solution-Processed Non-polymeric Organic Photodiodes. *Adv. Opt. Mater.* **3**, 50–56 (2015).
19. Leem, D.S. *et al.* Low dark current small molecule organic photodetectors with selective response to green light. *Appl. Phys. Lett.* **103**, 43305 (2013).
20. Lim, S.-J. *et al.* Organic-on-silicon complementary metal–oxide–semiconductor colour image sensors. *Sci. Rep.* **5**, 7708 (2015).
21. Armin, A. *et al.* Thick junction broadband organic photodiodes. *Laser Photon. Rev.* **8**, 924–932 (2014).
22. Pierre, A. *et al*. High Detectivity All-Printed Organic Photodiodes. *Adv. Mater.* **27**, 6411–6417 (2015).
23. Qi, J. *et al.* Optimization of Solubility, Film Morphology and Photodetector Performance by Molecular Side-Chain Engineering of Low-Bandgap Thienothiadiazole-Based Polymers. *Adv. Funct. Mater.* **24**, 7605–7612 (2014).
24. Ramuz, M. *et al*. High sensitivity organic photodiodes with low dark currents and increased lifetimes. *Org. Electron.* **9**, 369–376 (2008).
25. Saracco, E. *et al.* Work Function Tuning for High-Performance Solution-Processed Organic Photodetectors with Inverted Structure. *Adv. Mater.* **25**, 6534–6538 (2013).
26. Lee, K.H. *et al.* Green-Sensitive Organic Photodetectors with High Sensitivity and Spectral Selectivity Using Subphthalocyanine Derivatives. *ACS Appl. Mater. Interfaces* **5**, 13089–13095 (2013).
27. Zhu, X.-Y. *et al.* Charge Transfer Excitons at van der Waals Interfaces. *J. Am. Chem. Soc.* **137**, 8313–8320 (2015).
28. Banerji, N. Sub-picosecond delocalization in the excited state of conjugated homopolymers

and donor–acceptor copolymers. *J. Mater. Chem. C* **1**, 3052–3066 (2013).

29. Savoie, B. M. *et al*. Mesoscopic Features of Charge Generation in Organic Semiconductors. *Acc. Chem. Res.* **47**, 3385–3394 (2014).
30. Savoie, B. M. *et al.* Unequal Partnership: Asymmetric Roles of Polymeric Donor and Fullerene Acceptor in Generating Free Charge. *J. Am. Chem. Soc.* **136**, 2876–2884 (2014).
31. Zhong, Y. *et al.* Efficient Organic Solar Cells with Helical Perylene Diimide Electron Acceptors. *J. Am. Chem. Soc.* **136**, 15215 (2014).
32. Zhong, Y. *et al.* Molecular helices as electron acceptors in high-performance bulk heterojunction solar cells. *Nat. Commun.* **6**, 8242 (2015).
33. Hwang, I. *et al*. Ultrafast relaxation of charge-transfer excitons in low-bandgap conjugated copolymers. *Chem. Sci.* **3**, 2270–2277 (2012).
34. Hwang, I.-W. *et al.* Ultrafast Electron Transfer and Decay Dynamics in a Small Band Gap Bulk Heterojunction Material. *Adv. Mater.* **19**, 2307–2312 (2007).
35. Grancini, G. *et al.* Hot exciton dissociation in polymer solar cells. *Nat. Mater.* **12**, 29 (2012).
36. Ball, M. *et al.* Conjugated Macrocycles in Organic Electronics. *Acc. Chem. Res.* (2019). doi:10.1021/acs.accounts.9b00017
37. Gregg, B. A. Transport in Charged Defect-Rich π-Conjugated Polymers. *J. Phys. Chem. C* **113**, 5899–5901 (2009).
38. Wang, G.-W. *et al*. Synthesis and X-ray structure of dumb-bell-shaped C120. *Nature* **387**, 583–586 (1997).
39. Komatsu, K. *et al.* Mechanochemical Synthesis and Characterization of the Fullerene Dimer C120. *J. Org. Chem.* **63**, 9358–9366 (1998).
40. Huang, C. *et al*. Perylene-3,4,9,10-tetracarboxylic Acid Diimides: Synthesis, Physical Properties, and Use in Organic Electronics. *J. Org. Chem.* **76**, 2386–2407 (2011).
41. Würthner, F. Perylene bisimide dyes as versatile building blocks for functional supramolecular architectures. *Chem. Commun.* 1564–1579 (2004). doi:10.1039/B401630K
42. Würthner, F. *et al.* Perylene Bisimide Dye Assemblies as Archetype Functional Supramolecular Materials. *Chem. Rev.* **116**, 962–1052 (2016).
43. Kozma, E. *et al*. Perylene diimides based materials for organic solar cells. *Dye. Pigment.* **98**, 160–179 (2013).
44. Langhals, H. *et al*. Cyclophanes as Model Compounds for Permanent, Dynamic Aggregates – Induced Chirality with Strong CD Effects. *European J. Org. Chem.* **1998**, 1915–1917 (1998).
45. Wang, W. *et al*. Cyclization and Catenation Directed by Molecular Self-Assembly. *J. Am. Chem. Soc.* **128**, 11150–11159 (2006).
46. Feng, J. *et al.* Cyclophanes of Perylene Tetracarboxylic Diimide with Different Substituents at Bay Positions. *Chem. Eur. J.* **14**, 7000–7010 (2008).
47. Shaller, A. D. *et al*. Tunable Molecular Assembly Codes Direct Reaction Pathways. *Angew.*

Chem. Int. Ed. **47**, 7705–7709 (2008).

48. Wang, W. *et al*. Twisted Perylene Stereodimers Reveal Chiral Molecular Assembly Codes. *J. Am. Chem. Soc.* **130**, 8271–8279 (2008).

49. Schlosser, F. *et al*. Perylene bisimide macrocycles and their self-assembly on HOPG surfaces. *Chem. Commun.* **46**, 8350–8352 (2010).

50. Lee, J.-E. *et al.* Structure–Property Relationship of Perylene Bisimide Macrocycles Probed by Atomic Force Microscopy and Single-Molecule Fluorescence Spectroscopy. *ACS Nano* **7**, 5064–5076 (2013).

51. Schlosser, F. *et al*. Redox-switchable Intramolecular π–π-Stacking of Perylene Bisimide Dyes in a Cyclophane. *Adv. Mater.* **25**, 410–414 (2013).

52. Brown, K. E. *et al*. Direct Observation of Ultrafast Excimer Formation in Covalent Perylenediimide Dimers Using Near-Infrared Transient Absorption Spectroscopy. *J. Phys. Chem. Lett.* **5**, 2588–2593 (2014).

53. Ham, S. *et al*. Reconstruction of the Molecular Structure of a Multichromophoric System Using Single-Molecule Defocused Wide-Field Imaging. *J. Phys. Chem. Lett.* **5**, 2830–2835 (2014).

54. Nicolai, H. T. *et al.* Unification of trap-limited electron transport in semiconducting polymers. *Nat. Mater.* **11**, 882–887 (2012).

55. Mandoc, M. M. *et al*. Trap-limited electron transport in disordered semiconducting polymers. *Phys. Rev. B* **75**, 193202 (2007).

56. Gregg, B. A. *et al*. Coulomb forces and doping in organic semiconductors. *Chem. Mater.* **16**, 4586–4599 (2004).

57. Ball, M. *et al.* Chiral Conjugated Corrals. *J. Am. Chem. Soc.* **137**, 9982–9987 (2015).

58. Jo, J. *et al.* Enhanced Efficiency of Single and Tandem Organic Solar Cells Incorporating a Diketopyrrolopyrrole-Based Low-Bandgap Polymer by Utilizing Combined ZnO/Polyelectrolyte Electron-Transport Layers. *Adv. Mater.* **25**, 4783–4788 (2013).

59. Ball, M. L. *et al.* Influence of Molecular Conformation on Electron Transport in Giant, Conjugated Macrocycles. *J. Am. Chem. Soc.* **140**, 10135–10139 (2018).

Chapter 6. Hollow Organic Capsules Assemble into Cellular Semiconductors

6.1. Preface

Chapter 6 is reproduced with permission from the authors: Boyuan Zhang, Raúl Hernández Sánchez, Yu Zhong, Melissa Ball, Maxwell W. Terban, Daniel Paley, Simon J. L. Billinge, Fay Ng, Michael L. Steigerwald, and Colin Nuckolls, published in *Nature Communications*.[1] Boyuan Zhang and Yu Zhong performed all device fabrication and characterization. Fay Ng synthesized all compounds. Raúl Hernández Sánchez performed XRD analysis. I performed DFT calculations and developed the HPLC method to separate the PDI isomers. Maxwell W. Terban performed PDF analysis.

6.2. Introduction

There is a growing class of electroactive, conjugated cyclic molecules that are being applied in several areas of materials science.[2–28] These cyclic, conjugated organic semiconductors have interior spaces that should be useful as a locus for guest inclusion to tune the electronic and optoelectronic properties.[12,25,27–29] Conjugated, cyclic semiconductors that incorporate PDIs have many benefits as the active elements in organic field effect transistors OFETs,[30] OPVs,[11,31] and OPDs.[10] It has been challenging to synthesis rigid PDI-based macrocycles that interconvert as the previous chapters have demonstrated.[5]

Chapter 6 focuses on a new electronic material whose molecular components are shape persistent and self-assemble into semiconducting films that are capable of detecting nuanced differences in small molecule guests. The macrocycle comprises a tetra-brominated bithiophene (BBr_4) and a PDI wound into a trimeric structure called **$(PBBr_4)_3$**. Figure 6.1a provides the structure of **$(PBBr_4)_3$**. These macrocycles exist as a single pair of enantiomers and are shape persistent to temperatures above 160 °C. Their capsular structure is capped on the ends by the alkyl sidechains and on the equator by the electronic components (the PDI and BBr_4 subunits). This is

shown in Figure 6.1b-g. We found that **(PBBr$_4$)$_3$**'s cellular films act as the active layer in OFETs, and the electrical response depends on the guest that occupies the interior space.

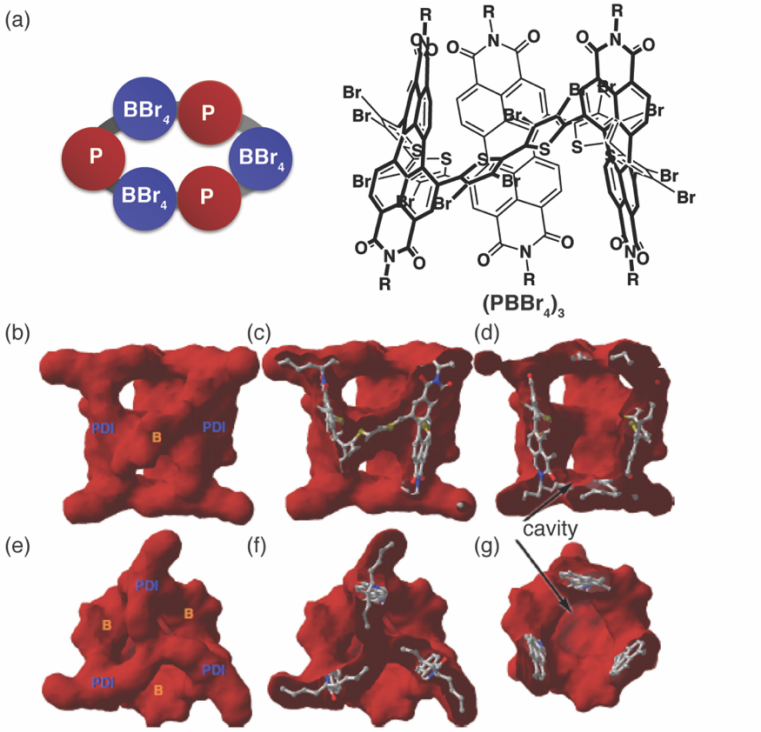

Figure 6.1. (a) Structure of **(PBBr$_4$)$_3$**; (b) – (g) van der Waals Surface of **(PBBr$_4$)$_3$** seen from the side and top, trimmed to reveal the cavity (g). R = $C_{11}H_{23}$ side chains.

6.3. Capsule Construction

We developed a synthesis of **(PBBr$_4$)$_3$** based on our own previous studies to make PDI-based macrocycles[5,11] that builds from the methodology originally pioneered for cyclothiophenes[2] and later for cycloparaphenylenes.[21,32] Our earlier studies suggested the bithiophenes adopt a syn geometry when incorporated into a macrocycle, which provides strain relief (Chapter 1B.6 and Chapter 2.6). With three sets of bithiophenes, **(PBBr$_4$)$_3$** possesses little strain (Chapter 1B.5). Figure 6.2 contains the scheme to synthesis **(PBBr$_4$)$_3$**. Using regio-pure *1,7*-dibromo PDI, we form **6.1** via a Stille coupling, and react **6.1** with $PtCODCl_2$, and after a ligand exchange and reductive elimination, afford intermediate **6.2** in a 15% yield. In addition to **6.2**, the reaction produces several different sized macrocycles raning from the trimeric species to a hexameric structure (Section 6.9).

We post-synthetically modify **6.2** with bromine atoms in the thiophene rings to encourage self-assembly through halogen bonding interactions to form **(PBBr$_4$)**.[33]

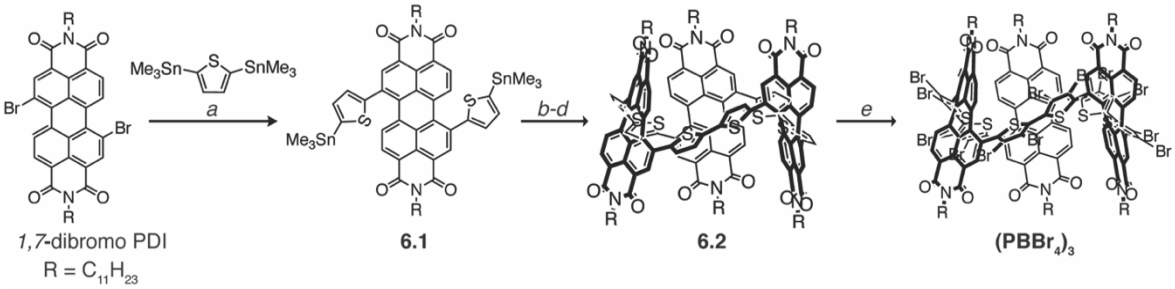

Figure 6.2. (a) Pd(PPh$_3$)$_4$, Toluene, 110 °C, 13 h, 69% yield; (b) PtCODCl$_2$, 1,2-dichloroethane, 85 °C, 72 h; (c) 1,1'-ferrocenediyl-bis(diphenylphophine), CH_2Cl_2, rt, 24 h; (d) PPh$_3$, Toluene, 110 °C, 48 h, 15% yield for **(PBBr$_4$)$_3$**; (e) Br$_2$, I$_2$, CH_2Cl_2, rt, 80% yield.

The *1,7*-dithienyl-PDI subunit (**6.1**) introduces an element of chirality:[5] it can exist in either a *P*- or *M*-helical conformations. This allows for the possibility of two pairs of enantiomers (*P,P,P*/*M,M,M* and *P,P,M*/*M,M,P*). However, in the reaction to form **6.2**, we only observe the (*P,P,P*/*M,M,M)* pair. We separate the two enantiomers of **6.2**, using a chiral stationary phase for HPLC, and monitor their interconversion as the samples are heated. The two enantiomers of **6.2** do not interconvert, even when heated up to 160 °C, and both **6.2** and **(PBBr$_4$)$_3$** exhibit an intense (and opposite) chiroptic response in their CD spectra (Figure 6.3).

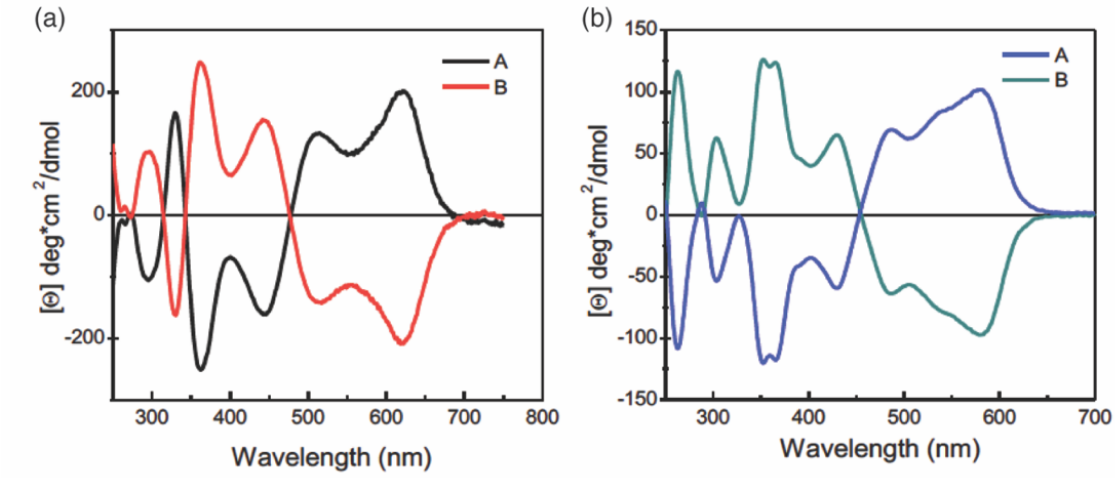

Figure 6.3. (a) CD of **6.2**; (b) CD of **(PBBr$_4$)$_3$**. Both spectra show each enantiomer preferentially absorbs left or right-handed circularly polarized light.

6.4. Capsule Structure.

We were able to grow single crystals of sufficient quality to yield the structures of **(PBBr$_4$)$_3$**. Figure 6.4 displays the structure of one of the two enantiomers of **(PBBr$_4$)$_3$** present in the solid-state: (*SSS*)-**(PBBr$_4$)$_3$**. The structure of **(PBBr$_4$)$_3$** is cylindrical with the three sets of bithiophenes and three PDIs forming the walls at the equator. The ends of the cylinder are capped with branched alkyl chains (Figure 6.4 and highlighted in green in Figure 6.5a). This creates windows on the side of the structure, displayed in Figure 6.1b,e. We estimate the interior volume of the capsule in **(PBBr$_4$)$_3$** (shown in Figure 6.1d,g) to be approximately 415 Å^3.[34]

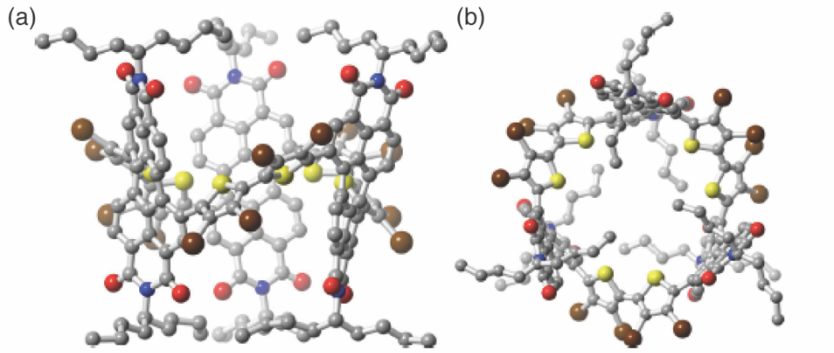

Figure 6.4. Molecular structure from SCXRD of **(PBBr$_4$)$_3$**. (a) Side and b, top view of (*SSS*)-**(PBBr$_4$)$_3$**. C, N, O, S, and Br atoms are colored in grey, blue, red, yellow, and brown, respectively. Hydrogen atoms have been removed to clarify the view. The alkyl chains on the imide are refined to only nine of the eleven carbon atoms due to disorder.

6.5. Cellular Solids from Capsular Nanostructures.

The packing structure in the solid state of **(PBBr$_4$)$_3$** (Figure 6.5) reveals why the bromines were necessary for long range crystallinity. The structure is composed of sheets of a honeycomb-like arrangement in the a,b plane (Figure 6.5a). The interactions that bind the cylinders within the a,b plane are from neighboring brominated thiophene rings and the adjacent carbonyl groups of an adjacent macrocycle (Figure 6.5c). The PDIs do not π-stack with each other, and halogen bonding from the functionalized thiophenes drives the self-assembly process. The cavity of **(PBBr$_4$)$_3$**

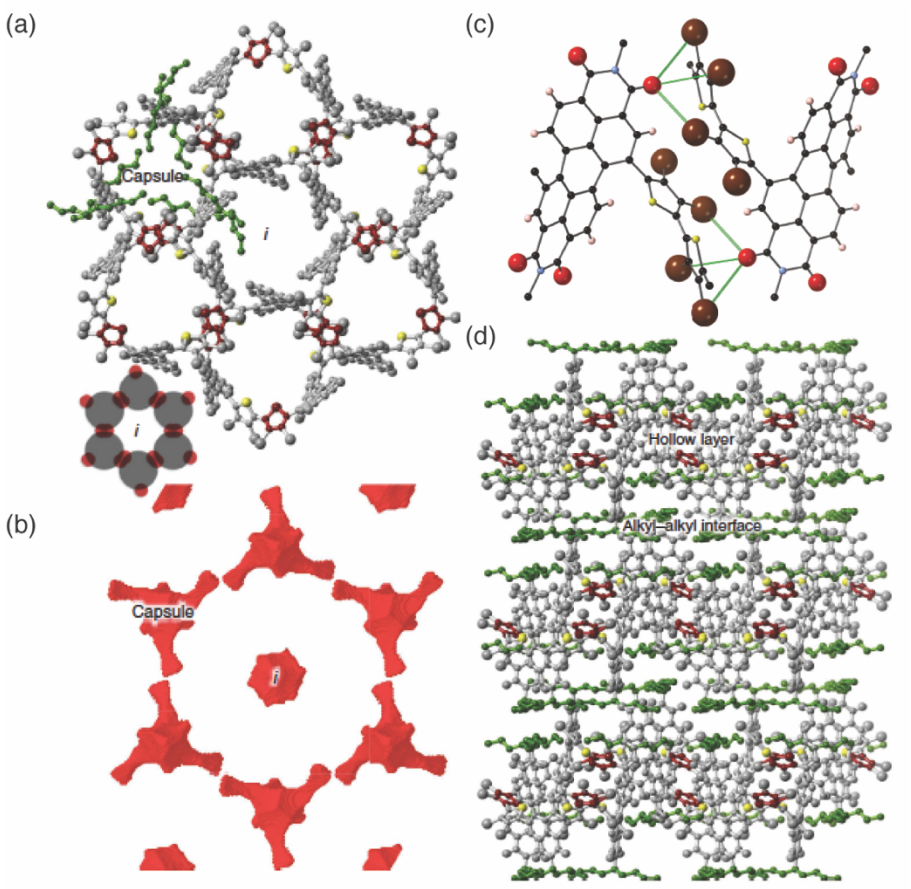

Figure 6.5. Structural packing of **$(PBBr_4)_3$**. (a) view of the honeycomb structure in the ab plane for **$(PBBr_4)_3$**. The capsule and *i* corresponds to the internal cavity of **$(PBBr_4)_3$** and the cavity formed by the packing of **$(PBBr_4)_3$**, respectively. The remaining sulfur atoms are colored in yellow to provide a marker to identify the macrocycle cavities. See bottom left cartoon. Highlighted in green are the imide side chains (some of the sidechains have been removed to clarify the view of the cavity). In red are the thiophene rings. (b) Surface map of the void space in the ab plane of **$(PBBr_4)_3$**. (c) Two molecules of **$(PBBr_4)_3$** showing the C=O…Br-C halogen interaction responsible for the 2D assembly. (d) View of the packing of **$(PBBr_4)_3$**. As shown, the vertical stacking follows the c axis. The alkyl sidechains of the imide are shown in green. Hydrogen atoms have been removed from all structures to clarify the view.

(labeled "capsule" in Figure 6.5a,b) is ~11.4 Å in diameter and is a three-fold symmetric chiral nanoenvironment for guest incorporation within the two-dimensional layer. Due to the packing of the subunits of **$(PBBr_4)_3$** into a hexameric cyclic structure, a second cavity forms at the center of each hexagon (labeled *i* in Figure 6.5a,b). These honeycomb two-dimensional, cellular sheets then stack through the packing of the alkyl side chains of the imides, (shown in green in Figure 6.5).

This packing arrangement propagates along the c-axis, hinting that these materials could likely be exfoliated to yield molecularly thin sheets of **$(PBBr_4)_3$**.

We find that **$(PBBr_4)_3$** self-assembly in cast thin films and powder samples is analogous to what we described above for the single crystal. Figure 6.6 compares the thin film and powder diffraction data for **$(PBBr_4)_3$** with the simulated pattern calculated from the SCXRD data. No other reflections are present in the films or powders indicating that the self-assembly motif using the halogen bonding is robust.

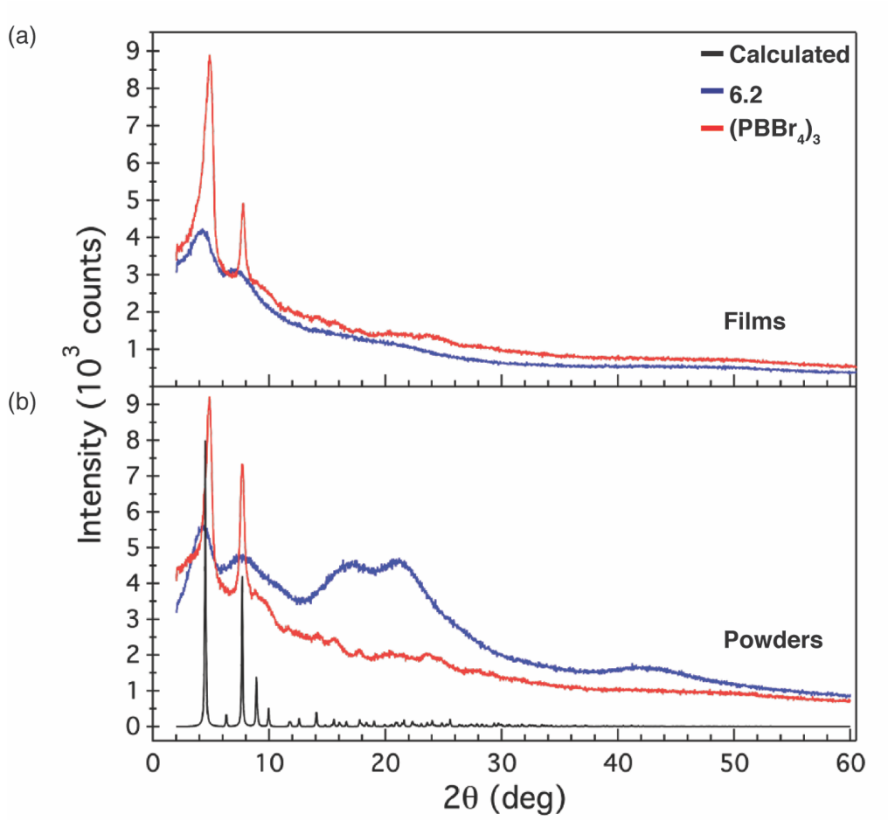

Figure 6.6. PXRD of **$(PBBr_4)_3$** and **6.1**. (a) Films drop cast from a chloroform solution; (b) data obtained from powder samples. The black line represents the predicted pattern for **$(PBBr_4)_3$**.

We performed pair distribution function (PDF) analyses on powders of **6.1** and **$(PBBr_4)_3$** to extract quantitative information about the long-range crystallinity of these new hollow semiconductors. We found that the crystalline domains for **$(PBBr_4)_3$** contain on average up to 23 to 27 capsules arranged in one direction relative to just a few capsules for **6.1** (Figure 6.9).

6.6. Electron Transport through Cellular Films.

Figure 6.7 displays transfer curves from an OFET constructed using a self-assembled thin film of **$(PBBr_4)_3$**. Details for the device dimensions and its properties can be found in the Appendix. The device exhibits electron transporting character and has a mobility of ~1.5 x 10^{-2} $cm^2V^{-1}s^{-1}$. The mobility of **$(PBBr_4)_3$** is more than 20 times greater than that of **6.1** (~6.8 x 10^{-4} $cm^2V^{-1}s^{-1}$) (Figure 6.10). We attribute this to the robust self-assembly process for **$(PBBr_4)_3$** described in Section 6.4. From the AFM height images, films of **6.1** display a smooth surface with RMS roughness of 0.347 nm; in contrast, **$(PBBr_4)_3$** displays a larger RMS roughness of 3.2 nm, presumably due to its more crystalline nature and better self-assembly properties (Figure 6.11).

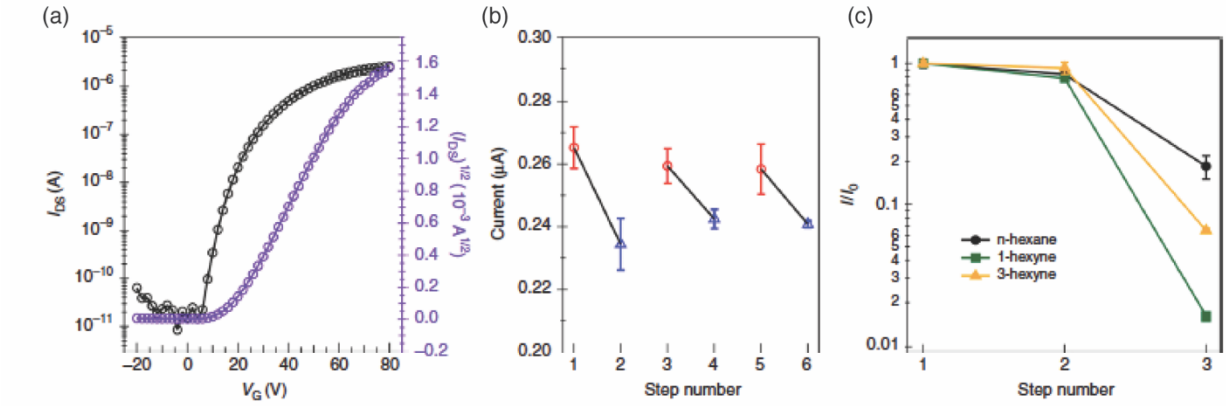

Figure 6.7. Charge transport for **$(PBBr_4)_3$**. (a) Transfer characteristics of OFET device for **$(PBBr_4)_3$**; (b) device cycling response under vacuum (red circles) and N_2 atmosphere (blue triangles); and (c) normalized behavior of the device response under vacuum (step 1), N_2 (step 2), and different analytes atmosphere (step 3: n-hexane, 3-hexyne and 1-hexyne). Error bars represent the standard error obtained in three measurements.

The exciting finding is that the devices show modulation in the drain current depending on what, if anything, is within the cavities of the macrocycles. Every potential guest tested had a measurable effect on the drain current in the device, but the absolute levels of the drain current varied depending on the guest. Figure 6.7b is a representative data set for a device measured sequentially in steps as the atmosphere is changed between vacuum and N_2. In certain cases, traditional OFETs show a differential response to nitrogen and vacuum that is from extrinsic

effects (moisture, oxygen, or dielectric effects).[35] We were curious whether the response to N_2 for **$(PBBr_4)_3$** was due to an extrinsic effect or due to the macrocycle's ability to sense the gas, and made a control FET device from **6.2**, which does not self-organize into cellular semiconducting films or crystals. We observe no response when comparing its response to nitrogen and vacuum (Figure 6.12a).

Incorporating more polarizable and functional guests causes more pronounced changes in the drain current. Figure 6.12b compares the effects of several different guests with a variety of functional groups such as ketones, alcohols, nitriles, alkynes, and alkanes. In each case we are able to differentiate the guest by the current in the device. Figure 6.7c highlights one striking example of how this material responds to a series of closely related hydrocarbons (3-hexyne, 1-hexyne, and n-hexanes). These hydrocarbons were chosen so that their length, size, and polarity were roughly similar to that of n-hexane, while having an additional functional group in them. We compare the transistor output for three devices exposed to n-hexane, 3-hexyne, or 1-hexyne, carried by nitrogen under their saturated vapor pressure (148, 99, and 138 mmHg at 25 °C, respectively).[36] In each case, the devices can both easily detect and distinguish each hydrocarbon. There is also specificity towards particular analytes; the trend in the device responses does not simply follow the vapor pressure.

For n-hexane and 3-hexyne the data was collected after the OFET was in contact with the vapor for ~70 minutes (Figure 6.8a). After this time, the drain current no longer decreased. The original current levels for n-hexane and 3-hexyne could be restored by removing the analyte by placing the devices in vacuum (Figure 6.8b) During these long exposures, we speculate that the guests infiltrate the films to reside in the active part of the films at the gate dielectric interface.[37,38]

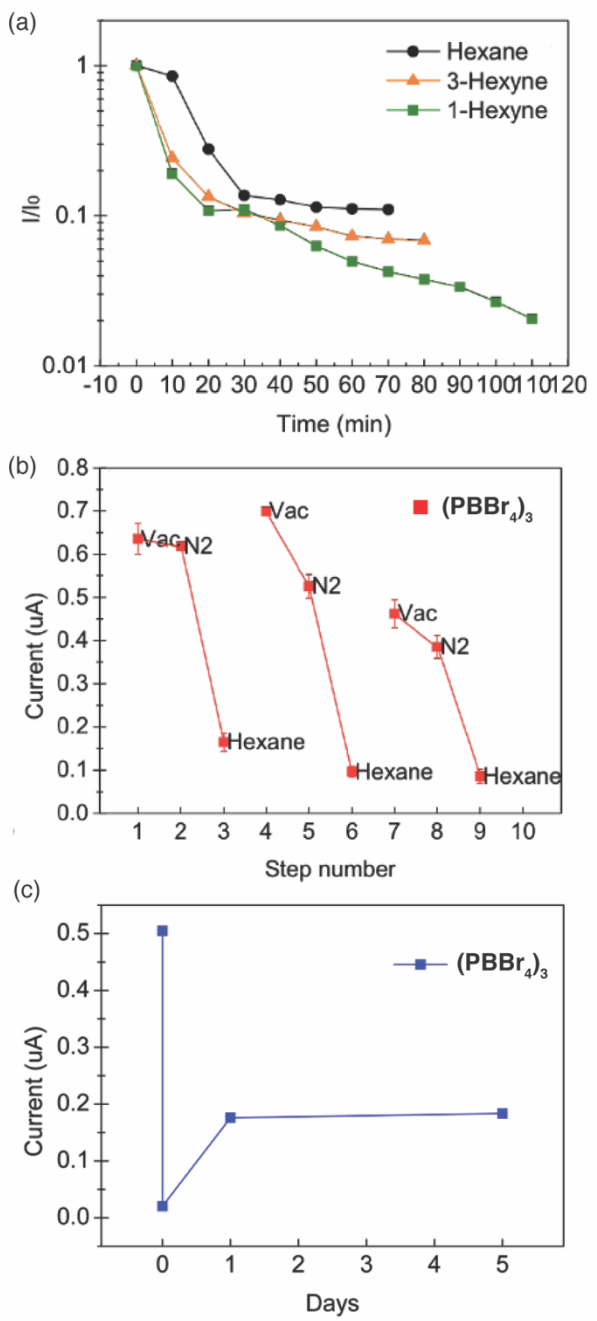

Figure 6.8. (a) I/I_0 for **$(PBBr_4)_3$** under n-hexane, 3-hexyne and 1-hexyne. (b) Device cycling response for **$(PBBr_4)_3$** under vacuum, N_2 and hexane atmosphere. Error bars represent the standard error obtained in three measurements. (c) Recovery response for **$(PBBr_4)_3$** under vacuum after exposure to 1-hexyne. The films do not recover their original current levels.

We tested the sensitivity of **$(PBBr_4)_3$** films and find that there is a linear response between vacuum and 20 ppt of the analyte in the atmosphere, after we observed a plateau region as the concentration reaches saturation (Figure 6.13). The guests can infiltrate the porous network

through the capsule's interior (~415 Å^3) or the *i*-sites (~110 Å^3). Note that n-hexane has a van der Waals molecular volume of ~113 Å^3.[39] The implication is that n-hexane would not fit into the *i*-site. In addition, most of the cellular nature of self-assembled **(PBBr$_4$)$_3$** comes from the capsule interior which is present in a 2:1 numerical ratio relative to the *i*-site. Given the 8-fold difference in volume between these two cavities we speculate that guests can be accommodated most feasibly at the capsules' interior. Using BET, we find that powders of **(PBBr$_4$)$_3$** have a surface area of 20 m^2g^{-1} (versus 1.2 m^2g^{-1} for **6.2**).

1-hexyne behaves differently than each of the other guests tested (Figure 6.8c). For the devices in an atmosphere of 1-hexyne, the current continues to drop and does not reach a plateau even at times that exceed 2 hours of exposure. In addition, the 1-hexyne devices do not recover to their original levels when placed in vacuum. We speculate that the terminal alkyne is undergoing a reaction under the device conditions that is not possible with the internal alkyne or the alkane. This offers the intriguing possibility that in addition to sensing, these nanoenvironments in these hollow semiconductors[40,41] can be used as nanoreactors.

6.7. Conclusion

We have described here a shape persistent, hollow macrocycle that self-assembles both in the solid state and thin films to form cellular organic semiconductors. The macrocycle is chiral and conformationally locked into a capsular structure, with ~415 Å^3 volume on its interior. The self-assembly of a brominated derivative of the trimer into cellular films forms the active layer in an organic field effect transistor device. Once assembled, these films have periodic, nanoscopic, cellular voids in them. Because the macrocyclic component in the film is conformationally locked, the self-assembled films maintain their interior, open spaces. The hollow films of **(PBBr$_4$)$_3$** are

responsive to the atmosphere in which the OFETs are measured. These studies chart a clear path to using the interior of the cellular organic semiconductors as gas sensors and nanoreactors.

6.8. Appendix – Supplementary Figures

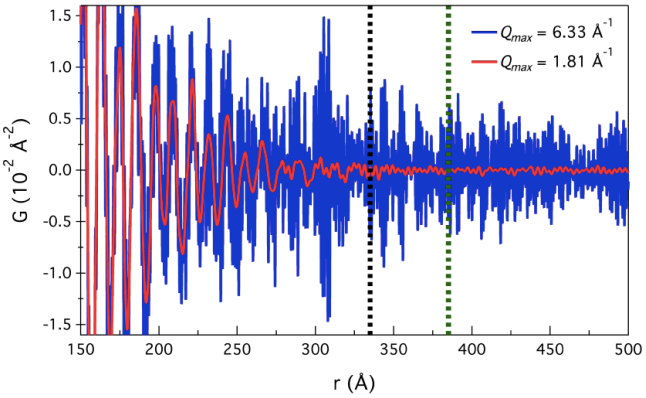

Figure 6.9. Coherence length for **$(PBBr_4)_3$**. We can approximate the coherence length lower bound at 335 Å (black dotted line) and upper bound at 385 Å (green dotted line).[42] The online Supporting Information contains the additional PDF analysis details and spectra for **6.2** and for **$(PBBr_4)_3$**.[1]

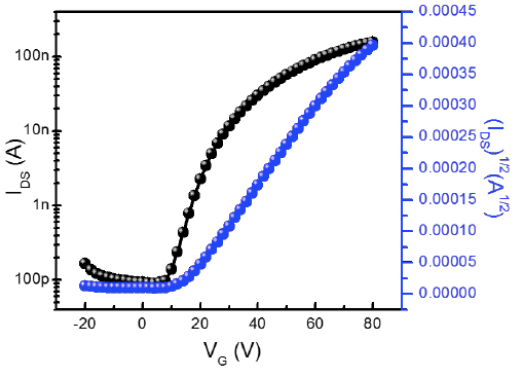

Figure 6.10. Transfer characteristics for **6.2**.

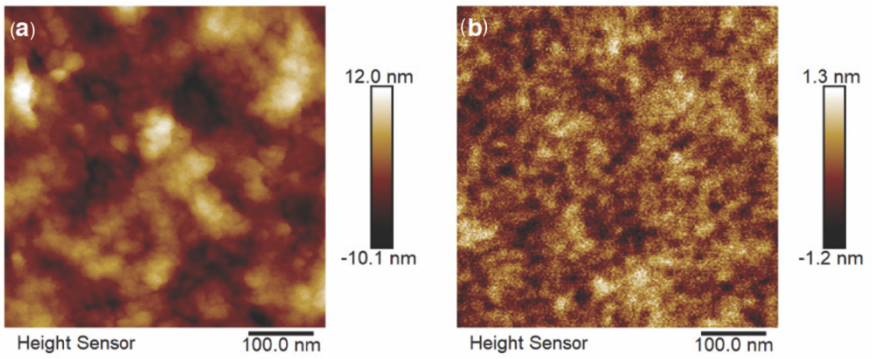

Figure 6.11. (a) AFM height images of spin-cast films for (a) **$(PBBr_4)_3$** and (b) **6.2**. The root mean square roughness are 3.2 nm for **$(PBBr_4)_3$** and 0.347 nm for **6.2**, respectively.

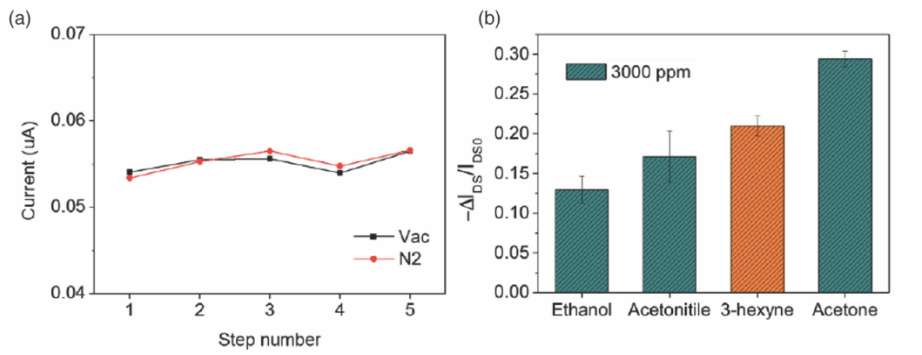

Figure 6.12. (a) Device cycling response for 6.2 under vacuum and N_2 atmosphere. (b) The average current of response for **$(PBBr_4)_3$** OFET to series of analytes at a concentration of 3000 PPM. Error bars represent the standard error obtained in three measurements.

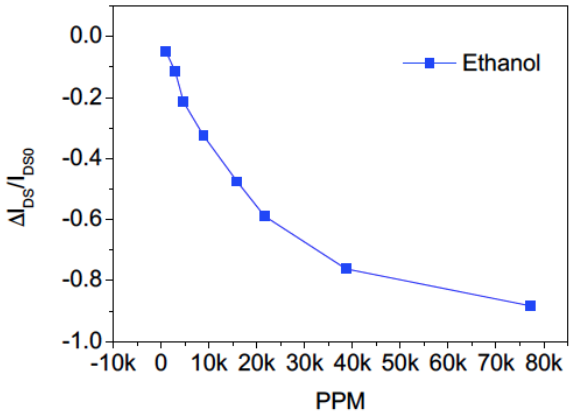

Figure 6.13. Sensitivity for **$(PBBr_4)_3$** OFET under different concentrations of ethanol.

6.9. General Experimental Information

All reactions were performed in oven-dried or flame-dried round bottom flasks, unless otherwise noted. The flasks were fitted with Teflon magnetic stir bar, rubber septa and reactions were conducted under a positive pressure of nitrogen, unless otherwise noted. Anhydrous and anaerobic solvents were obtained from Schlenk manifold with purification columns packed with activated alumina and supported copper catalyst (Glass Contour, Irvine, CA). Automated flash chromatography was performed using a Teledyne Isco Combiflash R_f200 and Redisep R_f Silica columns. Preparative HPLC purification was performed on a Waters Prep150 instrument equipped with a UV-vis detector, an automated fraction collector with either a Nacalai Tesque COSMOSIL

Buckyprep column (20 mm ID x 250 mm, 5 μm) or a COSMOSIL 5PBB column (20 mm ID x 250 mm, 5 μm).

Chiral Analyses and Purification. Racemic trimer **6.2** samples were resolved by an Agilent 1200 Series analytical HPLC equipped with a diode array detector (300 nm to 900 nm) and a CHIRALPAK IA-3 column (4.6 mm ID x 250 mm, 3μm) from Chiral Technologies; preparative purification was performed using CHIRALPAK IA-3 column (21 mm ID x 250 mm, 5μm) on Waters Prep150 instrument.

Materials. Pure regioisomeric 1,7-dibromoperylene-3,4,9,10-tetracarboxylicbisimides was synthesized (as a mixture of *1,7*- and *1,6*-regioisomers) according to known procedures,[43] and separated using COSMOSIL Buckyprep column (20 mm ID x 250 mm, 5 μm) on Waters Prep150 instrument. All chemicals were purchased from commercial sources and used without further purification unless otherwise specified.

Instrumentation. ^{1}H and ^{13}C NMR spectra were recorded on Bruker DRX400 (400 MHz) or a Bruker DMX500 (500 MHz) spectrometer. Chemical shifts for protons are reported in parts per million downfield from tetramethylsilane and are referenced to residual protium in the NMR solvent ($CHCl_3$: δ 7.26; CH_2Cl_2: δ 5.32; $C_2H_2Cl_4$: δ 6.00). Chemical shifts for carbon are reported in parts per million downfield from tetramethylsilane and are referenced to the carbon resonances of the solvent ($CDCl_3$ δ 77.0; $C_2H_2Cl_4$ δ 73.78). Data are represented as follows: chemical shift, multiplicity (s = singlet, d = doublet, t = triplet, m = multiplet, br = broad), coupling constants in Hertz, and integration. Some ^{1}H NMR and ^{13}C NMR were recorded at elevated temperatures (in K) to enhance peak resolution in the aromatic region. Resonances corresponding to the numerous aromatic carbon atoms in the reported compound sometimes overlap, thereby reducing the number of observed resonances. HRMS was performed on (1) a Waters XEVO G2-XS QTOF instrument

equipped with a UPC2 SFC inlet, and electrospray (ESI) and atmospheric pressure chemical (APCI) ionization sources; or (2) a Bruker UltrafleXtreme MALDI TOF instrument using dithranol matrix. Absorption spectra were obtained on Shimadzu UV 1800 UV-Vis spectrophotometer and emission spectra were recorded in a Fluorolog-3 spectrophotometer.

Cyclic voltammograms: CVs were recorded on a CHI600C electrochemical workstation using Ag/AgCl electrode as the reference electrode. 0.1 M solution tetrabutylammonium hexafluorophosphate, $[Bu_4N][PF_6]$, in dichloromethane was used as the supporting electrolyte. The thin film transistors were tested on the Agilent 4155C semiconductor parameter analyzer. CD spectra were recorded by a Jasco J-810 spectropolarimeter. It is assumed that the absolute energy level for Fc/Fc^+ redox potential is −4.80 eV with respect to vacuum level. The energy levels of the LUMO) and HOMO are calculated according to the following equation: $E_{LUMO} = -e(E_{red}+4.80)$ (eV), $E_{HOMO} = -e(E_{oxi}+4.80)$ (eV).[44]

AFM was performed with a PSIA XE100.

PXRD was collected on a PANalytical X'Pert^3 Powder Diffractometer. Data was collected on powder samples and films drop-cast from chloroform solution and p-xylene solution. For all data collection a Si zero-background holder was used.

Single crystal data for **$(PBBr_4)_3$** was collected on an Agilent SuperNova diffractometer using a mirror-monochromated Cu K_α radiation. The hexagonal-shaped crystals were mounted on a MiTeGen Kapton loop (polyimide). These were cooled to 100 K with an Oxford Cryosystems nitrogen flow apparatus. Data integration, scaling (ABSPACK) and absorption correction were perfomed in CrysAlisPro.[45] Structure solution was performed using ShelXS,[46] ShelXT,[47] or SuperFlip.[48] Subsequent refinement was performed by full-matrix least-squares on F^2 in ShelXL. Olex2[34] was used for viewing and to prepare CIF files. PLATON[49] was used for SQUEEZE,[50]

ADDSYM[51] and TwinRotMat. Details of crystallographic data and refinement parameters are given in Table 6.2. Due to heavy disorder of the alkyl imide chains in **$(PBBr_4)_3$**, only nine carbons (out of eleven) in each alkyl fragment were modeled. The cavity size of **$(PBBr_4)_3$** was calculated from the solvent accessible volume calculator in Olex2. By employing this functionality we found discrete pockets within the structure of **$(PBBr_4)_3$** which match the cavities of these molecules. Thus, the calculated cavity size of (*M,M,M*/*P,P,P*)- **$(PBBr_4)_3$** is 414.9 Å^3 (CalcSolv 3.0 Å probe, grid step 0.2 Å).

Table 6.1. Crystallographic data for $(PBBr_4)_3$.

	$(PBBr_4)_3$
Chemical formula	$C_{150}H_{132}Br_{12}N_6O_{12}S_6$
Formula weight	3361.89
Space group	*P–3*
a (Å)	23.028 (4)
b (Å)	23.028 (4)
c (Å)	19.626 (3)
α (deg)	90
β (deg)	90
γ (deg)	120
V (Å^3)	9013 (3)
Z	2
μ (mm^{-1})	4.21
T (K)	100

$R1^a$ ($wR2^b$)	0.157 (0.476)
Reflections	3155
Radiation type	Cu K_α

$^aR1 = [\Sigma w(F_o - F_c)^2/\Sigma wF_o^2]^{1/2}$; $^bwR2 = [\Sigma[w(F_o^2 - F_c^2)^2]/\Sigma w(F_o^2)^2]^{1/2}]$, $w = 1/[\sigma^2(F_o^2) + (aP)^2 + bP]$, where $P = [\max(F_o^2,0) + 2(F_c^2)]/3$

X-ray total scattering experiments (PDF analysis)

X-ray total scattering experiments were conducted on beamline 28-ID-2 at the National Synchrotron Light Source II at Brookhaven National Laboratory. An X-ray beam of energy 67.756 keV (λ = 0.18299 Å) was focused on samples loaded into Kapton capillaries. Scattered intensities were collected at room temperature, in rapid acquisition mode[52] on a Perkin-Elmer 2D flat panel detector (2048 x 2048 pixels and 200 x 200 μm pixel size) mounted orthogonal to the beam path. Data collection was carried out with a short (239.9734 mm) and a large (1552.689 mm) sample-to-detector distance to obtain improved Q-space resolution. Q is the magnitude of the scattering momentum transfer where for elastic scattering is defined as: $Q=(4\pi \sin(\theta))/\lambda$, for scattering angle 2θ and wavelength λ. A Ni standard sample was measured in both cases to calibrate the detector geometry. 2D intensities were azimuthally integrated to 1D intensities versus Q using Fit2D.[53] Scattering from an empty Kapton tube was measured for background subtraction. The PDF gives the scaled probability of finding atom-pairs in the material at a distance r apart. The program xPDFsuite with PDFGetX3[54,55] was used to obtain the PDFs from the experimental scattering intensities. The coherent scattering I(Q) was extracted through background subtraction and corrections to the raw intensities, then normalized by the atomic scattering factors to give the total scattering structure function S(Q) which is converted to the real-space pair distribution function (PDF), G(r), by

$$G(r) = \frac{2}{\pi}\int_{Q_{\min}}^{Q_{\max}} Q[S(Q) - 1](Q)\sin(Qr)\,dQ$$

where $Q_{\min}$ and $Q_{\max}$ are the minimum and maximum values of the scattering momentum transfer considered. These limits were determined by the Q-range accessible for the different detector configurations, 0.29–22.0 $Å^{-1}$ for the short sample-to-detector distance which gives a wide range of momentum transfer in order to achieve a high real-space resolution in the PDFs. The far sample-to-detector distance gives a smaller Q-range of 0.20–6.33 $Å^{-1}$, which gives a lower real space resolution, but provides a much better Q-resolution of the scattering which allows the resulting PDFs to be analyzed over longer real-space distances.[56,57] In this case, the $Q_{\max}$ was reduced further to decrease the noise level below any signal observable at high distances. The structural coherence of the sample was estimated from visual observation of the distance at which the structural signal became indistinguishable from the average atomic density, $G(r) = 0$.

It is important to note the following for the coherence length estimation: (1) all approximated coherence lengths are well below the resolution limit determined from fitting Ni measured with the same experimental setup, and (2) the approximated lengths may be underestimated as the presence of noise may still obscure some high-r signals.

Electron Transport. We first treat the substrate (300 nm of SiO_2 on a Si wafer) with OTS in order to passivate traps on the SiO_2 surface. Au source and drain electrodes are deposited on the film to make a bottom-contact configuration. We then spin-cast films of **6.2** and **$(PBBr_4)_3$** onto this surface at 1000 r.p.m. for 1 min, to form transistors using the silicon wafer as the global back gate for the device. The thickness of the organic films is 15−20 nm. OFETs made from thicker films (40−60 nm) exhibit nonlinear characteristic at low bias voltage. Finally, the film of **$(PBBr_4)_3$** was annealed under p-xylene vapor for 10 min and then annealed under inert atmosphere at 160 ^oC for 10 mins to optimize the device performance. The film of **6.2** was annealed under inert atmosphere

at 200 ^{o}C for 10 mins to optimize the device performance. Vapor annealing of p-xylene didn't show enhanced performance for **6.2**.

The mobility is calculated in the saturation regime using $I_{DS} = (W/2L)Ci\mu(V_G - V_T)^2$, where W and L are the width and length of the channel, Ci (11.5 nFcm^{-2}), μ, and V_T correspond to the capacitance per unit area of the gate insulator, the field effect mobility, and the threshold voltage, respectively. W = 105 μm and L = 20 μm for transistor devices. W = 2 mm and L = 10 μm for sensor devices.

The crystalline material **$(PBBr_4)_3$** provide a unique opportunity to study how thin film assembly and charge transport are affected by the dynamics of the semiconducting subunits. This is important because, if films can be made to maintain the open spaces on the interior of the hollow semiconductor, they could be used as a locus for guest incorporation to modulate the semiconducting properties. The crystalline material made here, **$(PBBr_4)_3$**, possesses an enormous amount of space within their interiors.

A saturated vapor of the analyte or odor is delivered to the thin film transistor using a bubbler. Nitrogen was used as the carrier gas. A sealed exposure chamber with a volume of 1.7 L was used; the flow rate of N_2 through the chamber was 0.2 Lmin^{-1}. Responsing experiments were conducted by fixing the drain voltage at the determined minimum saturation value and conducting gate sweeps. The gate was applied in a pulsed manner in order to reduce device hysteresis. The responses of these devices to analytes were investigated by plotting the percent change in drain current, $I_{DS}/I_{DS,0}$ (measured at V_G = 80 V, V_{DS} = 80 V) versus time of exposure to analytes. For concentration dependent measurement, the analyte concentration was set via a saturated vapor of the analyte or odor using a bubbler, subsequently diluted through a series of gas mass-flow

controllers (FMA-5506A and FMA-5514A). During the course of experiment, the total fow rate of the N_2 gas was set to a constant 500 standard cubic centimeter (SCCM).

6.10. Synthetic Procedures and Characterizations

Synthesis of **6.1**: A solution of 1,7-dibromoperylene-3,4,9,10-tetracarboxylicbisimides (1.145 g, 1.34 mmol, 1.00 equiv) in toluene (15 mL) was degassed under nitrogen for 20 minutes. In a separate flask, a solution of 2,5-bis(trimethylstannyl)thiophene (2.64g, 6.44 mmol, 4.81 equiv) in toluene (20 mL) was degassed under nitrogen for 20 minutes. The 2,5-bis(trimethylstannyl)thiophene solution was transferred under nitrogen to the dibromoperylene solution, and degassed for 40 minutes. Tetrakis(triphenylphosphine)palladium(0) (70 mg, 0.06 mmol, 4 mol%) was added, and the resultant solution was degassed for 20 minutes. The mixture was placed in oil bath set at 115 ^oC for 13 h under nitrogen. The resultant blue reaction mixture was concentrated via rotoevaporation under reduced pressure. The product was purified using C_{18} reverse phase column chromatography (DCM:acetonitrile 1:1) to yield blue-purple solid **6.1** (1.10 g, 0.93 mmol, 69%). **^{1}H NMR** (500 MHz, $CDCl_3$): δ 8.65 (br, 2H); 8.21 (br, 2H); 8.12 (d, J = 8 Hz, 2H); 7.38 (d, J = 3 Hz, 2H); 7.22 (d, J = 3Hz, 2H); 5.16 (m, 2H); 2.26-2.22 (m, 4H); 1.83 (m, 4H); 1.28 (m, 24H); 0.85 (m, 12H); 0.46*(s, 18H). **^{13}C NMR** (100 MHz, $CDCl_3$): δ 164.59; 163.47; 149.25; 141.92*; 136.82; 136.16; 135.47; 134.83; 133.61; 132.95; 130.01; 129.41; 129.20; 128.39; 128.04; 122.71; 122.57; 122.01; 121.83; 54.57; 32.28; 31.70; 26.53; 22.51; 14.00; -8.02*. **IR** (ATR-ZnSe) [cm $^{-1}$] 3025, 2966, 2929, 2909, 2842, 2723, 2244, 1628, 1427, 1371. **HRMS** (APCI+) calculated m/z for $[C_{60}H_{74}N_2O_4S_2Sn_2+H]^+$ 1189.3225; found 1189.3237. *Tin satellite peaks visible.

Synthesis of Trimer **6.2**: A solution of stannane **6.1** (833 mg, 0.70 mmol, 1.00 equiv) and dichloro(1,5-cyclooctadiene)platinum (262 mg, 0.70 mmol, 1.00 equiv) in 1,2-dichloroethane (180

mL, 3.9 mM) was placed in oil bath set at 85 °C under N_2 for 3 days. The blue solution was concentrated to a dark blue solid that was washed with hexane. The resultant solid was dried under vacuum. It was combined with 1,1′-ferrocenediyl-bis(diphenylphosphine) (550 mg, 1.00 mmol, 1.43 equiv) in CH_2Cl_2 (100 mL). The solution was set to stir under N_2 for 2 days. The solution was concentrated, and redissolved in toluene (100 mL) and combined with triphenylphosphine (2.01 g, 7.12 mmol, 10.17 equiv). The resultant solution was set to reflux under N_2 for 2 days. The reaction mixture was concentrated under reduced pressure, the resultant dark blue solid was subjected to Soxhlet extraction: hexane, methanol, acetone, and CH_2Cl_2. The CH_2Cl_2 extract contained the cyclic and acyclic compounds. The resultant solid was first purified by alumina chromatography using gradient of 50% CH_2Cl_2/hexane to 80% CH_2Cl_2/hexane. The resultant fractions with cyclic and acyclic compounds were purified into its individual cyclic components by HPLC with a 5PBB column eluting with 27% CH_2Cl_2/hexane. Trimer **6.2** (90 mg, 0.035 mmol, 15% yield); tetramer (62 mg, 0.018 mmol, 10% yield); pentamer (32 mg, 0.007 mmol, 5% yield); hexamer (26 mg, 0.005 mmol, 4% yield). The remaining mass balance is higher order cyclic and acyclic oligomers.

Trimer **6.2**: **^{1}H NMR** (500 MHz, CD_2Cl_2): δ 8.48-8.47 (br, 6H); 8.37 (d, J = 8.1 Hz, 6H); 8.23 (br, 6H); 7.57 (d, J = 3.7 Hz, 6H); 7.43 (d, J = 3.7 Hz, 6H); 5.07-5.04 (m, 6H); 2.12 (br, 12H); 1.74 (br, 12H); 1.26-1.21 (m, 72H); 0.80-0.71 (m, 36H). **^{13}C NMR** (100 MHz, $CDCl_3$): δ 164.21; 163.17; 144.32; 139.55; 135.94; 135.23; 134.17; 133.18; 131.89; 130.60; 129.87; 129.38; 128.77; 128.05; 127.79; 125.16; 125.16; 122.84; 122.22; 54.65; 32.19; 31.59; 26.49; 22.42; 13.92. **IR** (ATR-ZnSe) [cm $^{-1}$] 2924.4; 2856.6; 1696.9; 1655.7; 1584.9; 1455.0; 1400.9; 1321.2; 1243.0; 1180.2; 1118.0; 974.9; 911.8; 859.2; 832.8; 810.1; 756.7; 713.5. **HRMS** (MALDI, dithranol matrix) calculated m/z for $[C_{162}H_{168}N_6O_{12}S_6]^-$ 2581.1039; found 2581.1036.

Tetramer: **^{1}H NMR** (500 MHz, $C_2D_2Cl_4$, 333K): δ 8.60 (s, 8H); 8.41 (d, J = 8.2 Hz, 8H); 8.31(d, J = 8.2 Hz, 8H); 7.51 (d, J = 3.7 Hz, 8H); 7.33 (d, J = 3.7 Hz, 8H); 5.14-5.09 (m, 8H); 2.19-2.16 (m, 16H); 1.90-1.87 (m, 16H); 1.31-1.27 (m, 96H); 0.83-0.82(m, 48H). **^{13}C NMR** (100 MHz, $CDCl_3$): δ 164.31; 163.22; 144.16; 139.22; 135.91; 135.19; 134.04; 132.55; 132.21; 130.24; 129.69; 128.99; 128.41; 128.01; 125.69; 122.82; 122.24; 54.69; 32.22; 31.63; 26.50; 22.46; 13.93. **IR** (ATR-ZnSe) [cm $^{-1}$] 2923.3; 2855.9; 1696.9; 1655.9; 1584.6; 1454.6; 1401.4; 1320.7; 1241.7; 1179.6; 1118.9; 973.8; 926.6; 860.3; 832.7; 809.9; 755.6; 715.7. **HRMS** (MALDI, dithranol matrix) calculated m/z for $[C_{216}H_{224}N_8O_{16}S_8]^-$ 3441.4721; found 3441.4648.

Pentamer: **^{1}H NMR** (500 MHz, CD_2Cl_2): δ 8.59-8.57 (br, 10H); 8.35 (d, J = 8.2 Hz, 10H); 8.25 (br, 10H); 7.40 (d, J = 3.6 Hz, 10H); 7.35 (d, J = 3.6 Hz, 10H); 5.08 (br, 10H); 2.16-2.13 (m, 20H); 1.76-1.75 (m, 20H); 1.26-1.17 (m, 120H); 0.76-0.73 (m, 60H). **^{13}C NMR** (100 MHz, $CDCl_3$): δ 164.37; 163.28; 143.59; 139.25; 135.98; 135.26; 134.15; 132.69; 132.27; 130.33; 129.70; 129.09; 128.70; 128.10; 125.60; 123.02; 122.83; 122.30; 122.06; 54.63; 32.18; 31.63; 26.48; 22.45; 13.96. **IR** (ATR-ZnSe) [cm $^{-1}$] 2925.7; 2856.1; 1699.1; 1658.4; 1586.2; 1403.5; 1323.6; 1275.6; 1260.9; 750.7. **HRMS** (MALDI, dithranol matrix) calculated m/z for $[C_{270}H_{280}N_{10}O_{20}S_{10}]^-$ 4031.8402; found 4031.8465.

Hexamer: **^{1}H NMR** (500 MHz, $CDCl_3$): δ 8.62 (br, 12H); 8.36 (d, J = 8.2 Hz, 12H); 8.28 (br, 12H); 7.37-7.33 (m, 24H); 5.10 (br, 12H); 2.18-2.16 (m, 24H); 1.79-1.77 (m, 24H); 1.52-1.19 (m, 144H); 0.78-0.77 (m, 72H). **^{13}C NMR** (100 MHz, $CDCl_3$): δ 164.41; 163.28; 143.56; 139.26; 136.04; 135.35; 134.28; 132.89; 132.37; 131.20; 130.41; 129.74; 129.17; 128.74; 128.20; 127.95; 125.81; 122.93; 122.34; 54.72; 32.24; 31.67; 26.53; 22.48; 13.98. **IR** (ATR-ZnSe) [cm $^{-1}$] 2952.0; 2923.1; 2856.0; 1696.9; 1655.9; 1585.2; 1455.7; 1402.7; 1321.6; 1246.6; 1180.0; 1121.2; 862.4;

833.4; 757.8. **HRMS** (MALDI, dithranol matrix) calculated m/z for $[C_{324}H_{336}N_{12}O_{24}S_{12}]^-$ 5162.2084; found 5162.2105.

Interconversion study of both enantiomers of trimer **6.2**: The enantiomers of trimer **6.2** was separated on CHIRALPAK IA-3 column (21 mm ID x 250 mm, 5μm) on Waters Prep150 instrument eluting with 24% dichloromethane in hexane. Each enantiomer (1 mg each) labeled **trimer-entA** (shorter retention time, t = 14.7 min) and **trimer-entB** (longer retention time, t = 28.0 min) was dissolved in 1 mL of anhydrous 1,2-dichlorobenzene, sparged under N_2 for 30 minutes. It was placed in oil bath set at 160 ^oC for 19 hours. The solvent was distilled off under high vacuum reduced pressure. ^{1}HNMR was identical to starting enantiomer and the chiral HPLC trace exhibited same retention time.

Synthesis of **$(PBBr_4)_3$**: A solution of trimer **6.2** (60 mg, 0.023 mmol) in CH_2Cl_2 (5 mL) was set stirring in a vial. Excess bromine (0.5 mL) was added, followed by a crystal of iodine. The reaction was capped and left to stir for 3 days. The solvent and bromine was purged under air. The resultant red solid was dissolved in chloroform and purified by small silica gel column chromatography, eluting with 100% chloroform to yield dark violet solids (65 mg, 0.018 mmol, 80% yield). **^{1}H NMR** (400 MHz, $CDCl_3$): δ 8.77-8.74 (br, 6H); 8.36-8.33 (br, 6H); 8.07 (d, J = 8 Hz, 6H); 5.09-5.06 (m, 6H); 2.14-2.06 (m, 12H); 1.83 (br, 12H); 1.25 (br, 72H); 0.80-0.77 (m, 36H). **^{13}C NMR** (100 MHz, $CDCl_3$): δ 163.98; 163.61; 162.89; 162.48; 140.20; 135.36; 134.61; 133.31; 132.95; 130.86; 130.37; 129.52; 128.47; 128.07; 123.48; 122.78; 117.27; 116.26; 54.86; 32.07; 31.56; 26.51; 22.45; 13.94. **IR** (ATR-ZnSe) [cm^{-1}] 3005.9; 2986.5; 2923.4; 2851.9; 1696.9; 1656.4; 1584.9; 1394.5; 1320.0; 1260.8; 862.9; 811.9; 750.5. **HRMS** (MALDI, dithranol matrix) calculated m/z for $[C_{162}H_{156}Br_{12}N_6O_{12}S_6]^-$ 3516.0306; found 3516.0356

6.11. NMR Spectra of Compounds

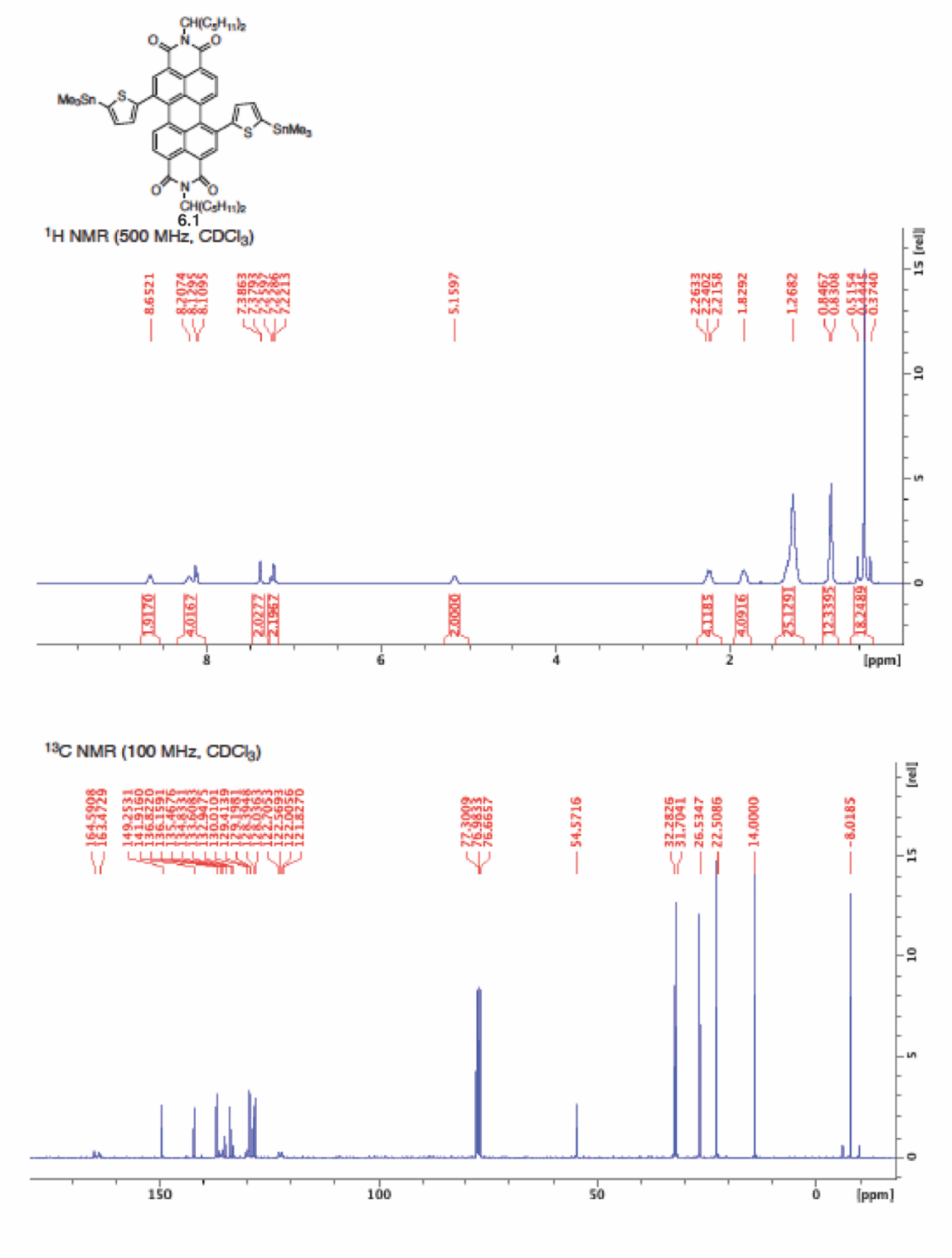

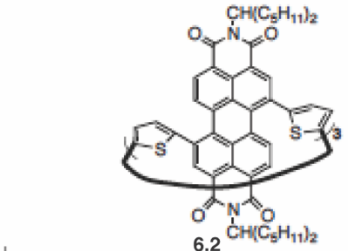

6.2

^{1}H NMR (500 MHz, CD_2Cl_2)

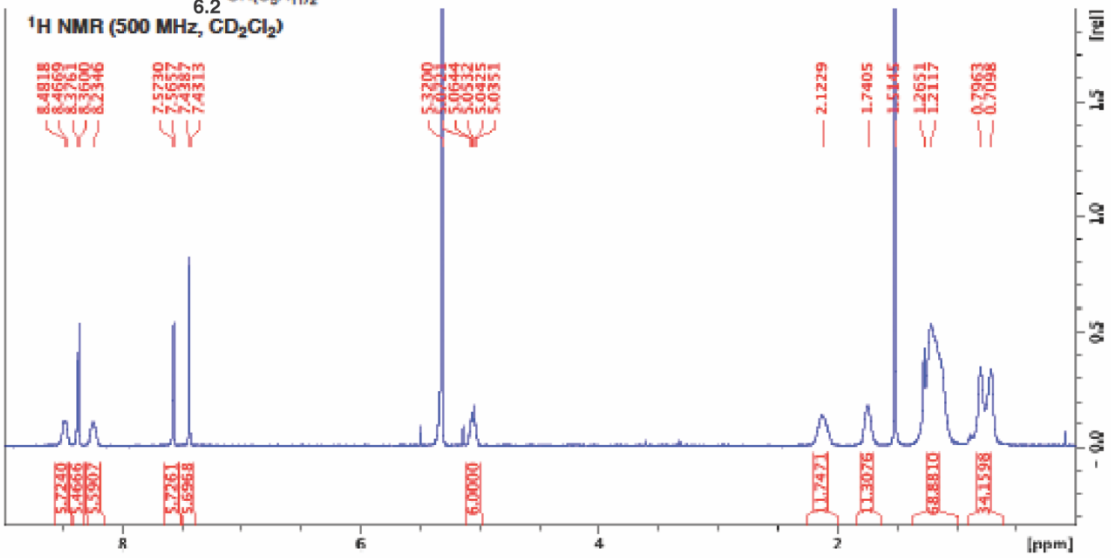

COSY (400 MHz, $CDCl_3$)

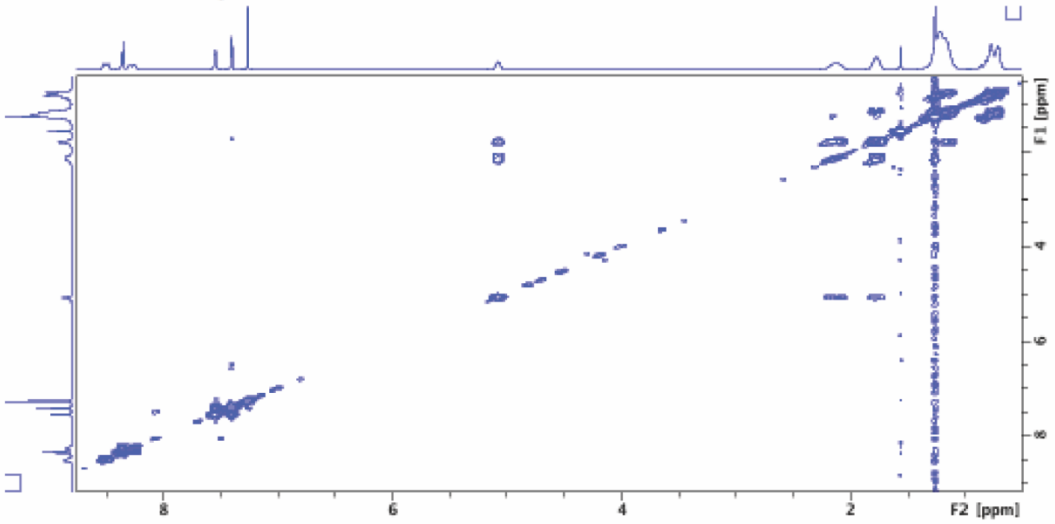

^{13}C NMR (100 MHz, $CDCl_3$) **Trimer 1**

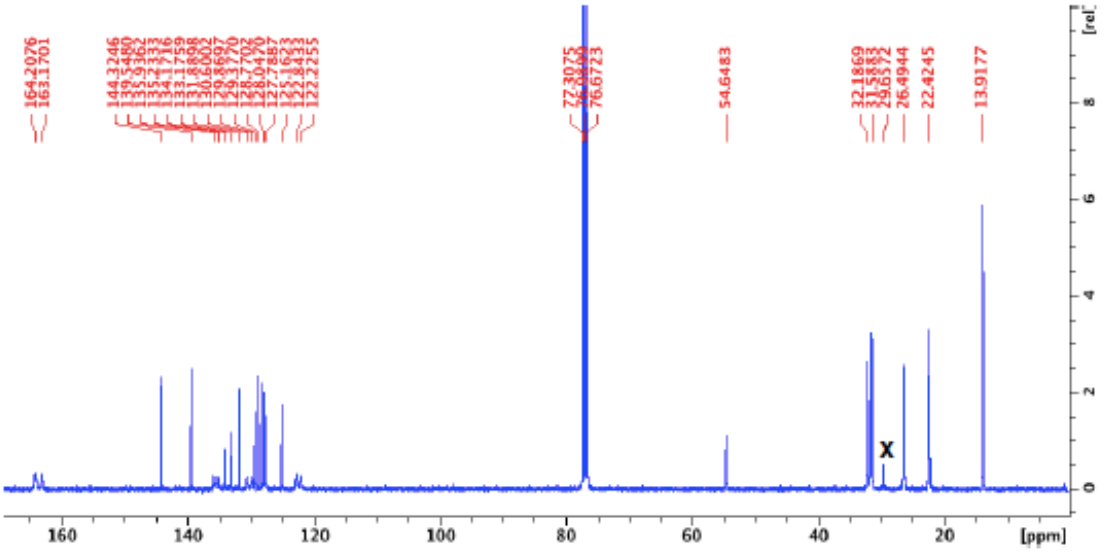

Chiral HPLC trace of trimer 1

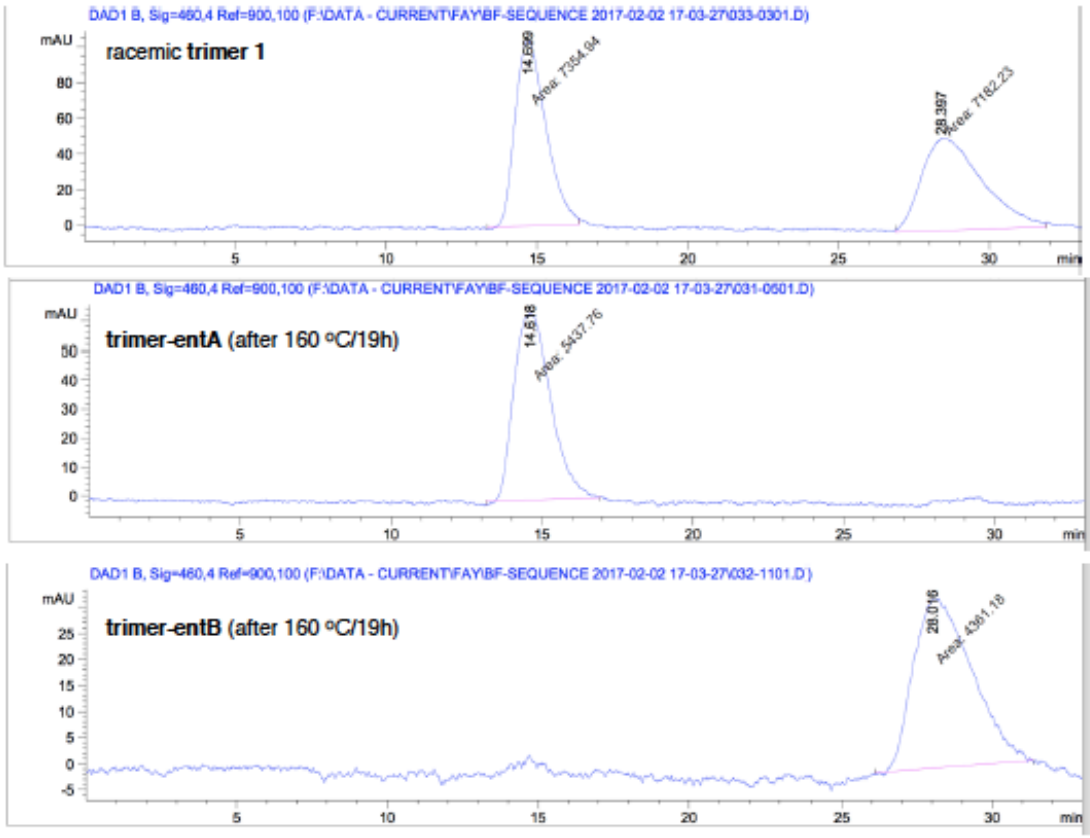

Tetramer

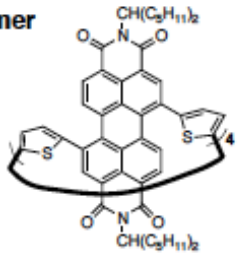

^{1}H NMR (500 MHz, $C_2D_2Cl_4$, 333K)

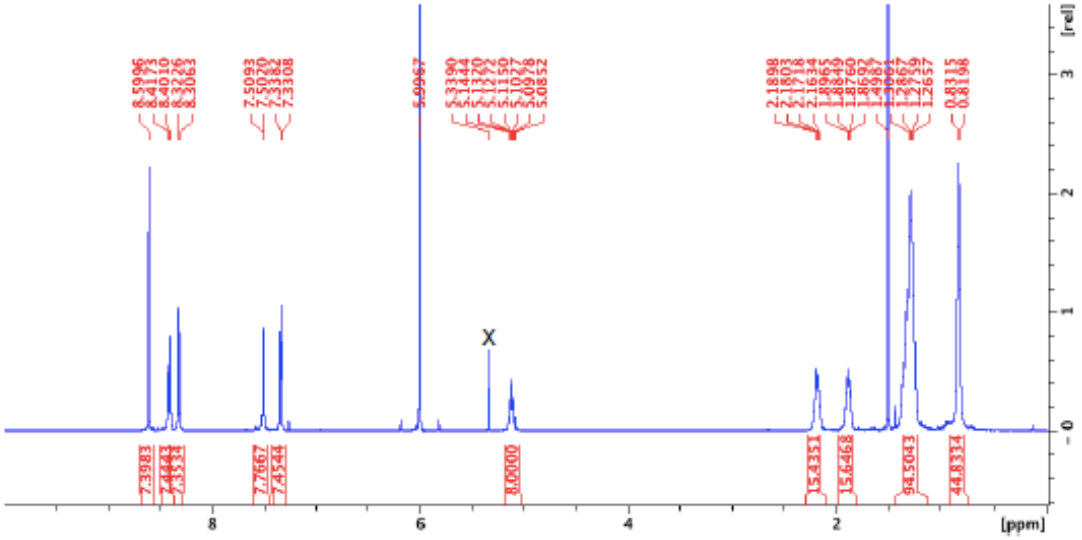

^{13}C NMR (100 MHz, $CDCl_3$)

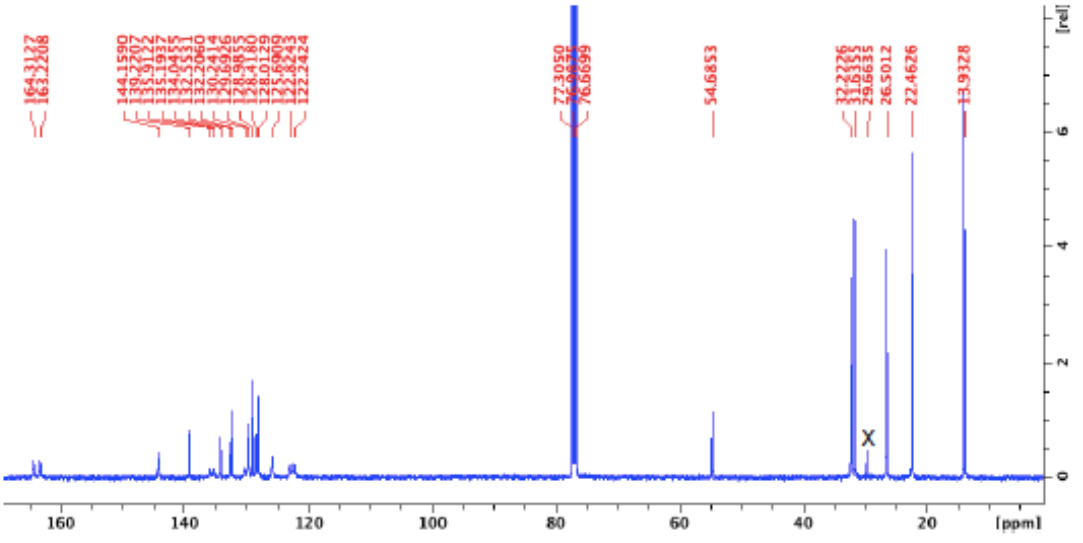

Pentamer

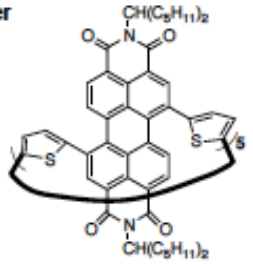

^{1}H NMR (500 MHz, CD_2Cl_2)

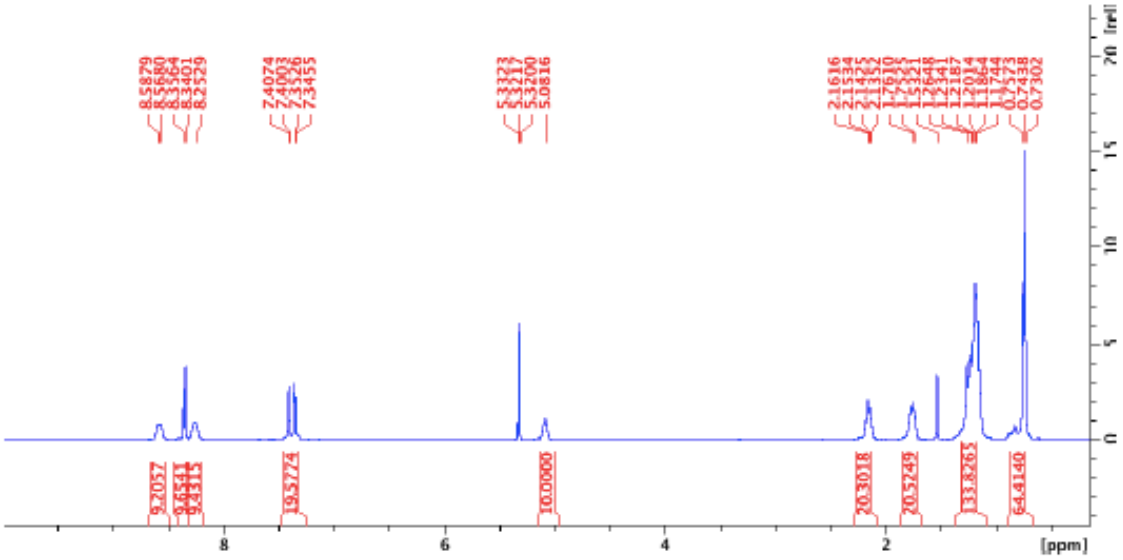

^{13}C NMR (100 MHz, $CDCl_3$)

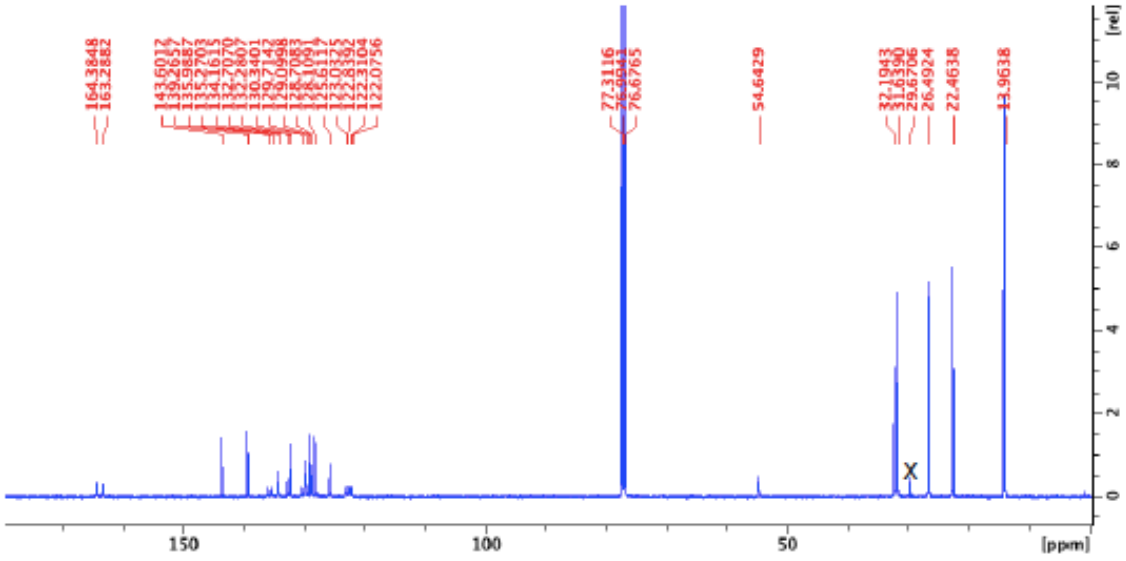

Hexamer

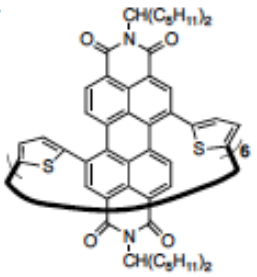

^{1}H NMR (500 MHz, $CDCl_3$)

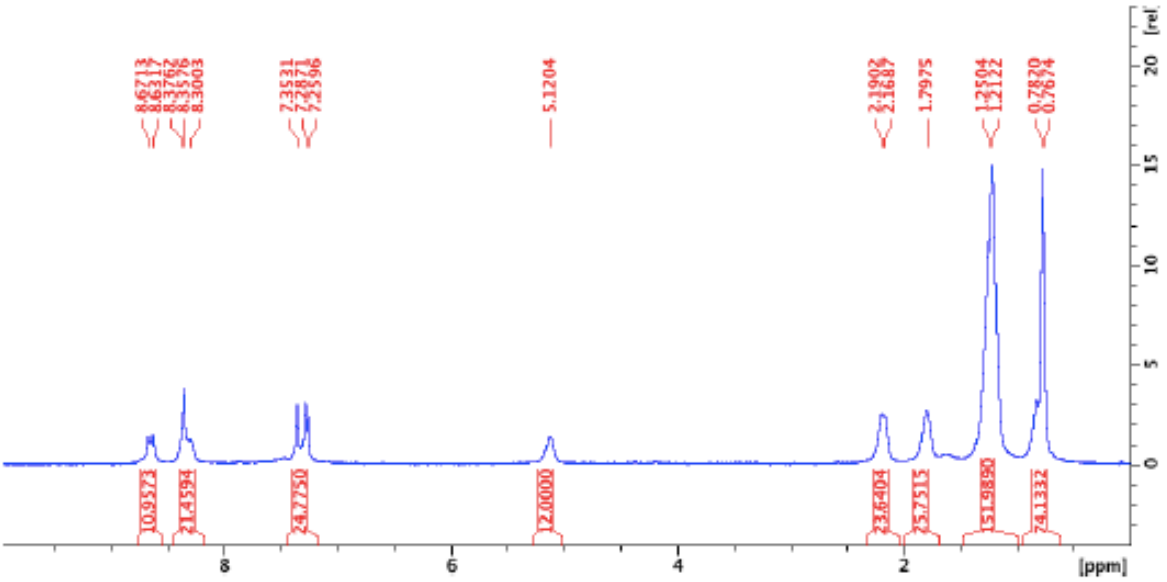

^{13}C NMR (100 MHz, $CDCl_3$)

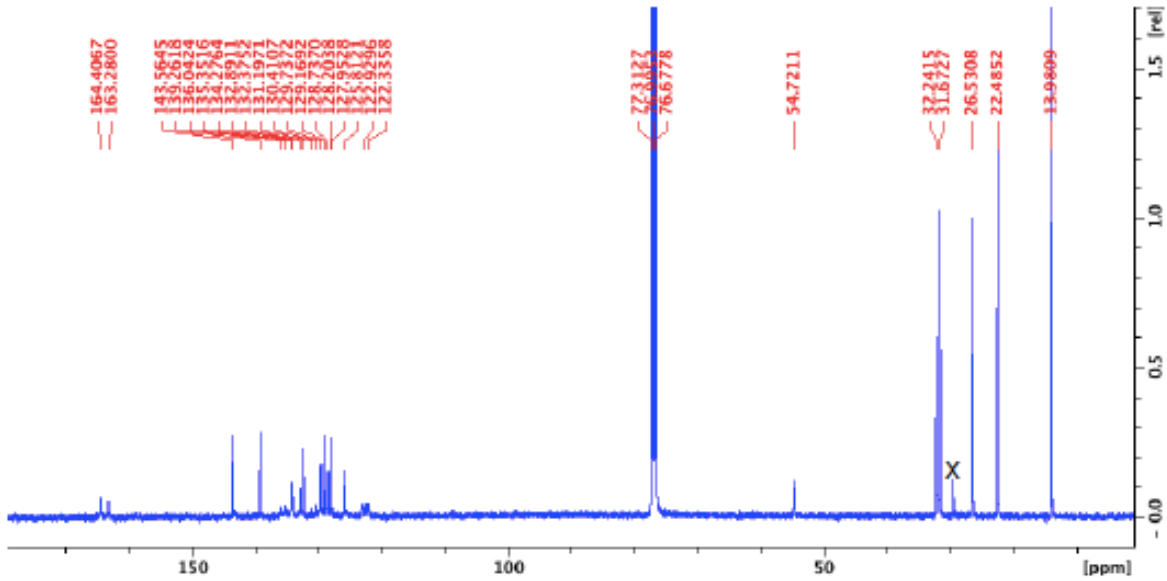

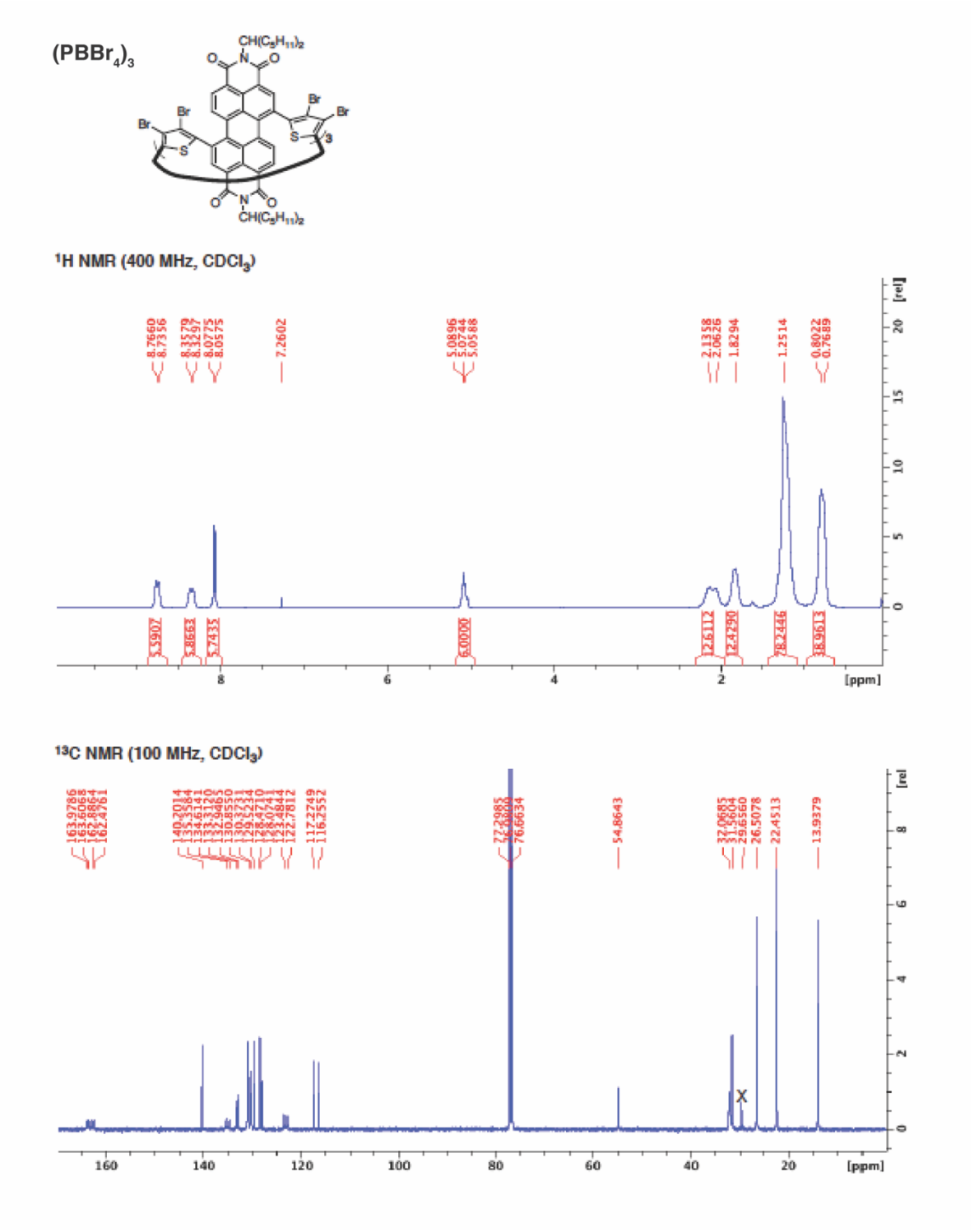

6.12. DFT Output

All quantum chemical calculations were performed using Jaguar, version 8.3, Schrodinger, Inc., New York, NY, 2013. (See A. D. Bochevarov, E. Harder, T. F. Hughes, J. R. Greenwood, D. A.

Braden, D. M. Philipp, D. Rinaldo, M. D. Halls, J. Zhang, R. A. Friesner, "Jaguar: A High Performance Quantum Chemistry Software Program with Strengths in Life and Materials Sciences", Int. J. Quantum Chem., 2013, 113(18), 2110-2142). All geometries were optimized using the B3LYP functional and the LACVP** basis set.

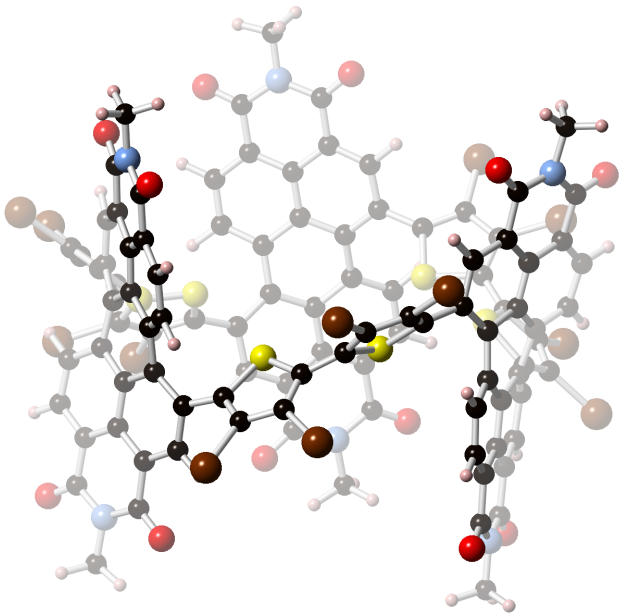

$(PBBr_4)_3$

Final Heat of Formation: -7687.0083

Br	-11.07353	3.05844	-0.23637
Br	-11.93869	3.46266	3.15296
Br	-8.48656	-0.88369	-4.04970
Br	-10.80890	-0.40223	-1.44883
Br	4.23672	3.23274	-0.88615
Br	1.79296	5.04959	-2.67498
Br	5.30854	-2.57089	0.97605
Br	4.31135	-0.46729	-1.68291
Br	-3.05497	-3.40898	11.33508
Br	-6.38367	-4.16710	10.51682
Br	0.87547	1.11359	11.50628
Br	-2.44482	0.17504	12.15510
C	-9.33767	3.24094	5.42546
C	-9.40297	1.92425	4.90928
C	-9.16817	0.83267	5.77151
C	-8.62842	1.08765	7.07171
C	-8.64150	2.41378	7.58827
C	-9.03450	3.48441	6.74887
C	-8.06639	0.03691	7.86304

C	-7.71193	0.31862	9.18462
C	-7.82682	1.60905	9.71899
C	-8.25714	2.66005	8.92599
C	-9.49938	-0.56456	5.46372
C	-8.81960	-1.60031	6.17630
C	-7.93528	-1.30052	7.26315
C	-10.48131	-0.92308	4.53613
C	-10.74878	-2.26193	4.22537
C	-10.00544	-3.27343	4.80971
C	-9.02629	-2.95154	5.77786
C	-8.22905	-3.97019	6.35017
C	-7.23209	-3.63607	7.24103
C	-7.05906	-2.31098	7.71072
C	-5.85637	-2.07422	8.53944
C	-9.56127	1.78415	3.44596
C	-9.07143	1.31119	0.99267
C	-10.13844	2.15725	1.19198
C	-10.42343	2.40218	2.57208
C	-8.44813	0.83379	-0.23512
C	-6.72642	0.28831	-2.02923
C	-8.00806	-0.09409	-2.34572
C	-8.97526	0.18922	-1.33036
C	-5.17460	-1.28404	-3.13110
C	-3.96057	-1.64237	-3.67946
C	-2.90796	-0.69778	-3.73468
C	-3.13262	0.62472	-3.26029
C	-4.45546	1.03626	-2.90050
C	-5.44755	0.04746	-2.73306
C	-1.64162	-1.06783	-4.24243
C	-0.61166	-0.14245	-4.25707
C	-0.79568	1.12603	-3.69214
C	-2.01908	1.51231	-3.13969
C	-2.22550	2.80002	-2.46091
C	-3.55936	3.31769	-2.46751
C	-4.67930	2.48426	-2.77498
C	-3.78592	4.68687	-2.15386
C	-5.07199	5.25210	-2.31573
C	-6.11677	4.45856	-2.76037
C	-5.92531	3.08595	-2.96582
C	-1.20653	3.56457	-1.85481
C	-1.47533	4.89969	-1.46795
C	-2.71357	5.47371	-1.66964
C	0.10130	2.99726	-1.46244
C	1.88886	1.57740	-0.34176
C	2.38510	2.69606	-0.96862
C	1.37777	3.48278	-1.61274

C	2.54715	0.52847	0.42693
C	3.13326	-1.11610	2.27379
C	3.88040	-1.27034	1.13203
C	3.54261	-0.35674	0.08376
C	2.83794	-3.32561	3.34276
C	2.54861	-4.13628	4.42291
C	2.31556	-3.55707	5.69429
C	2.45047	-2.14956	5.85785
C	2.97364	-1.36075	4.78797
C	3.03873	-1.93296	3.50059
C	1.93828	-4.36425	6.79260
C	1.66640	-3.77604	8.01649
C	1.69603	-2.38205	8.15447
C	2.04054	-1.54597	7.08961
C	2.04368	-0.07834	7.19056
C	2.92627	0.61651	6.30065
C	3.45842	-0.01755	5.13497
C	1.29689	0.67647	8.12088
C	1.60767	2.04643	8.30475
C	2.61885	2.66681	7.60165
C	3.28025	1.96981	6.56389
C	4.26940	2.61589	5.78558
C	4.86820	1.93886	4.73477
C	4.44619	0.64552	4.39942
C	-3.52396	-1.37070	9.28407
C	-4.04545	-2.42019	10.00572
C	-5.36533	-2.79296	9.60330
C	-2.22110	-0.72073	9.37786
C	0.10471	0.17342	8.84045
C	-0.27978	0.35125	10.14919
C	-1.59594	-0.12240	10.44696
C	-3.75381	-3.03975	-4.14546
C	-1.41755	-2.43617	-4.77158
C	-2.92880	6.89972	-1.31338
C	-5.30798	6.69122	-2.02938
C	2.95504	4.08335	7.90248
C	4.67809	4.00837	6.10148
C	2.40753	-5.60312	4.22257
C	1.84905	-5.83730	6.64324
C	-8.33312	4.03245	9.48606
C	-9.06411	4.88169	7.25847
C	-10.24907	-4.68828	4.42997
C	-8.40455	-5.39201	5.95374
C	-2.23912	-4.69109	-5.18263
C	-9.67075	-7.04535	4.62499
C	1.97632	-7.81610	5.22954

C	-4.39942	8.83668	-1.20927
C	4.39916	6.02908	7.43356
C	-8.80226	6.40309	9.18526
H	-9.52884	4.08924	4.77898
H	-7.34300	-0.47703	9.81971
H	-7.56185	1.81008	10.75173
H	-11.05295	-0.14969	4.03882
H	-11.51876	-2.52652	3.50823
H	-6.57095	-4.42231	7.58373
H	0.34330	-0.43066	-4.68372
H	0.03865	1.81593	-3.67921
H	-7.08857	4.91509	-2.91565
H	-6.77047	2.48092	-3.27181
H	-0.70049	5.49879	-1.00347
H	1.40657	-4.41402	8.85473
H	1.44406	-1.94916	9.11446
H	1.04943	2.63701	9.02027
H	5.64571	2.43905	4.16718
H	4.90250	0.15106	3.55118
H	-3.14412	-5.27438	-5.03015
H	-8.96361	-7.67496	5.15982
H	2.19965	-8.07365	4.19690
H	-5.42885	9.09733	-1.44347
H	3.78378	6.39086	8.25397
H	-9.14251	7.07841	8.40381
H	-5.92932	-2.05243	-3.01117
H	2.90329	-3.77953	2.36086
H	-1.39929	-5.13655	-4.64477
H	-1.98239	-4.64902	-6.24359
H	-9.53579	-7.14759	3.54580
H	-10.69792	-7.32567	4.86908
H	0.96584	-8.13656	5.49382
H	2.67826	-8.30312	5.90990
H	-3.70579	9.44527	-1.79371
H	-4.19218	9.00359	-0.14978
H	4.26076	6.65201	6.54707
H	5.45667	6.05069	7.70605
H	-7.81568	6.70218	9.54654
H	-9.49355	6.41084	10.03083
N	-2.48894	-3.33613	-4.67786
N	-4.21114	7.41845	-1.53547
N	3.99121	4.64998	7.14282
N	2.08855	-6.35902	5.36280
N	-8.73749	5.05338	8.61340
N	-9.42728	-5.65526	5.02730
O	-11.11744	-5.02182	3.63506

O	-7.70685	-6.28815	6.40827
O	-8.06324	4.28705	10.65152
O	-9.36645	5.83001	6.54729
O	-4.63313	-3.88657	-4.07512
O	-0.35634	-2.78958	-5.26623
O	1.58015	-6.58510	7.57349
O	2.56485	-6.12826	3.12941
O	2.37256	4.72116	8.76817
O	5.56854	4.59148	5.49820
O	-2.04493	7.60896	-0.85323
O	-6.39595	7.22019	-2.20797
S	-8.37950	0.85963	2.54020
S	-6.71582	1.02359	-0.43922
S	0.14310	1.53685	-0.49714
S	1.99070	0.19344	2.05421
S	-4.67061	-0.87885	8.04886
S	-1.18671	-0.62416	7.96230

6.13. References

1. Zhang, B. *et al.* Hollow organic capsules assemble into cellular semiconductors. *Nat. Commun.* **9**, 1957 (2018).
2. Krömer, J. *et al.* Synthesis of the First Fully α-Conjugated Macrocyclic Oligothiophenes: Cyclo[n]thiophenes with Tunable Cavities in the Nanometer Regime. *Angew. Chem. Int. Ed.* **39**, 3481–3486 (2000).
3. Nakao, K. *et al.* Giant Macrocycles Composed of Thiophene, Acetylene, and Ethylene Building Blocks. *J. Am. Chem. Soc.* **128**, 16740–16747 (2006).
4. Darzi, E. R. *et al.* Synthesis, Properties, and Design Principles of Donor–Acceptor Nanohoops. *ACS Cent. Sci.* **1**, 335–342 (2015).
5. Ball, M. *et al.* Chiral Conjugated Corrals. *J. Am. Chem. Soc.* **137**, 9982–9987 (2015).
6. Ito, H. *et al*. Thiophene-Based, Radial pi-Conjugation: Synthesis, Structure, and Photophysical Properties of Cyclo-1,4-phenylene-2 ',5 '-thienylenes. *Angew. Chem. Int. Ed.* **54**, 159–163 (2015).
7. Xue, J. Y. *et al.* Aromatic hydrocarbon macrocycles for highly efficient organic light-emitting devices with single-layer architectures. *Chem. Sci.* **7**, 896–904 (2016).
8. Kayahara, E. *et al*. Synthesis and Characterization of [n]CPP (n=5, 6, 8, 10, and 12) Radical Cation and Dications: Size-Dependent Absorption, Spin, and Charge Delocalization. *J. Am. Chem. Soc.* **138**, 338–344 (2016).
9. Kayahara, E. *et al*. Size Dependence of {[}n]Cycloparaphenylenes (n=5-12) in Electrochemical Oxidation. *Chem. Asian J.* **11**, 1793–1797 (2016).
10. Zhang, B. *et al.* Rigid, Conjugated Macrocycles for High Performance Organic Photodetectors. *J. Am. Chem. Soc.* **138**, 16426–16431 (2016).
11. Ball, M. *et al.* Macrocyclization in the Design of Organic n-Type Electronic Materials. *J.*

Am. Chem. Soc. **138**, 12861–12867 (2016).

12. Van Raden, J. M. *et al*. Synthesis and characterization of a highly strained donor-acceptor nanohoop. *Org. Biomol. Chem.* **14**, 5721 (2016).
13. Peeks, M. D. *et al*. Aromatic and antiaromatic ring currents in a molecular nanoring. *Nature* **541**, 200-203 (2017).
14. Zang, L. *et al*. One-Dimensional Self-Assembly of Planar π-Conjugated Molecules: Adaptable Building Blocks for Organic Nanodevices. *Acc. Chem. Res.* **41**, 1596–1608 (2008).
15. Izumi, T. *et al.* Efficient Blue Electroluminescence from a Single-layer Organic Device Composed Solely of Hydrocarbons. *Chem. Asian J.* **12**, 730–733 (2017).
16. Nishigaki, S. *et al.* Synthesis, Structures, and Photophysical Properties of Alternating Donor–Acceptor Cycloparaphenylenes. *Chem. Eur. J.* **23**, 7227–7231 (2017).
17. Thakellapalli, H. *et al.* Synthesis and Properties of Conjugated Macrocycles Containing 2,7-Bis(2-thienyl)-9H-fluoren-9-one Units. *Org. Lett.* **19**, 2674–2677 (2017).
18. Li, T. *et al.* Synthesis, solvent-dependent emission and two- photon absorption of a triangular -[D-pi-A](3)- macrocycle. *Org. Chem. Front.* **4**, 737–742 (2017).
19. Van Raden, J. M. *et al*. 2,2′-Bipyridyl-Embedded Cycloparaphenylenes as a General Strategy To Investigate Nanohoop-Based Coordination Complexes. *J. Am. Chem. Soc.* **139**, 2936–2939 (2017).
20. Li, C. *et al.* A diketopyrrolopyrrole-based macrocyclic conjugated molecule for organic electronics. *J. Mater. Chem. C* **7**, 3802–3810 (2019).
21. Kayahara, E. *et al.* Gram-Scale Syntheses and Conductivities of {[}10]Cycloparaphenylene and Its Tetraalkoxy Derivatives. *J. Am. Chem. Soc.* **139**, 18480–18483 (2017).
22. Zhang, F. *et al*. Giant Cyclo n thiophenes with Extended pi Conjugation. *Angew. Chem. Int. Ed.* **48**, 6632–6635 (2009).
23. Fenwick, O. *et al.* Linear and Cyclic Porphyrin Hexamers as Near-Infrared Emitters in Organic Light-Emitting Diodes. *Nano Lett.* **11**, 2451–2456 (2011).
24. Zhang, F. *et al.* Molecular and electronic structure of cyclo[10]thiophene in various oxidation states: polaron pair vs. bipolaron. *Chem. Sci.* **2**, 781–784 (2011).
25. Iyoda, M. *et al*. Conjugated Macrocycles: Concepts and Applications. *Angew. Chem. Int. Ed.* **50**, 10522–10553 (2011).
26. Jiang, H.-W. *et al.* Cyclic 2,12-Porphyrinylene Nanorings as a Porphyrin Analogue of Cycloparaphenylenes. *J. Am. Chem. Soc.* **137**, 2219–2222 (2015).
27. Kuwabara, T. *et al*. Curved Oligophenylenes as Donors in Shape-Persistent Donor–Acceptor Macrocycles with Solvatofluorochromic Properties. *Angew. Chem. Int. Ed.* **54**, 9646–9649 (2015).
28. Chen, Q. *et al.* Strain-Induced Stereoselective Formation of Blue-Emitting Cyclostilbenes. *J. Am. Chem. Soc.* **137**, 12282–12288 (2015).
29. Iwamoto, T. *et al*. Size-Selective Encapsulation of C60 by [10]Cycloparaphenylene:

Formation of the Shortest Fullerene-Peapod. *Angew. Chem. Int. Ed.* **50**, 8342–8344 (2011).

30. Ball, M. L. *et al.* Influence of Molecular Conformation on Electron Transport in Giant, Conjugated Macrocycles. *J. Am. Chem. Soc.* **140**, 10135–10139 (2018).

31. Ball, M. *et al.* Conjugated Macrocycles in Organic Electronics. *Acc. Chem. Res.* (2019). doi:10.1021/acs.accounts.9b00017

32. Iwamoto, T. *et al*. Selective and Random Syntheses of n Cycloparaphenylenes (n=8-13) and Size Dependence of Their Electronic Properties. *J. Am. Chem. Soc.* **133**, 8354–8361 (2011).

33. Cavallo, G. *et al.* The Halogen Bond. *Chem. Rev.* **116**, 2478–2601 (2016).

34. Dolomanov, O. V, *et al*. {\it OLEX2}: A complete structure solution, refinement and analysis program. *J. Appl. Crystallogr.* **42**, 339–341 (2009).

35. Su, W.-C. *et al.* Characterization of intrinsic hysteresis of pentacene-based organic thin-film transistor through in-situ real-time electrical measurement. *Jpn. J. Appl. Phys.* **53**, 03CC03 (2014).

36. Yaws, C. L. *et al*. Chapter 1 - Vapor Pressure – Organic Compounds. in (ed. Yaws, C. L. B. T.-T. Y. H. of V. P. (Second E.) 1–314 (Gulf Professional Publishing, 2015).

37. Hsieh, J. C. *et al*. Response characteristics of lead phthalocyanine gas sensor: effects of film thickness and crystal morphology. *Thin Solid Films* **322**, 98–103 (1998).

38. Sakai, G. *et al*. Theory of gas-diffusion controlled sensitivity for thin film semiconductor gas sensor. *Sensors Actuators B Chem.* **80**, 125–131 (2001).

39. Zhao, Y. H. *et al*. Fast Calculation of van der Waals Volume as a Sum of Atomic and Bond Contributions and Its Application to Drug Compounds. *J. Org. Chem.* **68**, 7368–7373 (2003).

40. Crone, B. *et al.* Electronic sensing of vapors with organic transistors. *Appl. Phys. Lett.* **78**, 2229–2231 (2001).

41. Huang, W. *et al.* Highly Sensitive NH3 Detection Based on Organic Field-Effect Transistors with Tris(pentafluorophenyl)borane as Receptor. *J. Am. Chem. Soc.* **134**, 14650–14653 (2012).

42. Farrow, C. L. *et al.* PDFfit2 and PDFgui: computer programs for studying nanostructure in crystals. *J. Phys. Condens. Matter* **19**, 335219 (2007).

43. Rajasingh, P. *et al*. Selective Bromination of Perylene Diimides under Mild Conditions. *J. Org. Chem.* **72**, 5973–5979 (2007).

44. You, J. B. *et al.* A polymer tandem solar cell with 10.6% power conversion efficiency. *Nat. Commun.* **4**, 10 (2013).

45. *CrysAlis Pro*. (2013).

46. Sheldrick, G. M. A short history of {\it SHELX}. *Acta Crystallogr. Sect. A* **64**, 112–122 (2008).

47. Sheldrick, G. M. {\it SHELXT} {--} Integrated space-group and crystal-structure determination. *Acta Crystallogr. Sect. A* **71**, 3–8 (2015).

48. Palatinus, L. *et al*. {\it SUPERFLIP} {--} a computer program for the solution of crystal structures by charge flipping in arbitrary dimensions. *J. Appl. Crystallogr.* **40**, 786–790 (2007).

49. Spek, A. L. Structure validation in chemical crystallography. *Acta Crystallogr. Sect. D* **65**, 148–155 (2009).

50. Sheldrick, G. M. Phase annealing in {\it SHELX}-90: direct methods for larger structures. *Acta Crystallogr. Sect. A* **46**, 467–473 (1990).

51. Le Page, Y. {\it MISSYM}1.1 {--} a flexible new release. *J. Appl. Crystallogr.* **21**, 983–984 (1988).

52. Betteridge, P. W. *et al*. {\it CRYSTALS} version 12: software for guided crystal structure analysis. *J. Appl. Crystallogr.* **36**, 1487 (2003).

53. Hammersley, A. P. *et al*. Two-dimensional detector software: From real detector to idealised image or two-theta scan. *High Press. Res.* **14**, 235–248 (1996).

54. Yang, X. *et al*. *PDFgetXgui: a program for pair distribution function transformation and visualization*. (2014).

55. Juhás, P. *et al*. {\it PDFgetX3}: a rapid and highly automatable program for processing powder diffraction data into total scattering pair distribution functions. *J. Appl. Crystallogr.* **46**, 560–566 (2013).

56. Toby, B. H. *et al*. Accuracy of pair distribution function analysis applied to crystalline and non-crystalline materials. *Acta Crystallogr. Sect. A* **48**, 336–346 (1992).

57. Qiu, X. *et al*. Reciprocal-space instrumental effects on the real-space neutron atomic pair distribution function. *J. Appl. Crystallogr.* **37**, 110–116 (2004).

Chapter 7. Chiral PDI as Electron Deficient Moiety in Locked Cycloparaphenylene

7.1. Preface

Chapter 7 contains work from a collaboration between the Nuckolls Laboratory and the Yamago Laboratory at Kyoto University. I synthesized **PPh_6-PhHex** while in Kyoto University with invaluable assistance from Sun Liansheng. I performed all compound characterizations. Nathanial Schuster performed the CD analysis. I performed the DFT calculations, with valuable input from Dr. Michael Steigerwald.

7.2. Introduction

This manuscript describes a new donor/acceptor macrocycle that incorporates PDI and is shape persistent and chiral. Conformationally rigid and chiral macrocycles remain a challenging synthetic target as they require the design of a rigid scaffold in order to impede isomerization between stereoisomers. Chapter 6 described **$(PBBr_4)_3$** as a sensor and nanoreactor[1] with small molecule guests, and we envision additional potential uses within catalysis,[2] sensing,[1,3,4] and applications requiring preferential absorption of light; such as, circularly polarized light (CPL) emitters[5–8] with macrocyclic host with larger cavities. Isobe and coworkers too have synthesized conformationally rigid arene-based macrocycles.[9–11] Here we show the design and synthesis of the first chiral, donor/acceptor nanobelt that incorporates a PDI as the electron acceptor moiety (part of the system that has low energy empty space available to accept an electron), and an alkoxy-substituted CPP belt as the donor moiety (part of the molecule that possesses a large density of high energy electrons).

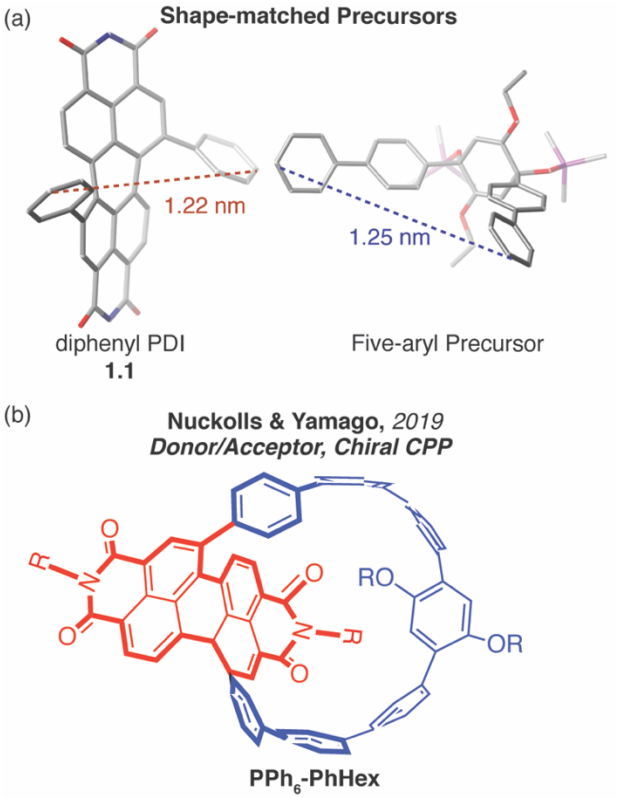

Figure 7.1. (a) The two pieces that were joined to make **PPh$_6$-PhHex**: a diphenyl PDI (Compound **1.1**) and five-aryl precursor that possess analogous distance between substituents; (b) a PDI-substituted CPP called **PPh$_6$-PhHex**, where the PDI is the electron poor and the belt is the electron rich portion of the molecule. Red = relative electron poor subunit = lower energy available space to accept an electron and blue = relative electron rich subunit e.g. larger density of high energy electrons. R = $C_{11}H_{23}$ for PDI and R = OC_6H_{13} for aryl ring.

7.3. Design of Conformationally Restricted Macrocycle

We used DFT to calculate the aryl-aryl distance in **1.1** (1.22 nm), and chose a five-aryl CPP precursor (**7.2**) that was best matched to form a one-to-one complex (Figure 7.1a).[12] We call this molecule **PPh$_6$-PhHex**. Relative to unsubstituted CPPs,[13–15] the addition of a PDI molecule results in strong absorption in the visible range up to 700 nm for **PPh$_6$-PhHex**. Using HPLC and CD experiments, we find **PPh$_6$-PhHex** exists as a pair of enantiomers that are conformationally rigid and do not racemize up to temperatures of 100 °C.

Our previous work consisted of the design and synthesis of chiral donor/acceptor macrocycles, with a PDI as the relative electron deficient moiety and a phenyl-bithiophene-phenyl

or phenyl moiety as the electron rich part of the molecule.[16–20] PDI has many advantages as electronic materials.[21–25] Due to their n-type behavior and broad absorption of visible light, we have used these macrocycles in electronic applications such as OFETs, OPVs, OPDs, and sensors. The motivation for the design of **PPh$_6$-PhHex** was to create a chiral, conformationally rigid molecule.

PPh$_6$-PhHex was a challenging synthetic target due to the large amount of strain in the macrocycle. We performed homodesmotic calculations to assess the strain energy in **PPh$_6$-PhHex**, and found **PPh$_6$-PhHex** possesses 63 kcal/mol of strain energy (Section 7.13.3). This is similar to an **[8]**- and **[10]CPP** with similar sized cavities.[15] Homodesmotic calculations compute the enthalpy difference between the macrocycle and an acyclic analog. The design of **PPh$_6$-PhHex** was inspired by the Yamago[12] and Jasti[6,26] laboratories who use an unstrained borylated precursor as a means to access conformationally strained and rigid CPPs (Section 1B.3). Previous syntheses in the Nuckolls' laboratory used a bis-platinated PDI (**2.2**) in the macrocyclization step[19] that is formed from a double transmetalation of 1,7-Bis[4-(tributylstannyl)-phenyl]-PDI.

7.4. Synthesis of PPh$_6$-PhHex

We use a cross coupling strategy in the synthesis of **PPh$_6$-PhHex**. Figure 7.2 shows the synthesis of **PPh$_6$-PhHex**. Compounds **2.2** and **7.2** were reacted with K_3PO_4 in tetrahydrofuran (THF) at 55 °C for 48 hours. We isolated intermediate compound **7.3** in a 6% yield, and proceeded to the reductive aromatization of **7.3** using $SnCl_2$ and HCl to yield our target compound **PPh$_6$-PhHex** as a teal solid. We also isolate the precursor to **SI-7.1** also in a 6% yield (Figure 7.6 and 7.7). This byproduct suggests there is some degree of reversibility in the transmetalation step of the reaction sequence. Section 7.13 contains the details of the calculations to assess the strain energy, synthesis, and characterization of **PPh$_6$-PhHex**.

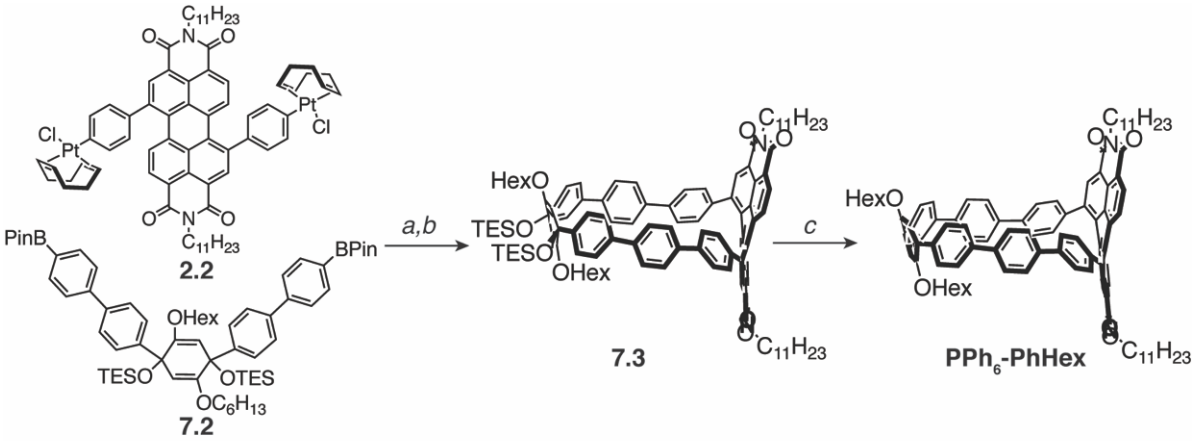

Figure 7.2. Synthesis of **PPh$_6$-PhHex**. Compounds **2.2** and **7.2** are reacted in equimolar ratios to afford intermediate **7.3** in a 6% yield. **PPh$_6$-PhHex** is obtained after an aromatization step. key: [a]K_3PO_4, THF, 55 °C, 48 h; [b]PPh_3, toluene, 100 °C, 22 h, 6% yield (2 steps); [c]$SnCl_2$, HCl (50% yield).

7.5. Strain Originates from Aryl-PDI Dihedral

Figure 7.3 shows the lowest energy geometry calculated using the 6-31G/B3LYP basis set. **PPh$_6$-PhHex** possesses an elliptiform cavity that measures 12.3 Å along its long axis from the PDI to the alkoxy-substituted aryl ring (Figure 7.3). The aryl rings are arranged with their π-surfaces directed to the cavity, and form a concave surface for the perimeter of the macrocycle. Analogous to other bay-substituted PDI molecules, the two phenyl rings attached to the PDI are on the same face of the PDI molecule: this is an important design feature as it facilitates macrocyclization.[19] We observe two important features about the PDI-aryl bond once the diphenyl PDI is constricted into a macrocyclic framework: 1) the torsional angle between the phenyl group and the PDI moiety is reduced for **PPh$_6$-PhHex** relative to diphenyl PDI, at 26° and 54°, respectively; and 2) the aryl-aryl distance (highlighted in orange circles in Figure 7.3b) decreases once the diphenyl PDI is restricted within a macrocycle. DFT measurements show this is 0.97 nm instead of 12.2 nm (Figure 7.1a) in a relatively unstrained diphenyl PDI. The relatively more coplanar linkage between the PDI and aromatic belt increases electronic coupling between the two moieties.

7.6. Size-Dependent Isomerization

Due to the substitution in the bay position of the PDI, **PPh$_6$-PhHex** is chiral, and exists as a (*P*)- **PPh$_6$-PhHex** and (*M*)- **PPh$_6$-PhHex** in solution. We have synthesized chiral PDI-based macrocycles that have been conformationally locked[1] or exhibit dynamic stereochemistry.[19] Chiral PDI-based macrocycles isomerize through an "intramolecular somersault,' that is, where a chiral (*P* or *M*) PDI molecule rotates its diimide head around its transverse axis through the plane of the cavity to convert to the opposite enantiomer (*M* or *P*). The ability to isomerize is dependent upon the rigidity of the macrocycle and the size of the cavity (Chapter 1B.5). If the diameter of the cavity is large enough, then the macrocycle exhibits dynamic stereochemistry using the intramolecular somersault mechanism, yet when the cavity is smaller, the macrocycle is conformationally locked and shape persistent. Our studies suggest that cavities with the long axis measuring at least 15 Å can isomerize in solution, while cavities at 11 Å or shorter are conformationally restricted.

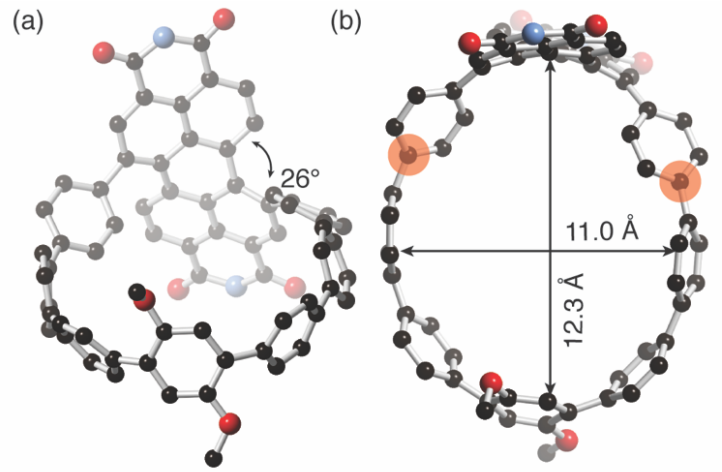

Figure 7.3. DFT calculations showing (a) the twisting of (*P*)- **PPh$_6$-PhHex**. The torsional angle is reduced in **PPh$_6$-PhHex**. (b) The cavity measures 12.3 Å along the long axis from PDI to alkoxy-substituted aryl ring. Orange circles indicate the distance between the PDI phenyl appendages. Red = oxygen, blue = nitrogen, black = carbon, and yellow = sulfur. Hydrogens and side chains have been removed for clarity. Computations at the using 6-31G/B3LYP level of theory.

7.7. CD Measurements Show PPh_6-PhHex is Conformationally Locked

We employed chiral HPLC to study the dynamics of **PPh_6-PhHex**. Using a CHIRALPAK® IA-3 column (4.6 mm I.D. x 250 mm, 3 μm), we isolate two peaks in a 1:1 ratio (Figure 7.4a), and use CD spectroscopy to confirm that the two peaks are (*P*)- **PPh_6-PhHex** and (*M*)- **PPh_6-PhHex**. Figure 7.4b shows each enantiomer of **PPh_6-PhHex** preferentially absorbs left- or right-handed circularly polarized light.

We also performed a variable temperature CD experiment, where the sample is heated and monitored by CD spectroscopy, to study the isomerization process in **PPh_6-PhHex**. We heated an optically pure sample of Enantiomer 2 of **PPh_6-PhHex** to temperatures to 100 °C (over three hours) and saw no evidence of isomerization. This suggests **PPh_6-PhHex** is conformationally restricted and unable to perform an intramolecular somersault.

Both the CD spectrum and UV-Vis spectrum show three broad groups of electronic transitions: alkoxy-substituted aryl → PDI, aryl belt → PDI, and PDI → PDI at lower wavelengths. Figure 7.4c contains the UV-Vis spectrum. The lowest energy transition is characterized by the promotion of an electron from the alkoxy-substituted aryl ring (HOMO) to a PDI-centered orbital (LUMO). Figure 4a,b shows the HOMO and LUMO molecular orbitals for **PPh_6-PhHex**. The Appendix contains the calculated absorption spectrum without thermal broadening to best visualize the electronic states (Figure 7.8) and the TD-DFT information used for the assignment of the electronic states.

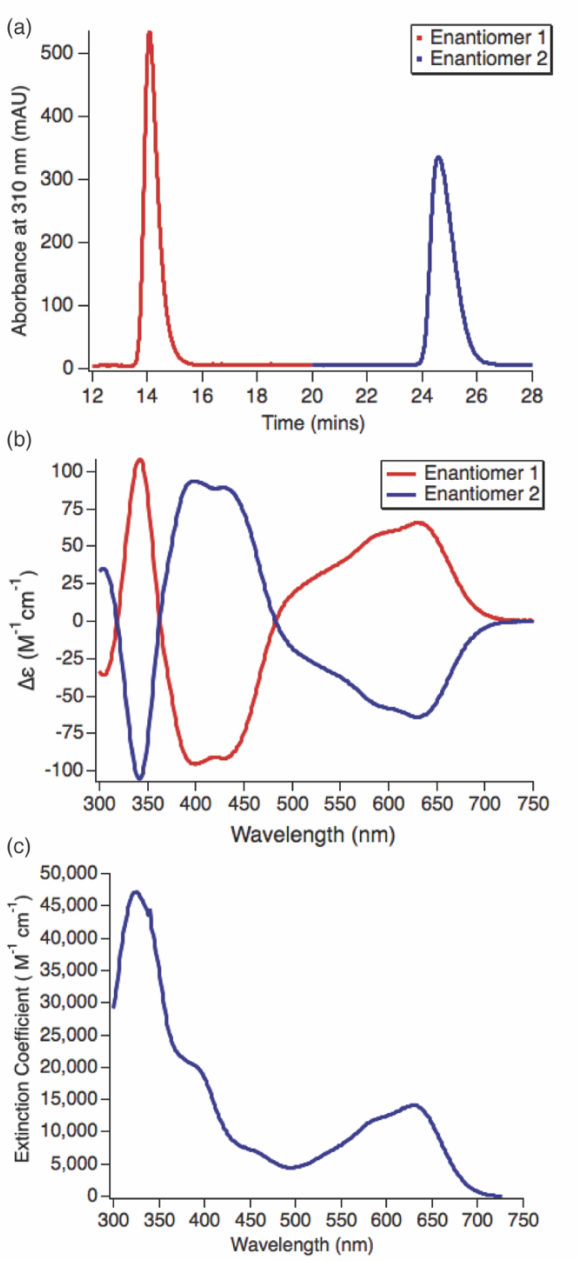

Figure 7.4. (a) HPLC chromatogram showing the retention times of both (*P*)- **PPh$_6$-PhHex** and (*M*)- **PPh$_6$-PhHex** with a mobile phase of 18% DCM/82% Hexanes using an IA-3 Chiralpak column. We call them Enantiomer 1 and 2, arbitrarily assigned; (b) CD chromatogram (*P*)- **PPh$_6$-PhHex** and (*M*)- **PPh$_6$-PhHex** in toluene (1 cm path length, 10^{-6} M for Enantiomer 1 and 10^{-5} M for Enantiomer 2); and (c) UV-Vis absorption spectrum of **PPh$_6$-PhHex** (dichloromethane, 1.0 cm path length, 1.37 x 10^{-5} M).

7.8. Incorporation of PDI Alters Electronic Structure of PPh$_6$-PhHex

The incorporation of a diphenyl PDI moiety into a CPP nanobelt has a profound effect on the electronic structure. While **[8]**- and **[10]CPP** are yellow in solution, **PPh$_6$-PhHex** is teal

reflecting its ability to absorb visible light: the onset of absorption is at 680 nm for **PPh$_6$-PhHex**. The narrowing of the energy gap for **PPh$_6$-PhHex** reflects the incorporation of a PDI moiety into the nanobelt and a lowering in the LUMO energy level, as both the LUMO/LUMO+1/LUMO+2 reside on a PDI-centered orbital. Other donor/acceptor CPPs too showed a narrowing of the HOMO/LUMO level due to the incorporation of strong electron withdrawing subunits,[27–29] but the effect from PDI incorporation greatly enhances this effect.

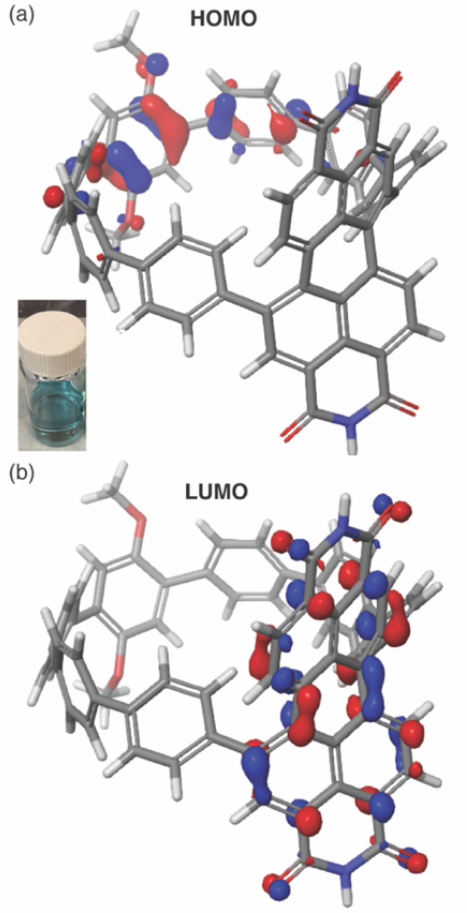

Figure 7.5. (a) HOMO energy level showing a high density of high energy electrons on the hexoxy-substituted aryl ring and (b) LUMO energy level showing unoccupied low energy space on the PDI. Red = oxygen, blue = nitrogen, black = carbon, and yellow = sulfur. Hydrogens and side chains have been removed for clarity.

It is also interesting to compare the UV-Vis spectrum of an **1.1** with **PPh$_6$-PhHex** (Figures 7.8 and 7.9). From TDDFT, we assign the second excited state as a promotion of an electron from a PDI-centered orbital to a PDI-centered orbital for **PPh$_6$-PhHex**, which is analogous to the lowest

energy transition for **1.1**. We believe this transition is shifted towards lower energy in **PPh$_6$-PhHex** because of the orientation of the PDI with respect to the adjacent phenyls: the phenyls pi-surfaces are more conjugated to the PDI core in **PPh$_6$-PhHex** as the torsional angle is less relative to **1.1**.

7.9. Conclusion

In conclusion, we have synthesized a chiral donor/acceptor CPP nanobelt called **PPh$_6$-PhHex**. The nanobelt comprises a PDI moiety as the relatively electron deficient subunit and an alkoxy-substituted aryl belt as the electron rich portion. We have shown that incorporation of a PDI into the belt causes a profound effect on the electronic structure of the macrocycle relative to CPPs. **PPh$_6$-PhHex** is teal in solution and has an onset of absorption into the visible. The macrocycle, too, is conformationally locked, and does not show evidence of racemization at elevated temperatures. This study reveals the importance of substituting CPPs with chiral, electroactive groups, and highlights the effects on the electronic structure. Future studies will include host/guest chemistry with chiral analytes and sensing applications.

7.10. Appendix – Supplementary Figures

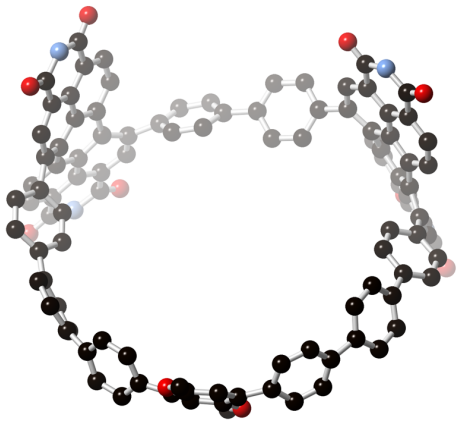

Figure 7.6. DFT minimized geometry for **SI-7.1**. Red = oxygen, blue = nitrogen, black = carbon, and yellow = sulfur. Hydrogens and side chains have been removed for clarity.

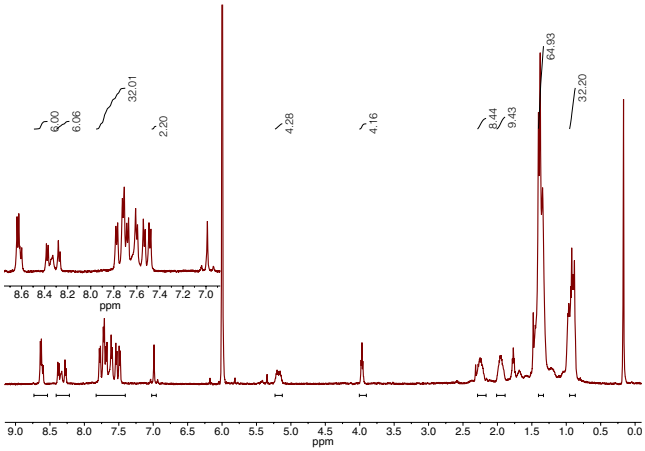

Figure 7.7. Proton NMR and chemical structure of the major byproduct from the reaction **SI-7.1**. This byproduct suggests there is some degree of reversibility in the reaction. It contains two bis-platinum, diphenyl-PDIs and one belt linker. ^{1}H NMR taken in $C_2D_2Cl_4$ at 410 K. HRMS (MALDI^{-}) calculated m/z for $[C_{158}H_{164}N_4O_{10}]^{-}$ is 2276.873, found 2277.274.

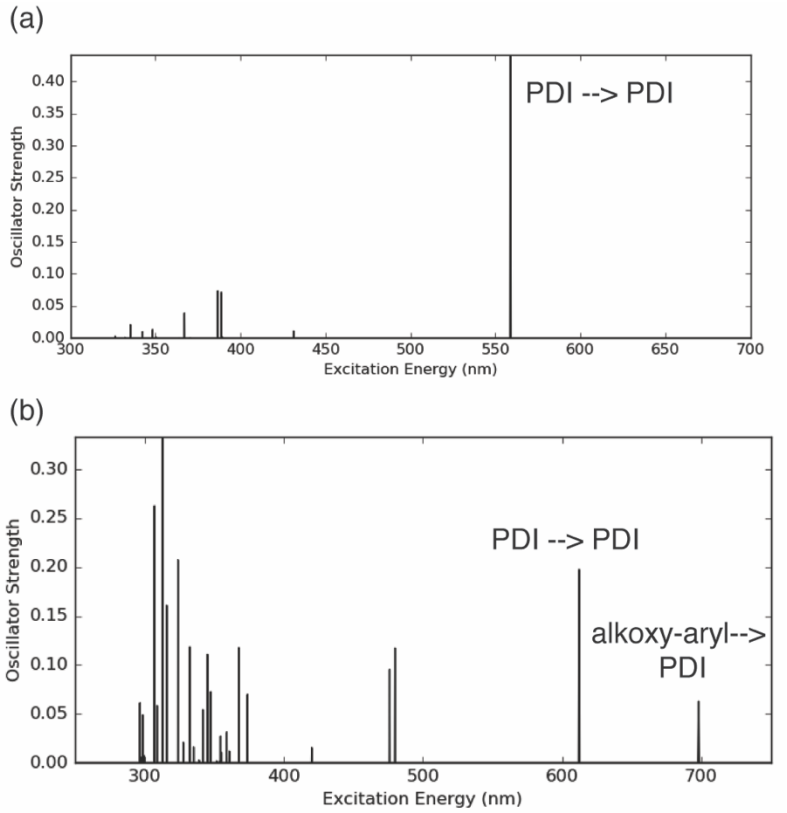

Figure 7.8. (a) The calculated UV-Vis for **1.1** (b) and **PPh$_6$-PhHex**. The PDI→ PDI transition is shifted to lower energy in the macrocycle as a result of a higher energy HOMO.

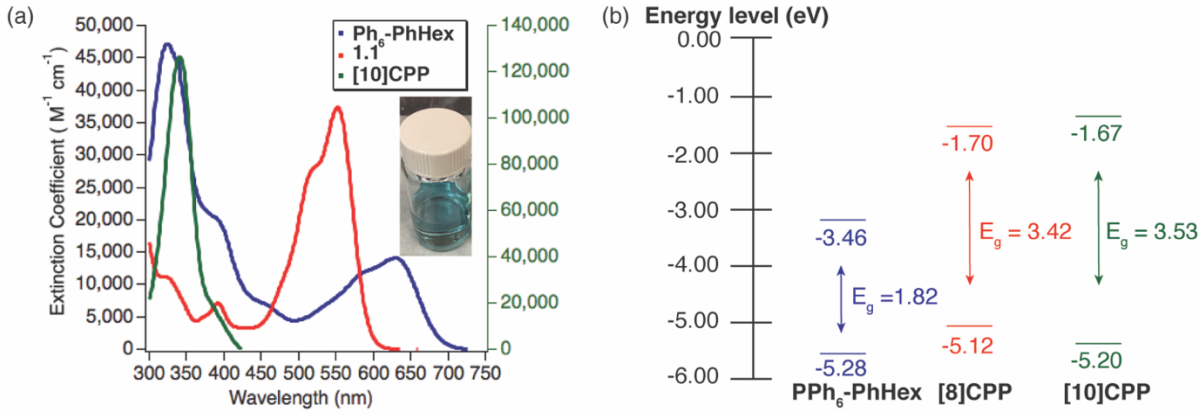

Figure 7.9. (a) UV-vis absorption spectrum of **PPh$_6$-PhHex** (DCM, 1.0 cm path length, 1.37 x 10^{-5} M), diphenyl-PDI (**1.1**), and [10]CPP; (b) HOMO-LUMO energy gaps for the three compounds showing the electronic effect of incorporating a PDI moiety into a CPP nanobelt.

7.11. General Experimental Information

Synthesis. All reactions were performed in oven-dried or flame-dried round bottom flasks, unless otherwise noted. The flasks were fitted with rubber septa and reactions were conducted under a positive pressure of nitrogen or argon, unless otherwise noted. Anhydrous and anaerobic solvents were obtained from a Glass Contour solvent system consisting of a Schlenk manifold with purification columns packed with activated alumina and supported copper catalyst. Reaction monitoring by TLC was performed on J.T. Baker Baker-flex Silica Gel IB2-F (25 mm x 75 mm) TLC plates. TLC visualization was accomplished by visible observation and irradiation with a UV lamp. Commercial reagents were used without further purification. Pt(COD)Cl$_2$ was purchased from Strem Chemicals, and all other reagents were purchased from Sigma-Aldrich.

Purification. Automated flash chromatography was performed using a Teledyne Isco Combiflash Rf200 and Redisep Rf Silica and Alumina columns.

Spectrometers. ^{1}H NMR spectra were recorded on a Bruker 400 or 500 MHz spectrometer. ^{13}C NMR spectra were recorded on a Bruker 125 or 100 MHz spectrometer with complete proton decoupling. NMR spectra were recorded at 300 K unless otherwise noted. Chemical shifts are reported in parts per million (ppm) Data are represented as follows: chemical shift, multiplicity (s

= singlet, d = doublet, dd= doublet of doublets, t = triplet, m = multiplet), coupling constants in Hz, and integration. Broadening (br) of peaks in the ^{1}H NMR spectrum is due to rotational isomers about the imide side chains. Multiple peaks for the same carbon in the ^{13}C NMR spectrum arise due to rotational isomers about the imide side chains that have been seen previously.[19,30] **1.1** was previously presented in Chapters 1, 3, and 4.[16] HRMS was performed on a (1) Waters XEVO G2-XS QTOF instrument equipped with a UPC SFC inlet, and ESI and APCI ionization sources; or (2) a Bruker UltrafleXtreme MALDI TOF/TOF instrument using a dithranol matrix. UV-vis absorption spectra were recorded on a Shimadzu UV-1800 spectrophotometer using a 1.0 cm quartz cell. IR spectra were recorded on a Perkin Elmer Spectrum400 FTIR spectrometer using a PIKE ATR attachment.

Chirality Analysis: Analytical HPLC was performed on an Agilent 1200 Series instrument equipped with a diode array detector (300 nm to 900 nm) and a CHIRALPAK® IA-3 column (4.6 mm I.D. x 250 mm, 3 μm) from Chiral Technologies. The mobile phase was 28% DCM and 78% hexanes.

7.12. Synthetic Procedures and Characterization

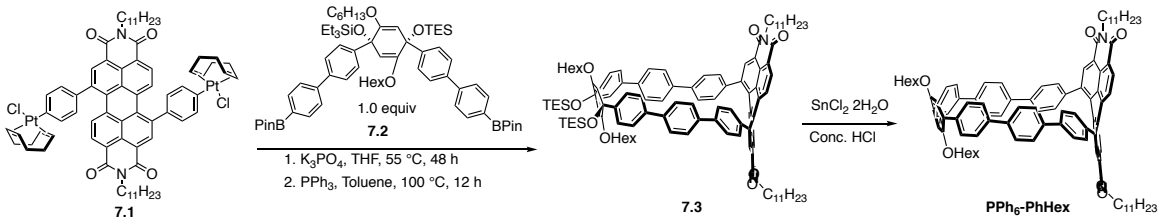

Synthesis of **PPh_6-PhHex**: 1,7-Bis[4-(Pt(COD)Cl)-phenyl]-PDI (**2.2**)[19] (0.261 mMol, 0.415 g) and **7.2** (0.261 mMol, 0.286 g) are added to an oven dried round bottom flask equipped with a stir bar in equimolar amounts. Oven-dried K_3PO_4 (0.276, 1.31 mmol) was added and the solids were exposed to three cycles of purging with N_2/vacuum. 87.0 ml of THF was added and the mixture was sparged with nitrogen for 30 min before being added to an oil bath at 55 ºC and allowed to stir

for 48 hours. Crude mixture was then removed from oil bath and concentrated. The crude was extracted with ethyl acetate and brine to remove the salts and then triphenylphosphine (5.21 mmol, 1.52 g) and toluene (87.0 mL) were added to the flask. Mixture was sparged with nitrogen for 15 min then placed in a 100 ºC oil bath and allowed to stir overnight. The crude mixture was concentrated, followed by re-precipitation from dichloromethane using methanol. and then purified by column chromatography (48 g Redisep Rf Alumina) using a gradient from 0% to 100% CH_2Cl_2/hexanes. The polar fractions were further purified with prepatory TLC. Product was a dark green solid (0.0280 g, 6.3%). Due to the stability of the intermediate, we proceeded to the reductive aromatization step immediately. Intermediate **7.3** sparged for one hour in 1.5 ml THF while a separate flask containing $SnCl_2$ (0.010 g, 0.044 mmol) and Conc. HCl (0.007 μL) in 3 ml of THF was also sparged. A stock solution was made by scaling up the $SnCl_2$ and HCl by three (0.030 $SnCl_2$ and 0.022μL HCl in 3 ml of THF). Using a syringe, 1 ml of the stock solution was added to the reaction and allowed to stir overnight. Reaction was quenched with 2M NaOH and extracted with ethyl acetate. A prepatory TLC was ran (70%DCM/30%hexanes) and isolated a teal solid (0.006 g, 42% yield). **^{1}H NMR** (400 MHz, 380 K, $C_2D_2Cl_4$) δ 8.74 (s, 2H), 8.58 (d, J = 7.9 Hz, 2H), 8.37 (d, J = 7.9 Hz, 2H), 7.70 (d, J = 8.7 Hz, 4H), 7.64 (d, J = 8.5 Hz, 4H), 7.55 (d, J = 8.5 Hz, 4H), 7.50 (d, J = 8.7 Hz, 4H), 7.31 (d, J = 8.5 Hz, 4H), 7.15 (d, J = 8.5 Hz, 4H), 6.91 (s, 2H), 5.19 (br m, 2H), 3.98 (t, J = 6.5 Hz, 4H), 2.25 (br m, 4H), 1.97 (br m, 4H), 1.82 (br m, 4H), 1.39 (br m, 36H)*, 0.96 (br m, 18H)*. **^{13}C NMR** (100 MHz, 380 K, $C_2D_2Cl_4$) δ 164.42, 164.08, 152.27, 142.18, 140.07, 139.62, 139.20, 138.40, 138.14, 138.74, 135.25, 134.77, 132.83, 130.54, 129.64, 129.60, 129.43, 129.16, 129.07, 128.93, 128.61, 127.13, 126.67, 122.86, 122.42, 116.54, 70.42, 55.04, 53.47, 32.73, 32.66, 31.91, 31.80, 31.60, 29.66, 26.76, 25.92, 22.62, 22.53, 22.48, 22.46, 13.97, 13.91, 13.86. **HRMS** (MALDI-) calculated m/z for $[C_{100}H_{104}N_2O_6]^-$ is 1428.789, found

1428.706. *Integrations are high in the aliphatic region due to H grease overlapping with spectral peaks.

7.13. NMR Spectra of Compounds

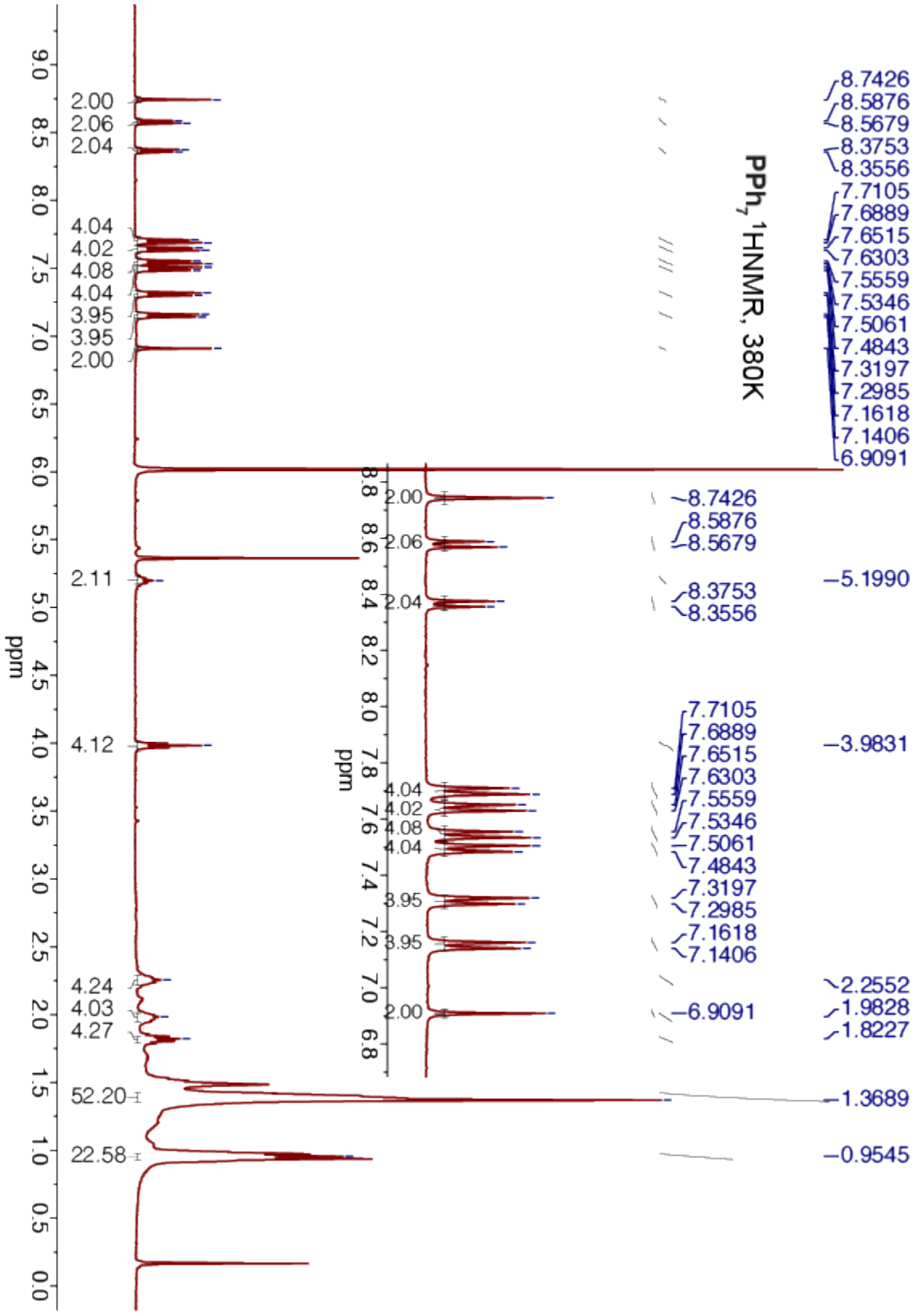

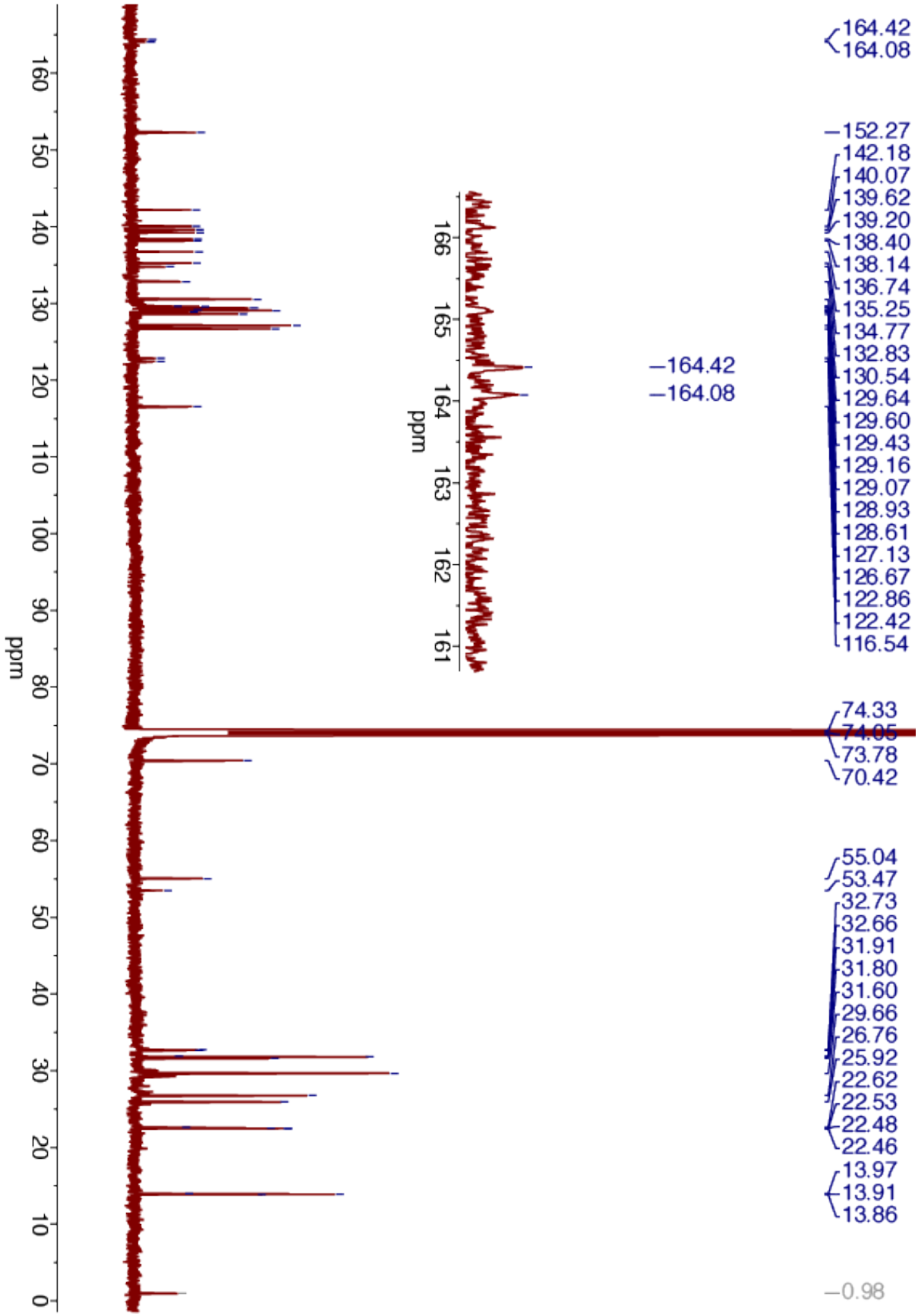
164.42
164.08
152.27
142.18
140.07
139.62
139.20
138.40
138.14
136.74
135.25
134.77
132.83
130.54
129.64
129.60
129.43
129.16
129.07
128.93
128.61
127.13
126.67
122.86
122.42
116.54
74.33
74.05
73.78
70.42
55.04
53.47
32.73
32.66
31.91
31.80
31.60
29.66
26.76
25.92
22.62
22.53
22.48
22.46
13.97
13.91
13.86
0.98
164.42
164.08
ppm
ppm

7.14. DFT Output

All quantum chemical calculations were performed using Jaguar, version 8.3, Schrodinger, Inc., New York, NY, 2013. (See A. D. Bochevarov, E. Harder, T. F. Hughes, J. R. Greenwood, D. A. Braden, D. M. Philipp, D. Rinaldo, M. D. Halls, J. Zhang, R. A. Friesner, "Jaguar: A High Performance Quantum Chemistry Software Program with Strengths in Life and Materials Sciences", Int. J. Quantum Chem., 2013, 113(18), 2110-2142). All geometries were optimized using the B3LYP functional and the 6-31G basis set. In the following pages, we include for each molecule its optimized geometry and total energy. The geometry optimization for **1.1** is provided in Chapter 1B. The TDDFT excited state calculations for **PPh_6-PhHex** present the thirty lowest energy roots and 15 lowest energy roots for **1.1**. We also provide the results of the homodesmotic reaction employed in order to calculate strain within **PPh_6-PhHex**.

Minimized Geometries for Compounds

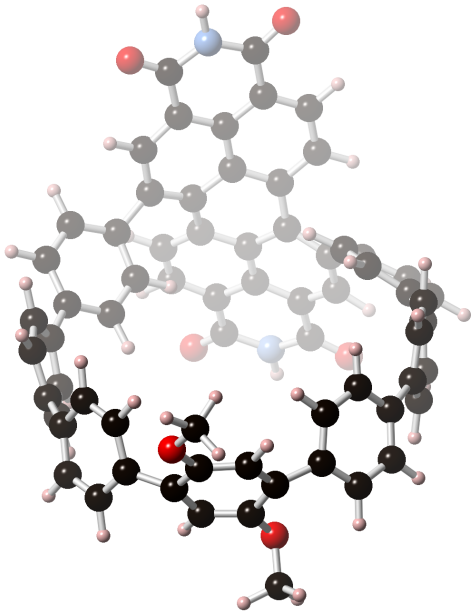

PPh_6-PhHex

Final Heat of Formation = -3176.308485

C	-1.21660	-0.70690	1.58610
C	-1.65860	-1.72350	0.73350

C	-1.93590	-1.51390	-0.61980
C	-1.85370	-0.21620	-1.15630
C	-1.18550	0.74810	-0.36770
C	-0.83320	0.50990	0.95860
C	-2.76910	0.21170	-2.25090
C	-3.52230	1.37650	-2.00750
C	-4.70180	1.63500	-2.68820
C	-5.19500	0.74270	-3.65530
C	-4.34420	-0.31170	-4.03490
C	-3.15940	-0.57600	-3.34970
C	-6.64330	0.79120	-3.99090
C	-7.39920	1.96990	-3.84240
C	-8.77940	1.92550	-3.68050
C	-9.47160	0.70380	-3.70230
C	-8.74520	-0.44420	-4.05860
C	-7.35970	-0.40240	-4.19020
C	-10.80200	0.53710	-3.05770
C	-10.92730	0.99870	-1.73540
C	-11.94370	0.55340	-0.90680
C	-12.92240	-0.34990	-1.36340
C	-12.89100	-0.67490	-2.73530
C	-11.84380	-0.25880	-3.55870
C	-13.68950	-1.15940	-0.37200
C	-13.94240	-2.51380	-0.70760
C	-14.26200	-3.46750	0.23650
C	-14.52220	-4.86440	-0.18420
C	-14.62390	-5.53330	2.23970
C	-14.33740	-4.13030	2.61810
C	-14.20630	-3.13850	1.61540
C	-13.97620	-1.78340	1.97930
C	-13.72440	-1.46990	3.35180
C	-13.85660	-2.47750	4.31130
C	-14.18430	-3.78830	3.95370
C	-13.91780	-0.76790	0.97130
C	-13.83150	0.91930	2.80530
C	-13.37690	-0.09330	3.70760
C	-12.65630	0.29410	4.86340
C	-12.77480	1.64250	5.28280
C	-13.45050	2.59210	4.54430
C	-13.92400	2.26810	3.24600
C	-14.44440	3.26100	2.38030
C	-14.80330	2.92420	1.08270
C	-14.61780	1.62000	0.61010
C	-14.59130	4.65650	2.85910
C	-13.56000	3.98000	5.05130
C	-11.56330	-0.51530	5.47480

C	-11.04060	-0.23210	6.75250
C	-9.76080	-0.64230	7.12370
C	-8.94520	-1.37110	6.24070
C	-9.53160	-1.78460	5.02870
C	-10.79870	-1.36730	4.65270
C	-7.47470	-1.51840	6.38890
C	-6.69580	-0.44700	6.86090
C	-5.32460	-0.39310	6.62460
C	-4.67000	-1.40180	5.89570
C	-5.42170	-2.55140	5.58690
C	-6.78880	-2.60960	5.82790
C	-3.37150	-1.18290	5.20480
C	-2.56020	-2.23730	4.74570
C	-3.07420	0.09920	4.70830
C	-2.18730	0.28070	3.65570
C	-1.56490	-0.81710	3.03070
C	-1.67390	-2.05830	3.68540
C	-14.12010	0.60860	1.43800
H	-1.97610	-2.67090	1.15600
O	-0.21010	1.43130	1.75470
H	-1.02300	1.72960	-0.79690
O	-2.51410	-2.54310	-1.33860
H	-2.57390	-1.44270	-3.62980
H	-4.64200	-0.98060	-4.83670
H	-3.25550	2.01700	-1.17370
H	-5.31000	2.47310	-2.36530
H	-6.82110	-1.33580	-4.31940
H	-9.25240	-1.40410	-4.09660
H	-9.32160	2.84370	-3.47420
H	-6.89500	2.92860	-3.77640
H	-13.66000	-1.31320	-3.15990
H	-11.81680	-0.59300	-4.59230
H	-11.91270	0.83370	0.13800
H	-10.14080	1.61680	-1.31590
H	-13.83280	-2.85200	-1.73110
H	-14.88620	-6.72760	0.59250
H	-14.29880	-4.56200	4.70550
H	-13.69240	-2.23800	5.35460
H	-12.28450	1.97670	6.18980
H	-15.20690	3.69870	0.43930
H	-14.86170	1.38940	-0.42040
H	-14.23470	5.83620	4.49840
H	-11.14830	-1.61450	3.65780
H	-8.93460	-2.34220	4.31430
H	-9.37670	-0.35330	8.09820
H	-11.61730	0.36460	7.45300

H	-4.94980	-3.36790	5.04990
H	-7.34520	-3.48610	5.50790
H	-4.77210	0.48560	6.94200
H	-7.18360	0.40500	7.32620
H	-3.64680	0.95450	5.05330
H	-2.07970	1.26840	3.22590
H	-1.13180	-2.91780	3.30280
H	-2.67580	-3.23080	5.16980
N	-14.70360	-5.76780	0.86430
N	-14.14670	4.88300	4.16380
O	-13.17830	4.34470	6.15310
O	-15.06180	5.56710	2.19480
O	-14.57800	-5.23560	-1.34680
O	-14.78460	-6.44450	3.03770
C	0.18520	2.66820	1.18160
C	-1.58380	-3.51730	-1.80390
H	0.71220	3.20820	1.96980
H	0.86060	2.51890	0.32980
H	-0.67790	3.26200	0.85360
H	-2.16910	-4.27470	-2.33280
H	-0.84700	-3.07270	-2.49010
H	-1.04300	-3.99600	-0.97450

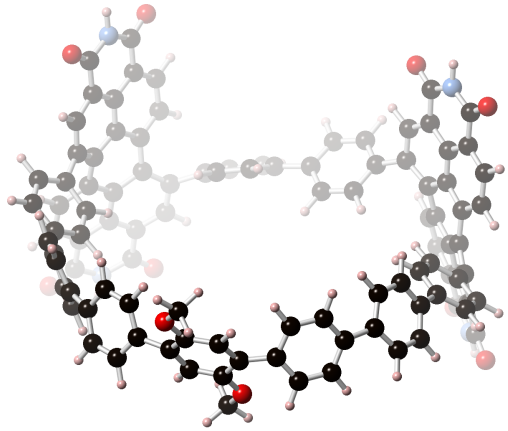

SI-7.1

Final Heat of Formation = -4968.401876

C	-0.329708	-0.069824	3.476209
C	-0.368715	-1.142230	2.576126
C	0.257980	-1.107857	1.331319
C	0.924808	0.067533	0.909940
C	1.076249	1.088120	1.867116
C	0.483501	1.031359	3.129684
C	1.199353	0.323001	-0.529092

C	0.919302	1.595898	-1.064854
C	0.794475	1.801405	-2.433132
C	0.914139	0.736459	-3.345460
C	1.370940	-0.485563	-2.821343
C	1.523437	-0.686521	-1.453899
C	0.346782	0.809361	-4.718102
C	0.582980	-0.177874	-5.692848
C	-0.245109	-0.313254	-6.803900
C	-1.336990	0.545936	-7.008216
C	-1.460443	1.637993	-6.132191
C	-0.646987	1.761277	-5.015461
C	-13.730676	-1.243864	-3.947456
C	-13.087752	-0.820838	-2.770830
C	-13.548130	-1.199636	-1.518129
C	-14.666476	-2.040790	-1.378840
C	-15.339513	-2.424795	-2.549248
C	-14.888629	-2.021211	-3.808993
C	-14.921714	-2.645258	-0.038204
C	-14.950580	-4.057226	0.027207
C	-14.852861	-4.741028	1.223451
C	-14.913390	-6.224292	1.234076
C	-14.437530	-6.185929	3.701177
C	-14.358476	-4.708168	3.643314
C	-14.596572	-4.028253	2.422339
C	-14.561553	-2.604026	2.383357
C	-14.145119	-1.884997	3.549892
C	-13.923991	-2.597857	4.732052
C	-14.050070	-3.989435	4.786796
C	-14.891645	-1.915416	1.172318
C	-14.797274	0.225800	2.463597
C	-14.033266	-0.422214	3.485802
C	-13.290723	0.369448	4.392424
C	-13.597283	1.747444	4.476219
C	-14.518772	2.350864	3.644599
C	-15.091095	1.615442	2.575510
C	-15.932969	2.241000	1.622127
C	-16.418530	1.511338	0.548983
C	-16.054294	0.169716	0.382342
C	-16.297271	3.670775	1.776014
C	-14.834794	3.790882	3.815548
C	-12.067930	-0.097476	5.104851
C	-11.674209	0.400973	6.358826
C	-10.392490	0.174084	6.859356
C	-9.445499	-0.559411	6.127223
C	-9.870609	-1.125620	4.910999
C	-11.142407	-0.898072	4.411173

C	-8.003227	-0.619366	6.467737
C	-7.330508	0.516101	6.949674
C	-5.940723	0.585412	6.944676
C	-5.161653	-0.473423	6.448402
C	-5.834760	-1.659698	6.105054
C	-7.221427	-1.732107	6.115709
C	-3.737672	-0.305542	6.065210
C	-2.849654	-1.390382	5.961742
C	-3.297662	0.929350	5.557032
C	-2.108091	1.041649	4.848414
C	-1.307444	-0.084744	4.595388
C	-1.663809	-1.281851	5.241641
C	-15.241744	-0.492420	1.306640
H	-0.998992	-1.984719	2.827978
O	0.604506	2.020694	4.070385
H	1.640411	1.967741	1.582475
O	0.165066	-2.141462	0.438983
H	1.817181	-1.664834	-1.098720
H	1.519532	-1.334713	-3.480268
H	0.696886	2.421057	-0.395503
H	0.524383	2.792299	-2.783907
H	-0.853764	2.563848	-4.316316
H	-2.246735	2.369378	-6.293321
H	-0.092800	-1.154015	-7.473602
H	1.381423	-0.899145	-5.551051
H	-16.212019	-3.067476	-2.480972
H	-15.416063	-2.361224	-4.694523
H	-13.005675	-0.884482	-0.632218
H	-12.203376	-0.195342	-2.846607
H	-15.013780	-4.637010	-0.887720
H	-14.762180	-7.823832	2.508169
H	-13.889000	-4.530369	5.712906
H	-13.644839	-2.062945	5.630140
H	-13.076084	2.372132	5.192532
H	-17.071269	2.005161	-0.162387
H	-16.420862	-0.367550	-0.482636
H	-15.952675	5.294062	2.982118
H	-11.399406	-1.285309	3.431587
H	-9.159083	-1.676915	4.305049
H	-10.119474	0.592621	7.823857
H	-12.370057	0.992992	6.945220
H	-5.267426	-2.507830	5.734818
H	-7.706449	-2.647639	5.789354
H	-5.457011	1.500162	7.274019
H	-7.902027	1.390082	7.248489
H	-3.947895	1.796196	5.621416

H	-1.843555	1.991851	4.401574
H	-1.025580	-2.155089	5.137583
H	-3.109044	-2.345142	6.410683
N	-14.716322	-6.811058	2.483827
N	-15.715321	4.314636	2.869489
O	-14.382547	4.493995	4.706061
O	-17.049256	4.272947	1.025857
O	-15.117979	-6.911589	0.245322
O	-14.277663	-6.844681	4.717066
C	1.458198	3.118610	3.793720
C	-0.658700	-3.252646	0.750717
H	1.450080	3.738087	4.691967
H	2.485485	2.789815	3.590426
H	1.099196	3.713833	2.943751
H	-0.600005	-3.917216	-0.112948
H	-0.302380	-3.787926	1.640272
H	-1.703502	-2.954507	0.905379
C	-2.440360	0.203543	-7.939446
C	-3.759239	0.453469	-7.514663
C	-4.850107	-0.000183	-8.233620
C	-4.686266	-0.733035	-9.422786
C	-3.374619	-0.944760	-9.878323
C	-2.274930	-0.483266	-9.152784
C	-5.881455	-1.415367	-9.989041
C	-5.758873	-2.785467	-10.314297
C	-6.859351	-3.588232	-10.539779
C	-6.669432	-5.010742	-10.917786
C	-9.156749	-5.336393	-10.789405
C	-9.302899	-3.914544	-10.392340
C	-8.163305	-3.075414	-10.316518
C	-8.313672	-1.695647	-9.997816
C	-9.607241	-1.202193	-9.627199
C	-10.700184	-2.069403	-9.701072
C	-10.555703	-3.402907	-10.099229
C	-7.171387	-0.835444	-10.006288
C	-8.720031	1.100804	-9.694235
C	-9.752274	0.210425	-9.249415
C	-10.856880	0.746265	-8.547797
C	-11.061374	2.144099	-8.579481
C	-10.171489	3.005864	-9.184438
C	-8.950036	2.507403	-9.704712
C	-7.963939	3.385840	-10.217480
C	-6.759264	2.878363	-10.674670
C	-6.493127	1.508386	-10.592617
C	-8.217260	4.843814	-10.268862
C	-10.454693	4.460310	-9.193276

C	-11.695466	0.003098	-7.560119
C	-13.077501	0.214985	-7.419324
C	-13.770426	-0.241195	-6.295157
C	-13.101103	-0.902079	-5.255309
C	-11.731583	-1.169176	-5.430026
C	-11.045872	-0.737506	-6.557122
C	-7.435277	0.606618	-10.087627
H	-3.207476	-1.486692	-10.805191
H	-1.274951	-0.674917	-9.531164
H	-5.847415	0.156777	-7.836584
H	-3.927192	0.940260	-6.560170
H	-4.777237	-3.245307	-10.354270
H	-7.732816	-6.723052	-11.294878
H	-11.416036	-4.059155	-10.173999
H	-11.687320	-1.702648	-9.452085
H	-11.922656	2.572814	-8.078543
H	-6.026090	3.567577	-11.079454
H	-5.532490	1.141421	-10.927805
H	-9.628491	6.247199	-9.768735
H	-9.977650	-0.915771	-6.633489
H	-14.830827	-0.024533	-6.199503
H	-13.613363	0.779917	-8.177211
N	-7.845657	-5.751816	-11.026244
N	-9.448254	5.249381	-9.748931
O	-11.477959	4.964759	-8.756541
O	-7.431711	5.662880	-10.720346
O	-5.583174	-5.527619	-11.129365
O	-10.089370	-6.114498	-10.915339
H	-11.193658	-1.701681	-4.651356

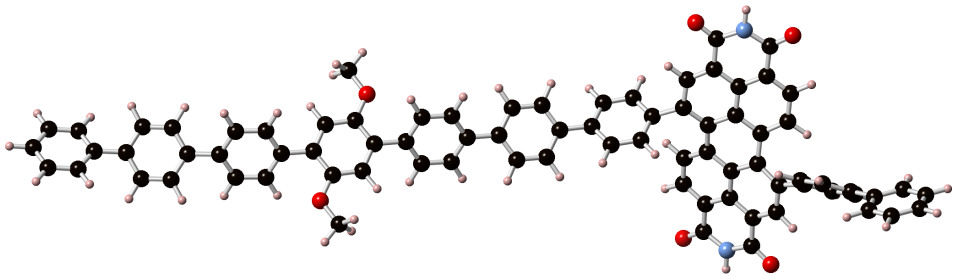

PPh$_6$-PhHex Acyclic Analog for Homodesmotic Calculations

Final Heat of Formation = -3639.730299

C	3.120776	-1.376616	1.091177
C	3.489349	-2.116950	-0.042196
C	4.821942	-2.355211	-0.382253
C	5.857653	-1.848930	0.430197

C	5.487466	-1.100818	1.557315
C	4.157775	-0.854601	1.893767
C	7.300415	-2.073648	0.163828
C	8.225832	-1.039752	0.386952
C	9.592549	-1.249393	0.252558
C	10.104283	-2.507155	-0.106889
C	9.177243	-3.530726	-0.362694
C	7.808810	-3.319893	-0.238160
C	11.564904	-2.744988	-0.176282
C	12.441431	-2.074159	0.692134
C	13.813480	-2.277032	0.632535
C	14.377640	-3.166818	-0.294132
C	13.503109	-3.847603	-1.156577
C	12.128897	-3.639771	-1.100107
C	-18.804327	1.578101	0.000885
C	-17.450222	1.913078	-0.176501
C	-16.443280	1.257965	0.520145
C	-16.745808	0.230824	1.427588
C	-18.097659	-0.091381	1.622530
C	-19.107310	0.574888	0.934113
C	-15.670784	-0.624334	2.010682
C	-15.787233	-1.995741	1.696591
C	-14.824184	-2.916030	2.041868
C	-15.032311	-4.343653	1.698804
C	-12.791398	-4.864309	2.694173
C	-12.618487	-3.422668	3.000484
C	-13.632172	-2.485425	2.674521
C	-13.468967	-1.099092	2.983844
C	-12.218502	-0.663042	3.532509
C	-11.270733	-1.629062	3.880725
C	-11.465480	-2.989873	3.627670
C	-14.547869	-0.182314	2.746242
C	-13.153468	1.617259	3.805551
C	-11.992611	0.773907	3.762212
C	-10.728270	1.348599	4.016716
C	-10.657025	2.677237	4.488673
C	-11.776146	3.455798	4.671269
C	-13.048798	2.950668	4.308877
C	-14.203752	3.761865	4.450100
C	-15.442310	3.251376	4.112212
C	-15.549623	1.966456	3.573811
C	-14.098695	5.144646	4.975924
C	-11.622641	4.831607	5.202261
C	-9.391844	0.733185	3.766340
C	-8.422190	0.739086	4.780409
C	-7.111649	0.358039	4.520224

C	-6.703304	-0.015224	3.230490
C	-7.684905	-0.051257	2.224198
C	-9.002807	0.308956	2.486309
C	-5.277643	-0.293073	2.934830
C	-4.269474	0.408273	3.616055
C	-2.927374	0.208586	3.325419
C	-2.521395	-0.695481	2.330243
C	-3.529506	-1.406074	1.655925
C	-4.875489	-1.209200	1.949709
C	-1.086925	-0.873214	2.008163
C	-0.575771	-2.097728	1.551081
C	-0.178871	0.190883	2.151410
C	1.173557	0.036632	1.875160
C	1.685741	-1.189597	1.418081
C	0.775937	-2.248738	1.260059
C	-14.434908	1.151067	3.361477
H	2.697245	-2.480598	-0.684379
O	3.786438	-0.152364	3.010414
H	6.277876	-0.738625	2.200430
O	5.200265	-3.040586	-1.506642
H	7.124649	-4.139601	-0.421150
H	9.534820	-4.522869	-0.621936
H	7.865184	-0.048811	0.646468
H	10.272921	-0.416973	0.404858
H	11.484150	-4.167755	-1.796228
H	13.904503	-4.557447	-1.872723
H	14.462078	-1.720396	1.301440
H	12.040635	-1.396038	1.437456
H	-18.363096	-0.888956	2.309054
H	-20.139229	0.274807	1.086123
H	-15.407632	1.529356	0.343739
H	-17.182887	2.701775	-0.872223
H	-16.653030	-2.348172	1.147355
H	-14.119246	-6.175689	1.839451
H	-10.713314	-3.720947	3.902980
H	-10.351921	-1.325030	4.358419
H	-9.689670	3.115568	4.706285
H	-16.320836	3.870455	4.256949
H	-16.531632	1.603164	3.312858
H	-12.722724	6.499650	5.670092
H	-9.728391	0.306969	1.679259
H	-7.400853	-0.313523	1.209748
H	-6.392577	0.353689	5.332349
H	-8.701846	1.042282	5.785350
H	-3.259249	-2.099284	0.865166
H	-5.623655	-1.786495	1.413945

H	-2.179413	0.762244	3.884073
H	-4.541456	1.144627	4.366096
H	-0.541101	1.165774	2.462994
H	1.842437	0.879779	1.998074
H	1.142925	-3.220432	0.942438
H	-1.234062	-2.956958	1.462605
N	-13.990157	-5.194631	2.062052
N	-12.808717	5.554459	5.312501
O	-10.554998	5.326012	5.529205
O	-15.049727	5.896706	5.120593
O	-16.027799	-4.776763	1.139577
O	-11.967280	-5.725735	2.959773
C	4.797578	0.337249	3.874074
C	4.194965	-3.500837	-2.392586
H	4.275174	0.844587	4.686669
H	5.405873	-0.475828	4.290534
H	5.457465	1.053440	3.367188
H	4.721358	-3.998282	-3.208919
H	3.522048	-4.220588	-1.908604
H	3.599923	-2.671930	-2.797591
C	18.651526	-3.608669	-0.522242
C	17.877167	-3.630134	-1.681791
C	16.492605	-3.498679	-1.604955
C	15.847983	-3.348775	-0.366422
C	16.643861	-3.324552	0.790851
C	18.027798	-3.455486	0.715370
H	19.731264	-3.707142	-0.582839
H	18.353964	-3.734909	-2.651905
H	15.902860	-3.483842	-2.516164
H	16.167214	-3.233357	1.762348
H	18.619584	-3.441244	1.626130
C	-21.885539	3.402820	-2.376425
C	-22.133505	3.071022	-1.044719
C	-21.135116	2.487451	-0.268911
C	-19.866423	2.223678	-0.808253
C	-19.631624	2.562212	-2.151047
C	-20.629735	3.146517	-2.926160
H	-22.664948	3.856033	-2.981421
H	-23.105972	3.273106	-0.605835
H	-21.332910	2.254944	0.773134
H	-18.669445	2.335472	-2.599845
H	-20.429335	3.390846	-3.965213

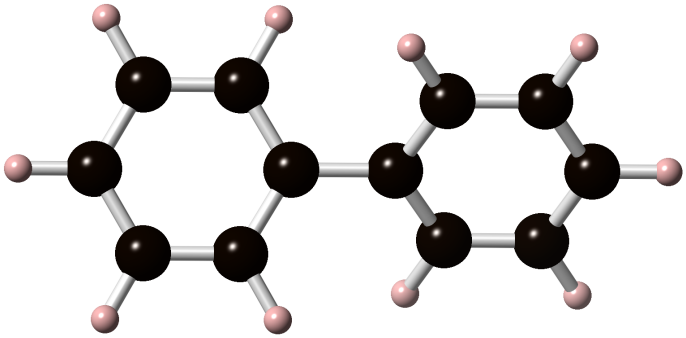

Biphenyl

FINAL HEAT OF FORMATION = -463.321476

C	-1.140470	-0.387961	1.464750
C	-1.141173	-0.387029	2.857959
C	0.000000	0.000000	3.561339
C	1.141173	0.387029	2.857959
C	1.140470	0.387961	1.464750
C	0.000000	0.000000	0.742532
C	0.000000	0.000000	-0.742532
C	1.140470	-0.387961	-1.464750
C	1.141173	-0.387029	-2.857959
C	0.000000	0.000000	-3.561339
C	-1.141173	0.387029	-2.857959
C	-1.140470	0.387961	-1.464750
H	-2.025300	-0.716471	0.927586
H	-2.032468	-0.698615	3.395283
H	0.000000	0.000000	4.647453
H	2.032468	0.698615	3.395283
H	2.025300	0.716471	0.927586
H	2.025300	-0.716471	-0.927586
H	2.032468	-0.698615	-3.395283
H	0.000000	0.000000	-4.647453
H	-2.032468	0.698615	-3.395283
H	-2.025300	0.716471	-0.927586

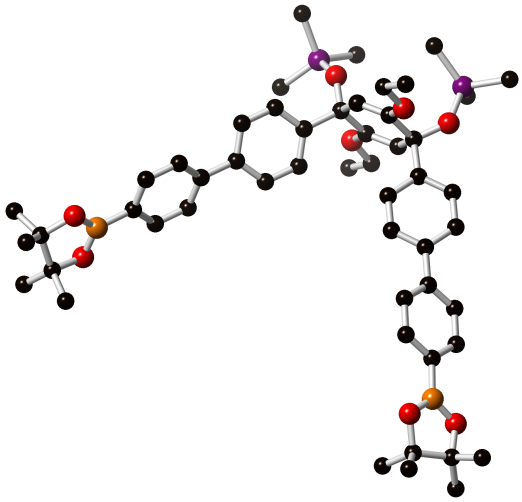

Five-Aryl Precursor (7.2)

Final Heat of Formation = -3254.65918

B	10.47009	-1.01958	-0.13630
B	1.46007	-11.90187	0.42225
C	0.26168	0.07333	-0.12649
C	-0.15369	-0.45579	-1.48140
C	-1.02572	-1.45046	-1.69135
C	-1.71240	-2.21774	-0.57138
C	-1.32557	-1.66790	0.78211
C	-0.45789	-0.66891	0.98799
C	-1.29766	-3.70270	-0.60631
C	1.79418	-0.06824	-0.02873
C	-1.52745	2.90150	1.98740
C	1.56415	2.73334	2.03354
C	0.11625	4.25394	-0.22018
C	-5.79411	-1.60109	-1.35089
C	-4.56119	-0.50946	1.24741
C	-3.69037	0.66404	-1.46473
C	-2.23596	-4.72992	-0.49145
C	-1.82789	-6.06091	-0.40266
C	-0.47052	-6.41355	-0.42709
C	0.46401	-5.37358	-0.57116
C	0.05881	-4.04706	-0.65571
C	2.60716	0.81230	-0.75393
C	3.99061	0.67197	-0.76603
C	4.62448	-0.36142	-0.05697
C	3.80536	-1.24573	0.66145
C	2.41932	-1.10361	0.67431
C	6.10016	-0.51560	-0.07387
C	-0.02149	-7.81884	-0.26908
C	6.79324	-0.99965	1.04898

C	8.17470	-1.15786	1.02643
C	8.92823	-0.83195	-0.11339
C	8.23486	-0.33940	-1.23163
C	6.85217	-0.18774	-1.21565
C	1.13485	-8.29179	-0.91444
C	1.59134	-9.58934	-0.70843
C	0.91133	-10.47762	0.14241
C	-0.25850	-10.01034	0.76510
C	-0.71480	-8.71139	0.56692
C	12.54508	-1.75458	0.46940
C	12.64447	-0.83551	-0.80960
C	1.55881	-14.05742	1.16978
C	2.94128	-13.63468	0.53677
C	1.64707	-14.71042	2.54749
C	0.69813	-14.91474	0.23221
C	3.52674	-14.62259	-0.46960
C	3.99943	-13.25870	1.58349
C	13.46335	-1.41131	-1.96283
C	13.10663	0.59389	-0.49596
C	13.52192	-1.41465	1.59281
C	12.61285	-3.25370	0.14704
C	-0.63923	-0.81304	3.37978
C	-0.82614	-1.34196	-4.07224
C	-0.02531	-0.15073	4.59938
C	-1.38674	-2.07170	-5.27853
H	0.31312	0.06387	-2.30862
H	-1.80885	-2.17234	1.61038
H	-1.50795	3.81623	2.59161
H	-2.42297	2.93890	1.35792
H	-1.62961	2.05136	2.66748
H	1.53720	3.58982	2.71844
H	1.61159	1.82015	2.63111
H	2.48675	2.80021	1.44979
H	0.12033	5.19096	0.34836
H	1.02307	4.23417	-0.83391
H	-0.74404	4.27757	-0.89710
H	-6.61620	-0.87806	-1.30066
H	-5.62796	-1.85176	-2.40325
H	-6.11993	-2.51247	-0.83891
H	-5.42157	0.16448	1.33765
H	-4.79001	-1.41563	1.81903
H	-3.70413	-0.01756	1.71635
H	-4.46495	1.43402	-1.36322
H	-2.75551	1.06673	-1.06440
H	-3.54352	0.47772	-2.53366
H	-3.29003	-4.48034	-0.47650

H	-2.58134	-6.83981	-0.32793
H	1.52510	-5.60410	-0.57601
H	0.80911	-3.26718	-0.74259
H	2.14682	1.62498	-1.30654
H	4.59110	1.39070	-1.31556
H	4.25553	-2.07417	1.20026
H	1.82266	-1.81811	1.23140
H	6.24427	-1.23289	1.95572
H	8.68502	-1.53387	1.90909
H	8.79084	-0.08413	-2.12977
H	6.34272	0.16295	-2.10835
H	1.67371	-7.63626	-1.59234
H	2.49392	-9.92488	-1.21219
H	-0.80447	-10.67247	1.43177
H	-1.59892	-8.36798	1.09614
H	2.20573	-15.65122	2.49952
H	2.12939	-14.05517	3.27451
H	0.64047	-14.93396	2.91191
H	1.10177	-15.92597	0.12410
H	-0.31052	-14.98926	0.64741
H	0.62133	-14.46286	-0.76064
H	3.74938	-15.58225	0.00886
H	2.84751	-14.79857	-1.30518
H	4.46087	-14.22221	-0.87354
H	4.36961	-14.13824	2.11895
H	4.84402	-12.78320	1.07746
H	3.60198	-12.54888	2.31426
H	14.50794	-1.55487	-1.66675
H	13.06349	-2.36721	-2.30481
H	13.44474	-0.71695	-2.80752
H	14.16834	0.62667	-0.23338
H	12.95151	1.21816	-1.38001
H	12.53161	1.02647	0.32742
H	14.55791	-1.54539	1.26242
H	13.39451	-0.38923	1.94314
H	13.35154	-2.08391	2.44077
H	13.62088	-3.55808	-0.15029
H	12.33139	-3.82061	1.03854
H	11.91881	-3.52029	-0.65489
H	-0.40662	-1.88636	3.35580
H	-1.73246	-0.70799	3.37888
H	0.26726	-1.44123	-4.02109
H	-1.06286	-0.26932	-4.11004
H	-0.41447	-0.61723	5.50968
H	1.06257	-0.26079	4.59302
H	-0.26455	0.91583	4.62995

H	-0.96016	-1.65895	-6.19802
H	-1.14520	-3.13688	-5.22984
H	-2.47422	-1.96710	-5.32229
O	-0.10447	1.46094	-0.12746
O	-3.12933	-2.16862	-0.74005
O	11.19267	-1.48759	0.93669
O	11.25434	-0.74355	-1.23196
O	0.87952	-12.77828	1.30951
O	2.59550	-12.40908	-0.16720
O	-1.41141	-1.92193	-2.90599
O	-0.09611	-0.18617	2.21345
Si	0.03253	2.76439	0.93359
Si	-4.23031	-0.90433	-0.57122

Fifteen Lowest Roots for PPh_6-PhHex

Restricted Singlet Excited State 1:

Excitation energy = 0.0582865269 hartrees 1.58605709 eV 781.71 nm

excitation	X coeff.
255 => 256	-0.99815

Transition dipole moment (debye):
X= 3.1852 Y= 0.5014 Z= 0.1987 Tot= 3.2306

Oscillator strength, f= 0.0628

Restricted Singlet Excited State 2:

Excitation energy = 0.0664619655 hartrees 1.80852210 eV 685.56 nm

excitation	X coeff.
254 => 256	-0.99060

Transition dipole moment (debye):
X= 0.5680 Y= 3.3374 Z= 4.1652 Tot= 5.3675

Oscillator strength, f= 0.1976

Restricted Singlet Excited State 3:

Excitation energy = 0.0847408081 hartrees 2.30591471 eV 537.68 nm

excitation	X coeff.
251 => 256	-0.15475
252 => 256	-0.48188
253 => 256	0.85385

Transition dipole moment (debye):
X= 1.8126 Y= -2.9241 Z= -1.2539 Tot= 3.6617

Oscillator strength, f= 0.1172

Restricted Singlet Excited State 4:

Excitation energy = 0.0854358977 hartrees 2.32482906 eV 533.30 nm

excitation	X coeff.
251 => 256	0.16296
252 => 256	0.84009
253 => 256	0.50322

Transition dipole moment (debye):
X= -2.0862 Y= -2.5268 Z= -0.2840 Tot= 3.2890

Oscillator strength, f= 0.0954

Restricted Singlet Excited State 5:

Excitation energy = 0.0968336355 hartrees 2.63497729 eV 470.53 nm

excitation	X coeff.
247 => 256	-0.11134
251 => 256	-0.95230
252 => 256	0.23462

Transition dipole moment (debye):
X= 1.2199 Y= 0.0436 Z= -0.2270 Tot= 1.2416

Oscillator strength, f= 0.0154

Restricted Singlet Excited State 6:

Excitation energy = 0.1087785382 hartrees 2.96001463 eV 418.86 nm

excitation	X coeff.
248 => 256	-0.18354
250 => 256	-0.79096
255 => 257	-0.37365
255 => 258	0.32656
255 => 259	-0.10935
255 => 260	0.10452

Transition dipole moment (debye):
X= 0.8321 Y= -2.3136 Z= -0.4138 Tot= 2.4933

Oscillator strength, f= 0.0698

Restricted Singlet Excited State 7:

Excitation energy = 0.1106178912 hartrees 3.01006597 eV 411.90 nm

excitation	X coeff.
250 => 256	0.48080
254 => 257	-0.11400
254 => 259	-0.11414
254 => 260	-0.17503
255 => 257	-0.70542
255 => 258	0.38129
255 => 259	-0.17280

Transition dipole moment (debye):
X= 0.9845 Y= 1.1220 Z= -2.8430 Tot= 3.2110

Oscillator strength, f= 0.1177

Restricted Singlet Excited State 8:

Excitation energy = 0.1127214092 hartrees 3.06730561 eV 404.21 nm

excitation	X coeff.
239 => 256	0.12110
244 => 256	0.10394
247 => 256	-0.32382
248 => 256	-0.14972
249 => 256	-0.54087
250 => 256	0.10494
251 => 256	0.12693
254 => 257	0.52293
255 => 257	0.19326
255 => 258	0.38200
255 => 259	-0.13434

Transition dipole moment (debye):
X= -0.6730 Y= 0.0377 Z= -0.7526 Tot= 1.0103

Oscillator strength, f= 0.0119

Restricted Singlet Excited State 9:

Excitation energy = 0.1133028915 hartrees 3.08312854 eV 402.14 nm

excitation	X coeff.
239 => 256	-0.14503
247 => 256	-0.23631
248 => 256	-0.12056
249 => 256	-0.58068
254 => 257	-0.21000
254 => 258	-0.20761
254 => 260	0.10566
255 => 257	-0.36310
255 => 258	-0.53300
255 => 259	0.12869

Transition dipole moment (debye):

X= -0.7894 Y= -0.5668 Z= 1.3186 Tot= 1.6381

Oscillator strength, f= 0.0314

Restricted Singlet Excited State 10:

Excitation energy = 0.1144901191 hartrees 3.11543465 eV 397.97 nm

excitation	X coeff.
239 => 256	-0.13464
241 => 256	-0.51302
242 => 256	-0.10266
243 => 256	-0.51893
244 => 256	-0.27751
249 => 256	-0.27508
254 => 257	-0.36486
255 => 257	0.23149
255 => 258	0.21378

Transition dipole moment (debye):
X= 0.8609 Y= 0.1565 Z= -0.3385 Tot= 0.9382

Oscillator strength, f= 0.0104

Restricted Singlet Excited State 11:

Excitation energy = 0.1147216476 hartrees 3.12173486 eV 397.16 nm

excitation	X coeff.
239 => 256	-0.16787
241 => 256	0.31357
242 => 256	0.28068
243 => 256	0.38360
244 => 256	0.15509
249 => 256	-0.21965
254 => 257	-0.56653
255 => 257	0.32355
255 => 258	0.31268

Transition dipole moment (debye):

X= 1.3765 Y= 0.2586 Z= -0.5778 Tot= 1.5151

Oscillator strength, f= 0.0272

Restricted Singlet Excited State 12:

Excitation energy = 0.1149342514 hartrees 3.12752011 eV 396.43 nm

excitation	X coeff.
241 => 256	0.33619
242 => 256	-0.86831
242 => 257	-0.13053
242 => 258	-0.10951
244 => 256	0.17906
254 => 257	-0.16998

Transition dipole moment (debye):
X= 0.3434 Y= 0.0392 Z= -0.0600 Tot= 0.3508

Oscillator strength, f= 0.0015

Restricted Singlet Excited State 13:

Excitation energy = 0.1156296372 hartrees 3.14644252 eV 394.05 nm

excitation	X coeff.
245 => 256	-0.10525
247 => 256	-0.25270
248 => 256	-0.84940
249 => 256	0.32228
250 => 256	0.19302
254 => 257	-0.11443

Transition dipole moment (debye):
X= -0.1518 Y= -0.2555 Z= 0.2542 Tot= 0.3911

Oscillator strength, f= 0.0018

Restricted Singlet Excited State 14:

Excitation energy = 0.1170384589 hartrees 3.18477851 eV 389.30 nm

excitation	X coeff.
239 => 256	0.19612
245 => 256	-0.11356
246 => 256	0.22981
247 => 256	0.58092
248 => 256	-0.33149
249 => 256	-0.31899
254 => 258	0.52475

Transition dipole moment (debye):
X= 2.4451 Y= -0.0311 Z= -0.1510 Tot= 2.4500

Oscillator strength, f= 0.0725

Restricted Singlet Excited State 15:

Excitation energy = 0.1178521197 hartrees 3.20691934 eV 386.61 nm

excitation	X coeff.
241 => 256	-0.19450
244 => 256	0.47240
245 => 256	0.16076
247 => 256	-0.46261
248 => 256	0.15593
249 => 256	0.12112
254 => 257	-0.15347
254 => 258	0.60073
254 => 259	0.13593

Transition dipole moment (debye):
X= 3.0120 Y= -0.0284 Z= 0.1510 Tot= 3.0159

Oscillator strength, f= 0.1106

Restricted Singlet Excited State 16:

Excitation energy = 0.1189447489 hartrees 3.23665130 eV 383.06 nm

excitation	X coeff.
238 => 256	0.40710
239 => 256	-0.21382
241 => 256	0.12301
242 => 256	-0.10295
243 => 256	0.15780
244 => 256	-0.47246
245 => 256	-0.20207
246 => 256	-0.48059
247 => 256	-0.15802
254 => 258	0.39657
254 => 259	0.12360
254 => 261	0.10464

Transition dipole moment (debye):
X= 2.0911 Y= 0.0086 Z= 0.2063 Tot= 2.1013

Oscillator strength, f= 0.0542

Restricted Singlet Excited State 17:

Excitation energy = 0.1198773413 hartrees 3.26202843 eV 380.08 nm

excitation	X coeff.
238 => 256	-0.35487
239 => 256	0.22765
241 => 256	-0.19609
244 => 256	0.30004
245 => 256	-0.53408
246 => 256	-0.59787
249 => 256	-0.11312

Transition dipole moment (debye):
X= -0.2772 Y= 0.0406 Z= 0.1330 Tot= 0.3101

Oscillator strength, f= 0.0012

Restricted Singlet Excited State 18:

Excitation energy = 0.1199662091 hartrees 3.26444664 eV 379.80 nm

excitation	X coeff.
241 => 256	-0.18733
243 => 256	0.18536
245 => 256	0.73759
246 => 256	-0.49579
247 => 256	0.23577
248 => 256	-0.21589

Transition dipole moment (debye):
X= 0.1117 Y= 0.4384 Z= -0.0359 Tot= 0.4539

Oscillator strength, f= 0.0026

Restricted Singlet Excited State 19:

Excitation energy = 0.1213525740 hartrees 3.30217155 eV 375.46 nm

excitation	X coeff.
240 => 256	-0.11159
241 => 256	0.51286
242 => 256	0.26817
243 => 256	-0.64587
244 => 256	0.13079
245 => 256	0.14921
246 => 256	-0.28715
255 => 258	0.11662
255 => 259	0.23039

Transition dipole moment (debye):
X= -0.6209 Y= -0.9309 Z= 0.1742 Tot= 1.1324

Oscillator strength, f= 0.0161

Restricted Singlet Excited State 20:

Excitation energy = 0.1223193303 hartrees 3.32847833 eV 372.50 nm

```
 excitation     X coeff.
------------   ---------
 241 =>  256     0.16791
 243 =>  256    -0.22451
 254 =>  258     0.14036
 254 =>  259    -0.14804
 254 =>  260    -0.18663
 255 =>  258    -0.36045
 255 =>  259    -0.74717
 255 =>  260     0.30477

 Transition dipole moment (debye):
   X=     1.3481     Y=    -0.8463     Z=    -2.6178  Tot=     3.0637

 Oscillator strength, f=     0.1185

--------------------------------------------------------------------------------
 Restricted Singlet Excited State  21:
---------------------------------------

 Excitation energy =  0.1240850806 hartrees      3.37652684 eV      367.19 nm

 excitation     X coeff.
------------   ---------
 235 =>  256    -0.11338
 236 =>  256     0.11295
 238 =>  256    -0.54146
 239 =>  256     0.44934
 241 =>  256     0.22544
 244 =>  256    -0.51755
 245 =>  256     0.14115
 247 =>  256    -0.29066
 254 =>  257    -0.12488
 254 =>  258     0.11904

 Transition dipole moment (debye):
   X=     1.2049     Y=    -0.1719     Z=    -0.3823  Tot=     1.2757

 Oscillator strength, f=     0.0208

--------------------------------------------------------------------------------
 Restricted Singlet Excited State  22:
---------------------------------------

 Excitation energy =  0.1255336538 hartrees      3.41594452 eV      362.96 nm
```

```
 excitation     X coeff.
------------   ---------
 254 =>  259    -0.14559
 255 =>  259     0.43344
 255 =>  260     0.86608

 Transition dipole moment (debye):
   X=    -3.9252     Y=     0.3219     Z=    -0.7051  Tot=     4.0010

 Oscillator strength, f=     0.2074

-------------------------------------------------------------------------
 Restricted Singlet Excited State  23:
---------------------------------------

 Excitation energy =  0.1288198393 hartrees      3.50536618 eV      353.70 nm

 excitation     X coeff.
------------   ---------
 231 =>  256    -0.12222
 237 =>  256     0.13934
 239 =>  256     0.18586
 240 =>  256     0.61824
 250 =>  256    -0.19456
 254 =>  259    -0.42351
 254 =>  260    -0.37166
 254 =>  262     0.11659
 255 =>  259     0.20630
 255 =>  260    -0.17478

 Transition dipole moment (debye):
   X=    -0.0209     Y=    -2.2297     Z=     2.6706  Tot=     3.4791

 Oscillator strength, f=     0.1609

-------------------------------------------------------------------------
 Restricted Singlet Excited State  24:
---------------------------------------

 Excitation energy =  0.1300416816 hartrees      3.53861420 eV      350.37 nm

 excitation     X coeff.
------------   ---------
 238 =>  256    -0.21495
 239 =>  256    -0.35749
 253 =>  258    -0.11940
```

253 => 261 -0.12034
254 => 258 0.25214
254 => 259 -0.54664
254 => 260 0.51780
254 => 261 -0.35180
255 => 261 -0.11124

Transition dipole moment (debye):
X= 4.9750 Y= -0.2687 Z= 0.0166 Tot= 4.9823

Oscillator strength, f= 0.3331

Restricted Singlet Excited State 25:

Excitation energy = 0.1316641678 hartrees 3.58276430 eV 346.06 nm

excitation	X coeff.
238 => 256	-0.45876
239 => 256	-0.48446
240 => 256	0.27419
253 => 257	-0.38595
254 => 257	0.32177
254 => 259	0.29147
254 => 260	-0.18753
254 => 261	0.19834
255 => 260	0.10369

Transition dipole moment (debye):
X= -1.9442 Y= 0.4324 Z= -0.5733 Tot= 2.0725

Oscillator strength, f= 0.0584

Restricted Singlet Excited State 26:

Excitation energy = 0.1324709935 hartrees 3.60471914 eV 343.95 nm

excitation	X coeff.
235 => 256	-0.12572
236 => 256	-0.15562
237 => 256	0.13534

```
 238 =>  256     0.12727
 239 =>  256     0.19132
 240 =>  256     0.56340
 252 =>  258    -0.13145
 254 =>  259     0.41430
 254 =>  260     0.49172
 255 =>  259    -0.17697
 255 =>  260     0.17755

 Transition dipole moment (debye):
   X=     0.0105     Y=     2.1344     Z=    -3.8284  Tot=     4.3832

 Oscillator strength, f=     0.2626

--------------------------------------------------------------------------------
 Restricted Singlet Excited State  27:
---------------------------------------

 Excitation energy =  0.1357698237 hartrees      3.69448488 eV      335.59 nm

  excitation     X coeff.
 ------------   ---------
 231 =>  256     0.15289
 233 =>  256     0.57543
 233 =>  257    -0.10493
 234 =>  256     0.50902
 235 =>  256    -0.29135
 236 =>  256    -0.30117
 240 =>  256    -0.11971
 253 =>  257     0.25268
 255 =>  261     0.16982

 Transition dipole moment (debye):
   X=     0.5689     Y=    -0.4352     Z=     0.0853  Tot=     0.7213

 Oscillator strength, f=     0.0073

--------------------------------------------------------------------------------
 Restricted Singlet Excited State  28:
---------------------------------------

 Excitation energy =  0.1362057533 hartrees      3.70634712 eV      334.52 nm

  excitation     X coeff.
 ------------   ---------
 232 =>  256    -0.28325
```

```
 233 =>  256    -0.11462
 234 =>  256    -0.22779
 235 =>  256     0.10114
 236 =>  256     0.13164
 238 =>  256    -0.14321
 239 =>  256    -0.14843
 240 =>  256     0.17804
 252 =>  257    -0.11286
 253 =>  257     0.72385
 253 =>  258    -0.21098
 254 =>  261     0.10141
 255 =>  261     0.30217

 Transition dipole moment (debye):
   X=     1.5741     Y=     0.4449     Z=    -0.8893  Tot=     1.8619

 Oscillator strength, f=      0.0487

-------------------------------------------------------------------------
 Restricted Singlet Excited State  29:
---------------------------------------

 Excitation energy =  0.1365059830 hartrees      3.71451679 eV      333.78 nm

  excitation     X coeff.
 ------------   ---------
 232 =>  256     0.71272
 233 =>  256    -0.44527
 234 =>  256     0.24268
 236 =>  256    -0.20522
 252 =>  257    -0.10840
 253 =>  257     0.14489
 253 =>  258    -0.10107
 255 =>  261     0.24610

 Transition dipole moment (debye):
   X=     0.4408     Y=     0.1291     Z=    -0.4373  Tot=     0.6342

 Oscillator strength, f=      0.0057

-------------------------------------------------------------------------
 Restricted Singlet Excited State  30:
---------------------------------------

 Excitation energy =  0.1370926065 hartrees      3.73047963 eV      332.35 nm
```

excitation X coeff.

232 => 256	-0.14594
238 => 256	0.10924
239 => 256	0.13092
252 => 257	-0.27395
253 => 257	-0.36456
253 => 258	0.12363
254 => 259	-0.12783
254 => 260	0.28502
254 => 261	0.12759
255 => 261	0.74361

Transition dipole moment (debye):
X= -1.1523 Y= 1.0473 Z= -1.3823 Tot= 2.0821

Oscillator strength, f= 0.0613

Diphenyl PDI: 15 roots

Restricted Singlet Excited State 1: 2.2184 eV 558.90 nm

excitation X coeff.

148 => 149	0.99526

excitation Y coeff.

148 => 149	-0.11694

Transition dipole moment (debye):
X= -0.4696 Y= -1.0485 Z= 7.1546 Tot= 7.2462

Oscillator strength, f= 0.4417

Restricted Singlet Excited State 2: 2.8743 eV 431.35 nm

excitation X coeff.

147 => 149	0.98872
148 => 152	0.10632

Transition dipole moment (debye):

X= -0.1041 Y= -0.9812 Z= -0.1883 Tot= 1.0045

Oscillator strength, f= 0.0110

Restricted Singlet Excited State 3: 3.1824 eV 389.59 nm

excitation	X coeff.
142 => 149	-0.31441
142 => 150	0.14324
143 => 149	0.63564
143 => 150	0.11923
144 => 149	0.21519
145 => 149	0.62260

Transition dipole moment (debye):
X= -0.2710 Y= -0.1021 Z= -0.2166 Tot= 0.3616

Oscillator strength, f= 0.0016

Restricted Singlet Excited State 4: 3.1891 eV 388.77 nm

excitation	X coeff.
142 => 149	0.56460
143 => 149	0.31947
144 => 149	0.17470
146 => 149	-0.70387
148 => 153	0.10858

Transition dipole moment (debye):
X= 2.0350 Y= -0.3321 Z= 1.2756 Tot= 2.4246

Oscillator strength, f= 0.0711

Restricted Singlet Excited State 5: 3.2070 eV 386.60 nm

excitation	X coeff.
142 => 149	-0.63899
143 => 149	-0.28563
146 => 149	-0.66473
148 => 153	0.11843

Transition dipole moment (debye):
X= 2.1038 Y= -0.3601 Z= 1.2253 Tot= 2.4611

Oscillator strength, f= 0.0737

Restricted Singlet Excited State 6: 3.3417 eV 371.02 nm

excitation	X coeff.
138 => 149	0.26560
140 => 149	0.11743
141 => 149	-0.39974
142 => 149	-0.25528
143 => 149	0.34059
144 => 149	0.21632
145 => 149	-0.55581
148 => 150	-0.44547

Transition dipole moment (debye):
X= 0.0313 Y= 0.0092 Z= -0.0727 Tot= 0.0797

Oscillator strength, f= 0.0001

Restricted Singlet Excited State 7: 3.3470 eV 370.44 nm

excitation	X coeff.
138 => 149	0.11717
140 => 149	0.21502
141 => 149	-0.83478
142 => 149	0.12451
143 => 149	-0.17352
145 => 149	0.25723
148 => 150	0.32667

Transition dipole moment (debye):
X= 0.1328 Y= 0.0911 Z= 0.0482 Tot= 0.1681

Oscillator strength, f= 0.0004

Restricted Singlet Excited State 8: 3.3770 eV 367.14 nm

```
 excitation     X coeff.
------------   ---------
 143 =>  149     0.36802
 144 =>  149    -0.91855

 Transition dipole moment (debye):
   X=     0.5227     Y=    -0.2921     Z=     1.6381  Tot=     1.7441

 Oscillator strength, f=     0.0390
--------------------------------------------------------------------------------

 Restricted Singlet Excited State   9:     3.4073 eV       363.88 nm

 excitation     X coeff.
------------   ---------
 138 =>  149    -0.38444
 139 =>  149    -0.23525
 142 =>  149    -0.19648
 143 =>  149     0.29386
 145 =>  149    -0.44634
 148 =>  150     0.66885

 Transition dipole moment (debye):
   X=     0.0383     Y=     0.0983     Z=     0.0675  Tot=     0.1253

 Oscillator strength, f=     0.0002
--------------------------------------------------------------------------------

 Restricted Singlet Excited State  10:     3.5375 eV       350.49 nm

 excitation     X coeff.
------------   ---------
 138 =>  149    -0.11686
 139 =>  149     0.45963
 148 =>  151    -0.84632
 148 =>  152     0.17064

 Transition dipole moment (debye):
   X=     0.1216     Y=    -0.3065     Z=    -0.0839  Tot=     0.3403

 Oscillator strength, f=     0.0016
--------------------------------------------------------------------------------

 Restricted Singlet Excited State  11:     3.5599 eV       348.28 nm

 excitation     X coeff.
```

```
 ------------   ---------
  137 =>  149    -0.28905
  140 =>  149     0.89672
  141 =>  149     0.22500
  148 =>  153     0.11724

 Transition dipole moment (debye):
   X=    -0.5693     Y=     0.1511     Z=    -0.7894  Tot=     0.9850

 Oscillator strength, f=     0.0131
-------------------------------------------------------------------------------

 Restricted Singlet Excited State  12:     3.6205 eV       342.45 nm

  excitation     X coeff.
 ------------   ---------
  134 =>  149    -0.25434
  135 =>  149     0.26883
  137 =>  149     0.25816
  138 =>  149     0.32261
  139 =>  149    -0.67228
  148 =>  151    -0.43601

 Transition dipole moment (debye):
   X=    -0.5592     Y=    -0.6180     Z=     0.1435  Tot=     0.8458

 Oscillator strength, f=     0.0098
-------------------------------------------------------------------------------

 Restricted Singlet Excited State  13:     3.6977 eV       335.30 nm

  excitation     X coeff.
 ------------   ---------
  134 =>  149     0.12970
  135 =>  149     0.42122
  136 =>  149     0.17323
  137 =>  149     0.70094
  139 =>  149     0.34950
  140 =>  149     0.22810
  148 =>  151     0.11886
  148 =>  153    -0.18693

 Transition dipole moment (debye):
   X=    -0.9648     Y=     0.3198     Z=     0.6670  Tot=     1.2157

 Oscillator strength, f=     0.0207
```

Restricted Singlet Excited State 14: 3.7333 eV 332.11 nm

excitation	X coeff.
135 => 149	0.15716
136 => 149	-0.92852
136 => 150	0.17919
137 => 149	0.12880
138 => 149	-0.12173
142 => 151	-0.10866

Transition dipole moment (debye):
X= 0.1581 Y= -0.0489 Z= 0.2034 Tot= 0.2623

Oscillator strength, f= 0.0010

Restricted Singlet Excited State 15: 3.7993 eV 326.33 nm

excitation	X coeff.
136 => 149	-0.12848
138 => 149	0.77486
139 => 149	0.24378
141 => 149	0.19878
148 => 150	0.44444
148 => 152	0.15439

Transition dipole moment (debye):
X= 0.1437 Y= 0.4263 Z= 0.0212 Tot= 0.4504

Oscillator strength, f= 0.0029

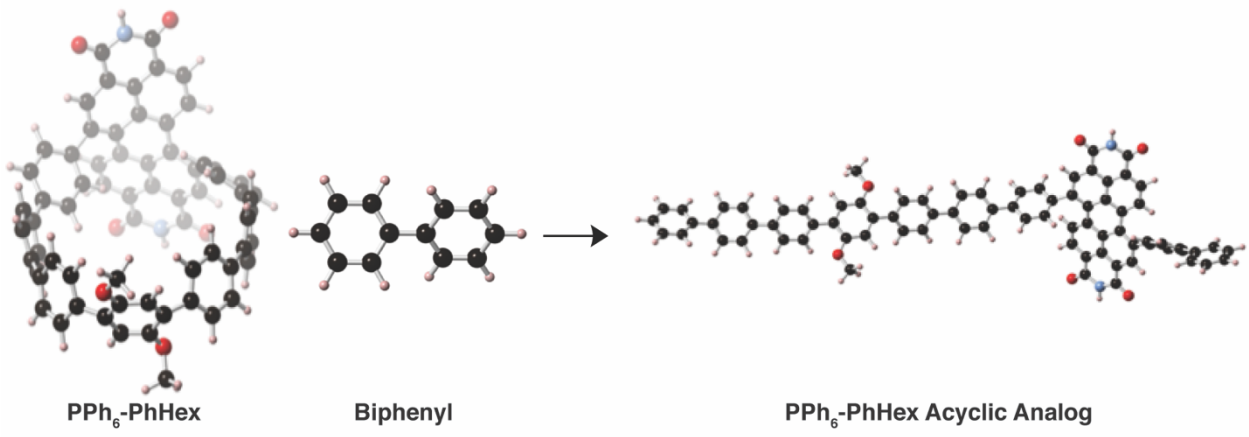

Table 7.1. Homodesmotic Calculations for Strain

Compound	Total energy	Strain energy (hartree)	Strain energy (kcal/mol)
PPh_6-PhHex	-3639.3085	0.100	63
Biphenyl	-463.3215	-	-
PPh_6-PhHex Acyclic Analog	-3639.7302	-	-

Table 7.1: Energies for the Homodesmotic Reaction (enthalpy).

7.15. References

1. Zhang, B. *et al.* Hollow organic capsules assemble into cellular semiconductors. *Nat. Commun.* **9**, 1957 (2018).
2. Hitosugi, S. *et al.* Asymmetric Autocatalysis Initiated by Finite Single-Wall Carbon Nanotube Molecules with Helical Chirality. *Org. Lett.* **16**, 645–647 (2014).
3. Matsuno, T. *et al*. Self-Sorting of Two Hydrocarbon Receptors with One Carbonaceous Ligand. *Angew. Chem. Int. Ed.* **55**, 15339–15343 (2016).
4. Matsuno, T. *et al*. Ratchet-free solid-state inertial rotation of a guest ball in a tight tubular host. *Nat. Commun.* **9**, 1907 (2018).
5. Sato, S. *et al.* Chiral intertwined spirals and magnetic transition dipole moments dictated by cylinder helicity. *Proc. Natl. Acad. Sci.* **114**, 13097–13101 (2017).
6. Wu, D. *et al*. Cycloparaphenylenes (CPPs): An Overview of Synthesis, Properties, and Potential Applications. *Asian J. Org. Chem.* **7**, 2161–2181 (2018).
7. Nojima, Y. *et al*. Stereogenic cyclic oligonaphthalenes displaying ring size-dependent handedness of circularly polarized luminescence (CPL). *Chem. Commun.* **55**, 2749–2752 (2019).
8. Xu, W. *et al.* Synthesis and Characterization of a Pentiptycene-Derived Dual Oligoparaphenylene Nanohoop. *Angew. Chem. Int. Ed.* **58**, 3943–3947 (2019).
9. Nakamura, T. *et al*. Double-Circularly Connected Saloph-Belt Macrocycles Generated from

a Bis-Armed Bifunctional Monomer. *J. Am. Chem. Soc.* (2019). doi:10.1021/jacs.9b00171

10. Hitosugi, S., *et al*. Bottom-up synthesis of finite models of helical (n,m)-single-wall carbon nanotubes. *Nat. Commun.* **2**, (2011).
11. Hitosugi, S. *et al*. Atropisomerism in a Belt-Persistent Nanohoop Molecule: Rotational Restriction Forced by Macrocyclic Ring Strain. *Chem. Asian J.* **7**, 1550–1552 (2012).
12. Kayahara, E. *et al.* Gram-Scale Syntheses and Conductivities of [10]Cycloparaphenylene and Its Tetraalkoxy Derivatives. *J. Am. Chem. Soc.* **139**, 18480–18483 (2017).
13. Kayahara, E. *et al*. Synthesis and Characterization of 5 Cycloparaphenylene. *J. Am. Chem. Soc.* **136**, 2284–2287 (2014).
14. Segawa, Y. *et al.* Concise Synthesis and Crystal Structure of 12 Cycloparaphenylene. *Angew. Chem. Int. Ed.* **50**, 3244–3248 (2011).
15. Iwamoto, T. *et al*. Selective and Random Syntheses of n Cycloparaphenylenes (n=8-13) and Size Dependence of Their Electronic Properties. *J. Am. Chem. Soc.* **133**, 8354–8361 (2011).
16. Ball, M. *et al.* Macrocyclization in the Design of Organic n-Type Electronic Materials. *J. Am. Chem. Soc.* **138**, 12861–12867 (2016).
17. Ball, M. L. *et al.* Influence of Molecular Conformation on Electron Transport in Giant, Conjugated Macrocycles. *J. Am. Chem. Soc.* **140**, 10135–10139 (2018).
18. Zhang, B. *et al.* Rigid, Conjugated Macrocycles for High Performance Organic Photodetectors. *J. Am. Chem. Soc.* **138**, 16426–16431 (2016).
19. Ball, M. *et al.* Chiral Conjugated Corrals. *J. Am. Chem. Soc.* **137**, 9982–9987 (2015).
20. Ball, M. *et al.* Conjugated Macrocycles in Organic Electronics. *Acc. Chem. Res.* (2019). doi:10.1021/acs.accounts.9b00017
21. Ball, M. *et al.* Contorted Polycyclic Aromatics. *Acc. Chem. Res.* **48**, 267–276 (2015).
22. Nolde, F. *et al*. Synthesis and self-organization of core-extended perylene tetracarboxdiimides with branched alkyl substituents. *Chem. Mater.* **18**, 3715–3725 (2006).
23. Zhong, Y. *et al.* Helical Ribbons for Molecular Electronics. *J. Am. Chem. Soc.* **136**, 8122–8130 (2014).
24. Meng, D. *et al.* High-Performance Solution-Processed Non-Fullerene Organic Solar Cells Based on Selenophene-Containing Perylene Bisimide Acceptor. *J. Am. Chem. Soc.* **138**, 375–380 (2016).
25. Wu, Q. *et al*. Covalently Bound Clusters of Alpha-Substituted PDI—Rival Electron Acceptors to Fullerene for Organic Solar Cells. *J. Am. Chem. Soc.* **138**, 7248–7251 (2016).
26. Darzi, E. R. *et al*. An Operationally Simple and Mild Oxidative Homocoupling of Aryl Boronic Esters To Access Conformationally Constrained Macrocycles. *J. Am. Chem. Soc.* **139**, 3106–3114 (2017).
27. Darzi, E. R. *et al.* Synthesis, Properties, and Design Principles of Donor–Acceptor Nanohoops. *ACS Cent. Sci.* **1**, 335–342 (2015).
28. Nishigaki, S. *et al.* Synthesis, Structures, and Photophysical Properties of Alternating

Donor–Acceptor Cycloparaphenylenes. *Chem. Eur. J.* **23**, 7227–7231 (2017).

29. Van Raden, J. M. *et al*. Synthesis and characterization of a highly strained donor-acceptor nanohoop. *Org. Biomol. Chem.* **14**, 5721 (2016).

30. Rajasingh, P. *et al*. Selective Bromination of Perylene Diimides under Mild Conditions. *J. Org. Chem.* **72**, 5973–5979 (2007).

Chapter 8. The Influence of Molecular Conformation on Electron Transport in Giant, Conjugated Macrocycles.

8.1. Preface

Chapter 8 is reproduced with permission from the authors: Melissa Ball, Boyuan Zhang, Qizhi Xu, Daniel W. Paley, Fay Ng, Michael L. Steigerwald and Colin Nuckolls published in the *Journal of the American Chemical Society*.[1] Copyright 2018 American Chemical Society. I carried out the synthesis and characterization of all compounds. Boyuan Zhang and Qizhi Xu performed all device fabrication and characterization.

8.2. Introduction

This manuscript describes the direct connection between the molecular conformation of a macrocycle and its macroscopic charge transport properties. The macrocycles studied here are the merger of two classes of electronic materials: conjugated macrocycles[2–28] and electron transporting hPDI ribbons.[29–31] Conjugated macrocycles are emerging as efficacious materials for electron transport in OFETs, OPVs, OPD, and sensors.[12,32–34] Thus far, the most successful conjugated macrocycles in devices consist of multiple copies of PDI monomers with various spacers that are wound into a macrocycle. Our goal here is to substitute monomeric PDI subunits with oligomeric hPDI subunits. The hPDI nanoribbons are known to have extraordinary properties in devices requiring efficient charge transport, such as solar cells and photodetectors,[35–39] making them exciting candidates for incorporation into a conjugated macrocycle construction.

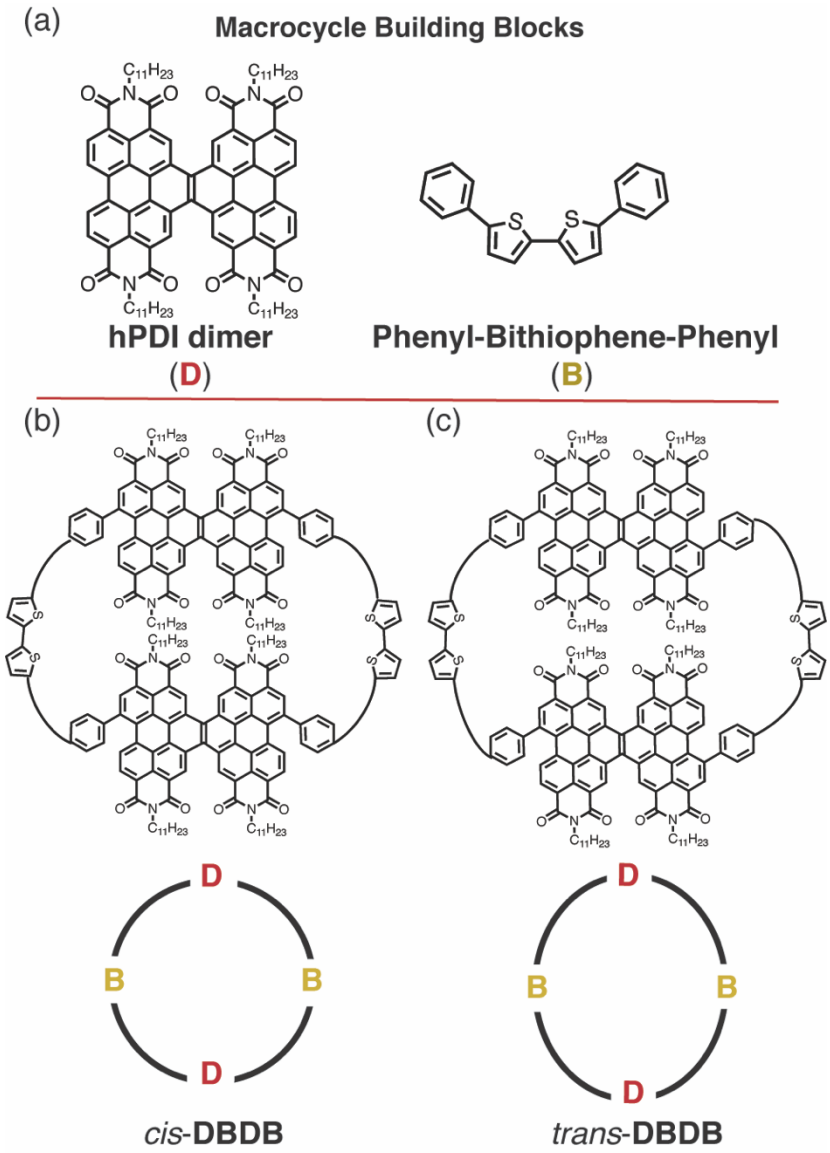

Figure 8.1. (a) Macrocycle building blocks comprising a phenyl-bithiophene-phenyl linker (B) and an hPDI dimer (D). The macrocycles are formed from these two molecular components wrapped into a -D-B-D-B- arrangement; (b) chemical structure of *cis*-**DBDB**; and (c) *trans*-**DBDB**.

Here we reveal the first of new, giant macrocycles that incorporate hPDI ribbons (Figure 8.1). Both structures comprise hPDI dimers (**D**) that are connected with a phenyl-bithiophene-phenyl linker (**B**) to form the macrocycles with the structure **DBDB** (the "c" denoting a cyclic structure). The connectivity of the two macrocycles differ between the hPDI monomer and the linker group (**B**), resulting in the formation of two, giant macrocycles: *cis*-**DBDB** (Figure 8.1b) and *trans*-**DBDB** (Figure 8.1c). We create amorphous thin films from each of these macrocycles

and compare how both the molecular structure and conformation affect charge transport. We find that both macrocycles form thin films that exhibit n-type semiconducting behavior in OFET devices. The remarkable finding is that the seemingly small change in the connectivity between hPDI dimer and the linker group results in a pronounced difference in the conductance of the films: the electron mobility of *cis*-**DBDB** is over four-times greater than that of *trans*-**DBDB**. As both films are amorphous, the difference in mobility is a direct consequence of the different molecular conformations available to the two isomers: the cis isomer's more flexible structure is better able to make intermolecular contacts than the trans isomer's more rigid structure.

8.3. Regio-pure Synthesis To Create DBDB

Figure 8.2 displays the scheme for *cis*-**DBDB** and *trans*-**DBDB**. Both syntheses begin from the cis and trans dibrominated dimers (hPDI-Br_2 **8.1a** and **8.2a**) that are formed as a 1:1 mixture in the bromination of the parent hPDI dimer.[29] The separation of **8.1a** and **8.2a** proved to be a challenging step in part because the two regioisomers are indistinguishable by ^{1}H-NMR or UV/vis spectroscopy. Moreover, we were unable to find conditions using standard silica gel chromatography to separate **8.1a** and **8.2a**; however, chiral HPLC proved to be successful in the separation of the two regioisomers (Figures 8.8-10 Table 8.1).

Using these regio-pure building blocks, we completed the syntheses of *trans*-**DBDB** and *cis*-**DBDB** (Figure 8.2). The approach to their syntheses utilizes square planar platinum atoms to form multi-nuclear macrocycles that form conjugated macrocycles through a reductive elimination process. We isolate the macrocycles in 6% yield for *trans*-**DBDB** and 12% yield for *cis*-**DBDB**. Both *trans*-**DBDB** and *cis*-**DBDB** are dark purple solids with a metallic sheen.

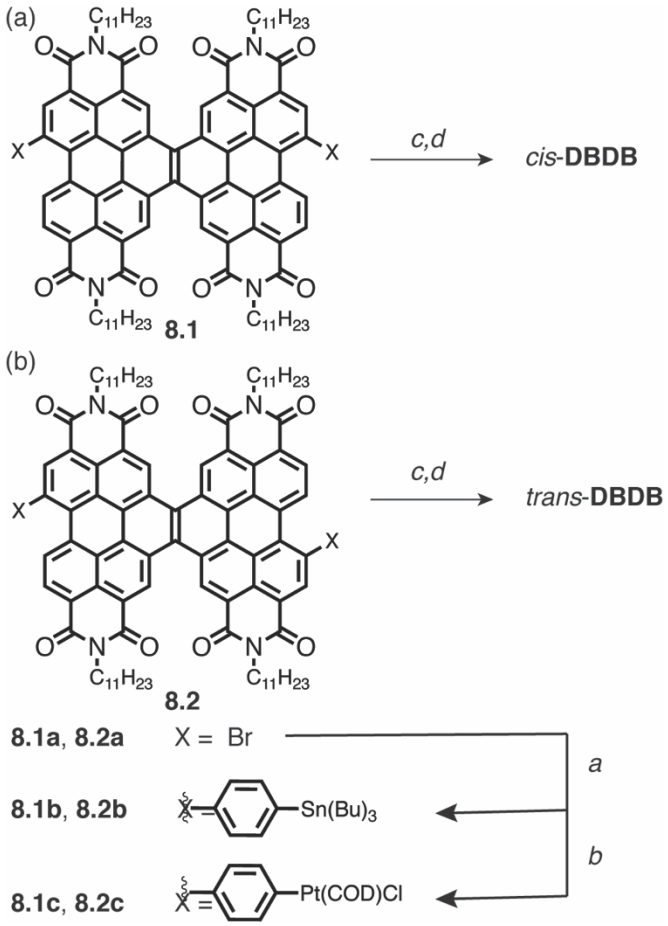

Figure 8.2. Synthesis of **DBDB**. key: a) 1,4-bis(tributylstannyl)benzene, P-(2-furyl)$_3$, Pd_2dba_3, THF, 55 °C, 12 h; b) $Pt(COD)Cl_2$, toluene, 100 °C, 12 h; c) 5,5′-bis(tributylstannyl)-2,2′-bithiophene, THF, 55 °C, 40 h. (d) PPh_3, toluene, 100 °C, 12 h.

8.4. Cis-DBDB Four-fold Increase in Carrier Mobility

We next explore how the connectivity of the macrocycles influences charge transport in thin films. From the potential of the first reduction peak in the cyclic voltammogram, we estimate the lowest unoccupied molecular orbital (LUMO) energy level to be –3.80 eV and –3.82 eV for *trans*-**DBDB** and *cis*-**DBDB** (Figure 8.11), respectively. These values are similar to the parent hPDI dimer and common n-type semiconductors like [6,6]-phenyl C_{61}-butyric acid methyl ester ($PC_{61}BM$).[29] This data suggests both macrocycles are promising n-type semiconductors.

Figure 8.3 contains a schematic of the OFET device, and displays the gate sweep for the devices from *trans*-**DBDB** and *cis*-**DBDB**. The remarkable finding is *cis*-**DBDB** shows a four-fold

increase in mobility relative to *trans*-**DBDB**, using the methods developed by McCulloch and Choi.[40,41] The *cis*-**DBDB** based transistor has a mobility of ~5.3 x 10^{-3} $cm^2/V•s$ relative to ~1.3 x 10^{-3} $cm^2/V•s$ for *trans*-**DBDB** (Figure 8.3). The devices in Figure 8.3 are the highest mobility for each isomer. To confirm the statistical relevance of this data, we measured seven devices and averaged the data for both *trans*-**DBDB** and *cis*-**DBDB** (Table 8.2). The averaged data, too, showed the cis isomer has a four-fold increase in electron mobility. We tested **8.1a** and **8.2a**, too, to see if there was a difference in mobility within the acyclic fragments, and found that the mobilities of the two are essentially identical (Figure 8.13). This suggests that the difference in mobility between *cis*-**DBDB** and *trans*- **DBDB** has to do with the molecular conformation of each macrocycle.

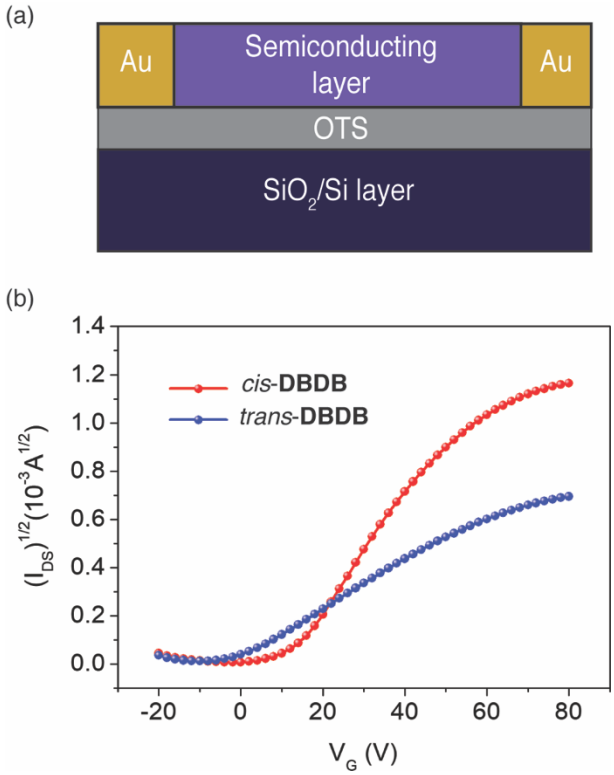

Figure 8.3. (a) Schematic of the OFET device and (b) transfer characteristics for *trans*-**DBDB** and *cis*-**DBDB**, showing a four-fold increase in electron mobility for the latter.

To understand why *cis*-**DBDB**'s mobility is much greater than *trans*-**DBDB**, we consider two factors that have a significant and general impact on charge transport in thin films: (1) the film

morphology and (2) the molecular and electronic structure of the molecule. We conclude that the films as we have prepared them are amorphous, and the electronic structures of the two macrocycles are essentially identical. These points suggest that it is the molecular structures and their associated dynamics that determine device performance.

8.5. Both Macrocycles are Amorphous by PXRD, AFM, and DSC

It is well-established that a thin film's crystallinity and morphology will influence the charge transport characteristics, and thus we first investigate the film morphology under device fabrication for each macrocycle.[42] We used a combination of differential scanning calorimetry (DSC), PXRD, and AFM to investigate the film morphology and crystallinity (Figure 8.14). Broad and featureless transitions in the DSC occur below 160 °C for both *trans*-**DBDB** and *cis*-**DBDB**. PXRD of both films suggests that both films are amorphous, lacking any obvious signs of crystallinity for both *trans*-**DBDB** and *cis*-**DBDB**. The AFM images, too, showed both films possess a smooth surface, with a root mean square roughness of 1.39 nm and 1.36 nm for *trans*-**DBDB** and *cis*-**DBDB**, respectively. Given this data, the essential point is that the origin of the difference in device performance cannot be due to the film morphology. We next investigate the electronic and molecular structure of the molecules as a source of the difference.

8.6. DFT Shows Pronounced Difference in Geometries

DFT calculations reveal that there is a marked difference between the lowest energy structures of both macrocycles. *Trans*-**DBDB** possesses an upright conformation (Figure 8.4a), where the hPDI dimer subunits are vertically arranged with respect to the macrocyclic plane. In contrast, *cis*-**DBDB** adopts a tent shape (Figure 8.4b), where the hPDI dimer subunits collapse across the macrocycle. The two macrocycles show a pronounced difference in their shapes: while both are elliptical, the eccentricity of *trans*-**DBDB** is greater than that of *cis*-**DBDB** (Figure 8.4c).

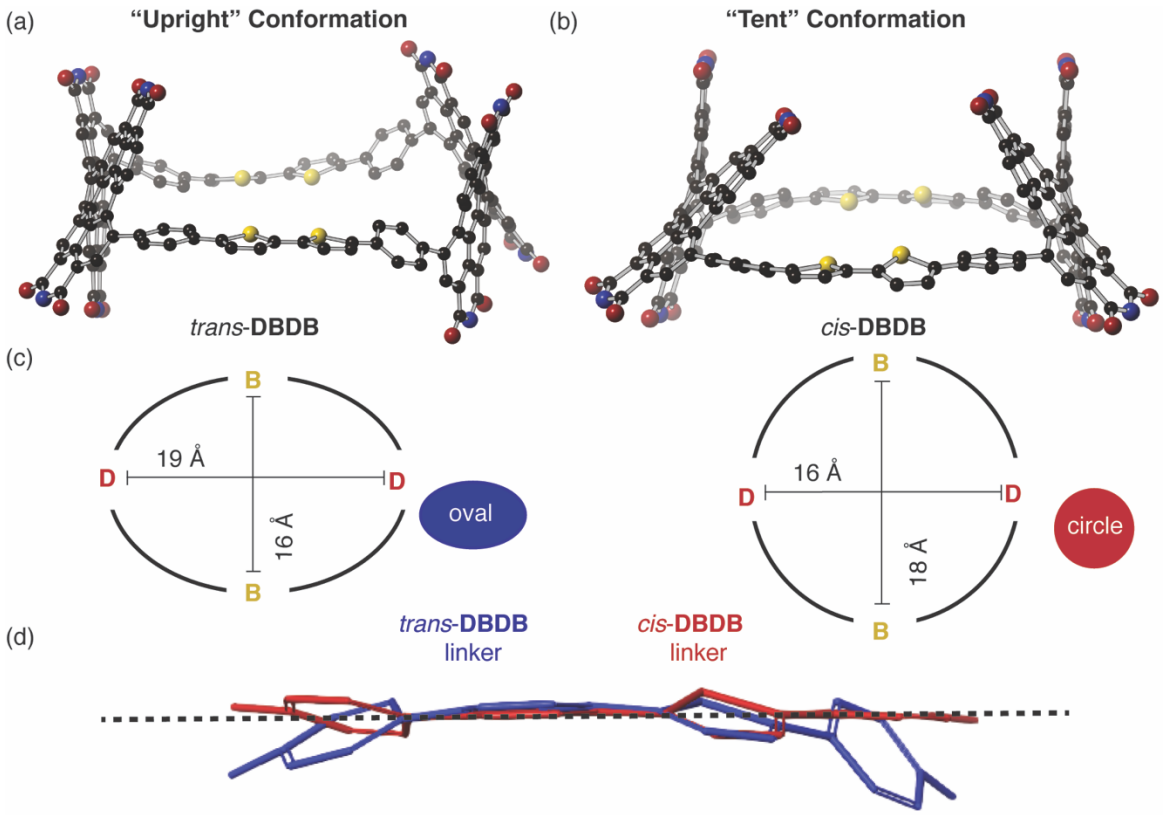

Figure 8.4. (a) DFT calculated lowest energy geometry for *trans*-**DBDB**; (b) and *cis*-**DBDB**. Red = oxygen, blue = nitrogen, black = carbon, and yellow = sulfur. Hydrogens and side chains have been removed for clarity; (c) Schematics of both *trans*-**DBDB** and *cis*-**DBDB**, respectively; (d) an overlay of the tetracyclic linker of both *trans*-**DBDB** and *cis*-**DBDB**. *trans*-**DBDB** shows a pronounced bowing relative to the cis isomer. Dashed black line indicates no bowing.

From the elongation and the upright structure for *trans*-**DBDB**, we reasoned that it was more strained than *cis*-**DBDB**. Calculations using a homodesmotic[24,43–45] series reveal that the strain energy difference between *trans*-**DBDB** and *cis*-**DBDB** is 9 kcal/mol, with the former structure possessing 18.6 kcal/mol of strain relative to just 9.5 kcal/mol for *cis*-**DBDB** (Table 8.3). To put this number into context, *trans*-**DBDB** contains a similar amount of strain to **PBPB**,[12] highlighting *cis*-**DBDB**'s conformational flexibility. We can visualize the strain in the two isomers from the difference in their tetracyclic linkers (phenyl-bithiophene-phenyl) connecting the hPDI subunits (Figure 8.4d). It is apparent from the over-lay that the tetracyclic linker bows in order to accommodate the rigidity of the *trans*-**DBDB** macrocycle (blue model). This is not the case for the

cis isomer (red model) where the tetracyclic linker is essentially flat and less strained relative to *trans*-**DBDB**.

8.7. Variable Temperature NMR Studies

The difference in strain for the two macrocycles affects the dynamics in solution. From variable temperature ^{1}HNMR measurements, we observe *trans*-**DBDB** is much less floppy than *cis*-**DBDB**. Both macrocycles possess different conformers that are able to interconvert through an "intramolecular somersault" process, where a hPDI subunit rotates through the center of the cavity (denoted with green arrows in Figure 8.5b,c).[12]

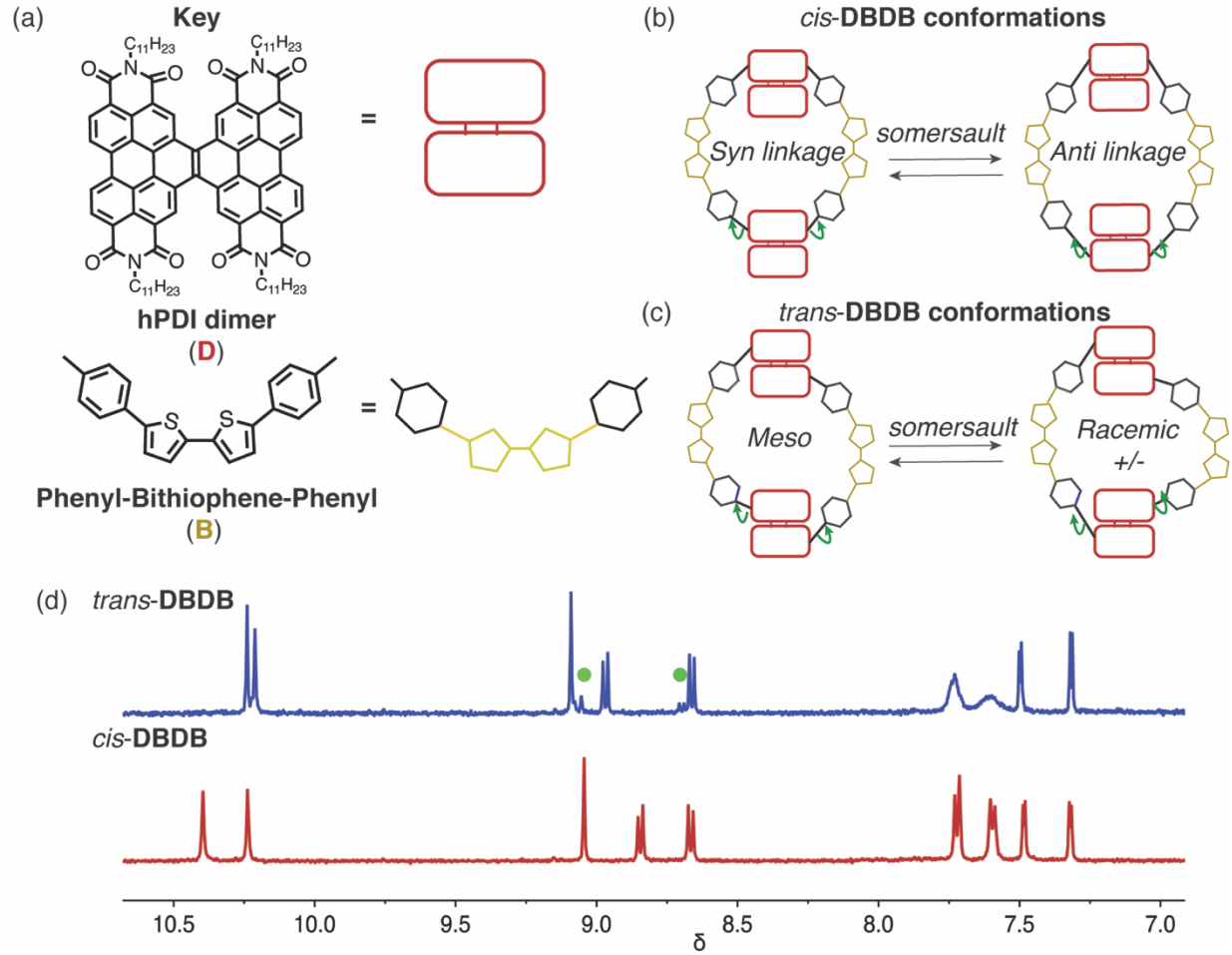

Figure 8.5. (a) Molecular building blocks for **DBDB** macrocycles; (b) Schematics the two conformers of *cis*-**DBDB**; (c) and *trans*-**DBDB** that interconvert through a somersault mechanism; and (d) VT-NMR of both macrocycles at 380 K. *trans*-**DBDB** shows the presence of both conformers at 380 K at 9.1 and 8.7 ppm, denoted with green circles.

Yet the intramolecular somersault dynamics differ for *trans*-**DBDB** and *cis*-**DBDB**. While the ^{1}H-NMR resonances for *cis*-**DBDB**'s two conformers fully coalesce at 380 K, the NMR shows the presence of both diastereomers for *trans*-**DBDB** (denoted with green circles in Figure 8.5d). Figure 8.15 contains further coalescence details. This suggests the activation barrier for the somersault process is higher for *trans*-**DBDB** than for *cis*-**DBDB**. We believe this reflects the geometries of each macrocycle: the cis isomer's "tent" shape is less rigid, and the hPDI subunits are more able to rotate through the cavity relative to the trans isomer's upright, rigid scaffold.

8.8. Rigidity Evident in the UV-Vis spectrum

The floppiness of the *cis*-**DBDB** relative to *trans*-**DBDB** is evident in both their UV-Vis and fluorescence spectra. While *trans*-**DBDB** retains features of a vibrational progression, characteristic of the unsubstituted PDI dimer,[29] *cis*-**DBDB** possesses a broadened spectrum. T*rans*-**DBDB**'s lowest energy transition, too, is shifted to lower energy shifted relative to *cis*-**DBDB** by approximately 20 nm. Both structural features reflect *trans*-**DBDB**'s more rigid, strained conformation.

8.9. VT-OFET Shows Larger Temperature Dependence for Cis

As both films are amorphous with no crystalline features, the disparity in transport properties reflects the differences in molecular structure between *trans*-**DBDB** and *cis*-**DBDB** geometries. The cis isomer's "tent" shape is conformationally flexible, aiding its ability to transport charge more effectively than the more rigid trans isomer. *cis*-**DBDB**'s less strained and floppy structure allows it to make better intermolecular contacts with neighboring molecules, resulting in higher mobility. We tested this hypothesis using temperature dependent transport measurements on films of pure *cis*-**DBDB** and *trans*-**DBDB** to temperatures as low as 250 K. We find that the mobility of *cis*-**DBDB** films is much more sensitive to temperature than is that of the

trans isomer (Figure 8.6). The slope of the change in current in the device with decreasing temperature is an order of magnitude steeper for the cis isomer relative to a shallow slope for the trans isomer (Figure 8.6). When we plot electron mobility verses temperature and analyze the data according to McCulloch and Choi,[40,41] we find the slope remains more steep for *cis*-**DBDB**, albeit the difference is less stark due to the higher threshold voltage for *trans*-**DBDB**. The structure of *cis*-**DBDB**, which is quite flexible at room temperature, stiffens as the temperature decreases; in contrast, the trans isomer is already rigid, making it less susceptible to temperature changes.

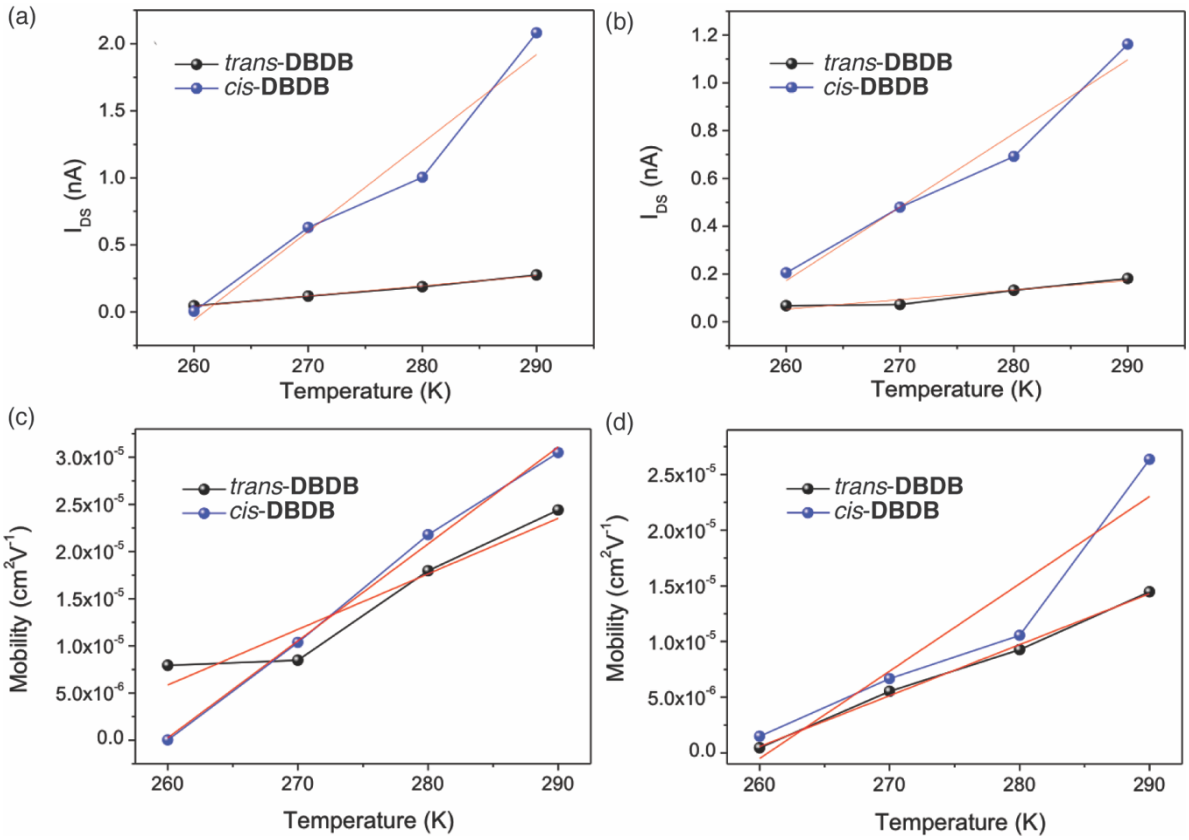

Figure 8.6. The dependence of source-drain current of the *cis*-**DBDB** and *trans*-**DBDB**-based OFET on temperature (a) from 290 K to 250 K and (b) from 250 K to 290 K, measured at gate voltage of 40V and bias voltage of 80V. The slope of the best fit line for a) is 6.6 x 10^{-2} and 7.6 x 10^{-3} for *cis*-**DBDB** and *trans*-**DBDB**, suggesting the cis corral is more temperature sensitive than the trans corral. The dependence of mobility of the *cis*-**DBDB** and *trans*-**DBDB**-based OFET on temperature (c) from 290 K to 250 K and (d) from 250 K to 290 K, measured at bias voltage of 80 V.

8.10. Conclusion

In summary, we describe two n-type, electronic materials made from giant conjugated macrocycles comprising hPDI dimers and bithiophenes in an alternating pattern. We find that there is a marked difference in the electron transporting properties of the two macrocycles. Creating amorphous films of both macrocycles, we were able to probe the effects of conformation on transport and find that the *cis*-**DBDB**'s conformational flexibility enhances its ability to transport charge relative to *trans*-**DBDB**. These materials will serve as the electron accepting semiconducting material in organic photovoltaics, taking advantage of their ability to transport electrons and open cavities.

8.11. Appendix – Supplementary Figures

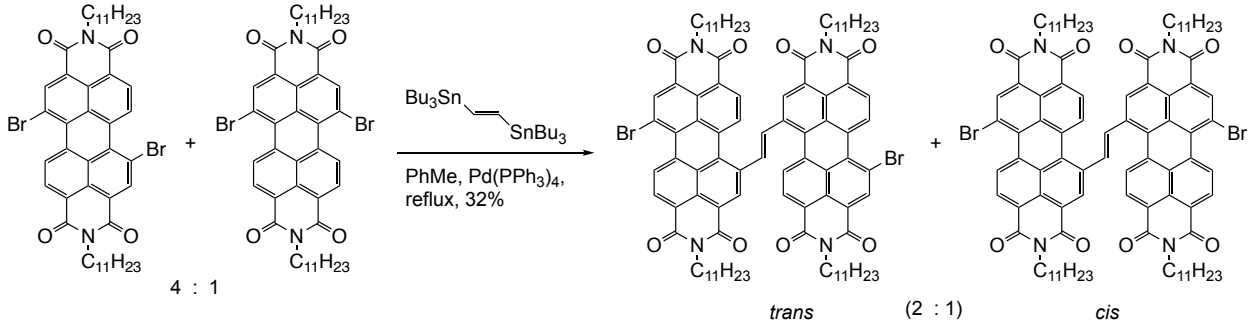

A solution of dibromoPDI (4:1 trans/cis) (850 mg, 1.00 mmol, 4.00 equiv) and *trans*-1,2-bis(tributylstannyl)ethene (150 mg, 0.25 mmol, 1.00 equiv) in toluene (20 mL) was degassed under Argon for 30 minutes. Tetrakis(triphenylphosphine)palladium(0) (100 mg, 0.09 mmol) was added, and the resultant solution was degassed for 15 minutes. The mixture was refluxed for overnight under Argon. The black reaction mixture was filtered through celite. The solvent was removed under reduced pressure and the product was purified using silica gel column chromatography (DCM:hexane 6:4) to yield dark purple solid (126 mg, 0.08 mmol, 32%) as an inseparable 2:1 mixture of regioisomers. See ^{1}H NMR spectrum for regioisomeric distribution.

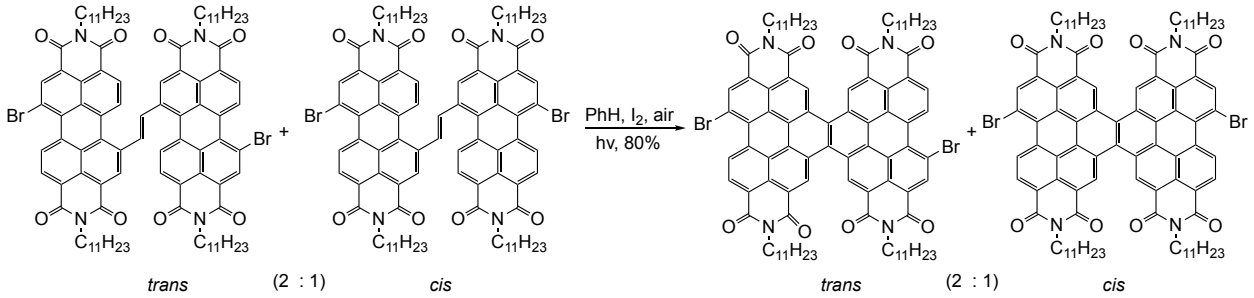

In standard photocyclization glassware, uncyclized dimer mixture (120 mg, 0.076mmol, 1.00 equiv) was dissolved in 150 mL toluene and iodine (150 mg, 0.59 mmol, 7.76 equiv) was added. The resultant purple solution was photoirradiated using 450W mercury lamp for 10 hours. The resultant pink reaction mixture extracted with saturated sodium bicarbonate (2 X 100 mL), brine (100 mL) and concentrated under reduced pressure. The residue was treated with 50 mL methanol to crash out dark red solid. The red solid was purified using silica gel column chromatography (gradient mobile phase: DCM:hexane 2:8 to DCM:hexane 6:4) to yield dark red solid (96 mg, 0.061 mmol, 80 %) that is spectroscopically identical to $hPDI_2Br_2$ from dibromination of $hPDI_2$.

Figure 8.7: Synthetic details for the two dibromo $hPDI_2$ isomers (**8.1a** and **8.2a**) showing an enriched mixture of 8.2a (2:1 trans:cis).

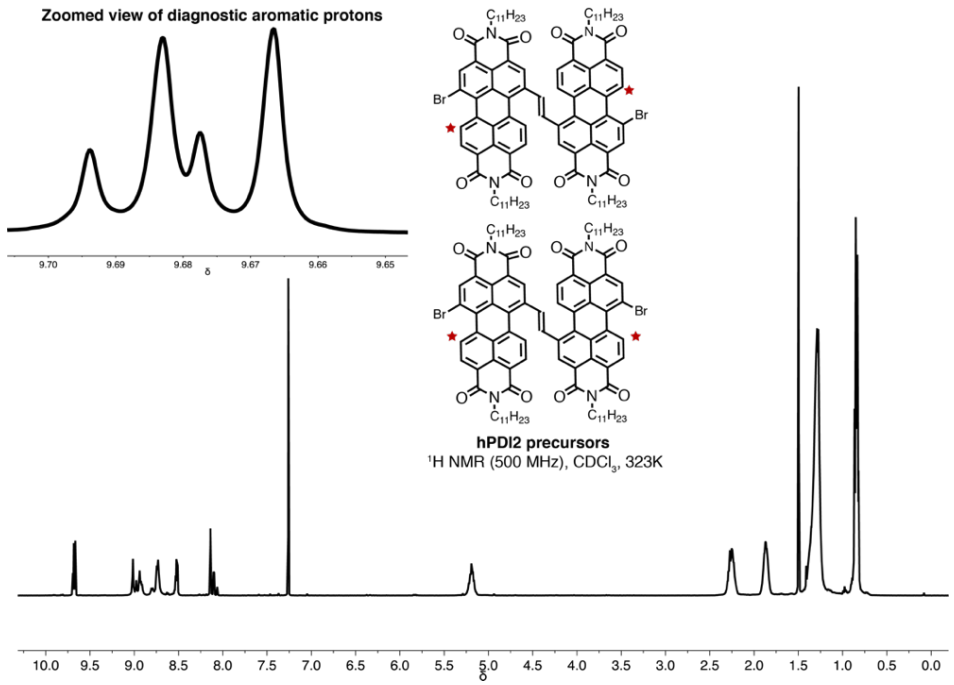

Figure 8.8. ^{1}H NMR spectrum of the enriched mixture of **8.2a**:**8.1**a's precursors, showing an approximate 2:1 ratio of the downfield protons at 9.65-9.70 ppm. These peaks correspond to the red starred protons that are deshielded due to the bromine atoms.

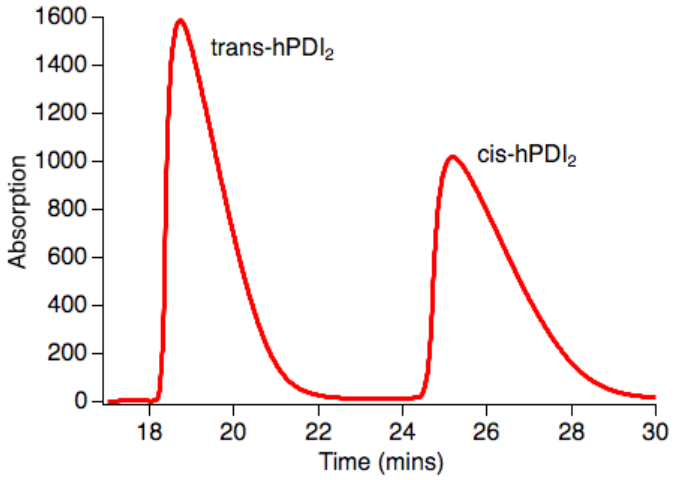

Figure 8.9: The two dibromo hPDI$_2$ isomers are separated using a CHIRALPAK® IA-3 column (4.6 mm I.D. x 250 mm, 3 μm), using an isocratic method of 22% methylene chloride: 78% hexanes. Using an enriched mixture (2:1 trans isomer:cis isomer), we were able to confirm the first peak from HPLC is **8.2a**.

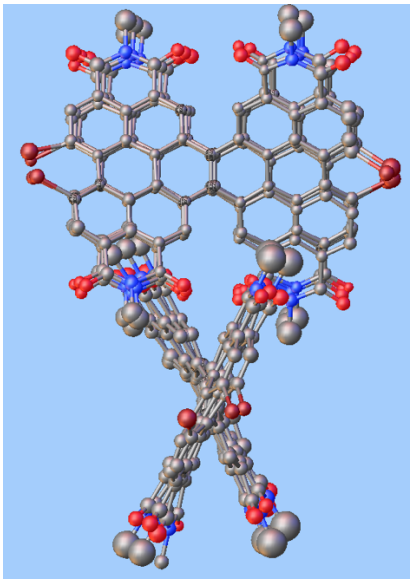

Figure 8.10. Thermal ellipsoid plot of hPDI-Br_2. The two independent sites are disordered over 4 and 3 positions. All atoms were refined with isotropic ADPs due to the extensive disorder. Thermal ellipsoids are depicted at the 40% level. The $C_{11}H_{23}$ side chains were omitted from the refinement. Hydrogen atoms are omitted for clarity.

Table 8.1. Table of crystallographic data for Compound **8.2a**

Compound	Compound **8.2a**
Formula	$C_{54}H_{22}Br_2N_4O_8$ + side chains + solvent
MW	1014.57
Space group	P-1
a (Å)	15.4448(11)
b (Å)	19.9037(13)
c (Å)	26.3807(18)
α (°)	86.411(5)
β (°)	82.181(6)
γ (°)	79.782(6)
V (Å3)	7900.6(9)
Z	4
ρcalc (g cm-3)	0.853
T (K)	100
λ (Å)	1.54184
2θmin, 2θmax	7, 90
Nref	41264

R(int), R(σ)	.0679, .0809
μ(mm-1)	1.600
Size (mm)	.12 x .04 x .03
Tmax, Tmin	.954, .831
Data	12531
Restraints	3167
Parameters	1940
R1(obs)	0.1673
wR2(all)	0.5119
S	1.846
Peak, hole (e- Å-3)	1.03, -0.81

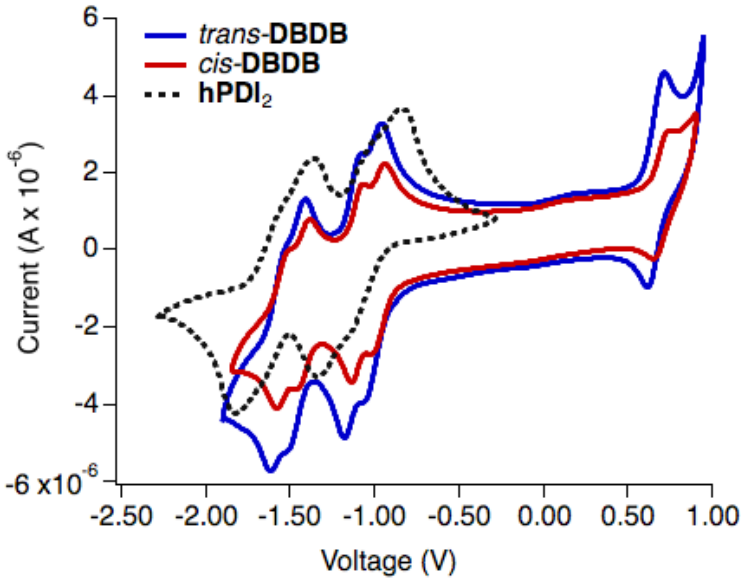

Figure 8.11. CV for *cis*-**DBDB** and *trans*-**DBDB** relative to a hPDI monomer.

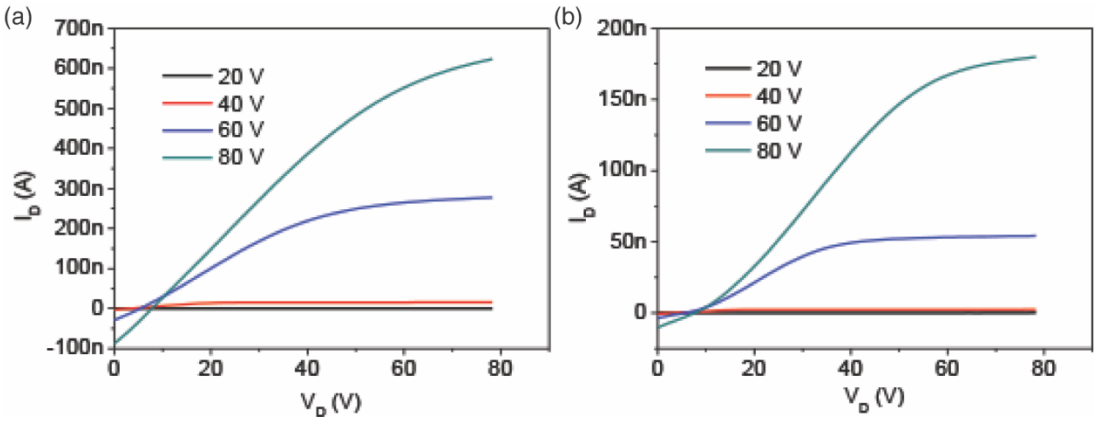

Figure 8.12. Output curves for (a) cis-**DBDB** and (b) trans-**DBDB**. Both devices show current saturation at 80 V.

	cis-**DBDB** Highest/average	*trans*-**DBDB** Highest/average
Mobility (cm^2V^{-1})	4.1×10^{-3} / $2.7 \pm 1.2 \times 10^{-3}$	9.9×10^{-4} / $8.2 \pm 1.4 \times 10^{-4}$

Table 8.2. Transfer characteristics for (a) *cis*-**DBDB** and (b) *trans*-**DBDB**.

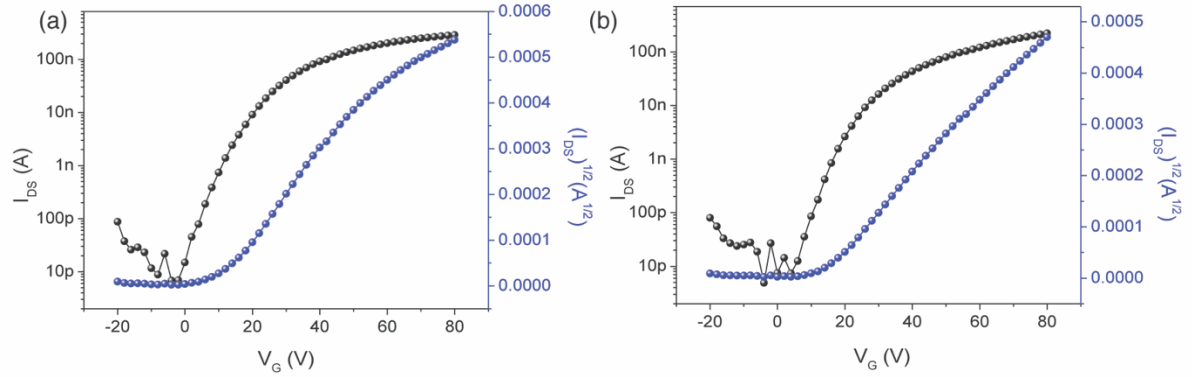

Figure 8.13. Transfer curves for (a) **8.1a** and (b) **8.2a**. The mobilities are essentially identical at 2.0×10^{-3} and 1.6×10^{-3} for **8.1a** and **8.2a**, respectively.

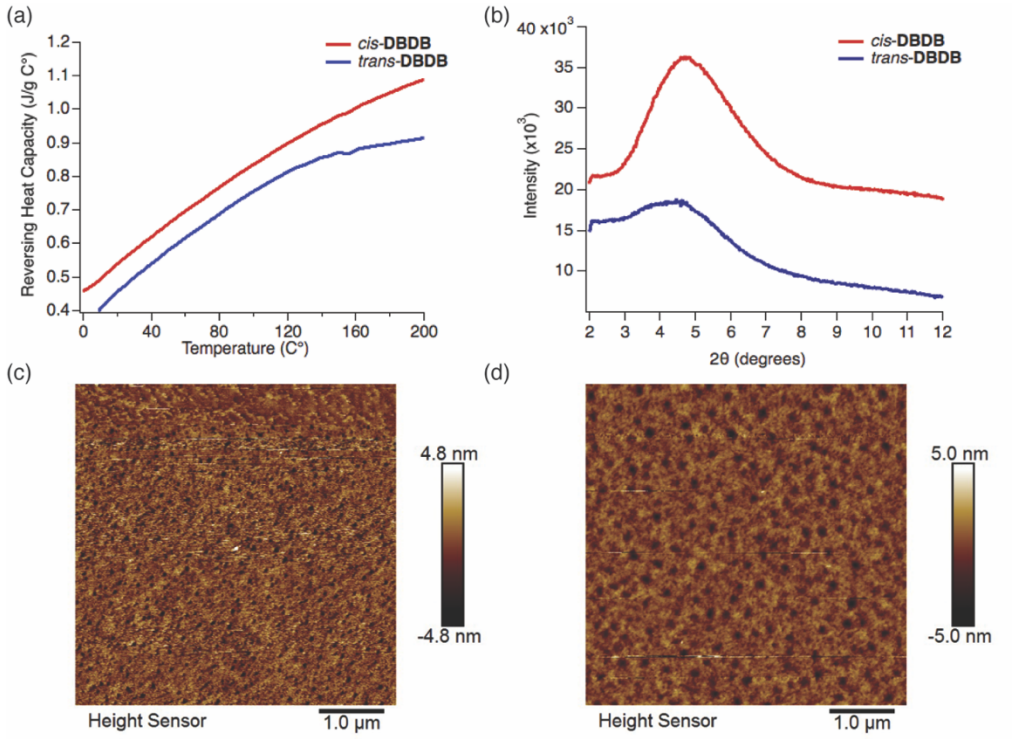

Figure 8.14. (a) DSC showing broad features at temperatures below 160 °C; (b) PXRD of *cis*-**DBDB** and *trans*-**DBDB** at three temperatures, showing the materials are amorphous at higher temperatures ~160 °C; (c) AFM of height images of cis-**DBDB** and (d) trans-**DBDB**.

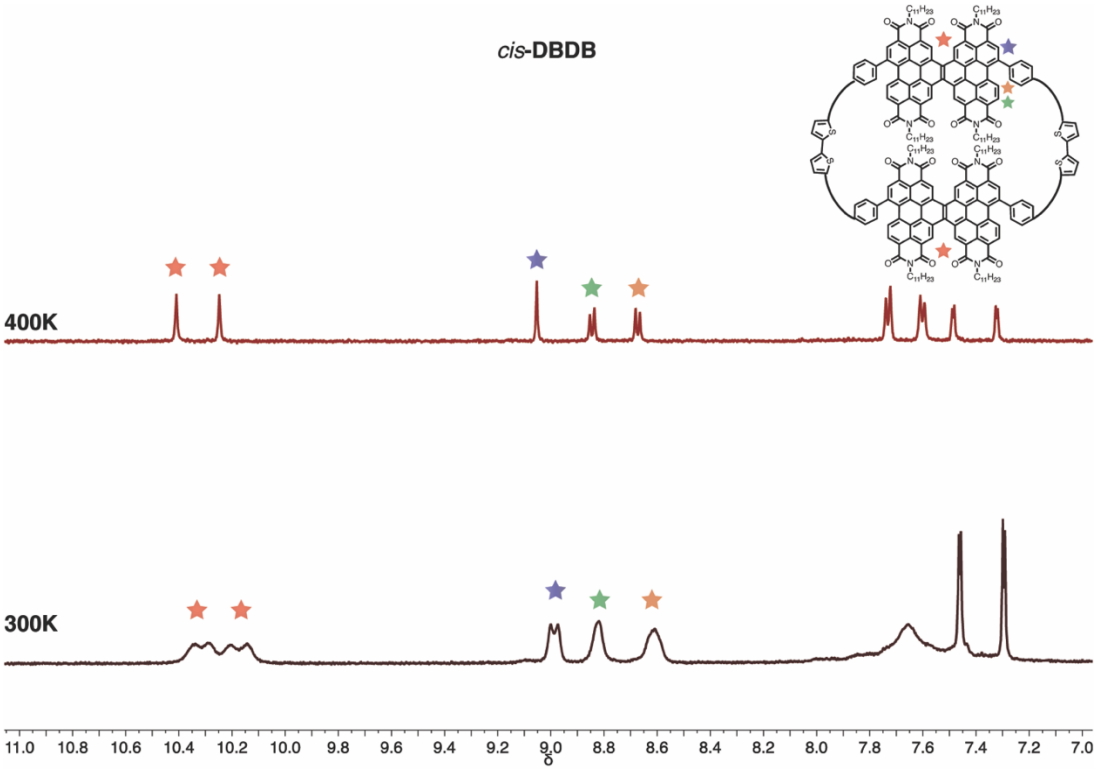

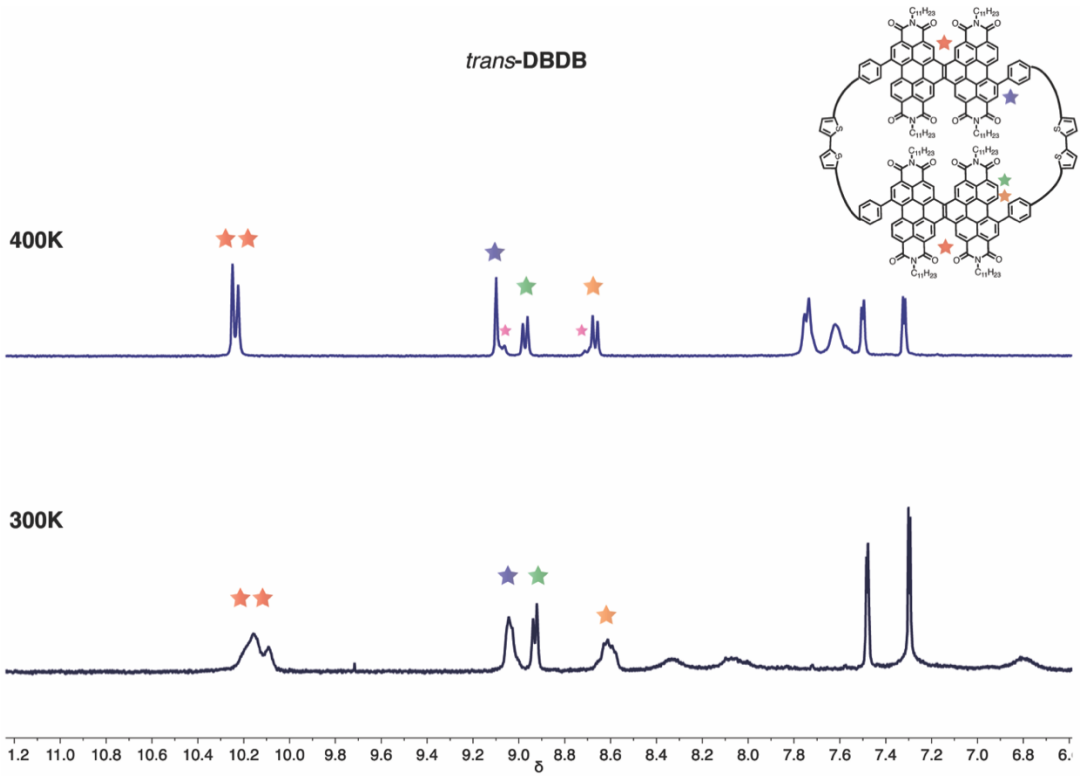

Figure 8.15. VT-NMR for *cis*-**DBDB** and *trans*-**DBDB**. Both room temperature spectra show the presence of multiple conformers. Yet, at 400K, the spectrum for *cis*-**DBDB** shows coalescence, while *trans*-**DBDB** shows multiple peaks at 8.7 and 9.1 ppm, denoted with pink stars.

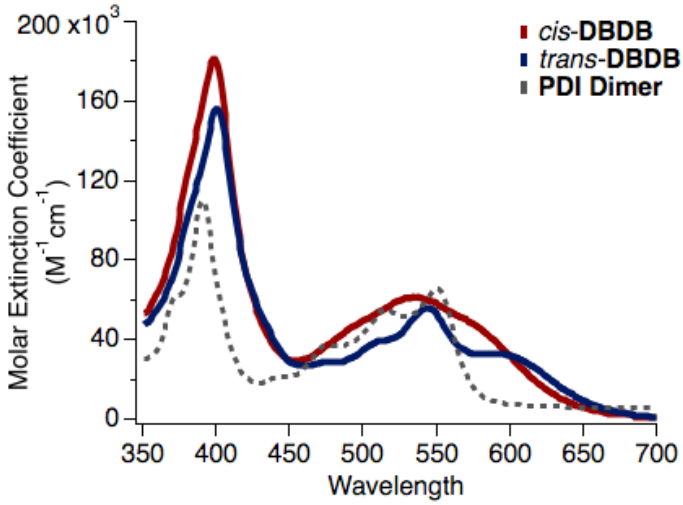

Figure 8.16. UV-Vis absorption spectra for *cis*-**DBDB**, *trans*-**DBDB**, and a $hPDI_2$.

8.12. General Experimental Information

Synthesis. All reactions were performed in oven-dried or flame-dried round bottom flasks, unless otherwise noted. The flasks were fitted with rubber septa and reactions were conducted

under a positive pressure of nitrogen or argon, unless otherwise noted. Anhydrous and anaerobic solvents were obtained from a Glass Contour solvent system consisting of a Schlenk manifold with purification columns packed with activated alumina and supported copper catalyst. Reaction monitoring by TLC was performed on J.T. Baker Baker-flex Silica Gel IB2-F (25 mm x 75 mm) TLC plates. TLC visualization was accomplished by visible observation and irradiation with a UV lamp. Commercial reagents were used without further purification. $Pt(COD)Cl_2$ was purchased from Strem Chemicals, and all other reagents were purchased from Sigma-Aldrich.

Purification. Automated flash chromatography was performed using a Teledyne Isco Combiflash Rf200 and Redisep Rf Silica and Alumina columns.

Spectrometers. ^{1}H NMR spectra were recorded on a Bruker 400 or 500 MHz spectrometer. ^{13}CNMR spectra were recorded on a Bruker 125 or 100 MHz spectrometer with complete proton decoupling. NMR spectra were recorded at 300 K unless otherwise noted. Chemical shifts are reported in parts per million (ppm) Data are represented as follows: chemical shift, multiplicity (s = singlet, d = doublet, dd= doublet of doublets, t = triplet, m = multiplet), coupling constants in Hz, and integration. Broadening (br) of peaks in the 1H NMR spectrum is due to rotational isomers about the imide side chains. The synthesis of **8.1a** and **8.2a** was previously reported.[29] The separation of the two isomers is provided in Figures 8.7-8.9. Broadening (br) of peaks in the ^{1}H NMR spectrum is due to rotational isomers about the imide side chains.[12,46] HRMS was performed on a (1) Waters XEVO G2-XS QTOF instrument equipped with a UPC SFC inlet, and ESI and APCI ionization sources; or (2) a Bruker UltrafleXtreme MALDI TOF/TOF instrument using a dithranol matrix. UV-vis absorption spectra were recorded on a Shimadzu UV-1800 spectrophotometer using a 1.0 cm quartz cell. IR spectra were recorded on a Perkin Elmer Spectrum400 FTIR spectrometer using a PIKE ATR attachment.

Atomic force microscopy. AFM measurements were carried out in scan analysis mode on a Bruker Multi-Mode AFM at ambient conditions. A commercial silicon cantilever (SCANASYST-AIR, Bruker) was used in this study with a typical radius of curvature of ~8nm and a nominal spring constant of ~0.4 Nm^{-1}.

Cyclic Voltammetry. CVs were recorded on a CH166 electrochemical workstation using an Ag/AgCl electrode as the reference electrode at room temperature. Experiments were performed in CH_2Cl_2 with NBu_4PF_6 as the supporting electrolyte at a scan rate of 0.1 V/s.[47]

Thin film transistors. To create the devices, we first silanize the substrate (300 nm of SiO2 on a Si wafer) with OTS Au is deposited onto the substrate as bottom-contact source and drain electrodes (40 nm) with a width of 115 μm and length of 10 μm. Next, we spin-cast organic films onto the surface at 3,000 r.p.m. for 1 min, to form transistors using the silicon wafer as the global back gate for the device. Finally, the samples were annealed under inert atmosphere at 160℃ for 10 minutes to optimize device performance. The thin film transistors were tested on the Agilent 4155C semiconductor parameter analyzer.

The mobility is calculated in the saturation regime using $IDS = (W/2L)C_i\mu(V_G - V_T)_2$, where W and L are the width and length of the channel, C_i (11.5 $nFcm^{-2}$), μ, and V_T correspond to the capacitance per unit area of the gate insulator, the field effect mobility, and the threshold voltage, respectively. W = 115 μm and L = 10 μm for transistor devices. The data is fitted using the methods developed by McCulloch and Choi to avoid overestimated mobilities.[40,41]

Temperature dependence measurement. Temperature-dependent current-voltage measurements were realized in a vacuum cryogenic probe station (Lakeshore TTP4). Computer-controlled source units were used S3 to apply DC potentials (Yokogawa 7651). Current measurements were obtained using a current preamplifier (Stanford Research System SR570) and

a digital multimeter (Keysight 34401A). All device measurements were performed in vacuum (P < 1×10-4 Torr) at different temperatures.

Single crystal X-ray diffraction. Data for all compounds was collected on an Agilent SuperNova diffractometer using mirror-monochromated Cu Kα radiation. Data collection, integration, scaling (ABSPACK) and absorption correction (multi-scan) were performed in CrysAlisPro.[48] Structure solution was performed using ShelXT.[49] Subsequent refinement was performed by full-matrix least-squares on F4 in ShelXL.[50] Olex2[51] was used for viewing and to prepare CIF files. PLATON[52] was used extensively for SQUEEZE.[53]

A toluene solution of hPDI2 – Br_2 - trans was diluted with methanol by vapor diffusion to afford bright red prisms. Part of a crystal (0.12 x 0.04 x 0.03 mm) was separated carefully, mounted with Paratone oil, and cooled to 100 K on the diffractometer. Complete data (99.7%) were collected to 1.1 Å, outside of which resolution there was little usable data. 41264 reflections were collected (12531 unique, 7287 observed) with R(int) 6.8% and R(sigma) 8.1% after multiscan absorption correction (Tmax 0.954, Tmin 0.831).

The structure solved readily in P-1 but showed signs of extensive disorder. Each of the two independent molecules was a mixture of PPP and PPM isomers (+ enantiomers) and was further disordered by a twofold rotation around the helical axis, which is not a point symmetry operator of the molecule but is an approximate symmetry of the van der Waals surface. For each site, these 4 possible isomers + orientations were introduced as fragments with DFT-optimized geometry and subsequently allowed to refine with all 1,2- and 1,3- distances restrained to match their DFT geometry. One site had all 4 possibilities occupied and the other had 3 of the 4 possibilities occupied.

The $C_{11}H_{23}$ side chains were not possible to locate in view of the extensive disorder of the hPDI cores. Thus they were modeled as methyl groups and the rest of the chains were treated as a diffuse contribution to the overall scattering using Platon SQUEEZE.

All ADPs were modeled isotropically because the data/parameters ratio was already poor due to the low resolution of the diffraction and the numerous overlapping disordered positions. All C-H hydrogens were placed in calculated positions and refined with riding coordinates and isotropic ADPs. The final refinement (12531 data, 3167 restraints, 1940 parameters) converged with R1 (Fo > 4σ(Fo)) = 16.7%, wR2 = 51.2%, S = 1.85. The largest Fourier features were 1.03 and -0.81 e- A-3.

8.13. Synthetic Procedures and Characterization

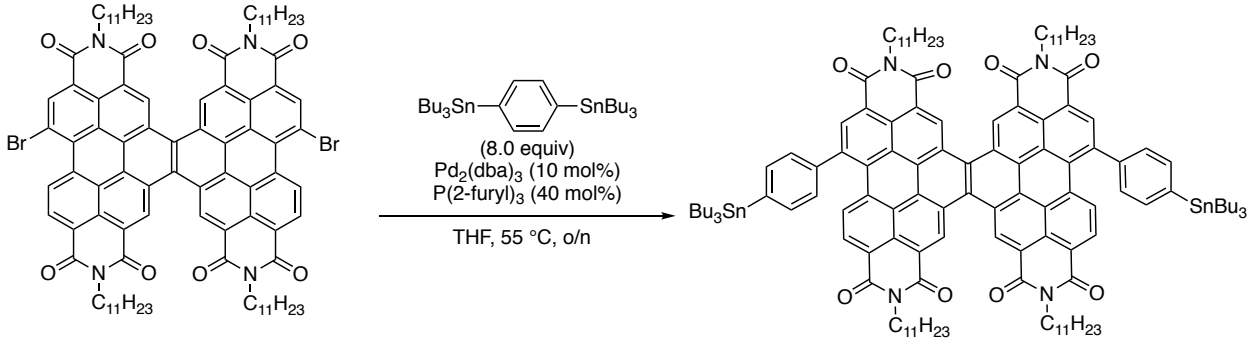

8.1a **8.1b**

Synthesis of Bis[4-(tributylstannyl)-phenyl]-hPDI$_2$-Cis (**8.1b**): Regiopure **8.1a** (1.00 equiv, 0.196 mmol, 0.308 g), 1,4-bis(tributylstannyl)benzene (8.00 equiv, 1.56 mmol, 0.895 mL), tri(2-furyl)phosphine (0.400 equiv, 0.0784 mmol, 0.0180 g) and THF (24 mL) were added to an oven-dried two-neck 100 mL round bottom flask equipped with a stir bar. The mixture was degassed for thirty minutes. While under N_2, tris(dibenzylideneacetone)dipalladium (0.100 equiv, 0.0196 mmol, 0.0180 g) was added. The mixture was further degassed for ten minutes before being placed in a 55 °C oil bath and allowed to stir overnight. The crude mixture was concentrated and purified by column chromatography using a gradient from 0% to 80% CH_2Cl_2/hexanes to yield **8.1b** as a

magenta solid (0.246 g, 0.115 mmol, 59% yield). **^{1}H NMR** (400 MHz, $CDCl_3$) δ 10.29 (s, br, 4H), 9.05 (s, br, 2H), 8.69 (d, J = 8.5 Hz, 2H), 8.60 (d,br, 2H), 7.78* (d, J = 7.2 Hz, 4H), 7.66 (d, J = 7.1 Hz, 4H), 5.31 (m, 4H), 2.34 (m, br, 8H), 1.95 (m, br, 8H), 1.69* (m, 12H), 1.45** (m, 12H), 1.32** (m, br, 48H), 1.23*,** (m, 12H), 1.00 (tr, 18H), 0.84 (m, br, 24H).**^{13}C NMR** (100 MHz, $CDCl_3$) δ 164.9, 163.9, 143.2, 142.7, 142.6, 138.4*, 135.4, 134.8, 134.2, 133.9, 133.3, 131.8, 130.0*, 128.0, 126.9, 126.8, 126.3, 126.2, 126.1, 126.0, 125.9, 125.5, 123.8, 123.5, 122.1, 121.5, 55.1, 55.0, 32.4, 31.8, 29.2*, 27.4*, 26.7, 22.6, 14.1, 14.1, 13.8, 9.8*. **IR** (cm^{-1}) 2957, 2924, 2859, 1703, 1661, 1593, 1323, 1264, 126. **HRMS** (APCI+) calculated m/z for $[C_{136}H_{164}N_4O_8Sn_2+Na]^+$ is 2172.0547, found 2172.0491. *Tin satellite peaks visible. ** Overlapping peaks in the ^{1}HNMR.

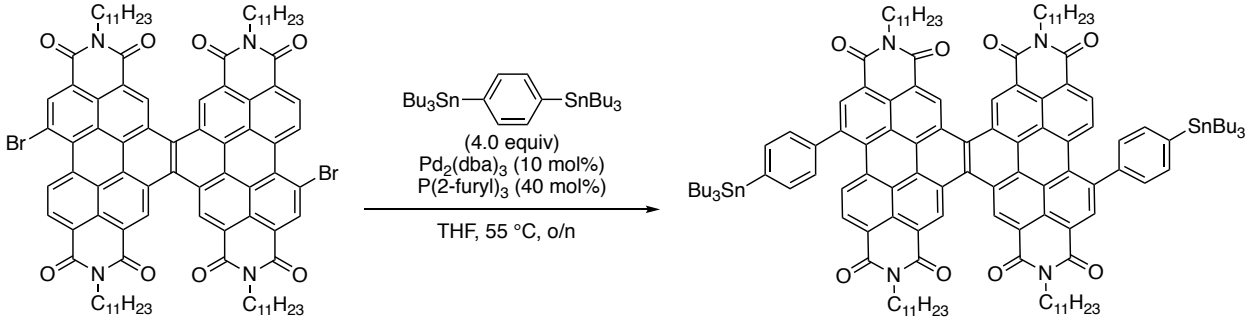

8.2a **8.2b**

Synthesis of Bis[4-(tributylstannyl)-phenyl]-hPDI$_2$-Cis (**8.2b**): Regiopure **8.2a** (1.00 equiv, 0.451 mmol, 0.710 g), 1,4-bis(tributylstannyl)benzene (4.00 equiv, 1.80 mmol, 1.03 mL), tri(2-furyl)phosphine (0.400 equiv, 0.180 mmol, 0.0419 g) and THF (45 mL) were added to an oven-dried two-neck 100 mL round bottom flask equipped with a stir bar. The mixture was degassed for thirty minutes. While under N_2, tris(dibenzylideneacetone)dipalladium (0.100 equiv, 0.0451 mmol, 0.0413 g) was added. The mixture was further degassed for ten minutes before being placed in a 55 °C oil bath and allowed to stir overnight. The crude mixture was concentrated and purified by column chromatography using a gradient from 0% to 80% hexanes to CH_2Cl_2 to yield **8.2b** as a magenta solid (0.657 g, 0.306 mmol, 68% yield). **^{1}H NMR** (400 MHz, $CDCl_3$) δ 10.30 (s, br,

4H), 9.05 (s, br, 2H), 8.69 (d, J = 8.5 Hz, 2H), 8.59 (d, br, 2H), 7.77* (d, J = 7.3 Hz, 4H), 7.66 (d, J = 7.2 Hz, 4H), 5.31 (m, 4H), 2.34 (m, br, 8H), 1.94 (m, br, 8H), 1.69* (m, 12H), 1.47 (m, 12H), 1.32 (m, br, 48H), 1.23* (m, 12H), 1.00 (tr, 18H), 0.84 (m, br, 24H). **^{13}C NMR** (100 MHz, $CDCl_3$) δ 164.9, 163.9, 143.2, 142.7, 142.5, 138.4*, 134.2, 133.9, 133.2, 131.8, 130.5, 130.0, 128.8, 128.0*, 126.9, 126.8, 126.7, 126.3, 126.3, 126.1, 126.0, 125.9, 125.5, 124.0, 123.4, 122.2, 121.5, 55.1, 55.0, 32.4, 31.8, 29.2*, 27.4*, 26.7, 22.6, 14.1, 14.1, 13.8, 9.8*. **IR** (cm^{-1}) 2955, 2924, 2855, 1701, 1661, 1597, 1322, 1268. **HRMS** (APCI+) calculated m/z for $[C_{136}H_{164}N_4O_8Sn_2+Na]^+$ is 2172.0542, found 2172.0491.*Tin satellite peaks visible.

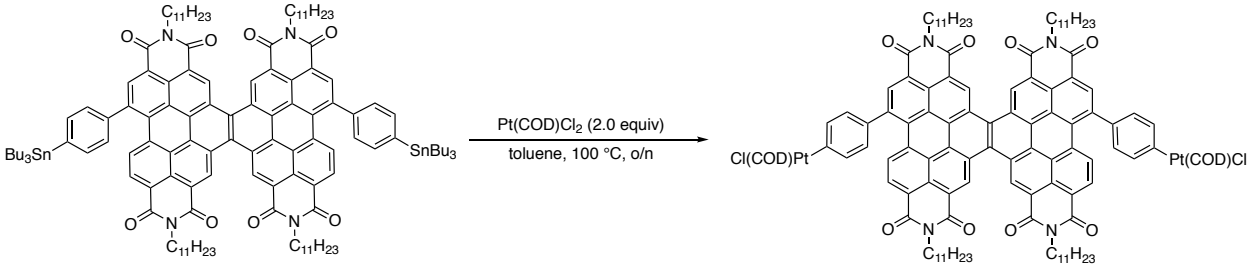

8.1b **8.1c**

Synthesis of Bis[4-(Pt(COD)Cl)-phenyl]-hPDI$_2$-cis (**8.1c**): **8.1b** (1.00 equiv, 0.0700 mmol, 0.150 g) was added to an oven-dried two-neck, 100 mL round bottom flask equipped with a stir bar. Dichloro(1,5-cyclooctadiene)platinum(II) (2.00 equiv, 0.140 mmol, 0.0522 g) was added to the flask with anhydrous toluene (7.00 mL). The mixture was degassed for thirty minutes and then placed in a 100 °C oil bath and allowed to stir overnight. The crude mixture was allowed to cool to room temperature and concentrated *in vacuo*. The crude mixture is recrystallized from methanol before being purified by column chromatography using a gradient from 0% to 100% CH_2Cl_2/hexanes to elute the desired product. The product is a purple solid (0.100 g, 0.0445 mmol, 64% yield). **^{1}H NMR** (400 MHz, $CDCl_3$) δ10.26 (s, br, 4H), 9.04 (s, br, 2H), 8.68 (d, J = 8.5 Hz, 2H), 8.59 (d, br, 2H), 7.57 (d, J = 7.8 Hz, 4H), 7.44 (d, J = 7.6 Hz, 4H), 5.95 (s, 4H), 5.31 (m, br, 4H), 4.85 (s, 4H), 2.82 (m, br, 4H), 2.65 (m, br, 4H), 2.51 (m, br, 8H), 2.33 (m, br, 8H), 1.94 (m,

br, 8H), 1.31 (m, br, 48H), 0.84 (m, br, 24H). **^{13}C NMR** (100 MHz, $CDCl_3$) δ 165.0, 163.9, 145.7, 142.9, 139.0, 136.0, 134.5, 133.9, 133.2, 131.7, 129.9, 128.5, 128.3, 126.8, 126.8, 126.2, 126.1, 126.1, 126.0, 125.9, 125.5, 123.9, 123.4, 122.0, 121.4, 116.0, 87.9, 55.0, 54.9, 32.4, 32.3, 31.8, 28.1, 26.7, 22.6, 14.1. **IR** (cm^{-1}) 2953, 2924, 2858, 1701, 1660, 1595, 1324, 1246. **HRMS** (ESI+) calculated m/z for $[C_{122}H_{134}Cl_2N_4O_8Pt_2+Na]^+$ is 2265.8772, found 2265.8774.

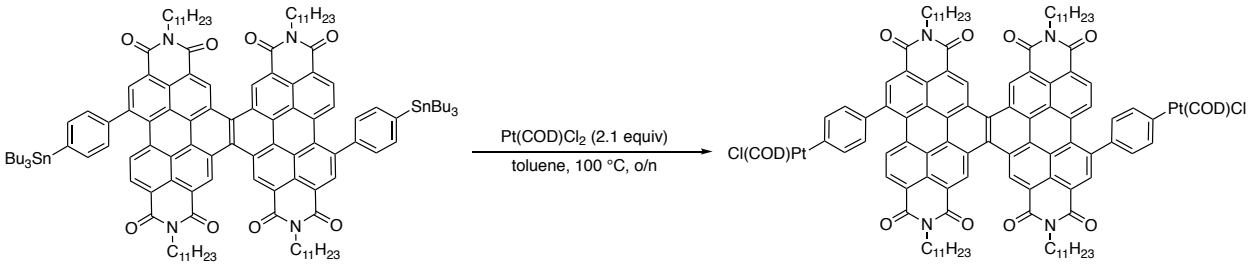

8.2b **8.2c**

Synthesis of Bis[4-(Pt(COD)Cl)-phenyl]-hPDI$_2$-trans (**8.2c**): **8.2b** (1.00 equiv, 0.0758 mmol, 0.163 g) was added to an oven-dried two-neck, 100 mL round bottom flask equipped with a stir bar. Dichloro(1,5-cyclooctadiene)platinum(II) (2.10 equiv, 0.159 mmol, 0.0596 g) was added to the flask with anhydrous toluene (8.00 mL). The mixture was degassed for thirty minutes and then placed in a 100 °C oil bath and allowed to stir overnight. The crude mixture was allowed to cool to room temperature and concentrated *in vacuo*. The crude mixture is recrystallized from methanol before being purified by column chromatography using a gradient from 0% to 100% CH_2Cl_2/hexanes to elute the desired product. The product is a purple solid (0.130 g, 0.0579 mmol, 76% yield). **^{1}H NMR** (400 MHz, $CDCl_3$) δ 10.27 (s, br, 4H), 9.04 (s, br, 2H), 8.68 (d, J = 8.6 Hz, 2H), 8.58 (d, br, 2H), 7.57 (d, J = 7.7 Hz, 4H), 7.44 (d, J = 7.7 Hz, 4H), 5.95 (s, 4H), 5.30 (m, br, 4H), 4.84 (s, 4H), 2.82 (m, br, 4H), 2.65 (m, br, 4H), 2.51 (m, br, 8H), 2.33 (m, br, 8H), 1.94 (m, br, 8H), 1.31 (m, br, 48H), 0.85 (m, br, 24H). **^{13}C NMR** (100 MHz, $CDCl_3$) δ 165.0, 164.0, 145.7,

142.9, 139.0, 136.0, 134.5, 134.0*, 133.0*, 131.7, 129.9, 129.1, 128.3, 126.8, 126.8, 126.7, 126.3, 126.2, 126.0, 125.9, 125.9, 125.5, 124-121*, 116.0, 87.9, 55.0, 54.9, 32.4, 32.3, 31.8, 28.1, 26.7, 22.6, 14.1. **IR** (cm^{-1}) 2970, 2954, 2928, 2924, 2853, 1739, 1701, 1660, 1595, 1322, 1232. **HRMS** (ESI+) calculated m/z for $[C_{122}H_{134}Cl_2N_4O_8Pt_2+Na]^+$ is 2265.8772, found 2265.8772. *Between 134-133 ppm and 124-121 ppm, there are broad signals that likely represent the quaternary carbons of the aromatic core of the dimer. Used the corresponding cis isomer (*cis*-**DBDB**) as a guide.

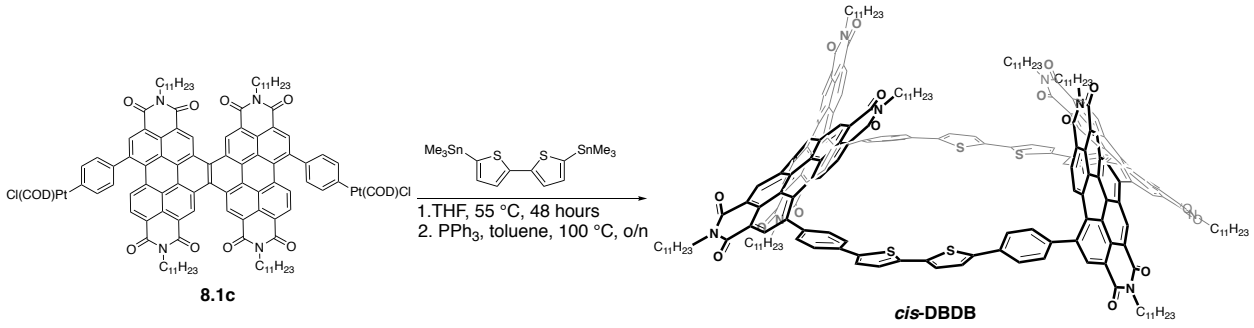

8.1c ***cis*-DBDB**

Synthesis of *cis*-**DBDB**: Bis[4-(Pt(COD)Cl)-phenyl]-hPDI$_2$-cis (**8.1c**) (1.00 equiv, 0.0771 mmol, 0.172 g), commercially available 5,5′-bis(trimethylstannyl)-2,2′-bithiophene (1.00 equivalent, 0.0771 mmol, 0.0379 grams) and THF (26.0 mL) were added to an oven-dried 50 mL round bottom flask. The mixture was degassed for thirty minutes, and stirred in a 55 °C oil bath for 48 h. The crude mixture was concentrated and triphenylphosphine (20.0 equiv, 1.54 mmol, 0.450 g) was added to the flask with toluene (26.0 mL). The mixture was degassed for ten minutes, then stirred for overnight in a 100 °C oil bath. The crude mixture was first purified by column chromatography (24 g Redisep Rf Silica) using a gradient from 0% to 100% CH_2Cl_2/hexanes at 35 mL/min. Fractions that contained *cis*-**DBDB** were collected and further purified on by preparative TLC using 70%:30% CH_2Cl_2/hexanes. The solids were re-precipitated from methanol, followed by hexanes. The product is a dark purple solid (0.0150 g, 0.00448 mmol, 12% yield). **^{1}H NMR** (500 MHz, 400K, $C_2D_2Cl_4$) δ 10.41 (s, 4H), 10.25 (s, 4H), 9.05 (s, 4H), 8.85 (d, J = 8.4 Hz, 4H), 8.67 (d, J = 8.3 Hz, 4H), 7.73 (d, J = 8.1 Hz, 8H), 7.60 (d, J = 7.8 Hz, 8H), 7.49 (d, J = 4.0 Hz, 4H),

7.32 (d, J = 4.1 Hz, 4H), 5.37 (m, 4H), 5.23 (m, 4H), 2.41 (m, br, 8H), 2.28 (m, br, 8H), 2.05 (m, br, 8H), 1.94 (m, br, 8H), 1.33* (m, br, 96H), 0.93 (tr, 24H), 0.80 (tr, 24H). **^{13}C NMR** (100 MHz, 400K, $C_2D_2Cl_4$) δ□164.4, 164.3, 164.1, 142.7, 141.9, 141.7, 137.8, 134.4, 134.3, 133.5, 133.0, 132.7, 132.6, 130.5, 130.3, 128.9, 127.4, 127.2, 127.2, 127.1, 127.0, 126.6, 126.3, 126.2, 126.0, 125.9, 125.6, 125.0, 124.1, 124.0, 123.7, 123.4, 122.4, 122.4, 55.6, 55.3, 32.8, 32.6, 31.8, 31.6, 26.7, 26.6, 22.4, 22.3, 13.8, 13.7. **IR** (cm^{-1}) 2957, 2924, 2855, 1702, 1660, 1595, 1321. **HRMS** (MALDI-) calculated m/z for $[C_{228}H_{228}N_8O_{16}S_4]^-$ is 3461.6156, found 3461.6205. *Integration is higher due to overlapping peak with both H_20, and/or a small amount of grease.

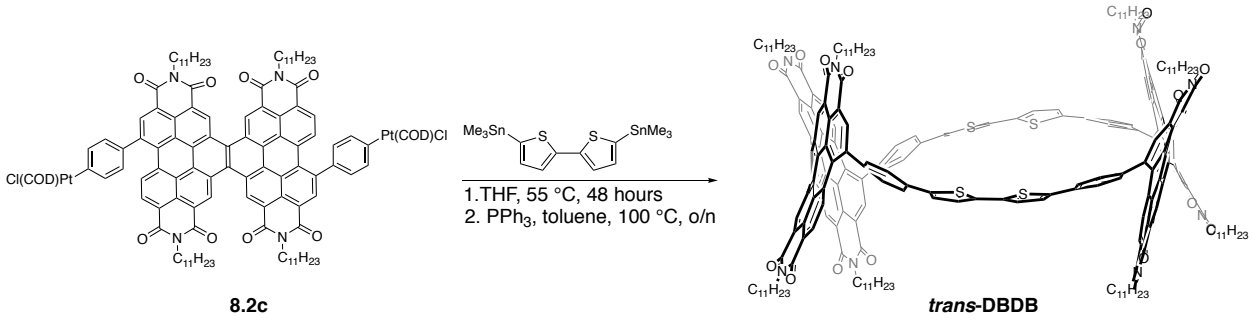

8.2c ***trans*-DBDB**

Synthesis of *trans*-**DBDB**: Bis[4-(Pt(COD)Cl)-phenyl]-hPDI$_2$-trans (**8.2c**) (1.00 equiv, 0.0922 mmol, 0.207 g), commercially available 5,5′-bis(trimethylstannyl)-2,2′-bithiophene (1.00 equivalent, 0.0922 mmol, 0.0450 grams) and THF (31.0 mL) were added to an oven-dried 150. mL round bottom flask. The mixture was degassed for thirty minutes and, then, stirred in a 55 °C oil bath for 48 h. The crude mixture was concentrated and triphenylphosphine (20.0 equiv, 1.84 mmol, 0.538 g) was added to the flask with toluene (31.0 mL). The mixture was degassed for ten minutes, then stirred for overnight in a 100 °C oil bath. The crude mixture was first purified by column chromatography (24 g Redisep Rf Silica) using a gradient from 0% to 100% CH_2Cl_2/hexanes at 35 mL/min. Fractions that contained *trans*-**DBDB** were collected and further purified on by preparative TLC using 70%:30% CH_2Cl_2/hexanes. To remove a small impurity, the product mixture was further purified using a COSMOSIL Buckyprep column (20 mm I.D. x 250

mm, 5 μm), using an isocratic method of 50% methylene chloride:50% hexanes. The solids were re-precipitated from methanol, followed by hexanes. The product is a dark purple solid (0.0100 g, 0.00289 mmol, 6% yield). **^{1}H NMR** (400 MHz, 400 K, $C_2D_2Cl_4$) δ [*major stereoisomer*] 10.25 (s, 4H), 10.22 (s, 4H), 9.10 (s, 4H), 8.97 (d, J = 8.4 Hz, 4H), 8.67 (d, J = 8.4 Hz, 4H), 7.75 (d, J = 8.2 Hz, 8H), 7.61 (d, J = 8.1 Hz, 8H), 7.50 (d, J = 4.0 Hz, 4H), 7.32 (d, J = 3.9 Hz, 4H), 5.39 (m, 4H), 5.20 (m, 4H), 2.45 (m, br, 8H), 2.24 (m, br, 8H), 2.05 (m, br, 8H), 1.96 (m, br, 8H), 1.37* (m, br, 96H), 0.94* (tr, br, 24H), 0.83 (tr, br, 24H). [*distinguishable minor stereoisomer peaks*] 9.06, 8.71. **^{13}C NMR** (100 MHz, 400K, $C_2D_2Cl_4$) δ 164.4, 164.1, 164.0, 142.6, 142.0, 141.3, 137.4, 134.4, 134.2, 133.5, 132.7, 132.6, 132.5, 130.6, 130.4, 130.4, 130.4, 130.1, 128.9, 127.2, 127.1, 127.1, 127.0, 126.8, 126.5, 126.1, 125.2, 125.1, 124.9, 124.5, 124.2, 123.4, 122.8, 122.4, 122.1, 55.6, 55.3, 33.0, 32.8, 32.6, 32.4, 31.8, 31.7, 31.7, 26.7, 26.7, 26.7, 22.5, 22.4, 22.3, 13.9, 13.8, 13.7. **IR** (cm^{-1}) 2956, 2924, 2854, 1703, 1661, 1594, 1320. **HRMS** (MALDI-) calculated m/z for $[C_{228}H_{228}N_8O_{16}S_4]^-$ is 3461.61516, found 3461.6384. *Integration is higher due to overlapping peak with both H_20, and/or a small amount of grease.

8.14. NMR Spectra of Compounds

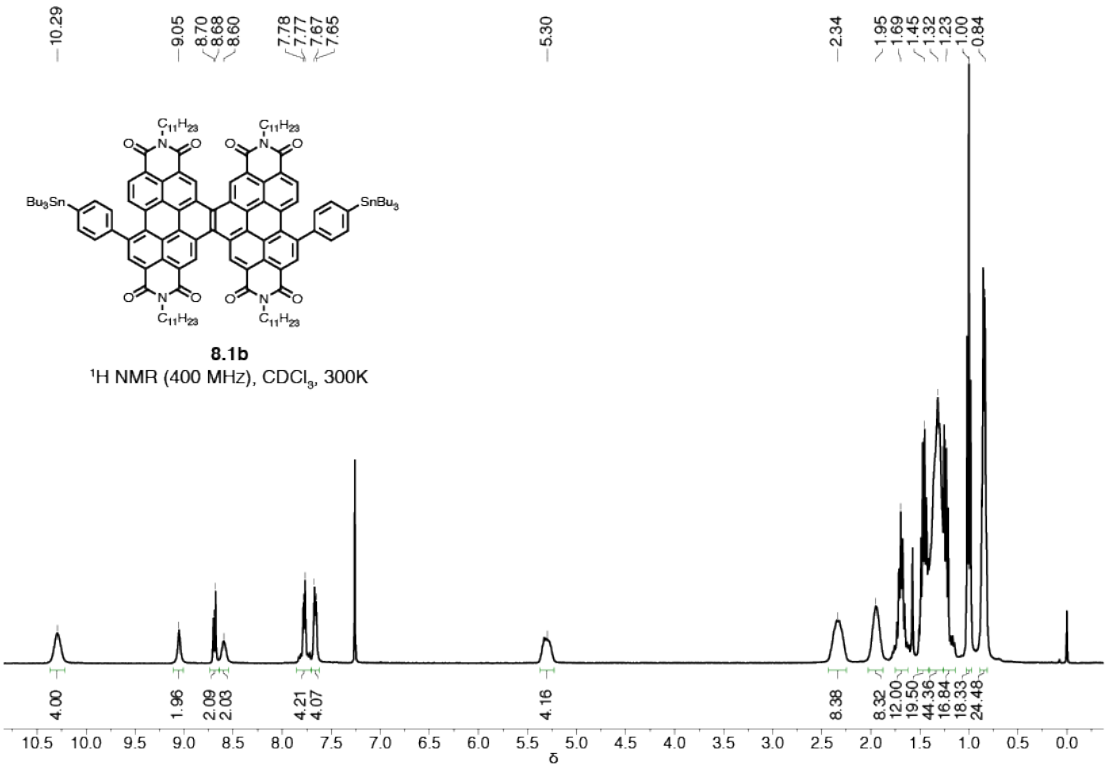

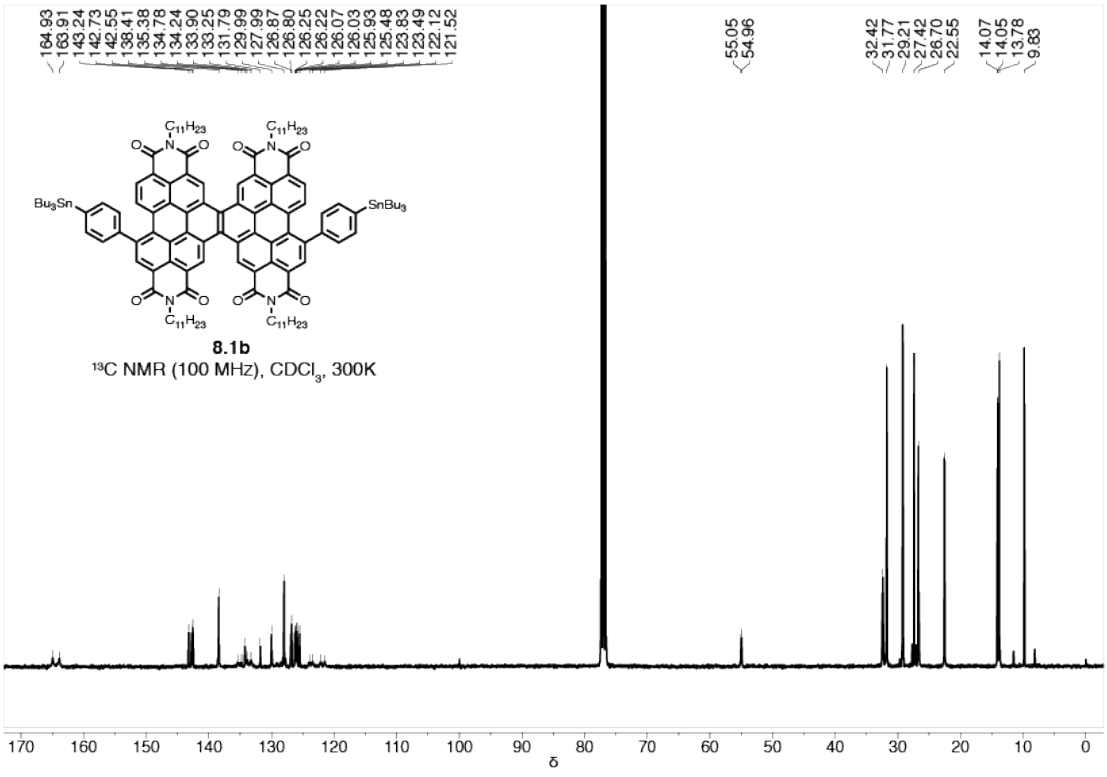

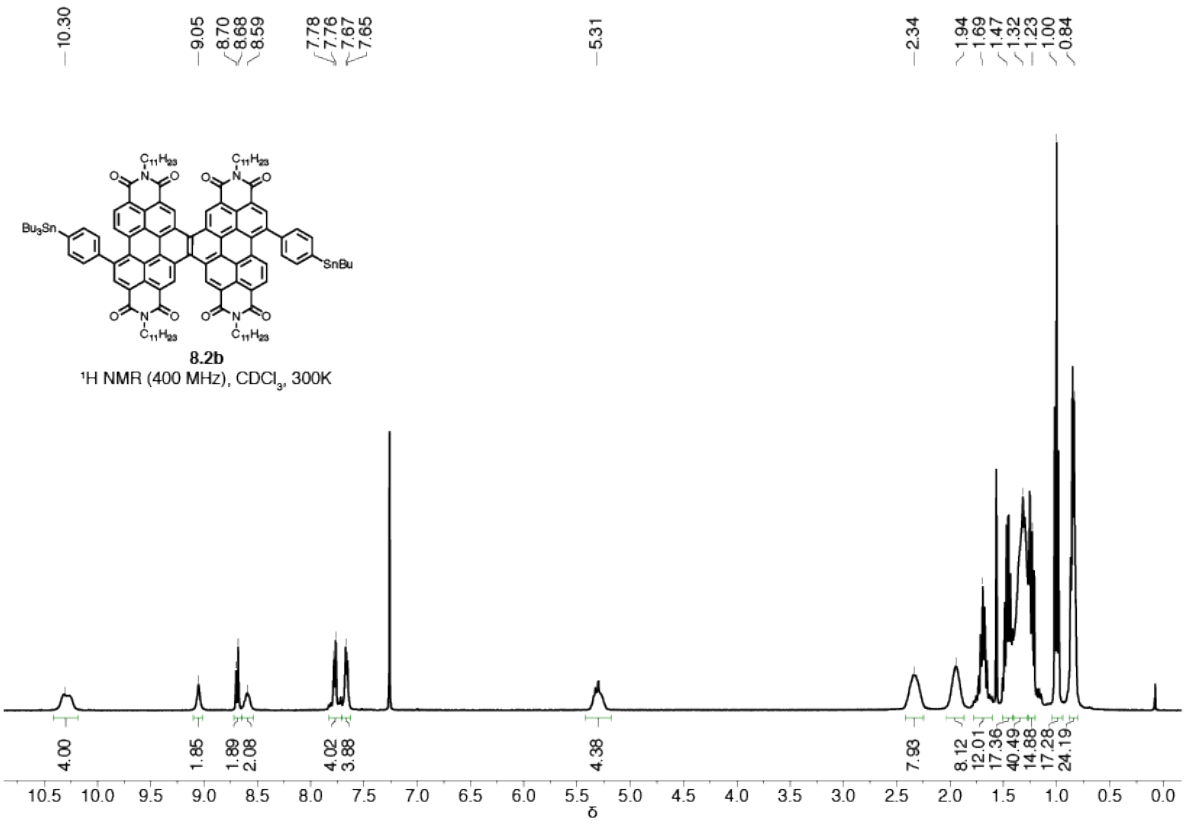
10.30
9.05
8.70
8.68
8.59
7.78
7.76
7.67
7.65
5.31
2.34
1.94
1.69
1.47
1.32
1.23
1.00
0.84
Bu3Sn
SnBu
8.2b
1H NMR (400 MHz), CDCl3, 300K
4.00
1.85
1.89
2.08
4.02
3.88
4.38
7.93
8.12
12.01
17.36
40.49
14.88
17.28
24.19
δ

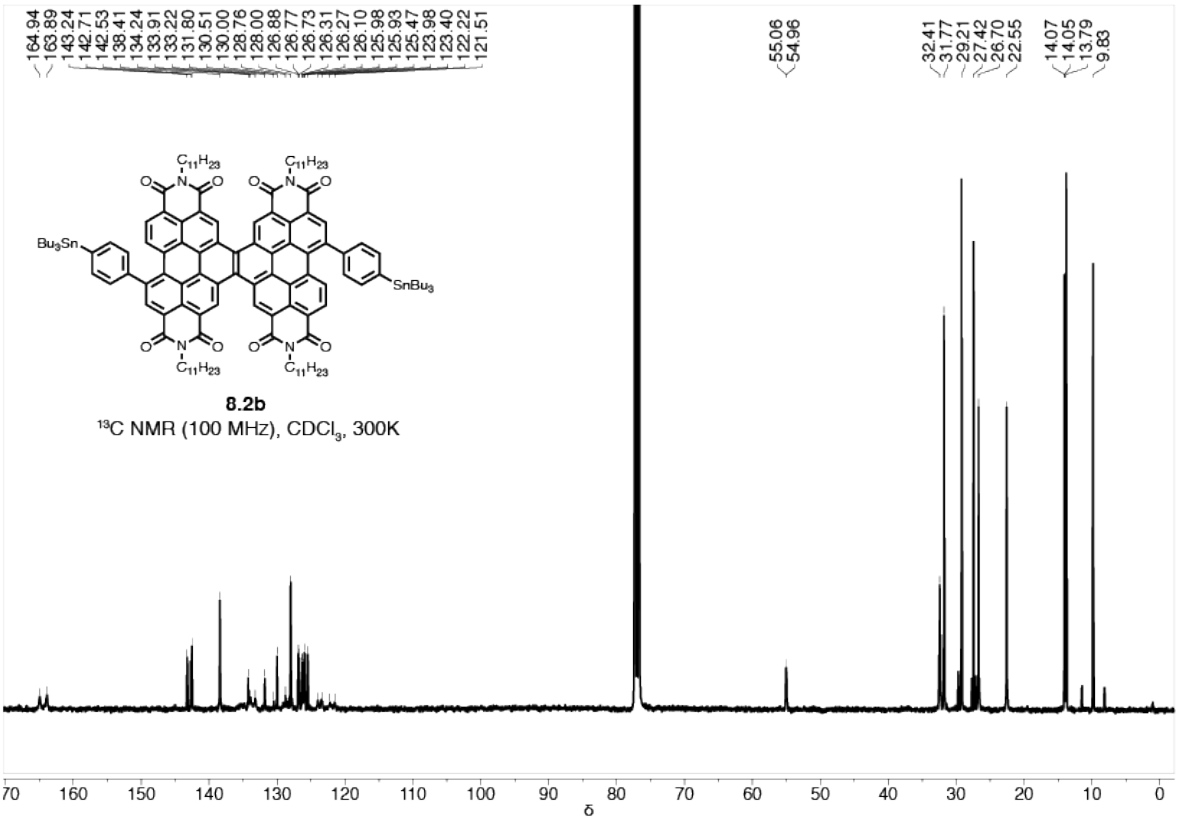
164.94
163.89
143.24
142.71
142.53
138.41
134.24
133.91
133.22
131.80
130.51
130.00
128.76
128.00
126.88
126.77
126.73
126.31
126.27
126.10
125.98
125.93
125.47
123.98
123.40
122.22
121.51
55.06
54.96
32.41
31.77
29.21
27.42
26.70
22.55
14.07
14.05
13.79
9.83
Bu3Sn
SnBu3
8.2b
13C NMR (100 MHz), CDCl3, 300K
δ

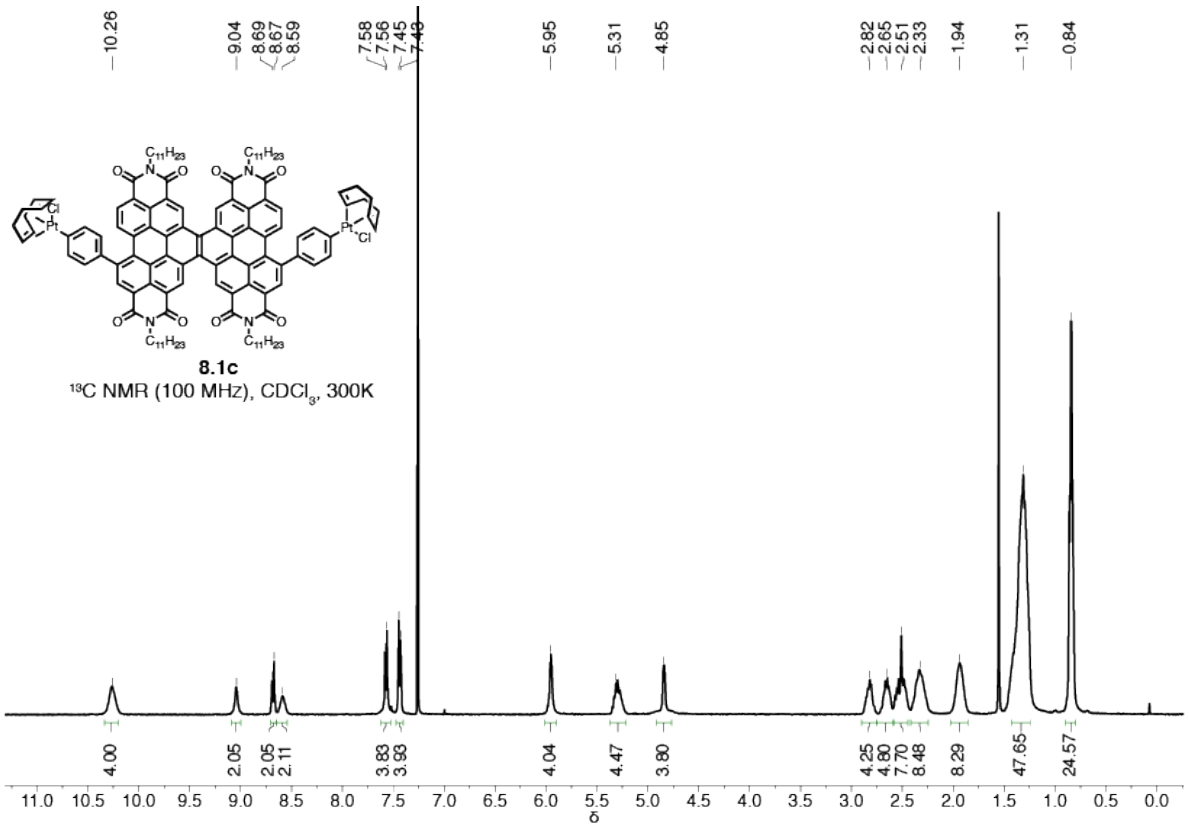

8.1c

^{13}C NMR (100 MHz), $CDCl_3$, 300K

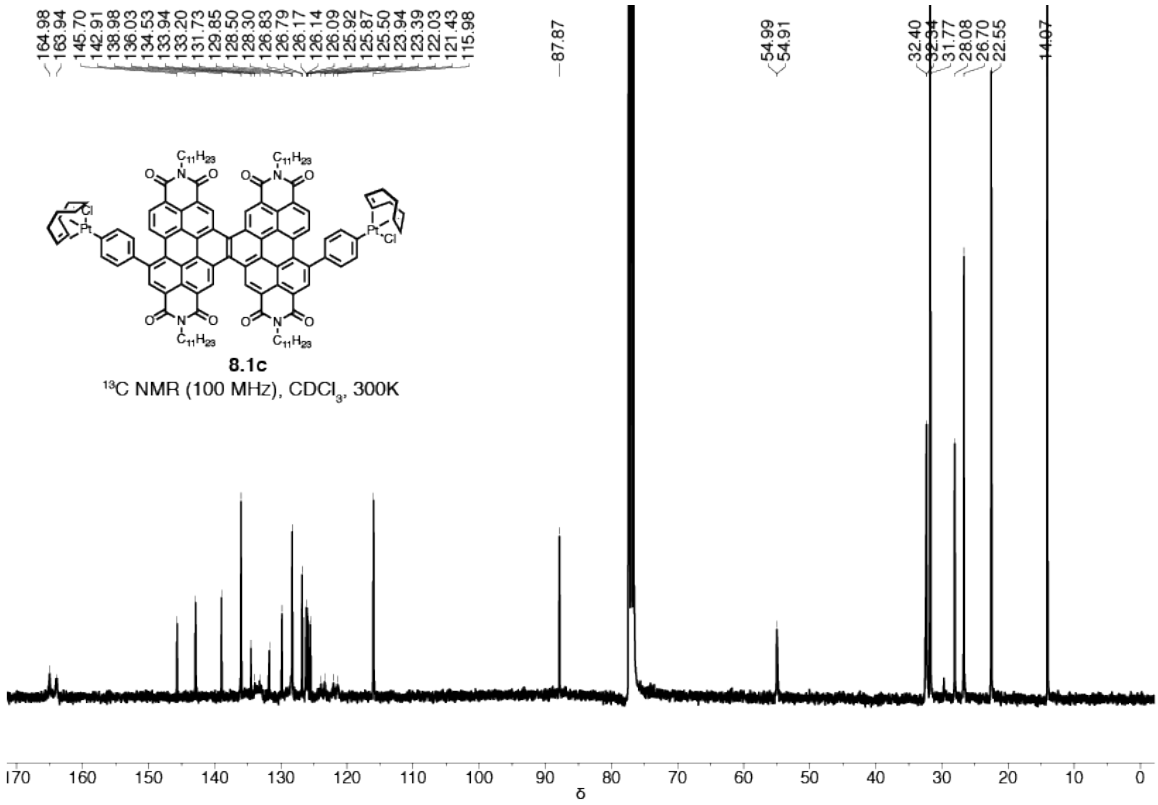

8.1c

^{13}C NMR (100 MHz), $CDCl_3$, 300K

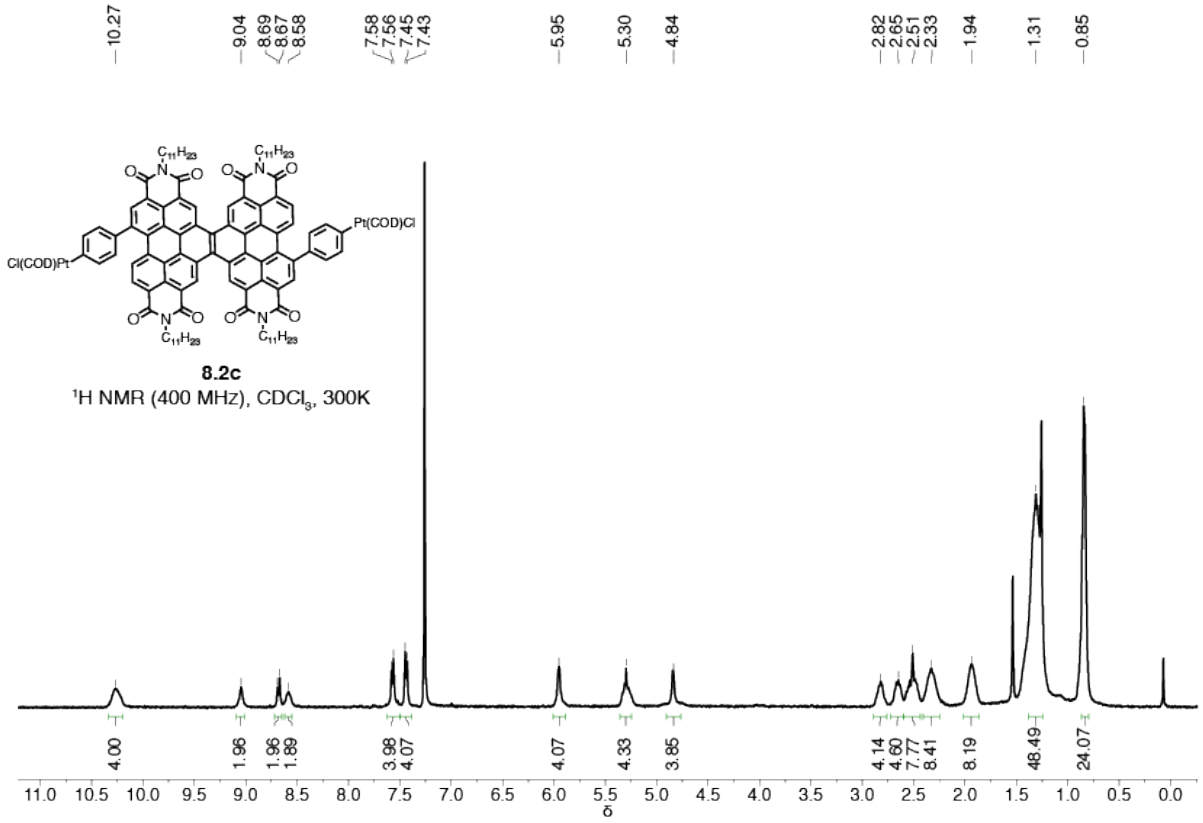
10.27
9.04
8.69
8.67
8.58
7.58
7.56
7.45
7.43
5.95
5.30
4.84
2.82
2.65
2.51
2.33
1.94
1.31
0.85
Cl(COD)Pt
Pt(COD)Cl
8.2c
1H NMR (400 MHz), CDCl3, 300K
4.00
1.96
1.96
1.89
3.98
4.07
4.07
4.33
3.85
4.14
4.60
7.77
8.41
8.19
48.49
24.07
δ

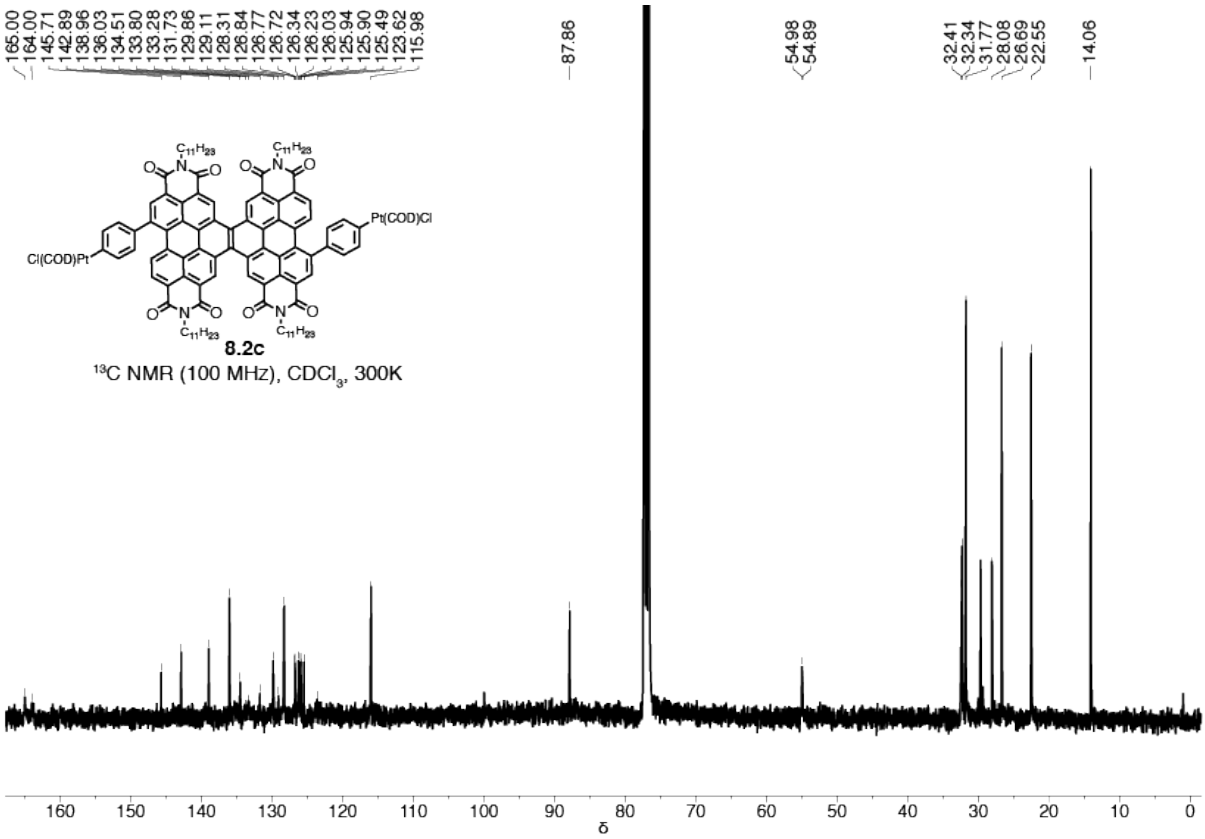
165.00
164.00
145.71
142.89
138.96
136.03
134.51
133.80
133.28
131.73
129.86
129.11
128.31
126.84
126.77
126.72
126.34
126.23
126.03
125.94
125.90
125.49
123.62
115.98
87.86
54.98
54.89
32.41
32.34
31.77
28.08
26.69
22.55
14.06
Cl(COD)Pt
Pt(COD)Cl
8.2c
13C NMR (100 MHz), CDCl3, 300K
δ

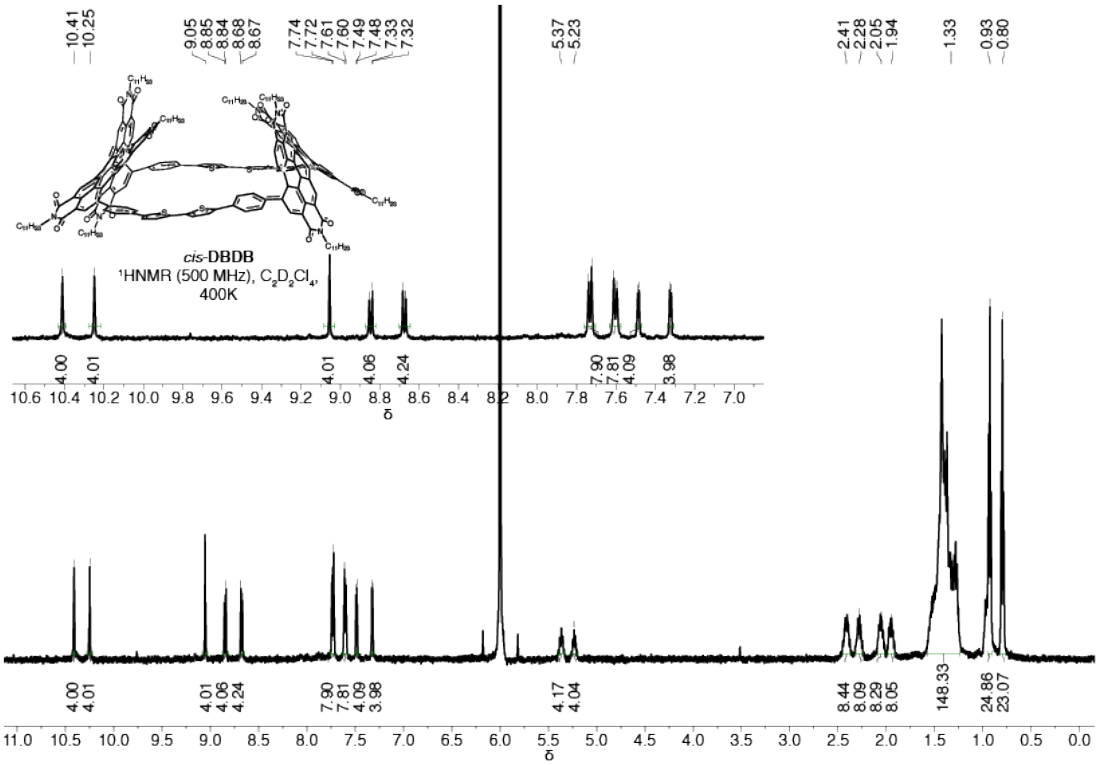
cis-DBDB
¹HNMR (500 MHz), C2D2Cl4, 400K
δ

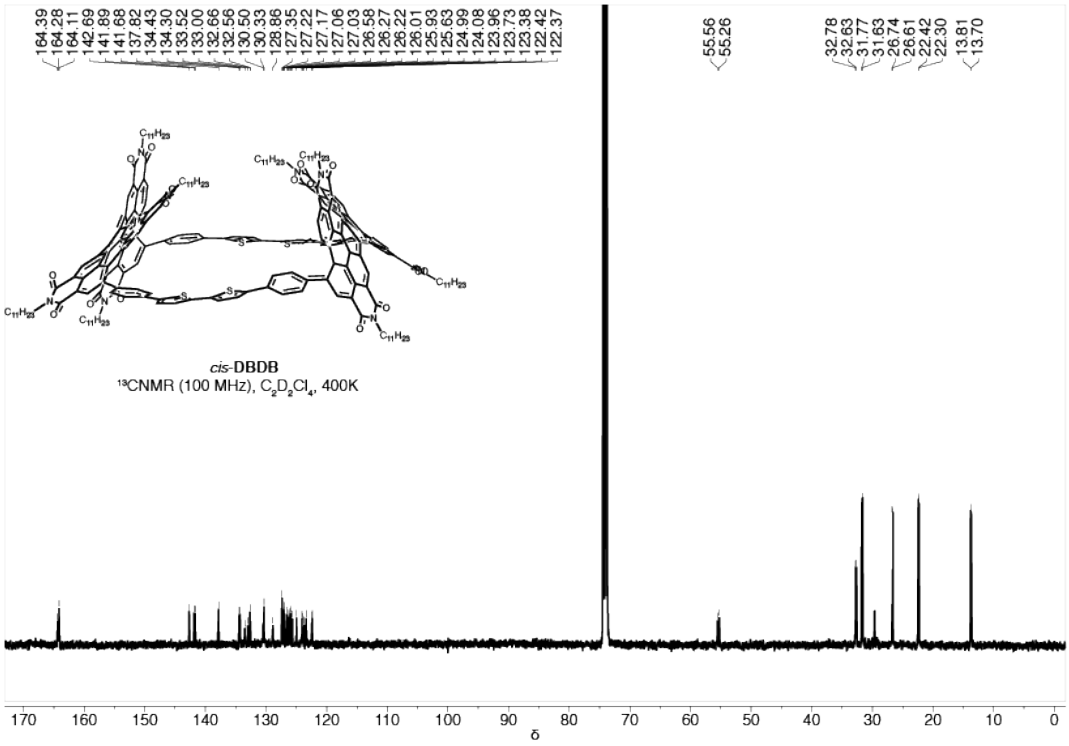
cis-DBDB
¹³CNMR (100 MHz), C2D2Cl4, 400K
δ

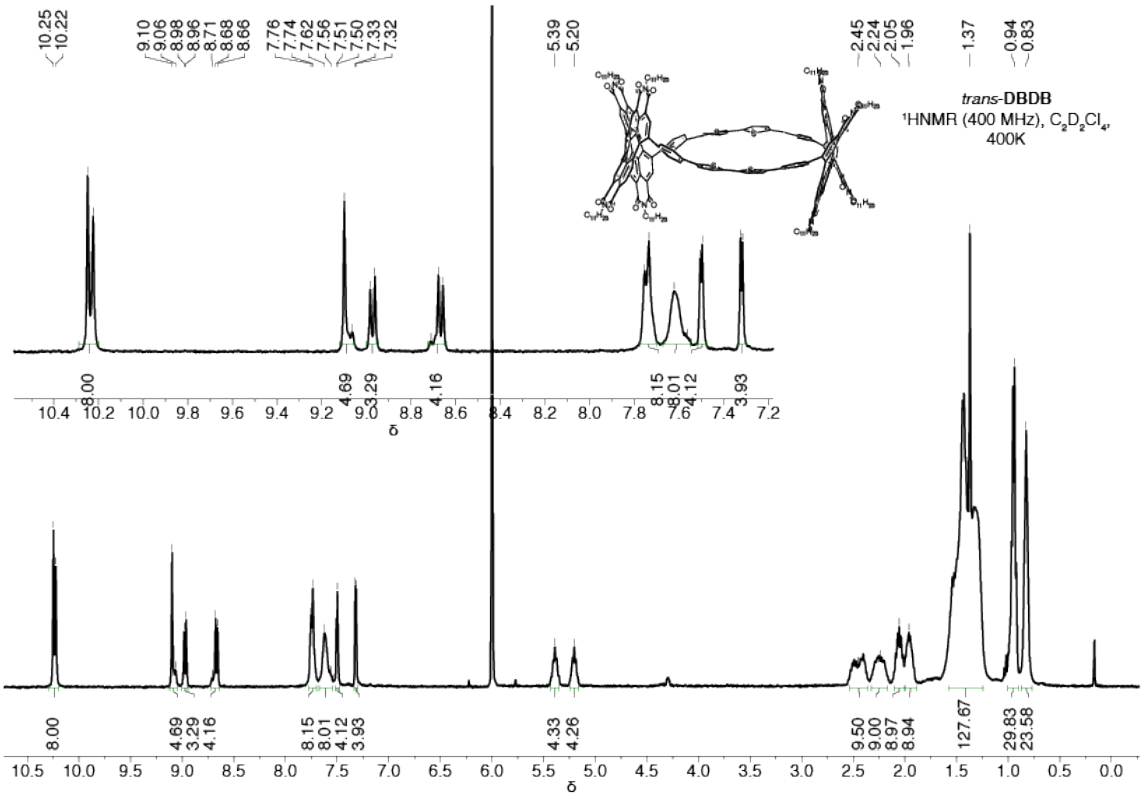
10.25
10.22
9.10
9.06
8.98
8.96
8.71
8.68
8.66
7.76
7.74
7.62
7.56
7.51
7.50
7.33
7.32
5.39
5.20
2.45
2.24
2.05
1.96
1.37
0.94
0.83
trans-DBDB
¹HNMR (400 MHz), C2D2Cl4,
400K
8.00
4.69
3.29
4.16
8.15
8.01
4.12
3.93
4.33
4.26
9.50
9.00
8.97
8.94
127.67
29.83
23.58
δ

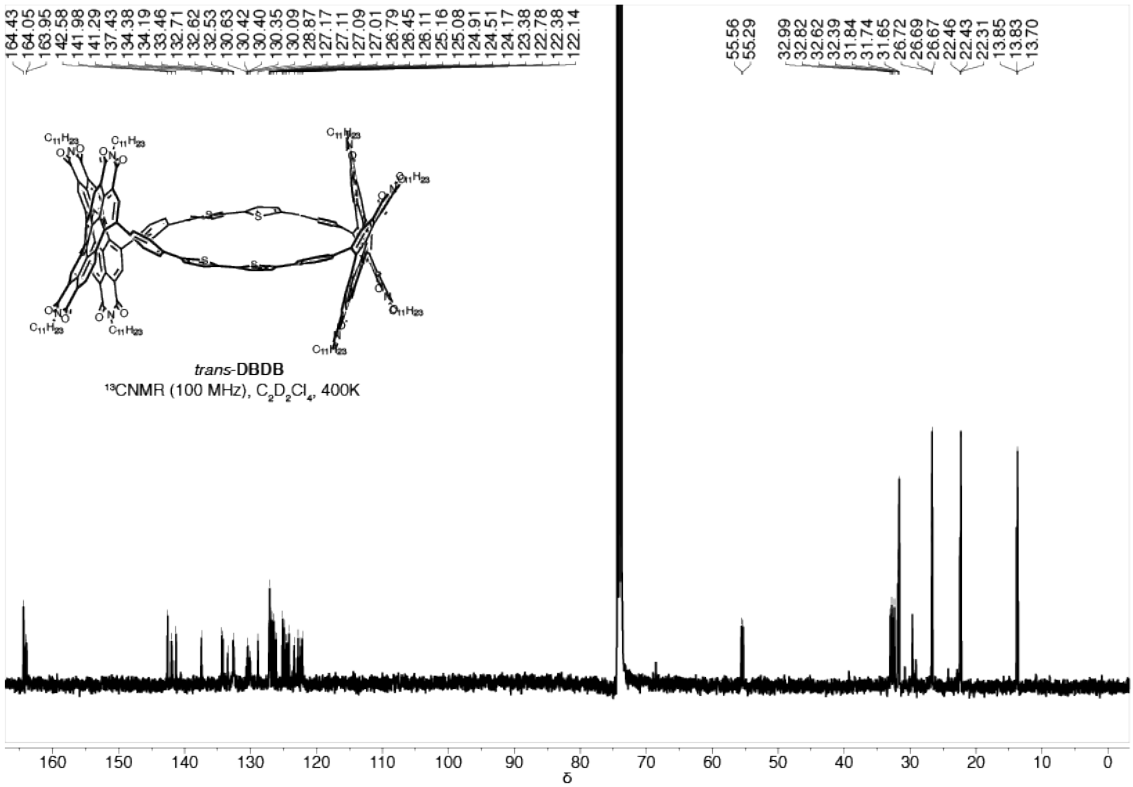
164.43
164.05
163.95
142.58
141.98
141.29
137.43
134.38
134.19
133.46
132.71
132.62
132.53
130.63
130.42
130.40
130.35
130.09
128.87
127.17
127.11
127.09
127.01
126.79
126.45
126.11
125.16
125.08
124.91
124.51
124.17
123.38
122.78
122.38
122.14
55.56
55.29
32.99
32.82
32.62
32.39
31.84
31.74
31.65
26.72
26.69
26.67
22.46
22.43
22.31
13.85
13.83
13.70
trans-DBDB
¹³CNMR (100 MHz), C2D2Cl4, 400K
δ

8.15. DFT Output

All quantum chemical calculations were performed using Jaguar, version 8.3, Schrodinger, Inc., New York, NY, 2013. (See A. D. Bochevarov, E. Harder, T. F. Hughes, J. R. Greenwood, D. A. Braden, D. M. Philipp, D. Rinaldo, M. D. Halls, J. Zhang, R. A. Friesner, "Jaguar: A High Performance Quantum Chemistry Software Program with Strengths in Life and Materials Sciences", Int. J. Quantum Chem., 2013, 113(18), 2110-2142). All geometries were optimized using the B3LYP functional and the 6-31G basis set. The geometry optimizations can be found in reference 1.[1] I provide the results of the homodesmotic reaction employed in order to calculate strain within the two $hPDI_2$ macrocycles.

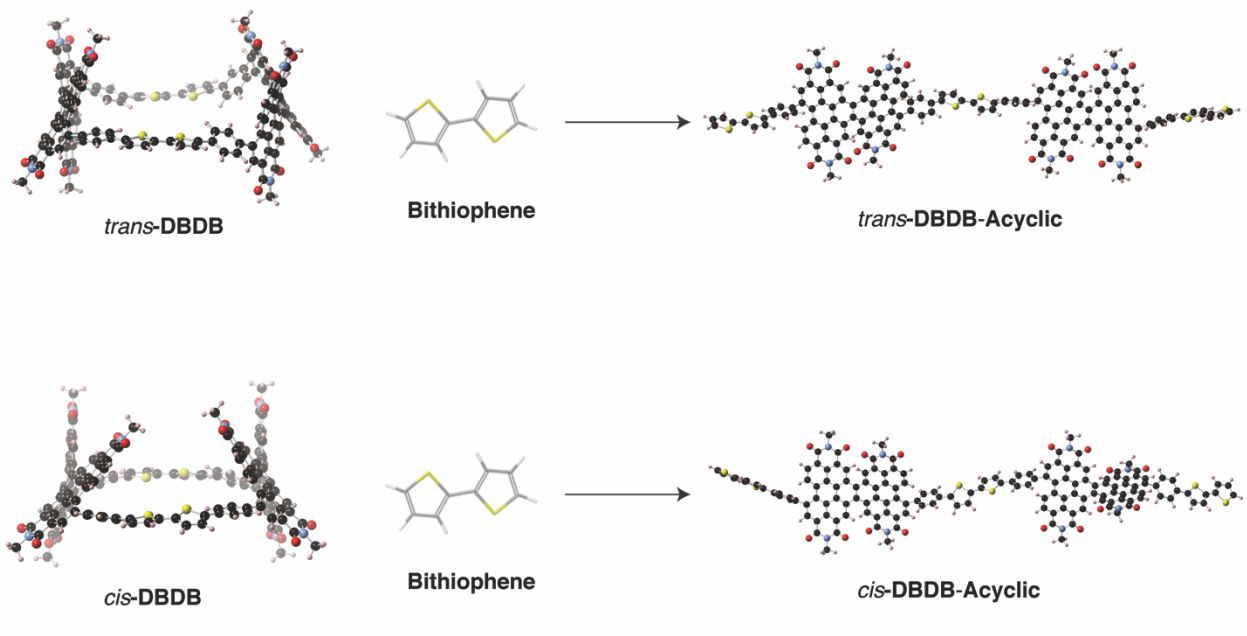

Table 8.3. Homodesmotic Calculations for Strain

Compound	Total energy (hartree)	Strain energy (hartrees)	Strain energy (kcal/mol)
trans-**DBDB**	-8915.8024	0.0296	18.575
trans-**DBDB**-Acyclic	-10020.6588	-	-
Bithiophene	-1104.8268	-	-
cis-**DBDB**	-8915.8154	0.0151	9.476
cis-**DBDB**-Acyclic	-10020.6573	-	-

Table 8.3: Calculated enthalpy from DFT using B3LYP functional and the 6-31G basis set

8.16. References

1. Ball, M. L. *et al.* Influence of Molecular Conformation on Electron Transport in Giant, Conjugated Macrocycles. *J. Am. Chem. Soc.* **140**, 10135–10139 (2018).
2. Krömer, J. *et al.* Synthesis of the First Fully α-Conjugated Macrocyclic Oligothiophenes: Cyclo[n]thiophenes with Tunable Cavities in the Nanometer Regime. *Angew. Chem. Int. Ed.* **39**, 3481–3486 (2000).
3. Nakao, K. *et al.* Giant Macrocycles Composed of Thiophene, Acetylene, and Ethylene Building Blocks. *J. Am. Chem. Soc.* **128**, 16740–16747 (2006).
4. Ishii, Y. *et al.* Size-selective synthesis of 9 - 11 and 13 cycloparaphenylenes. *Chem. Sci.* **3**, 2340–2345 (2012).
5. Hitosugi, S. *et al*. Bottom-up Synthesis and Thread-in-Bead Structures of Finite (n,0)-Zigzag Single-Wall Carbon Nanotubes. *J. Am. Chem. Soc.* **134**, 12442–12445 (2012).
6. Omachi, H. *et al*. Synthesis of Cycloparaphenylenes and Related Carbon Nanorings: A Step toward the Controlled Synthesis of Carbon Nanotubes. *Acc. Chem. Res.* **45**, 1378–1389 (2012).
7. Kayahara, E. *et al*. Selective Synthesis and Crystal Structure of [10]Cycloparaphenylene. *Org. Lett.* **14**, 3284–3287 (2012).
8. Hitosugi, S. *et al*. Atropisomerism in a Belt-Persistent Nanohoop Molecule: Rotational Restriction Forced by Macrocyclic Ring Strain. *Chem. Asian J.* **7**, 1550–1552 (2012).
9. Kayahara, E. *et al*. Synthesis and Characterization of [5]Cycloparaphenylene. *J. Am. Chem. Soc.* **136**, 2284–2287 (2014).
10. Yamago, S. *et al*. Organoplatinum-Mediated Synthesis of Cyclic pi-Conjugated Molecules: Towards a New Era of Three-Dimensional Aromatic Compounds. *Chem. Rec.* **14**, 84–100 (2014).
11. Evans, P. J. *et al*. Efficient room-temperature synthesis of a highly strained carbon nanohoop fragment of buckminsterfullerene. *Nat. Chem.* **6**, 404–408 (2014).
12. Ball, M. *et al.* Chiral Conjugated Corrals. *J. Am. Chem. Soc.* **137**, 9982–9987 (2015).
13. Chang, S.-W. *et al*. A donor-acceptor conjugated block copolymer of poly(arylenevinylene)s by ring-opening metathesis polymerization. *Chem. Commun.* **51**, 9113–9116 (2015).
14. Jasti, R. *et al*. Synthesis, Characterization, and Theory of 9 -, 12 -, and 18 Cycloparaphenylene: Carbon Nanohoop Structures. *J. Am. Chem. Soc.* **130**, 17646-17647 (2008).
15. Ito, H. *et al*. Thiophene-Based, Radial pi-Conjugation: Synthesis, Structure, and Photophysical Properties of Cyclo-1,4-phenylene-2 ',5 '-thienylenes. *Angew. Chem. Int. Ed.* **54**, 159–163 (2015).
16. Chen, Q. *et al.* Strain-Induced Stereoselective Formation of Blue-Emitting Cyclostilbenes. *J. Am. Chem. Soc.* **137**, 12282–12288 (2015).
17. Jiang, H.-W. *et al.* Cyclic 2,12-Porphyrinylene Nanorings as a Porphyrin Analogue of

Cycloparaphenylenes. *J. Am. Chem. Soc.* **137**, 2219–2222 (2015).

18. Darzi, E. R. *et al.* Synthesis, Properties, and Design Principles of Donor–Acceptor Nanohoops. *ACS Cent. Sci.* **1**, 335–342 (2015).
19. Asai, K. *et al*. A Cyclic Octithiophene Containing B,B'-linkages. *Chem. Commun.* **51**, 6096 (2015).
20. Kuwabara, T. *et al*. Curved Oligophenylenes as Donors in Shape-Persistent Donor–Acceptor Macrocycles with Solvatofluorochromic Properties. *Angew. Chem. Int. Ed.* **54**, 9646–9649 (2015).
21. Van Raden, J. M. *et al*. Synthesis and characterization of a highly strained donor-acceptor nanohoop. *Org. Biomol. Chem.* **14**, 5721 (2016).
22. Zhang, F. *et al*. Giant Cyclo n thiophenes with Extended pi Conjugation. *Angew. Chem. Int. Ed.* **48**, 6632–6635 (2009).
23. Omachi, H. *et al*. A Modular and Size-Selective Synthesis of [n]Cycloparaphenylenes: A Step toward the Selective Synthesis of n, n Single-Walled Carbon Nanotubes. *Angew. Chem. Int. Ed.* **49**, 10202–10205 (2010).
24. Iwamoto, T. *et al*. Selective and Random Syntheses of n Cycloparaphenylenes (n=8-13) and Size Dependence of Their Electronic Properties. *J. Am. Chem. Soc.* **133**, 8354–8361 (2011).
25. Iwamoto, T. *et al*. Size-Selective Encapsulation of C60 by [10]Cycloparaphenylene: Formation of the Shortest Fullerene-Peapod. *Angew. Chem. Int. Ed.* **50**, 8342–8344 (2011).
26. Sprafke, J. K. *et al.* Belt-Shaped π-Systems: Relating Geometry to Electronic Structure in a Six-Porphyrin Nanoring. *J. Am. Chem. Soc.* **133**, 17262–17273 (2011).
27. Segawa, Y. *et al.* Concise Synthesis and Crystal Structure of 12 Cycloparaphenylene. *Angew. Chem. Int. Ed.* **50**, 3244–3248 (2011).
28. Segawa, Y. *et al*. [9]Cycloparaphenylene: Nickel-mediated Synthesis and Crystal Structure. *Chem. Lett.* **40**, 423–425 (2011).
29. Zhong, Y. *et al.* Helical Ribbons for Molecular Electronics. *J. Am. Chem. Soc.* **136**, 8122–8130 (2014).
30. Ball, M. *et al.* Contorted Polycyclic Aromatics. *Acc. Chem. Res.* **48**, 267–276 (2015).
31. Sisto, T. J. *et al.* Long, Atomically Precise Donor–Acceptor Cove-Edge Nanoribbons as Electron Acceptors. *J. Am. Chem. Soc.* **139**, 5648–5651 (2017).
32. Ball, M. *et al.* Macrocyclization in the Design of Organic n-Type Electronic Materials. *J. Am. Chem. Soc.* **138**, 12861–12867 (2016).
33. Zhang, B. *et al.* Rigid, Conjugated Macrocycles for High Performance Organic Photodetectors. *J. Am. Chem. Soc.* **138**, 16426–16431 (2016).
34. Zhang, B. *et al.* Hollow organic capsules assemble into cellular semiconductors. *Nat. Commun.* **9**, 1957 (2018).
35. Zhong, Y. *et al.* Efficient Organic Solar Cells with Helical Perylene Diimide Electron Acceptors. *J. Am. Chem. Soc.* **136**, 15215 (2014).

36. Zhong, Y. *et al.* Molecular helices as electron acceptors in high-performance bulk heterojunction solar cells. *Nat. Commun.* **6**, 8242 (2015).

37. Edison, C. *et al.* Cove-Edge Nanoribbon Materials for Efficient Inverted Halide Perovskite Solar Cells. *Angew. Chem. Int. Ed.* **56**, 14648–14652 (2017).

38. Zhong, Y. *et al.* Helical Nanoribbons for Ultra-Narrowband Photodetectors. *J. Am. Chem. Soc.* **139**, 5644–5647 (2017).

39. Peurifoy, S. R. *et al.* Three-Dimensional Graphene Nanostructures. *J. Am. Chem. Soc.* **40**, 9341-9345 (2018).

40. McCulloch, I. *et al*. Avoid the kinks when measuring mobility. *Science (80-.).* **352**, 1521 LP – 1522 (2016).

41. Choi, H. H. *et al*. Critical assessment of charge mobility extraction in FETs. *Nat. Mater.* **17**, 2 (2017).

42. C.D., D. *et al*. Organic Thin Film Transistors for Large Area Electronics. *Adv. Mater.* **14**, 99–117 (2002).

43. George, P. *et al*. An alternative approach to the problem of assessing stabilization energies in cyclic conjugated hydrocarbons. *Theor. Chim. Acta* **38**, 121–129 (1975).

44. Bachrach, S. M. *et al*. DFT Study of Cycloparaphenylenes and Heteroatom-Substituted Nanohoops. *J. Org. Chem.* **75**, 6595–6604 (2010).

45. Segawa, Y. *et al.* Theoretical Studies on the Structures and Strain Energies of Cycloparaphenylenes. *Org. Lett.* **12**, 2262–2265 (2010).

46. Rajasingh, P. *et al*. Selective Bromination of Perylene Diimides under Mild Conditions. *J. Org. Chem.* **72**, 5973–5979 (2007).

47. You, J. B. *et al.* A polymer tandem solar cell with 10.6% power conversion efficiency. *Nat. Commun.* **4**, 10 (2013).

48. *CrysAlis Pro*. (2013).

49. Sheldrick, G. M. {\it SHELXT} {--} Integrated space-group and crystal-structure determination. *Acta Crystallogr. Sect. A* **71**, 3–8 (2015).

50. Sheldrick, G. M. Crystal structure refinement with {\it SHELXL}. *Acta Crystallogr. Sect. C* **71**, 3–8 (2015).

51. Dolomanov, O. V *et al*. {\it OLEX2}: A complete structure solution, refinement and analysis program. *J. Appl. Crystallogr.* **42**, 339–341 (2009).

52. Spek, A. L. Structure validation in chemical crystallography. *Acta Crystallogr. Sect. D* **65**, 148–155 (2009).

53. van der Sluis, P. *et al*. BYPASS: an effective method for the refinement of crystal structures containing disordered solvent regions. *Acta Crystallogr. Sect. A* **46**, 194–201 (1990).

Chapter 9. Conjugated PDI Macrocycles as Electronic Hosts

9.1. Preface

Chapter 9 contains unpublished work on **PBPB** and its utility as a host system. Dr. Timothy Andrew Barendt from Oxford University was integral to this work, and performed all spectroscopy presented and I synthesized all compounds. The second half of this chapter briefly describes initial work I performed while a visiting student in Kyoto University in 2018. I believe both show the potential of these materials as chiral hosts within a range of applications and scope to design interesting structures in the future

9.2. Introduction

This study uses **PBPB** as an electronic host for fullerenes.[1] Fullerenes stand out amongst the carbon nanomaterials as desirable components within organic electronic materials due to their unique electrochemical and photophysical properties.[2–8] This has motivated the use of self-assembly with a rationally designed hosts as a means to incorporate fullerenes into electronically active systems and materials.[9–15]

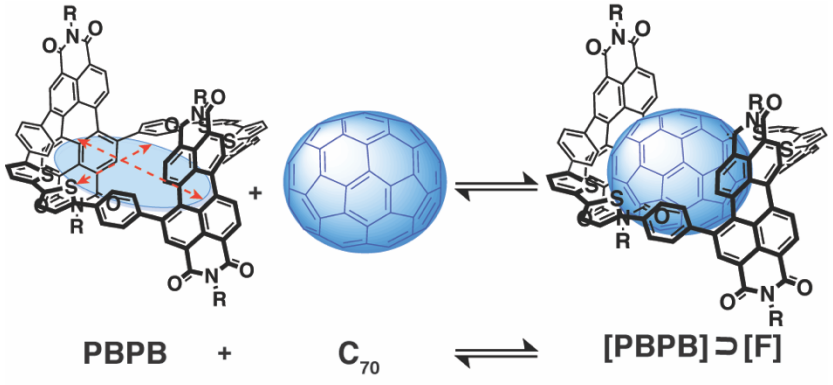

Figure 9.1. The recognition of fullerenes C_{70}, C_{60} or **PCBM** by bis-PDI macrocycle **PBPB** to form a supramolecular complex (R = $C_{11}H_{23}$).

To date, a number of fullerene receptors have been constructed, thereby establishing several principles of host design in order to maximize guest affinities.[9,11–29] These include; 1) a large, preorganized and typically macrocyclic cavity to accommodate the fullerene; 2) extensive

π-conjugation that facilitates convex-concave intermolecular aromatic stacking interactions; and 3) the integration of electron donating heteroatoms to provide electronic complementarity with the electron deficient guest.

We have investigated the dynamics and electronic properties of **PBPB**, and found the macrocycle possesses many of the desirable characteristics for strong, non-covalent recognition of fullerenes, namely; 1) a large inner nano-space with a persistent elliptical geometry; 2) π-conjugation that extends throughout the concave aromatic framework; and 3) Lewis basic sulfur atoms that are directed into the cavity and available for lone pair–π interactions. Experimental NMR, absorption and emission spectroscopies, mass spectrometry and theoretical molecular modelling are used to characterize and quantify the resulting supramolecular complexes in the solution phase. A preference for **C_{70}** fullerene is revealed. Furthermore, an insight into the electronic communication between macrocyclic host and fullerene guest is provided from UV–Vis absorption and fluorescence emission spectroscopies and supported by density functional theory calculations. As such these findings have significant implications for the generation of conducting organic electronic materials composed from supramolecular assemblies of electron donor and acceptor units.

9.3. NMR Spectroscopy Shows Formation of Supramolecular Complex

The ability of **PBPB** to form a supramolecular complex with fullerenes (**F**) **C_{60}**, **C_{70}** and [6,6]-Phenyl C_{61} butyric acid methyl ester (**PCBM**) was investigated by NMR spectroscopy in d_8-toluene solution. Initial proton NMR titrations, in which up to ten equivalents of fullerene (**F**) guest were titrated into a 0.5 mM solution of macrocyclic **PBPB** host, showed three features indicative of non-covalent interactions and formation of the supramolecular complex [**PBPB**] ⊃ [**F**] with all guests (Figure 9.2a-d and Figure 9.8-Figure 9.11, NMR data provided for all complexes in the

Appendix). Our attempts to grow single crystals of the supramolecular complexes were unsuccessful, so we employed DFT to elucidate how **F** guest rests within the cavity of **PBPB** (Figure 9.2a).

The largest perturbations were the downfield shifts of peaks associated with phenyl aromatic protons H_d and H_e (up to $\Delta\delta$ = 0.18 ppm, Figure 9.2b). We believe this is indicative of the formation of strong intermolecular aromatic stacking (π-π) interactions between the concave surface of the fullerene guest and convex belt of the macrocyclic host. Analogous effects have been observed in fullerene receptors also containing extensive π-conjugation such as CPP and porphyrin-based systems.[16,26,28] Downfield shifts of the $H_{a\text{-}c}$ proton signals (PDI-based protons), too, suggest a close approach between **PBPB** and the fullerene guests (Figure 9.2e).

The second interaction consists of lone pair donation from the thiophene bridges of **PBPB** to the fullerene (S:π interactions), made possible by the Lewis basic sulfur atoms of the heterocycles being directed towards the guest in the cavity (Figure 9.2c). Both cyclothiophenes and sulfur-based macrocycles have shown this interaction contributes to the stabilization of the supramolecular fullerene complexes involving these hosts.[11,12,30] The thiophene proton shift is much less pronounced relative to the neighboring phenyl rings ($\Delta\delta$ H_i = 0.02 - 0.05 ppm) because the sulfur lone pairs are orthogonal to the aromatic system of the macrocycle. Analogous to literature reports, we observe an upfield shift in the heterocycle's protons as they are outside the binding pocket.

Interaction 3 involves the methylene protons of the $C_{11}H_{23}$ side chains of **PBPB**. While there are significant changes in the alkyl region, the clearest occur with protons labelled H_f, H_g, and $H_{f'}$, and $H_{g'}$ in Figure 9.2d and 9.12 and 9.13. These sixteen protons exist as a diastereotopic set of resonances that, in the absence of any fullerene guest, produce two broad peaks (δ = 2.16

ppm and 1.83 ppm, $H_f/H_{f'}$ and $H_g/H_{g'}$ respectively) of equal integration. (Figure 9.12 and 9.13).[1] However, upon fullerene recognition both of these signals are further split into two broad peaks, giving, in total, four signals that each integrate to four protons (H_f, H_g, $H_{f'}$, $H_{g'}$)

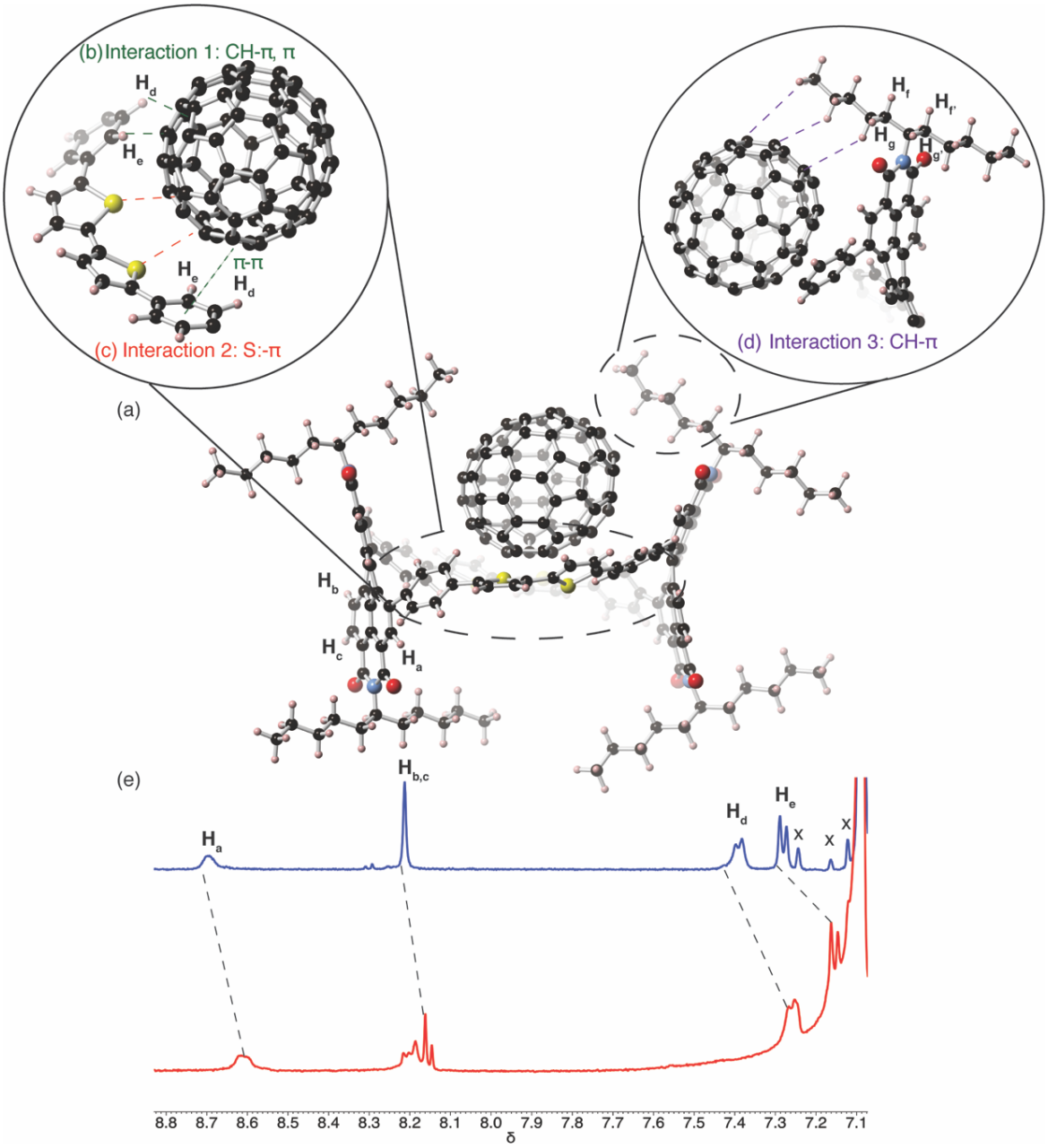

Figure 9.2. (a) DFT structure of the supramolecular complex showing non-covalent interactions present. (b) CH-π interactions from aryl rings to **C_{70}**; (c) sulfur lone pair-π interactions; (d) CH-π interaction between methylene and fullerene; and (e) Truncated ^{1}H NMR spectra from the titration of 1 eq. of **C_{70}** fullerene guest into a 0.5 mM host solution of **PBPB** (start point = red, end point = blue, d_8-toluene, 298 K, 500 MHz.

Our hypothesis is that fullerene encapsulation within the macrocyclic cavity renders the internal and external environments of the macrocycle inequivalent by restricting free rotation of the sidechains, rendering $H_f/H_{f'}$ and $H_g/H_{g'}$ to become inequivalent.

To better understand the role of the alkyl side chains, we prepared **PBPB** with 2,6-diisopropyl phenyl substituents (*aryl*-**PBPB**) at the imide positions and studied the binding of C_{70} (Figure 9.14). Fullerene recognition was shown to be over an order of magnitude weaker (Table 9.1), confirming the integral role of the flexible alkyl side chains to a) allow ease of access to the cavity and b) undergo additional CH–π non-covalent interactions to accommodate the fullerene guest. The side chains help form a macrocyclic cage around the fullerene.

We qualified the importance of the macrocyclic cavity by performing NMR titrations studies on a diphenyl PDI (Compound **1.1**),[31] and observe no evidence of a supramolecular complex between **1.1** and C_{70} (Figure 9.15). This suggest the cavity is critical to form a supramolecular complex. We also investigated the importance of size complementarity between host and guest in [**PBPB**] ⊃ [**F**] by performing analogous ^{1}H NMR spectroscopic titration experiments with *trans*-**DBDB** and $\mathbf{C_{70}}$. From DFT, the cavity for *trans*-**DBDB** measures 19 Å from $hPDI_2$ to $hPDI_2$ and 16 Å along the short axis between the bithiophenes vs. 16 Å and 12 Å respectively for **PBPB** (Figure 1B.4 and Figure 8.4). Analogous to **PBPB**, *trans*-**DBDB** possesses the three key interactions described: 1) four aryl rings that can participate in π-π interactions; 2) $C_{11}H_{23}$ branched side-chains that can stabilize a supramolecular complex through CH-π interactions; and 3) four sulfur groups with their lone pairs directed to the center of the cavity. The ^{1}H NMR spectra exhibited modest shifts in the corresponding aryl groups ($\Delta\delta$ H_a = 0.01 ppm), indicative of weak binding and negligible formation of complex **DBDB ⊃ C70**, and despite **DBDB**

possessing analogous functionality responsible for strong interactions between **PBPB** and **F** guests (Figure 9.16).

Job's plot analysis of the titration data revealed the maximum chemical shift change occurred when the fullerene mole fraction χ (**F**) = 0.5, indicating 1:1 host:guest stoichiometric binding for all guests investigated in this study (Figure 9.16). The supramolecular complexes were also studied by ESI mass spectrometry (Figures 9.17). Solutions of macrocycle and fullerene mixtures revealed peaks for 1:1 and 1:2 host:guest complexes ([**PBPB**] ⊃ [**F**] and [**PBPB**] ⊃ [**2F**]), the former being of significantly higher intensity relative to the latter. An indication of the robustness of complex [**PBPB**] ⊃ [**F**] was provided by ESI MS/MS experiments; large collision energies (80-100 eV) were required to break the intermolecular interactions and observe peaks for discrete macrocycle and fullerene components (Figures 9.18).

Table 9.1. Fullerene Association Constants

	K_a (M^{-1})
C_{70}	9,278
C_{60}	2,119
PCBM	1,336[a]
C_{70}/*aryl*-**PBPB**	591

Table 9.1: Fullerene association constants (K_a, M^{-1}) for macrocycle **PBPB** determined by ^{1}HNMR spectroscopy in d8-toluene using chemical shift data of H_d unless otherwise stated (298 K, 500 MHz). Errors < 7%. Chemical shift of thiophene proton H_h used due to spectral overlap of H_d.

We quantified fullerene recognition with macrocyclic host **PBPB** using Bindfit,[32] following H_d proton (Table 9.1). Interestingly, the association constant for C_{70} was over four times that of C_{60}, at 9,278 M^{-1} relative to 2,119 M^{-1}, respectively. This suggests the ellipsoidal cavity of **PBPB** provides a better size and shape complementarity for the less spherical fullerene guest. There is also potential for an enhanced electronic contribution to complexation: C_{70} is more

electron deficient than C_{60} (vide infra for photophysics).[33] Binding with PCBM, too, is also observed despite the additional steric bulk arising from covalent functionalization of the carbon cage.

Carbon NMR spectroscopy was used to further characterize fullerene complexation by macrocycle **PBPB**. Analysis of host solutions containing a small excess (1.5 eq.) of $\mathbf{C_{60}}$ or $\mathbf{C_{70}}$ guest in *d8*-toluene revealed upfield shifts of the ^{13}C NMR fullerene signals, consistent with a ring current effect from the diamagnetic aromatic system of the macrocycle (Figure 9.20). We note that $\mathbf{C_{70}}$ fullerene exhibits a larger maximum perturbation than $\mathbf{C_{60}}$ ($\Delta\delta_{max}$ = 0.18 *vs.* 0.09 ppm). Therefore, to further probe fullerene selectivity of **PBPB** in solution, a competition experiment was performed by combining **PBPB**, $\mathbf{C_{60}}$ and $\mathbf{C_{70}}$ in a 1:1.5:1.5 stoichiometric ratio (Figure 9.20b). In agreement with ^{1}H NMR calculated K_a values, a larger proportion of the maximum possible ^{13}C NMR shift was observed for $\mathbf{C_{70}}$ ($\Delta\delta/\Delta\delta_{max}$ = 67%) than for $\mathbf{C_{60}}$ (44%).

9.4. Photophysics Between PBPB and Fullerenes

In order to provide insight into electronic communication between macrocyclic host and fullerene guest, UV-Vis absorption spectra were recorded for macrocycle **PBPB** (μM concentration) in the presence of an excess of C_{70} (Figure 9.3) and C_{60} guests in toluene (Figure 9.21). The addition of up to 100 equivalents of fullerene caused a decrease in intensity of the lowest energy absorption band and a concomitant increase in absorptions at longer wavelength generating an isosbestic point at λ = 650 nm indicative of the establishment of a thermodynamic equilibrium between host and host–guest complex.

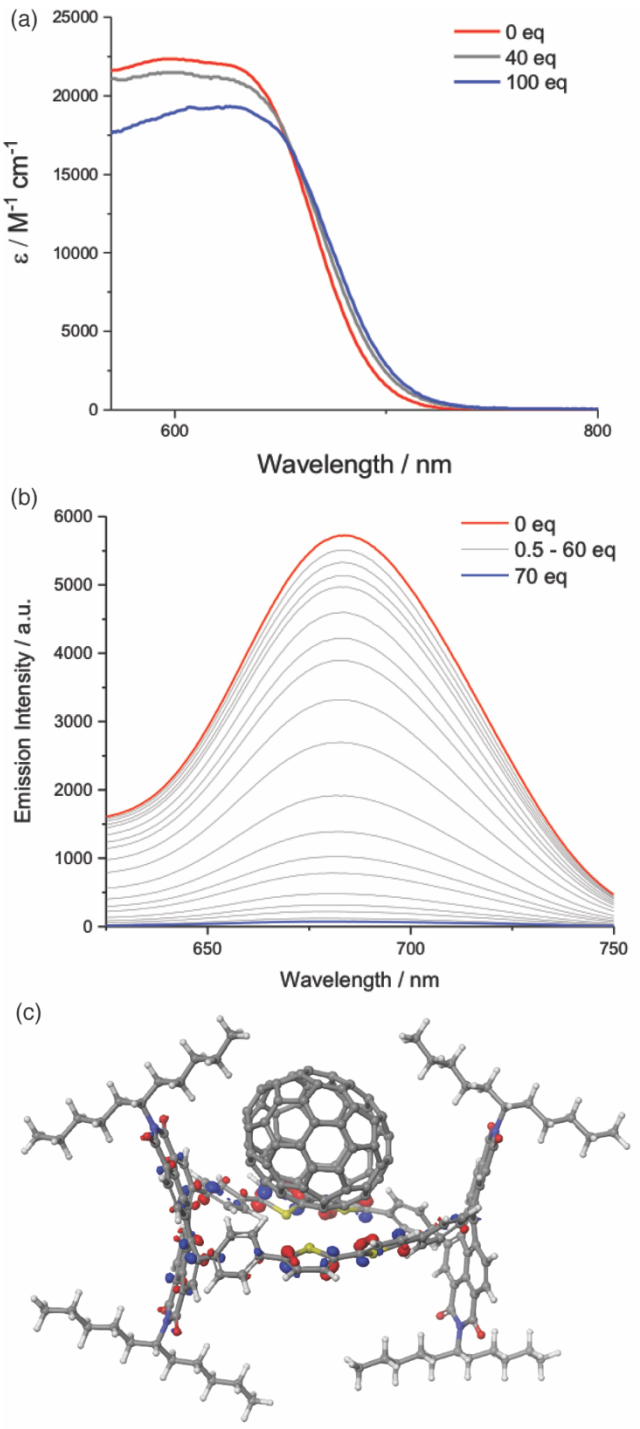

Figure 9.3. (a) Electronic absorption spectra of **PBPB** upon the addition of C_{70} (toluene, corrected for C_{70} absorptions); (b) Fluorescence emission spectra of **PBPB** upon the titration with C_{70} (toluene, 4 μM, λex = 600 nm); and (c) HOMO energy level showing electron delocalization.

TDDFT calculations show the HOMO is **PBPB**-based, suggesting there is a high density of high energy electrons on the perimeter of the macrocycle. Relative to the free macrocycle, the

complex shows a high degree of electron delocalization across the bithiophenes and PDI in the HOMO. We characterize the low energy transition in the absorption spectrum as a promotion of an electron from the HOMO (macrocyclic-based) to a purely PDI-based LUMO. Upon addition of fullerene guest, we observe a decrease in absorption at low energy wavelengths. A possible explanation for the decrease in absorption at this wavelength is that the proximal fullerene guest also possesses empty, low energy orbitals available to accept an electron. As such, this effect is most pronounced with $\mathbf{C_{70}}$ because, while it forms the strongest intermolecular complex, it is also more electron deficient than $\mathbf{C_{60}}$.[33] The change in absorption could also reflect geometrical changes in **PBPB** upon fullerene encapsulation: electron delocalization is greater in the complex relative to the free macrocycle[1] and could result in ground state electron transfer.

Fluorescence emission host–guest titration experiments revealed the influence of fullerene binding on the excited state of **PBPB** (host concentration maintained at 4 μM throughout, Figure 9.3b and Figure 9.22 and Figure 9.22). Both $\mathbf{C_{60}}$ and $\mathbf{C_{70}}$ recognition induced significant quenching of fluorescence emission due to intermolecular energy and/or electron transfer[34–39] from host to guest due to their electronic complementarity. The stronger recognition of $\mathbf{C_{70}}$ by **PBPB** was manifested in a near depletion (99%) of fluorescence emission after 70 equivalents of guest, while an equal molar ratio of $\mathbf{C_{60}}$ resulted in a smaller decrease (57%).

9.5. Potential Applications for PBPB-Fullerene Complex

Chapter 9 describes the supramolecular complexation of fullerene (**F**) guests by a conjugated PDI-bithiophene-based macrocycle (**PBPB**) in solution (Figure 9.1). Qualitative evidence for the non-covalent interactions that promote this encapsulation is, in part, provided by a detailed analysis of perturbations to the ^{1}H and ^{13}C NMR spectra and is supported by mass spectrometry and DFT calculations. The importance of geometric and electronic complementarity

to the formation of [**PBPB**] ⊃ [**F**] is highlighted through comparisons with analogous, yet inferior, PDI-based acyclic and macrocyclic receptors. These principles also explain the > 4-fold preference of **PBPB** for $\mathbf{C_{70}}$ over $\mathbf{C_{60}}$ fullerenes. Electronic absorption and fluorescence emission spectroscopies revealed electronic communication between the **PBPB** macrocycle (donor) and fullerene (acceptor) in the ground and excited state. This, and the fact **PBPB** was demonstrated to be a potent receptor for the fullerene **PCBM**, paves the way for these donor–acceptor supramolecular complexes to be integrated into organic electronic materials for enhancing the performance of OFET and OPV devices.

9.6. Future Directions for Conjugated Macrocycles

The success of both $\mathbf{(PBBr_4)_3}$ and **PBPB** as a hosts systems is exciting as one relatively under-explored area for the conjugated macrocycles is applications that utilize the cavities; for example, one can envision using the cavity as a chiral environment for catalysis.[40] Each of the macrocycles created possess different electronic and physical structures, providing an opportunity to select guests that are electronically and size-matched to each host.

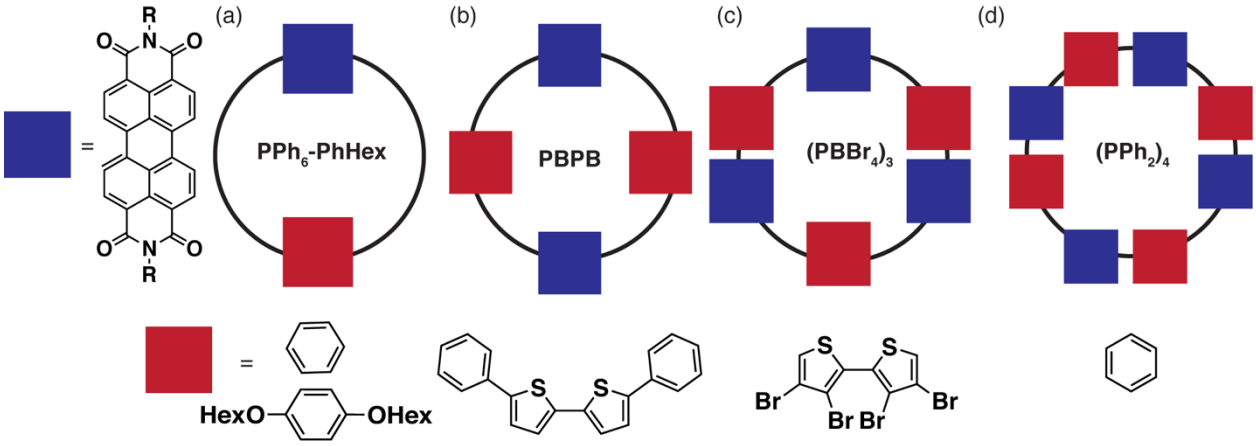

Figure 9.4. Schematic of (a) $\mathbf{PPh_6}$**-PhHex**; (b) **PBPB**; (c) $\mathbf{(PBBr_4)_3}$; and (d) $\mathbf{(PPh_2)_4}$.

One promising idea would be to incorporate phenanthroline into a conjugated macrocycle. Phenanthroline moieties (**PA**) are ubiquitous in catalysis and host-guest applications, making this linker a strong candidate for inclusion into a macrocyclic design.[41,42] The phenanthroline nitrogen

long pair are orthogonal to the π-plane of the macrocycle and do not contribute significant electron density to the frontier orbitals. This suggests the lone pair could be available for host-guest/coordination/sensing interactions.

Figure 9.5 shows the first synthesis attempted to make a macrocycle that comprised a PDI (**P**) and **PA** moiety. I first synthesized Compound **9.1** using a literature procedure using 1,4-benzenediboronic acid bis(pinacol) ester and 2,9-dichloro-1,10-phenanthroline. The macrocyclization step was inspired by our synthesis of **PPh$_6$-PhHex**. Compound **2.2** and **9.1** are then reacted in equimolar ratios for two days.[43,44] After extraction to remove the salts, the intermediate platinum complex is subjected to reductive elimination. Upon workup, however, the target compound **9.2** was not isolated; instead, both Compounds **9.3** and **9.4** were detected by MALDI. In addition to these two major byproducts, MALDI too showed several additional combinations of PDI and **9.1** (Figure 9.23) after the column was spiked with NEt_3. Further purification using GPC was unsuccessful; the macrocycles did not appear to be stable. The multiple byproducts is a curious result; it suggests that there is reversibility in the macrocyclization step, analogous to Chapter 7.[45]

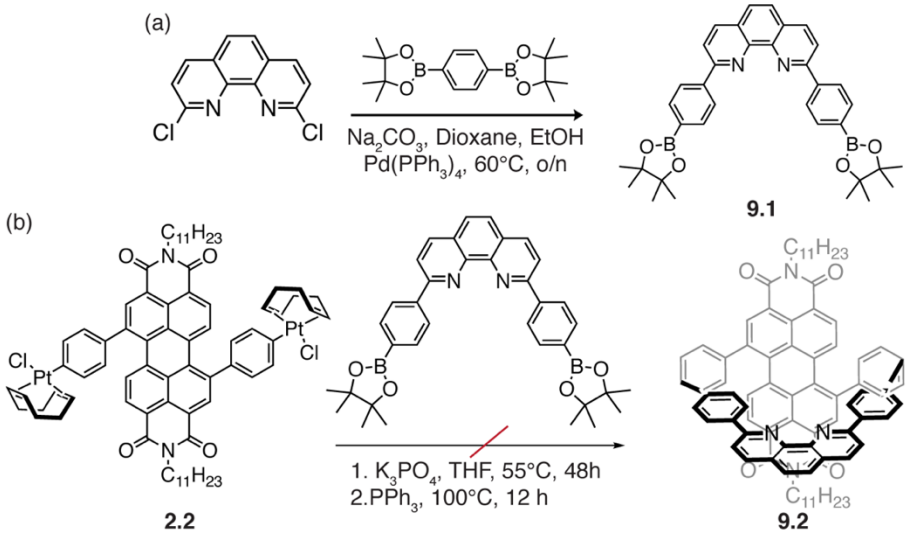

Figure 9.5. (a) Literature synthesis to make **9.1**; (b) First synthesis to make macrocycle **9.2**.

One plausible reason we do not observe the targeted macrocycle could be due to strain. The aryl to aryl distance measures 8.39 Å in **9.2** relative to 12.2 Å in an unstrained diphenyl PDI. Chapter 1B discussed the implications a tighter distance between the two aryl rings adjacent to the PDI. The smallest conjugated macrocycle isolated has an aryl-aryl distance of 0.97 nm. According to DFT, both **9.3** and **9.4** have much wider aryl-aryl distances, presumably relieving strain, and stabilizing the complex and formation. Figure 9.5 shows the three energy minimized structures and their aryl-aryl distances.

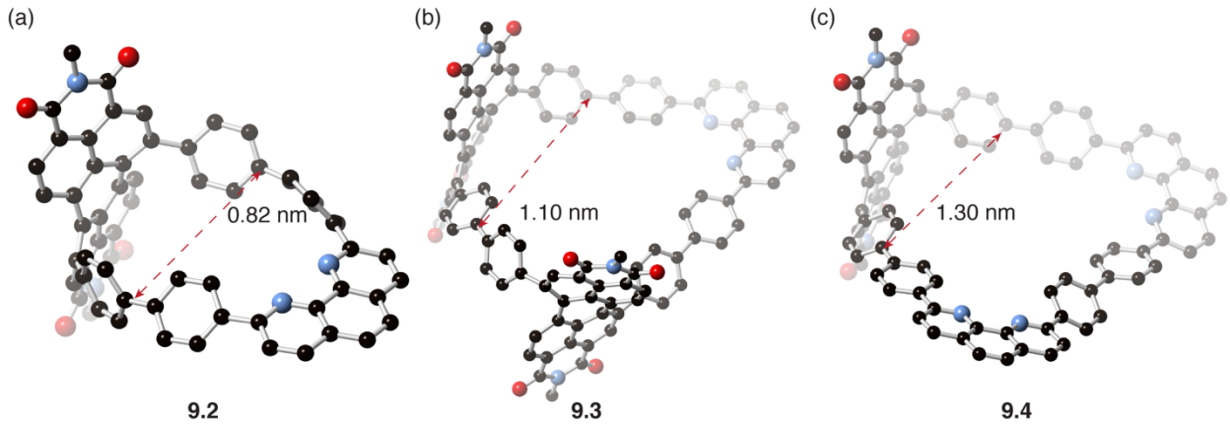

Figure 9.6. The DFT energy minimized structures for (a) **9.2**; (b) **9.3**; and (c) **9.4**. One hypothesis for not forming **9.2** could be due to strain. The aryl-aryl distance serves as a quick tool to assess strain. The smallest PDI-based macrocycle synthesized has an aryl-aryl distance at 0.97 nm.

A rational synthesis is required in order to try and isolate either product in high yield. One potential synthesis is proposed in Figure 9.6. Compound **9.1** and excess **SI-3.6** could be coupled through a Suzuki reaction to form **9.5**. This intermediate provides several opportunities to create interesting topologies. Using a nickel-based homocoupling approach, one could form **9.3**.[41] There is precedent for this approach forming a phenanthroline-incorporated CPP.[41] One could also envision using Compound **9.5** to form a catenane structure by first exchanging the bromides for BPin, followed by the addition of copper(I) to coordinate two molecules of **9.5** geometry.[42] This intermediate (**9.6**) could then be subjected to a oxidative homocoupling strategy[43] for catenane

formation. This is one example of how we could incorporate different ligands to build in additional functionality utilizing the nano-space rendered by the macrocyclic design.

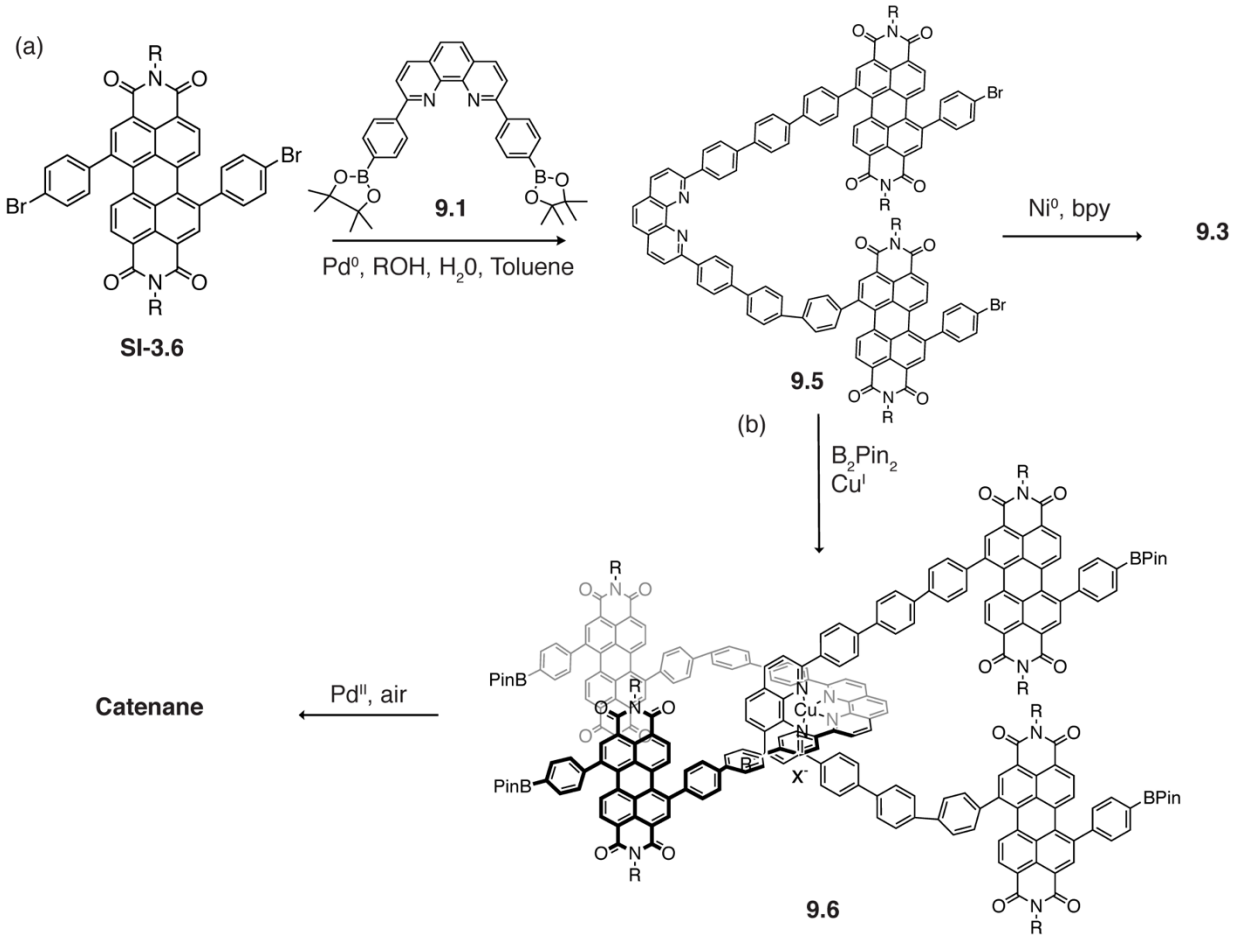

Figure 9.7. (a) A proposed synthesis to form **9.2** using a nickel-based strategy; (b) one could also employ oxidative coupling conditions to yield a catenane structure.

Over the past five years, I have asked myself the question of how fundamental physical organic concepts impact organic electronics – it has been both illuminating and fun to study classroom principles in the laboratory. In particular, the conjugated macrocycles described in this thesis allowed me to explore rigidity, strain, and chirality as they applied to device properties. We found that the cyclic design resulted in interesting properties in each application, which prompted a five-year long discovery process that is ongoing. I look forward to seeing the directions this program takes in the coming years.

9.7. Appendix – Supplementary Figures

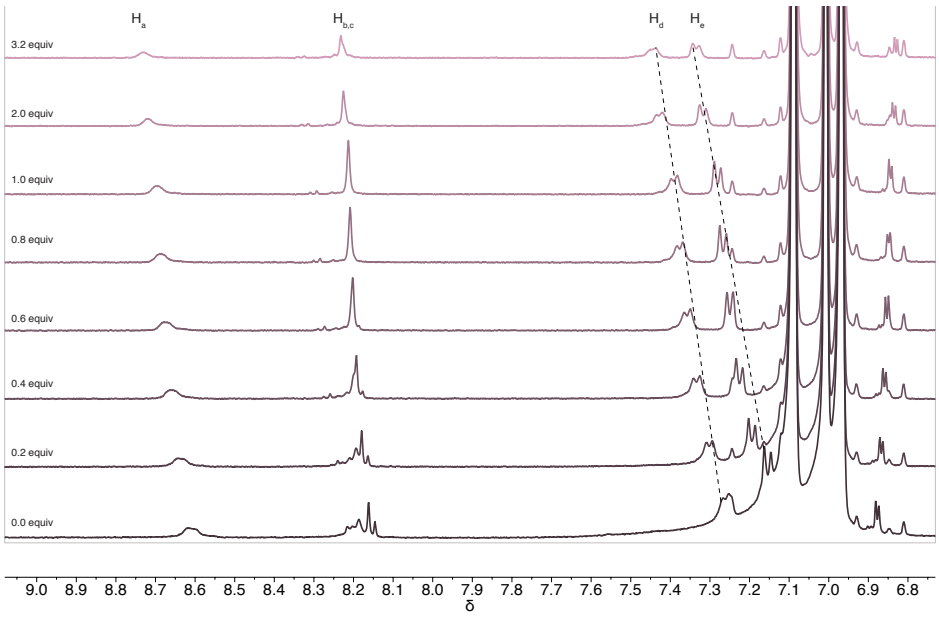

Figure 9.8. The ^{1}H NMR of **PBPB** and **C_{70}** from 0.0 to 3.2 equivalents. The aryl protons shift dramatically as the concentration of **C_{70}** increases.

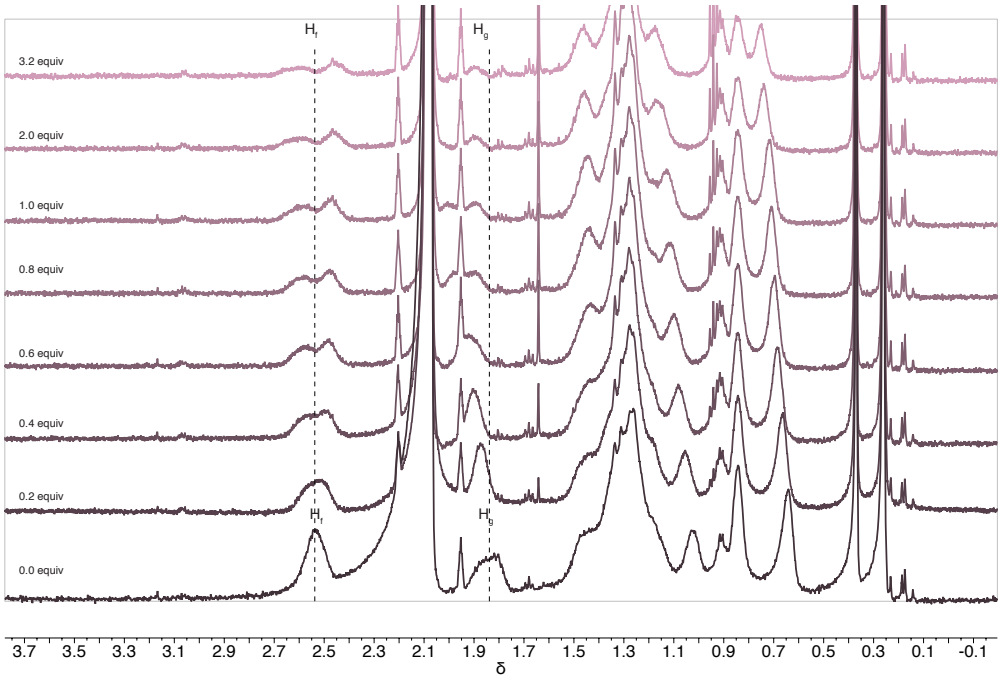

Figure 9.9. The ^{1}H NMR of **PBPB** and C_{70} from 0.0 to 3.2 equivalents. The alkyl protons split into two as the concentration of C_{70} increases, indicative of outside and inside environments for methylenes.

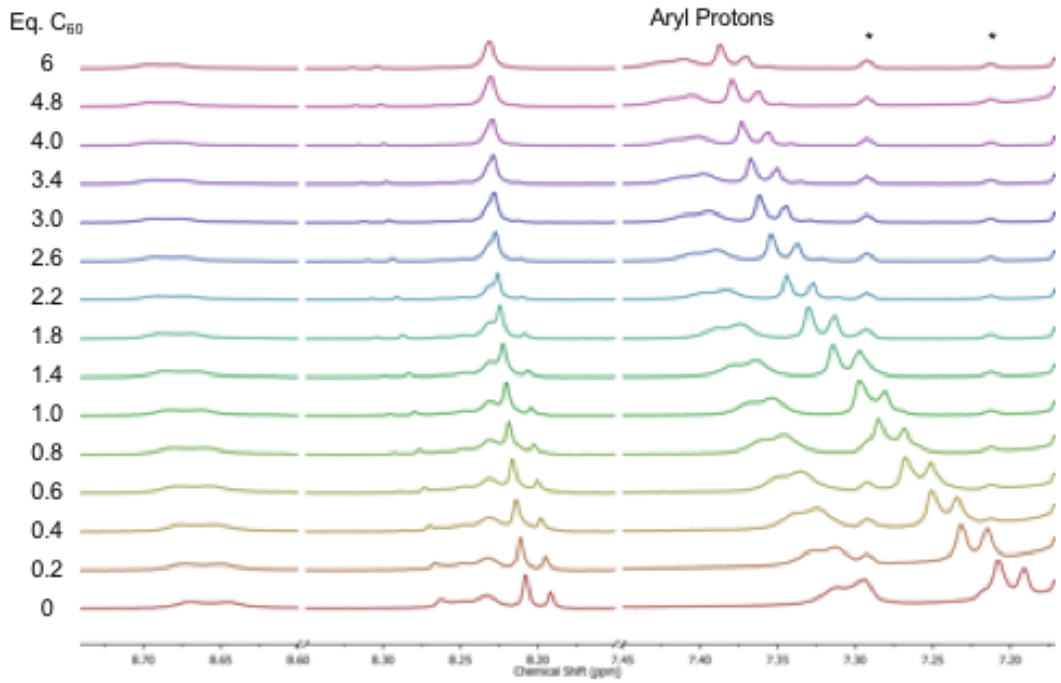

Figure 9.10. The ^{1}H NMR of **PBPB** and **C_{60}** from 0.0 to 6 equivalents.

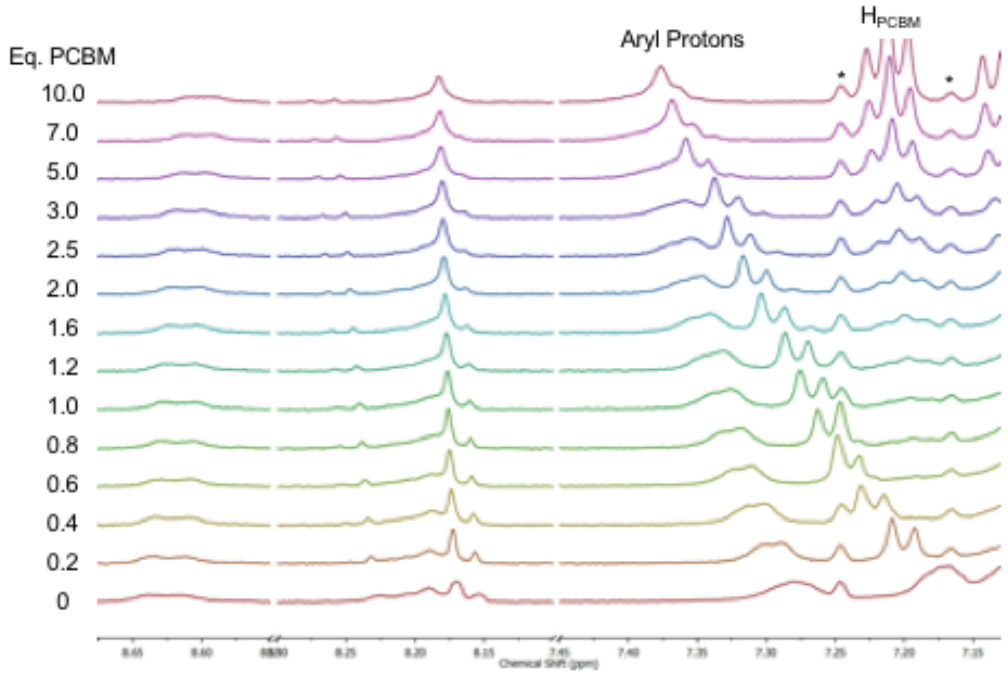

Figure 9.11. The ^{1}H NMR of **PBPB** and **PCBM** from 0.0 to 6 equivalents.

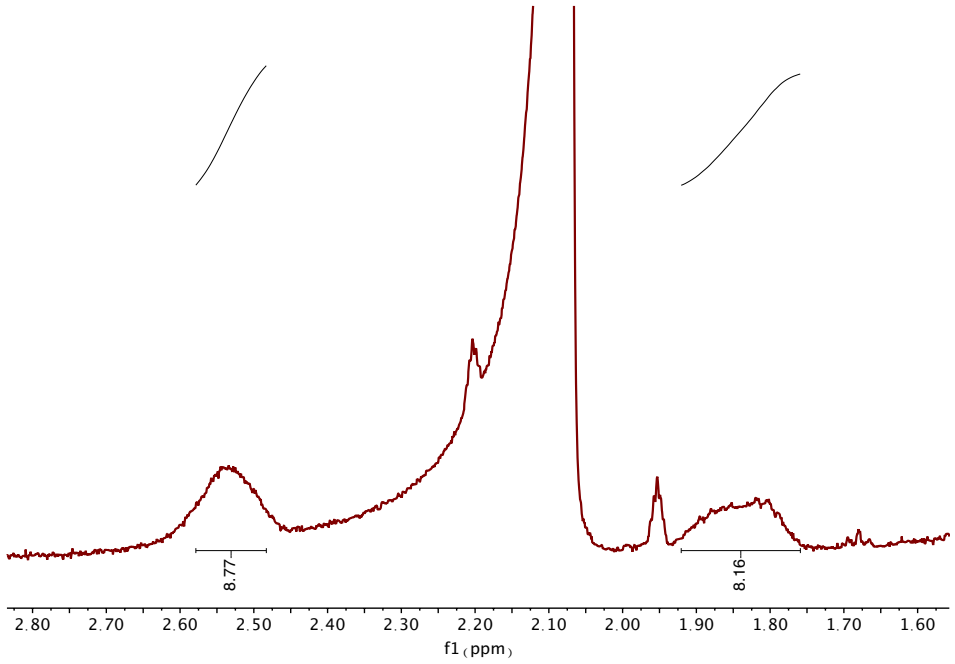

Figure 9.12. The ^{1}H NMR of **PBPB** alkyl region showing the methylene protons ortho to the methine (H_f and H_g) as two broad peaks as they are diastereotopic. Each integrates to eight protons.

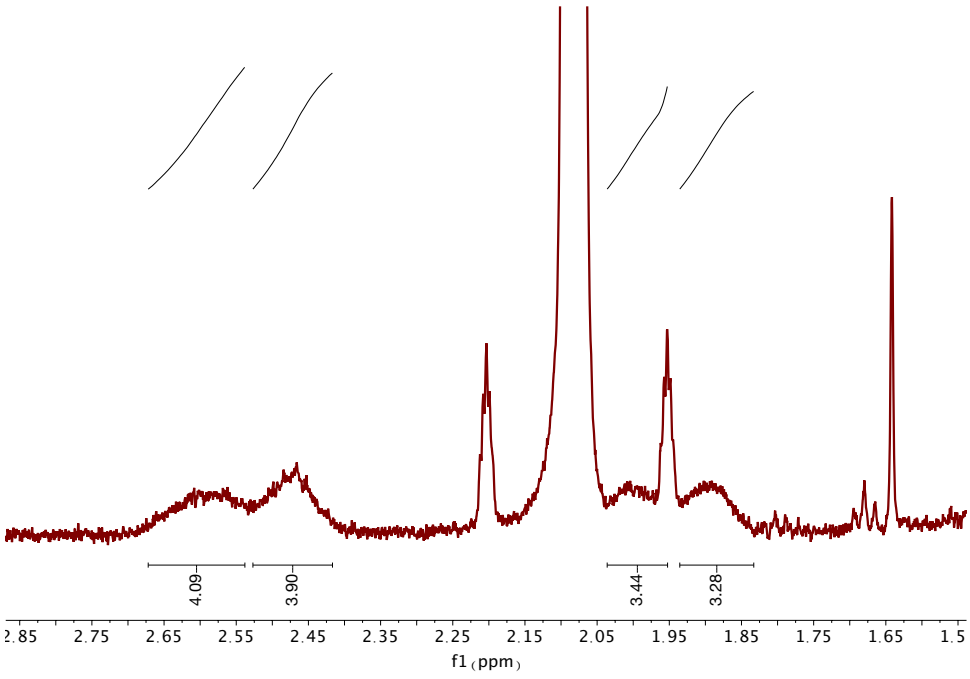

Figure 9.13. The ^{1}H NMR of **PBPB** and 1.0 equivalent of **C_{70}**. The methylene protons (H_f and H_g) ortho to the methine split into two broad peaks and are now inequivalent.

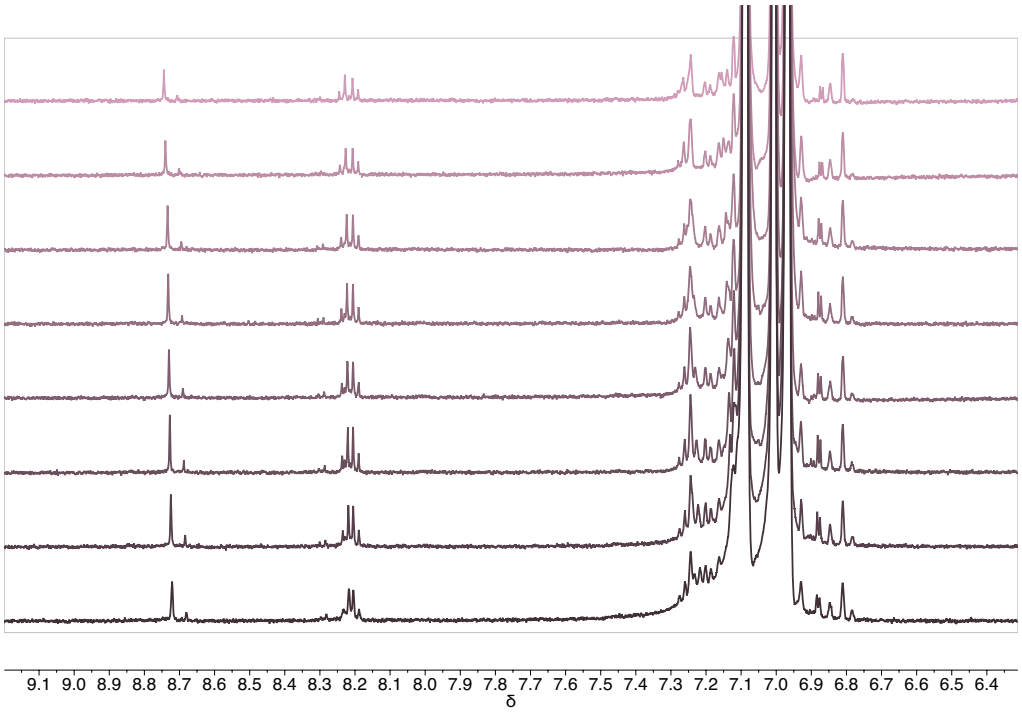

Figure 9.14. The ^{1}H NMR of *aryl*-**PBPB** up to 3.4 equivalent of $\mathbf{C_{70}}$.

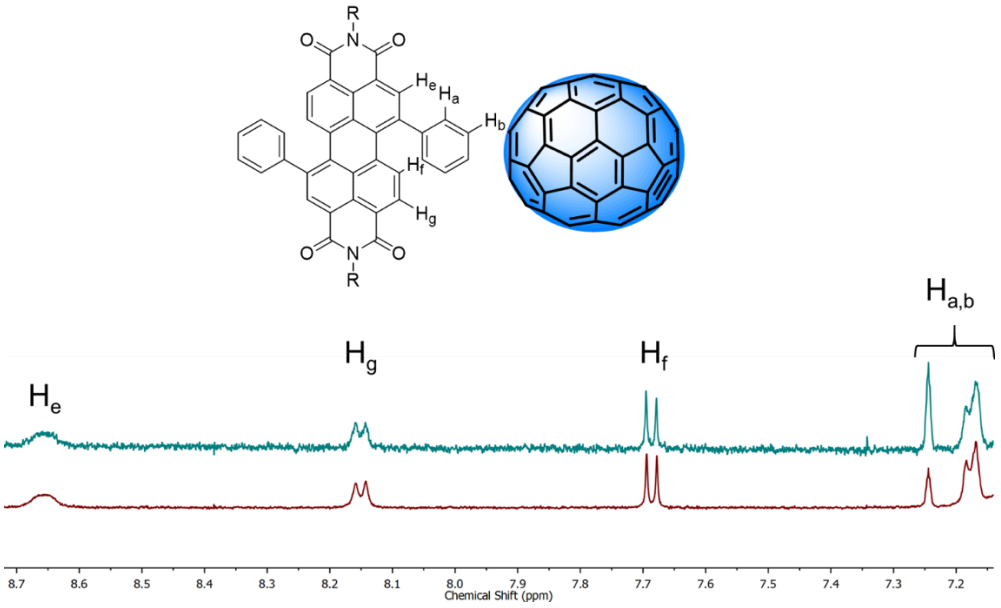

Figure 9.15. Truncated ^{1}H NMR spectra of Compound **3.4** (bottom) and after the addition of four equivalents of $\mathbf{C_{70}}$ fullerene (top) (d8-toluene, 298 K, 500 MHz, R = $C_{11}H_{23}$).

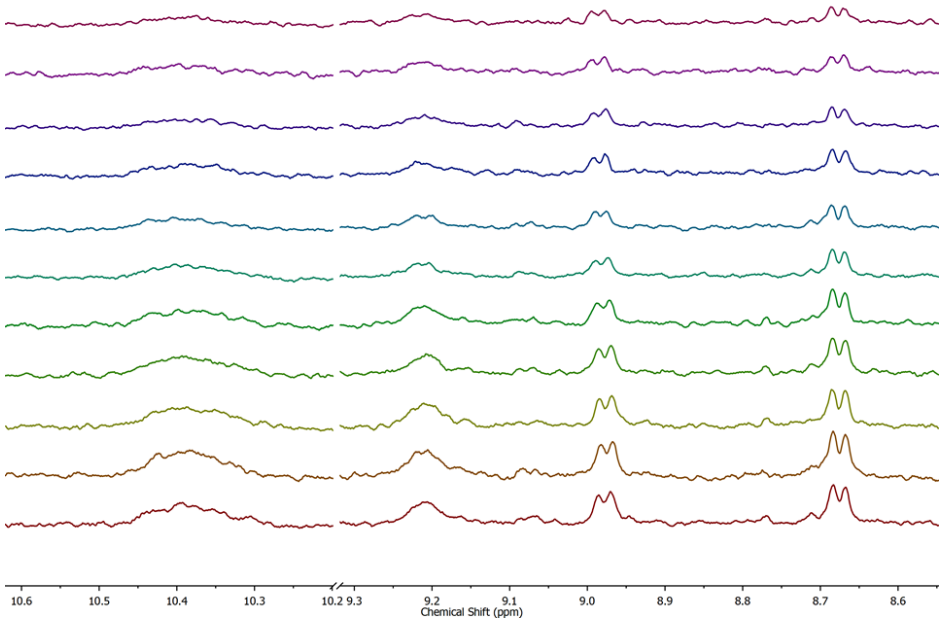

Figure 9.16. Truncated ^{1}HNMR spectra of *trans*-**DBDB** (Chapter 8) and after the addition of four equivalents of **C$_{70}$** fullerene (d$_8$-toluene, 298 K, 500 MHz). $\Delta\delta$ H$_a$ = 0.01 ppm and so too small to be accurately fitted.

(a) [**PBPB**] ⊃ [**C$_{70}$**]

K_a = 9,278 (7%)

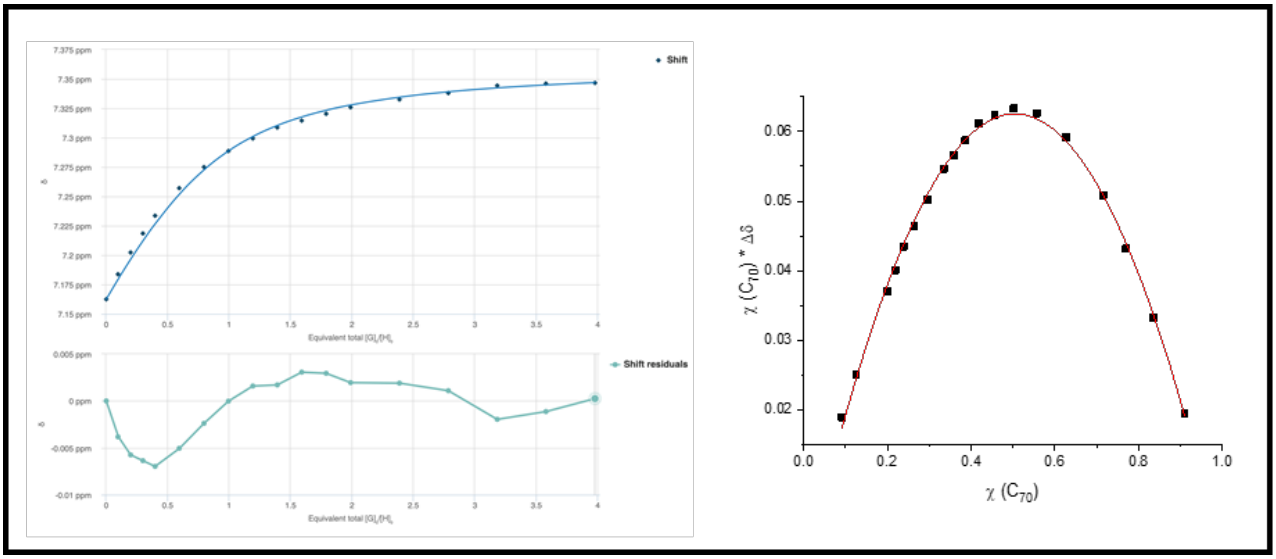

(b) [**PBPB**] ⊃ [**C$_{60}$**]

K_a = 2,119 (1%)

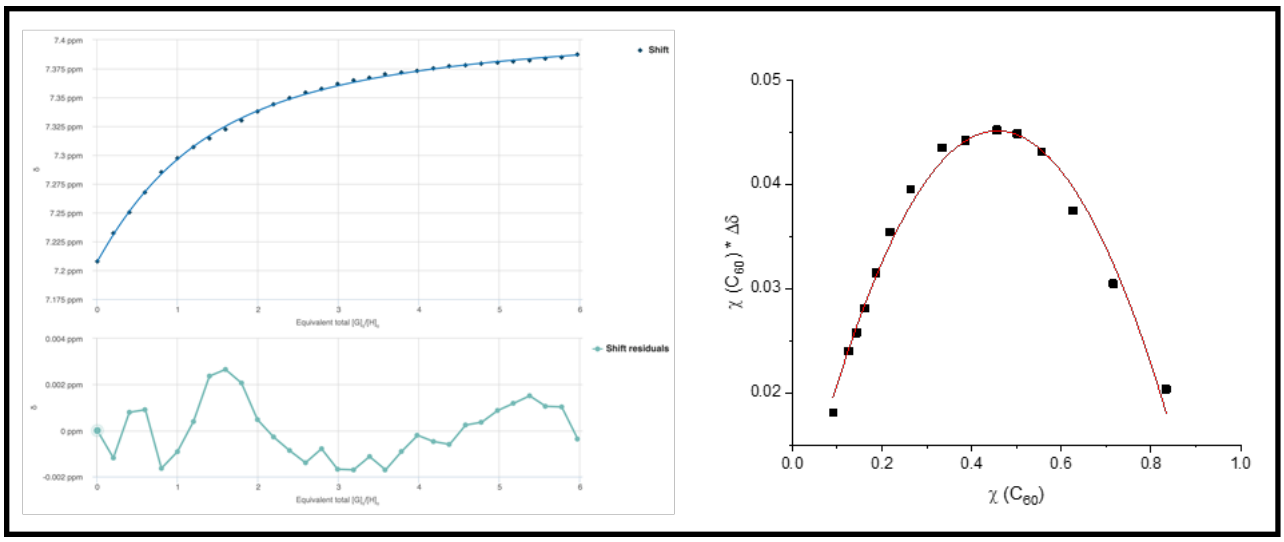

(c) [**PBPB**] ⊃ [**PCBM**]

K_a = 1,336 (2%)

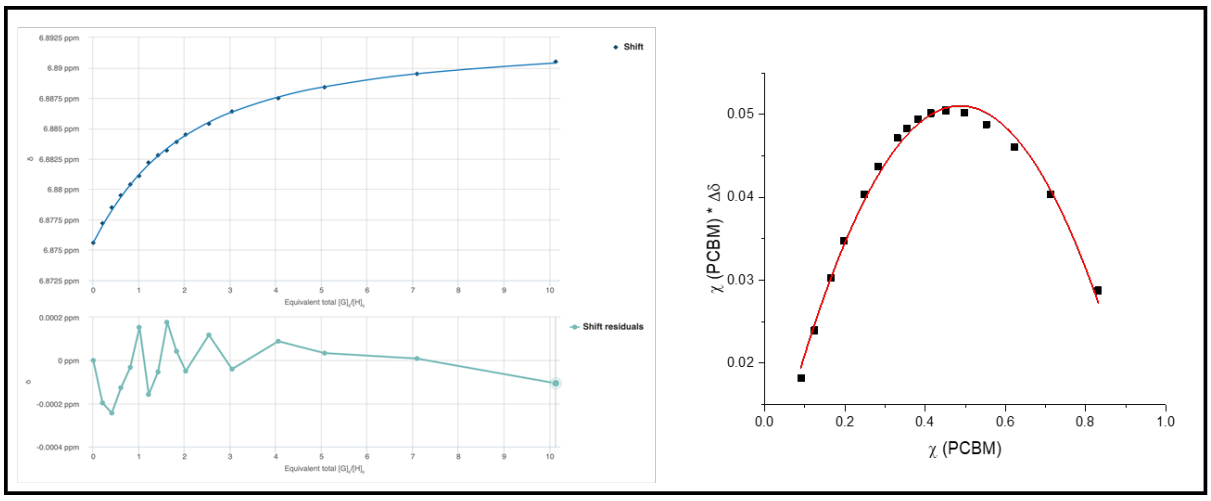

(d) [*aryl*-**PBPB**] ⊃ [**C70**]

K_a = 591 (1%)

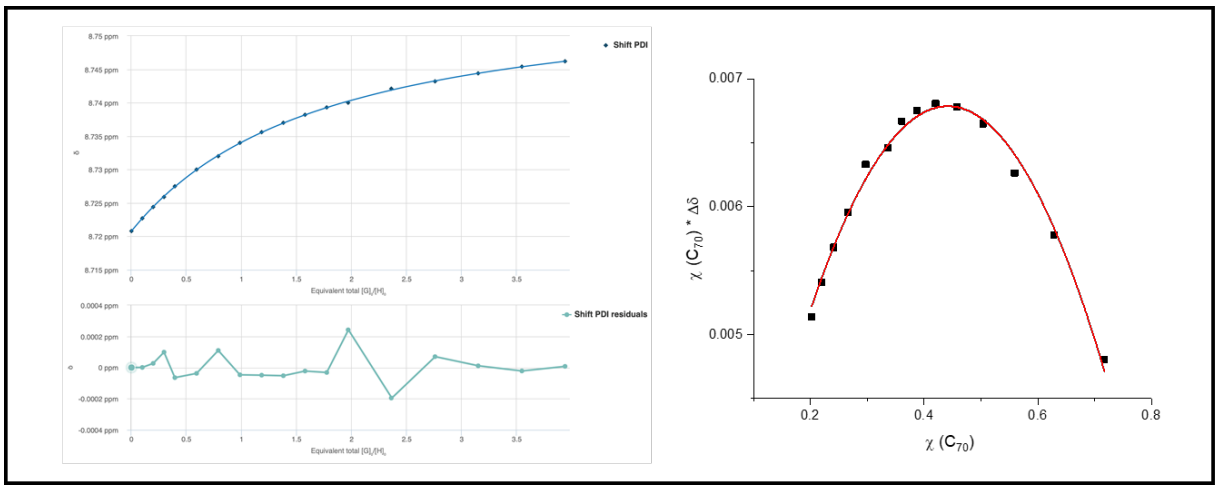

Figure 9.17. ^{1}H NMR spectroscopic titration curves and residuals for **PBPB** and *aryl*-**PBPB** upon titration with fullerene guests. Solid points represent experimental data, continuous line represents theoretical binding isotherm. Errors for association constants are given in brackets. Job's plots for complexes indicate a 1:1 binding stoichiometry; the maximum change in chemical shift occurs when the mole fraction of fullerene guest χ (F) = 0.5.

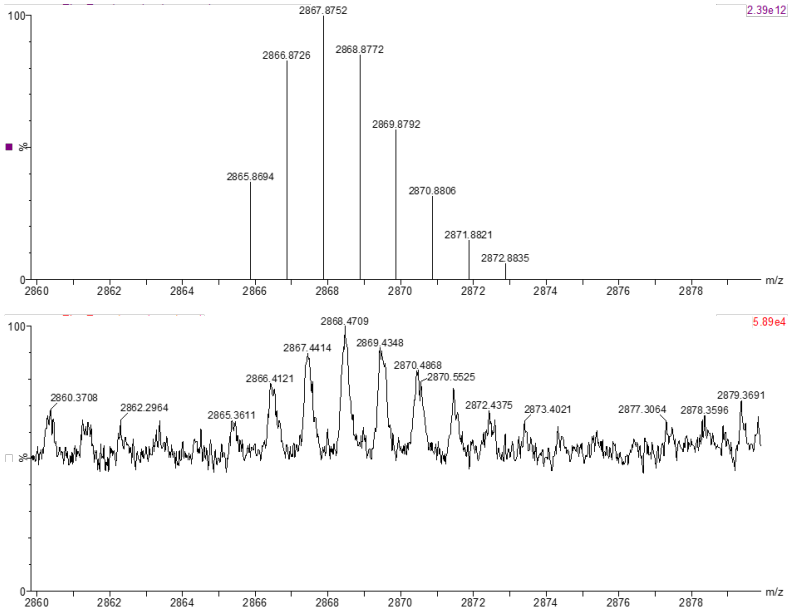

Figure 9.18. Top: The theoretical ESI mass spectrum of the 1:1 stoichiometric host guest complex [**PBPB**] ⊃ [**C$_{70}$**]. Bottom: Experimental ESI mass spectrum of the 1:1 stoichiometric host guest complex [**PBPB**] ⊃ [**C$_{70}$**].

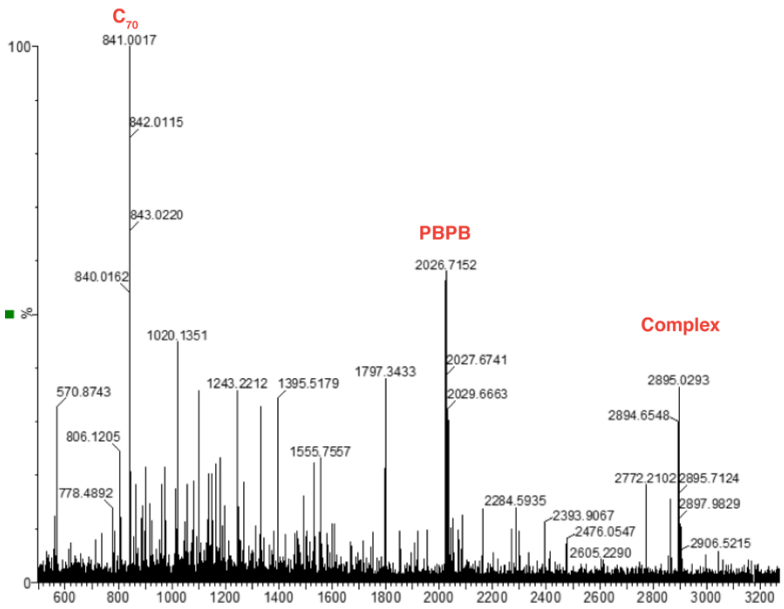

Figure 9.19. The ESI MS/MS spectrum of [**PBPB**] ⊃ [**C70**] as the complex is broken into its constituent parts (collision energy = 80-100 eV).

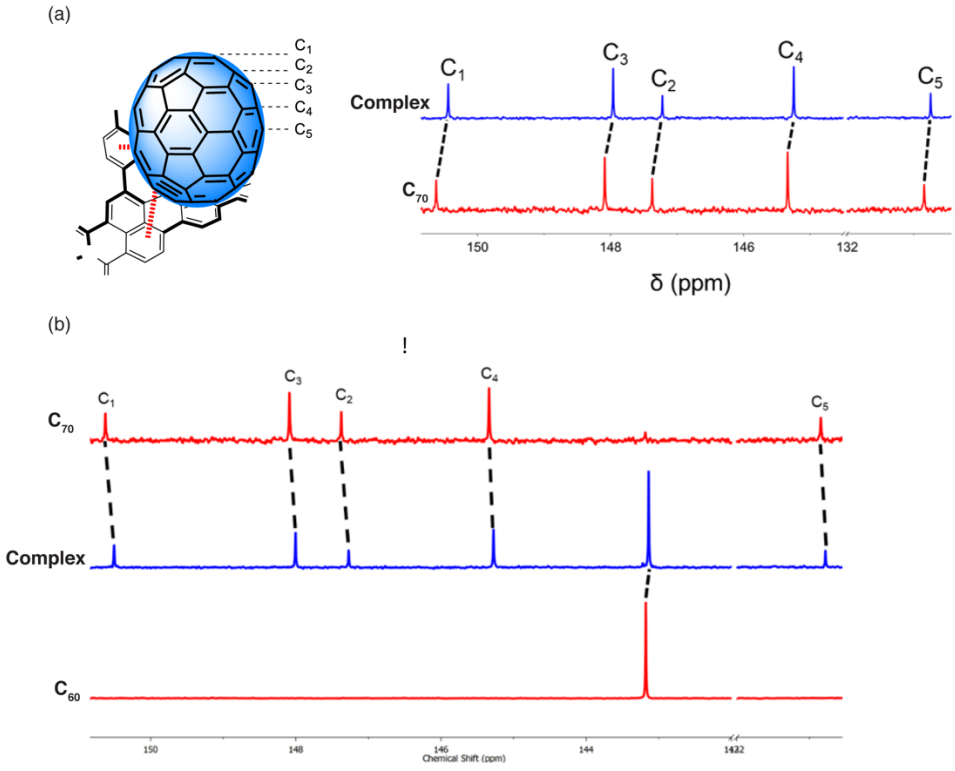

Figure 9.20. (a) Truncated ^{13}C NMR spectra showing **C70** fullerene and a 1:1.5 **PBPB**:**C70** stoichiometric mixture (d8-toluene, 298 K, 125 MHz). Carbon labels for **C70** are also given. (b) Truncated ^{13}C NMR spectra showing **C60** fullerene, **C70** fullerene and a 1:1.5:1.5 **PBPB**:**C60**:**C70** stoichiometric mixture (d_8-toluene, 298 K, 125 MHz).

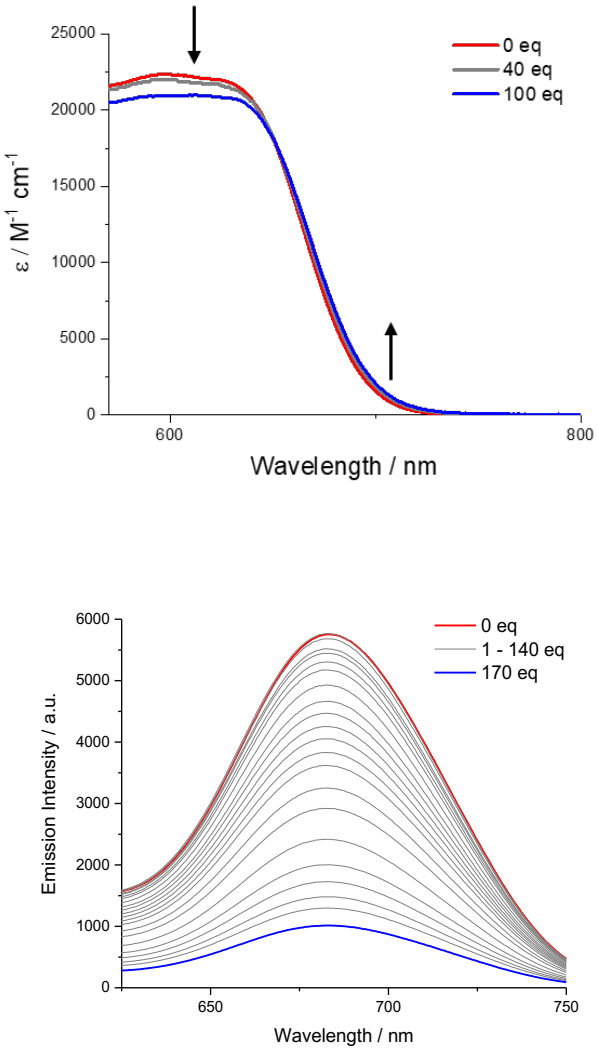

Figure 9.21. (top) Electronic absorption spectrum for **PBPB** upon addition of C_{60} correct for C_{60} absorptions; (bottom) Florescence emission spectrum of **PBPB** with titration of C_{60} (toluene, 4 μM, λ_{ex} = 600 nm).

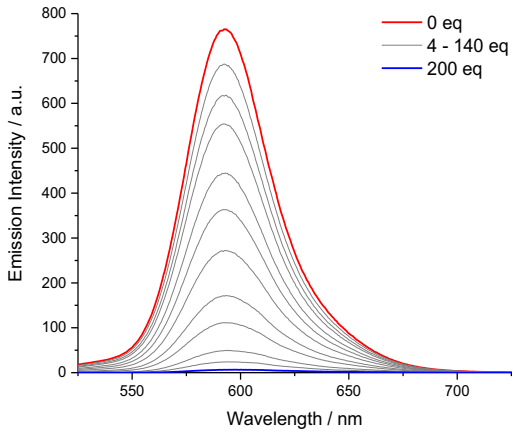

Figure 9.22. Florescence emission spectrum of **3.4** with titration of C_{60} (toluene, 4 μM, λ_{ex} = 600 nm).

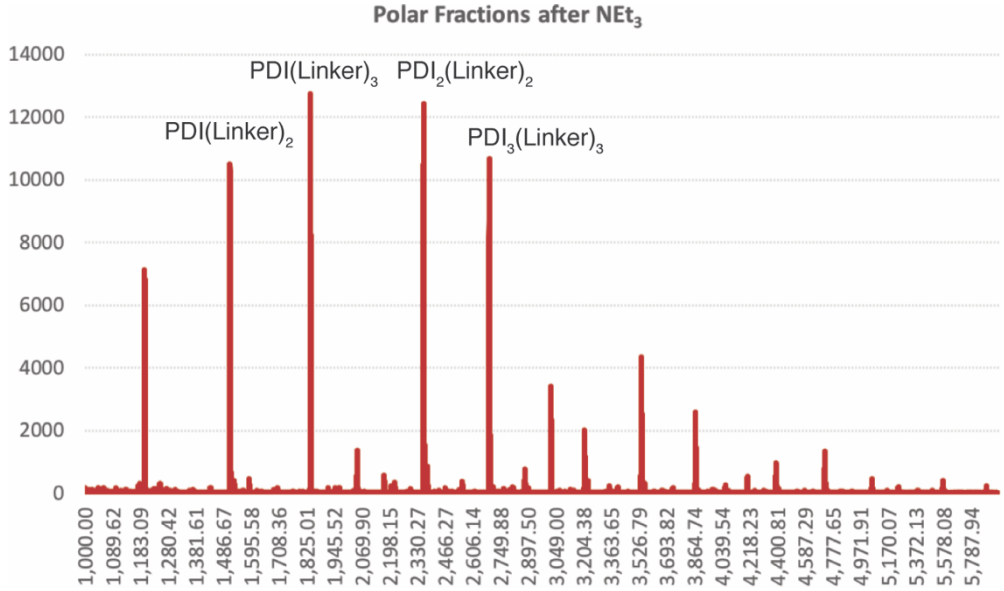

Figure 9.23. MALDI from first attempt to synthesize PDI-phenanthroline macrocycle showing many products formed due to the reversibility of the reaction.

9.8. General Experimental Information

Synthesis. All reactions were performed in oven-dried or flame-dried round bottom flasks, unless otherwise noted. The flasks were fitted with rubber septa and reactions were conducted under a positive pressure of nitrogen or argon, unless otherwise noted. Anhydrous and anaerobic solvents were obtained from a Glass Contour solvent system consisting of a Schlenk manifold with

purification columns packed with activated alumina and supported copper catalyst. Reaction monitoring by thin layer chromatography (TLC) was performed on J.T. Baker Baker-flex Silica Gel IB2-F (25 mm x 75 mm) TLC plates. TLC visualization was accomplished by visible observation and irradiation with a UV lamp. Commercial reagents were used without further purification. $Pt(COD)Cl_2$ was purchased from Strem Chemicals, and all other reagents were purchased from Sigma-Aldrich. Compounds **3.4** (Chapter 3), *trans*-**DBDB** (Chapter 8) and **PBPB** (Chapter 2) have been characterized elsewhere in this thesis.

Purification. Automated flash chromatography was performed using a Teledyne Isco Combiflash Rf200 and Redisep Rf Silica columns. Preparative HPLC was performed on a Waters Prep150 instrument equipped with a UV-vis detector (335 nm), an automated fraction collector, and a Nacalai Tesque COSMOSIL Buckyprep column (20 mm I.D. x 250 mm, 5 μm).

Spectrometers. ^{1}H NMR spectra were recorded on a Bruker 400 or 500 MHz spectrometer. ^{13}C NMR spectra were recorded on a Bruker 125 or 100 MHz spectrometer with complete proton decoupling. NMR spectra were recorded at 300 K unless otherwise noted. Chemical shifts are reported in parts per million (ppm) Data are represented as follows: chemical shift, multiplicity (s = singlet, d = doublet, dd= doublet of doublets, t = triplet, m = multiplet), coupling constants in Hz, and integration. HRMS was performed on a Waters XEVO G2XS instrument equipped with a UPC SFC ESI and APCI ionization, and a QToF mass spectrometer. Absorption spectra were obtained on Shimadzu UV 1800 UV-Vis spectrophotometer and emission spectra were recorded in a Fluorolog-3 spectrophotometer.

9.9. NMR Spectra of *aryl*-PBPB

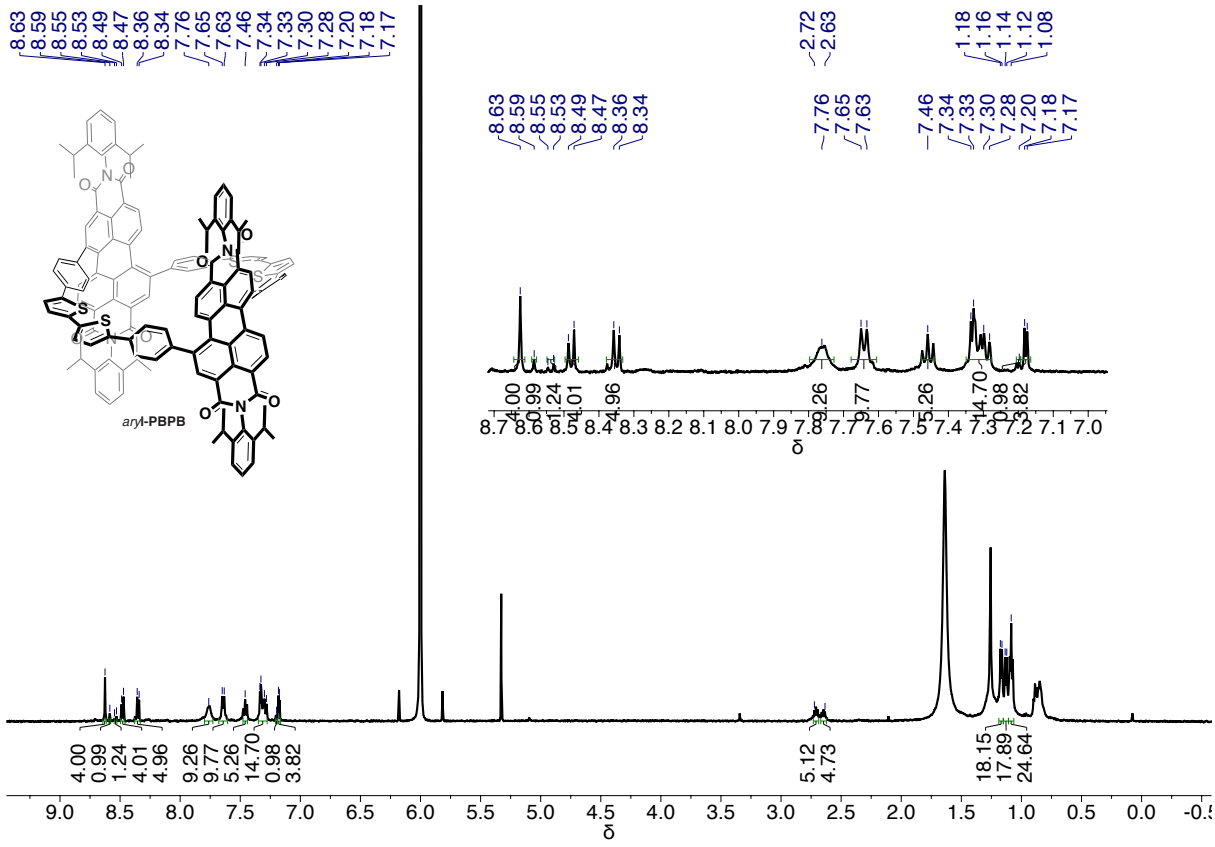

9.10. DFT Output

All quantum chemical calculations were performed using Jaguar, version 8.3, Schrodinger, Inc., New York, NY, 2013. (See A. D. Bochevarov, E. Harder, T. F. Hughes, J. R. Greenwood, D. A. Braden, D. M. Philipp, D. Rinaldo, M. D. Halls, J. Zhang, R. A. Friesner, "Jaguar: A High Performance Quantum Chemistry Software Program with Strengths in Life and Materials Sciences", Int. J. Quantum Chem., 2013, 113(18), 2110-2142). All geometries were optimized using the B3LYP functional and the 6-31G basis set. Below contains the optimized geometry for **PBPB** and **C_{70}**, followed by the 30 lowest roots from TDDFT. The optimized geometry and excited state calculations for free **PBPB** can be found at the original reference and in Chapter 2.[1]

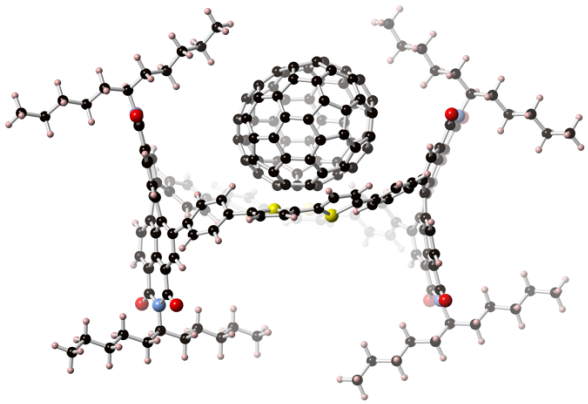

PBPB-C_{70} Complex

Final Heat of Formation: -10188. 507539

C	15.124211	0.422396	-2.251470
C	14.577263	0.974609	-1.073298
C	14.370439	2.371112	-1.091596
C	14.443244	3.129872	-2.301740
C	14.728112	2.514977	-3.543959
C	15.200018	1.179271	-3.467956
C	15.020352	0.257013	-4.566973
C	14.852095	-1.076525	-4.032468
C	14.900536	-0.962568	-2.595554
C	14.080056	-1.752628	-1.807513
C	13.439621	-1.181934	-0.643418
C	13.709785	0.142683	-0.235834
C	12.697579	0.760516	0.533111
C	12.568295	2.198035	0.554225
C	13.384070	2.986760	-0.238507
C	12.854309	4.150958	-0.909825
C	13.496807	4.216744	-2.203301
C	12.781786	4.624411	-3.317164
C	12.979049	3.947878	-4.579761
C	13.963277	2.934309	-4.723330
C	13.719187	1.980063	-5.739484
C	14.282041	0.652466	-5.668938
C	13.364700	-0.268979	-6.290861
C	13.206434	-1.551512	-5.786454
C	13.970604	-1.971726	-4.632405
C	13.107262	-2.786044	-3.808463
C	13.170776	-2.687923	-2.421541
C	11.961372	-2.676991	-1.631711
C	12.142680	-1.780163	-0.502284
C	11.045224	-1.031888	0.001477
C	11.383723	0.188815	0.648093
C	10.444934	1.284086	0.727306

C	11.173502	2.529433	0.692588
C	10.653877	3.638438	0.035939
C	11.508506	4.477444	-0.777152
C	10.755609	4.889773	-1.945203
C	11.382976	4.960889	-3.185884
C	10.715832	4.457182	-4.361925
C	11.700377	3.844752	-5.226933
C	11.366242	2.732643	-6.044508
C	12.442990	1.880653	-6.388425
C	12.219201	0.493750	-6.716123
C	10.950665	-0.054066	-6.638962
C	10.776333	-1.388424	-6.112557
C	11.881921	-2.122733	-5.691250
C	11.823161	-2.902771	-4.473226
C	10.658844	-2.876970	-3.712397
C	10.731621	-2.762048	-2.271619
C	9.625611	-1.948098	-1.823848
C	9.746918	-1.120371	-0.678647
C	8.882140	-0.000535	-0.651250
C	9.222462	1.189305	0.092256
C	8.676711	2.331075	-0.592356
C	9.376431	3.529283	-0.626540
C	9.437790	4.297308	-1.847046
C	8.788891	3.829821	-2.981589
C	9.446163	3.911853	-4.265002
C	9.105526	2.736598	-5.032188
C	10.020254	2.154181	-5.946278
C	9.844182	0.768466	-6.203819
C	8.982996	-0.051015	-5.394807
C	9.562701	-1.379857	-5.328784
C	9.508892	-2.112235	-4.149253
C	8.880879	-1.536236	-2.984130
C	8.234783	-0.276275	-3.049122
C	8.142017	0.407190	-1.811394
C	8.020723	1.837875	-1.769482
C	8.086705	2.563705	-2.940357
C	8.246738	1.926462	-4.227021
C	8.278201	0.501453	-4.297272
H	19.036641	-2.140778	0.189127
H	3.319116	1.227391	3.308180
H	4.419866	5.642004	1.093435
H	19.934693	4.973345	2.259069
H	20.302659	2.381410	2.067109
H	19.855430	0.312036	0.495655
H	13.090141	-3.488072	1.304644
H	16.264253	-5.843290	-0.432078

H	17.828697	-4.054115	0.112839
H	14.642332	-1.828777	1.955501
H	7.236548	-2.235751	0.802217
H	3.606567	3.208840	1.506785
H	3.496373	-1.381441	3.311009
H	8.673431	-4.163633	1.085977
C	10.970599	9.821331	1.464467
C	11.040724	9.999075	2.920062
C	12.286203	9.779706	3.576018
C	13.441283	9.960986	1.408350
C	9.947651	10.421371	3.688240
C	11.150621	10.046951	5.747994
C	13.487644	9.570852	2.827264
C	9.786151	9.564167	0.736234
C	13.463831	9.260839	5.648366
C	12.175762	10.062173	0.750945
C	14.549615	8.876935	4.893074
C	13.259655	11.016428	-2.787466
C	10.002294	10.462016	5.085722
C	14.598238	9.001427	3.478561
N	11.991731	11.080248	-3.391140
C	14.529954	10.606165	-0.687304
C	14.589753	10.265083	0.669852
C	13.311364	10.650029	-1.348440
C	10.780060	10.784539	-2.722902
C	12.292707	9.701512	4.996537
C	11.170146	9.969262	7.230019
C	11.344656	-6.467341	4.533211
C	12.580767	-6.708037	5.167651
C	13.462182	-6.304758	-1.266032
C	17.204916	5.952363	2.120012
C	15.667419	8.223846	2.791215
C	16.079990	6.298327	1.357856
C	17.237807	-1.636837	1.286427
C	14.143895	-3.746284	1.195481
C	12.128212	10.341019	-0.643262
C	10.872697	10.391842	-1.295094
C	9.937538	-7.416545	-1.589612
C	12.340068	9.365961	9.331923
O	14.483861	8.651522	7.698080
C	9.757175	9.885236	-0.642345
N	11.179784	-8.074853	-3.627008
C	9.946294	-8.036924	-2.937867
C	18.161609	2.149012	1.851810
S	16.647220	-0.194814	2.110735
H	15.433479	10.824653	-1.246354

C	13.499612	9.107441	7.128291
O	9.699498	10.863559	-3.293176
C	8.722336	8.682679	1.300808
H	10.098007	7.691097	2.645443
O	14.279541	11.274580	-3.416275
C	12.362528	-7.489687	-3.150290
C	12.473935	-6.157752	2.372029
C	11.888281	11.597886	-4.796090
C	7.121644	6.340934	1.776511
C	8.760437	-6.858904	0.452853
C	6.645950	7.427081	1.009471
C	13.685703	-6.328084	3.059292
C	11.133960	-6.930295	-1.019567
C	10.174715	-6.845311	6.734087
C	9.124496	7.650580	2.179798
C	13.748189	-6.612872	4.425364
C	8.761366	-7.367325	-0.852903
C	17.664861	6.870855	3.078462
C	16.789422	-3.948332	0.408211
C	7.418058	8.564007	0.785166
C	16.921522	8.002184	3.388742
C	9.929999	-6.403822	1.074603
C	8.361611	6.520920	2.407723
C	13.486643	-5.824965	0.060076
C	12.331691	-6.919870	-1.778433
C	18.486782	-1.399353	0.756732
O	8.928583	-8.515875	-3.424080
O	10.200716	10.304648	7.899700
N	12.352680	9.490700	7.838394
O	9.154269	-6.839286	7.412204
C	7.883964	-4.004831	1.808406
C	16.376188	-2.800998	1.117669
C	12.635752	-7.104113	6.597826
C	5.851673	-3.507603	3.618419
N	11.410054	-7.267940	7.264987
C	6.629244	-4.652587	3.742254
O	13.385292	-7.471286	-3.826319
C	14.553862	-4.915927	0.519555
C	18.060237	0.723698	1.630614
C	6.107670	-2.556039	2.615784
C	11.391889	-7.869486	8.636341
S	16.778287	3.221748	1.837420
C	15.319091	7.407160	1.697374
C	19.136777	4.260912	2.079725
O	13.702144	-7.334862	7.155395
C	5.027939	4.895106	1.589191

C	7.745393	-4.871917	2.912382
C	7.075004	-2.890579	1.651881
C	4.579520	3.574725	1.813329
C	5.518774	2.759010	2.403918
C	15.032328	-2.738159	1.509223
C	15.902787	-4.982372	0.124749
C	5.367242	1.331626	2.622296
C	11.266732	-6.226750	3.130481
C	6.337015	5.117587	1.953304
C	4.316961	-0.725969	3.041222
C	18.939797	-0.072305	0.930120
C	5.558828	-1.195744	2.686969
S	7.022329	3.644156	2.653734
C	4.210473	0.687469	3.009605
S	6.613704	0.154989	2.302302
C	17.820043	4.631563	1.968522
C	19.334283	2.862183	1.985001
C	8.896705	-5.713214	3.336855
H	9.142308	10.762097	5.673752
H	8.859798	9.709342	-1.224386
H	15.381389	8.437945	5.427061
H	17.268959	8.665138	4.175392
C	9.986343	-6.075039	2.508787
C	8.994834	-5.990505	4.723858
C	11.145514	-6.457751	0.322663
H	8.746121	5.756499	3.077531
C	10.156946	-6.460837	5.299858
H	15.759751	5.649362	0.547991
C	12.384328	-6.076509	0.902725
H	14.390530	7.573950	1.167179
H	8.164690	-5.778553	5.384291
H	14.614586	-6.297263	2.509843
H	5.658247	7.383819	0.566024
H	7.851236	-7.749920	-1.301575
H	7.011949	9.354606	0.159535
H	18.577880	6.663068	3.629135
H	14.700640	-6.792731	4.911830
H	14.311205	-6.150149	-1.923357
H	7.832114	-6.860080	1.009778
H	6.398526	-5.337724	4.551070
H	5.068665	-3.317543	4.345592
C	11.194924	-8.788495	-4.946681
H	10.811243	11.642252	-4.962615
C	12.447018	13.031481	-4.917594
C	12.488378	10.622803	-5.825480
C	13.448397	10.208205	9.996184

H	11.379225	9.801143	9.609485
C	12.350932	7.891127	9.776844
C	11.413596	-7.814662	-6.121265
C	11.959034	-9.301866	8.624489
C	12.070693	-6.957116	9.678239
H	10.327405	-7.919685	8.872197
H	10.184484	-9.191396	-5.026440
H	9.030424	10.700935	3.186888
H	15.552232	10.263382	1.165073
C	12.191507	-9.964590	-4.935898
H	11.397202	-8.421314	-7.037648
C	10.342874	-6.718726	-6.219260
H	12.413742	-7.374696	-6.058995
H	12.092963	-10.464114	-5.909679
H	13.217000	-9.586586	-4.883734
C	11.938281	-10.980653	-3.813441
H	12.225581	13.361951	-5.941976
C	11.842619	14.031333	-3.922595
H	13.535994	13.018990	-4.822309
H	12.491189	11.154445	-6.787587
H	13.535338	10.413717	-5.584622
C	11.687493	9.322938	-5.987839
H	14.426509	9.755584	9.814753
C	13.460918	11.678233	9.551418
H	13.267400	10.160060	11.078765
H	13.303168	7.428968	9.498369
H	12.307063	7.890300	10.874480
C	11.176991	7.072019	9.222266
H	11.807928	-9.704056	9.636055
C	11.287322	-10.229313	7.602386
H	13.040098	-9.273760	8.456711
H	11.970619	-7.458003	10.651799
H	13.142535	-6.893042	9.467823
C	11.461229	-5.550283	9.759557
C	10.432706	-5.881184	-7.502371
H	9.345562	-7.175531	-6.152088
H	10.425023	-6.047773	-5.352964
C	12.831688	-12.226263	-3.897415
H	12.101522	-10.499958	-2.839242
H	10.883033	-11.289296	-3.828704
C	12.316589	15.474412	-4.145303
H	10.745752	13.989493	-3.980576
H	12.101188	13.733154	-2.897037
C	12.153795	8.468228	-7.175733
H	11.747686	8.723997	-5.068366
H	10.625103	9.570726	-6.117956

C	14.485827	12.541084	10.300465
H	13.679744	11.731057	8.476505
H	12.457621	12.109067	9.677273
C	11.121889	5.632608	9.750476
H	10.233115	7.583075	9.456940
H	11.237714	7.042552	8.125779
C	11.771351	-11.683095	7.682376
H	10.196615	-10.198202	7.740063
H	11.473150	-9.851782	6.587432
C	12.054382	-4.684266	10.879672
H	11.610756	-5.034582	8.800680
H	10.373736	-5.628613	9.892435
C	9.336214	-4.810112	-7.591022
H	11.420469	-5.400468	-7.563075
H	10.364018	-6.543463	-8.377783
C	12.566346	-13.228330	-2.764684
H	12.681707	-12.721854	-4.867743
H	13.888649	-11.921725	-3.875302
C	9.384231	-3.992079	-8.885189
H	8.353004	-5.292836	-7.499321
H	9.420353	-4.133782	-6.729612
C	13.439299	-14.484680	-2.843039
H	12.730812	-12.731365	-1.798375
H	11.506360	-13.518387	-2.779558
H	8.590152	-3.238339	-8.912404
H	10.342140	-3.468333	-8.989620
H	9.262009	-4.633900	-9.765710
H	13.221738	-15.175102	-2.020750
H	13.274241	-15.025820	-3.782074
H	14.505314	-14.232187	-2.791244
C	11.711041	16.465832	-3.141169
H	13.413146	15.513744	-4.075020
H	12.065907	15.791974	-5.168198
C	11.236753	7.266452	-7.440925
H	12.196697	9.093962	-8.079961
H	13.181156	8.117433	-7.001820
C	12.183227	17.908682	-3.348413
H	10.615337	16.424438	-3.208626
H	11.962326	16.143558	-2.120636
C	11.697851	6.393047	-8.611673
H	11.172194	6.655579	-6.531532
H	10.218198	7.629218	-7.635613
H	11.730132	18.587499	-2.617696
H	13.271695	17.989335	-3.245317
H	11.919882	18.273637	-4.348408
H	11.015789	5.551640	-8.775578

H	11.744951	6.968618	-9.544015
H	12.696284	5.978512	-8.429630
C	11.116938	-12.587414	6.627698
H	12.863622	-11.711761	7.557332
H	11.569154	-12.086447	8.685700
C	11.438679	-3.278537	10.933179
H	11.909214	-5.183893	11.849224
H	13.142637	-4.599155	10.744128
C	11.594270	-14.041334	6.690749
H	10.025301	-12.554321	6.749405
H	11.321284	-12.178933	5.627682
C	12.006908	-2.402918	12.054948
H	11.596267	-2.779391	9.966502
H	10.349869	-3.366323	11.053020
H	11.108750	-14.655038	5.924062
H	12.677402	-14.110765	6.535022
H	11.372021	-14.491598	7.665629
H	11.543845	-1.410397	12.061556
H	11.834555	-2.855769	13.038886
H	13.088758	-2.263095	11.942098
C	14.513273	13.995999	9.809535
H	14.267685	12.523595	11.378073
H	15.487268	12.101537	10.187335
C	9.929186	4.843642	9.190678
H	12.055605	5.110603	9.495660
H	11.068923	5.642457	10.848740
C	15.531463	14.872302	10.545747
H	14.734224	14.008117	8.733174
H	13.510667	14.432099	9.915934
C	9.865371	3.396005	9.686595
H	8.997720	5.362585	9.455372
H	9.976453	4.850975	8.092769
H	15.521196	15.900604	10.168705
H	15.319492	14.911252	11.620547
H	16.550001	14.485364	10.425310
H	9.001544	2.868289	9.268344
H	10.764617	2.837706	9.400986
H	9.783987	3.352158	10.778974

TDDFT Output for 30 Lowest Roots

Restricted Singlet Excited State 1:

Excitation energy = 0.0575100274 hartrees 1.56492747 eV 792.27 nm

excitation X coeff.

```
------------   ---------
 746 =>  749    -0.10745
 748 =>  749     0.93795
 748 =>  750    -0.28549

 Transition dipole moment (debye):
   X=     0.5066     Y=    -0.0922     Z=     3.8091  Tot=     3.8437

 Oscillator strength, f=     0.0877

--------------------------------------------------------------------------------
 Restricted Singlet Excited State   2:
---------------------------------------

 Excitation energy =  0.0606414457 hartrees      1.65013770 eV      751.36 nm

  excitation     X coeff.
------------   ---------
 748 =>  749     0.27441
 748 =>  750     0.91951
 748 =>  751    -0.21721
 748 =>  752    -0.11629

 Transition dipole moment (debye):
   X=     3.5602     Y=     0.2888     Z=    -1.4775  Tot=     3.8655

 Oscillator strength, f=     0.0935

--------------------------------------------------------------------------------
 Restricted Singlet Excited State   3:
---------------------------------------

 Excitation energy =  0.0616435373 hartrees      1.67740600 eV      739.14 nm

  excitation     X coeff.
------------   ---------
 748 =>  750    -0.23889
 748 =>  751    -0.89632
 748 =>  752    -0.17238
 748 =>  753    -0.29460

 Transition dipole moment (debye):
   X=    -1.2780     Y=    -0.3623     Z=     0.4317  Tot=     1.3968

 Oscillator strength, f=     0.0124
```

Restricted Singlet Excited State 4:

Excitation energy = 0.0628412198 hartrees 1.70999659 eV 725.06 nm

excitation	X coeff.
748 => 751	-0.11876
748 => 752	0.94676
748 => 753	-0.27216

Transition dipole moment (debye):
X= 0.4435 Y= -0.0132 Z= -0.2155 Tot= 0.4932

Oscillator strength, f= 0.0016

Restricted Singlet Excited State 5:

Excitation energy = 0.0646824193 hartrees 1.76009818 eV 704.42 nm

excitation	X coeff.
747 => 751	0.13968
748 => 751	-0.35602
748 => 752	0.20590
748 => 753	0.89019

Transition dipole moment (debye):
X= 0.1324 Y= 0.0296 Z= 0.1107 Tot= 0.1751

Oscillator strength, f= 0.0002

Restricted Singlet Excited State 6:

Excitation energy = 0.0657336955 hartrees 1.78870486 eV 693.15 nm

excitation	X coeff.
746 => 749	-0.14846
747 => 749	0.97767

Transition dipole moment (debye):
X= -1.2422 Y= -5.0308 Z= -1.2131 Tot= 5.3220

Oscillator strength, f= 0.1921

Restricted Singlet Excited State 7:

Excitation energy = 0.0679481166 hartrees 1.84896233 eV 670.56 nm

excitation	X coeff.
746 => 750	0.18304
747 => 750	-0.96613

Transition dipole moment (debye):
X= 0.0409 Y= -2.4380 Z= 1.1339 Tot= 2.6891

Oscillator strength, f= 0.0507

Restricted Singlet Excited State 8:

Excitation energy = 0.0694372836 hartrees 1.88948462 eV 656.18 nm

excitation	X coeff.
747 => 751	0.94322
747 => 753	0.22882
748 => 753	-0.14952

Transition dipole moment (debye):
X= 0.0879 Y= 0.3072 Z= -0.1368 Tot= 0.3476

Oscillator strength, f= 0.0009

Restricted Singlet Excited State 9:

Excitation energy = 0.0703871399 hartrees 1.91533153 eV 647.32 nm

excitation	X coeff.

747 => 752 0.95926
747 => 753 -0.23151

Transition dipole moment (debye):
X= -0.0904 Y= 0.4241 Z= -0.2290 Tot= 0.4904

Oscillator strength, f= 0.0017

Restricted Singlet Excited State 10:

Excitation energy = 0.0713236376 hartrees 1.94081493 eV 638.83 nm

excitation	X coeff.
746 => 749	-0.97084
747 => 749	-0.13613
748 => 749	-0.13229

Transition dipole moment (debye):
X= 2.0902 Y= -1.6402 Z= 1.6768 Tot= 3.1418

Oscillator strength, f= 0.0727

Restricted Singlet Excited State 11:

Excitation energy = 0.0723772617 hartrees 1.96948550 eV 629.53 nm

excitation	X coeff.
746 => 750	-0.12712
746 => 751	0.13484
747 => 751	0.25563
747 => 752	-0.20334
747 => 753	-0.90820

Transition dipole moment (debye):
X= -0.3088 Y= 0.3810 Z= 0.2518 Tot= 0.5513

Oscillator strength, f= 0.0023

Restricted Singlet Excited State 12:

Excitation energy = 0.0734500072 hartrees 1.99867639 eV 620.33 nm

excitation	X coeff.
746 => 750	-0.88972
746 => 751	0.27220
746 => 752	0.20410
747 => 750	-0.17378
747 => 753	0.18026

Transition dipole moment (debye):
X= -0.5897 Y= 0.5790 Z= 4.3633 Tot= 4.4409

Oscillator strength, f= 0.1495

Restricted Singlet Excited State 13:

Excitation energy = 0.0740039569 hartrees 2.01375013 eV 615.69 nm

excitation	X coeff.
745 => 751	0.16039
746 => 750	-0.29822
746 => 751	-0.88889
746 => 753	-0.22828
747 => 753	-0.12065

Transition dipole moment (debye):
X= -0.0768 Y= 0.3021 Z= 1.8618 Tot= 1.8877

Oscillator strength, f= 0.0272

Restricted Singlet Excited State 14:

Excitation energy = 0.0750234086 hartrees 2.04149082 eV 607.32 nm

excitation	X coeff.
745 => 752	0.21671
746 => 750	-0.20187

746 => 752 -0.91516
746 => 753 0.16932

Transition dipole moment (debye):
X= -0.2348 Y= 0.3632 Z= 1.3373 Tot= 1.4054

Oscillator strength, f= 0.0153

Restricted Singlet Excited State 15:

Excitation energy = 0.0768266753 hartrees 2.09056020 eV 593.07 nm

excitation	X coeff.
742 => 752	-0.16519
743 => 751	-0.14085
744 => 751	0.14147
744 => 752	-0.15353
745 => 751	0.29753
745 => 752	-0.14769
745 => 753	-0.24748
746 => 751	-0.15729
746 => 752	0.11588
746 => 753	0.81316

Transition dipole moment (debye):
X= -0.1549 Y= 0.3611 Z= -0.1351 Tot= 0.4155

Oscillator strength, f= 0.0014

Restricted Singlet Excited State 16:

Excitation energy = 0.0772261905 hartrees 2.10143156 eV 590.00 nm

excitation	X coeff.
742 => 751	-0.14141
742 => 752	-0.17917
742 => 753	-0.11253
743 => 752	-0.31821
744 => 751	0.49924
745 => 750	-0.19415

745 => 752 0.66353
746 => 752 0.25150

Transition dipole moment (debye):
X= -0.0023 Y= 0.0917 Z= -0.1720 Tot= 0.1949

Oscillator strength, f= 0.0003

Restricted Singlet Excited State 17:

Excitation energy = 0.0772767679 hartrees 2.10280784 eV 589.61 nm

excitation	X coeff.
742 => 751	0.23048
742 => 752	-0.24916
743 => 751	0.34079
744 => 751	0.14057
744 => 752	0.24876
744 => 753	-0.25801
745 => 751	-0.67466
745 => 753	-0.16484
746 => 751	-0.23128
746 => 753	0.19406

Transition dipole moment (debye):
X= -0.2082 Y= -0.1127 Z= 0.1785 Tot= 0.2965

Oscillator strength, f= 0.0007

Restricted Singlet Excited State 18:

Excitation energy = 0.0780985018 hartrees 2.12516836 eV 583.41 nm

excitation	X coeff.
742 => 752	-0.39524
743 => 752	0.16936
743 => 753	0.23874
744 => 751	0.34820
744 => 752	-0.14034
745 => 751	0.17150

745 => 752 -0.40047
745 => 753 -0.42630
746 => 751 0.13783
746 => 752 -0.11651
746 => 753 -0.42926

Transition dipole moment (debye):
X= 0.2032 Y= 0.0128 Z= 0.0713 Tot= 0.2157

Oscillator strength, f= 0.0004

Restricted Singlet Excited State 19:

Excitation energy = 0.0783937783 hartrees 2.13320324 eV 581.21 nm

excitation	X coeff.
742 => 751	0.60323
743 => 751	-0.12333
743 => 752	0.11951
744 => 752	0.63117
744 => 753	0.28381
745 => 751	0.27678

Transition dipole moment (debye):
X= 0.0813 Y= 0.1870 Z= -0.1903 Tot= 0.2790

Oscillator strength, f= 0.0006

Restricted Singlet Excited State 20:

Excitation energy = 0.0793435582 hartrees 2.15904807 eV 574.25 nm

excitation	X coeff.
742 => 752	0.11713
742 => 753	0.18600
743 => 749	0.14588
743 => 750	-0.26871
744 => 751	0.43017
745 => 749	-0.43796
745 => 750	0.63991

745 => 753 0.14400

Transition dipole moment (debye):
X= 0.4430 Y= -0.6923 Z= 0.6589 Tot= 1.0534

Oscillator strength, f= 0.0091

Restricted Singlet Excited State 21:

Excitation energy = 0.0799075748 hartrees 2.17439574 eV 570.20 nm

excitation	X coeff.
742 => 752	0.20273
742 => 753	0.47632
743 => 750	0.11941
743 => 751	0.14829
743 => 753	-0.14436
744 => 751	0.49596
744 => 752	-0.10729
745 => 749	0.33952
745 => 750	-0.31074
745 => 751	-0.11686
745 => 752	-0.23560
745 => 753	0.30176

Transition dipole moment (debye):
X= -0.1971 Y= 0.4948 Z= -0.5053 Tot= 0.7342

Oscillator strength, f= 0.0044

Restricted Singlet Excited State 22:

Excitation energy = 0.0801574394 hartrees 2.18119490 eV 568.42 nm

excitation	X coeff.
742 => 751	0.56279
742 => 753	0.11351
743 => 752	-0.16175
743 => 753	0.13222
744 => 750	0.21426

744 => 752 -0.56339
744 => 753 0.38607
745 => 749 -0.12030
745 => 751 -0.16399
745 => 752 0.11932
745 => 753 -0.12428

Transition dipole moment (debye):
X= 0.0678 Y= 0.1004 Z= 0.1501 Tot= 0.1929

Oscillator strength, f= 0.0003

Restricted Singlet Excited State 23:

Excitation energy = 0.0808063308 hartrees 2.19885214 eV 563.86 nm

excitation	X coeff.
742 => 750	-0.21610
742 => 752	0.48626
742 => 753	-0.75290
744 => 751	0.26242
744 => 752	-0.12271
745 => 752	-0.14274

Transition dipole moment (debye):
X= -0.1337 Y= 0.1607 Z= -0.2572 Tot= 0.3315

Oscillator strength, f= 0.0009

Restricted Singlet Excited State 24:

Excitation energy = 0.0814116035 hartrees 2.21532244 eV 559.67 nm

excitation	X coeff.
743 => 749	0.12266
743 => 750	0.16020
745 => 749	-0.78173
745 => 750	-0.54579
745 => 752	-0.15169

Transition dipole moment (debye):
X= 0.0555 Y= -0.2123 Z= 1.5257 Tot= 1.5414

Oscillator strength, f= 0.0200

Restricted Singlet Excited State 25:

Excitation energy = 0.0821100011 hartrees 2.23432681 eV 554.91 nm

excitation	X coeff.
742 => 749	0.45164
743 => 749	-0.15026
744 => 749	-0.74898
744 => 750	0.40004

Transition dipole moment (debye):
X= 0.0510 Y= -0.1237 Z= 0.1713 Tot= 0.2174

Oscillator strength, f= 0.0004

Restricted Singlet Excited State 26:

Excitation energy = 0.0826620185 hartrees 2.24934797 eV 551.20 nm

excitation	X coeff.
742 => 749	-0.88522
744 => 749	-0.36555
744 => 750	0.23863

Transition dipole moment (debye):
X= -0.1895 Y= -0.1198 Z= -0.0019 Tot= 0.2242

Oscillator strength, f= 0.0004

Restricted Singlet Excited State 27:

Excitation energy = 0.0833227139 hartrees 2.26732641 eV 546.83 nm

```
 excitation     X coeff.
------------   ---------
 742 =>  750     0.25769
 743 =>  749    -0.15693
 743 =>  750    -0.13708
 744 =>  749    -0.48738
 744 =>  750    -0.76512
 744 =>  752    -0.18649

 Transition dipole moment (debye):
   X=     0.0013     Y=    -0.1128     Z=     0.4322  Tot=     0.4467

 Oscillator strength, f=     0.0017

-------------------------------------------------------------------------
 Restricted Singlet Excited State  28:
---------------------------------------

 Excitation energy =  0.0838719224 hartrees      2.28227113 eV      543.25 nm

 excitation     X coeff.
------------   ---------
 748 =>  754    -0.98794

 Transition dipole moment (debye):
   X=     0.0298     Y=    -0.0636     Z=    -0.0815  Tot=     0.1076

 Oscillator strength, f=     0.0001

-------------------------------------------------------------------------
 Restricted Singlet Excited State  29:
---------------------------------------

 Excitation energy =  0.0841914008 hartrees      2.29096458 eV      541.19 nm

 excitation     X coeff.
------------   ---------
 742 =>  750     0.13863
 743 =>  749     0.92226
 744 =>  749    -0.22666
 745 =>  749     0.18094

 Transition dipole moment (debye):
   X=    -0.2429     Y=     0.6862     Z=    -4.5972  Tot=     4.6544
 Oscillator strength, f=     0.1882
```

```
-------------------------------------------------------------------------
 Restricted Singlet Excited State  30:
 ------------------------------------

 Excitation energy =  0.0845547724 hartrees      2.30085242 eV      538.86 nm

  excitation     X coeff.
 ------------   ---------
  742 =>  750    -0.90033
  742 =>  753     0.16493
  743 =>  749     0.14839
  744 =>  750    -0.30324

 Transition dipole moment (debye):
   X=    -0.0231     Y=     0.2851     Z=    -1.1256  Tot=     1.1614

 Oscillator strength, f=     0.0118

 -------------------------------------------------------------------------
```

9.11. References

1. Ball, M. *et al.* Chiral Conjugated Corrals. *J. Am. Chem. Soc.* **137**, 9982–9987 (2015).
2. Haddon, R. C. *et al.* C60 thin film transistors. *Appl. Phys. Lett.* **67**, 121–123 (1995).
3. Savoie, B. M. *et al.* Unequal Partnership: Asymmetric Roles of Polymeric Donor and Fullerene Acceptor in Generating Free Charge. *J. Am. Chem. Soc.* **136**, 2876–2884 (2014).
4. Anthony, J. E. *et al*. n-Type Organic Semiconductors in Organic Electronics. *Adv. Mater.* **22**, 3876–3892 (2010).
5. Huang, Q. *et al.* Photoconductive Curved-Nanographene/Fullerene Supramolecular Heterojunctions. *Angew. Chem. Int. Ed.* **58**, 6244 (2019).
6. Li, H. *et al.* High-Mobility Field-Effect Transistors from Large-Area Solution-Grown Aligned C60 Single Crystals. *J. Am. Chem. Soc.* **134**, 2760–2765 (2012).
7. Zhang, Y. *et al*. Development of fullerenes and their derivatives as semiconductors in field-effect transistors: exploring the molecular design. *J. Mater. Chem. C* **6**, 3514–3537 (2018).
8. Zhao, Y., Guo, Y. & Liu, Y. 25th Anniversary Article: Recent Advances in n-Type and Ambipolar Organic Field-Effect Transistors. *Adv. Mater.* **25**, 5372–5391 (2013).
9. Tremblay, N. J. *et al.* Photovoltaic Universal Joints: Ball-and-Socket Interfaces in Molecular Photovoltaic Cells. *ChemPhysChem* **11**, 799–803 (2010).
10. Kang, S. J. *et al.* A Supramolecular Complex in Small-Molecule Solar Cells based on Contorted Aromatic Molecules. *Angew. Chem. Int. Ed.* **51**, 8594–8597 (2012).
11. Shimizu, H. *et al.* A Saturn-Like Complex Composed of Macrocyclic Oligothiophene and C60 Fullerene: Structure, Stability, and Photophysical Properties in Solution and the Solid

State. *Chem. Eur. J.* **24**, 3793–3801 (2018).

12. Toyota, S. *et al*. Exploration of Nano-Saturns: A Spectacular Sphere–Ring Supramolecular System. *Chem. Eur. J.* **25**, 6878–6890 (2019).
13. Lu, X. *et al.* Bowl-Shaped Carbon Nanobelts Showing Size-Dependent Properties and Selective Encapsulation of C70. *J. Am. Chem. Soc.* **141**, 5934–5941 (2019).
14. Ferrero, S. *et al*. Dual-Tweezer Behavior of an Octapodal Pyrene Porphyrin-Based System as a Host for Fullerenes. *J. Org. Chem.* **84**, 6183–6190 (2019).
15. Selmani, S. & Schipper, D. J. π-Concave Hosts for Curved Carbon Nanomaterials. *Chem. Eur. J.* **25**, 6673–6692 (2019).
16. Xu, Y. *et al.* Concave–Convex π–π Template Approach Enables the Synthesis of [10]Cycloparaphenylene–Fullerene [2]Rotaxanes. *J. Am. Chem. Soc.* **140**, 13413–13420 (2018).
17. Würthner, F. *et al.* Perylene Bisimide Dye Assemblies as Archetype Functional Supramolecular Materials. *Chem. Rev.* **116**, 962–1052 (2016).
18. Liu, Z. *et al*. Surveying macrocyclic chemistry: from flexible crown ethers to rigid cyclophanes. *Chem. Soc. Rev.* **46**, 2459–2478 (2017).
19. Shi, Y. *et al.* Selective Extraction of C70 by a Tetragonal Prismatic Porphyrin Cage. *J. Am. Chem. Soc.* **140**, 13835–13842 (2018).
20. Jiao, T. *et al.* Guest recognition enhanced by lateral interactions. *Chem. Sci.* **10**, 5114–5123 (2019).
21. Samanta, J. *et al*. Cofacial Organic Click Cage to Intercalate Polycyclic Aromatic Hydrocarbons. *Org. Lett.* **18**, 3394–3397 (2016).
22. Wu, Y. L. *et al.* Electron Delocalization in a Rigid Cofacial Naphthalene-1,8:4,5-bis(dicarboximide) Dimer. *Angew. Chem. Int. Ed.* **53**, 9476–9481 (2014).
23. Haino, T. *et al*. Fullerenes Enclosed in Bridged Calix[5]arenes. *Angew. Chem. Int. Ed.* **37**, 997–998 (1998).
24. Spenst, P. *et al*. A Perylene Bisimide Cyclophane as a "Turn-On" and "Turn-Off" Fluorescence Probe. *Angew. Chem. Int. Ed.* **54**, 10165–10168 (2015).
25. Spenst, P. *et al*. Perylene Bisimide Cyclophanes with High Binding Affinity for Large Planar Polycyclic Aromatic Hydrocarbons: Host-Guest Complexation versus Self-Encapsulation of Side Arms. *Chem. Eur. J.* **23**, 1667–1675 (2017).
26. Song, J. *et al*. A Porphyrin Nanobarrel That Encapsulates C60. *J. Am. Chem. Soc.* **132**, 16356–16357 (2010).
27. Xia, J. *et al*. Gram-scale synthesis and crystal structures of [8]- and [10]CPP, and the solid-state structure of C60@[10]CPP. *Chem. Sci.* **3**, 3018–3021 (2012).
28. Iwamoto, T. *et al*. Size-Selective Encapsulation of C60 by [10]Cycloparaphenylene: Formation of the Shortest Fullerene-Peapod. *Angew. Chem. Int. Ed.* **50**, 8342–8344 (2011).
29. Ball, M. *et al.* Contorted Polycyclic Aromatics. *Acc. Chem. Res.* **48**, 267–276 (2015).

30. Shimizu, H. *et al.* Synthesis, Structures, and Photophysical Properties of π-Expanded Oligothiophene 8-mers and Their Saturn-Like C60 Complexes. *J. Am. Chem. Soc.* **137**, 3877–3885 (2015).

31. Ball, M. *et al.* Macrocyclization in the Design of Organic n-Type Electronic Materials. *J. Am. Chem. Soc.* **138**, 12861–12867 (2016).

32. Bindfit. Available at: http://supramolecular.org.

33. Diao, G. *et al*. The electrochemical reduction of fullerenes, C60 and C70. *Talanta* **43**, 1633–1637 (1996).

34. Kishi, N. *et al*. Selective host-guest interactions of a transformable coordination capsule/tube with fullerenes. *Angew. Chem. Int. Ed.* **53**, 3604—3607 (2014).

35. Tashiro, K. & Aida, T. Metalloporphyrin hosts for supramolecular chemistry of fullerenes. *Chem. Soc. Rev.* **36**, 189–197 (2007).

36. Ke, X.-S. *et al*. Flattened Calixarene-like Cyclic BODIPY Array: A New Photosynthetic Antenna Model. *J. Am. Chem. Soc.* **139**, 13950–13956 (2017).

37. Moreira, L. *et al.* Unveiling the nature of supramolecular crown ether–C60 interactions. *Chem. Sci.* **6**, 4426–4432 (2015).

38. Hua, J. *et al*. Novel soluble and thermally-stable fullerene dyad containing perylene. *J. Mater. Chem.* **14**, 1849–1853 (2004).

39. Baffreau, J. *et al*. Fullerene C60–Perylene-3,4:9,10-bis(dicarboximide) Light-Harvesting Dyads: Spacer-Length and Bay-Substituent Effects on Intramolecular Singlet and Triplet Energy Transfer. *Chem. Eur. J.* **14**, 4974–4992 (2008).

40. Hitosugi, S. *et al.* Asymmetric Autocatalysis Initiated by Finite Single-Wall Carbon Nanotube Molecules with Helical Chirality. *Org. Lett.* **16**, 645–647 (2014).

41. Fan, Y.-Y. *et al.* An isolable catenane consisting of two Möbius conjugated nanohoops. *Nat. Commun.* **9**, 3037 (2018).

42. Dietrich-Buchecker, C. *et al.* Quantitative Formation of [2]Catenanes Using Copper(I) and Palladium(II) as Templating and Assembling Centers: The Entwining Route and the Threading Approach. *J. Am. Chem. Soc.* **125**, 5717–5725 (2003).

43. Darzi, E. R. *et al*. An Operationally Simple and Mild Oxidative Homocoupling of Aryl Boronic Esters To Access Conformationally Constrained Macrocycles. *J. Am. Chem. Soc.* **139**, 3106–3114 (2017).

44. Kayahara, E. *et al.* Gram-Scale Syntheses and Conductivities of {[}10]Cycloparaphenylene and Its Tetraalkoxy Derivatives. *J. Am. Chem. Soc.* **139**, 18480–18483 (2017).

45. Shekhar, S. *et al*. Distinct electronic effects on reductive eliminations of symmetrical and unsymmetrical bis-aryl platinum complexes. *J. Am. Chem. Soc.* **126**, 13016–13027 (2004).